Institut für Physikalische und Theoretische Chemie

Jan Haubrich

Adsorption and Selective Hydrogenation of α,β-unsaturated Aldehydes on Pt(111) and Pt-Sn Model Catalysts

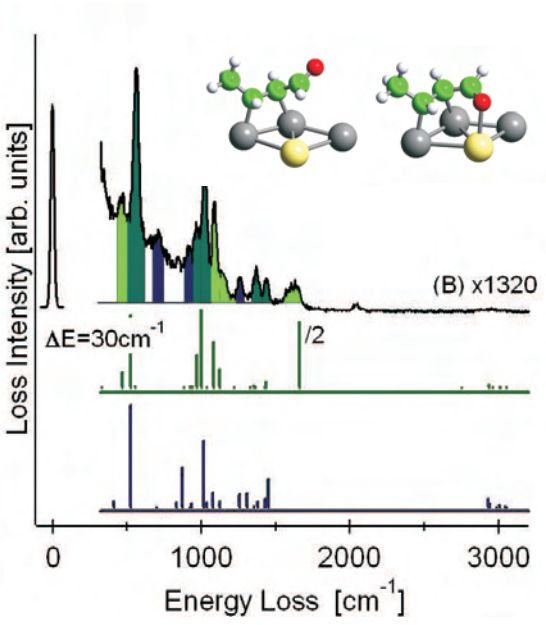

Universität Bonn 2006

Adsorption and Selective Hydrogenation of α,β-unsaturated Aldehydes on Pt(111) and Pt-Sn Model Catalysts

Dissertation

zur Erlangung des Doktorgrades (Dr. rer. nat.)

der Mathematisch-Naturwissenschaftlichen Fakultät

der Rheinischen Friedrich-Wilhelms-Universität Bonn

vorgelegt von

Jan Haubrich

aus Aachen

Bonn 2006

1. Referent: Prof. Dr. K. Wandelt
2. Referent: Prof. Dr. T. Bredow

Tag der Promotion: 04.05.2007
Erscheinungsjahr der Dissertation: 2007

Everything should be made as simple as possible, but not simpler.
Albert Einstein.

Contents

Chapter 1

Combining Vibrational Studies with Theoretical Calculations in Surface Science

Studies of complex interacting systems such as the adsorption of α,β-unsaturated aldehydes on model catalyst surfaces are a present day challenge. Although numerous studies have been published on the catalytical properties of systems like crotonaldehyde and prenal on Pt(111) single crystals or ordered Pt-Sn surface alloys in recent years, these systems still remain under debate. Gaining insight into the molecule-surface bonding is a prerequisite to understand the different hydrogenation activities and selectivities on various catalysts. In addition to the already complex adsorption behavior on monometallic surfaces, alloying effects encountered on bimetallic catalysts lead to new modifications of the molecule-substrate interactions and can change the properties of the catalysts dramatically.

The adsorption and the selective hydrogenation of crotonaldehyde and prenal on a Pt(111) single crystal surface and two ultra-thin Sn-Pt(111) surface alloys are studied in this work with two complementary approaches: The High Resolution Electron Energy Loss Spectroscopy (HREELS) and Density Functional Theory (DFT) calculations. On the one hand, HREELS has proven to be a powerful tool to characterize molecule-surface interactions and surface processes experimentally. On the other hand, using DFT it is possible to study adsorption energies, adsorption structures and vibrational spectra from a theoretical point. The properties and stability of various possible adsorption structures can be explored as a function of coverage. Also experimentally short-lived intermediates become accessible. Combining both powerful approaches, it is possible to gain new insights into molecule-surface interactions, modifications by alloying effects and the surface processes.

First, a brief overview on the importance of surface studies in the field of catalysis is presented in Chap. 2. With a focus on the adsorption, interaction and reactivity of the molecules prenal and crotonaldehyde on various catalysts and single crystal surfaces, a review of previous results of both high pressure and also vacuum studies is given in Chap. 2.2. After a general introduction to the experimental techniques employed throughout this thesis (Chap. 3), the basics of the Density Functional Theory (DFT) will be discussed in Chap. 4. Additionally, details on the computation of vibrational normal modes are given in Chap. 4.6. The characterization and preparation of the Pt and Pt-Sn model catalysts used in this work is described in Chap. 5.

New TPD (Temperature Programmed Desorption) Spectroscopy measurements concerning crotonaldehyde (Chap. 6) on Pt(111) show the desorption of intact molecules at low temperatures. Between 200 K and 300 K highly complex HREELS spectra are measured. Since crotonaldehyde exists in the gas phase in four rota-isomers, the DFT calculations of potential adsorption modes on the pure Pt surface result in a large set of 19 stable structures. Comparison of the computed HREELS spectra to the experimental data suggests a mixture of various adsorption modes coexisting on the surface. Several adsorption modes of η^2, η^3 and η^4 hapticity (see Chapts. 6 and 7) have to be taken into account in order to interpret these spectra successfully. The decomposition pathway of crotonaldehyde observed with HREELS and TPD leads to many vibrational loss signals, which are correlated with five specific surface intermediates. On the Pt-Sn surface alloys much larger sets of conceiveable adsorption structures have to be treated in the DFT calculations, but most of them turn out to be un- or weakly stable. Due to the still relatively high adsorption energies obtained by DFT for the remaining structures on both Pt-Sn alloys, crotonaldehyde is still chemisorbed here. On the $Pt_2Sn(111)$, the reversibly chemisorbed species at low temperatures are mainly interpreted as η^2 species. Desorption of intact crotonaldehyde initiates a phase change and enables the population of η^2 and η^3 configurations at higher temperatures. On $Pt_3Sn(111)$, crotonaldehyde behaves very similar compared to Pt_2Sn and is also bound in a variety of flat adsorption modes.

The studies of prenal (Chap. 7) adsorbed on Pt(111) show several different desorption states from the surface. While desorption of intact prenal is observed below 200 K, also strongly adsorbed species are found on the surface, which start to decompose at higher temperatures. The HREELS spectra obtained at low temperatures are interpreted as a combination of flat η^4 and η^3 adsorption modes as well as lower coordinated η^2 species. As for crotonaldehyde, several fragments stemming from the decomposition have been identified by the combination of HREELS and DFT. This allows to propose a decomposition pathway for prenal on Pt(111). On the $Pt_3Sn/Pt(111)$ surface alloy, experiments and DFT total energy calculations clearly lead to the conclusion that a change in the coordination type compared to Pt(111) occurs. Here prenal is chemisorbed in two vertical η^1 top-adsorption geometries, bonded via the aldehydic oxygen to the surface Sn. In contrast, on the $Pt_2Sn/Pt(111)$ surface alloy prenal is found to be only physisorbed. Both, theory and experiment have difficulties to reach a doubtless conclusion when considered on their own. Yet the combination of the results from both approaches allows to conclude that prenal is physisorbed in this case.

Generally the DFT analysis of the experimental HREELS data provides not only the identification of certain adsorption structures and the characterization of their vibrational properties, but furthermore gives deeper insights in the specific interactions to the surfaces. By an analysis of the energetic contributions to the adsorption energy of the various possible configurations (see Sec. 6.2.2), the interaction strength of the surface species with the substrate can be estimated and their vibrational properties understood in more detail.
Finally the conclusions drawn from the combined approach of experiments and theoretical calculations presented in this thesis are summarized in Chap. 8.

Chapter 2

The Importance of Studies on Catalysis

The field of heterogeneous catalyis has been of great importance in both industrial applications and science for decades now [1, 2, 3, 4, 5].

Catalytic processes and catalysts represent the heart of chemical and oil processing industry. Presently about 70% of all chemical processes used in industry are catalytic and this number is even significantly higher for newly introduced processes. The yearly turnover of the world catalyst market amounted to already US$ 10 billion in 1994. The many bulk production processes like ammonia synthesis (*Haber-Bosch* using iron as primary catalyst, with potassium hydroxide as a promoter), synthesis of nitric acid (gauze of 90% platinum and 10% rhodium), sulphuric acid (V_2O_5 on a ceramic base) or acetic acid (rhodium or iridium) or hydocarbon cracking in fuel production (zeolithes) employing heterogeneous catalysis possess a giant impact factor on economy. In the light of increasing global competition during the recent decade, the optimization of production processes gained a lot of attention and forced the catalysts development to become a highly sophisticated field in science. Developing efficient catalysts and improving those further requires a deep understanding of the underlying microscopical processes.

Numerous studies have been dedicated to homogeneous and heterogeneous catalytical processes employing a variety of techniques in order to elucidate the underlying chemical and physical basics. Recently, the importance of catalysis in science has again been underlined by awarding the 2005 *Nobel Price* in chemistry to Yves Chauvin, Robert H. Grubbs and Richard R. Schrock "for the development of the metathesis method in organic synthesis". The *Chauvin* mechanism of this reaction uses homogeneous, low valency transition metal catalysts based, for instance, on Mo, W (Schrock), Ru (Grubbs) or Ta. It is basically an exchange reaction between two olefines forming two new olefins and proceeds via carbene (alkylidene) complexes and metallacyclobutane intermediates.

Common approaches to study heterogeneous catalysis include experiments under "real" as well as under (ultra-high) vacuum (UHV) conditions. While the "real-life" experiments are performed at elevated reactant pressures ranging from a few mbar to several hundred bar and temperatures up to 1000 K, the pressure range of the UHV investigations is strongly limited. Nonetheless, the various potent experimental techniques available in the UHV approach are of great value not only to investigate the initial stages of any heterogeneous catalytical process itself: the interaction of the reactants and products with the catalyst itself. The characterization of the adsorption states of the considered molecules on the catalysts is a prerequisite for understanding the reaction mechanism, from which finally the catalyst selectivity and its activity originate. Sometimes UHV experiments even permit to identify reaction intermediates, which otherwise

are hardly accessible, and thus can ultimately prove elementary reaction mechanisms.
In the following sections the general approach to characterize catalytical reactions using UHV experiments on model catalysts with its advantages and also its shortcomings will be discussed briefly. Thereafter the focus will be shifted to the selective hydrogenation of α,β-unsaturated aldehydes and a chronological overview of the studies in this field of catalysis will be given.

2.1 Bridging Gaps: The Pressure Gap and the Materials Gap

"Real-life" catalysts are compositionally and structurally heterogeneous materials that consist of a catalytically active metal or alloy on an oxidic support such as Al_2O_3, SiO_2, TiO_2, zeolithes or on active charcoal ([1, 4, 5, 6, 7] and references therein). Sometimes their complexity is even enhanced by addition of promoters, which can increase both the selectivity and activity of the catalyst and also can lead to an improvement of the stability against catalyst coking. The typically chosen promotors can be separated into three distinctive groups: electropositive alkali metal compounds, other transition metals and non-transition metal additives. Many other factors like the metal-support interactions, the oxidation state of the metal phase(s), the size of the active metal particles or the catalyst sintering are known to strongly affect the catalyst chemistry. On the one hand these systems are important to determine the kinetic and thermodynamic parameters of the catalytic reactions and the product yields. Yet on the other hand, their complexity is the origin of many difficulties encountered in investigations of the elementary reaction steps and of the interactions of the reactant and product molecules with the catalyst. In addition, unlike in high pressure experiments, which can employ both disperse metals and single crystal metal samples, physical limitations of many typical UHV techniques require the use of conducting and well-ordered samples. Therefore, model systems have to be found, which mimick the chemistry and properties of the "real" catalyst under vacuum conditions closely and at the same time allow to overcome several complexity factors.
Mostly single crystal samples of the interesting metals are employed as model catalyst. Like their industrial archetype, also model catalysts can be altered by vapor deposition of promotors from Knudsen-cell sources or by molecular beam epitaxy. Sometimes, especially when other metals are used as promotors, they are found to form ordered alloys with the substrate [1, 6, 7, 8, 9, 10, 11, 12, 13, 14, 15]. During the recent decade it has even been shown that also clusters on oxidic supports can be employed as model catalysts. They can be grown easily by vapor deposition of metals on an ultrathin oxide layer, which itself can serve as a template for the preordering of the seeding clusters and usually is prepared on a clean metallic substrate [16, 17, 18, 19].
Nonetheless, replacing realistic systems by model catalysts introduces an uncertainty as to the transferability of UHV results to the "real-life" chemistry of the catalytic process. This problem is usually termed the "materials gap". Furthermore mimicking catalytical processes under UHV conditions undeniably leads often to the controversy, whether the results obtained at low pressures on ordered model catalyst surfaces are significant for "real" catalytic systems "beyond" the so-called "pressure gap". The reason for these concerns doubting the transferability of results between vacuum and high pressure experiments originates from several examples, in which investigations showed that the monolayer adsorption of reactants on single crystals lead to no or only to stochiometric reactions that are different from the results observed at high pressures. One famous example for this phenomenon is the *Fischer-Tropsch* synthesis forming hydrocarbons over transition metal catalysts from carbon monoxide and hydrogen. It is also well-known that instead of bond synthesis reactions, on many clean metal surfaces dissociation and decomposition processes are favored under UHV conditions. Yet there are also other examples proving the value of the model catalyst concept. For instance the cyclotrimerisation of acetylene to benzene has been reproduced successfully on Pd(111) by Janssens et al. [20],

while on Pt(111) or Pt-Sn surface alloys such a reaction could not be initiated under similar circumstances [21].
Although today it is generally accepted in surface science that the basics of bonding, structure and reactivity derived from vacuum studies also apply at high pressures, the key step, showing that the important factors, which characterize catalysts at real conditions, are not missed at low pressures, has been achieved only within the past 10 years [5]. This key step was achieved in part by introducing the concept of "generation and isolation of reaction intermediates" at cryogenic temperatures. In such two-dimensional matrix isolation experiments, even highly reactive, short-lived species that have been postulated as reaction intermediates in heterogeneous catalysis, can be trapped and accumulated to relatively high surface coverages until the sample is being heated up to initiate a reaction. The short life time and the resulting low coverages translating in problems for spectroscopical identification heretofore are avoided and elementary reaction steps can be investigated in detail, even in case of reactions, which usually do not occur under low pressure conditions. It has been demonstrated that the high surface precoverages of intermediate fragments accessible in this manner promote bimolecular coupling reactions like for i.e. the formation of carbon-carbon bonds in the coupling of CH fragments forming acetylene on Ni(111) [22].
The entire potential of the matrix isolation approach in surface catalysis has yet to be exploited fully in order to interpret high pressure spectroscopical experiments. Furthermore, the method can also be applied to high pressure experiments. Importantly, this approach has allowed to establish a close connection between high pressure chemistry and the UHV experiments and proven the value of the UHV model catalyst studies.

2.2 The Selective Hydrogenation of α,β-unsaturated Aldehydes

The selective hydrogenation of α,β-unsaturated aldehydes like acrolein, crotonaldehyde (2-butenal) or prenal (3-methyl 2-butenal) to α,β-unsaturated alcohols is an important catalytic process for the industrial production of fine chemicals used mainly in the fields of pharmacology, perfumes and flavors [1, 2, 4]. As shown in Fig. 2.1, both double bonds of prenal can be hydrogenated: The hydrogenation of the C=O bond gives the unsaturated alcohol while the hydrogenation of the C=C double bond leads to a saturated aldehyde. The unsaturated alcohol and the saturated aldehyde can be hydrogenated in a second step to the saturated alcohol. The difficulties in the control of the selectivity in this reaction arise from the thermodynamical preference to hydrogenate the C=C double bond [12, 23]. Therefore the thermodynamically less favorable hydrogenation of the C=O bond has to be performed at low temperatures under kinetic control. Currently, the only method to obtain the unsaturated alcohols in high yield ($> 90\%$) in the laboratory is by reduction using metal hydrides like the derivates of $NaBH_4$ or $LiAlH_4$ [24], but this method is of course too expensive and hardly feasable in industrial scale chemistry. In this respect, the challenging creation of a sophisticated catalyst that is able to produce the unsaturated alcohols with high selectivity and activity bears a great impact to the chemical industry.
Both experimentally and theoretically the investigation of the hydrogenation and adsorption of α,β-unsaturated aldehydes is a highly complex and difficult task. The multifunctionality of the molecules with their two double bonds allows a huge variety of different interactions with a substrate. The variety of coordination geometries ranges from pure $\eta^2 - di\sigma$ and $\eta^2 - \pi$ interactions (the hapticity η^x refers to the number of molecule-surface bonds) of either the C=C or C=O double bonds to low coordinated η^1-top interactions of the aldehydic oxygen with the substrate atoms, to $di\sigma$(C3,O) metallacycles bonded via the terminal atoms and to η^3 and η^4 adsorption structures, which again can consist of combinations of $di\sigma$ and π interactions. The

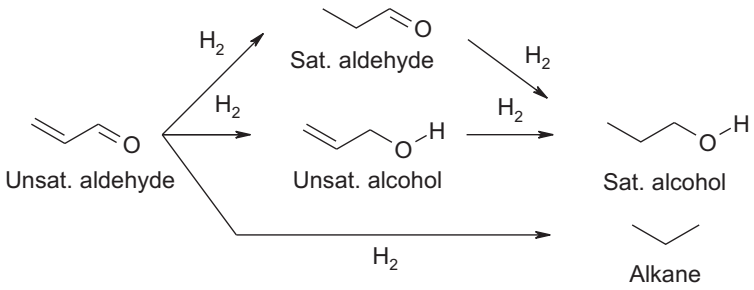

Figure 2.1: Hydrogenation reactions of α, β-unsaturated aldehydes.

sheer number of conceivable binding geometries will even be multiplied when promotors like Fe or Sn can change the adsorption sites, rendering conclusions on the adsorption geometry and interaction mechanisms highly problematic from a purely experimental point of view. Likewise the total energy calculations are discussed in the following result in sets of different adsorption modes, which possess similar adsorption energies and can therefore hardly be identified or excluded by this criterium. Yet also the experimental handling of such molecules turns out to be problematic, since they can undergo aldol condensations resulting in oligomerisation or formation of polymer films when activated sufficiently. This has also been observed during this work, especially when Cu gaskets have been employed in the leak valves used for dosing the crotonaldehyde or prenal into the vacuum chamber. Exchanging these Cu gaskets against Ag improved the situation somewhat.

From the results of reactivity studies obtained on supported catalysts, it is known that Pd, Rh or Ni are hardly selective towards the unsaturated alcohols, but Pt, Ru or Ir on the contrary show an increased selectivity [2, 6, 7, 8, 12, 14, 15, 25, 26, 27, 28, 29, 30, 31, 32, 33]. It has also been shown that the selectivity is greatly influenced by many factors such as the nature of the support, the size of the supported particles, the presence of electropositive species on the surface, the presence of promoters and the reaction conditions. Therefore one aims at a minimum effort. Especially adding promoters and alloying a catalyst with other components is a promising route to tune the productivity of a catalyst to an optimum.

The gas phase hydrogenation of crotonaldehyde and prenal over Pt(111) and $Pt_{80}Fe_{20}(111)$ single crystals was studied by Beccat et al. [25] using mass spectrometry and Auger electron spectroscopy. Their results indicated that the selectivity towards the unsaturated alcohol depends mainly on kinetical parameters, but is also increased by the alloying with Fe. Yet the reason for the increase of selectivity, i.e. the effect of alloying, could not be explained by their results. The predominant product measured in their experiments was the saturated aldehyde. However, these authors found that the selectivity towards the unsaturated alcohol is increased slightly for prenal. This is ascribed to the substitution of the C=C bond with an additional methyl group compared to crotonaldehyde.

Although the selectivity observed in similar hydrogenation experiments over titania supported Pt catalysts could be described by a surface electronic gas model by Makouangou et al. [26], these authors could also not conclude about the properties of the interaction and the active site of the catalyst.

Deeper insights on the structural dependence of the reactivity and the active sites were presented by Birchem et al. [27, 28], who investigated with two studies the selectivity of the hydrogenation of prenal on a well-ordered Pt(111) as well as a stepped Pt(553) surface by low pressure adsorption, thermal desorption and high pressure hydrogenation experiments. The results on the Pt(111) surface show that the selectivity towards the formation of the unsaturated alcohol

is highest at low conversion. Based on kinetic models, the selectivities towards the different products are assigned to different adsorbed surface species, which could not be determined further. Also the influence of the partial pressures of the aldehyde and hydrogen on the reactivity were considered. On Pt(553) these authors found that the structural effects of steps lead to an increase of the reactivity that can be explained by the higher activity of the low-coordination step atoms for hydrogen dissociation. The selectivity on this surface is mainly governed by structural factors: While the step atoms have been identified as the active sites of the production of the saturated aldehyde, the flat terraces have been suggested to lead to the formation of the saturated alcohols. Alloying the Pt(553) surface with Sn induces a change in the selectivity. At low coverages, tin is found to be located near the step edges and a local reconstruction of the surface occurs. The shift of the selectivity to the production of the saturated alcohol measured is ascribed mainly to electronic effects due to partially oxidized tin moieties. At high coverages, tin islands grow on the terraces. The authors suggest that steric and electronic effects of these tin islands cause a higher selectivity towards the unsaturated alcohol.

Further studies of the hydrogenation of acrolein, crotonaldehyde and prenal on SiO_2 and Al_2O_3 supported Pt catalysts by Marinelli et al. [6, 7], confirmed the trend of increasing the selectivity by substitution of the C=C bond with methyl groups, especially when Fe is added as a promotor. Marinelli et al. concluded that increased selectivity towards the unsaturated alcohol is related to a predominant bonding through the C=O group. The selectivity in the hydrogenation of α,β-unsaturated aldehydes is thus governed by the availability of sites on the catalyst, which can activate the aldehydic function, while the C=C bond remains essentially unperturbed. In contrast, these authors found that ensemble size effects are much less important. The effect of substitution is found to be mainly of steric origin, since the additional methyl groups do not cause a change in the activity.

Recently Borgna et al. [14] performed in situ reaction studies on silica-supported Pt-Co bimetallic catalysts with various Pt/Co ratios. The electronic states of Pt and Co characterized by X-ray photoelectron spectroscopy and near-edge X-ray absorption fine structure (NEXAFS) revealed that cobalt is primarily forming octahedrally coordinated Co^{2+} moieties in the reduced catalyst. Upon reduction of the catalyst with 1-2 mbar of hydrogen, Co is reduced completely and forms alloyed Pt-Co particles. The *d*-density of states of Co is increased by alloying, which is ascribed by the authors to electron transfer or rehybridization of the Co orbitals. Experiments on the hydrogenation of crotonaldehyde showed that also the Co particles have a promoting effect and improve the selectivity towards the unsaturated alcohol. This is explained by the formation of $Pt^{\delta-}$-$Co^{\delta+}$ species on the surface, which are considered to be crucial to the adsorption of the aldehyde via the C=O group and favor its activation.

Newer studies on TiO_2 supported Pt catalyst reduced in situ at varying temperatures by Coloma et al. [30] aimed at the determination of the adsorption sites of crotonaldehyde on the catalyst surface. Although these authors reported the displacement of preadsorbed CO from top and bridge sites by crotonaldehyde in their FTIR (Fourier Transform Infrared) experiments, they failed to conclude on the exact adsorption site of crotonaldehyde. Nonetheless, they showed the importance of the metal-support interaction, which on increase due to reduction at higher temperatures led to improved selectivities towards the unsaturated aldehyde.

Also reaction studies performed on catalysts based on transition metals other than Pt have been performed with crotonaldehyde or prenal and present insights on the reaction mechanism and active sites. Noteworthy for instance is a study performed by Reyes et al. [32] on the gas phase hydrogenation of crotonaldehyde over Rh/Ti_2 catalysts that were prepared under varying conditions. Interestingly these authors suggested that crotonaldehyde adsorbed in a η^1-top geometry is being hydrogenated to the unsaturated alcohol. These authors also detected a carboxylate intermediate and CO arising from the reaction process, which poison the catalyst surface.

Lately Iwasa et al. [15] used Pd-based monometallic and alloyed catalysts to investigate the

influence of the crystallite size and alloying effects on the hydrogenation of crotonaldehyde by XRD, SEM and gas phase hydrogenation experiments in a flow reactor. The results of their investigations indicated that Pd/ZnO catalyst show a much higher selectivity towards the unsaturated aldehyde compared to Pd/Al_2O_3 or Pd/SiO_2 catalyst, but still the major product was the saturated aldehyde.

Although many experiments on the hydrogenation process have been performed on supported catalysts, there is still little known on the basic interaction of the aldehydes and the products with the catalyst and the elementary reaction mechanism. As described in the previous section, the drawbacks of using supported catalysts are that these are more difficult to probe with standard surface science techniques and that their structure and composition increase the complexity of the investigation significantly. For this reason, numerous investigations on well-defined model catalyst surfaces in UHV have been performed by other groups.
To investigate catalytical processes or alloying effects with this approach, either ordered bulk alloys such as Pt_3Sn [34] can be used or ultra thin Pt-Sn alloy films can be prepared by physical vapor deposition (PVD) of tin [10, 12, 13, 28, 35, 36, 37, 38, 39, 40, 41, 42] on a monocrystalline Pt sample. At this point, only a brief summary of the studies on the Pt-Sn surface and bulk alloys and their preparation shall be given while a more specific discussion of the model catalyst surfaces employed throughout this work will follow in Chap. 5.3.
Generally, two different ultra-thin surface alloys can be prepared on a Pt(111) substrate by deposition of tin and subsequent heating of the sample. According to Paffett et al., heating low tin precoverages to 1000 K results in the formation of a $Pt_2Sn(111)$ surface alloy with a $(\sqrt{3} \times \sqrt{3})R30°$ structure (surface tin fraction 33%), while a $Pt_3Sn(111)$ surface alloy with a $p(2 \times 2)$ periodicity (surface tin fraction 25%) evolves when larger amounts of tin were deposited previously [35]. Both structures also evolve sequentially upon heating a tin film on Pt(111) with the $Pt_2Sn(111)$ being stable at temperatures around 700 K and transforming into a $Pt_3Sn(111)$ surface alloy around 1000 K (this work, see Chap. 5.3). Low energy alkali ion scattering (LEIS) experiments on the Sn-Pt system by Overbury et al. [38, 43] showed that both surface alloys consist of a single alloy layer with the Sn protruding the Pt by about 22 pm.
Somewhat contradictory results have been obtained by Galeotti et al. [34] in X-ray photoelectron diffraction (XPD) experiments. Using high tin precoverages (4-5 monolayer) these authors found the formation of a $p(2 \times 2)$ bulk alloy like surface formed already around 400 K. Indeed, in a few of the LEED experiments with high tin exposures performed here a weak diffraction pattern corresponding to a $p(2 \times 2)$ structure was visible around 500 K before a transition to a $(\sqrt{3} \times \sqrt{3})R30°$ LEED pattern occurred around 575 K. Latest surface X-ray diffraction (SXRD) results also support these results [44].
The alloying effects, i.e. the influence of the Sn atoms on the adsorption properties of these surface alloys, are widely discussed in the literature. On the one hand, in several studies the influence is considered mainly as a site blocking effect [35], while on the other hand also numerous investigations suggest that the electronic situation changes strongly [12, 39]. Delbecq et al. [45] found in their calculations that by alloying platinum with tin, the overlap of the Pt-*d*-orbitals forming the *d*-band is weakened and the density of states (DOS) at the Fermi edge decreases. This is consistent with the results of STM experiments of Batzill et al. [39] and UPS measurements by Paffett et al. [37]. Observing a shift of the *d*-band centre to lower energies (-1.93 eV for Pt(111), -2.09 eV for Pt_3Sn and -2.12 eV for $Pt_2Sn(111)$) these authors expected a decrease in the binding energies and an electron transfer from the more electropositive Sn to Pt (see also [46]).

In order to develop a deeper understand of the elementary hydrogenation mechanisms of α,β-unsaturated aldehydes, the adsorption of such molecules on the Pt and Pt-Sn model catalyst surfaces was investigated in a number of UHV experiments [12, 13, 47, 48, 49] and several

theoretical works [45, 50, 51, 52, 53, 54, 55].
TPD and RAIRS (Reflection-Absorption Infrared Spectroscopy) measurements by de Jesús et al. indicate flat adsorption geometries for both acrolein and crotonaldehyde on Pt(111) [48]. The measured shifts of the vibrational bands in their experiments suggest that acrolein is adsorbed mainly via the C=O group while crotonaldehyde shows a strong diσ(CC) interaction to the surface, but no clear conclusion towards the observed adsorption geometries could be drawn. After providing thermal activation energy, de Jesús et al. found a decarbonylation reaction of the adsorbed crotonaldehyde forming propylene and CO, which desorb subsequently around 340 K and 440 K. Also the desorption of H_2 was measured by TPD in two steps at 280 K and 440 K arising from the dehydrogenation of unidentified surface species.
Other studies on crotonaldehyde reveal a very complex adsorption behaviour. The high-resolution XPS and DFT investigations of Janin et al. point to an η^3 adsorption geometry of crotonaldehyde on Pt(111) with an interaction through the C=C bond and a coordination of the aldehydic oxygen to Pt [13, 49]. The alloying effect of Sn is observed in a strong decrease of the calculated adsorption energies accompanied by a change of the preferred adsorption structure. Switching to the $Pt_3Sn(111)$ surface alloy, the authors interpret the measured changes in the XPS spectra as a change to a mixture of an η^3 adsorption structure with O-Sn interaction (see Chap 6.1.3) and a vertical form bonded only by an oxygen lone pair (η^1-top-OSn). Finally, on the Sn richer $Pt_2Sn(111)$ surface alloy, the latter adsorption geometry is most abundant.
Recently Jerdev et al. probed the hydrogenation reaction of crotonaldehyde employing XPS, LEED and gas chromatographic analysis, finding that the selectivity on Pt(111), $Pt_3Sn(111)$ and $Pt_2Sn(111)$ at the chosen reaction conditions is similar [12]. Therefore these authors suggest that the selectivity of the hydrogenation is not solely due to the Sn-Pt alloy formation. In contrast, their results showed that the activity of the catalyst is nearly doubled on alloying, but depend hardly on the surface alloy formed (the activity was 10% higher in the case of the tin richer $(\sqrt{3}\times\sqrt{3})R30°$ versus the $p(2\times2)$ surface structure). The primary hydrogenation product desorbing from these model catalyst was the saturated aldehyde. The analysis of the reaction kinetics showed that the hydrogen partial pressure is involved in the rate-limiting elementary steps for the production of all products except the alkane (butan), i.e. the saturated aldehyde as well as the saturated and unsaturated alcohols, and approximate activation energies were given for butane (46.8 kJ/mol) and butanal (35.9 kJ/mol) formation.

In several works Delbecq and Sautet et al. have studied the adsorption of acrolein, crotonaldehyde and prenal on Pt(111) by means of calculations based on cluster models [50] and density functional theory (DFT) with periodic boundaries [45, 51]. The authors argued that at low coverages prenal assumes a flat adsorption mode with molecule-surface interactions by the C=C and C=O bonds (η^3 and η^4 adsorption structures, see Chap. 7.1.3), while at the higher coverage, the prenal molecule might switch to a more vertical geometry. This can be realized by interacting with the substrate via the C=C double bond only ($\eta^2 - di\sigma(CC)$) or even solely by the aldehydic oxygen atom (η^1-top). For low as well as medium coverages crotonaldehyde is expected to be oriented parallel to the surface in certain η^3 and η^4 adsorption geometries. Higher coverages above 1/6 monolayer have not been considered by these authors. Since both aldehydes interact mainly with the C=C bond, the results underline the low selectivity toward the unsaturated alcohol found for Pt(111).
In a later study, Delbecq and Sautet et al. considered the adsorption of acrolein, crotonaldehyde and prenal on the $Pt_2Sn/Pt(111)$ and $Pt_3Sn/Pt(111)$ surface alloys [45]. According to their DFT calculations, the adsorption energy is always lowered by alloying of Pt(111) with Sn, leading to an enhancement of the reactivity. As mentioned above, the decreases in the interaction energies have been interpreted by electronic effects, i.e. shifts of the d-band centre to lower energies. While for crotonaldehyde and acrolein the preferred adsorption structures are the η^3 form with an interaction of the aldehydic oxygen with Sn as well as the $\eta^2 - di\sigma(CC)$ form, prenal is

expected to be adsorbed in the η^1-top configuration on an underlying Sn atom (η^1-top-OSn). Importantly, a significant electron transfer from Sn to Pt is found in their calculations. On the Pt_2Sn/Pt(111) surface alloy, Sn looses 0.42 e^- and Pt gains 0.13 e^-; on Pt_3Sn/Pt(111) the electron loss of Sn is more pronounced (0.53 e^-), while Pt is less polarized (0.10 e^-).
Recent HREELS and periodical DFT studies on the vibrational properties of acrolein on the Pt(111) surface showed a mixture of adsorption types present at low temperatures [53]. As a function of the coverage of acrolein, different adsorption modes could be identified. At high coverage a phase of $\eta^2 - di\sigma(CC)$-(s)-trans and -(s)-cis acrolein is present on the surface. Turning to the low coverage phase, a mixture of η^3 and η^4 adsorption modes is measured in accordance with previous total energy calculations [51]. For all observed adsorption structures a full vibrational analysis has been performed by these authors and an interpretation of the measured loss signals has been proposed.
Hirschl et al. studied the adsorption and induced segregation effects of prenal on the $Pt_{80}Fe_{20}$(111) bulk alloy surface, concluding that prenal assumes flat adsorption geometries with $\eta^2 - di\sigma(CC)$, η^3 and η^4 coordination on this alloy [52]. The interaction of the aldehydic oxygen with the electropositive Fe in the η^3 and η^4 adsorption structures was found to strongly stabilize the bonding to the surface in comparison with Pt(111) and induced significant changes in the segregation profile [52]. Any vertical top adsorption geometry turned out not to be competitive in the framework of their DFT calculations. The main result was, however, that the hydrogenation to the unsaturated acohols is unlikely using such catalysts.
An investigation of the reactivity of acrolein/Pt(111) published lately by Loffreda et al. [55] discussed the effects governing the reactivity of this molecule from the theoretical point of view. Employing the computed activation energies for the various possible monohydrogenation pathways for a kinetical model, these authors were able to reproduce the low selectivity of the hydrogenation towards propenol on this model catalyst. Importantly the desorption step of the product molecules turned out to be crucial for the product yield. Although the unsaturated alcohol seemed to be produced more selectively due to more favorable reaction energetics, its higher adsorption energy led to an accumulation on the surface. The saturated aldehyde propanal is in contrast adsorbed only weakly. Although it is not the most abundant reaction product on the catalyst, its facile desorption seemed to account for the high product yield.

Despite the number of investigations published on the reactivity and the adsorption of α,β-unsaturated aldehydes such as prenal and crotonaldehyde on the Pt(111) single crystal surface and the Sn-Pt/Pt(111) surface alloys, a deep understanding of the adsorption and interaction with the catalysts is still lacking. The binding properties of the molecules to the various catalyst surfaces and the alloying effects of Sn are still debated. Yet to reach a good knowledge of the reactivity and catalytical properties, it is a prerequisite to understand the molecule-surface interaction on such model catalysts. This evident lack of understanding motivated the investigations on the adsorption and molecular interaction on these model catlaysts in this work.

Chapter 3

Experimental Methods

A variety of experimental methods has been used in this work to characterize the properties of the unsaturated aldehydes on the model catalyst surfaces. These methods and the basic experimental setup will be described in this chapter.

3.1 The Experimental Setup

The experimental setup, i.e. the UHV chamber (Fig. 3.2) used for most of the measurements presented here, is primarily pumped by a turbomolecular pump with a pumping speed of 530 l/s. The rough vacuum is generated by a two-stage rotary vane pump (suction capacity of 8 m^3/h), to which a Pirani manometer is attached. Additionally an ion-getter pump (400 l/s) with an integrated titanium-sublimation pump is attached at the bottom of the UHV chamber. The base pressure reached after 54h bake-out at 150°C with this pumping system is below $10^{-10}\,mbar$ ($10^{-8}\,Pa$). An ionisation manometer is used to determine the pressure in the main chamber.
The Pt(111) single crystalline sample is held by twisted tantalum wires (diameter 0.25 mm), which are spot-welded to two molybdenum rods. The temperature of the sample can be varied in the range between 90 K and 1400 K. The temperature is controlled by a PID (proportional, integral and differential) controller (cp. Eurotherm) and is measured using a NiCr-Ni thermocouple (type K). The sample is cooled by a liquid nitrogen cryostat mounted to the sample holder and can be heated directly. The manipulator, to which the sample-holder is fixed, allows the sample to be translated in all three dimensions with high precision as well as rotated around the vertical axis.
The UHV chamber is equipped with various experimental techniques, which are arranged on three different levels. The upper level houses a three-grid low-energy electron diffraction (LEED, cp. Fisons) optics, used for characterizing the Pt-Sn surface alloys prepared in this thesis, and an Auger electron spectrometer (AES, cp. Perkin-Elmer). The AES spectrometer is mainly employed to check the sample surface region for cleanliness and also to determine the amount of tin deposited on the surface from the Sn-evaporator mounted in the intermediate level of the UHV chamber. In this level also a sputter gun required for sample cleaning, a quartz microbalance (QMB, cp. Baltec) and a quadrupole mass-spectrometer (QMS, cp. Balzers) are fitted to the setup. The QMS is used for the analysis of residual gases and temperature programmed desorption (TPD) experiments. It is pumped differentially in order to maintain a sufficiently low partial background pressure of the desorbing molecules in the QMS, which is required for well defined peak positions and steep high temperature flanks of the desorption signals and for data analysis using the Redhead approach [56].
On the lowest level, shielded by mu-metal walls to reduce magnetic stray fields, the high-

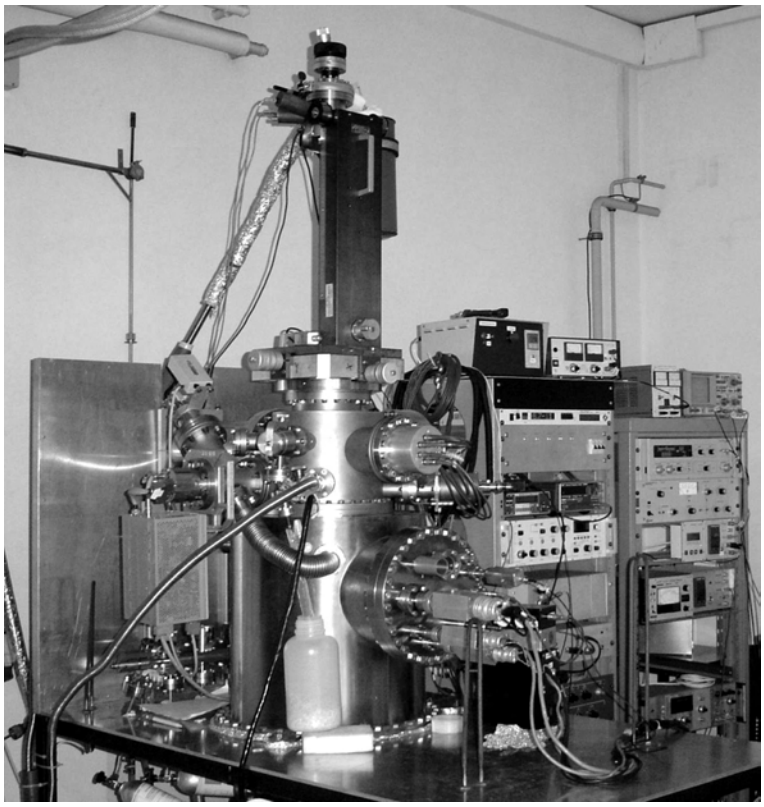

Figure 3.1: The UHV chamber.

resolution electron energy loss spectrometer (HREELS, IB 2000 from cp. VSW) is positioned. This is the central experimental method used in this setup and will therefore be described in more detail below.

3.2 High-Resolution Electron Energy Loss Spectroscopy (HREELS)

The high-resolution electron energy loss spectroscopy (HREELS) presents one of the most powerful tools in surface analytics to study adsorption processes and binding properties. By comparison of gas phase vibrations with the spectra obtained from adsorbed molecules, information on the type and strength of the interactions with the surface and the effects exerted by the surface onto the molecule can be deduced. Vibrations can be excited by photons (reflection absorption infrared spectroscopy, RAIRS), electrons (HREELS) or atoms (helium atom energy loss spectroscopy, HAELS). The advantages of using electrons for the excitation is their high sensitivity and the accessibility of the low frequency vibrations. With HREELS it is possible to detect coverages as low as 1/1000 of a monolayer of CO on Pt(111) [57]. Furthermore, via different excitation mechanisms described in the following sections, also dipole-inactive vibrations can be excited. But this comes at the expense of lower resolutions compared to the other methods. While HREELS regularly operates with resolutions above 16 cm^{-1} (ca 2 meV), IRAS and atom scattering can reach resolutions below 0.8 cm^{-1} (0.1 meV) [58], making them supe-

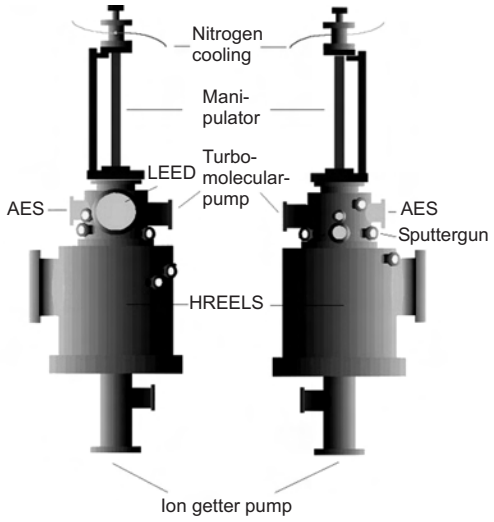

Figure 3.2: Schematic view of the UHV chamber used for the experiments in this thesis.

rior techniques for resolving close-lying vibrational frequencies, which are for example typically obtained in the $\nu(CH)$ stretching region between 2600 cm^{-1} and 3500 cm^{-1}.
Yet HREELS studies are not only limited to vibrations of adsorbates on metallic surfaces. Exceeding such studies, HREELS can also be used to characterize metallic and semi-conductor substrates by their surface phonons and electronic excitations. Also resonant electron scattering processes can be investigated. This variety of applications renders HREELS a very potent method in surface science.

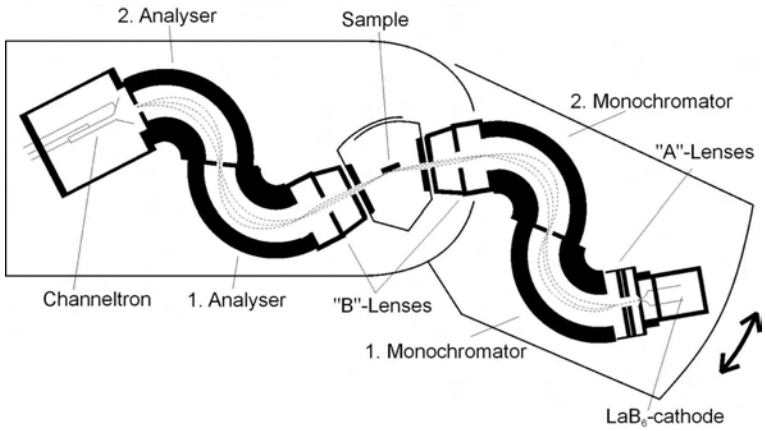

Figure 3.3: Scheme of the Ibach-type HREELS spectrometer used in the current experiments.

The HREELS spectrometer can be divided up into five major sections (Fig. 3.3): In the first section the LaB_6 cathode is housed. It is connected via a focusing lens-system ("A"-lenses) to two successive cyclindric 127° deflectors forming the premonochromator and the monochromator parts. The electron beam having been monochromatized in this section is then focused by

another set of electrostatic lenses ("B"-lenses) onto the sample in the central scattering chamber. In the dipolar operation mode, the incident beam hits the sample surface at an angle of 60° off the surface normal and is reflected back in mirror geometry. A similar set of "B"-lenses focuses the scattered electrons onto the entrance slit of the analyser section, which also consists of two 127° analysers (analyser and postanalyser parts). Finally the electrons are detected by a channeltron operated at a voltage of 2.0 kV. The monochromator section of the spectrometer is rotatable against the analyser deflectors with the rotational axis being the center of the scattering chamber. The primary energy of the electrons emitted from the cathode is generally a few eV. Depending on the excitation mechanism observed, the scattering cross sections and, thus, measured loss intensities depend on the selected primary electron energy. The different excitation meachnisms will be described in the following section 3.2.1.

3.2.1 Interaction Mechanisms in HREELS

Generally three limiting cases of inelastic interaction mechanisms of the incident electrons with the sample have to be taken into account [57]. At long distances from the surface, the dipolar scattering occurs. The scattered intensity is strongly focused in the specular direction, so that these losses are recorded experimentally in the mirroring geometry. At short distances, the impact scattering is dominant. It causes weaker signals, which are recorded at large diffraction angles. Multiple scattering events and diffraction of electrons in the first layers near the surface are important for the description of these energy losses. Finally also resonant scattering can occur, if an electron is trapped in an intermediate step. Such negative ion states lead to strong increases of the scattering intensity at the resonant loss energies.

3.2.1.1 The Dipolar Scattering Regime

The basic model underlying the theoretical description of the dipolar scattering mechanism is the interaction of a long-range electric field $\vec{E}$, which is generated by the time-dependent modulation of the electric dipole moment $\vec{\mu}$ of a vibrating molecule, with an incident electron above the surface [57]. The vibration of the molecule with the frequency ω_0 (the lifetime of the excited state is supposed to be infinite) induces an oscillation of the static dipole moment $\vec{\mu}$. The component $\vec{P}$ of $\vec{\mu}$ orthogonal to the surface is changed to $\vec{P}(t) = \vec{P}_0 + \vec{p}\exp(i\omega_0 t)$. On a polarizable surface, $\vec{p}$ induces a collinear image dipole. The incident electron in the vacuum above the surface sees the potential:

$$V(r) = 2\frac{p\,z}{r^3}e^{-i\omega_0 t} + c.c. \tag{3.1}$$

with the factor 2 coming from the image dipole. Here z denotes the unit vector normal to the surface.
The potential $V(r)$ can further be separated into two terms containing surface parallel and orthogonal contributions:

$$V(r) = p\,e^{-i\omega_0 t}\iint\frac{\mathrm{d}^2Q_\parallel}{\pi}e^{i\vec{Q}_\parallel\vec{r}_\parallel}e^{-Q_\parallel z} + c.c. \tag{3.2}$$

Here $\vec{Q}_\parallel$ denotes a two-dimensional wave vector in the surface plane (xy) and $\vec{r}_\parallel$ the projection of $\vec{r}$ onto the surface. Equation 3.2 shows that the dipole potential is synthesized from linear combinations of two-dimensional waves localized at the surface. Each component with a wave vector $\vec{Q}_\parallel$ has a field extending into the vacuum with a distance $l(\vec{Q}_\parallel) = Q_\parallel^{-1}$, which is largest for long wavelengths. Since the electrostatic potential V must satisfy the *Laplace*-equation

$$\Delta V \;=\; 0, \tag{3.3}$$

a z-dependence $e^{-Q_\parallel z}$ is required. An electron approaching the surface with the energy E_i and the wave vector $\vec{k}_i$ is scattered at the potential V and exits into the final state $E_f \;=\; E_i \pm \hbar\omega_0$ with $\vec{k}_\parallel^{\,f} \;=\; \vec{k}_\parallel^{\,i} + \vec{Q}_\parallel$ according to the *Born* approximation.
If an electron entering orthogonally emerges after the inelastic scattering at a small angle Θ_S, $Q_\parallel$ is given by $Q_\parallel \;\approx\; k_i\Theta_S$. The time spend by the electron (velocity v_0) in the field can be approximated by

$$\Delta t \;=\; \frac{2l(\vec{Q}_\parallel)}{v_0} \;\approx\; \frac{2}{\left|\vec{k}_i\right|\Theta_S\, v_0} \;=\; \frac{\hbar}{E_i\Theta_S} \tag{3.4}$$

Here a factor of 2 enters because the electron experiences the potential field as it approaches as well as after the scattering process. For very small dwell times of the electron in the scattering potential, $\Delta t\omega_0 \;<<\; 1$ corresponding to large Θ_S, the excitation probably is small since the electron passes too fast. Similarly, in the adiabatic limit $\Delta t\omega_0 \;>>\; 1$, the excitation probability becomes very small. Instead, a maximum is found for $\Delta t\omega_0 \;=\; 1$, which results in a scattering angle of $\Theta_S \;=\; \hbar\omega_0/E_i$. Under experimental conditions, when $\hbar\omega_0 << E_i$, the scattered beam is thus strongly focused in the specular direction.

A detailed theory of the dipolar scattering mechanism reveals that the exact scattering angle is given by $\Theta_S \;=\; \hbar\omega_0/2\,E_i$. The precise derivation of the scattering cross section [57] starts with defining a perturbation of the charge density ρ_0 in the ground state.

$$\rho'(\vec{x},t) \;=\; \rho_0(\vec{x}) \;+\; \rho_1(\vec{x},t)\,\text{with}\int \rho_1(\tilde{\mathrm{x}},\mathrm{t})\mathrm{d}^3\mathrm{x} = 0 \tag{3.5}$$

Within ρ_1, the vibrational motions, fluctuations of the charge density of free carriers or interband transitions in the bulk will be included. With the crystal surface in the xy plane and the bulk below $z < 0$, an approaching electron senses the potential

$$\varphi(\vec{x},t) \;=\; e\int_{z'<0+\delta z} d^3x'\,\frac{\rho_1(\vec{x}',t)}{|\vec{x}-\vec{x}'|} \tag{3.6}$$

The integral is extended slightly into the vacuum to include any charge redistribution in the surface region induced by the fluctuations in the bulk. Since the perturbed density ρ_1 obeys charge conservation, the leading contribution to the potential at large distances in the vacuum will have dipolar character. The validity of equation 3.6 requires that the time-scale of charge fluctuations and their transmittance between different positions $\vec{x}$ is instant, which is generally ensured, because the interaction distance of an incident electron is $l_0 << c/\omega_0$. Thus no retardation effects have to be introduced in the derivation.
By using the identity relation

$$\frac{1}{|\vec{x}-\vec{x}'|} \;=\; 2\pi\int\frac{d^2Q_\parallel}{Q_\parallel}\,e^{i\vec{Q}_\parallel\vec{x}_\parallel}\,e^{-Q_\parallel\left|z-z'\right|} \tag{3.7}$$

the potential sensed by the electron in the vacuum can be rewritten in terms of wave vector transfers $Q_\parallel$:

$$\varphi(\vec{x},t) \;=\; 2\pi e\int\frac{d^2Q_\parallel}{Q_\parallel}\,e^{i\vec{Q}_\parallel\vec{x}_\parallel}\,e^{-\vec{Q}_\parallel\vec{z}}\int_{z'<0+}\rho_1\left(\vec{Q}_\parallel\vec{z}',t\right)e^{\vec{Q}_\parallel\vec{z}'}dz' \tag{3.8}$$

Here, too, the surface parallel components of basis of the disturbed density are transformed into the wave vector space.

$$\rho_1\left(\vec{Q}_\parallel \vec{z}', t\right) = \int d^2x_\parallel \, e^{-i\vec{Q}_\parallel \vec{x}_\parallel} \rho_1(\vec{x}, t) \tag{3.9}$$

Again it is seen that the potential showing a spatial behavior of $e^{i\vec{Q}_\parallel \vec{x}_\parallel}$ must according to the *Laplace* equation 3.3 decay like $e^{\vec{Q}_\parallel \vec{z}'}$ into the vacuum. Thus the potential extends like $l_0(Q_\parallel) \approx Q_\parallel^{-1}$ into the vacuum. In a given electron scattering process with the wave vector transfer $Q_\parallel$, the probability of interaction is created by the right-hand side of equation 3.8. This can be understood from the conservation of the wave vector components of the electron: The surface parallel components are fully conserved in this event, but for the perpendicular component there is no restricting relationship. Yet the direction of the emerging electron is still uniquely defined by the combination of $Q_\parallel$ and the energy on the exiting pathway $E_s = E_i - \hbar\omega_0$.
In the following step of the theoretical derivation the potential has to be inserted into the *Schrödinger* equation and using perturbation theory in first order the scattering cross sections can be obtained [59]. If the electron approaches the surface with $\vec{k}_i$ and emerges after the inelastic scattering $E_s = E_i - \hbar\omega_0$ with $\vec{k}_f$, four distinct scattering events can contribute to the scattering cross section (Fig. 3.4).

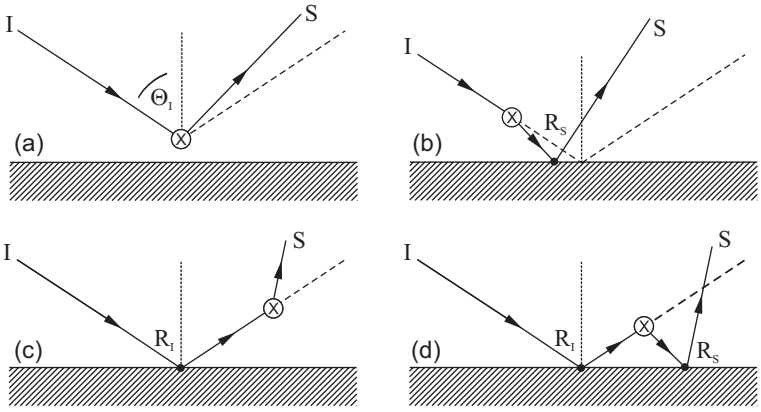

Figure 3.4: The four scattering events of the incident electron (I) in the dipolar regime. The scattering event by the vibration into the final state (S) is marked by the crossed circle. The elastic diffractions from the surface of the sample are labeled with their corresponding reflectivities.

Basically the incident electron can either be scattered back at larger distances from the surface into the vacuum by the oscillating electric field without striking the surface (Fig. 3.4(a)) or it can experience additional diffraction events when approaching or leaving the surface region (Fig. 3.4(b)-(d)). The description of these diffractions requires the knowledge of the reflectivity of the surface, i.e. the reflection probabilities $|R_i|$ and $|R_s|$, which can be obtained for instance from LEED data.
The weight of matrix elements M of the four events can be estimated by a few coarse assumptions. For a vibrational scattering with an energy loss of 150 meV of a primary electron impacting with an energy of 5 eV, $Q_\parallel$ is approximately $10^{-6}\,cm^{-1}$. The magnitudes of the normal component of the incident and the scattered electron $k_\perp^i$ and $k_\perp^f$ are both in the order of $10^{-8}\,cm^{-1}$. Thus it is found that the events (b) and (c) form the leading contributions to the scattering process [57, 59].

$$\begin{aligned}
M^{(a)}(S \to I) &= \int_0^\infty dz\, e^{-(Q_\parallel + ik_\perp^i + ik_\perp^s)z} &= \left(Q_\parallel + ik_\perp^i + ik_\perp^s\right)^{-1} \\
M^{(b)}(S \to I) &= \int_0^\infty dz\, e^{-(Q_\parallel - ik_\perp^i + ik_\perp^s)z} &= \left(Q_\parallel - ik_\perp^i + ik_\perp^s\right)^{-1} \\
M^{(c)}(S \to I) &= \int_0^\infty dz\, e^{-(Q_\parallel + ik_\perp^i - ik_\perp^s)z} &= \left(Q_\parallel + ik_\perp^i - ik_\perp^s\right)^{-1} \\
M^{(d)}(S \to I) &= \int_0^\infty dz\, e^{-(Q_\parallel - ik_\perp^i - ik_\perp^s)z} &= \left(Q_\parallel - ik_\perp^i - ik_\perp^s\right)^{-1}
\end{aligned} \tag{3.10}$$

Weighting the scattering amplitudes by the matrix elements (Eqs. 3.10) for the events (b) and (d), the scattering efficiency per solid angle and per unit energy $d^2S/d\hbar\omega\, d\Omega$ can be calculated. This function describes the scattering probability from the initial state into the solid angle $d\Omega$ and the energy range $d\hbar\omega$. The difficulty in calculating the scattering efficiency arises from the determination of the perturbed charge density ρ_1. Using the fluctuation-dissipation theorem, Mills showed that the charge density fluctuations can be related to the dielectric response function of the crystal via their correlated electric field [59] (for the formulation of the relationships see [57]).

$$\rho_1(\vec{x}, t) = \frac{1}{4\pi} \nabla \vec{E}(\vec{x}, t) \tag{3.11}$$

In order to study surface scattering effects as wells as bulk scattering, a simple "two-layer model" has been established. Therefore one considers a semi-infinite bulk substrate with an isotropic dielectric constant $\epsilon_b(\omega)$. The choice of $\epsilon_b(\omega)$ depends on the nature of the substrate, which may be a metal, an insulator or semi-conductor. Upon the substrate, an ad-layer with a certain thickness d and the spatially not varying dielectric constant $\epsilon_s(\omega)$ is assumed. With $d \to 0$, the model can describe electronic scattering events such as interband transitions or phonon excitations in the substrate. With a finite ad-layer present, besides the vibrational scattering from adsorbed molecules also layer-effects on substrates such as depletion layers of semi-conductors can be investigated. One of the general results of this theoretical formulation is the separation of the scattering efficiencies into bulk and surface layer events:

$$\frac{d^2S}{d\hbar\omega\, d\Omega(k_s)} = \frac{d^2S_b}{d\hbar\omega\, d\Omega(k_s)} + \frac{d^2S_s}{d\hbar\omega\, d\Omega(k_s)} \tag{3.12}$$

The term $d^2S_s/d\hbar\omega\, d\Omega(k_s)$ on the right hand side is used to derive loss intensities I_{inel} arising from vibrational excitations of adsorbed molcules in the inelastic scattering event. The loss intensities I_{inel} are normalized relatively to the intensity of the elastically reflected electron beam I_{el}. Since only the electrons approaching the analyzer within the acceptance angle ϑ_c are detected, a spectrometer dependent "technical" function $F_b(\hat{\vartheta}_c)$ is required to determine the detected intensity.

$$\begin{aligned}
F_b(\hat{\vartheta}_c) &= \frac{2}{\pi} \int_0^{2\pi} d\varphi \int_0^{\hat{\vartheta}_c} d\hat{\vartheta}\, \hat{\vartheta}\, \frac{\left[\left(\sin(\Theta_i) - \hat{\vartheta}\cos(\Theta_i)\cos(\varphi)\right)^2 + \hat{\vartheta}^2 \sin^2(\varphi)\right]}{\left[1+\hat{\vartheta}^2\right]^2} \\
&= \left(\sin^2(\Theta_i) - 2\cos^2(\Theta_i)\right) \frac{\hat{\vartheta}_c^2}{1+\hat{\vartheta}_c^2} + \left(1 + \cos^2(\Theta_i)\right) \ln(1 + \hat{\vartheta}_c^2)
\end{aligned} \tag{3.13}$$

with $\hat{\vartheta} = \vartheta/\vartheta_E$ being a reduced scattering angle. ϑ_E is the angle between the specular direction and the vector of the exiting (scattered) electron. For a simple model of an adsorbed layer with a single (perpendicular) vibrational frequency, the linear response theory allows to approximate

the loss function necessary in equation 3.13 from the high-frequency limit ϵ_∞ of $\epsilon_s(\omega)$, the ion-plasma frequency ω_p and the transverse eigenfrequency ω_T of the adsorbed molecules, which is equal to their mechanical eigenfrequency [57]. Assuming a low coverage situation without mechanical coupling of the vibrations, ω_T and the dynamic dipole moment are independent of the (surface) concentration and the high-frequency limit can be set $\epsilon_\infty \approx 1$.
In the limit $\hbar\omega >> k_B T$ the normalized loss intensity is obtained by subsequent integration of $d^2S_s/d\hbar\omega\, d\Omega(k_s)$:

$$\frac{I_{inel}}{I_{el}} = \frac{S_s}{|R_i|^2} = \frac{4\pi}{a_0}\,\frac{\Theta_{surf}\sqrt{1-2\vartheta_E}}{E_i\,\cos(\Theta_i)}\,|\langle 0\,|\mu_\perp|\,\nu\rangle|^2\,F(\hat{\vartheta}_c) \tag{3.14}$$

where $|\langle 0\,|\mu_\perp|\,\nu\rangle|^2$ is the expectation value of the perpendicular component of the dynamic dipole moment and a_0 the Bohr radius. Θ_{surf} is the surface concentration or coverage of the substrate by adsorbed molecules. Expression 3.14 will later be of use to calculate the normalized loss intensities from the vibrational analysis by Density Functional Theory described in chapter 4.7, where vibrational frequencies and the dynamic dipole moments are computed in the harmonic approximation.

The selection rules in the dipolar limit can be deduced starting with *Fermi´s Golden Rule* [60]. Accordingly, the transition probability from the vibrational state $|\lambda\rangle$ of an adsorbed species into the state $\langle\nu|$, induced by the scattering of an incident electron $|\Psi_{k_i}\rangle$, ω_i into its final state $\langle\Psi_{k_f}|$,ω_f, is given by

$$w = \frac{2\pi}{\hbar^2}\left\langle \lambda\Psi_{k_f}\left|\hat{H}\right|\nu\Psi_{k_i}\right\rangle^2 \delta(\omega_0+\omega_f-\omega_i) \text{ with } \hat{\mathrm{H}} = -\mu\mathrm{E} \tag{3.15}$$

Here again μ is the dynamic dipole moment of the vibrating molecule and E the time dependent electric field scattering the primary electrons.
The transition matrix element can be decoupled into two state products, containing the z-component of the dynamic dipole moment μ_z and the scattering potential $V(r)$ (see eq. 3.1),

$$\langle\lambda\,|\mu_z|\,\nu\rangle^2 \text{ and } \langle\Psi_{\mathrm{k_f}}\,|\mathrm{V(r)}|\,\Psi_{\mathrm{k_i}}\rangle^2 \tag{3.16}$$

which is justified by the experimental observation that the **relative** loss intensities are independent of the primary energy of the incident electrons. Since the scattering process is symmetric under time-reversal, the time-dependent potential must be even. Both electron wave functions can be described in a plane wave basis set of the form $\exp(ikr)$, which also are of *gerade* symmetry. Thus the transition matrix element of the electrons is always *gerade* and the selection rules must arise from the vibrational transition probability.
The dynamic dipole moment $\mu_z \propto q\hat{z}$ transforms like a translation in the z direction. From the group tables it is understood that this translation always belongs to a totally symmetric representation and, thus, must be *gerade*. Therefore, the selection rules in the dipolar scattering mechanism depend only on the symmetry properties of the two vibrational states considered. Assuming again $\hbar\omega >> k_B T$, the transition with an energy loss $E_s < E_i$ occurs from the vibrational ground state of the molecule to a certain excited state. The ground state of a neutral molecule is generally of even symmetry. Thus it is finally concluded that the transition in the dipolar limit is only allowed, if the excited state of the molecule also transforms totally symmetric and therefore belongs to one of the irreducible respresentations A', A_1 or A_g.

3.2.1.2 The Impact Scattering Regime

The picture of the impact scattering mechanism is more complicated, since kinematical processes and multiple scattering events have to be included in the theoretical description [57]. Impact scattering leads to loss signals, which are detectable out of the mirror geometry.
In the theoretical description of this scattering mechanism, the outgoing wave is of the form $f(\vec{k}_s, \vec{k}_i)\cdot\exp(ik_s r)$. Invoking the adiabatic approximation, i.e. assuming the crystal to be macroscopic but nonetheless finite in dimension and that the positions of the scattering nuclei $\{\vec{R}_i\}$ are fixed, the Schrödinger equation for the electron can be solved. The probability of the electron to emerge with certain wave vectors k_s is described by the scattering amplitude $f(\vec{k}_s, \vec{k}_i, \{\vec{R}_i\})$. If the crystal is periodic and ordered layers of adsorbates are present, the calculation of the scattering amplitudes are determined by kinematics (Bragg scattering) encountered in the low-energy electron diffraction (LEED). For wave vector components parallel to the surface the wave vector is conserved within a reciprocal lattice vector, while for the direction normal to the surface the lack of translational symmetry leads to a breakdown of conservation. In fact the inelastically scattered electrons considered here appear as a diffuse background, since they do not emerge in the Bragg directions as they are scattered by emission or absorption of a vibrational quantum.
Thermal vibrations of the scattering nuclei can be included in the theoretical description by expanding f into powers of the displacement $dR_{i\alpha}$ (with cartesian components α) of the nuclei from the equilibrium positions R_i^0, because these amplitudes are small:

$$f\left(\vec{k}_s, \vec{k}_i, \left\{\vec{R}_i\right\}\right) = f\left(\vec{k}_s, \vec{k}_i, \left\{\vec{R}_i^0\right\}\right) + \sum_{i\alpha}\left(\frac{\partial f}{\partial R_{i\alpha}}\right)_0 dR_{i\alpha} + ... \tag{3.17}$$

Introducing the normal coordinates $\vec{Q}_s$ for the vibrations of the system, equation 3.17 can be expressed in terms of annihilation and creation operators a_s and a_s^+ of vibrational quanta, showing that single scattering events are described by the linear terms here. If we consider the events, in which just one vibrational quantum is emitted, one can introduce the matrix element

$$\begin{aligned} M\left(\vec{k}_i, \vec{k}_s, \vec{Q}_\parallel^\alpha\right) &= \left\langle n_s + 1 \left| f\left(\vec{k}_s, \vec{k}_i, \left\{\vec{R}_i\right\}\right)\right| n_s\right\rangle \\ &= \sqrt{(n_s+1)\,\tfrac{\hbar}{2N\omega_s}}\left(\tfrac{\partial f}{\partial Q_s}\right) \end{aligned} \tag{3.18}$$

where

$$\left(\frac{\partial f}{\partial Q_s}\right) = \sum_{i\alpha}\left(\frac{\partial f}{\partial R_{i\alpha}}\right)_0 \frac{\xi_{ia}^s}{\sqrt{M_i}} \tag{3.19}$$

and N is the number of unit cells in the system and ξ_{ia}^s is the amplitude of displacement (normalized over all motions i and components α, $\sum_{i\alpha}|\xi_{ia}^s| = 1$). From *Bose-Einstein* statistics, the occupation number is given by $n_s = [\exp(\hbar\omega_s/k_BT) - 1]^{-1}$.
The translational symmetry assumed for the systems considered here allows the set of vibrational normal modes to be identified by wave vector $Q_\parallel^\alpha$ in the irreducible Brillouin zone. Vibrational quantum numbers other than the wave vector parallel to the surface are included in the indices α. An expression for the probability of scattering an electron into the solid angle $d\Omega$ by the vibrational quantum $\vec{Q}_s^\alpha$ is given by

$$\frac{dS_\alpha\left(\vec{k}_i, \vec{k}_s\right)}{d\Omega} = \frac{mE_i\,\cos^2(\Theta_s)}{2\pi^2\hbar^2\,\cos(\Theta_i)}\,A\left|M\left(\vec{k}_i, \vec{k}_s, \vec{Q}_\parallel^\alpha\right)\right|^2 \tag{3.20}$$

Here A denotes the surface area of the crystal. Again, the wave vector components parallel to the surface are conserved within a reciprocal lattice vector $\vec{Q}_\parallel^\alpha = \vec{k}_\parallel^s - \vec{k}_\parallel^i - \vec{G}_\parallel$.

This expression is still quite general for electron scattering from adsorbate vibrations and describes both the small angle and the impact scattering regimes. To apply this equation further to the impact scattering mechanism, where penetration of the electrons into the crystal is highly important, the derivatives $\partial f/\partial R_{i\alpha}$ have to be calculated at the equilibrium geometry. The variation of the derivates depends on the change of the scattering potential $(\partial V(\{\vec{R}_i\})/\partial R_{i\alpha})_0$ or $(\partial V(\{\vec{Q}\})/\partial Q_s)_0$ in the normal coordinate space respectively.
A rather simple approach for evaluation of these derivates is the "muffin tin" model [57]. The potential is approximated by spherical potential wells with certain radii R_0 centered on the nuclei positions. Thus the potential of the substrate and the adsorbate layer can be constructed from a linear superposition of nonoverlapping spheres. Inside the spheres, the potential is nonzero. In between, a constant background potential below the vacuum potential, equivalent to the inner potential, is assumed. In this form the physical model is also used in the theoretical analysis of low-energy electron diffraction and angular-resolved photoelectron spectroscopy (ARPES). In the theoretical analysis of the impact scattering as seen in HREELS, the model has to be enhanced by including the change of the crystal potential induced by the nuclear displacements of the vibrational motions. If multiple scattering events and all possible approaches and exit paths of the electron are included in the calculation by means of Green´s functions, a transition probability between the electron states, formulated using plane waves, can be obtained:

$$\frac{\partial V\left(\left\{\vec{Q}\right\}\right)}{\partial Q_s} = \left\langle \Psi_{\vec{k}_s} \left| \frac{\partial V}{\partial Q_s} \right| \Psi_{\vec{k}_i} \right\rangle \tag{3.21}$$

This equation, forming the transition matrix elements, permits the formulation of the impact scattering selection rules. The time-reversal invariance of the scattering process together with certain assumptions discussed below lead to the result that the scattering amplitude in the specular direction vanishes for certain vibrational normal modes that fullfill certain symmetry requirements.

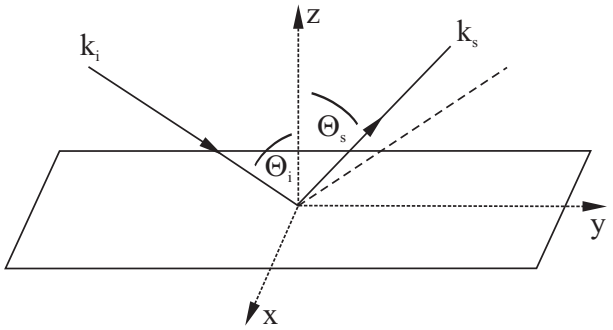

Figure 3.5: The scattering geometry assumed for the discussion of the selection rules in impact scattering.

Assuming that the emerging electrons appear in the specular direction, they obey $\left|\vec{k}_s\right| = \left|\vec{k}_i\right|$ and $E_s = E_i$. The wave vector components of the incident electron can be separated into parallel and normal parts $\vec{k}_i = \vec{k}_{\|} + \hat{z}k_z$. Similarly $\vec{k}_s = \vec{k}_{\|} - \hat{z}k_z$ are the components of the exiting electron. The plane wave functions Ψ of the electrons of the form $\exp(ikr)$ are labeled additionally according to their z-component. Reversing the scattering event in time with the operator $\hat{K}$ transforms

$$\hat{K}\Psi^{(-)}_{\vec{k}_i} = \Psi^{(+)}_{-\vec{k}_i} = \left(\Psi^{(-)}_{\vec{k}_i}\right)^* \tag{3.22}$$

and similarly $\Psi^{(+)}_{\vec{k}_s}$ into its complex conjugate $\left(\Psi^{(+)}_{\vec{k}_s}\right)^*$.
If the xy-plane is the surface of the sample (Fig. 3.5) and the xz-plane the corresponding scattering plane, a reflection symmetry operator in the yz-plane $\hat{R}_{yz}$ transforms the plane waves of the incident and exiting electron states according to

$$\begin{aligned} \hat{R}_{yz}\Psi^{(-)}_{\vec{k}_i} &= \Psi^{(-)}_{\vec{\tilde{k}}_s} \quad , \quad \vec{\tilde{k}}_i = -\vec{k}_{\|} + \hat{z}k_z \\ \hat{R}_{yz}\Psi^{(+)}_{\vec{k}_s} &= \Psi^{(+)}_{\vec{\tilde{k}}_i} \quad , \quad \vec{\tilde{k}}_s = -\vec{k}_{\|} + \hat{z}k_z \end{aligned} \tag{3.23}$$

Now it is recognized easily that the combination of the symmetry operators transform the incident electron wave functions into the emerging waves and vice versa:

$$\begin{aligned} \hat{K}\hat{R}_{yz}\Psi^{(-)}_{\vec{k}_i} &= \hat{K}\Psi^{(-)}_{\vec{\tilde{k}}_i} = \Psi^{(+)}_{\vec{k}_s} \\ \hat{K}\hat{R}_{yz}\Psi^{(+)}_{\vec{k}_s} &= \hat{K}\Psi^{(+)}_{\vec{\tilde{k}}_s} = \Psi^{(-)}_{\vec{k}_i} \end{aligned} \tag{3.24}$$

If the symmetry of the derivative is *ungerade* under the operation $\hat{R}_{yz}$, then $\hat{R}_{yz}$ and $\partial V/\partial Q_s$ form an anti-commutator relationship. Using identities of 3.24 and the symmetry of the potential, equation 3.21 can be expanded

$$\begin{aligned} \frac{\partial V(\{\vec{Q}\})}{\partial Q_s} &= \iiint d^3r\, \Psi^{(+)}_{\vec{k}_s}\, \hat{R}^{-1}_{yz}\hat{R}_{yz}\, \frac{\partial V}{\partial Q_s}\, \Psi^{(-)}_{\vec{k}_i} \\ \frac{\partial V(\{\vec{Q}\})}{\partial Q_s} &= -\iiint d^3r\, \Psi^{(+)}_{\vec{k}_s}\, \hat{R}^{-1}_{yz}\, \frac{\partial V}{\partial Q_s}\, \hat{R}_{yz}\, \Psi^{(-)}_{\vec{k}_i} \end{aligned} \tag{3.25}$$

Here it is appreciated that the impact scattering rule depends on the symmetry of the derivative of the scattering potential. Due to the *ungerade* behavior towards $\hat{R}_{yz}$, the scattering amplitude vanishes in the specular direction:

$$\begin{aligned} \hat{R}^{-1}_{yz}\frac{\partial V}{\partial Q_s}\hat{R}_{yz} &= -\frac{\partial V}{\partial Q_s} \\ \Rightarrow \frac{\partial f}{\partial Q_s} &= -\frac{\partial f}{\partial Q_s} \\ \Rightarrow \frac{\partial f}{\partial Q_s} &= 0 \end{aligned} \tag{3.26}$$

Thus for scattering vibrational normal modes, which transform *ungerade* with respect to the yz-plane, the scattered intensity vanishes in the specular direction. It has to be underlined that this result is only strictly valid for the assumption of an elastic scattering $E_s = E_i$. Similarly it can be shown that for normal modes Q_s *ungerade* under a twofold rotation along the z-axis or Q_s *ungerade* under a reflection symmetry $\hat{R}_{xz}$, the scattering amplitude vanishes, too.
A major drawback of the "muffin tin" model is the ignorance of the changes in the shape of the spherical potential wells during the vibrational motion. In this approach it is assumed that the potential wells follow the motion of the nuclei instantaneously and without changes of their shape. The dynamic dipole moments of vibrations encountered in the dipolar scattering are effectively prevented by this "static" model, rendering it unsuitable for the description of dipolar scattering. While experimentally a continuous transition from the impact scattering regime to the dipolar regime is observed, the theoretical models fail to reproduce this transition.

With a few simple approximations, an estimate of the intensities observed in the impact scattering regime can be made [57]. A rough estimate of the inelastically scattered intensity of a

vibrational mode with the amplitude $\vec{u}$ (i.e. the displacement from the equilibrium position), the wave vector transfer $\vec{Q}_s$ and the intensity of the elastic beam I_{el} is given by

$$I_{inel} \approx \frac{1}{2}\left(\vec{Q}_s\vec{u}\right)^2 I_{el} \tag{3.27}$$

This approximation is invoked by the depletion of a diffracted beam by thermal scattering as described by the *Debye-Waller factor* (Eq. 3.28). The vibrational scattering deflects a part of the incident electrons away from the specular direction into the diffuse thermal background. Thus the depletion of the specular beam can be approximated according to equation 3.27.

$$\exp\left(-\frac{1}{2}\left\langle\left(\vec{Q_s\vec{u}}\right)^2\right\rangle\right) \tag{3.28}$$

In the scattering regime, large scattering angles are encountered, which allow to set $\left|\vec{Q}_s\right| \approx \left|\vec{k}_i\right|$, the incident wave vector. For monolayer coverages, also I_{el} can be approximated by I_i instead of the exact term $I_i \left|R_i^2\right|$, since a single scattering event deflects the electron into sufficiently large angles so that a backreflection by the substrate is not necessary. Since the impact scattering mechanism produces a uniform intensity throughout the whole solid angle, the current detected by the spectrometer with the acceptance angle ϑ_c is roughly $\pi\vartheta_c^2/4\pi$. Furthermore replacing $\vec{u}^2$ by the zero-point amplitude $\hbar/2M_r\omega_s$, where M_r denotes the reduced mass, the estimate of the loss intensity is obtained:

$$I_{inel} = I_i \frac{m_e E_i}{\hbar\omega_s M_r}\frac{\vartheta_c^2}{4} \tag{3.29}$$

This estimate is justified for $\hbar\omega_s >> k_BT$. Comparing this result to the loss intensities in the dipolar regime, it is seen that the rate for impact scattering is much lower than the dipolar losses [57], especially when strong dipole scatterers such as the CO stretching vibration are explored. Often a relative difference in the range of 10^{-2} is found in the experimental spectra. However, when weak dipole scatterers like the $\nu(CH)$ stretching vibrations are considered, the impact and dipole scattering features may become equally intense. From equation 3.29 it is recognized that the loss intensities due to the impact scattering increase with lower loss energies $\hbar\omega_s$ and also with the primary electron energy E_i.

The molecular adsorption complexes of crotonaldehyde and prenal are generally of low symmetry. With the exception of the top adsorption modes bound to Pt via the aldehydic oxygen, which can transform like C_s, basically all adsorption geometries are of C_1 symmetry and thus all their vibrational normal modes are dipole active. For this reason additional measurements out of the mirroring geometry have not been performed in the framework of this thesis.

3.2.1.3 The resonant scattering

The resonant scattering (negative ion resonance scattering) mechanism is well known from electron collisions between electrons and ions in the gas phase. Since the lifetime of such resonant states (*Shape* or *Feshbach* resonances) is much shorter in molecules adsorbed on surfaces, such scattering events are less frequently detected with HREELS. Generally in this mechanism the scattered electron is interimly trapped in the molecule, forming a negative ion. Such a state can occur, when the energy of the quasi-bound state in the potential is equal to the kinetic energies of the colliding electron and the molecule. The resonance energies can be obtained from extensive Configuration-Interaction (CI) calculations using the R-matrix scattering approach, but due to the high computational cost of CI this approach is limited to small systems.

3.2.1.4 General Considerations

From the comparison of the HREELS spectra recorded in and out of specular geometry, it is possible to identify adsorption sites or coordination geometries simply from symmetry arguments [57]. On the one hand, the specular geometry is dominated by the dipolar scattering mechanism with its according selection rule, so that only totally symmetric modes with a dynamic dipole moment normal to the surface are recorded. On the other hand, in the impact scattering regime, different selection rules are valid.
The analysis of the differences in the vibrational frequencies of molecules in the gas phase and their adsorbed counterparts, binding strengths can be obtained. This is possible by either directly analyzing the molecule-metal stretching vibrations or by looking at internal modes of an adsorbate, which are indirectly affected. Typically the frequency shifts of double-bonds interacting with surfaces are very sensitive to the adsorption strength and the adsorption mode. In addition, the scattering intensities can reveal a specific orientations of adsorbed molecules.

3.2.2 Fermi Resonances, Vibrational Couplings and Davydov Splitting

If two or more vibrational normal modes of the same symmetry race are close in frequencies to each other, they can couple by the anharmonic terms in their vibrational potentials. Like in the text book case of coupled springs, the shift of the vibrational frequencies away from each other is stronger the smaller the initial difference between the undisturbed frequencies is. Such vibrational couplings are not only well known for polyatomic molecules in the gas phase, but also for adsorbed molecules. Often interactions between a normal mode and overtones of other vibrations, having similar frequencies, are observed. The overtone of the second vibrational mode can show increased intensity in such a case. The two coupling states do not necessarily have to belong to the same symmetry to interact. Such couplings are regularly referred to as *Fermi resonances* in the literature [61].
Typically even the charateristical group vibrations of groups like CH_3, CH_2 or $C = C$ normal modes can vary sizably in gas phase spectra from their usual frequencies. This can be understood by Fermi resonances, which result from the coupling of the pure group vibrations of the same symmetry. The normal modes of the molecule are then formed by linear combination of the vibrational modes of the subgroup, combined with different weights. In the case of ethene (point group D_{2h}) for instance, the $\nu(C = C)$, the $\delta_s(CH_2)$ and the $\omega_s(CH_2)$ belong to the totally symmetric representation A_g. Therefore, these vibrational normal modes are allowed to couple. The coupling depends on the difference in the eigenfrequencies of the modes, which in turn can be influenced by the adsorption on a surface or a change of the substituents. Notably, a hydrogen-deuterium exchange in a molecule influences the couplings and thus the isotopic shifts of the vibrational frequencies. Even the frequencies of normal modes of a single molecule present in different adsorption geometries are sometimes difficult to correlate. This can be due to the varying prefactors, with which the normal modes are composed from the group vibrations in the different adsorption complexes [57].

The vibrational coupling can render the analysis of vibrational spectra problematic. This is especially true for the complex functional molecules like the α,β-unsaturated aldehydes studied in this thesis. The DFT-calculations performed to determine the frequencies and eigenvectors (normal modes) of the vibrations in the different adsorption sites carried out in this thesis have been performed in the framework of the *Harmonic Force Approach* (Chap. 4.6). In this theoretical approach the anharmonic effects are ignored.

Finally, the *Davydov splitting* (or factor-group splitting), which is typical for electronical and

vibrational levels in solid state physics, can lead to significant changes in the vibrational spectra. It is encountered in cases, in which more than one molecular species is present in a unit cell, where it may interact with other equivalent molecular moities. Also changes in the orientation of an adsorption structure, for i.e. the rotation of a η^2-diσ(CC) bonded moiety (characteristical for ethene and other alkenes) along the six nearest-neighbor directions on a (111) surface, contributes to such a splitting phenomenon. The interaction of the molecular entities in the unit cell causes a splitting or broadening of the individual levels. Hence for vibrational levels, aside from the dispersion in the vibrational *Brillouin* zone, the splitting of the normal modes also disperses the signal intensity observed and may cause an overall broadening of the measured signals.

3.3 Temperature Programmed Desorption (TPD)

Although the temperature programmed desorption (TPD) is experimentally a rather simple method, it can give valuable information on desorption processes such as the activation energy of desorption and it can identify different desorption states.
In order to perform this experiment, the sample is first exposed to a defined dosage of the adsorbate. Then the sample is heated with a linear temperature ramp ($dT/dt = const.$) while the partial pressure of the desorbing molecules is measured parallely with a quadrupole mass-spectrometer (QMS). If the pumping rate of the vacuum system is sufficiently high, no readsorption occurs and the rate of desorption $d\Theta/dt$ is proportional to the partial pressure of the desorbing particles. The sample is placed directly in front of a cylindrical aperture, which covers the entrance of the QMS and has a diameter slightly smaller than the single crystal. In this manner desorption from the rims of the sample or from the sample holder can be minimized. By differential pumping of the mass spectrometer itself, a high pumping rate is ensured and the background of the TPD spectra is reduced further. Various other factors influence the accuracy of the TPD experiments, but are difficult to estimate and to correct. Especially the varying ionization probabilities of different desorbing particles, the acceptance angle of the QMS or the effective ion yield of the secondary electron multiplier (which depends on the applied high voltage) cause problems analysing the obtained TPD spectra quantitatively.
Performing TPD experiments for different initial adsorbate coverages Θ, information on adsorption states, sticking coefficients, coverage limits and adsorbate-surface interactions as well as adsorbate-adsorbate interactions can be deduced. The potential of this technique includes studies of surface reactions, which can even be done by co-adsorption of different adsorbates like for example studies of hydrogenation reactions by co-adsorption of hydrogen and unsaturated reactants. In this case it is called temperature programmed reaction spectroscopy (TPRS). The analysis of TPD spectra is complicated by the fact that no general microscopic description of the desorption processes exists. From a purely theoretical point of view the desorption can be modelled quantum-chemically by *kinetic Monte-Carlo* simulations. This approach allows to introduce complex elementary steps besides the inclusion of precursor states.
In a first approximation the desorption process can be described by the Polanyi-Wigner equation 3.30, which is derived from a phenomenological *Arrhenius ansatz*:

$$-\frac{d\Theta}{dt} = \nu(\Theta)\cdot\Theta^m\cdot\exp\left(-\frac{E_{des}(\Theta)}{RT}\right) \tag{3.30}$$

Here $\nu(\Theta)$ is the coverage dependent frequency factor, m the order (cf. Fig. 3.6) and $E_{des}(\Theta)$ the activation energy of the desorption process, which can depend on the coverage. In the literature several evaluation procedures are described to analyze the different parameters [62, 63, 64, 65, 66]. Although this phenomenological approach allows an interpretation of these parameters, it does not necessary lead to a deeper microscopical understanding of the involved elementary

processes in the desorption. A detailed description of the prevalent desorption models is given in [67].

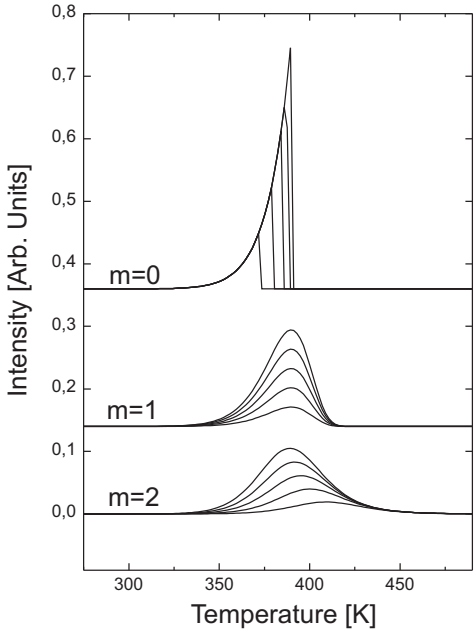

Figure 3.6: Simulated TD Spectra of processes of 0., 1. and 2. order desorption processes.

In this work only an estimation of the desorption energies has been performed. Assuming that the frequency factor ν and the desorption energy E_{des} are coverage independent, Redhead [56] showed that a simple correlation between the desorption energy and the temperature at the maximum of a desorption signal can be established by differentiation of the Polanyi-Wigner equation:

$$\frac{E_{des}}{RT} = \ln\left(\frac{m\nu\Theta^{m-1}}{\beta}T\right) - \ln\left(\frac{E_{des}}{RT}\right) \tag{3.31}$$

For a desorption of 1^{st} order, like in the case for desorption of non-dissociatively adsorbed molecules and values of ν/β between $10^{-8}\,K^{-1}$ and $10^{-13}\,K^{-1}$ this equation can be approximated by

$$\frac{E_{des}}{RT} = \ln\left(\frac{\nu}{\beta}T\right) - 3.64 \tag{3.32}$$

Since the exact frequency factors are unknown in this work, a value of $10^{-13}\,Hz$ is assumed. This value is in the range of typical molecular vibrational frequencies. In these experiments a heating rate of $\beta = 2\,K/s$ was chosen. Although relatively slow, this heating rate allows a favorable resolution of close desorption maxima.

3.4 Low Energy Electron Diffraction (LEED)

A tool to study surface structures with long-range periodicity is the low energy electron diffraction (LEED). The electrons with kinetic energies E_{kin} between 20 and 500 eV used in this method have a low penetration depth of only 2 to 5 atomic layers [68] and are thus highly surface sensitive. Since their wavelength given by the *de Broglie* equation

$$\lambda = \frac{h}{p} = \frac{h}{\sqrt{2 \cdot m_e \cdot E_{kin}}} \tag{3.33}$$

is in the range of interatomic distances, the electrons (mass m_e) are diffracted. Both elastic and inelastic scattering processes occur on the surface, so that a grid system has to be used to filter the inelastically scattered electrons and to accelerate the elastically diffracted ones (Fig. 3.7). The electrons are generated by a cathode emitting a parallel, monochromatic beam that is focused orthogonally onto the sample surface.

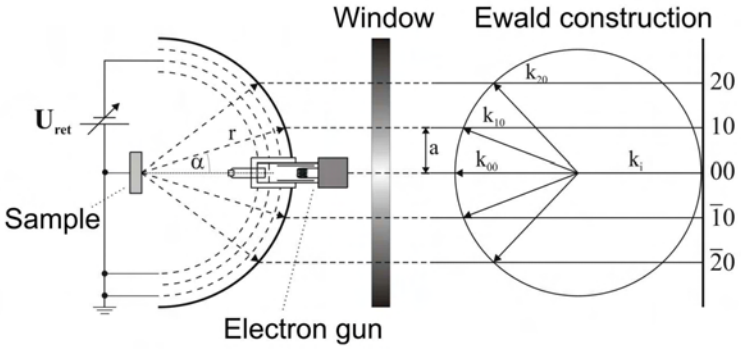

Figure 3.7: Schematical drawing of the LEED optics used in this thesis.

From the elastically scattered electrons, information on the surface periodicity and symmetry is deduced. Also relative angles between the substrate and any superstructure are accessible. By recording LEED intensities as a function of the primary electron energy, as it is done in LEED-IV experiments, even the exact atom positions and knowledge of deeper layers can be gained.
The scattering process can be considered as a diffraction of an incident plane wave with a wave vector $\vec{k_i}$ by a 2 dimensional lattice. Whenever the difference between the incident wave vector $\vec{k_i}$ and the diffracted wave vector $\vec{k_f}$ corresponds to a lattice vector $\vec{G}$ in the reciprocal space (Eqn. 3.34), constructive interference is observed.

$$\vec{k_i} - \vec{k_f} = \vec{G} \tag{3.34}$$

This can also be shown by the *Ewald construction* depicted in Fig. 3.7: Drawing a circle with the radius $\left|\vec{k_i}\right|$ around a point of the reciprocal space, one obtains all LEED reflexes as intersections of the circle with the lattice rods of the reciprocal lattice. Therefore the observed LEED images exhibit the same symmetry and periodicity like in the reciprocal space. The angle under which LEED spots are observed is given by the Bragg equation 3.35.

$$n \cdot \lambda = d_{hk} \cdot sin(\alpha) \tag{3.35}$$

Here n is the order of diffraction, λ the wave length of the incident beam and d_{hk} the distance of the surface lattice rods. Replacing the wave length λ in the Bragg equation by the kinetic

energy of the primary electrons, a relationship is obtained, which, at a given distance of the sample to the LEED screen l, allows the determination of the lattice vectors from the distance r of the central (00) spot to another LEED spot.

$$sin(\alpha) = \frac{n}{d_{hk}[nm]}\sqrt{\frac{1.5eV}{E}} = \frac{r}{l} \tag{3.36}$$

Often additional reflexes are recorded or different spots are suppressed by destructive interference. These phenomena arise from multiple-scattering events, for example caused by linear combinations of the lattice vectors of the substrate and superstructures.
In order to describe the properties of the superstructures $\{a_z, b_z\}$ with respect to the substrate lattice $\{a_s, b_s\}$, Park and Madden [69] have established a general matrix notation:

$$\begin{bmatrix} a_z \\ b_z \end{bmatrix} = \begin{bmatrix} m_{11} & m_{12} \\ m_{21} & m_{22} \end{bmatrix} \cdot \begin{bmatrix} a_s \\ b_s \end{bmatrix} \tag{3.37}$$

If the coefficients m_{ij} are integer numbers, the atoms or molecules occupy periodically the same adsorption sites. Rational numbers m_{ij} are found in the case of commensurate coincidence structures, while incommensurate superlattice are characterized by irrational matrix elements.
For the superlattices of the alloy surfaces studied in this work, a more convenient notation by Wood [70] is used. Yet this notation is restricted to commensurate superlattices, in which the angle enclosed between basis vectors of the respective lattices are equal. The length of the basis vectors of the superlattice is given relative to the lattice vectors of the substrate (Eqn. 3.38). For expressing a rotation of the superlattice against the substrate basis, an additional rotational angle α has to be given in the notation.

$$(|a_z| \,/\, |a_s| \times |b_z| \,/\, |b_s|)R\alpha \tag{3.38}$$

3.5 Auger Electron Spectroscopy (AES)

The Auger electron spectroscopy provides a valuable tool to characterize the elementary composition of the surface region of solids. The excitation of an electron from an inner shell of an atom leads to a hole state, which is filled by an electron from higher atomic levels in the following step (Fig. 3.8). The energy liberated in this process can be relaxed in two competing processes: Either by X-ray fluorescence or it can be transferred onto a third electron, which then is emitted as Auger electron. The latter is called Auger process. Since the kinetic energy of the Auger electron is independent of the energy of the excitation, it is charateristic for each chemical element. The expectation that this process can be described as an "internal photo effect" is inconsistent with the fact that Auger processes are not subject to the selection rules of optical transitions [68]. The first process, the emission of X-ray radiation during relaxation, i.e. X-ray fluorescence, is used in the energy dispersive X-ray analysis (EDX). This technique is less surface sensitive due to the much greater escape length of photons and the deeper entry path of the higher energetic primary electrons compared to the Auger electrons.
Auger transitions are identified by a triple of letters indicating the participating energy levels. The first letter represents the shell from which the electron is excited. The second letter stands for the electronic level from which an electron relaxes into the core hole and the third letter defines the electronic level, from which an electron is finally emitted in the Auger process. If bonding or valence shell electrons are involved, the letter V is used. Subshells, if known, can be indicated by adding subscripts. If two or three participating electrons originate from the same shell, the transitions are usually referred to as *Coster-Kronig* transitions. Generally Auger processes show a sizeable energy uncertainty since three electronic transitions are involved in

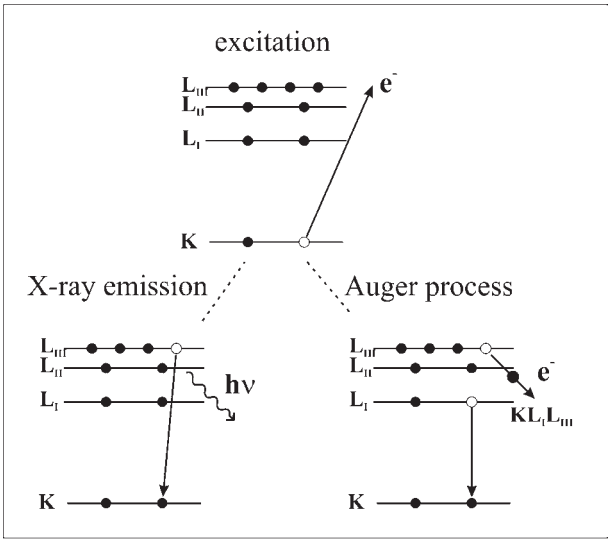

Figure 3.8: The competing X-ray fluorescence and Auger process.

the whole mechanism. The kinetical energy E_{kin} of the Auger electron emitted from the KLL process shown in Fig. 3.8 is given by

$$E_{kin} = E_K - E_{L(I)} - E_{L(III)} + E_R - \phi \tag{3.39}$$

where ϕ is the work function of the solid. E_R is a correction term and describes several effects leading to a shift of the measured Auger peak. These effects include interactions with energy bands of the solid, hole-hole interactions and matrix effects exerted by the chemical environment, which lead to a different screening of the core potential. Typical primary electron energies of $1\,keV \leq E_{kin} \leq 3\,keV$ do not only ensure a high surface sensitivity, but also an optimal ionization cross section, leading to high yields of Auger electrons.

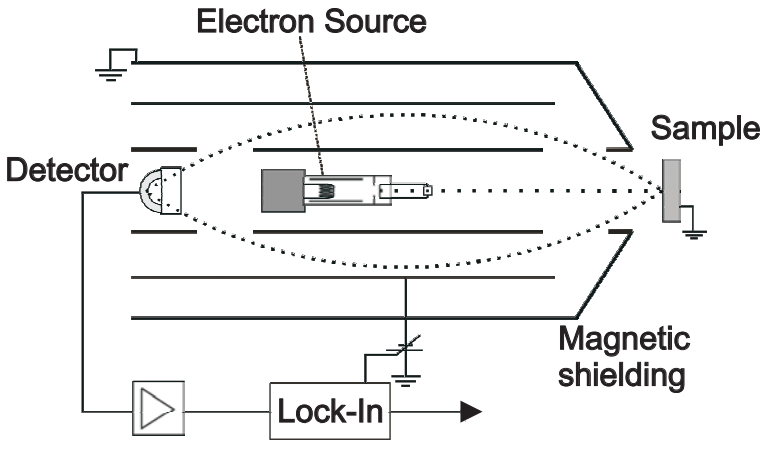

Figure 3.9: A technical scheme of an Auger Electron Spectrometer (AES).

The Auger electron spectrometer consists of a cathode emitting a focused electron beam onto the sample. It is mounted axially inside a cylindrical mirror analyzer (CMA), which performs the energy selection of the detected Auger electrons. A channeltron acts as a secondary electron multiplier and is placed in the back of the analyser.
Since Auger signals show a low intensity compared to the slowly increasing background of secondary electrons, the signal to noise ratio has to be optimized using lock-in technique by a modulation of the primary energy ramp on the CMA with a sinosoidal potential $\Delta V = k\,\sin(\omega t)$ while the recorded signal of the channeltron is amplified phase- and frequency-sensitively. The intensity I recorded as a function of the potential $V + \Delta V$ can be expanded in a Taylor series:

$$\begin{aligned} I(V + \Delta V) &= I(V) + \textstyle\sum_{i=1}^{n} \frac{d^n I(V)}{dV^n} \frac{\Delta V^n}{n!} \\ &= I(V) + I'(V)\,\Delta V + I''(V)\,\frac{\Delta V^2}{2!} + I'''(V)\,\frac{\Delta V^3}{3!} + \ldots \end{aligned} \tag{3.40}$$

Applying only small modulation amplitudes k, terms of order $n \geq 3$ can be neglected. By collecting the terms of different harmonics remaining, one obtains:

$$I(V + \Delta V) = I_0(V) + I'(V)\,k\,\sin(\omega t) + \tfrac{1}{4} I''(V)\,k^2\,\cos(2\omega t) \tag{3.41}$$

where $I_0(V)$ also contains terms constant in time arising from the higher expansion terms. The derivative spectrum of the dI/dV recording mode appears as prefactor to the first harmonic term. By tuning the CMA voltage to the first harmonic, the derivative spectrum is obtained. The size of the chosen modulation amplitude k influences the measured intensity as well as the resolution of the spectra. Larger modulation amplitudes result in increased peak intensities but also worsen the achievable energy resolution. A modulation amplitude of 1.25 V has been used in the current experiments.

3.6 The Tin Evaporator

The deposition of Sn on the Pt(111) sample is achieved by vaporization from a Knudsen cell. This cell is constructed from a Al_2O_3 crucible with a diameter of 5 mm (Fig. 3.10). It is filled with a tin wire and closed by a 2-hole ceramic. In order to monitor the temperature during the deposition process, a type K thermoelement can be fixed to the backside of the crucible. The Knudsen cell is heated by a tungsten wire (diameter 0.3 mm) wrapped around the crucible. Shielding the front of the water cooling jacket, a rotatable shutter is placed and allows to control the deposition time.

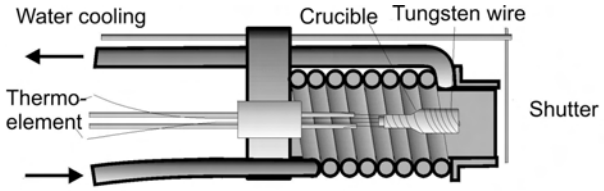

Figure 3.10: The Sn evaporator with the Knudsen cell.

The temperature of the Knudsen cell and thus the Sn evaporation rate is adjusted by the heating current. With a current of ∼6 A at ∼12 V, a deposition rate of ca. 1 ML per 15 min at a crucible temperature of ∼1300 K was achieved in the current geometry of this experimental setup [71].

Chapter 4

Theoretical Methods

The independent determination of many physical and chemical properties from experiments or from theory alone is sometimes a difficult task. Often only the combination of both, theoretical calculations and experiments, allows deeper insights into the microscopic description of complex physical and chemical problems. Various theoretical methods are available today. Of these, especially the density functional theory (DFT) has proven to be capable of dealing with large systems up to a few hundred atoms while still being an *ab initio* approach. Switching to periodic systems, it is possible to express the electronic wave functions into plane-waves (Chap. 4.3). With this intuitive expansion, one can reproduce electronic band structures (Bloch states) in periodic solids as well as on surfaces. The interaction of the core electrons with the ions is treated in the framework of the pseudopotential theory (Chap. 4.5).
In this chapter an overview over some DFT methods implemented in the *Vienna ab initio Simulation Package* (VASP) [72, 73, 74] shall be given. Furthermore it will be shown how the vibrational EELS and RAIRS spectra can be calculated from the ground state properties of the adsorption complexes (Chap. 4.6).

4.1 Density Functional Theory (DFT)

The properties of a system of N_e electrons and N_I nuclei can be derived from the solutions of the time-independent many-body *Schrödinger* equation

$$\hat{H}(\{\vec{r}\},\{\vec{R}\})\,\Psi(\{\vec{r}\},\{\vec{R}\}) \;=\; E_{tot}(\{\vec{R}\})\,\Psi(\{\vec{r}\},\{\vec{R}\}) \tag{4.1}$$

with the electron and nuclear coordinates $\{\vec{r}\}$ and $\{\vec{R}\}$. The *Hamiltonian* $\hat{H}$ of such a system can be written in a sum containing the kinetic energies of electrons and nuclei, the *Coulomb* interactions of electrons with each other, nuclei with each other plus finally the electron-nulcear electrostatic interaction terms.

$$\begin{aligned}\hat{H} \;=\; & -\tfrac{\hbar^2}{2m_e}\textstyle\sum_{i=1}^{N_e}\Delta_i \;-\; \tfrac{\hbar^2}{2M_j}\sum_{j=1}^{N_I}\Delta_j \;+\; \tfrac{e^2}{2}\sum_{i=1}^{N_I}\sum_{j\neq i}^{N_I}\tfrac{Z_i Z_j}{\left|\vec{R}_i-\vec{R}_j\right|} \\ & +\tfrac{e^2}{2}\sum_{i=1}^{N_e}\sum_{j\neq i}^{N_e}\tfrac{1}{|\vec{r}_i-\vec{r}_j|} \;+\; e^2\sum_{i=1}^{N_I}\sum_{j=1}^{N_e}\tfrac{Z_i}{\left|\vec{R}_i-\vec{r}_j\right|}\end{aligned} \tag{4.2}$$

Here m_e and M_I denote the masses of an electron and the nuclei, respectively, and Z_i is the charge of the nucleus i.
Using the *Born-Oppenheimer* (adiabatic) approximation [75], this equation can be simplified conveniently. Since the electron mass is roughly a factor of 1000 smaller than the nuclear masses, the nuclei can be considered static in the time frame of electron movement. The electrons are

permanently in their equilibrium and adjust instantly to any nuclear displacements. Therefore the total wave function can be decoupled into electronic and nuclear parts

$$\Psi(\{\vec{r}\},\{\vec{R}\}) \;=\; \tilde{\Psi}(\{\vec{r}\})\,\Phi(\{\vec{R}\}). \tag{4.3}$$

The positions and velocities of the nuclei can be treated classically. Then the total energy of the system is given by the linear superposition $E_{tot} \;=\; E_{kin}(\{R_I\}) + E_{el}^{ion-ion}(\{R_I\}) + E_{el}(\{R_I\})$. With the errors introduced by the adiabatic approximation in the order of $\sqrt{m_e/M_I}$, properties such as the vibrational frequencies can still be obtained with a precision of a few percent.
Now the *Schrödinger* equation has to be solved for all electrons in a static potential generated by the fixed nuclei. The exact analytical solution of the *Schrödinger* equation is possible only for smallest systems like H or He. For larger systems, one has to refer to numerical procedures, which still allow to achieve an accurate solution of the many-body problems. Yet the size of the quantum chemically treatable systems remains very limited, because the configuration space being the basis of the electronic wave functions generally scales exponentially. Compared to more extensive methods such as the *Configuration Interaction* scheme (CI) or the *Coupled-Cluster* theory (CC), which scale with the number of basis functions N as N^5 to N^7, the DFT approach provides a cheaper, yet still reasonably accurate tool to determine the physical and chemical observables. DFT generally has a much smaller scaling factor of typically N^3.

Basically, DFT approaches quantum chemical problems treating the electron density as variational parameter to minimize the total energy. The Density Functional Theory is based on two theorems formulated by P. Hohenberg, W. Kohn and L. J. Sham in 1964/65, which can be summarized as follows:

- Every observable in a quantum system can be calculated from the electron density of the system alone. (Hohenberg/Kohn) [76]
- The density of the interacting system can be approximated by the density of an auxilary system of noninteracting particles, which move in an external potential field. (Kohn/Sham) [77]

The consequence of the first statement is that all physical information is stored in the electron density. Once we know the exact electron density of a system, we principally can obtain all observables of interest. Yet for obtaining the exact electron density, there is no direct solution available. Here the second theorem will become of great importance, approximating the electron density by a noninteracting electron gas.
The electron density replacing the many-particle wavefunction from eq. 4.3 is given in a basis of orthonormal wavefunctions ϕ_i by

$$\rho(\vec{r}) \;=\; \sum_{i=1}^{N} |\phi_i(\vec{r})|^2 \qquad \text{with} \qquad \int \rho(\tilde{\mathrm{r}})\mathrm{d}\tilde{\mathrm{r}} \;=\; \mathrm{N}. \tag{4.4}$$

Note that this definition conserves the number of particles N. Following from the Hohenberg-Kohn theorem, the exact total energy is obtained by applying the variational principle to the electron density.

$$\frac{\delta E_{HK}}{\delta \rho(\vec{r})} \;=\; 0 \Leftrightarrow \rho(\vec{r}) \;=\; \rho_{exact}(\vec{r}) \tag{4.5}$$

Thus for the exact ground state density, the total energy E_{HK} has a minimum.

E_{HK} can be divided up into a term $F[\rho]$ containing the kinetic energy and the electron-electron interactions plus a term depending on an external potential V_{ext}. This is justified, since the external potential does not explicitly depend on the wave functions ϕ_i, but only on the electronic density ρ.

$$E_{HK}(\rho) \;=\; F[\rho] \;+\; \int V_{ext}(\vec{r})\,\rho(\vec{r})d\vec{r} \tag{4.6}$$

The first term is universal for all Coulombic systems, being valid for all external potentials. Therefore, the form of the external potential V_{ext} determines the electronic density. In fact, according to Hohenberg and Kohn, the electronic density, in turn, also defines the external potential:

$$V_{ext}(\vec{r}) \leftrightarrow \rho(\vec{r}). \tag{4.7}$$

The part of equation 4.6, which has to be minimized finally, is reduced to $F[\rho]$. Thus one is no longer confronted with finding the multi-particle wave function to a certain Hamiltonian, but instead has "only" to determine the universal form of the functional $F(\rho)$ valid for all quantum chemical problems.
The problem arising at this point is the definition of the universal functional $F(\rho)$, of which the exact form is unknown. Kohn and Sham suggested to split $F(\rho)$ into two terms, the kinetic energy $T[\rho]$ and the electron-electron interactions $V_{ee}[\rho]$, separating eq. 4.6 into:

$$\begin{aligned} E_{HK}(\rho) \;&=\; T[\rho] \;+\; V_{ee}[\rho] \;+\; \int V_{ext}(\vec{r})\,\rho(\vec{r})d\vec{r} \\ &=\; T[\rho] \;+\; J[\rho] \;+\; \tilde{E}_{xc}[\rho] \;+\; \int V_{ext}(\vec{r})\,\rho(\vec{r})d\vec{r} \end{aligned} \tag{4.8}$$

$V_{ee}[\rho]$ itself consists of the Coulombic electron-electron repulsions $J[\rho]$ and a "corrective" term $\tilde{E}_{xc}[\rho]$. While the effects of $T[\rho]$ and $J[\rho]$ are usually large, $\tilde{E}_{xc}[\rho]$ exerts only a small influence. Setting up the wavefunction ϕ in eq. 4.4 by an antisymmetric product in form of a *Slater* determinant $|\phi_{SD}\rangle$, the functionals on the left hand side can be approximated. The density ρ satisfying $\rho \rightarrow \phi_{SD}$ is called *n-representable*. Kohn and Sham showed that from n-representable densities created from antisymmetric wavefunctions, most of the kinetic energy of $T[\rho]$ can be obtained similarly to the *Hartee-Fock* theory:

$$T[\rho] \;=\; T_{SD}[\rho] \;+\; T_c[\rho] \;=\; -\frac{1}{2}\sum_{i=1}^{N} \left\langle \phi_i \left| \nabla^2 \right| \phi_i \right\rangle \;+\; T_c[\rho]. \tag{4.9}$$

The "noninteracting" kinetic energy $T_{SD}[\rho]$ is corrected by a term $T_c[\rho]$, which is assumed to be small. The approach using an antisymmetric wavefuntion allows to evaluate $J[\rho]$ easily, too. Thus the only unknown terms in eqs. 4.8 and 4.9 are $\tilde{E}_{xc}[\rho]$ and $T_c[\rho]$. Since both terms are expected to be small, they can be combined to the *Exchange-Correlation* funtional $E_{xc}[\rho]$:

$$\begin{aligned} E_{HK}(\rho) \;&=\; T_{SD}[\rho] \;+\; J[\rho] \;+\; T_c[\rho] \;+\; \tilde{E}_{xc}[\rho] \;+\; \int V_{ext}(\vec{r})\,\rho(\vec{r})d\vec{r} \\ &=\; T_{SD}[\rho] \;+\; J[\rho] \;+\; E_{xc}[\rho] \;+\; \int V_{ext}(\vec{r})\,\rho(\vec{r})d\vec{r}. \end{aligned} \tag{4.10}$$

The *Exchange-Correlation* funtional will be discussed more closely in chapter 4.2.

From the minimization requirement

$$\frac{\delta E_{HK}(\rho)}{\delta \phi_i} \;=\; 0 \tag{4.11}$$

applied to eq. 4.10, one obtains a new set of equations in the form of single-particle *Schrödinger* equations for all ϕ_i (building the derivatives of each term with respect to ϕ_i).

$$\left[-\frac{1}{2}\nabla^2 + v_{ext} + v_J + v_{xc}\right] \phi_i \;=\; \epsilon_i \phi_i \tag{4.12}$$

These are the *Kohn-Sham* equations. Neither the eigenfunction ϕ_i nor the ϵ_i, called the *Kohn-Sham* eigenvalues, have any direct physical meaning except for their connection to the total density. Nonetheless, with *Koopmans* theorem, the *Kohn-Sham* eigenvalue of the highest occupied molecular orbital (HOMO) relative to the vacuum level represents an approximation to the ionisation potential. The different potentials v can be combined to an effective potential v_{eff}

$$\left[-\frac{1}{2}\nabla^2 + v_{eff}\right] \phi_i \;=\; \epsilon_i \phi_i, \tag{4.13}$$

showing that the noninteracting particles represented by the ϕ_i move in an effective potential field. Once the form of the *Exchange-Correlation* potential v_{xc} is known, these equations can be solved self-consistently [74], similar to the *Hartee-Fock* theory. Therefore the operator given in brackets is called the *Kohn-Sham* Fock operator.

4.2 Exchange-Correlation Functionals

The only unknown in the DFT formalism is the exact form of the *Exchange-Correlation* functional $E_{xc}[\rho]$ and its corresponding derivative, the *Exchange-Correlation* potential v_{xc}. Basically, the *Exchange-Correlation* functional contains the electron exchange energy, treated exactly in the *Hartee-Fock* formalism, but it completely neglects any correlation parts, which consist of the difference between the kinetic energies of the noninteracting and the interacting electrons [78]. Many approximations to the *Exchange-Correlation* potential exist. A comprehensive review of these approximations is given in [79]. These approximations to the *Exchange-Correlation* potential can be separated into three groups:

- the local (spin) density approximation (LDA or LSDA),
- the generalized gradient approximation (GGA),
- and the hybrid functionals including *Hartree-Fock* exchange contributions.

In the local density approximation, it is assumed that the contribution of E_{xc} at a point $\vec{r}$ in space depends only on the density $\rho(\vec{r})$ at this certain point. It can be derived from the exchange and correlation term of uniform electron gas (UEG) with a certain density at a given point. The E_{xc} functional in the LDA approximation is also local in the sense that it is multiplicative:

$$E_{xc}^{LDA}[\rho] \;=\; \int \epsilon_{xc}^{LDA}(\rho(\vec{r}))\, \rho(\vec{r})\, d\vec{r}. \tag{4.14}$$

Despite the simplicity of this approximation, it gives good results for electronic properties, especially in the case of metallic solids, where electronic density varies only slowly. As soon as the electronic density shows strong variations, such as for semi-conductors, the errors introduced by this approximation grow sizable. Yet the LDA functionals give still acceptable results in such cases and can be well compared to results obtained from HF calculcations. Typical LDA functionals are the B88 (Becke, 1988 [80]), the VWN (Vosko-Wilk-Nusair, 1980 [81]) and the PW92 (Perdew-Wang, 1992 [82]) approximations. Notably, the Vosko-Wilk-Nusair functional was obtained by fitting E_{xc} to the results of Monte-Carlo calculations for a uniform (homogeneous) electron gas. Using the spin-decomposed density $\rho(n\uparrow, n\downarrow)$, the VWN

functional can be rewritten in the local spin density approximation LSDA. Here the exchange part effects only electrons of the same spin, while the correlation term involves all electrons.

To improve the behaviour of DFT in cases with strongly varying electronic densities, various E_{xc} functionals in the generalized gradient approximation (GGA) have been developed. Generally, they represent a compromise between purely local functionals and non-local functionals, since they include the gradient of the density $\nabla\rho$, which offers some non-local information (Eqn. 4.15; ϵ_{xc}^{GGA} is usually termed the "enhancement factor"). This gradient varies strongly in the vicinity of nuclear potentials, while at larger distances from the potentials the slope will become small.

$$E_{xc}^{GGA}[\rho] \;=\; \int \epsilon_{xc}^{GGA}(\rho(\vec{r}), \nabla\rho(\vec{r}))\,\rho(\vec{r})\,d\vec{r}. \tag{4.15}$$

Among such "semi-local" functionals, especially the PW86 (Perdew, 1986 [83]), PW91 (Perdew-Wang, 1991 [82]), the LYP (Lee-Yang-Parr, 1988 [84]) and the PBE (Perdew-Burke-Ernzerhoff, 1996 [85]) have to be named. The PW86 functional, based on the exact properties of the UEG, is one parameter functional fitted to the accurate energy of Ne. Similarly, the LYP functional, which is based on the correlation properties of the He atom, is a one parameter functional.
The PW91 presents a parameter free functional. It uses only UEG data and exact conditions, thus it is purely *ab-initio*. This functional is known to give reasonably precise results for total energies as well as for physical properties like dipole moments or the density of states [78, 82]. Also long-range interactions are described correctly by PW91 as the asymptotic behavior is reproduced by its kernel. Therefore this functional has been used for the calculations performed throughout this work. In a few cases, the quality of the results obtained have been compared to results from similar calculations performed using the PBE functional. These calculations yielded qualitatively the same results. Total energies, calculated vibrational frequencies and loss intensities differ by less then 2%. These benchmark calculations will be discussed in the following chapters.
Finally, the PBE functional corrects *some* of the short-comings occuring for small and large density gradients in the PW91 functional on which it is based. The chemisorption energies computed with PBE are known to change only marginally compared to PW91 [78].
In recent years, the semi-local GGA and also the local LDA functionals have been combined with the *Hartee-Fock* exchange [78, 86], forming the *hybrid* functionals. This development originated from several deficiencies, from which the previously available functionals lacked. Although the GGA and LDA functionals are able to achieve a sufficient accuracy in the treatment of most of the typical chemical problems, notably the LDA kernels failed to correctly reproduce binding energies or barrier heights necessary for studies of reactivity. The quality of the GGA results is generally better, but still can be refined. The discrepancies are due to the derivation, which is based on the assumption of a uniform electron gas. This is a situation, which is clearly not consistent with the electron density present in molecules. Moreover, since DFT does not make any statements about excited states, these functionals systematically underestimate band gaps of semi-conductors. Therefore new approximations had to be developed to overcome these shortcomings of the Kohn-Sham theory.
This was achieved by a modification of already existing functionals by including partial contributions of the nonlocal *Hartee-Fock* exchange. With the "generalised" Kohn-Sham scheme developed by Seidl et al. [87], a framework is available, in which nonlocal potentials like the *Fock* exchange operator can be used in the single-particle Kohn-Sham equations. This approach indeed improved the situation for the calculation of band gaps with DFT. Yet since the HF exchange does not incorporate dynamical correlation effects, but only the correlation arising from *Pauli* principle, the necessity for further improvements still remained. Combining the underestimation of band gaps in DFT with the fact that the HF theory systematically overestimates

these gaps in the electronic density of states, one could expect that a well conceived mixture of both theories might lead to an improvement.
Both contributions can be combined using an exact relation between E_{xc} of a noninteracting reference system and the real fully interacting system, which is given by the *adiabatic connection formula* [88]. This equation 4.16 uses the inter-electronic coupling strength parameter λ to "switch" the Coulomb interaction "on or off".

$$E_{xc}[\rho] \;=\; \int_{\lambda=0}^{1} d\lambda\, \epsilon_{xc}^{\lambda} - J[\rho] \tag{4.16}$$

The $\lambda = 0$ limit of the adiabatic connection formula is known exactly, because this is the exact exchange of the Kohn-Sham determinant. It is given by E_x^{HF}. The $\lambda = 1$ limit on the other side can be well estimated from the LSDA potential and amounts to exchange and correlation E_{xc}^{LSDA}.
Becke used as a first approximation a half-and-half mixture of the nonlocal HF exchange energy of the Kohn-Sham orbitals and the LSDA (SVWN) potential energy of exchange and correlation in his functional [89].

$$E_{xc}^{HH}[\rho] \;=\; \frac{1}{2}E_x^{HF} \;+\; \frac{1}{2}E_{xc}^{LSDA} \tag{4.17}$$

With this functional a reasonable accuracy for chemical problems was achieved, yet it failed to reproduce the uniform gas limit. Total energies computed with this functional proved to be rather poor, too. To correct these errors, Becke developed a more flexible scheme by the introduction of gradient correction terms and weighting all terms with three semi-empirical factors, which he fitted to experimental data of a set of molecules [89]. Commonly his functional is denoted B3WP91 in the literature:

$$E_{xc}^{B3PW91}[\rho] \;=\; E_{xc}^{LSDA} \;+\; a_0\left(E_x^{exact} - E_x^{SVWN}\right) \;+\; a_x\Delta E_x^{B88} \;+\; a_c\Delta E_c^{PW91} \tag{4.18}$$

It uses the Becke 88 GGA exchange contribution [80] together with the difference between PW91 and LSDA correlation ΔE_c^{PW91}.
Today a slight variation of this functional proposed by Stevens et al. [90] has gained popularity.

$$E_{xc}^{B3LYP}[\rho] \;=\; (1-a_0)\,E_{xc}^{LSDA} \;+\; a_0E_x^{exact} \;+\; a_x\Delta E_x^{B88} \;+\; a_cE_c^{LYP} \;+\; (1-a_c)\,E_c^{VWN} \tag{4.19}$$

Since the LYP correlation functional [84] includes both nonlocal (gradient corrected) and local terms, a factor of $(1 - a_c)$ has been applied to the purely local VWN correlation functional [81]. The resulting B3LYP functional has been shown to give very accurate results for binding energies, even for weakly bound systems, for bond lengths and many other physical properties [78].
Hybrid functionals have not yet gained popularity in solid state physics. This might be because the implementation of the exact exchange part of the hybrid functionals in plane-wave codes has been regarded as being too inefficient. Recently a method was published by Chawla and Voth [91], which allows an efficient implementation of the exact exchange in plane-wave algorithms. Such attempt to implement hybrid functionals into the VASP code is currently being made [78] (see also the official VASP homepage at the University of Vienna, *http://cms.mpi.univie.ac.at/VASP/*).
Two more issues of the previously discussed exchange-correlation functionals have to be mentioned here in order to raise the awareness to the accuracy of the results being presented in the following chapters. Firstly, a major deficiency of the present exchange-correlation functionals in the context of this thesis is insufficient treatment of nonbonded interactions as for example the *Van der Waals* (VdW) type [92, 93, 94, 95, 96, 97]. Although contributing only weakly to the adsorption energies, these long-ranged interactions can play a major role in processes, in

which the chemical bonds are also weak. This may be the case in the adsorption of molecules on rather inert surfaces or the interaction of saturated molecules (for i.e. alkanes) with other systems. VdW interactions originate from a long-range correlation of the electrons of a chemical systems, which can be either distant and thus non-overlapping or simultaneously chemically interacting. Generally DFT in its *exact* formalism includes the nonbonding interactions, yet due to the long-ranged character the local (LDA) and semi-local functionals fail to capture their essence [92, 93, 94, 95, 96, 97]. The GGA functionals include a part of the attractive *London* dispersion forces, but their results show an underestimation of the nonbonded interactions, which is unsystematic when compared to state-of-the-art CCSD(T) calculations [92]. Therefore new approaches have been studied in the past, including this attractive contribution explicitly. For the interaction of atoms or molecules the text-book example of a Lennard-Jones term, $E_{VdW} = -C_6/R^6$, can be used [95, 98, 99, 100]. The parameter C_6 depends on the polarizabilities of the two particles. For particles on surfaces, a related approach using a distance dependency of R^{-3} can be followed. Although the parameters of these non-standard methods are basically accessible from *ab initio* calculations, they have to be treated with care in each case.

Approaches proposed by other groups include the formulation of new GGA functionals, which are based on the augmentation of standard LDA, GGA (PW91) or hydrid kernels (B3LYP) by nonlocal correlation parts. The nonlocal contributions can be approximated for example from a combination of the PW91 (sound physical basis) and the B88 GGAs (which leads to good results for thermochemical and structural parameters in B3LYP, but miss the London dispersion forces) (X3LYP) [96] or from isotropic dielectric functions [93, 94, 97] (vdW-DF). The problems arising from the deficiency of the standard DFT functionals will be discussed later on in the sections dealing with the interaction of prenal and crotonaldehyde with the $Pt_2Sn(111)$ surface alloy, which are rather weak and thus might lead to a non-neglectable underestimation of the adsorption energies.

Secondly, a basic deficiency encountered with the commonly used exchange-correlation functionals is the unphysical self-interaction of an electron with itself. In HF theory as well as the exact derivation of the DFT equations, the interaction of an electron with itself via the Coulomb energy is perfectly cancelled by a corresponding term from the exchange-correlation energy. Yet caused by the introduction of the local or semi-local approximations, these terms fail to cancel each other completely. The correction of these errors has lead to the development of the Self-Interaction Correction (SIC) functionals [101, 102], which add a new term describing the self-interaction energies of all electrons to the exchange-correlation functionals to improve the cancellation. Applying such functionals leads to considerably better agreement of the exchange and the correlation energies with the *exact* values and also eigenvalues show an improved comparability to the ones obtained from HF theory. Nonetheless, also the SIC functionals come with some systematic deficiencies and finally lead to strongly increased computational costs. So one must decide in each particular case, whether the improvement of accuracies outweights the increased computational effort.

4.3 The Supercell Approach and Plane Waves

Naturally the choice to model periodic systems is the supercell approach. It uses the inherent translational symmetry of the considered system in all three space dimensions. The periodic boundary conditions imposed in this way enable to approximate the electronic wave functions, which are used to solve the Kohn-Sham equations, by plane waves. Therefore expanding the single-particle wave functions in sums of plane waves constrains the Kohn-Sham orbitals and all cell periodic functions such as the charge density or the potential to satisfy Bloch's theorem.

The theorem of Bloch implies that the electronic wave functions of the band n at a point $\vec{k}$ in

the Brillouin Zone (BZ) comply with eq. 4.20 for all translational vectors $\vec{\tau}$, which leave the Hamiltonian $\hat{H}$ invariant.

$$\Psi_{n,\vec{k}}(\vec{r}+\vec{\tau}) \;=\; \Psi_{n,\vec{k}}(\vec{r})\, e^{i\vec{k}\vec{\tau}} \tag{4.20}$$

Here a cell periodic part $u_{n,\vec{k}}(\vec{r})$ can be introduced, which also depends on the position $\vec{k}$ in the BZ and the band n:

$$\Psi_{n,\vec{k}}(\vec{r}) \;=\; u_{n,\vec{k}}(\vec{r})\, e^{i\vec{k}\vec{r}}. \tag{4.21}$$

The cell periodic function u can be expanded into plane waves (eq. 4.22) with a given cutoff vector $\vec{G}$ (eq. 4.23).

$$u_{n,\vec{k}}(\vec{r}) \;=\; \frac{1}{N^{1/2}} \sum_{\vec{G}} c_{\vec{G},n,\vec{k}}\, e^{i\vec{G}\vec{r}} \tag{4.22}$$

$$\frac{\hbar^2}{2m_e} \left|\vec{G}+\vec{k}\right|^2 < E_{cutoff} \tag{4.23}$$

All plane waves $\left|\vec{G}+\vec{k}\right|$, which have a lower kinetic energy than the cutoff energy, are included in the expansion of the wave function and thus form the basis set.
Finally, inserting eq. 4.22 in eq. 4.21, one obtains for the electronic wave functions the general expression

$$\Psi_{n,\vec{k}}(\vec{r}) \;=\; \frac{1}{N^{1/2}} \sum_{\vec{G}} c_{\vec{G},n,\vec{k}}\, e^{i(\vec{G}+\vec{k})\vec{r}}\,. \tag{4.24}$$

The plane wave basis sets are very convenient and bring about certain advantages of both technical and also practical origin:

- Firstly, many typical solids exhibit electronic band-structures, which can be understood from a free-electron gas model. The wave functions applicable to this free-electron picture are represented by plane waves.

- The transformation of the (plane) wave functions from real space into reciprocal space and vice versa can be performed highly efficient using the Fast Fourier Transformation (FFT) routines. Expressions such as the total energy can thus be implemented technically very simply. Therefore also the evaluation of expressions like $\hat{H}\,\Psi_{n,\vec{k}}(\vec{r})$ is highly efficient using the FFT routines (see further [78] and references therein).

- Since only the coefficients $c_{\vec{G},n,\vec{k}}$ need to be stored on harddisks during the calculation, the memory requirements are comparably small (The RAM requirements are in contrast large as both the charge density and the plane waves need to be handled).

- The basis set convergence can be checked very easily by increasing the kinetic cutoff vector $\vec{G}$ of the included plane waves.

- Additional correction terms to account for spatial variations as seen in the case of localized basis sets are avoided when using a plane wave basis, because the latter is independent of the atomic positions.

Despite these advantages, a serious drawback of this *Ansatz* has to be solved first: Plane waves are well suited to describe a free-electron situation, but this expansion is troublesome when considering strongly localized electrons in a potential well like the nuclear potential, where the wave functions vary drastically. For this reason a plane wave expansion becomes prohibitively large in order to obtain reasonably converged results when including core electrons.
It is commonly assumed that the core electrons do not participate in the chemically interesting inter-atomic interactions. A solution to the problem of strongly localized electrons can thus be anticipated by eliminating the core electrons from the plane wave DFT calculations. This solution leads to the pseudopotentials, which will be the topic of chapter 4.5.

4.4 Brillouin Zone Sampling and Smearing Methods

Due to the dispersion in the Brillouin Zone, many physical properties like the charge density, the density of states (DOS) and various matrix elements have to be evaluated using integrals over the Brillouin Zone [103]. These integrals are technically solved by weighted sums over discrete points k_i in the Brillouin Zone. The weighting coefficients $w_{\vec{k}_i}$ in those sums depend on the K selected k-points and thus also the symmetry of the Brillouin Zone.

$$A(\epsilon) \propto \int_{BZ} A_{n\vec{k}}(\epsilon)\Theta(\epsilon_{n\vec{k}} - \epsilon)d\vec{k} \quad \leftrightarrow \quad \sum_{i=1}^{K} w_{\vec{k}_i} A_{n\vec{k}_i}(\epsilon)\Theta(\epsilon_{n\vec{k}_i} - \epsilon) \quad \forall m \in \{1, 2, ...\} \tag{4.25}$$

Here $\Theta(\chi)$ is the Dirac step function giving the occupancy of a band n at a point k in the BZ:

$$\Theta(\chi) = \begin{cases} 1, & \forall \chi \leq 0 \\ 0, & \forall \chi > 0 \end{cases} \tag{4.26}$$

Since the properties such as the wave function usually do not vary drastically between neighboring k-points, a summation over a limited number of *special* k-points is already a good approximation to the true integral.
In this thesis the method of the Monkhorst Pack [104] has been used to set up the special k-point meshes in the BZ. Its idea is to interpolate an equally spaced mesh in the BZ. Depending on the symmetry of the system and the number of special k-points selected, the mesh has to be centered on the Γ point of the unit cell. For instance in the case of a hexagonal cell, uneven numbered k-point meshes are automatically set up to be centered on the Γ point, while for even meshes one has to make sure that the origin of the mesh is shifted accordingly. This is necessary in order to avoid a breaking of the symmetry of the system, which would lead to non-equal distribution of the special k-points throughout the IBZ.
Using the symmetry of the superlattice one can reduce the number of required k-points further. In this case, the whole (Reducible) Brillouin Zone is mapped onto the Irreducible Brillouin Zone (IBZ), which is defined as the smallest subspace necessary to reproduce the complete system using its corresponding symmetry operations. Finally, after the selection of the special k-points in the IBZ has been performed, their proper weighting coefficients $w_{\vec{k}_i}$ are calculated.
Another problem of the integration of properties in the BZ (see eq. 4.25) arises from the Dirac step function Θ, which is discontinuous at the Fermi-level. The discontinuity leads to a painfully slow convergence with respect to the number of k-points included. On the one hand, the integral can be solved for completely filled bands using only a few k-points. This for instance is the case for insulators or semi-conductors. On the other hand, for metals, the concept of partial occupancies has been introduced, replacing the Dirac step function by a smooth partial occupancy or "smearing" function $f(\epsilon_{n\vec{k}})$. *Ansatz* 4.27 results in a much improved convergence behavior and smaller sets of k-points required to retain the precision of the integrals.

$$A(\epsilon) \propto \sum_{i=1}^{K} w_{\vec{k}_i} A_{n\vec{k}_i}(\epsilon)\Theta(\epsilon_{n\vec{k}_i} - \epsilon) \leftrightarrow \sum_{i=1}^{K} w_{\vec{k}_i} A_{n\vec{k}_i}(\epsilon) f(\epsilon_{n\vec{k}}) \quad \forall m \in \{1, 2, ...\} \tag{4.27}$$

In order to define $f(\epsilon_{n\vec{k}})$, several methods have been established. Among the Finite Temperature approaches the Fermi-Dirac functions [105] (eq. 4.28) and the Gaussian function (eq. 4.29) have to be recalled.

$$f\left(\frac{\epsilon_{n\vec{k}} - \epsilon}{\sigma}\right) = \frac{1}{\exp\left(\frac{\epsilon_{n\vec{k}} - \epsilon}{\sigma}\right) + 1} \tag{4.28}$$

$$f\left(\frac{\epsilon_{n\vec{k}} - \epsilon}{\sigma}\right) = \frac{1}{2}\left(1 - erf\left[\frac{\epsilon_{n\vec{k}} - \epsilon}{\sigma}\right]\right) \tag{4.29}$$

Since these functions are commonly used in solid state calculations, they shall be discussed here shortly. As it turns out, the total energy is no longer variational (minimal) when using these smearing methods. To solve this drawback, a generalized free energy functional F is introduced:

$$F = E - \sum_{n\vec{k}_i} w_{\vec{k}_i} \sigma S\left(f_{n\vec{k}_i}\right). \tag{4.30}$$

In the Fermi-Dirac statistics the term $S\left(f_{n\vec{k}_i}\right)$ can be interpreted as the generalized entropy of a system of non-interacting electrons at a finite temperature T, which can be defined via the smearing parameter $\sigma = k_B T$. Yet in the case of Gaussian smearing, σ (and hence also S and F) is of no physical meaning. Nonetheless, with both methods an extrapolation towards $\sigma \to 0$ can be performed:

$$E_0 \approx E(\sigma \to 0) = \frac{1}{2}\left(F(\sigma) + E(\sigma)\right). \tag{4.31}$$

A second drawback of these two approaches is the fact that the calculated forces are the derivatives of the free energy F. They are just an approximation to the forces found at the ground state forces, where $E_0 = E$.
A further development of the Gaussian smearing is represented by the method of Methfessel and Paxton [106]. The idea behind this approach is to expand the Dirac step function in a set of orthogonal functions. The term of zeroth order is given by the Gaussian smearing function. The functions of higher order are derived from Hermite-polynomials of the corresponding order j.

$$f_N(x) = f_0(x) + \sum_{j=1}^{N} \frac{(-1)^j}{j! 4^j \sqrt{\pi}} H_{2j-1}(x)\, e^{-x^2} \tag{4.32}$$

With this approach the extrapolation of $\sigma \to 0$ can usually be omitted, because the deviation of F from E (the entropy term) is generally small for a reasonable σ.

$$E_0 \approx E(\sigma \to 0) = \frac{1}{N+2}\left((N+1)F(\sigma) + E(\sigma)\right). \tag{4.33}$$

Hence the forces obtained from the derivatives of $F(\sigma)$ represent a good approximation to the ground state forces in the case of the Methfessel-Paxton method. In practice it is seen that for metals already a smearing function of the order $N = 1$ or $N = 2$ is sufficient to reach reasonably precise results with a fast convergence, if the parameter σ has been chosen carefully (see further details in the *VASP Guide*). Therefore also the forces computed for metallic systems using this method are close to the real forces.

Finally the linear tetrahedron method to solve the integration eq. 4.25 and its corrections by Blöchl [107] shall be described here in short. It divides the BZ into linked tetrahedra, whose corners are formed by k-points. The function $A_{n\vec{k}_i}$, which is to be integrated, is interpolated linearly between two k-points of such a tetrahedron. In the last step of the linear tetrahedron method, the interpolated function is integrated. This method has been revised and its shortcomings corrected by Blöchl [107]. He introduced the corrected effective weights $f(\epsilon_{n\vec{k}})$ for each band n in the BZ and also proposed a correction for the quadratic errors that were inherent previously. Again a major drawback of this method is the calculation of the forces. Like for the smearing methods described above, the energy obtained here is no longer variational with respect to the partial occupancies and thus the first derivatives represent only an approximation to the true forces at the ground state. Nonetheless, the linear tetrahedron method with Blöchl corrections is in pratice advantageous for the computation of total energies or the investigation of the DOS of a periodic system.

4.5 Pseudopotential Theory

The separation of the electronic shells into valence electrons and core electrons is a proven chemical concept, based on the assumption that the valence electrons mainly determine the chemical properties of an element. The core electrons occupy inner, chemically inert shells of the atoms. Their main effect is to shield the valence electrons from the nuclear charge. Therefore, if one invokes a frozen core approximation, these core electrons can be eliminated from electronic structure calculations, replacing them instead by an effective core potential (ECP) acting on the valence electrons.
The wavefunctions of the valence electrons ϕ_v normally vary rapidly in the core region, a phenomenon induced by the requirement of the orthogonality $\langle \phi_c | \phi_v \rangle = 0$ between the core wavefunctions ϕ_c and valence states. If this requirement is removed, obviously also the constraint disappears. So one can replace the true valence wavefunctions by pseudo wavefunctions, which vary smoothly around the nucleus [108, 109].

4.5.1 Norm-conserving and Ultra-soft Pseudopotentials

By projecting the true wavefunctions on a set of pseudo wavefunctions, the core states can be eliminated and the valence electrons can be replaced by their pseudo wavefunctions:

$$|\psi_v\rangle = |\phi_v\rangle + \sum_c \beta_c |\psi_c\rangle \qquad \text{with} \qquad \beta_c = \langle \psi_c | \psi_v \rangle . \tag{4.34}$$

In this manner, the rapid changes of ϕ_v in the spatially limited core region are eliminated in the replacing pseudo wavefunction ψ_v. To project states onto the core states, a projection operator $\hat{P}$ is defined [108]:

$$\hat{P} = \sum_{\acute{c}} |\psi_{\acute{c}}\rangle \langle \psi_{\acute{c}}| \tag{4.35}$$

This projection operator shall satisfy two requirements, which can be easily proven:

$$\begin{aligned} \left(1 - \hat{P}\right) |\psi_c\rangle &= 0 \qquad \text{and} \\ \left(1 - \hat{P}\right) |\phi_v\rangle &= |\psi_v\rangle . \end{aligned} \tag{4.36}$$

Since the ψ_v (and of course also the ψ_c) obey the *Schrödinger* equation $\hat{H} |\psi_v\rangle = E |\psi_v\rangle$, substituting eq. 4.34, one can write:

$$\begin{aligned}
\hat{H}\,|\phi_v\rangle \quad &- \quad \hat{H}\sum_c \beta_c\,|\psi_c\rangle \,+\, E\sum_c \beta_c\,|\psi_c\rangle \quad = \quad E\,|\phi_v\rangle \\
\Leftrightarrow \hat{H}\,|\phi_v\rangle \quad &- \quad \sum_c \beta_c E_c\,|\psi_c\rangle \,+\, E\sum_c \beta_c\,|\psi_c\rangle \quad = \quad E\,|\phi_v\rangle \\
\Leftrightarrow \hat{H}\,|\phi_v\rangle \quad &- \quad \sum_c \beta_c\,(E_c \,-\, E)\,|\psi_c\rangle \quad = \quad E\,|\phi_v\rangle \\
\Leftrightarrow \left(\hat{T} + \hat{V}\right)|\phi_v\rangle \quad &- \quad \sum_c \beta_c\,(E_c \,-\, E)\,|\psi_c\rangle \quad = \quad E\,|\phi_v\rangle\,.
\end{aligned} \tag{4.37}$$

Here the pseudopotential $\hat{V}^{PS}$ can be defined using eq. 4.34:

$$\hat{V}^{PS} \,=\, \hat{V} \,+\, \sum_c \beta_c\,(E_c \,-\, E)\,|\psi_c\rangle\,\langle\psi_c|\,. \tag{4.38}$$

with which a pseudo-*Schrödinger* equation, usually referred to as the pseudopotential (PP) equation can be formulated:

$$\left(\hat{T} \,+\, \hat{V}^{PS}\right)|\phi_v\rangle \,=\, E\,|\phi_v\rangle\,. \tag{4.39}$$

This equation provides the same eigenvalues as the exact all-electron *Schrödinger* equation, but the core levels are missing.

Although with this equation the original goal is met, it still has two weaknesses. One is connected to $\hat{V}^{PS}$, which contains a nonlocal operator $\hat{P}$ as well as the unknown eigenvalues E. The other weakness is derived from eq. 4.34, using the orthogonality between true core and valence states:

$$\langle\phi_v|\phi_v\rangle \,-\, \left\langle\psi_{\acute{c}}|\hat{P}|\psi_{\acute{c}}\right\rangle \,=\, \langle\psi_v|\psi_v\rangle \tag{4.40}$$

Evidently, if the pseudo wavefunction is normalized, the true wave function is not. This difference between the exact density and the pseudo charge density, called orthogonalization hole, is a result of the nonlocality of $\hat{V}^{PS}$.

Basically there are to ways to build suitable pseudopotentials: either by means of empirical model potentials, or through derivation from all-electron *ab initio* calculations. Today typically used pseudo potentials belong to the latter group.

Assuming a spherical screening, the radial *Kohn-Sham* equations

$$\left[-\frac{1}{2}\frac{d^2}{dr^2} \,+\, \frac{l(l+1)}{2r^2} \,+\, V\,(\rho(r))\right]\psi_{nl}(r) \,=\, E_{nl}\psi_{nl}(r), \tag{4.41}$$

with

$$V\,(\rho(r)) \,=\, -\frac{Z}{r} \,+\, V^J\,(\rho(r)) \,+\, V_{xc}^{LDA}\,(\rho(r)) \tag{4.42}$$

and the wavefunctions $\psi_{nl}(r) \,=\, rR_l(r)$, can be solved.
This method has been extended to the GGA approach [110, 111]. In order to be considered an *ab initio* pseudopotential, the PP must be constructed in such a manner that they satisfy four general conditions [112, 113, 114]:

- Valence pseudo wavefunctions generated from the PP should be nodeless;

- Norm conservation: Beyond a chosen cut-off radius r_c, the normalised radial pseudo wavefunction must be equal (or converge rapidly) to the normalised all-electron wavefunction [113]:

$$R_{nl}^{PS}(r) \;=\; R_{nl}^{AE}(r) \qquad \forall\, r \geq r_c \tag{4.43}$$

- For a given atomic configuration, the eigenvalues of the exact and associated pseudo wavefunction must be the same, i.e. $E^{PS} = E^{AE}$.

- The charge density of the exact and the pseudo wavefunctions in the core region $r \leq r_c$ must be conserved [112], i.e.

$$\int_0^{r_c} r^2 \left|R_{nl}^{PS}(r)\right|^2 dr \;=\; \int_0^{r_c} r^2 \left|R_{nl}^{AE}(r)\right|^2 dr. \tag{4.44}$$

Furthermore, the pseudo wavefuntion inside the core region is chosen in such a way that it represents the scattering properties of the all-electron wavefunction in an energy window around the atomic reference energy. This property is essentialy described by the logarithmic derivative $\chi_{l\epsilon}$ of the wave function and its energy dependence

$$\chi_{l\epsilon} \;=\; \frac{d}{dr} \ln\left(\psi_{l\epsilon}(r)\right) \;=\; \frac{1}{\psi_{l\epsilon}(r)} \frac{d}{dr} \psi_{l\epsilon}(r). \tag{4.45}$$

Here the choice of the core radius r_c controls the achieveable accuracy and the transverability of the PP, because the first order energy derivative of the logarithmic derivatives $\chi_{l\epsilon}$ of the pseudo and the all-electron wavefunctions have to conincide at r_c [112].
As shown by Topp and Hopfield [115], this criterion of the energy derivative of $\chi_{l\epsilon}$ is essentially equivalent to the norm conservation condition inside the core radius. Extending this concept, the *Norm-Conserving* pseudopotentials (NC-PP) have been established by Hamann et al. [112].

The NC-PP work well except for the first row transition metals. Due to the conservation of the charge density in the core region, the calculation of total energies may present a serious problem when using plane-wave basis sets. This becomes especially true for the first row transition metals, which are characterized by well localized d-electrons. The condition of norm conservation prohibts the use of large cut-off radii, which is basically caused by the fact that the valence wavefunctions are already nodeless and thus the construction of a PP only shifts the maximum of the wavefunctions. Several attempts have been performed to generate smooth PP in a plane-wave basis [116, 117, 118, 119]. Independently, Vanderbilt [118] and Blöchl [119] solved this problem dropping the norm conservation requirement. Using lower kinetic cut-offs for the plane-wave expansion and improving the smoothness and the matching of the logarithmic derivatives at several reference energies, they introduced the *Ultra-Soft* pseudopotentials (US-PP).

Finally, the pseudopotential itself is obtained by inverting the radial *Kohn-Sham* equation 4.41 with the correspondingly generated pseudo wavefunctions:

$$V_l^{PS}(r) \;=\; E_l \;-\; \frac{l(l+1)}{2r^2} \;+\; \frac{1}{2rR_l^{PS}(r)} \frac{d^2}{dr^2} \left[rR_l^{PS}(r)\right] \tag{4.46}$$

Because one gets a PP for each spherical quantum number l, they have to be combined in a single potential using projection operators that subsequently also enter in the DFT energy functionals.

4.5.2 The Projector Augmented-Wave Method (PAW)

The projector augmented-wave method aims to combine the advantages of the computationally less demanding pseudopotential approach with the precision of all-electron calculations, hence it can be considered a frozen-core all-electron method. As already mentioned, the wave functions of materials behave very differently in the different regions of space: While being smooth in the bonding region, they oscillate rapidly in the core region. This phenomenon is caused by the attractive potential of the nucleus; it is the source of the difficulty of electronic structure approaches to accurately describe the large variations in the core region whilst retaining this precision also in the bonding region. First established by Blöchl et al. [120], the PAW approach follows the strategy to separate the wave functions into two parts. In a sphere centered around a nucleus the wave functions is expanded into partial-waves; outside this sphere, the pseudo wave function is constructed in a plane wave basis or another convenient basis set. At the sphere radius itself, the values and the first derivatives of the partial-wave expansion and the envelope wave function coincide. Both connect smoothly to each other.
The linear transformation of the exact wave function $|\psi\rangle$ into the pseudo wave function $\left|\tilde{\psi}\right\rangle$ is given by

$$|\psi\rangle \;=\; \left|\tilde{\psi}\right\rangle - \sum_{N,i} \left|\tilde{\phi}_{N,i}\right\rangle c_{N,i} + \sum_{N,i} |\phi_{N,i}\rangle \, c_{N,i} \tag{4.47}$$

The ϕ are local wave functions and the $\tilde{\phi}$ are the partial waves. The indices N denote all atomic sites and i goes over all quantum numbers $\{l, m\}$ and refers to a particular reference energy ϵ. Thus the exact all-electron wave function is constructed from a pseudo wave function, a local "pseudo-onsite" and an all-electron onsite contribution. The variational quantities in the PAW method are the pseudo wave functions $\left|\tilde{\psi}\right\rangle$.
In equation 4.47 the expansion coefficients $c_{N,i}$ are defined by localized projector functions:

$$c_{N,i} \;=\; \left\langle \tilde{p}_i \,|\, \tilde{\psi} \right\rangle . \tag{4.48}$$

These projector functions must be dual to the pseudo wave functions

$$\left\langle \tilde{p}_{lm\epsilon} | \tilde{\phi}_{l'm'\epsilon'} \right\rangle \;=\; \delta_{l,l'} \, \delta_{m,m'} \, \delta_{\epsilon,\epsilon'}, \tag{4.49}$$

which allows to reconstruct the all-electron and the pseudo wave functions at an atomic site N easily from the plane-wave expanded pseudo wave function as

$$|\psi_N\rangle \;=\; \sum_i |\phi_{N,i}\rangle \, c_{N,i} \qquad \textit{and} \tag{4.50}$$

$$\left|\tilde{\psi}_N\right\rangle \;=\; \sum_i \left|\tilde{\phi}_{N,i}\right\rangle c_{N,i}. \tag{4.51}$$

The basic concept of constructing the exact wave function from a pseudo wave function, a pseudo-onsite and an all-electron onsite contribution is also valid for other physical properties such as the charge density, the kinetic energy, the exchange-correlation energy or the Hartree energy. Contrary to the pseudopotential methods described in the previous chapter, the operators $\hat{A}$ representing the physical properties in the PAW approach have to be traced back to their all-electron forms.

$$\tilde{A} \;=\; A + \sum_{N,i,j} |\tilde{p}_{N,i}\rangle \left(\left\langle \psi_{N,i} \left| \hat{A} \right| \psi_{N,j} \right\rangle - \left\langle \tilde{\psi}_{N,i} \left| \hat{A} \right| \tilde{\psi}_{N,j} \right\rangle \right) \langle \tilde{p}_{N,j}| \tag{4.52}$$

This equation is valid for local and quasilocal operators $\hat{A}$. Yet also the nonlocal operators are tractable in the PAW framework.
Technically, the PAW methods use smaller radial cutoffs (core radii) than the US PP and reconstruct the valence wave functions with all nodes in the core region. They are thus more accurate than ultrasoft pseudopotentials. Yet due to their smaller sphere radii, they also require somewhat larger basis sets (higher plane-wave energy cutoffs). In practice this increase in the basis set size is usually small for the light elements like H, C, N and O and thus is justified by the benefit in computational precision. Another advantage brought by the PAW approach is the controlablity of systematical errors. Transferability errors are generally negligible here, unlike in the case of the regular pseudopotentials, where a pseudopotential generated for an isolated atom is not guaranteed to be well suited for the calculation of a molecule. On the other hand, the converged results of the PAW method should not depend on such a reference system, because they employ the full density and potential. In comparison to the full-potential linearized augmented plane-wave (FLAPW) method, which treats all electrons essentially exact, the PAW pseudopotential reaches an almost similar accuracy, but at a much lower computational cost.
Lately the connection between the ultra-soft and the PAW pseudopotentials has been described by Kresse and Joubert [121], making this approach available in the newer VASP versions.
Throughout the calculations performed in this thesis the PAW method has been used. A comparison between the results actually obtained in this work and previous results by Delbecq et al. [45, 51] has been performed, yet one has to keep in mind that between both studies several parameters have been changed in the computations. Contrary to Delbecqs calculations employing ultrasoft pseudopotentials, *all* optimizations in this thesis are performed with additional dipole-corrections in the direction of the surface normal and smaller convergence thresholds on the residual forces at the stationary points (typically 0.01 $eV/\mathring{A}$).
For already known structures this leads to adsorption energies, which are within ± 8 kJ/mol compared to the results of Delbecq et al. [45, 51]. Notably the adsorption structures having strong permanent dipole moments normal to the surface show large deviations from previous data, a phenomenon clearly due to the additional z-dipole corrections. Concerning the bond lengths and bond angles, the actual results differ only slightly (approx. $< 1\%$) from the previous US-PP results. Again the biggest effect is seen when large permanent dipoles are involved. More detailed discussions of the actual results in comparison to previous studies will be given in the appropriate chapters.

4.6 Computation of Vibrational Frequencies

The determination of the vibrational frequencies is performed within the harmonic force approach [122]. In the classic picture of molecular vibrations, the total energy is separated into a kinetic (Chap. 4.6.1) and a potential energy part (Chap. 4.6.2). Solving the *Lagrange* equation of the vibrational motion, the vibrational frequencies and the corresponding *eigenvectors* are obtained (Chap. 4.6.3). Another approach to interpret the *eigenvectors* in the form of vibrational normal modes is to transform the basis of mass-weighted cartesian coordinates into internal coordinates. This transformation can be performed using the "*FG-method*" of Wilson [123], which is described in Sec. 4.6.4.

4.6.1 Kinetic Energy of Vibrations

A nonlinear system of N atoms possesses $(3N - 6)$ molecular vibrations plus additionally 3 rotations and 3 translations. The kinetic energy T of the N atoms can be expressed in the classical picture by a sum of their accelerations in a cartesian coordinate system

$$2T = \sum_{i=1}^{N} m_i \left(\left(\frac{dx_i}{dt} \right)^2 + \left(\frac{dy_i}{dt} \right)^2 + \left(\frac{dz_i}{dt} \right)^2 \right). \tag{4.53}$$

With the mass m_i of the atom i, a coordinate transformation into mass-weighted cartesian coordinates q_i^χ allows to remove the direct masses dependence of T:

$$q_i^\chi = \sqrt{m_i}\chi_i \qquad \forall \chi \in \{x, y, z\}. \tag{4.54}$$

This basis allows to express the kinetic energy in the simple form

$$2T = \sum_{i=1}^{N} \left(\left(\frac{dq_i^x}{dt} \right)^2 + \left(\frac{dq_i^y}{dt} \right)^2 + \left(\frac{dq_i^z}{dt} \right)^2 \right) = \sum_{i=1}^{3N} \dot{q}_i^2 \tag{4.55}$$

or written in the matrix formalism

$$2T = {}^t\dot{Q}\,\dot{Q} \tag{4.56}$$

where the Q is the N-dim column vector $Q = \{q_i^\chi\}$ containing the mass-weighted coordinates of the system. Similarly an expression for the potential energy of the system can be derived as shown in the next section.

4.6.2 Potential Energy of Vibrations

In the *Harmonic Force Approach* the potential energy for small displacements of the atoms dq_i ($d\chi_i$) can be expanded in a *Taylor*-series:

$$2V = 2V_e + 2\sum_{i=1}^{3N} \left(\frac{\partial V}{\partial q_i} \right)_e dq_i + \sum_{i=1}^{3N}\sum_{j=1}^{3N} \left(\frac{\partial^2 V}{\partial q_i \partial q_j} \right)_e dq_i\, dq_j + ... \tag{4.57}$$

with V_e the equilibrium energy of the system. The derivates are performed at the equilibrium geometry denoted here by the subscript e. At the equilibrium geometry, which is obtained by following the *Hellmann-Feynman* forces $\vec{F} = -Grad(V)$, the first derivatives are vanishing. Furthermore higher terms can be neglected.
With the force constants $\left(\frac{\partial^2 V}{\partial q_i \partial q_j}\right)_e = k_{ij}$ we obtain:

$$2V = 2V_e + \sum_{i=1}^{3N}\sum_{j=1}^{3N} k_{ij}\, dq_i\, dq_j \tag{4.58}$$

or with the $3N \times 3N$ force constant matrix $F = \{k_{ij}\}$

$$2V = 2V_e + {}^tQ\,F\,Q \tag{4.59}$$

The 2^{nd} derivatives of V with respect to the cartesian coordinates can be obtained from changes in the *Hellmann-Feynman* forces ΔF_{r_i} computed by VASP between the equilibrium position and the geometry in which the atom j is displaced by Δr_j:

$$k_{ij} = \frac{1}{\sqrt{m_j}\sqrt{m_i}} \frac{\partial V}{\partial r_j\, \partial r_i} = -\frac{1}{\sqrt{m_j}\sqrt{m_i}} \frac{\partial F_{r_i}}{\partial r_j} \approx -\frac{1}{\sqrt{m_j}\sqrt{m_i}} \frac{\Delta F_{r_i}}{\Delta r_j} \tag{4.60}$$

This links the differences in the *Hellmann-Feynman* forces to the *Hessian* matrix F of 2^{nd} derivatives, from which, by diagonalization, the vibrational frequencies are calculated. This will be shown in the following section.

4.6.3 Lagrange Equation of Vibrational Motion

In classical mechanics, the solution of the *Lagrange* equation of motion yields the equation of motion of a mechanical system. In this case the *Lagrangian* includes the kinetic and potential energy parts of the vibrating system and therefore its solution will lead to the vibrational motion. The *Lagrangian* has the form

$$\frac{d}{dt}\underbrace{\left(\frac{\partial T}{\partial \dot{q}_i}\right)}_{\partial E_{kin}/\partial v=p} + \frac{\partial V}{\partial q_i} = 0 \quad \forall i \in \{1, 2, ..., 3N\}. \tag{4.61}$$

Using $\frac{\partial T}{\partial \dot{q}_i} = \dot{q}_i$, derived from equation 4.55, and $\frac{\partial V}{\partial q_i} = \sum_{j=1}^{3N} k_{ij}\, q_i$ we obtain

$$\ddot{q}_i + \sum_{j=1}^{3N} k_{ij}\, q_j = 0 \quad \forall i \in \{1, 2, ..., 3N\}. \tag{4.62}$$

This is a set of 3N equations, which can be expressed in the matrix notation by

$$\ddot{Q} + FQ = 0 \tag{4.63}$$

The solutions of these 3N linear differential equations of 2^{nd} order in q are time-dependent harmonics of the general form

$$q_i = A_i cos(\sqrt{\lambda}t + \varphi_i) \quad \forall i \in \{1, 2, ..., 3N\} \tag{4.64}$$

with

- $\sqrt{\lambda} = \omega = 2\pi\nu = 2\pi\bar{\nu}$ the wavenumber
- A_i the amplitude
- φ_i the phase shift associated to q_i.

Inserting the general solution 4.64 into equation 4.62 we obtain a new set of linear equations

$$(\underbrace{k_{ij}\,\delta_{ij}}_{k_{ii}} - \lambda)q_i + \sum_{\substack{j=1 \\ j\neq i}}^{3N} k_{ij}\, q_j = 0 \quad \forall i \in \{1, 2, ..., 3N\} \tag{4.65}$$

or in the matrix notation

$$(F - 1_{3N}\lambda)Q = 0. \tag{4.66}$$

Evidently a non-trivial solution of this equation system is possible only in the case that the determinant of the left hand side vanishes: $|F - 1_{3N}\lambda| = 0$. This shows that in order to obtain the *eigenvectors* (normal modes) and *eigenvalues* λ_i (frequencies) of the vibrational modes one has to diagonalize the *Hessian* matrix F. Using the Schmidt-orthogonalization the diagonal matrix Λ containing all λ_i is obtained.

$$P^{-1}FP = \Lambda \tag{4.67}$$

P represents the transformation matrix of q_i from the cartesian basis into the internal coordinates ξ_i. One can furthermore transform equation 4.67 into the corresponding differential in the internal (normal) coordinate basis:

$$\ddot{Q} + (P^{-1}\Lambda P)Q = 0 \tag{4.68}$$

$$P\ddot{Q} + PP^{-1}\Lambda PQ = 0 \tag{4.69}$$

$$P\ddot{Q} + \Lambda PQ = 0 \tag{4.70}$$

$$\ddot{\Xi} + \Lambda\Xi = 0 \tag{4.71}$$

with $\Xi = PQ$ denoting the 3N column-vector containing the normal coordinates $\{\xi_i\}$.

4.6.4 The FG Method of Wilson

In the previous chapter the calculation of vibrational modes and frequencies by diagonalisation of the *Hessian* matrix expressed in cartesian basis has been discussed. Often it is more convenient for the analysis of vibrational normal modes, to express the vibrational motions in internal coordinates ξ_i, which are defined by the interatomic distances, deformation angles and dihedral angles. Therefore the (mass-weighted) cartesian coordinates q_i have to be transformed into the internal coordinates d_i. This basis change can be obtained by the following isomorphism employing the transformation matrix B with $dim(B) = (3N-6) \times 3N$ [123]:

$$B : \dot{D} \rightarrow \dot{Q} \qquad \dot{D} = B\dot{Q} \tag{4.72}$$

$$\dot{d}_i = \sum_{j=1}^{3N} b_{ij}\,\dot{q}_i = b_{ij}\,\dot{q}^j \quad \forall i \in \{1, 2, ..., 3N-6\} \tag{4.73}$$

The difficulties at this point arise from the transformation matrix B switching the coordinates between both basis spaces, which has to be known. In order to transform $3N$ cartesian coordinates into the $3N-6$ internal values, one has to "fill up" $\dot{D}$ with 6 additional coordinates. These correspond to 3 translations and 3 rotations of the complete system, which are of course ignored for the calculation of vibrations. Thus the center of the molecule has to remain fixed.

$$\sum_{i=1}^{N} m_i \frac{dx_i}{dt} = 0 \wedge \sum_{i=1}^{N} m_i \frac{dy_i}{dt} = 0 \wedge \sum_{i=1}^{N} m_i \frac{dz_i}{dt} = 0 \tag{4.74}$$

Furthermore all components of the angular momentum L_i of the system are require to be zero:

$$\sum_{i=1}^{N} m_i \left(y_i \frac{dz_i}{dt} - z_i \frac{dy_i}{dt} \right) \tag{4.75}$$

$$\sum_{i=1}^{N} m_i \left(z_i \frac{dx_i}{dt} - x_i \frac{dz_i}{dt} \right) \tag{4.76}$$

$$\sum_{i=1}^{N} m_i \left(x_i \frac{dy_i}{dt} - y_i \frac{dx_i}{dt} \right) \tag{4.77}$$

$$\tag{4.78}$$

Taking into account these additional 6 equations we obtain the correct $3N \times 3N$ matrix $\hat{B}$:

$$\dot{Q} = \hat{B}^{-1}\dot{D} \tag{4.79}$$

$\dot{\tilde{D}}$ is the $3N$ column-vector identical to $\dot{D}$ for $3N-6$ coordinates and completed by 6 zeros. This can be expressed by equation 4.80. Finally, for the internal coordinate vectors and inverted and the transposed transformation matrices, one has

$$\dot{\tilde{D}} = \begin{pmatrix} \dot{D} \\ \dot{D}_0 \end{pmatrix} \qquad {}^t\dot{\tilde{D}}^{-1} = \left({}^t\dot{D}\,{}^t\dot{D}_0\right). \tag{4.80}$$

$$\hat{B} = \begin{pmatrix} B \\ B_0 \end{pmatrix} \qquad \hat{B}^{-1} = (\bar{B}\ \bar{B}_0) \qquad {}^t\hat{B}^{-1} = \begin{pmatrix} {}^t\bar{B} \\ {}^t\bar{B}_0 \end{pmatrix} \tag{4.81}$$

Together with equation 4.72, the velocities in both coordinate spaces are transformed via

$$\dot{\tilde{D}} = \hat{B}\dot{Q} \Leftrightarrow \dot{Q} = \hat{B}^{-1}\dot{\tilde{D}}. \tag{4.82}$$

Using these equations the kinetic and the potential energy can be expressed in the basis D. For the kinetic part, one obtains from equation 4.56:

$$2T = {}^t\left(\hat{B}^{-1}\dot{\tilde{D}}\right)\hat{B}^{-1}\dot{\tilde{D}} = {}^t\,\dot{\tilde{D}}\,{}^t\hat{B}^{-1}\hat{B}^{-1}\dot{\tilde{D}}. \tag{4.83}$$

Together with equation 4.81 it is found that

$$2T = {}^t\,\dot{D}\,{}^t\bar{B}\bar{B}\,\dot{D} = {}^t\,\dot{D}\,\hat{G}^{-1}\,\dot{D}. \tag{4.84}$$

On the right hand side we defined the product as a $(3N-6)\times(3N-6)$ matrix representation $\hat{G}^{-1}$:

$${}^t\bar{B}\bar{B} = \left(B^tB\right)^{-1} = G^{-1}. \tag{4.85}$$

Similarly to equation 4.59 we obtain for the expression of the potential energy V:

$$2V = 2V_e + {}^t\,D\,\hat{F}\,D \tag{4.86}$$

with $\hat{F}$ the $(3N-6)\times(3N-6)$ force constant matrix.

Comparing the terms "2V" into both coordinate bases we find

$${}^tQFQ = {}^tD\hat{F}D \tag{4.87}$$

$${}^tQFQ = {}^t(BQ)\hat{F}(BQ) \tag{4.88}$$

$${}^tQFQ = {}^tQ\,{}^tB\hat{F}BQ \tag{4.89}$$

$$F = {}^tB\hat{F}B \tag{4.90}$$

The *Lagrangian* of the vibrational system transforms under change of the coordinate basis into internal coordinates $D = \{d_i\}$ into

$$\ddot{Q} + F\,Q = 0 \tag{4.91}$$

$$\ddot{Q} + ({}^tB\,\hat{F}\,B)\,Q = 0 \tag{4.92}$$

$$B\,\ddot{Q} + B\,({}^tB\,\hat{F}\,B)\,Q = 0 \tag{4.93}$$

$$\ddot{D} + B\,{}^tB\,\hat{F}\,D = 0 \tag{4.94}$$

$$\ddot{D} + \hat{G}\,\hat{F}\,D = 0 \tag{4.95}$$

Like in the case of the *Lagrangian* in the basis of mass-weighted cartesian coordinates we find that a non-trivial solution is only obtained if

$$\left|\hat{G}\hat{F} - \lambda 1_{3N}\right| = 0. \tag{4.96}$$

In this case the vibrational normal modes (*eigenvectors*) and the corresponding energies (*eigenvalues*) of these modes can be calculated simply by diagonalization of $\hat{G}\hat{F}$.

4.7 EELS and IR Intensities

In surface IR experiments such as RAIRS one finds that the absorption I is proportional to the change in the z-component of the dynamical dipole moment μ [57]:

$$I \propto \left(\frac{d\mu_z}{dq_i}\right)^2. \tag{4.97}$$

These variations of the dynamic dipole moment during the vibrational motions are evaluated similarly to the frequencies by finite differences $\Delta\mu_z/\Delta r_i$.
As already discussed in chapter 3.2.1.1, the complete description of loss intensities in HREELS experiments is more complicated. Ignoring the scattering and resonant excitation mechanisms, the normalized loss intensities in the specular reflection mode are given by equation 3.14. In this mode the dominant excitation mechanism is the long-range dipolar scattering.
Introducing a modified damping function $F(\omega_k)$ (see eq. 3.13), the normalized HREEL intensities can be approximated from the dynamic dipole moments computed with VASP by finite differences [53]:

$$\frac{I^k_{loss}}{I_{elastic}} \propto \Theta_{ads}\,\frac{F(\omega_i)}{\omega_k}\left(\frac{d\mu_z}{dq_k}\right)^2 = \Theta_{ads}\,\frac{F(\omega_k)}{\omega_k}\left(\sum_{i=1}^{3N}\frac{1}{\sqrt{m_i}}\frac{\partial\mu_z}{\partial\Delta r_i}\,P_{ki}\right)^2 \tag{4.98}$$

with P_{ki} a matrix of weights derived from the eigenvectors. The modified damping function is given by

$$F(\omega_i) = \sqrt{1-2\Theta_E}\left(\frac{\hat{\Theta}_c^2}{1+\hat{\Theta}_c^2}\left(sin^2(\Theta_I) - 2\,cos^2(\Theta_i)\right) + \left(1+cos^2(\Theta_I)\right)ln(1+\hat{\Theta}_c^2)\right). \tag{4.99}$$

$$with \qquad \hat{\Theta}_c = \frac{\Theta_c}{\Theta_E} \qquad \text{and} \qquad \Theta_{\mathrm{E}} = \frac{\hbar\omega_{\mathrm{k}}}{2\mathrm{E_I}}. \tag{4.100}$$

Here E_I is the primary energy of the incident electrons (typically 4.7eV have been used in this work), Θ_I the incident angle of the electrons towards the surface normal (60°) and Θ_c is the acceptance angle of the analyser (3°).

4.8 Employed Parameters of the Calculations of this Work

In the previous sections a general overview over theoretical methods for periodic DFT computations has been discussed. All these methods are implemented in the *Vienna ab initio Simulation package* (VASP) [72, 73, 74], an extensive *ab initio* quantum-mechanical molecular dynamics simulation program package that has been the primary theoretical tool used for the surface studies in this work. For comparison to the periodical DFT results, also a number of gas phase

calculations of the properties of prenal and crotonaldehyde have been performed using standard methods (i.e. HF, DFT, RI-DFT or CCSD(T)) implemented in other programs such as Molpro 2000 [124], Gaussian 2003 [125] or Turbomole 5.6 [126].

The VASP package, originally based on a program initially written by M. Payne at the MIT in Cambridge, has been revised and expanded massively since 1989 by G. Kresse and J. Furthmüller at the Institut für Materialphysik and Center for Computational Science of the University of Vienna. Starting in 1996, VASP was converted completely to *Fortran 90* and parallelized, making it a highly efficient *ab initio* quantum-mechanical code. Additional information on the capabilities of the VASP package can be obtained on the VASP homepage at the University of Vienna, *http://cms.mpi.univie.ac.at/VASP/*.

The periodic DFT computations in this thesis have been performed using the GGA functional Perdew-Wang 91 [82] together with PAW method to eliminate the core electrons. Various parameters influence the accuracy of the obtained results and need to be given here. For the plane-wave basis a cutoff of 400 eV was chosen to ensure a tight convergence of the plane-wave expansion (convergence threshold of 10^{-6} eV). The partial occupancies were determined by the smearing method of Methfessel and Paxton [106] with $\sigma = 0.25$. For most calculations, the electronic minimizations have been performed with a combination of the *blocked Davidson* algorithm within the first few iterations and the RMM-DIIS (*Residual Minimization Method-Direct Inversion in the Iterative Subspace* [127]) matrix diagonalization scheme during the final convergence phase. This minimization scheme is among the fastest available, yet in some cases, notably for adsorption complexes with large permanent dipole moments normal to the surface such as the top adsorption structures of the α,β-unsaturated aldehydes, stability problems were encountered. In such cases the typically less efficient but more robust *blocked Davidson* minimization algorithm was chosen.

All three considered surfaces, Pt(111), Pt_2Sn(111)/Pt(111) and Pt_3Sn(111)/Pt(111), were modeled by 4 layer-thick metallic slabs and a 5 layer vacuum with adsorption of the molecules on one side of the slab. The surface alloys were modelled by a single layer of the corresponding alloy structure above a Pt(111) bulk.

2D Brillouin zone integration was performed on sufficiently converged k-point grids, which are marked in parenthesis in the following. For the Pt(111) and the Pt_2Sn(111)/Pt(111) surfaces, both a medium coverage (3×3) cell ($3 \times 3 \times 1$ k-point grid, coverage of 1/9 monolayer (ML)) as well as a higher coverage situation represented by a 3×2 unit cell ($3 \times 5 \times 1$, coverage of 1/6 ML) have been considered. To establish the stability of the top adsorption modes of prenal on Pt(111) as a function of coverage, also a (2×2) unit cell ($5 \times 5 \times 1$, coverage of 1/4 ML) has been studied. In the case of Pt_3Sn(111)/Pt(111), a somewhat larger ($2\sqrt{3} \times 2\sqrt{3}$) supercell ($3 \times 3 \times 1$) with a rather low coverage of 1/12 ML was chosen.

The geometry optimizations of all stationary points were carried out using the *Conjugate Gradient* algorithm. All degrees of freedom of the two uppermost metal layers and the adsorbed molecule were relaxed whereas the two lowest metal planes were kept frozen. In order to obtain an accurate *Hessian* matrix for the vibrational analysis, a tight convergence threshold of 0.01 eV/Å was demanded.

Adsorption energies have been calculated from the difference of the well-converged total energies of the adsorbed complex and the energies of the optimized bare surface and the molecule relaxed in the gas phase (i.e. in a $14 \times 14 \times 20$ $Å^3$ box). No zero-point corrections have been applied to the total free energies given in this work.

In order to avoid spurious electrostatic interactions between the periodic images, dipole corrections along the z-axis normal to the slab surfaces have been introduced. Comparison to earlier results by Delbecq et al. [45, 51] yielded that these corrections have little impact on the geometry parameters and adsorption energies of optimized adsorption structures with small permanent dipole moments normal to the slab surfaces. In contrast, these corrections are found to be very important for systems exhibiting a large dipole moment component normal to the

surface. For such cases, the adsorptions energies are lowered by up to 20 kJ/mol. This and the tighter requirement for the convergence of the residual forces at stationary points has even lead to the destabilization of a few adsorption structures that where heretofore known in the literature [45, 51, 52, 78]. These phenomena will be discussed in detail in the following chapters.
The vibrational frequency analyses were performed by numerical computation of the 2^{nd} derivatives of the potential energy surface as described in section 4.6. For the numerical derivation, the atoms were displaced symmetrically along cartesian coordinates by ± 0.025 Å around the equilibrium geometry, which ensured that the computed frequencies were within the harmonic limit. Any coupling between molecular modes lying in the 0-300 cm^{-1} range and the surface phonons has been neglected by freezing the metal atoms of the slab [53]. As already mentioned previously, the HREELS loss intensities are calculated from the 1^{st} derivatives of the z-component of the dynamical dipole moments.
For the analysis of the experimental HREEL spectra, the focus is laid on the region between 300 cm^{-1} and 2000 cm^{-1} , because of the greater precision of the harmonic frequencies computed with DFT here. Below 300 cm^{-1} , the chosen slab models lead to systematic errors during the vibrational analysis. Although the slab models used here approximate the low-lying vibrations and hindered modes of the adsorbate reasonably well, thicker slabs have to be used and phonons have to be included in the vibrational analysis for a more detailed analysis in this frequency range. In benchmark calculations [128] it was observed that at least 6 layers, of which 4 have to be relaxed, are required to minimize the systematic errors. The inclusion of the relaxed substrate layers in the vibrational calculation allows to study the coupling of the low-lying vibrations to the surface phonons, which can lead to a splitting of normal modes and hence significant frequency shifts. In the frequency region above 2000 cm^{-1} the anharmonicity of the stretching vibrations and *Fermi* coupling complicates the vibrational analysis. In order to account for the anharmonic corrections, which vary usually between a few cm^{-1} and 100 cm^{-1} , it would be necessary to compute the potential energy curves along each normal coordinate affected with high precision. From the potential curves the corresponding anharmonic frequencies can be obtained. Yet this procedure has not been considered in this thesis, because on the one hand the computational effort in the light of a huge number of adsorption structures would be enormous, and on the other hand the ν(C-H) stretching region in the experimental HREEL intensities usually are only weak for the molecules considered here.
The precision in the intermediate frequency region extending from 300 cm^{-1} to 2000 cm^{-1} has been checked by the comparison of the gas phase vibrational spectra with the computed harmonic frequencies. In general the deviations are well below 15 cm^{-1} (<1.5 %) for all vibrational normal modes, whereas the deviation in the ν(C-H) stretching region is usually larger (up to 100 cm^{-1}). The computed IR and EELS intensities compare also quite well with the experiments, although the systematic errors encountered here are sometimes more significant. They can be assigned to various phenomena. Firstly, again the slab model and the chosen computational parameters must be quoted. Since the vibrational intensities are calculated from the dynamic dipole moments, which are essentially only small differences between the static dipole moments in the equilibrium geometry and the geometry distorted along a normal coordinate, they are easily influenced by the computational parameters. Therefore all parameters employed in this thesis, especially the displacements for the determination of the *Hessian* matrix, have been checked carefully in this respect. Moreover, *Davydov splitting* (see 3.2.2) causes additional deviations in all cases, in which more than one molecular entity is present in a single unit cell. This situation is encountered basically on all studied surfaces for crotonaldehyde and prenal in the actual investigations. The interaction of the various adsorption modes present in a single unit cell leads to a splitting and broadening of the vibrational levels compared to the isolated entities considered in the periodic DFT computations and hence also the intensities are being dispersed. Finally also experimental errors of the measured intensities due to contributions from impact scattering in the dipolar regime have to be kept in mind.

Chapter 5

The Pt(111) and Pt-Sn(111) surfaces

5.1 The Elements Pt and Sn

Platinum, first described by R. Watson in 1750, is a grey or silver-shining, ductile metal with a density of 21.45 g/cm^3. The melting point is 2041 K and it sublimates above 4098 K. While it can be dissolved in nitric acid or nitrohydrochloric acid at room temperature, it is very resistant against other elements such as sulphur or phosphorus except at high temperatures. It also alloys easily with elements like Sn or Pb at high temperatures. The electronic configuration of the *4d*-metal platinum is [Xe] $4f^{14}5d^{9}6s^{1}$. Fine-dispersed platinum absorbs great amounts of hydrogen and oxygen. In this form, platinum is regularly used as a catalyst for various technical processes. It plays an important role in the industrial production of sulphuric and nitric acid.

Tin, an *sp*-element with the electronic configuration [Kr] $4d^{10}5s^{2}p^{2}$, is a soft, silvery lustrous grey metal, with a high thermal conductivity. Its melting point is 505 K and it sublimates at 2875 K. From archaeological sources hints were obtained, that people have been using tin for at least 5500 years. It is known to exist in two phases: At room temperature the stable modification is the tetragonal β-tin (density 7.29 g/cm^3), which converts into the non-metallic cubic modification of α-tin below $13.2°C$. The latter modification is usually found as a grey powder. According to the Pauling electronegativity scale Sn (1.96) is slightly more electropositive [129] than Pt (2.28). Tin is dissolved by strong acids and bases. At higher temperatures it can be oxidized to white tinoxide. With an atomic radius of 3.01 Å , it is about 9% larger than platinum (2.77 Å). The surface energy of 5.6 10^{-5} J/cm^2 is sizeably smaller than the one of platinum with 18.1 10^{-5} J/cm^2.

5.2 The Pt(111) Single Crystal Surface

Platinum crystalizes in the cubic close-packed (fcc: face centered cubic, stacking sequence ABCABC...) and thus belongs to the space group Fm-3m (Fig. 5.1). Like in hexagonal close packing the coordination number of each atom is twelve. Six of the nearest neighbors coordinate hexagonally in a plane around the central platinum.
It has a lattice constant of 392 pm and a nearest neighbor distance of 277 pm. The {111}-surfaces of platinum show a hexagonal symmetry of the first layer. Taking into account the deeper layers, this symmetry is reduced to C_{3v}. On the pure Pt(111) surface, top, bridge and threefold hollow sites are available for coordination of adsorbates.

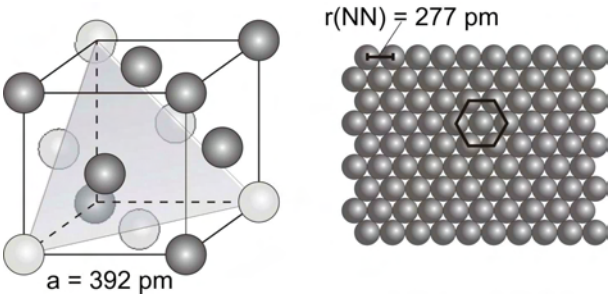

Figure 5.1: Unit cell and the (111) surface of platinum.

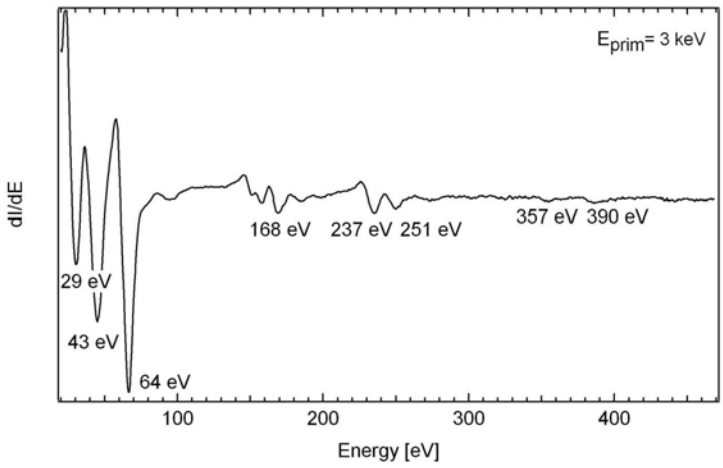

Figure 5.2: Auger spectrum of clean Pt(111) with a primary electron energy of 3 keV.

The clean platinum surfaces have been prepared by repeated cycles (3-6) of sputtering and annealing. The single crystal was sputtered for 10 min with argon ions of a kinetic energy of 3 keV and a sputtering current of 4 μA at 900 K. In order to heal sputtering defects and obtain a flat surface, the sample was heated afterwards to 1150 K for 5 min. In case the amount of tin deposited on the surface was sizeable, the first three sputtering cycles were carried out at 300 K, which avoids the diffusion of tin into the bulk. The surface was considered clean, when the AES spectrum (Fig. 5.2) showed no further signals of Sn, C, O or other elements.

5.3 The Sn-Pt(111) Surface Alloys

By deposition of tin on the Pt(111) surface, it is possible to obtain different ultra-thin surface alloys. The preparation of the surface alloys depends on the amount of tin deposited and the temperature the sample is heated to after deposition. According to Paffett et al., tin grows below 320 K in a Stranski-Krastanov mode on a Pt(111) substrate [35]. Starting from tin precoverages larger than the monolayer coverage of $\Theta_{Sn} = 0.6$ tin atoms per platinum atom, these authors observed the formation of a $Pt_2Sn(111)$ surface alloy with a $(\sqrt{3} \times \sqrt{3})R30^\circ$ structure ($\Theta_{Sn} = 0.33$) at 1000 K. Heating tin coverages between 0.25 ML and 0.6 ML to 1000 K, a $Pt_3Sn(111)$ surface alloy with a $p(2 \times 2)$ periodicity was obtained ($\Theta_{Sn} = 0.25$).

At tin exposures between these two limits, a LEED pattern consisting of a mixture of both structures was obtained upon annealing. Models of both surface alloys are shown in Fig. 5.3. STM experiments carried out by Batzill et al. [39] showed both surface alloys to be present in different domains after the preparation of the sample (Fig. 5.3). The platinum atoms are imaged as (light) protrusions.

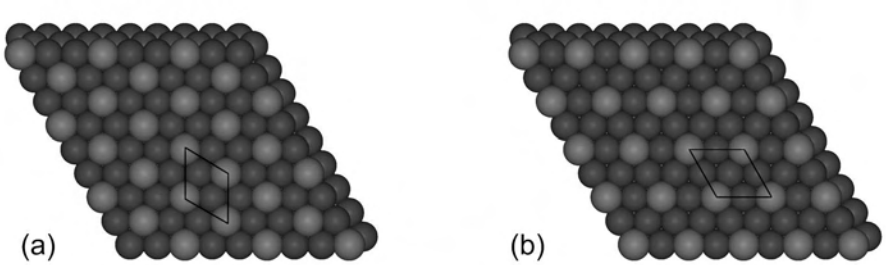

Figure 5.3: (a) Model of the $Pt_2Sn(111)/Pt(111)$ $(\sqrt{3} \times \sqrt{3})R30°$ surface. This surface shows only platinum top and bridge adsorption sites. (b) Model of the $Pt_3Sn(111)/Pt(111)$ $p(2 \times 2)$ surface. On this surface pure platinum threefold hollow sites are still present.

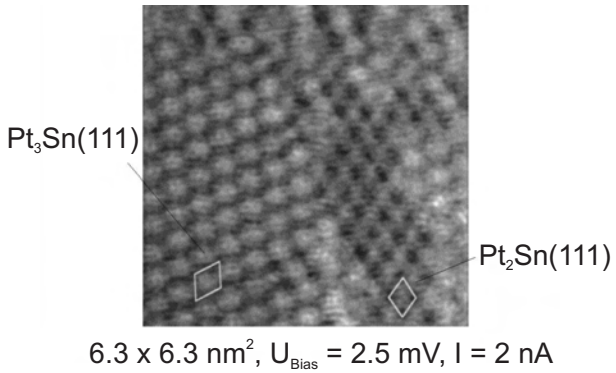

Figure 5.4: STM image of Sn-Pt(111) surface alloy [39].

Both the $Pt_2Sn(111)$ and the $Pt_3Sn(111)$ surface alloys do exist as possible surface phase on the Pt_3Sn bulk crystal, which was studied with I/V-LEED by Atrei et al. [130, 131] (Fig. 5.5). The Sn atoms on both alloy surfaces show a sizeable buckling. Atrei et al. [130] predict that the Sn atoms protrude the platinum by 23 pm and 30 pm on the $Pt_2Sn(111)$-$(\sqrt{3} \times \sqrt{3})R30°$ and $Pt_3Sn(111)$-$p(2 \times 2)$ surfaces, respectively. On the (111)-surface of the Pt_3Sn bulk alloy, the buckling is reduced to 11 pm.

Overbury et al. [38, 43] studied the Sn-Pt system with low energy alkali ion scattering. From their LEIS experiments these authors conlcude that the buckling on both surfaces is similar, i.e. 22 pm. They showed, that both surface alloys prepared on Pt(111) are single layer alloys, suggesting that the excess tin diffuses into the Pt bulk. At high tin coverages of 4-5 ML, Galeotti et al. [34] obtained contradictory results in their X-ray photoelectron diffraction (XPD) experiments, where a $p(2 \times 2)$ structure formed already around 400 K. Their analysis suggests, that the alloy formed is a bulk alloy surface. Indeed, the LEED experiments of higher tin exposures (Auger peak ratio $I_{Sn(430)}/(I_{Sn(430)} + I_{Pt(237)}) > 0.77$) performed in the present work

showed a weak diffraction pattern corresponding to a $p(2 \times 2)$ structure around 500 K. Yet the low transition temperature, at which this $p(2 \times 2)$ structure appears, indicates, that this is a different alloy than the one formed around 1000 K. Latest surface X-ray diffraction (SXRD) results support this indication [44].

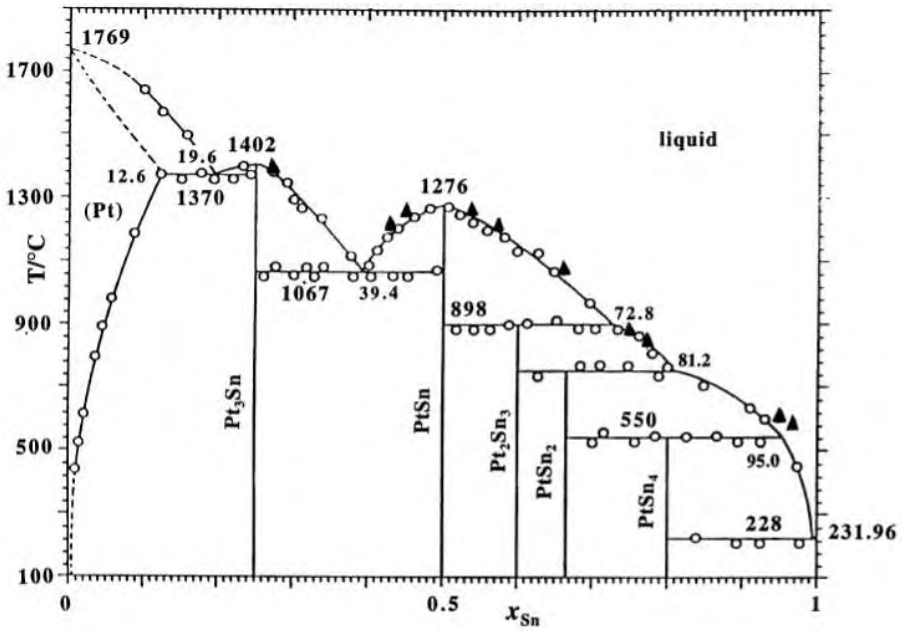

Figure 5.5: Phase diagramm of the Pt-Sn system reproduced from [131].

The influence of the tin atoms on the adsorption properties of these surface alloys is widely discussed in the literature. While Paffett et al. [35] consider the influence mainly as a site blocking effect, the investigations of Batzill et al. [39] lead to the conclusion that the electronic properties change strongly. The charge density at the Fermi edge is found in their STM experiments to be reduced. In agreement with the damping and the lowering obtained for the d-band center [132], the desorption energy for example for ethene on the Pt-Sn alloys decreases sizably.
The alloying of platinum with tin decreases the overlap of the Pt-d-orbitals forming the d-band. Recent studies of the density of states (DOS) of the Pt-Sn surface alloys by Delbecq et al. [45] pointed to a decrease of the DOS at the Fermi edge with increasing amount of Sn in the surface layer. These results are in good agreement with UPS measurements [37]. Consistent with the alloying of platinum with an electropositive metal, the d-band center shifts from -1.93 eV for Pt(111) to -2.09 eV for the Pt_3Sn alloy surface and to -2.12 eV for $Pt_2Sn(111)$ [50].
Assuming a conserved population of the d-band, a lowering of the d-band center is expected to lead to a decrease in binding energies and is correlated with an interaction of the Pt d-band with the Sn sp-bands. This gives rise to an electron transfer from Sn to Pt [46]. This electron transfer is also obtained in the theoretical calculation by Delbecq et al. [51]. These authors found that Sn looses 0.42 electrons and Pt gains 0.13 e^- in the case of the $(\sqrt{3} \times \sqrt{3})R30°$ surface. On the $p(2 \times 2)$ structure, the electron density of the Sn atoms decreases by 0.53 e^-, while the Pt atoms gain only 0.10 e^-. This means that the Pt atoms on the surface alloys are more negatively charged than on pure platinum. Similarly Rodriguez et al. [133] proposed in their analysis of the Pt-Sn bonds of the $Pt_2Sn(111)$ surface alloy an Sn(5s,5p) $\rightarrow$ Pt(6s,6p) charge transfer and

from this conclude on an increased electrophilic character of Sn opposed by a decreased donor and acceptor ability of Pt.
Theortical studies by Teraoka et al. [134] predict, that the $Pt_2Sn(111)/Pt(111)$ alloy is more stable than the $Pt_3Sn(111)/Pt(111)$ surface alloy. In the case of monolayer alloys, the computed order-disorder transition temperature for ordering to a $(\sqrt{3} \times \sqrt{3})R30°$ structure is higher then the temperature for forming a $p(2 \times 2)$ surface structure.

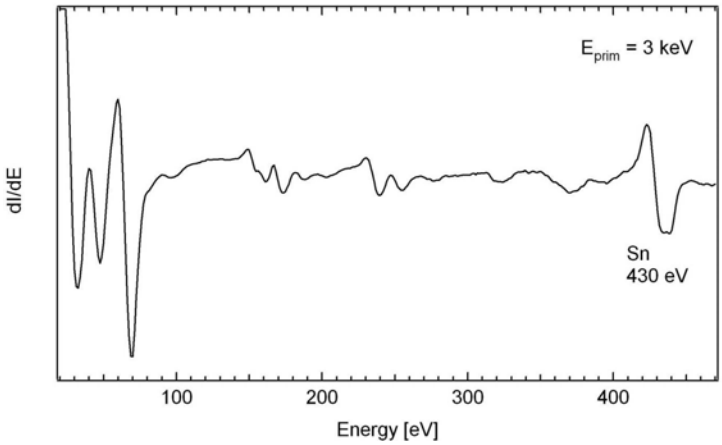

Figure 5.6: Auger spectrum of Sn deposited on the Pt(111) surface. The employed primary electron energy was 3 keV.

Depending on the amount of tin deposited at 300 K, the annealing temperatures, after which LEED experiments exhibited the images corresponding to the different alloy surfaces, varied. Generally the peak-to-peak intensity ratio of the Auger Sn peak at 430 eV ($M_4N_{45}N_{45}$) and the Pt signal at 237 eV recorded in the dI/dE mode were used to compare the amounts of tin deposited by means of the $I_{Sn}/(I_{Sn} + I_{Pt})$ ratio. For all tin depositions in this work the Sn evaporator was thermally equilibrated for 5 min prior to dosing and was operated without interruption. During the deposition of Sn, sometimes a build-up of impurities could be detected by AES. The AES spectra showed small signals of carbon, which were probably due to CO adsorbed from the background gas.
Figure 5.7 shows the development of the Auger intensity ratio $I_{Sn}/(I_{Sn} + I_{Pt})$ during annealing from 400 K to 1200 K in steps of 50 K (25 K resp.). The AES spectra were recorded with a primary electron energy of 3 keV. After each flashing step the sample was cooled down to 100 K again to perform LEED experiments using a beam energy of 130 eV. Between 800 K and 950 K the LEED patterns exhibited a $(\sqrt{3} \times \sqrt{3})R30°$ structure and between 1000 K and 1075 K the diffractron pattern of a $p(2 \times 2)$ superstructure was obtained.
In order to explore the temperature ranges of the different surface alloys as a function of the initial amount of Sn deposited on the Pt(111) face, several LEED annealing series were performed. The diagram constructed from these experiments showing the existence regimes is presented in Fig. 5.8. It is seen, that at low Sn coverages, only the $(\sqrt{3} \times \sqrt{3})R30°$ structure forms between 500 K and 600 K. With increasing Sn depositon, the temperature range, in which this surface alloy is stable, widens drastically. The $p(2 \times 2)$ structure generally evolves around 1000 K and exhibits only a small temperature interval of about 75 K, in which it is found to be stable. Between both temperature ranges, the LEED images show coexistence of both surface structures. Above 1075 K, the superstructure spots in the LEED images become increasingly diffuse and disappear. The Sn(430) signal in the AES spectra taken after the LEED spots of the

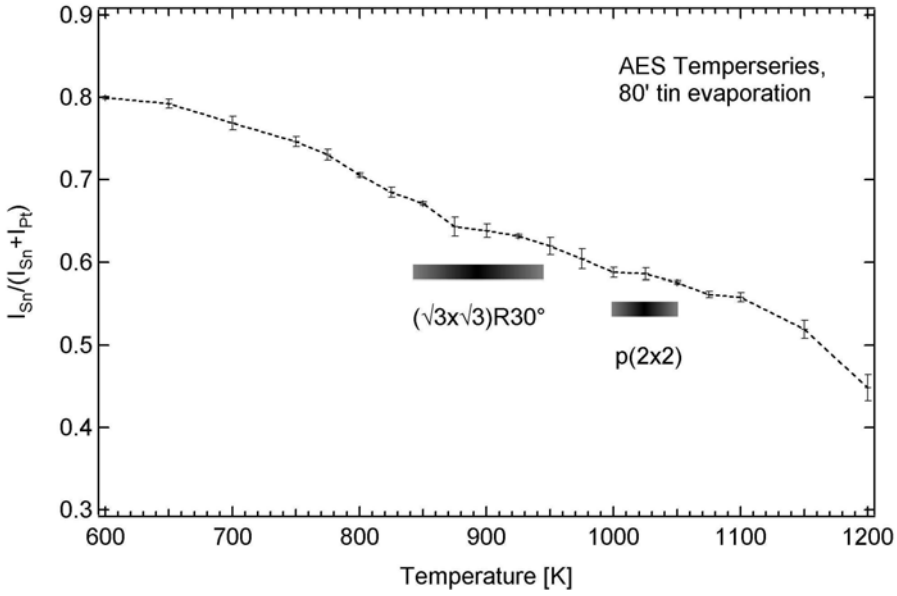

Figure 5.7: Auger annealing series of Sn deposited on Pt(111).

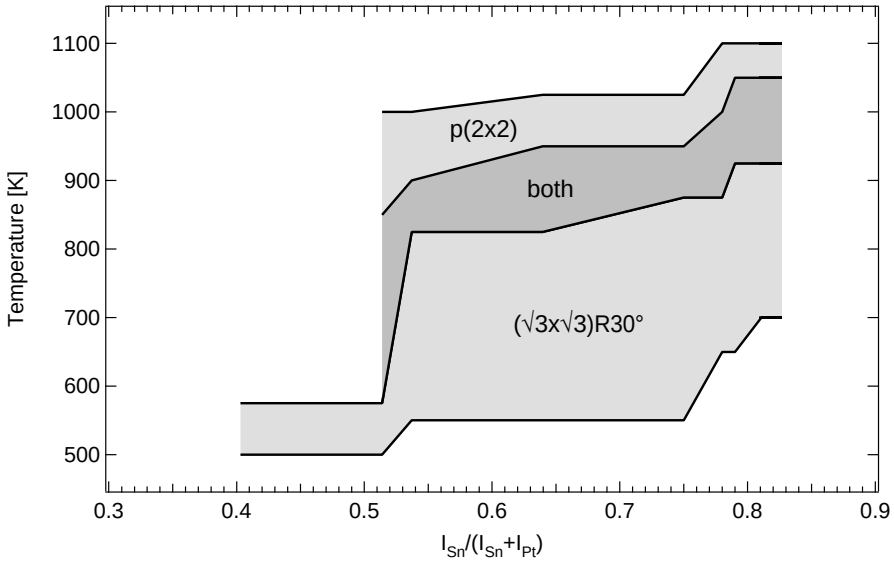

Figure 5.8: Diagram of Pt-Sn surface phases constructed from LEED annealing series.

superstructures disappeared are still significant, indicating that the tin diffuses into the bulk at temperature exceeding 1075 K.

Chapter 6

The Crotonaldehyde Adsorption

In this chapter the results on the experimental studies and the DFT calculations on the systems crotonaldehyde/Pt(111), crotonaldehyde/Pt_3Sn(111) and crotonaldehyde/Pt_2Sn(111) are presented. Crotonaldehyde was chosen as one of the two "model molecules" to investigate the adsorption and interaction properties of α, β-unsaturated aldehydes with model catalyst surfaces, which has to be understood in order to gain deeper insight into the selective hydrogenation processes in heterogeneous catalysis.
Crotonaldehyde exists in four rota-isomers in the gas phase as well as on surfaces: the E-(s)-trans, E-(s)-cis, Z-(s)-trans and the Z-(s)-cis forms (Fig 6.1). These four rota-isomers differ in the relative position of the methyl group with respect to the aldehydic group at the C=C double bond (E or Z) and the orientation of the C=O moiety relative to the C=C double bond along the connecting single bond ((s)-trans or (s)-cis). The isomerization of crotonaldehyde is also encountered on the surfaces. Together with the multifunctional interaction mechanisms via the C=C and C=O bonds this leads to huge sets of complex adsorption structures, which have to be considered on the three model catalyst surfaces.
Crotonaldehyde is also problematic from a purely experimental point of view, because it can form oligomeric or polymeric films. This phenomenon has been observed quite frequently in the course of the experimental studies, causing problems with reproducible dosing of crotonaldehyde through the leak valves or even a clogging of the valves. To a certain degree this oligomerisation was supressed by exchanging the copper gaskets inside the valves by silver gaskets.

6.1 Crotonaldehyde Adsorption on Pt(111)

The first section of this chapter deals with the characterization of the adsorption of crotonaldehyde on the Pt(111) surface. In the first part, the results of various TPD experiments performed in this work will be presented to give a general overview of the adsorption and thermal evolution of the system. Besides several adsorption states below 200 K, also a decomposition reaction with an onset below 300 K was observed. Although TPD allows only limited conclusions on this system when considered on its own, it is a tool of great value to assist the interpretation of the vibrational spectra shown in the following sections.
Just before switching to the HREEL spectra recorded on Pt(111) for several different coverages ranging from submonolayer to multilayer, the results of the DFT total energy calculations will be discussed. Using the computed HREEL spectra of all obtained stable adsorption configurations, the systematic analysis of the experimental HREEL spectra will be presented. The important adsorption structures forming the monolayer at low temperatures have been identified successfully with this strategy. Furthermore, multilayers of crotonaldehyde on the substrate have been

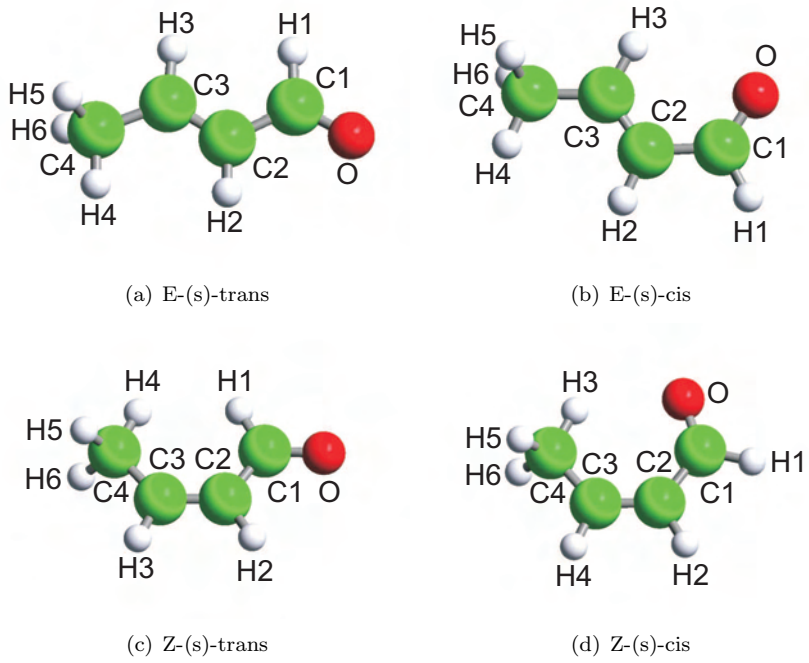

(a) E-(s)-trans (b) E-(s)-cis

(c) Z-(s)-trans (d) Z-(s)-cis

Figure 6.1: The four rota-isomers of crotonaldehyde in the gas phase.

characterized by comparison to gas phase IR spectra. For this reason, the spectroscopic properties of the four rota-isomers of crotonaldehyde in the gas phase were computed during this thesis (Sec. 6.1.3).
Combining TPD measurements, HREEL spectra and DFT calculations, an analysis of the decomposition process starting at higher temperatures was carried out. The identification of several intermediate fragments in the experimental HREEL spectra allows to suggest a scheme of decomposition reactions. Finally, coadsorption experiments of crotonaldehyde and D_2 aiming at achieving a hydrogenation of the molecule, are described, but instead of any hydrogenation products only an H-D exchange reaction was found.

6.1.1 TPD Results of Crotonaldehyde/Pt(111)

A principal knowledge on adsorption systems concerns desorption states and thermal evolution of adsorbed species on the surface. Therefore temperature programmed desorption (TPD) studies of crotonaldehyde adsorbed on Pt(111) at 100 K were performed. A comparably slow heating rate of 2 K/s, which allows a better temperature resolution of desorption states, was chosen for all experiments.
Firstly, one has to be aware that crotonaldehyde exhibits a typical fragmentation pattern in gas phase mass spectra, that depends on the method of ionization. A reference spectrum obtained by electron impact (EI) is shown in Fig. 6.2. It has been taken from the NIST internet database[1]. Whenever crotonaldehyde desorbs molecularly from the sample during TPD experiments, the EI ionization in the quadrupole mass spectrometer induces the molecule to undergo typical dissociations and rearrangements that lead to the fragments detected in this pattern. Thus the signals of this pattern can also be expected in the TPD spectra, if the crotonaldehyde molecules

[1] National Institute of Standards and Technology, MD, USA [135].

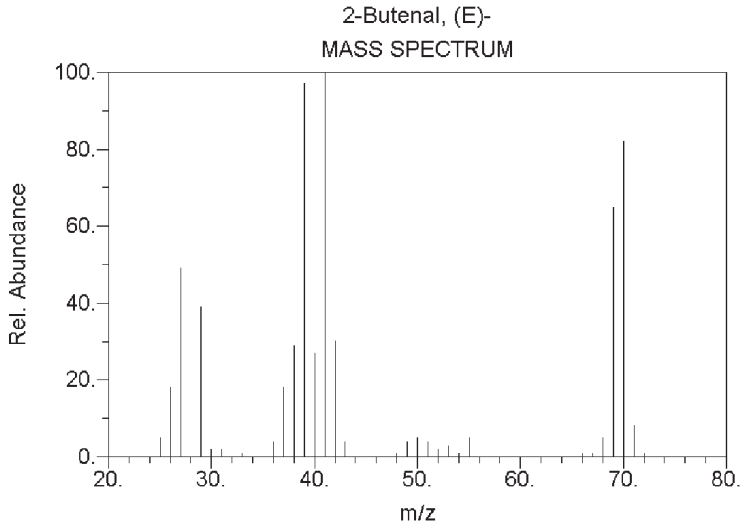

Figure 6.2: Fragmentation pattern of crotonaldehyde in the gas phase obtained by electron impact ionization (EI). The mass spectrum was taken from the NIST internet database [135].

desorb intact from the surface.

Since it was not known which species would desorb from the Pt(111) surface, the first step was to record *all* mass signals in the intervall between 1 amu and 75 amu (parental ion m/z = 70) simultaneously (Fig. 6.3) for different initial exposures. This was performed in the temperature range starting at the adsorption temperature (95-100 K) up to 800 K, at which most other hydrocarbons are usually decomposed to surface carbon species.

Shown in Fig. 6.3 is a relatively high initial precoverage of the sample with 3.3L crotonaldehyde. Several different desorption states of intact crotonaldehyde, CO, molecular hydrogen and propylene fragments are observed in all experiments. At ca 143 K and 165 K, the signals of 70 amu (crotonaldehyde parental ion), 41 amu, 39 amu (both propylene), 28 amu (CO) and 2 amu (H_2) can be identified (performing line scans, this information gets clearer; in the following paragraphs the signals will be shown separately and discussed in detail). The appearance of the complete fragmentation pattern indicates clearly that these are molecular desorption states of crotonaldehyde, which is bound comparably weakly to the substrate. In contrast to this, at temperatures above 200 K no more signals with m/z = 70 are detected. Around 275 K and 420 K the TPD shows the desorption of H_2, which must be originating from the decomposition of a surface species formed by the initial crotonaldehyde adsorption and is consistent with the desorption of CO at 397 K.

The experiments carried out with smaller crotonaldehyde precoverages show a similar behaviour except for the low temperature desorption peak of crotonaldehyde at 143 K, which therefore must correspond to a multilayer adsorption state. Thus it is recognized in these TPD experiments that crotonaldehyde is bound to Pt(111) in several different states. From the weakly bonded states it desorbs molecularly, whereas the more strongly adsorbed species decompose on the Pt(111) surface. The decomposition leads to the accumulation of CO and hydrogen, which desorb in subsequent steps at increasing temperatures.

After identification of all mass fragments emerging from the sample below 800 K, further experiments were performed with a focus on the signals with m/z = 70, 41, 39, 28 and 2. On the one hand this allowed a higher sampling rate for each signal, improving the signal/noise

ratio, and on the other hand also different sensitivities for each signal could be applied. For the set of the weaker signals of crotonaldehyde and propylene (70, 41, and 39 amu) that are hardly present in the background gas, a higher secondary electron multiplier (SEM) voltage could be employed without saturating the measured signals as compared to the TPD experiments of both CO (28 amu; yet also N_2 contributes to the background) and hydrogen (2 amu), which are always present significantly in the chamber background.

In order to analyze the data quantitatively by a comparison of the integrated peak areas of different mass signals one must keep in mind that the ionization probability of the different species is generally not similar and furthermore is temperature dependent (particle velocity in QMS $\propto \sqrt{T}$), too.

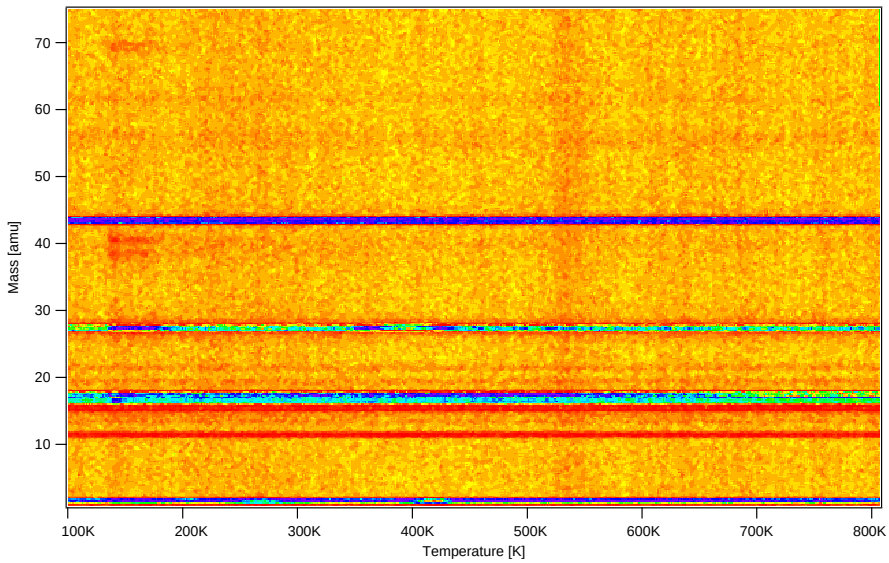

Figure 6.3: Overview TPD experiment of the mass range between 1 and 100 amu recorded after adsorption of 3.3L crotonaldehyde at 100 K on Pt(111).

Given the information of desorbing species, a series of TPD experiments with increasing crotonaldehyde precoverages from submonolayer to multilayer exposures were recorded in the temperature interval between 100 K and 800 K. Before presenting these TPD exposure series, an exemplary set of TPD spectra of a similar coverage compared to Fig. 6.3, shall be discussed in more detail to clarify the behaviour observed previously.
As displayed in Fig. 6.4, the TPD spectra of 3.0L crotonaldehyde adsorbed on Pt(111) at 100 K show three low temperature desorption states of intact crotonaldehyde. At 143 K, a desorption from a multilayer (α_1) of crotonaldehyde[2] takes place. At 177 K, a reversibly adsorbed layer (α_3) of crotonaldehyde on Pt(111) desorbs, while a badly resolved shoulder at 160 K might indicate another desorption state (α_2) to exist here. The origin of both the adlayer desorption and multilayer desorption will be discussed later on. As expected, all desorption signals of crotonaldehyde are accompanied by the corresponding peaks of m/z = 41, 39, 28 and 2.
Above 250 K, only fragments stemming from the decomposition process on the reactive Pt(111) surface are detected. Among the first dissociation reactions occurring must be the cleavages of C-H bonds, which would lead to a wide hydrogen desorption signal around 316 K (β_1). Although blank TPD of m/z = 2 and 28 carried out on a newly prepared Pt(111) surface lead only to

[2]The multilayer can be expected to correspond to a (frozen) condensed phase.

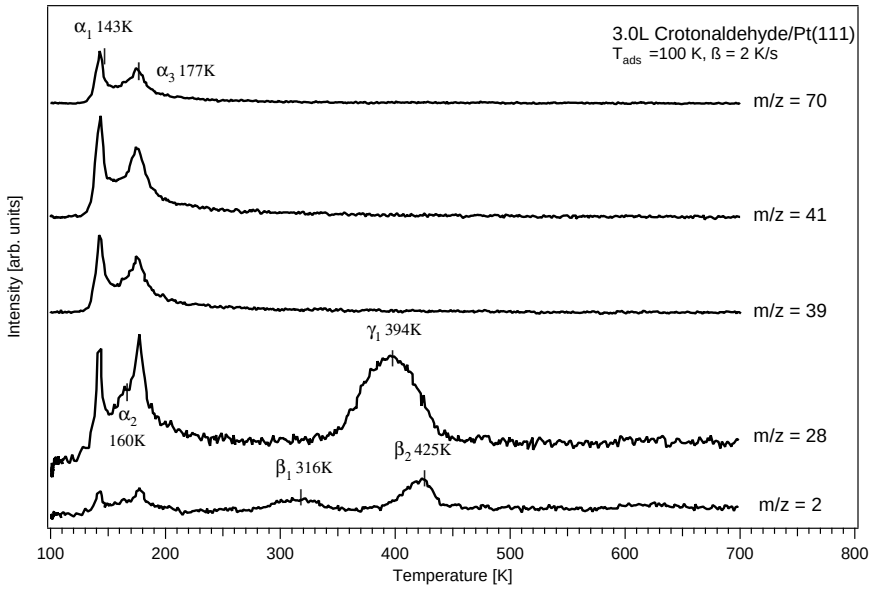

Figure 6.4: TPD experiment of 3.0L crotonaldehyde adsorbed at 100 K on Pt(111). Mind that the signals of m/z=28 and m/z=2 have been recorded with a lower channeltron voltage than m/z=39,41,70.

small desorption signals of H_2 and CO adsorbed from background gases, a small contribution from hydrogen coadsorption cannot be excluded for this desorption state. By comparison to reference measurements of H_2 desorption on Pt(111) carried out in this work, it is seen that this is a desorption limited process, which might be shifted to slightly lower temperatures by intermolecular interactions. This is in good agreement with the TPD spectra of H_2 on Pt(111) recorded by Paffett et al. [37], which show a second order associative hydrogen desorption peak shifting from 390 K at low hydrogen coverages to 315 K at higher coverage.
Around 397 K the desorption of CO (γ_1) suggests that this decomposition compound originates from a surface species, which has been formed from irreversibly adsorbed crotonaldehyde molecules. Whether the C-O moiety of this species is of aldehydic or hydroxy character cannot be distinguished on the basis of the TPD results. The HREEL spectra measured (Sec. 6.1.6) after annealing to this temperature range reveal several strongly bound crotonaldehyde structures that transform under loss of CO into pure hydrocarbons. These hydrocarbons undergo further transformations with increase of the temperature as evidenced by a second desorption peak (β_2) of H_2 around 425 K. This time the signal corresponds to a reaction limited desorption process of H_2 that has dissociated from the remaining surface species, since it appears at temperatures well above the typical H_2 desorption temperature [37].

In further TPD experiments, the coverage dependence of the different crotonaldehyde adsorption states and the decomposition process was investigated. An analysis of the desorption states of first order according to Redhead [56] yielded the activation energies of the desorptions. The results of these TPD coverage series will be summarized now.
The evolution of the crotonaldehyde desorption states with increasing exposure allows several important conclusions on the adsorbed species measured in the HREELS experiments in the sections 6.1.5 and 6.1.6. Firstly, at initial exposures below 1.5L (Fig. 6.5), no desorption signals of intact crotonaldehyde are observed. Since the sticking coefficients of strongly bonding molecules are usually close to unity, it is concluded that the first 1.5L crotonaldehyde form

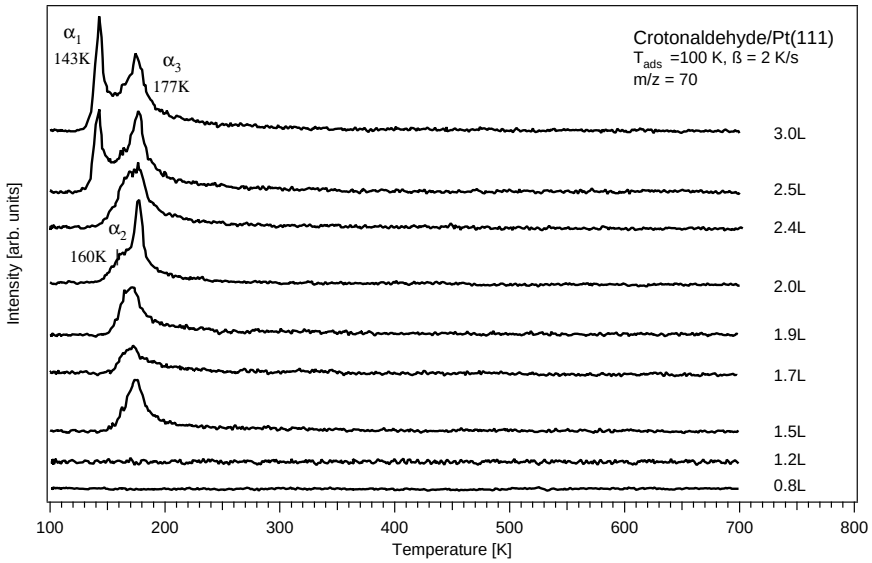

Figure 6.5: TPD spectra of m/z=70 as a function of crotonaldehyde exposure on Pt(111).

an irreversibly adsorbed monolayer, which decomposes at higher temperatures. Increasing the exposure up to ca 1.9L, the TPD series first shows the appearance of a desorption signal at 177 K (α_3) that may be interpreted as the desorption of a reversibly adsorbed species or a partial desorption process. This is a desorption signal of first order, because no significant shift of the desorption maximum can be recognized. Assuming a coverage independent frequency factor of $\nu = 10^{13}$ Hz, an activation barrier for the desorption process of 45.3 ± 1.1 kJ/mol is calculated for this state (estimated errors of the size of $\delta T_{max} \leq 4$ K, $\delta\beta \leq 0.05$ K/s). At exposures between 2.0L and ca 2.4L a low temperature shoulder of this desorption state is recognized at 160 K (α_2). Using the same assumptions, the activation barrier is estimated to be 41.9 ± 1.3 kJ/mol. Starting at about 2.5L the growth of the desorption signal from the physisorbed multilayer is observed at 143 K. Since no temperature shift of the desorption rate maximum is recognized with increasing exposures, a first order kinetics is applied, giving a desorption activation energy of 36.9 ± 1.3 kJ/mol for this process (although a multilayer desorption is usually of 0. order and should show a temperature shift). Hence the intramolecular interactions of crotonaldehyde in the physisorbed multilayer can be concluded to be sizable.[3]

Two factors render a quantitative analysis of the surface coverages from the TPD series difficult. Besides the sticking coefficients for crotonaldehyde, which are unknown, but can be expected to deteriorate significantly for each of the three weakly adsorbed states (α_1-α_3) compared to the strongly bonded crotonaldehyde phase, also the pumping speed of such a "heavy" molecule is slow. Yet a sufficiently high pumping speed is required for a satisfactory analysis of the integrals similar to the King method [62, 66]. Nonetheless the relative coverages of the different adsorption states can be estimated roughly with some simple assumptions.
From the integrated areas (Θ) of the desorption states of the TPD spectra (m/z = 70), a ratio of $\Theta(\alpha_2) : \Theta(\alpha_3)$ of $1 : 2(\pm 0.5)$ is derived. The correlation of the amount of desorbing crotonaldehyde relative to the amount of the irreversibly adsorbed species can be obtained

[3]Thermochemical investigations by Steele et al. [136] put the standard vaporization enthalpy of E-crotonaldehyde (boiling point ca 377 K, melting point 197 K [137]) at a very similar value of $\Delta_l^g H_m(298.15\text{ K}) = 37.70 \pm 0.12$ kJ/mol.

with a comparison to the exposures. As seen from TPD, the first 1.2L of crotonaldehyde form the irreversibly adsorbed phase, while an additional exposure of ca 0.5L can be assigned to the reversible adsorption state corresponding to α_3. The continued adsorption of up to ca 0.5L crotonaldehyde leads to the appearance of the intermediate desorption state α_2. The comparison of these values to the integral ratio suggests that the sticking coefficient of the intermediate state is about half of that of the reversible adlayer, hence $\sigma(\alpha_2) \approx 1/2\sigma(\alpha_3)$. At this point two more assumptions on the sticking coefficients have to be made. Usually it can be assumed that the sticking coefficient of a strongly bonded species is close to unity ($\sigma(irrev.) \equiv 1$).
Furthermore, the sticking coefficient of the much weaker bonded states can be expected to be lower, i.e. $\sigma(irrev.) > \sigma(\alpha_3)$. An estimtation might therefore be $\sigma(\alpha_3) \approx 1/2\sigma(irrev.)$. Correlating the exposures with the corresponding sticking coefficients one obtains a coverage ratio of $\Theta(irrev.) : \Theta(\alpha_2) : \Theta(\alpha_3) \approx 12 : 1 : 4$.
This allows the important conclusion, that the majority of the adsorbed crotonaldehyde forms an irreversible phase ($\Theta_{relative}(irrev.) = 70\%$), while only 24% desorb in the adlayer state α_3 and 6% in the intermediate adsorption state α_2. Varying the assumption in the interval $0.2 \leq \sigma(\alpha_3) \leq 1$ underlines this conclusion. For decreasing sticking coefficients, the amount of $\Theta_{relative}(irrev.)$ dominates even more obviously. At the upper limit, setting $\sigma(\alpha_3) \equiv 1$ and hence $\sigma(\alpha_2) \approx 0.5$, the fraction of irreversibly adsorbed crotonaldehyde amounts to 67% in contrast to 11% corresponding to $\Theta_{relative}(\alpha_2)$ and 22% for $\Theta_{relative}(\alpha_3)$.

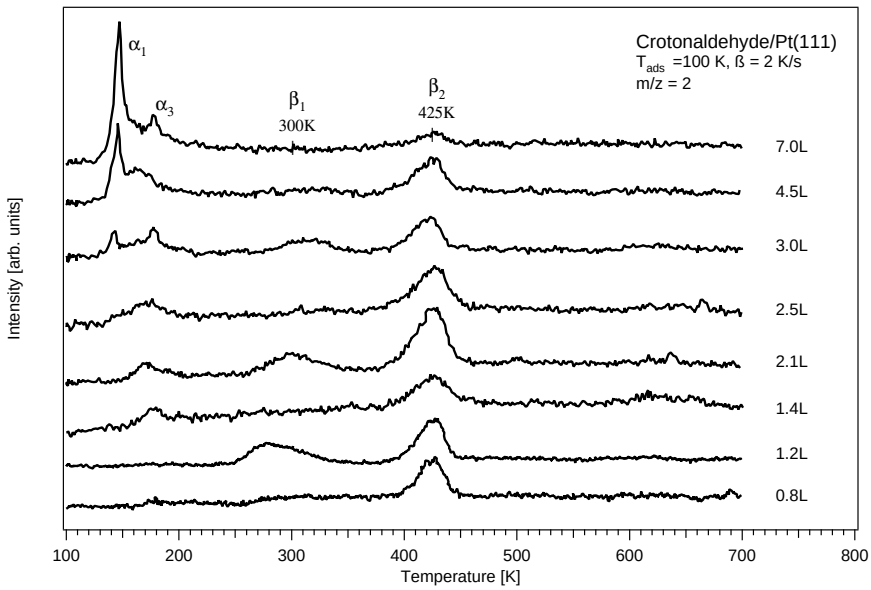

Figure 6.6: TPD spectra of m/z=2 as a function of crotonaldehyde exposure on Pt(111).

In the TPD spectra series for m/z = 2 (Fig. 6.6) a saturation of the signal at 425 K can be noticed. It is observed that the reproducibility of the spectra at similar initial exposures is rather unreliable in this case. Although the desorption state β_1 around 300 to 315 K is typically present, this signal is not always visible and tends to shift sizably. This could mean that this state arises partly from hydrogen coadsorption from the background gases. The appearance of the CO desorption detected around 400 K and the HREEL spectra discussed later prove that the aldehydic function is decomposed completely and with it at least the aldehydic hydrogen has to be dissociated from the molecule. Without any further H_2 desorption below 400 K, the hydrogen belonging to the aldehydic function has to either desorb before CO, or it could

rehydrogenate or rearrange to other surface species. Besides that also a possible influence from defect sites or steps and kinks on the Pt(111) surface can not be excluded at this time. Therefore, judging purely on the basis of the TPD data, the origin of the desorption state β_1 is not clear. Indeed, a precise interpretation of the HREELS spectra below 300 K reveals undoubtedly that the dissociation of the aldehydic hydrogen takes place between 275 K and 325 K concommitant with the onset of the appearance of CO on top- and bridge-adsorption sites starting at 300 K (see further sec. 6.1.7). Therefore it is concluded that the desorption state β_1 observed here arises from two processes with different kinetics, a reaction limited dissociation reaction and a desorption limited process, which have similar activation barriers.
The desorption state β_2, that has been assigned to a reaction limited desorption process arising from a H_2 dissociation from surface species present around 425 K, is always clearly identified and its peak maximum is rather independent of the coverage. Despite slight variations of this signal, the peak area reaches also a saturation at exposures of ca 1.4L in agreement with the exposure determined for the irreversibly adsorbed monolayer.

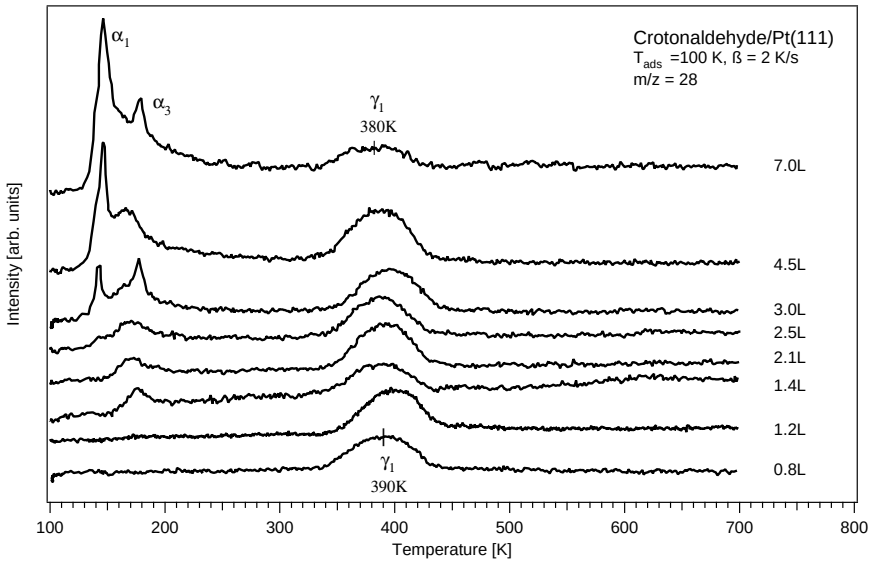

Figure 6.7: TPD spectra of m/z=28 as a function of crotonaldehyde exposure on Pt(111).

Further support for this observation is also gained from an exposure series and TPD spectra for m/z = 28 (Fig. 6.7). Apart from the CO signals originating from the fragmentation reaction of the crotonaldehyde parental ion in the mass spectrometer (α_1 and α_3), only a single desorption state is measured that is even seen after very small crotonaldehyde exposures (not displayed for clarity of Fig. 6.7). The desorption rate maximum shifts weakly from ca 390 K at low exposures to 380 K at high coverages, but small deviations from this trend are also seen. This might be due to intermolecular interactions of the CO adsorbed with other surface moieties on the Pt(111) surface just after the dissociation. According to the HREELS results, the fragmentation reaction of the aldehydic function starts at 300 K and is completed around 350 K. The emerging CO is thus bound to the surface before the desorption starts. This intermediate binding state to the surface renders CO to be a "probe" of the surface condition, making it very sensitive to any changes induced to the sample by crotonaldehyde adsorption and decomposition. An analysis of the activation energy for the desorption process of CO gives an estimate of 102.4 ± 1.5 kJ/mol at 0.8L ($\nu = 10^{13}$ Hz) and 99.7 ± 1.5 kJ/mol at 2.1L, which is in good agreement with TPD experiments of CO on Pt(111) performed by Paffet et al. [37], who measured CO desorption

between 450 K (125 kJ/mol) and 375 K (108 kJ/mol) for increasing coverages.
In order to further investigate the saturation effect, several coadsorption experiments with CO preadsorbed before crotonaldehyde exposure have been performed on Pt(111) (Fig. 6.8).

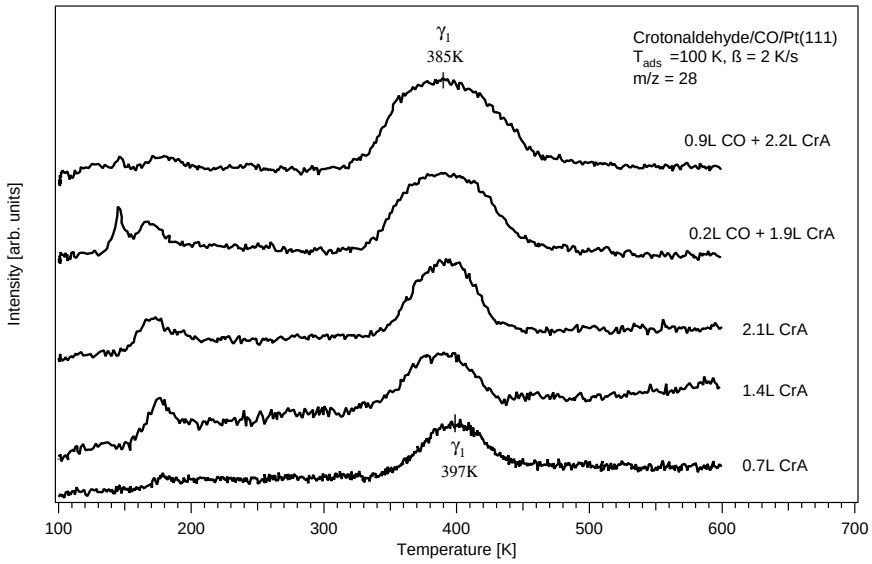

Figure 6.8: TPD spectra taken after crotonaldehyde and CO coadsorption experiments, m/z=28.

Here it becomes very obvious that in contrast to the previous TPD series of m/z = 28 a significant increase of the desorption peak area is achieved by coadsorption of even only very small amounts of CO. Also the temperatures of the CO desorption maxima are found to decrease only slightly to 385 K upon CO coadsorption[4]. In summary, these TPD experiments clearly strengthen the conclusion that it is definitely the irreversibly adsorbed crotonaldehyde layer, which undergoes a decomposition process at high temperatures.
Finally, the mass signals m/z = 39 and 41 are always observed in parallel (Fig. 6.9 and 6.10). These signals arise from propylene fragments, which can either develop from the crotonaldehyde parental ion in the mass spectrometer (α_1, α_2 and α_3), or can originate from molecular propylene desorbing from the surface, where it might be produced during the decomposition process. Like the hydrogen desorption state β_1, the propylene signal δ_1 around 330 K is not always measured in the TPD experiments. To make the situation even worse, δ_1 is quite wide (ca 40 K) but weak in intensity compared to the peaks arising from the crotonaldehyde desorption states. Therefore the origin of the propylene desorption state is not clear in this case.

Similar TPD studies on the system crotonaldehyde/Pt(111) have been reported by de Jesús et al. [48] for an initial multilayer adsorption. Despite a much lower temperature resolution in their TPD spectra, the results of this group agree qualitatively well with the present data. Besides multilayer desorption at 140 K, these authors measured the "monolayer" desorption state of intact crotonaldehyde as a wide signal with a maximum at 175 K and a high temperature tail extending up to 220 K. Also the decarbonylation process on the Pt surface was observed, with desorption states of CO at 420 K and H_2 at 280 and 440 K indicating a fragmentation of the

[4]Since it has not been the aim of the current studies, no further analysis of the intermolecular interactions of CO with other surface species present here or a possible displacement of preadsorbed CO by crotonaldehyde adsorption have been carried out.

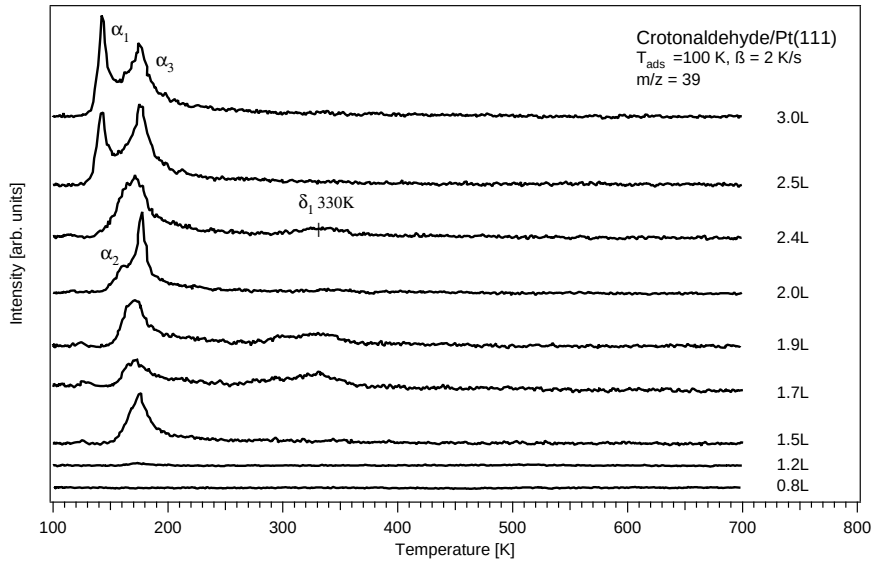

Figure 6.9: TPD spectra of m/z=39 as a function of crotonaldehyde exposure to Pt(111).

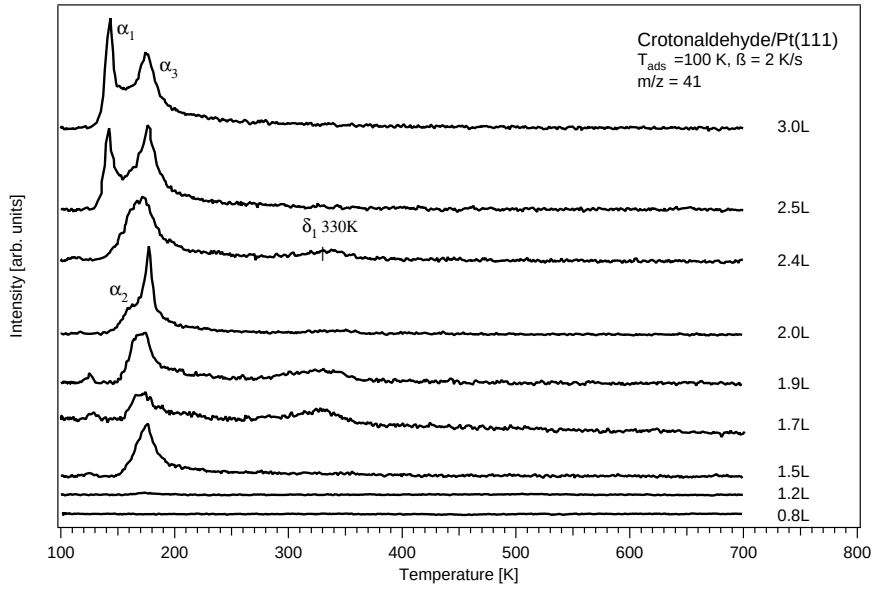

Figure 6.10: TPD spectra of m/z=41 as a function of crotonaldehyde exposure to Pt(111).

aldehydic backbone. Remarkebly, these authors detected in addition very weak signals of 39 and 41 amu corresponding to a propylene desorption around 340 K, but they could not determine whether this very small amount of propylene evolved during the decomposition. Possibly the remaining hydrocarbon moieties of crotonaldehyde formed alkylidyne (propylidyne) species on the surface, but these could hardly be detected in the RAIRS measurements carried out between 90 and 400 K. Their interpretation of their RAIRS measurements will be discussed more closely in the following sections.

Relative energies [kJ/mol]	E-(s)-trans	E-(s)-cis	Z-(s)-trans	Z-(s)-cis
RI-DFT BP86/SVP	0.0	4.5	10.1	9.0
RI-DFT BP86/TZVP	0.0	7.8	11.4	14.5
RI-DFT BP86/TZVPP	0.0	8.9	11.8	15.5
VASP DFT PW91	0.0	9.0	12.1	15.8
Molpro RHF/VDZ	0.0	13.8	16.9	20.7
Molpro CCSD/VDZ	0.0	11.9	13.9	16.5
Molpro CCSD(T)/VDZ	0.0	8.9	11.8	15.5

Table 6.1: Relative energies of the four crotonaldehyde rota-isomers relative to the E-(s)-trans form at various levels of theory.

6.1.2 Characterization of Crotonaldehyde in the Gas Phase

Before switching to the DFT results related to the adsorption of crotonaldehyde on Pt(111), the theoretical investigations of crotonaldehyde in the gas phase are presented. The four rota-isomers of crotonaldehyde (Fig. 6.1) have been calculated in the gas phase using various methods and different program packages with two aims: On the one hand, a characterization of crotonaldehyde in the gas phase provides the reference, to which changes in the geometry and the vibrational frequencies of the adsorption complexes can be compared. On the other hand, the quality of the results obtained with the periodic approach implemented in VASP is evaluated in comparison with the results of typical gas phase calculations performed with Turbomole [126] (RI-DFT) or Molpro [124] (coupled cluster, CCSD(T)).

First of all it is seen that the E-(s)-trans form is always the stabilomer at all levels of theory (Tab. 6.1). From the different gas phase optimizations using the resolution of identity formalism [138] together with the Becke-Perdew 86 [80, 81, 83] functional (RI-DFT BP86) implemented in the Turbomole program package [126], the influence of the size of the basis set is clearly visible. While in a small SVP (split valence plus polarization function) basis the Z-(s)-cis isomer (9.0 kJ/mol) is computed to be lower in energy than Z-(s)-trans crotonaldehyde (10.1 kJ/mol), this trend is reversed upon switching to larger basis sets of triple-ζ quality (TZVP, 11.4 and 14.5 kJ/mol). Obviously, the step from a SVP basis to a TZVP basis affects primarily the relative stability of the E-(s)-cis and Z-(s)-cis rota-isomers. A more flexible basis set with an additional polarization function (the TZVPP basis) slightly enhances this effect. Since the relative stabilities converge to errors of about 1 kJ/mol with respect to the size of the basis set, the TZVP results represent a good compromise between accuracy and computational cost.

Using the periodic DFT code VASP gas phase optimizations have been carried out, but here with a small trick: In order to minimize the intermolecular interactions and lift the periodic constraints, the molecule is computed in a sufficiently large vacuum box of a $20 \times 13 \times 13$ Å^3 volume. In the plane wave expansion the size of the basis is controlled by the kinetic energy cutoff of the plane waves included, which is chosen at 400 eV here. As Tab. 6.1 shows, the results obtained with VASP are of a similar quality like the RI-DFT/TZVPP calculations. Again E-(s)-trans is the most stable rota-isomer and the E-(s)-cis (9.0 kJ/mol), the Z-(s)-trans (12.1 kJ/mol) and the Z-(s)-cis (15.8 kJ/mol) forms are calculated somewhat higher in relative energy.

The results of the wave function based and strictly size-consistent CCSD(T)/cc-pVDZ optimizations carried out with the Molpro package [124] lead to the same sequence of relative stabilities of the four crotonaldehyde rota-isomers. One important result of the computationally more costly CCSD(T)/cc-pVDZ calculations is the observation that the electronic structures of the four rota-isomers are quite complex. Although the proper sequence in the relative energies of the four rota-isomers is already reproduced qualitatively at the RHF/cc-pVDZ level (restricted Hartree Fock), it is described pretty badly by the single reference approach: E-(s)-cis

Parameter	E-(s)-trans	E-(s)-cis	Z-(s)-trans	Z-(s)-cis
r(O-C1)	1.23	1.23	1.23	1.23
r(C1-C2)	1.46	1.47	1.46	1.47
r(C2-C3)	1.35	1.35	1.35	1.35
r(C3-C4)	1.49	1.49	1.49	1.49
r(C1-H1)	1.12	1.13	1.12	1.12
r(C2-H2)	1.09	1.09	1.09	1.09
r(C3-H3)	1.10	1.10	1.10	1.10
r(C4-H4)	1.10	1.10	1.10	1.09
r(C4-H5,6)	1.10	1.10	1.10	1.10
r(H-bond)				2.31
α(O-C1-C2)	124.8	125.2	123.3	126.8
α(C1-C2-C3)	121.0	122.2	125.7	127.5
α(C2-C3-C4)	126.0	125.8	128.5	128.3
α(O-C1-H1)	120.6	119.9	119.8	119.5
α(C1-C2-H2)	117.1	116.8	114.7	114.4
α(C2-C3-H3)	117.6	116.8	116.8	116.4
α(H4-C4-C3)	112.2	112.5	114.0	112.6
α(H5,6-C4-C3)	110.7	110.5	110.0	109.6
δ(O-C1-C2-C3)	180.0	0.0	180.0	0.0
δ(C1-C2-C3-C4)	180.0	180.0	0.0	0.0
δ(H1-C1-C2-C3)	0.0	180.0	0.0	180.0
δ(O-C1-C2-H2)	0.0	180.0	0.0	180.0
δ(C1-C2-C3-H3)	0.0	0.0	180.0	180.0
δ(H4-C4-C3-C2)	180.0	0.0	0.0	0.0
δ(H5-C4-C3-C2)	121.5	121.7	121.9	122.3
δ(H6-C4-C3-C2)	-121.5	-121.7	-121.9	-122.3

Table 6.2: Geometries of the four crotonaldehyde rota-isomers calculated in the gas phase using VASP. All distances r are given in Å and all angles in degree. The value r(H-bond) denotes the closest, non-covalent H-O distance observed between the hydrogen H4 of the methyl group and the aldehydic oxygen in Z-(s)-cis crotonaldehyde.

at 13.8 kJ/mol, Z-(s)-trans at 16.9 kJ/mol and the Z-(s)-cis at 20.7 kJ/mol. Including the singly and doubly excited configuration state functions (CSF), these values are improved considerably, giving 11.9 kJ/mol for the E-(s)-cis, 13.9 kJ/mol for the Z-(s)-trans and 16.5 kJ/mol for the Z-(s)-cis form. Furthermore adding the perturbative triple excitations changes these values only slightly to 11.8 kJ/mol for Z-(s)-trans and 15.5 for Z-(s)-cis whereas the E-(s)-cis is stabilized significantly at 8.9 kJ/mol. For the proper description of the E-(s)-trans and E-(s)-cis rota-isomers, about 975.000 configuration state functions (CSF) are generated by single and double excitations from the electronic ground state (reference) configuration in the coupled-cluster expansion. In contrast, for both Z rota-isomers about 1.89×10^6 CSFs are generated. The correlation-consistent cc-pVDZ basis sets [139], valence double-ζ basis sets augmented by polarization functions, are already large basis sets for these full CCSD(T) optimizations and so the relative energies obtained by this method are considered to be more reliable than the previous DFT results.

A comparison of the relative stabilities given above to values obtained from theoretical calculations and experiments by other groups reveals a good agreement in most cases. For crotonaldehyde, MNDO/AM1 calculations performed by Thakur et al. [140] put the energy of the E-(s)-cis form 0.1 kJ/mol above the E-(s)-trans form, while experimental studies estimate the difference to be between 7.1 kJ/mol [141] and 8.1 kJ/mol [142]. Hence the values presented in this work

agree very well with both experimental results, but the force-field calculations by Thakur et al. are evidently sizably to small. In the case of acrolein, Loncharich et al. [143] computed the energy difference between the (s)-trans and the (s)-cis form at 7.1 kJ/mol (RHF, 6-31G*). Latest DFT calculations [53] put this value at 9.6 kJ/mol compared to experimental data of 6.9 kJ/mol measured by Blom et al. [144] in the gas phase. The substitution of a methyl group on the β-carbon of acrolein therefore hardly influences the relative stabilities, since neither any significant change of the electronic structure nor any additional sterical strain occurs.
Also the geometry parameters of the four rota-isomers in the gas phase have been compared at the different levels of theory and represent reference data for the analysis of the interactions in the adsorption geometries encountered on the various model catalysts.
The bond lengths and bond angles obtained in the VASP optimizations are presented in Tab. 6.2. Certain variations characteristic for the configurations of the rota-isomers are observed. For instance it is seen that the distance r(C1-C2) and the bond angle α(O-C1-C2) are linked in a specific manner to the (s)-cis or (s)-trans configuration of the C1-C2 single bond, respectively. In the E-(s)-trans and Z-(s)-trans isomer both r(C1-C2) and α(O-C1-C2) are about 1% smaller than the values of E-(s)-cis and Z-(s)-cis crotonaldehyde. Likewise the computed values of r(C2-C3) and α(C1-C2-C3) are smaller in the E configurations than the Z rota-isomers. Since the distances of the C2=C3 double bond are very similar, the corresponding bond strength must be constant for all rota-isomers. In addition also the aldehydic C1=O bond is found to be quite constant in strength, even in the Z-(s)-cis isomer. The latter form exhibits a relatively short hydrogen-oxygen distance between one of the methyl protons (H4) and the aldehydic oxygen of 2.31 Å. Although this value is significantly longer than a typical hydrogen bond for i.e. in water (ca 1.9 Å), a weak interaction can not be ruled out, yet the distance r(C4-H4) of the hydrogen close to the aldehydic function hardly indicates that such an intramolecular hydrogen bond is formed. In general, all other C-H bond lengths and the remaining bond angles are found to depend only very weakly on the configuration of the corresponding rota-isomer and are thus rather uncharacteristic.
The dependencies of the geometrical parameters from the choice of the basis set and the methods are small; the bond lengths and angles vary only slightly (typically below 1%, although slightly larger deviations for angles are found than for distances). For this reason, the gas phase geometry parameters obtained with RI-DFT BP-86/TZVP are only given in Tab. B.1 of App. B and shall not be discussed here further.

Another important question involves the rotations around the C1-C2 and the C2=C3 bond axis, which transform the (s)-trans into (s)-cis and the E into Z configurations, respectively. The complete potential curves of both rotations have been calculated at the RI-DFT BP-86/TZVP and TZVPP levels to determine the activation barriers of the transformations. Additional single point computations of the transition states at the geometries obtained by the RI-DFT BP-86/TZVPP calculations carried out at the CCSD(T)/cc-pVDZ level give more precise estimates of the activation barriers. The transition states are found at rotation angles of $\pm 90°$ around the considered axis and are characterized by a single imaginary frequency corresponding to a rotation around this axis.
With a TZVP basis the energy barrier of a rotation around the C1-C2 axis transforming E-(s)-trans crotonaldehyde into the E-(s)-cis form is computed at 44.8 kJ/mol (TZVPP 53.0, see Fig. 6.11) relative to the E-(s)-trans ground state. For the same rotation, but from the Z-(s)-trans into the Z-(s)-cis rota-isomer, a somewhat lower activation barrier of 32.3 kJ/mol (TZVPP 35.2) relative to Z-(s)-trans has to be crossed. In agreement with the fact, that the bond C1-C2 is a conjugating single bond, these activation barriers correspond to bond orders intermediate between a single and a double bond.
As seen by the comparison of the barrier heights at the RHF, CCSD and CCSD(T)/cc-pVDZ levels, the expansion of the single reference configuration (the *Slater* determinant of the electronic

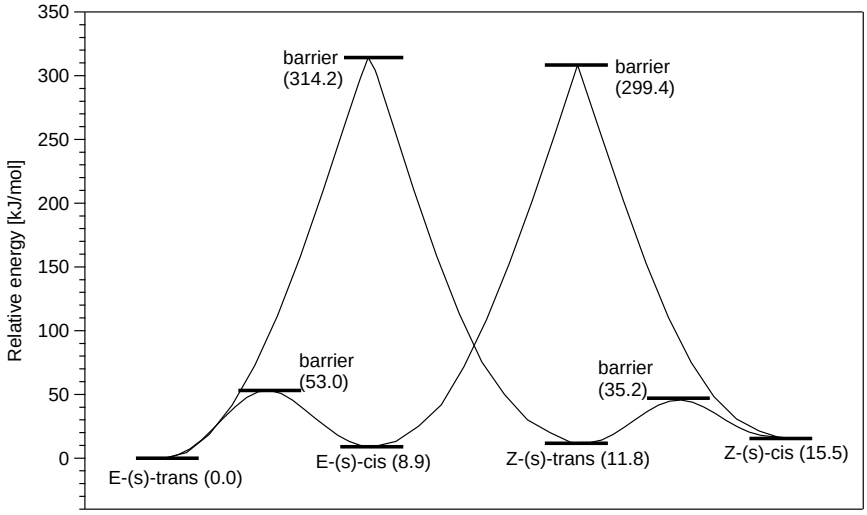

Figure 6.11: Schematic presentation of the relative stabilities of the four crotonaldehyde rota-isomers and the transition states of the rotation around the C1-C2 and C2=C3 axis (see text) at the RI-DFT BP86/TZVPP level of theory.

ground state) into the larger *Hilbert space* of singly and doubly excited configurations becomes even more important. While at the RHF level only 28.0 kJ/mol (E-(s)-trans to E-(s)-cis) and 9.8 kJ/mol (Z-(s)-trans to Z-(s)-cis) are computed for the activation energies, these values increase sizably at the CCSD level to 37.1 and 22.6 kJ/mol (both 1.89×10^6 CSFs). Finally, with the perturbative triple excitations of CCSD(T), values of 41.0 kJ/mol and 27.6 kJ/mol are obtained for the two rotational transition states. Together with the RI-DFT results, thus, a consistent picture is formed.

The smaller activation barrier found for the rotation around the C1-C2 axis in the Z isomers is no physical phenomenon, but simply a question of the reference state to which it is compared. If the energies of both transition states are calculated relative to E-(s)-trans crotonaldehyde, the two structures appear very close in energy at 41.0 kJ/mol and 39.4 kJ/mol respectively. This value of 40 kJ/mol can therefore be taken as a rough estimate of the contribution from the conjugation of the C1=O and C2=C3 double bond, which is broken up in the transition state geometry.

As can already be expected from the previous argumentation, the barrier heights of the rotation around the C2=C3 double bond are much higher. In fact, the value obtained for the transformation from the E-(s)-trans to the Z-(s)-trans rota-isomer in the TZVP basis amounts to 328.0 kJ/mol (TZVPP 324.6 kJ/mol) relative to E-(s)-trans and the one from E-(s)-cis to Z-(s)-cis is computed at 310.8 kJ/mol (TZVPP 309.2 kJ/mol).

The activation barriers of the rotations around both bond axis are thus much larger and no conversion between the four rota-isomers in the gas phase is expected in the electronic ground state at room temperature. Nonetheless, these conversions may become possible upon adsorption on a surface, especially when the adsorption energies are of the same order of magnitude or even larger than the energy barriers.

For the activation energy of the rotation around the conjugating C1-C2 axis, Thakur et al. find a small rotational barrier of 8.9 kJ/mol (MNDO/AM1) [140]. This finding does not match with the experimental results of 30.9 kJ/mol by De Groot et al. [142] and 68.6 kJ/mol by Durig et

al. [141], which even do not agree well with each other. The value of 42.4 computed at the CCSD(T) level in this thesis for the transformation from E-(s)-trans crotonaldehyde to the E-(s)-cis isomer shows a better agreement with the experimental study by De Groot et al. It also shows clearly, that the rotational barrier obtained by Thakur et al. using a force-field method results in an energy barrier wrong by an order of magnitude. Restricted Hartee-Fock calculations by Loncharich et al. [143] put the barrier height in acrolein to 37.2 kJ/mol (RHF, 6-31G*), so that no significant substitutional effect due to the additional methyl group is noticeable here.
For completeness also the potential hyperplanes for a rotation of the hydrogens of the methyl group around the C3-C4 axis have been computed in the E-(s)-trans isomer. At the RI-DFT BP-86/TZVP level a low energy barrier of 6.9 kJ/mol is obtained, which slightly increases to 7.8 kJ/mol with the larger TZVPP basis sets.

The insertion of the relative stabilities from CCSD(T)/cc-pVDZ in a *Boltzmann Ansatz* provides an estimate of the composition of the crotonaldehyde gas phase at room temperature. At 300 K, 98.4% of crotonaldehyde is in the E-(s)-trans form while the rest is composed of 1% E-(s)-cis, 0.4% Z-(s)-trans and 0.2% Z-(s)-cis. Using the results from the RI-DFT BP-86/TZVPP optimization, the value of E-(s)-cis crotonaldehyde increases to 2.7%, but the sum of the fractions of both Z configured rota-isomers remains far below 1%.
Therefore it can be expected, that E-(s)-trans and E-(s)-cis configured adsorption geometries will be most important on the various surfaces, yet this has to be validated first in the following sections.

6.1.3 DFT results of Crotonaldehyde/Pt(111)

From previous investigations [13, 45, 50, 51, 52, 53] in the recent years, already a number of possible adsorption geometries on the pure platinum surface were known at the beginning of this thesis. In the DFT studies of this work, a much larger number of conceivable adsorption structures has been included. Only such coordination geometries have been ignored that could be excluded either on qualitative arguments or due to previous studies, which reported only weak interaction strengths with the substrate (for i.e. complexes adsorbed solely via an agostic hydrogen bond). In this section all stable adsorption geometries obtained from the DFT optimizations will be described and their relative stabilities will be discussed. The adsorption energies from the total energy computations will be used to derive first hints on the adsorption modes that may be encountered on Pt(111). An analysis of the bond distances of the various stable adsorption structures reveals systematic bond length changes that can be traced back to specific configurations of the considered rota-isomers. These characteristic variations have to be seen in close connection to the adsorption energies and the energy cost of the distortions of both the molecule and the surface upon adsorption and will later on be correlated with the vibrational shifts in Sec. 6.1.5.

Altogether 36 possible adsorption geometries have been fully optimized and can be separated into six "coordination families". Each of the family shows a specific coordination to the atoms of the Pt(111) surface and can be realized for the different rota-isomers discussed in the previous section. Tab. 6.3 shows the adsorption energies of all considered coordination structures of crotonaldehyde on Pt(111) calculated from the DFT optimizations at theoretical coverage of $\Theta = 1/9$ (adsorbate periodicity 3×3). In order to permit a better understanding of the rather confusing nomenclature of the crotonaldehyde surfaces complexes, all stable structures have been plotted in Figs. 6.12 to 6.14.
In the first figure the families of η^1-top and η^2-diσ(CO) adsorption geometries are shown. The η^1-top adsorption represents the lowest coordination number, in which α, β-unsaturated alde-

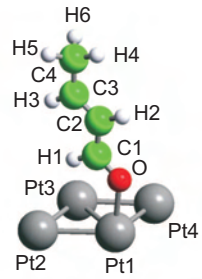

(a) η^1-top-E-(s)-trans

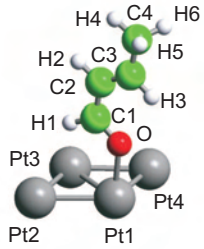

(b) η^1-top-E-(s)-cis

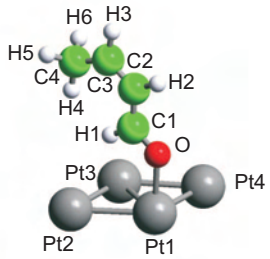

(c) η^1-top-Z-(s)-trans

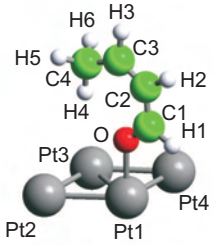

(d) η^1-top-Z-(s)-cis

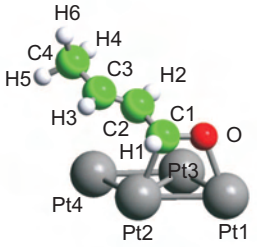

(e) η^2-diσ(CO)-E-(s)-trans

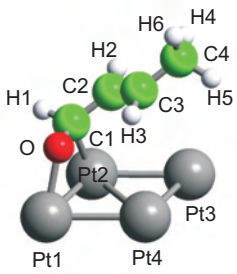

(f) η^2-diσ(CO)-E-(s)-cis

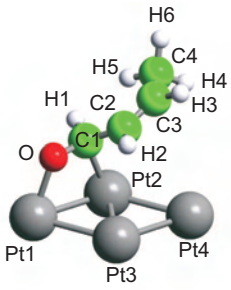

(g) η^2-diσ(CO)-Z-(s)-trans

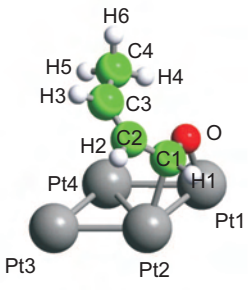

(h) η^2-diσ(CO)-Z-(s)-cis

Figure 6.12: The optimized adsorption geometries η^1 and η^2-diσ(CO) of crotonaldehyde on Pt(111).

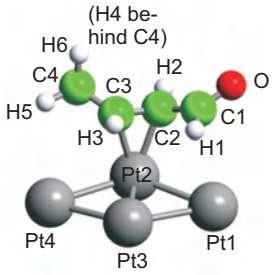

(a) η^2-π(CC)-E-(s)-trans

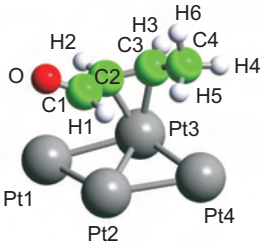

(b) η^2-π(CC)-Z-(s)-trans

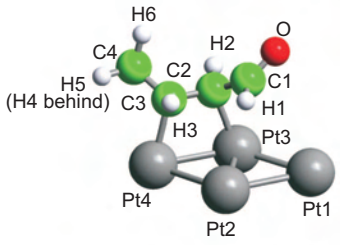

(c) η^2-diσ(CC)-E-(s)-trans

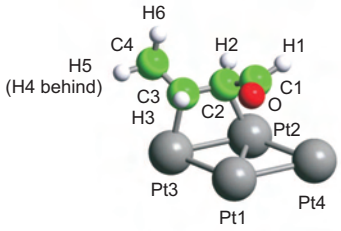

(d) η^2-diσ(CC)-E-(s)-cis

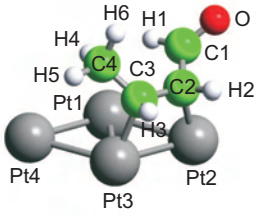

(e) η^2-diσ(CC)-Z-(s)-trans

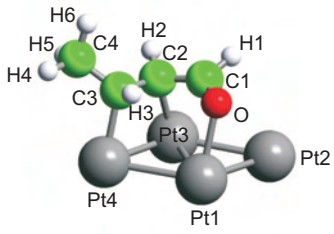

(f) η^3-diσ(CC)-σ(O)-E-(s)-cis

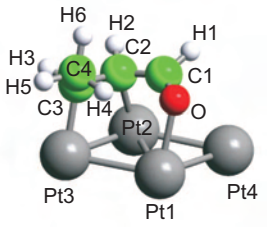

(g) η^3-diσ(CC)-σ(O)-Z-(s)-cis

Figure 6.13: The η^2-π(CC), η^2-diσ(CC) and η^3-diσ(CC)-σ(O)adsorption geometries of crotonaldehyd on Pt(111) optimized using VASP.

Adsorption energies [kJ/mol]	E-(s)-trans	E-(s)-cis	Z-(s)-trans	Z-(s)-cis
η^1-top	-23.5 (-28.1* [51])	-13.1	-24.4	-14.6
η^2-diσ(CO)	-20.6	-21.2	-14.2	-9.6
η^2-π(CC)	-44.4	unstable	-49.0	unstable
η^2-diσ(CC)	-76.0	-73.6	-66.0	unstable (-83.8 [51])
η^2-diσ(C3,O)	unstable	unstable	unstable	unstable
η^3-diσ(CC)-σ(O)	excluded	-76.9 (-79.0 [51])	excluded	-68.1
η^3-π(CC)-σ(O)	excluded	unstable	excluded	unstable
η^4-diσ(CC)-diσ(CO)	-80.2 (-79.8 [51])	excluded	-71.2	excluded
η^4-π(CC)-diσ(CO)	excluded	-68.7 (-71.2 [51])	excluded	-55.3

Table 6.3: Calculated adsorption energies of crotonaldehyde on Pt(111) at a theoretical coverage of $\Theta = 1/9$. The remark "excluded" refers to structures that have not been optimized because the initial geometry was already highly sterically strained. The reference values given in some cases are taken from Ref. [51]. Except for the values marked with an asterics the results of Delbecq et al. have been obtained without the use of dipole corrections.

hydes can be bonded sizably to a surface. The interaction mechanism is basically only a coordination of the aldehydic oxygen to a metal atom of the substrate with a Pt-O distance of 2.2 Å. This value is close to typical Pt-O bond lengths around 2.10 Å determined in organometallic complexes [145, 146]. The molecule is tilted up in a vertical position and the C2=O bond distance is slightly elongated by 2%. The hydrogen H1 of the aldehydic function points into a threefold hollow site in these structures and keeps a distance of around 2.87 Å from the surface atoms. Also a small distortion of the surface is induced by the η^1-top adsorption: the interacting Pt atoms are moved outward by about 0.07 Å. As seen in Tab. 6.3, the theoretical adsorption energies for the η^1-top configurations are rather weak. They are at about -23.5 kJ/mol for the η^1-top-E-(s)-trans and Z-(s)-trans structures and somewhat smaller for the E-(s)-cis and Z-(s)-cis complexes, which are computed at ca -14 kJ/mol.

At this point it is important to mention that all optimizations in Tab. 6.3 have been performed with dipole corrections to account for any unphysical interactions between the repeating slabs due to the periodic approach. These corrections are important in all cases, in which the adsorption structure has a strong dipole moment component normal to the surface, like for example for the η^1-top adsorption modes. Here the error may amount to up to 17 kJ/mol of additional, unphysical stabilization. For instance the computed adsorption energy of the η^1-top-E-(s)-trans complex is 41.5 kJ/mol without a dipole correction, which would render this to be a reasonably stable structure. But the inclusion of the correction lowers this value quite drastically to only 23.5 kJ/mol, leaving the structure in fact only weakly bound. For most of the other adsorption modes, the influence of the dipole corrections are below 2 kJ/mol. Nonetheless, the dipole corrections should not be neglected even in the flat adsorption structures, because they can sometimes influence the convergence process and may artificially stabilize adsorption structures. This has been observed in several critical cases like for i.e. the η^2-diσ(CC)-Z(s)-cis adsorption

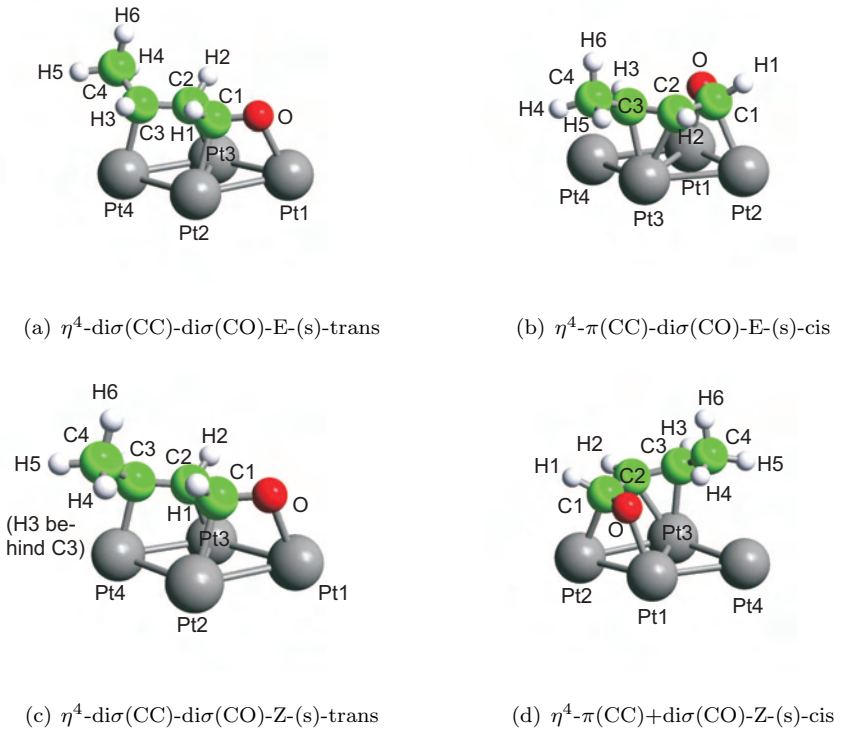

(a) η^4-diσ(CC)-diσ(CO)-E-(s)-trans

(b) η^4-π(CC)-diσ(CO)-E-(s)-cis

(c) η^4-diσ(CC)-diσ(CO)-Z-(s)-trans

(d) η^4-π(CC)+diσ(CO)-Z-(s)-cis

Figure 6.14: Optimized η^4-diσ(CC)-diσ(CO) and η^4-π(CC)+diσ(CO) adsorption geometries of crotonaldehyde on Pt(111).

complex (Tab. 6.14)and on the Pt-Sn surface alloys.

The coordination type η^2-diσ(CO) corresponds to a formation of two σ-bonds by interaction of the C1=O moiety with two neighboring Pt atoms. While the aldehydic part of the molecule is oriented parallel to the surface plane, the remaining C2=C3-C4 backbone is turned upwards by sterical repulsion. The O-Pt bond distances (Tab. 6.5) are quite short at an average of 2.09 Å in all four stable configurations and the C1-Pt bond lengths are computed at ca 2.25 Å. The surface atoms involved in the bonding are lifted up typically by ca 0.08 Å by the interaction to oxygen and 0.13 Å by the aldehydic carbon. This deformation of the surface induced by the adsorption is very typical and not really surprising for metals. In agreement with the expectations that can be derived from the coordination type, only r(C1-O) shows a significant elongation of a about 0.1 Å in the different geometries. Energetically the η^2-diσ(CO) are found to be also only weakly bonded to the surface with -9.6 to -21.2 kJ/mol. As known from previous theoretical studies, the η^2-π(CO) adsorption type is not stable on the Pt(111) and Pt-Sn surfaces [45, 51]. Therefore this coordination type has been excluded from the investigations in this work.

Another family of weakly bonded structures is given by the η^2-π(CC) type of coordination (Fig. 6.13). These structures are similar to the η^2-π(CC) adsorption complexes of ethylene found on many surfaces such as for instance $Pt_3Cu(111)$ [147]. Surprisingly, only the η^2-π(CC)-E-(s)-trans (-44.4 kJ/mol) and the Z-(s)-trans (-49.0 kJ/mol) forms are obtained to be stable structures here. During the optimization process, the E-(s)-cis and Z-(s)-cis geometries developed an additional coordination by the aldehydic oxygen towards a Pt atom and finally converged to a different coordination type, the η^4-π(CC)-diσ(CO) that will be described later in this section. The distortion of the molecular backbone of the crotonaldehyde rota-isomers upon adsorption is

primarily seen in the bond length r(C2-C3) (Tab. 6.5). By the adsorption, C2=C3 is lengthened sizably by 0.07 Å to ca 1.42 Å, which suggests a partial loss of its double bond character. Because the symmetry of the C2=C3 moiety is lowered by the substitution pattern by an aldehyde function and a methyl group, one could expect also the two C-Pt bonds not to be identical in this coordination type. Yet from the analysis of the optimized geometries, both distances r(C2-Pt) and r(C3-Pt) are found to be close to 2.22 Å. The interacting platinum atoms are pulled up very strongly from the surface plane by ca 0.31 Å. Small increases of the bond lengths are computed only for r(C1-C2) (ca 0.02 Å) and r(C3-C4) (ca 0.01 Å) in both configurations, while even the C-H bond distances are changed hardly.

Next, also well-known from the adsorption of alkenes on metal surfaces [148, 149, 150, 151, 152], is the family of η^2-diσ(CC) configurations (Fig. 6.13). The adsorption energies calculated from the DFT total energy studies are quite large between -76.0 kJ/mol (E-(s)-trans) and -66.0 kJ/mol (Z-(s)-trans) and indicate strongly bonded states of crotonaldehyde on the Pt(111) surface, which therefore are probable candidates to contribute to the HREEL spectra. The η^2-diσ(CC)-Z(s)-cis adsorption complex, which seemed to be stable in the preoptimization process with lighter convergence criteria on the residual forces acting on the atoms (< 0.05 eV/Å, no dipole corrections), evolved into an η^3-diσ(CC) geometry during the final optimization. The geometry parameters of the η^2-diσ(CC) structures also show a significant elongation of r(C2-C3) by about 0.15 Å, which can again be understood by the loss of double bond character upon the interaction (Tab. 6.4). Indeed, the relaxed bond length of ca 1.50 Å in all three configurations is very characteristic of a typical C-C single bond in hydrocarbons. Also the neighboring bonds C1-C2 and C3-C4 are computed with significantly increased bond distances of ca 1.49 Å and 1.52 Å, respectively. Matching with the much larger adsorption energy, the C-Pt bonds of the η^2-diσ(CC) adsorption modes are shorter than found for the η^2-π(CC) geometries. Here r(C2-Pt) and r(C3-Pt) vary both by about 0.01 Å around the median bond length of 2.14 Å. Due to the strong interaction of diσ-type configurations to the surface atoms, a large protrusion of the platinum of typically 0.18 Å (below C3) and 0.16 Å (C2) is induced.

Completely unstable on Pt(111) is the family of η^2-diσ(C3,O) coordination structures (not depicted). These geometries had been conceived as vertical, six-membered metallacycles, which are bound to the surface via the terminal oxygen and the carbon C3 and show a double bond rearrangement to C1=C2. As it turned out during the optimizations, the vertical structure quickly turned towards the surface to interact via the new C1=C2 π-bond, too. Finally the η^2-Diσ(C3,O) starting geometries evolved into higher coordinated η^3 and η^4 complexes.

More complicated to understand and handle are the families of higher coordinated species, namely the sets of η^3 and η^4 adsorption geometries. These are very typical for multi-functional molecules like α,β-unsaturated aldehydes and form very stable adsorption complexes on pure Pt(111). Both double bonds, C2=C3 and C1=O, interact with the catalyst surface in these species and are activated for hydrogenation. Commonly it is assumed that these highly coordinated adsorption structures are the precursors of the saturated hydrogenation products, the saturated alcohols or even the alkanes.

Two different kinds of η^3 adsorption modes are conceived on the Pt(111) surface, the η^3-π(CC)-σ(O) and the η^3-diσ(CC)-σ(O) coordination type, which is depicted in Fig. 6.13). This η^3-diσ(CC)-σ(O) can basically be divided into two parts: Two σ-bonds formed to underlying metal atoms, similar to the η^2-diσ(CC) configurations, plus an additional dative bond directed from the aldehydic oxygen to a third surface atom. The O-Pt interaction leads to a straining of the diσ(CC) part, which is observed by the asymmetric r(C2-Pt) and r(C3-Pt) bond distance (Tab. 6.6). Although the C3-Pt bond is computed at 2.12 Å, only 0.02 Å shorter compared to the η^2 complexes, r(C2-Pt) is found to be significantly elongated by ca 0.05 Å to 2.19 Å. Since C2 is closest to the aldehydic substituent, this effect must arise from sterical strain introduced by the additional interaction of the aldehydic function, which itself is quite long at ca 2.25 Å. The protrusions of the platinum atoms involved in the bonding are recognized to be very typical

for their configuration: Below the oxygen coordination a small outward shift of usually 0.03 Å is computed, while the diσ bonding induces characteristic protrusions of 0.13 Å (C2) and 0.15 Å (C3). The complex interaction mechanism also leads to several specific changes in C-C and C-H bond distances. To begin with the carbon backbone of the molecules, it is seen in Tab. 6.6 that both double bonds are elongated. The values of r(C1-O) are increased by 0.04 Å compared to the gas phase reference. Nearly exactly as in the η^2-diσ(CC) case, also r(C2=C3) is affected by the loss of the double bond character, amounting to around 1.50 Å here. The previously conjugating bond C1-C2 shows a small shortening of 0.02 Å and the methyl carbon bond C3-C4 is expanded sizably by 0.03 Å. It is also important to mention the significant shortening of one of the C-H bonds, namely the aldehydic C1-H bond. This phenomenon, since not observed in the η^2-diσ(CC) configurations, must be caused indirectly by the change of the electronic situation in the aldehydic function due to the additional O-Pt coordination rather than by sterical constraints. The calculated adsorption energies of both η^3-diσ(CC)-σ(O) adsorption complexes are relatively large. With -76.9 kJ/mol, the η^3-diσ(CC)-σ(O)-E-(s)-cis (-68.1 kJ/mol for η^3-diσ(CC)-σ(O)-Z-(s)-cis) is in fact the second most stable structure obtained in the DFT studies on Pt(111) in this work.

The η^3-π(CC) adsorption geometries, which only differ from the previous structures by a π(CC) interaction to a single underlying surface atom instead of forming two σ-bonds to two Pt centers, are consistently not stable during the optimizations and evolve into η^4 coordinated species. The latter set of adsorption complexes will be discussed now.

Even more diverse than the η^3 forms are the η^4 coordinated geometries, but only four structures belonging to two basic groups are found to be stable. The η^4-diσ(CC)-diσ(CO)-E-(s)-trans complex (Fig. 6.14) is the most stable structure obtained on Pt(111) at -80.2 kJ/mol. It is bonded to the surface through four σ-type bonds. Quite close in energy, slightly less stable than η^3-diσ(CC)-σ(O)-E-(s)-cis, follows the η^4-diσ(CC)-diσ(CO)-Z-(s)-trans adsorption mode at -71.2 kJ/mol. The two remaining structures of this coordination type, which have also been considered, ended up in the η^3-diσ(CC)-σ(O) configurations as discussed above.

The second group is the set of η^4-π(CC)-diσ(CO) adsorption configurations, which interact with three metal atoms of the substrate (Fig. 6.14). Of this type only the adsorption complexes of the E-(s)-cis and Z-(s)-cis rota-isomers turned out to be stable. The other two starting geometries lost the interaction of the C=O moiety with the surface during the optimization steps and developed into pure η^2-π(CC) adsorption modes. With -68.7 kJ/mol obtained for the binding energy of the η^4-π(CC)-diσ(CO)-E-(s)-cis geometry, this structure belongs to the group of strongly adsorbed crotonaldehyde species on Pt(111). The Z-(s)-cis form is adsorbed considerably weaker with an adsorption energy of -55.3 kJ/mol.

The major differences in the bond lengths specific to the two types of η^4 coordination are seen in the C1-C2, C2-C3, C3-C4 bond lengths as well as in the interactions of the C2=C3 moiety to the substrate (Tab. 6.6). The main reason for this is the weaker interaction in the π(CC) coordinated structures, which hence show a less perturbed carbon backbone and longer C-Pt bond distances. Indeed, r(C2=C3) is lengthened by ca 0.15 Å to 1.50 Å in the η^4-π(CC)-diσ(CO) adsorption complexes, while it is expanded by only ca 0.08 Å to 1.43 Å in the η^4-π(CC)-diσ(CO) structures. The elongation in the latter structures is similar to the ones computed for the η^2-π(CC) adsorption modes. In contrast the elongation in the η^4-π(CC)-diσ(CO) adsorption complexes is slightly smaller than in the η^2-diσ(CC) configurations. The bond distance variations of the neighboring C-C bonds of both coordination types are closely linked to the perturbance of the C2=C3 bond as visible in (Tab. 6.6). For this reason the expansions of r(C1-C2) and r(C3-C4) are somewhat smaller in the case of the η^4-π(CC)-diσ(CO) coordination. Also the C1=O bond distance is elongated significantly, but in contrast to the changes in r(C2-C3) the elongation of r(C1-O) is rather constantly 0.10 Å for all η^4 structures. An analysis of the bonds to the substrate reveals that r(O-Pt) varies only little around the value of 2.12 Å for all four adsorption geometries. This distance is much smaller compared to the η^3-diσ(CC)

species, but still a little larger than the one encountered in the pure η^2-diσ(CO) adsorption geometries. The underlying platinum atom is lifted up typically by 0.05 Å to 0.09 Å by the adsorption bond. Similarly the bond distance r(C1-Pt) of the carbon in the aldehydic function varies only slightly around 2.21 Å. Furthermore the bond lengths C2-Pt and C3-Pt of the C=C double bond moiety in the η^4 configurations behave similar to the η^2-diσ(CC) or η^2-π(CC) structures. It is noteworthy at this point that the variations of the π(CC) interactions in the η^4-π(CC)-diσ(CO) configurations do not show the same trend. Probably due to the sterical strain, r(C2-Pt) is elongated by about 0.04 Å, while r(C3-Pt) is in contrast shortened negligibly by ca 0.01 Å compared to the values obtained in the η^2-π(CC) geometries. Concerning the distortion of the surface by the Pt-C interactions, the atoms interacting with C1 and C2 are usually pulled up only weakly by 0.04 Å to 0.09 Å whereas the metal atoms below C3 or those involved in a π-type bond show much larger protrusions of 0.17 Å to 0.21 Å.

In a previous article on the system crotonaldehyde/Pt(111) Janin et al. [13] considered only a few potential adsorption geometries in order to investigate the adsorption energies as references for their XPS studies. Their computations, though performed with a periodic DFT code, too, produced quite different results than the optimizations in this work. All five structures these authors investigated belong either to the E-(s)-trans or to the E-(s)-cis rota-isomer of crotonaldehyde. In general these authors obtained a weaker bonding of crotonaldehyde to the Pt(111) surface with roughly 15 kJ/mol smaller adsorption energies and usually between 0.07 Å to 0.1 Å (ca 1 to 2%) longer bonds to the substrate. For the η^1-top-E-(s)-trans configuration, r(O-Pt) is calculated even at 2.37 Å in contrast to 2.22 Å obtained in this work. The reason for this disagreement might be twofold. On the one hand, Janin et al. used Vanderbilt Ultra-soft pseudo potentials in their optimizations, which might account for small deviations. On the other hand, probably far more important, might be the fact that these authors used only a two-layer slab for the model surface and therefore did not allow the surface metal layer to relax with the adsorbate. Without a relaxation of the surface Pt atoms, both the surface and the adsorbed molecule still inherit sizable stress and are therefore usually rather far from their local minimum on the potential hypersurface. For this reason the adsorption energies calculated by Janin et al. for the η^3-diσ(CC)-E-(s)-cis and η^2-diσ(CC) adsorption modes are consistently underestimated with -65.2 kJ/mol and -61.7 kJ/mol as compared to -76.9 kJ/mol and -76.0 kJ/mol in this work. Only the adsorption energy of the η^1-top-E-(s)-trans configuration (-23.8 kJ/mol) agrees quite well with the actual results, since the sterical strain between the aldehyde and the substrate in the vertical coordination types is rather small. Two other adsorption structures, which were found to be stable in their study (E_{ads} around -37 and 50 kJ/mol), could be eliminated in this work.

Of much greater importance for the validation of the actual results are the studies carried out by Delbecq et al. [51] in 2002. The adsorption energies calculated by these authors are also presented in Tab. 6.3. The main difference between their calculations and those carried out in this thesis concern the pseudo potentials and the convergence criteria. Delbecq et al. decided to use ultra-soft pseudo potentials and slightly less strict convergence criteria on the *Hellmann-Feynman* forces. In addition, dipole corrections in the direction of the surface normal were included only as single-point corrections on the η^1-top adsorption modes instead of being used during all optimizations. Nonetheless, with just one exception[5] the adsorption geometries and their relative energies agree excellently with the present results, showing deviations of less than 4 kJ/mol in the adsorption energies.

Owing to the complexity of the crotonaldehyde adsorption system, the conclusions from the total energy calculations alone are limited to suggestions of probable candidates, which could be present on Pt(111). The stable surface compounds obtained heretofore can be separated into

[5] Cf. the discussion of the η^2-diσ(CC) configurations above

Geometry	η^1-top-E-(s)-trans	η^1-top-E-(s)-cis	η^1-top-Z-(s)-trans	η^1-top-Z-(s)-cis	η^2-diσ(CC)-E-(s)-trans	η^2-diσ(CC)-E-(s)-cis	η^2-diσ(CC)-Z-(s)-trans
r(O-C1)	1.25	1.25	1.25	1.25	1.22	1.24	1.23
r(C1-C2)	1.44	1.45	1.44	1.45	1.50	1.49	1.49
r(C2-C3)	1.35	1.35	1.35	1.36	1.50	1.49	1.51
r(C3-C4)	1.48	1.48	1.49	1.49	1.52	1.52	1.52
r(C1-H1)	1.11	1.11	1.11	1.11	1.12	1.11	1.12
r(C2-H2)	1.09	1.09	1.09	1.09	1.10	1.10	1.10
r(C3-H3)	1.10	1.09	1.10	1.10	1.10	1.10	1.10
r(C4-H4)	1.10	1.10	1.10	1.09	1.10	1.10	1.10
r(C4-H5)	1.10	1.10	1.10	1.10	1.10	1.10	1.10
r(C4-H6)	1.10	1.10	1.10	1.10	1.11	1.11	1.11
r(O-M)	2.22	2.19	2.20	2.15	-	-	-
r(C1-M)	-	-	-	-	-	-	-
r(C2-M)	-	-	-	-	2.14	2.13	2.14
r(C3-M)	-	-	-	-	2.14	2.15	2.14
r(H-bond)				2.20			

Table 6.4: Bond distances of the optimized η^1 and η^2-diσ(CC) adsorption geometries of the crotonaldehyde on Pt(111). All distances r are given in Å.

three distinct groups according to their adsorption energies. Firstly, the strongly bound species (around -75 kJ/mol) include both η^4-diσ(CC)-diσ(CO), both η^3-diσ(CC)-σ(O), the η^4-π(CC)-diσ(CO)-E(s)-cis and the three η^2-diσ(CC) adsorption modes. These are the most probable candidates, which can be expected to be important for the following analysis of the experimental HREEL spectra. About 30% more weakly adsorbed are the two η^2-π(CC) complexes and the η^4-π(CC)-diσ(CO)-E(s)-cis geometry. Although it is not legitimate to exclude these structures purely on energetic grounds without looking at the coverage dependence, they can be expected to play only a secondary role. Finally, all remaining structures are adsorbed only very weakly with bond strengths of about -20 kJ/mol. Using, thus, the most probable candidates, a reasonable initial guess for the interpretation of the experimental HREEL spectra of crotonaldehyde adsorbed on Pt(111) is obtained. As will be shown in the next sections, the accurate comparison to the computed vibrational spectra of these surface complexes allows a reliable identification of specific adsorption modes even in mixed phases and an extensive analysis of the vibrational data.

Geometry	η^2-π(CC)-E-(s)-trans	η^2-π(CC)-Z-(s)-trans	η^2-diσ(CO)-E-(s)-trans	η^2-diσ(CO)-E-(s)-cis	η^2-diσ(CO)-Z-(s)-trans	η^2-diσ(CO)-Z-(s)-cis
r(O-C1)	1.23	1.23	1.33	1.33	1.34	1.33
r(C1-C2)	1.49	1.49	1.46	1.46	1.46	1.46
r(C2-C3)	1.42	1.43	1.35	1.35	1.36	1.36
r(C3-C4)	1.50	1.50	1.49	1.49	1.49	1.49
r(C1-H1)	1.13	1.12	1.11	1.11	1.11	1.11
r(C2-H2)	1.09	1.09	1.10	1.09	1.09	1.09
r(C3-H3)	1.10	1.09	1.10	1.09	1.09	1.10
r(C4-H4)	1.10	1.10	1.10	1.10	1.10	1.09
r(C4-H5)	1.10	1.10	1.10	1.10	1.10	1.10
r(C4-H6)	1.11	1.11	1.10	1.10	1.10	1.10
r(O-M)	-	-	2.10	2.09	2.09	2.10
r(C1-M)	-	-	2.25	2.25	2.23	2.28
r(C2-M)	2.22	2.22	-	-	-	-
r(C3-M)	2.22	2.22	-	-	-	-
r(H-bond)						2.25

Table 6.5: Bond length of the optimized η^2-π(CC) and η^2-diσ(CO) adsorption geometries of the crotonaldehyde on Pt(111). All distances r are given in Å.

Geometry	η^3-diσ(CC)-σ(O)-E-(s)-cis	η^3-diσ(CC)-σ(O)-Z-(s)-cis	η^4-diσ(CC)-diσ(CO)-E-(s)-trans	η^4-π(CC)-diσ(CO)-E-(s)-cis	η^4-diσ(CC)-diσ(CO)-Z-(s)-trans	η^4-π(CC)-diσ(CO)-Z-(s)-cis
r(O-C1)	1.27	1.27	1.33	1.34	1.33	1.33
r(C1-C2)	1.45	1.45	1.50	1.48	1.49	1.47
r(C2-C3)	1.49	1.50	1.49	1.42	1.50	1.43
r(C3-C4)	1.52	1.52	1.51	1.50	1.52	1.50
r(C1-H1)	1.11	1.11	1.11	1.11	1.11	1.11
r(C2-H2)	1.10	1.10	1.10	1.09	1.10	1.10
r(C3-H3)	1.10	1.10	1.10	1.09	1.10	1.10
r(C4-H4)	1.10	1.10	1.10	1.10	1.10	1.09
r(C4-H5)	1.10	1.10	1.10	1.10	1.10	1.10
r(C4-H6)	1.11	1.11	1.11	1.11	1.11	1.11
r(O-M)	2.26	2.24	2.12	2.12	2.11	2.13
r(C1-M)	-	-	2.22	2.19	2.22	2.22
r(C2-M)	2.19	2.18	2.16	2.28	2.15	2.26
r(C3-M)	2.12	2.11	2.14	2.21	2.13	2.21
r(H-bond)						2.34

Table 6.6: Bond length of the optimized η^3 and η^4 adsorption geometries of the crotonaldehyde on Pt(111). All distances r are given in Å.

6.1.4 Gas Phase IR and Multilayer HREEL Spectra

The HREEL spectra of crotonaldehyde multilayers on the Pt(111) surface and, subsequently, the surface alloys, are analyzed with numerical harmonic frequencies from DFT calculations and comparison to IR and Raman measurements of other groups in gas and liquid phases [140, 141, 153]. In Fig. 6.15 the HREEL spectrum of 4.5L crotonaldehyde adsorbed at 100 K on Pt(111) is confronted with the calculated IR spectra of the four crotonaldehyde rota-isomers (RI-DFT BP86/TZVP level). All rota-isomers of crotonaldehyde belong to the molecular point group C_s and therefore their 27 fundamental vibrations may be divided into 18 normal modes of A' symmetry and 9 of A" symmetry. For clarity, the normal modes belonging to the symmetry races A' and A" are depicted in Fig. 6.16 and 6.17. The vibrational modes shown for E-(s)-trans crotonaldehyde can in general not only be transfered to the remaining three rota-isomers, but also to the ones determined for the various adsorbed crotonaldehyde species. Although changes in the vibrational coupling due to differences in the particular geometries occur, the normal modes can still be understood very well on the basis of the gas phase normal coordinates.
The specific assignments of the vibrational normal modes of all four rota-isomers in the gas phase are presented in the Tabs. 6.7 and 6.8. They are based on the normal coordinate analysis performed on the equilibrium geometries obtained with the two DFT approaches discussed in Sec. 6.1.2, the VASP and the Turbomole RI-DFT BP86/TZVP molecular calculations.

The vibrational spectra can be divided into six frequency regions with distinct types of normal modes. Between 3100 cm^{-1} and 2700 cm^{-1} the ν(C-H) stretching region is located, followed between 1800 cm^{-1} and 1500 cm^{-1} by the ν(C=O) and ν(C=C) double bond stretching modes. From 1460 cm^{-1} to ca 1250 cm^{-1} the region of the in-plane (A') and out-of-plane (A") δ'(CH) and δ"(CH) deformation vibrations and the umbrella mode u(CH_3) expands. The characteristic stretching vibrations ν(C-C) of the carbon framework are typically found around 1100 cm^{-1}, whereas the other typical normal modes of the molecular backbone, namely the δ(OCC), δ(CCC) and the various torsion modes τ(C-C, CH_3), lie below 650 cm^{-1}. Mostly out-of-plane are the A" symmetric deformation modes of the γ(CH) type between ca 1050 cm^{-1} and 700 cm^{-1}.
Firstly, the results of the periodic VASP and the molecular RI-DFT computations are found to match extraordinarily well. Concerning the vibrational normal modes, no discrepancy in the assignment is found in either crotonaldehyde isomer. The vibrational frequencies ω of both computational approaches also agree excellently. At large the differences in the frequencies for a given structure vary by less than 10 cm^{-1} ($< 1.5\%$): Yet also some exceptions are noticed, but these are missing a systematic trend. The most important discrepancy is seen in the stretching vibration of the aldehydic hydrogen, i.e. ν(C1-H1), which is calculated at 2789 cm^{-1} (VASP) and 2766 cm^{-1} (RI-DFT) for E-(s)-trans crotonaldehyde. Measured IR and Raman spectra showed medium signals at 2805 and 2728 cm^{-1} [153] as well as 2808 and 2725 cm^{-1} [141], which were assigned in different manner by Durig et al. and Oelichmann et al. (see Tab. 6.9). While the latter considered the band at 2805 cm^{-1} to arise from the stretching mode ν(C1-H1) of the aldehydic hydrogen [153], Durig et al. had previously assigned the signal at 2725 cm^{-1} to this normal mode; the other signals, respectively, were concluded to arise from combination tones. In a more recent combined experimental and theoretical study carried out by IR and Raman spectroscopy and a normal coordinate analysis in the valence force field approximation, Thakur et al. [140] supported the assignments of Oelichmann et al. [153]. The values of 2789 cm^{-1} and 2766 cm^{-1} obtained in this thesis using VASP and RI-DFT, respectively, are in better agreement with the experimental bands around 2805 cm^{-1} (error of about 1%), hence this IR band is assigned to ν(C1-H1).

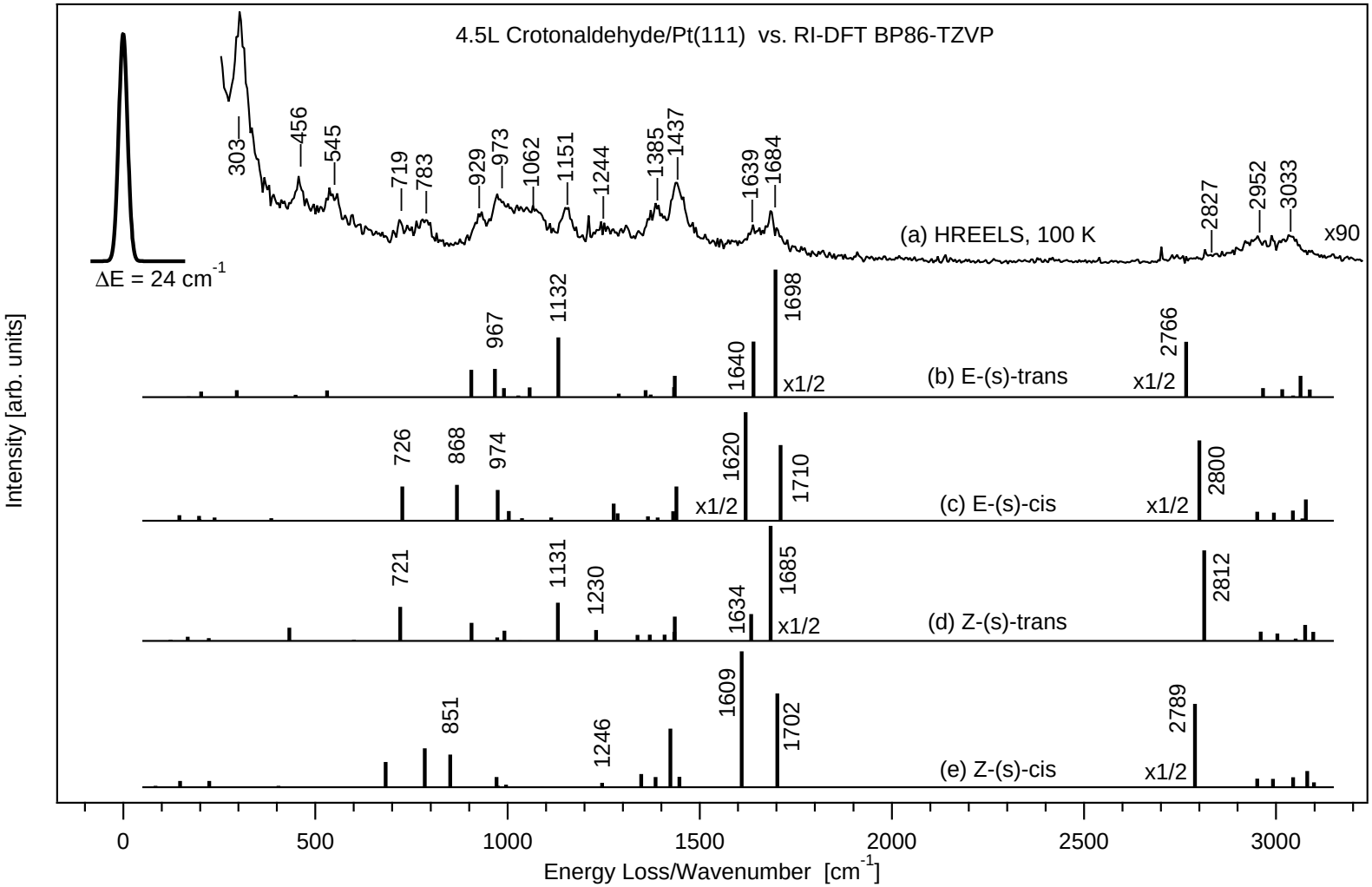

Figure 6.15: Comparison of the multilayer HREEL spectrum of 4.5L crotonaldehyde/Pt(111) at 100 K and the corresponding RI-DFT BP86/TZVP IR spectra (gas phase, numerical harmonic frequencies) of the four rota-isomers. The HREEL spectrum has been recorded in specular geometry at an incidence angle of 60° with a primary energy of 4.7 eV.

E-(s)-trans					E-(s)-cis				
VASP	RI-BP86/TZVP				VASP	RI-BP86/TZVP			
ω	ω	Inten.	Sym.	Assignment	ω	ω	Inten.	Sym.	Assignment
3097	3088	8.4	A'	ν(C2-H2)	3082	3077	23.4	A'	ν(C2-H2)
3067	3064	23.8	A'	ν(C4-H4)	3075	3068	2.2	A'	ν(C3-H3)
3042	3044	1.8	A'	ν(C3-H3)	3053	3043	11.1	A'	ν(C4-H4)
3007	3016	8.6	A"	ν_{as}(C4-H5,6)	3004	2994	8.7	A"	ν_{as}(C4-H5,6)
2965	2966	10	A'	ν_s(CH_3)	2965	2951	9.9	A'	ν_s(CH_3)
2789	2766	121.9	A'	ν(C1-H1)	2817	2800	177.6	A'	ν(C1-H1)
1706	1698	283.9	A'	ν(C=O)	1713	1710	83.7	A'	ν(C=O)
1642	1640	61.6	A'	ν(C=C)	1621	1620	240.8	A'	ν(C=C)
1433	1435	23.6	A'	δ'(CH_3)	1433	1439	37.8	A'	δ'(CH_3)
1426	1433	11.1	A"	δ"(CH_3)	1427	1431	10.5	A"	δ"(CH_3)
1369	1373	2.7	A'	δ(C1H1)	1382	1390	3.2	A'	δ(C1H1)
1357	1359	7.8	A'	u(CH_3)	1355	1365	4.6	A'	u(CH_3)
1287	1289	3.9	A'	δ(C3H3)	1284	1286	8.1	A'	δ_s(C2H2-C3H3)
1238	1236	0.3	A'	δ(C2H2)	1274	1277	18.7	A'	δ_{as}(C2H2-C3H3)
1143	1132	66.2	A'	ν(C1-C2)	1119	1113	3.4	A'	ν(C3-C4)
1078	1058	10.8	A'	ν(C3-C4)	1038	1038	2.5	A"	γ"(CH_3)
1029	1028	1.6	A"	γ"(CH_3)	1008	1003	10.7	A'	ν(C1-C2)
987	991	10.1	A"	γ(C1H1)	989	995	0.9	A"	γ(C1H1)
965	967	31.1	A"	γ_s(C2H2-C3H3)	970	975	33.8	A"	γ_s(C2H2-C3H3)
915	906	30.2	A'	γ'(CH_3)	871	868	39.6	A'	γ'(CH_3)
769	769	0.02	A"	γ_{as}(C2H2-C3H3)	747	750	0.1	A"	γ_{as}(C2H2-C3H3)
526	531	7.4	A'	δ(O-C1C2)	725	726	37.9	A'	δ(O-C1C2)
452	448	2.6	A'	δ(C2=C3-C4)	386	385	2.5	A'	δ(C2=C3-C4)
292	295	7.6	A"	τ(C2=C3)	225	238	3.3	A"	τ(C2=C3)
198	203	6.1	A'	δ(C1-C2=C3)	206	199	1.4	A"	τ(CH_3)
176	170	1	A"	τ(CH_3)	197	197	5.1	A'	δ(C1-C2=C3)
137	110	0.6	A"	τ(C1-C2)	134	146	6	A"	τ(C1-C2)

Table 6.7: Computed IR spectra of the two E-rota-isomers of crotonaldehyde in the gas phase (RI-DFT BP86/TZVP) compared with the frequencies from VASP. The harmonic frequencies ω are given in cm^{-1}. The assignments of both approaches are identical.

Z-(s)-trans					Z-(s)-cis				
VASP	RI-BP86/TZVP				VASP	RI-BP86/TZVP			
ω	ω	Inten.	Sym.	Assignment	ω	ω	Inten.	Sym.	Assignment
3101	3097	10.0	A'	ν(C2-H2)	3106	3098	5.7	A'	ν(C4-H4)
3082	3075	17.9	A'	ν(C4-H4)	3091	3081	18.1	A'	ν(C2-H2)
3057	3050	2.6	A'	ν(C3-H3)	3054	3044	11.2	A'	ν(C3-H3)
3013	3003	8.4	A"	ν_{as}(C4-H5,6)	3000	2992	9.4	A"	ν_{as}(C4-H5,6)
2976	2960	10.2	A'	ν_s(CH_3)	2966	2951	9.5	A'	ν_s(CH_3)
2825	2812	100.5	A'	ν(C1-H1)	2804	2789	184.8	A'	ν(C1-H1)
1687	1685	255.4	A'	ν(C=O)	1706	1702	104.0	A'	ν(C=O)
1634	1634	29.8	A'	ν(C=C)	1610	1609	150.8	A'	ν(C=C)
1435	1435	26.9	A'	δ'(CH_3)	1438	1447	11.8	A"	δ"(CH_3)
1428	1434	10.1	A"	δ"(CH_3)	1418	1423	65.0	A'	δ'(CH_3)
1406	1409	7.1	A'	δ(C1H1)	1404	1408	0.4	A'	δ(C1H1)
1364	1370	7.2	A'	u(CH_3)	1379	1385	11.3	A'	δ_{as}(C2H2-C3H3)
1333	1338	6.9	A'	δ_{as}(C2H2-C3H3)	1343	1348	14.7	A'	u(CH_3)
1228	1230	12.1	A'	δ_s(C2H2-C3H3)	1244	1246	5.2	A'	δ_s(C2H2-C3H3)
1136	1131	42.3	A'	ν(C1-C2)	1087	1090	1.1	A'	ν(C3-C4)
1033	1032	0.6	A"	γ"(CH_3)	1036	1036	0.6	A"	γ"(CH_3)
994	995	0.1	A"	γ(C1H1)	991	996	3.1	A"	γ(C1H1)
990	992	11.2	A'	γ'(CH_3)	981	975	1.6	A"	γ_{as}C2H2-C3H3)
971	973	4.0	A"	γ_{as}(C2H2-C3H3)	974	971	11.4	A'	ν(C1-C2)
911	906	20.2	A'	ν(C3-C4)	859	851	36.1	A'	γ'(CH_3)
717	721	37.6	A"	γ_s(C2H2-C3H3)	781	785	43.3	A'	δ(O-C1C2)
599	600	1.5	A'	δ(O-C1C2)	678	683	28.1	A"	γ_s(C2H2-C3H3)
426	432	14.8	A'	δ(C2=C3-C4)	399	404	1.6	A'	δ(C2=C3-C4)
324	330	0.0	A"	τ(C2=C3)	340	348	0.6	A"	τ(C2=C3)
210	222	3.2	A'	δ(C1-C2=C3)	227	224	7.0	A'	δ(C1-C2=C3)
166	168	4.7	A"	τ(C1-C2)	147	148	6.9	A"	τ(CH_3)
121	123	1.3	A"	τ(CH_3)	78	84	1.7	A"	τ(C1-C2)

Table 6.8: Computed IR spectra of the two Z-rota-isomers of crotonaldehyde in the gas phase (RI-DFT BP86/TZVP) compared with the frequencies from VASP. The harmonic frequencies ω are given in cm^{-1}. The assignments of both approaches are identical.

Experimental data E-(s)-trans				E-(s)-cis			gas ph.	liq.	HREELS
ω(exp.) [153]	ω(calc.) [140]	Sym.	Assignment [140]	ω(exp.) [153]	ω(calc.) [140]	Assignment [140]	ω(exp.) [141]	ω(exp.) [141]	ω(exp.) this w.
3058	3049	A'	ν_{as}(CH)	3058	3049	ν_{as}(CH)	3058	3042	3033
2995	3005	A'	ν_{s}(CH)	2995	3009	ν_{s}(CH)	2995	3002	-
2980	2967	A'	ν_{as}(CH_3)	2980	2967	ν_{as}(CH_3)	2980	2982	-
2963	2967	A"	ν_{as}(CH_3)	2963	2967	ν_{as}(CH_3)	2963	2944	2952
2938	2940	A'	ν_{s}(CH_3)	2938	2940	ν_{s}(CH_3)	2938	2916	-
2805	2789	A'	ν(CH-Ald.)	2805	2786	ν(CH-Ald.)	2725	2727	2827
(2728)				(2728)					
1720	1732	A'	ν(C=O)	1720	1733	ν(C=O)	1720	1693	1684
1649	1665	A'	ν(C=C)	1649	1654	ν(C=C)	1649	1641	1639
1455	1441	A'	δ_{as}(CH_3)	1455	1441	δ_{as}(CH_3)	1455	1444	1437
1455	1439	A"	δ_{as}(CH_3)	1455	1439	δ_{as}(CH_3)	1455	1444	-
1391	1406	A'	δ_{as}(CH_3), ρ(CH-Ald.)	1391	1401	δ_{as}(CH_3), ρ(CH-Ald.)	1391	1389	1385
1375	1382	A'	ρ(CH-Ald.), δ_{as}(CH_3)	1375	1380	ρ(CH-Ald.), δ_{as}(CH_3)	-	1375	-
1304	1291	A'	δ(CH)	1304	1286	δ(CH)	1304	1305	-
1253	1233	A'	δ(CH)	1253	1242	δ(CH)	1252	1253	1244
1147	1127	A'	ν(C-C)	1147	1141	ν(C-C)	1147	1147	1151
1074	1056	A'	ν(C-CH_3)	1074	1057	ν(C-CH_3)	1074	1075	1062
1042	1062	A"	ρ(CH_3)	1042	1062	ρ(CH_3)	1030	1042	1062
973	986	A"	ρ(C-CH_3)	973	988	ρ(CH_3)	973	966	973
973	983	A"	τ(CCH), ρ(CH)	973	988	τ(CCH), ρ(CH)	928	931	973
928	926	A'	ρ(CH-Ald.)	928	934	ρ(CH-Ald.)	780	780	929
780	762	A"	w(CCH)	780	761	w(CCH)	730	727	783
539	535	A'	δ(CCO)	539	558	δ(CCO)	554	542	545
464	484	A'	δ(CCC), ρ($CCCH_3$)	395	406	δ(CCC), ρ($CCCH_3$)	454	459	456
295	289	A"	τ(CCH), w(CCH)	295	277	τ(CCH), w(CCH)	295	297	303
230	231	A'	δ($CCCH_3$), d(CCC)	230	215	δ($CCCH_3$), d(CCC)	211	216	-
173	187	A"	τ(C-CH_3)	173	194	τ(C-CH_3)	139	145	-
122	114	A"	τ(CHO)	122	119	τ(CHO)	122	-	-

Table 6.9: Experimental and theoretical reference data on the vibrational normal modes of crotonaldehyde taken from the literature [140, 141, 153] confronted with the frequencies obtained from HREELS of a crotonaldehyde multilayer (4.5L) on Pt(111) at 100 K. The harmonic frequencies ω are given in cm^{-1}. Liq. refers to experiments performed in liquid phase.

The VASP results and the RI-DFT IR spectra of E-(s)-trans crotonaldehyde compare well to the experimental data of Oelichmann et al. Typically for the harmonic approximation, the frequencies of the ν(C-H) stretching modes are overestimated significantly by about 15 to 70 cm^{-1} (i.e. 1-2%) in the numerical calculations. This is mainly due to the shape of the potentials of these vibrations, which are usually affected by sizable anharmonic terms. The anharmonic terms of different fundamental bands and overtones may furthermore lead to *Fermi*-couplings and induce additional deviations. With errors of usually less than 15 cm^{-1} (1%), the region below 2000 cm^{-1} is described more precisely on the other hand. Since it contains many vibrations that will be highly sensitive to the interaction with a surface, the interpretation of the HREEL spectra of crotonaldehyde on the three model catalyst surfaces will focus on this region.
Thakur et al. expanded the focus of their investigation in order to expose specific bands from their semi-empirical vibrational computations, that might be helpful for a differentiation between the (s)-trans and the (s)-cis configurations of the E isomer. These authors also tried to correlate their results to previous experimental studies of Oelichmann et al., who measured two absorption signals at 464 cm^{-1} and 395 cm^{-1} , respectively. The outcome of the theoretical investigations of Thakur et al. showed only small differences in the computed frequencies for most of the normal modes, including ν(C2=C3)) and ν(C1=O). The only exceptions that were useful for the differentiation according to the outcome of this study were the δ(CCC) and ρ($CCCH_3$) vibrations computed at 484 cm^{-1} and 406 cm^{-1} for the (s)-trans and the (s)-cis forms. These were consequently assigned to the measured bands in the experiments of Oelichmann et al.
As can be easily recognized from the results of this study, the picture is more complicated than these authors expected. The identification of the four rota-isomers of crotonaldehyde in the gas phase is possible by several vibrational normal modes, which are influenced characteristically by the configuration along either the C2=C3 double bond or along the conjugating C1-C2 single bond. This shall be underlined at this point. In fact, for an identification of just one of the four forms always a combination of vibrational modes has to be assumed, since all sufficiently intense bands have at least one close "relative" in another isomer. Thus, for instance, the moderately intense γ_s(C2H2-C3H3) vibrations at 967 cm^{-1} (E-(s)-trans) and 974 cm^{-1} (E-(s)-cis) are characteristical for the E-configuration, while the somewhat weaker bands 1230 cm^{-1} (Z-(s)-trans) and 1246 cm^{-1} (Z-(s)-cis) assigned to δ_s(C2H2-C3H3) clearly identify the Z-configuration.
The differentiation between the (s)-trans and the (s)-cis forms is possible by several bands. Namely the set of bands at 1132 cm^{-1} (ν(C1-C2)), 1640 cm^{-1} (ν(C2=C3)) and 1698 cm^{-1} (ν(C1=O), E-(s)-trans) and 1131 cm^{-1}, 1634 cm^{-1} and 1685 cm^{-1} (Z-(s)-trans) is specific for the (s)-trans configuration. In contrast, the bands at 868 cm^{-1} (γ'(CH_3)), 1620 cm^{-1} (ν(C2=C3)) and 1710 cm^{-1} (ν(C1=O), E-(s)-cis) as well as the corresponding bands at 851 cm^{-1}, 1609 cm^{-1} and 1702 cm^{-1} (Z-(s)-cis) allow an identification of the (s)-cis forms. The weakly separated bands at 726/721 cm^{-1} and 2800/2812 cm^{-1} can be adducted additionally for the differentiation. The first low-lying signals indicate one of either the E-(s)-cis or the Z-(s)-trans forms, while signals around 2766 and 2789 cm^{-1} point towards the E-(s)-trans or Z-(s)-cis rota-isomers.
In most cases, the results of the IR and Raman investigations of Durig et al. match the results of this work very well, but aside from the erroneous assignment of the ν(C1-H1) vibration another discrepancy is disclosed: At 730 cm^{-1} (gas phase) and 727 cm^{-1} respectively, a band was assigned to the γ(C1-H1) wagging mode by Durig et al., but the actual results put this normal mode at 987 cm^{-1}. This latter value is closer to the results of Oelichmann et al. and the theoretical value of 928 cm^{-1} found by Thakur et al., too.

Finally, the HREEL spectra recorded for crotonaldehyde multilayers (Fig. 6.15) on the various surfaces are analysed by comparison to the experimental data and the theoretical results of this work. According to the TPD results given above, the exposure of 4.5L crotonaldehyde dosed

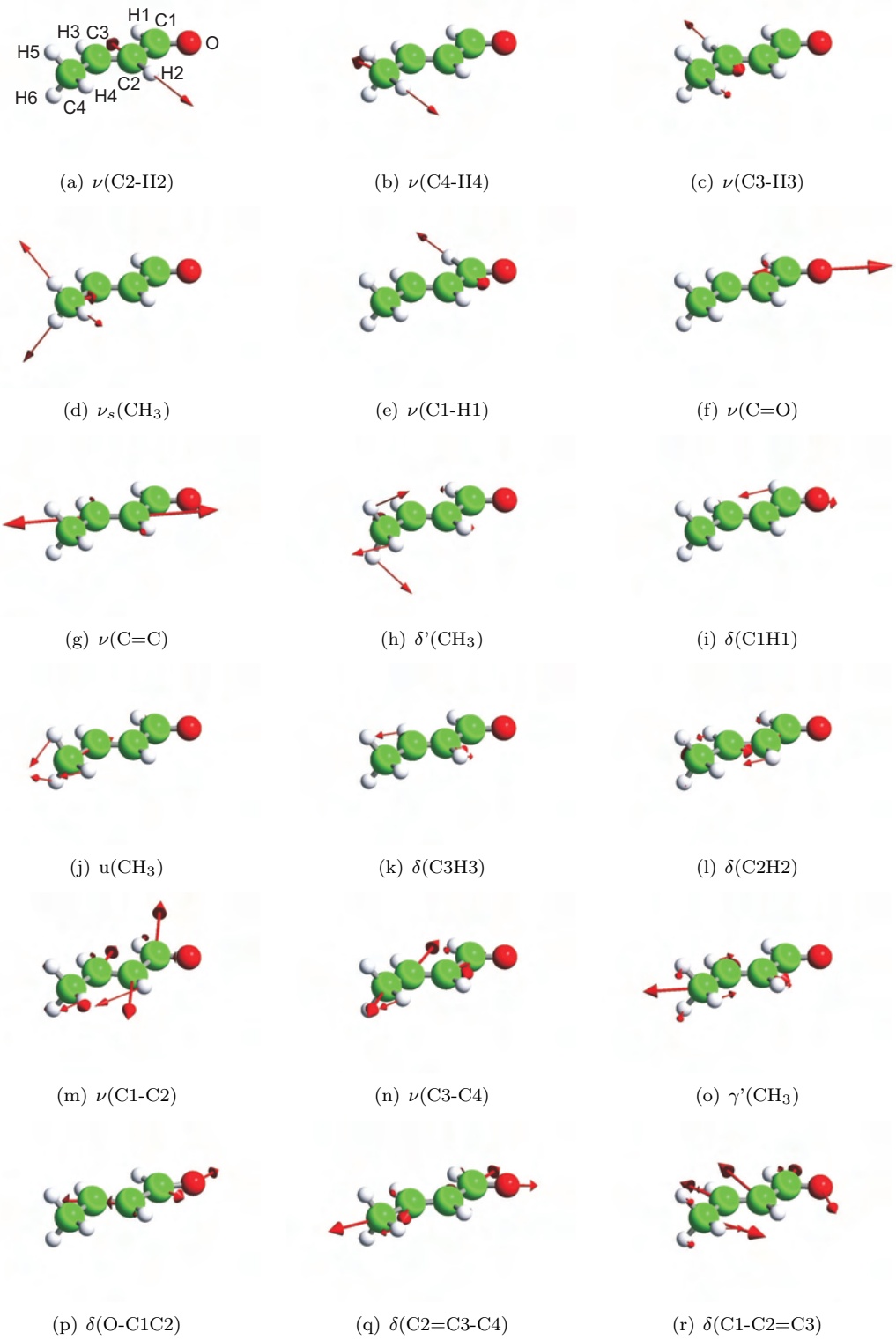

(a) ν(C2-H2) (b) ν(C4-H4) (c) ν(C3-H3)

(d) $\nu_s(CH_3)$ (e) ν(C1-H1) (f) ν(C=O)

(g) ν(C=C) (h) δ'(CH_3) (i) δ(C1H1)

(j) u(CH_3) (k) δ(C3H3) (l) δ(C2H2)

(m) ν(C1-C2) (n) ν(C3-C4) (o) γ'(CH_3)

(p) δ(O-C1C2) (q) δ(C2=C3-C4) (r) δ(C1-C2=C3)

Figure 6.16: A' symmetric vibrational normal modes of E-(s)-trans crotonaldehyde in the gas phase from the RI-DFT BP86/TZVP analysis. The vibrational normal modes of the three remaining rota-isomers correspond closely to the ones determined for the E-(s)-trans form.

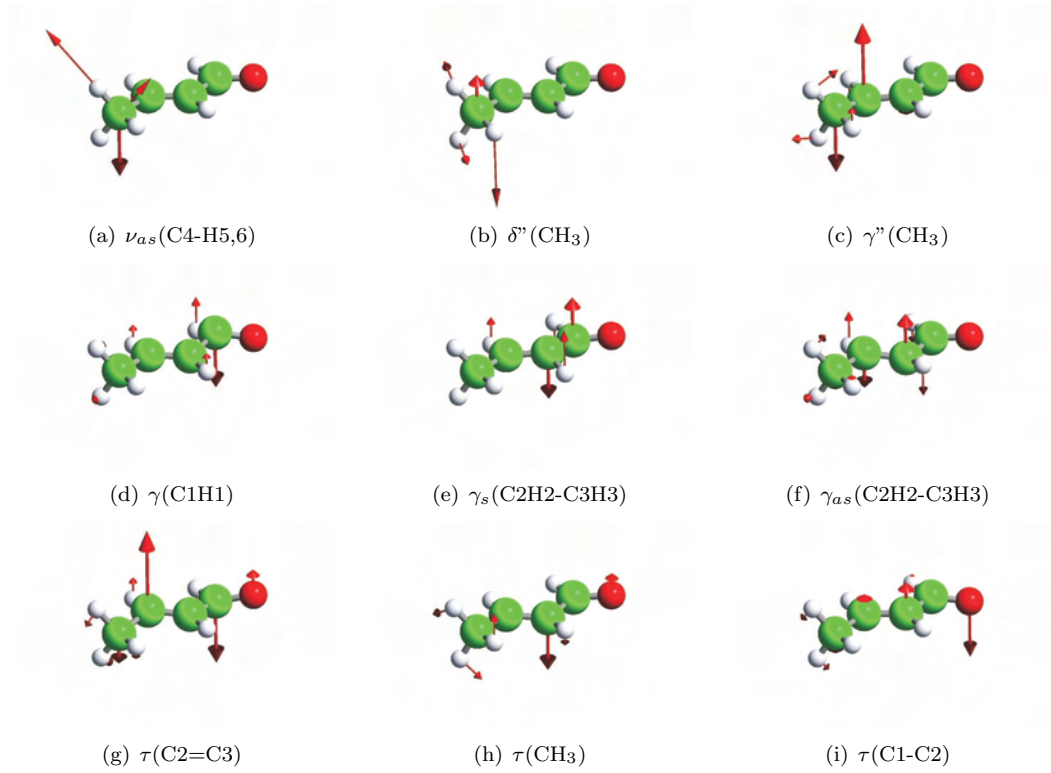

(a) ν_{as}(C4-H5,6) (b) δ"(CH_3) (c) γ"(CH_3)

(d) γ(C1H1) (e) γ_s(C2H2-C3H3) (f) γ_{as}(C2H2-C3H3)

(g) τ(C2=C3) (h) τ(CH_3) (i) τ(C1-C2)

Figure 6.17: A" symmetric vibrational normal modes of E-(s)-trans crotonaldehyde in the gas phase from the RI-DFT BP86/TZVP analysis.

in this case corresponds to about 1.5 times the exposure of the irreversibly adsorbed monolayer species. Since also the sticking coefficient can be expected to degrade for the multilayer adsorption, most of the vibrational loss peaks measured in this spectrum arise from the strongly chemisorbed structures. These can be correlated to the HREEL spectra recorded after annealing to higher temperatures or with the submonolayer exposures, which will be discussed in the next chapter.

Unless it is assumed that the multilayers of crotonaldehyde are totally disordered and therefore the molecular orientations is isotropic, the IR intensities of the RI-DFT calculations can not be compared directly to the HREELS intensities. Furthermore, as already mentioned in Chap. 4.7, one has to keep in mind that the intensities coming from IR data are decreased by a frequency dependent damping factor that is roughly proportional to ω^{-1}.

Basically it is seen, that all IR-active vibrational normal modes computed for E-(s)-trans crotonaldehyde are identified in the HREEL spectra, although they are not resolved very well. Especially in the region of the ν(C-H) stretching vibrations, the assignment is problematic. Concerning the experimental references, the agreement is closest with the IR and Raman data measured by Durig et al. in a liquid phase, but also the gas phase data match the HREELS results very well. The ν(C2=C3) and ν(C1=O) vibrations are observed at 1639 cm^{-1} and 1684 cm^{-1} in the HREEL spectra of this work. These frequencies are very similar to the values of 1641 cm^{-1} and 1693 cm^{-1} determined in the liquid [141].

Two of the experimentally measured loss peaks are somewhat surprising and not easy to interpret at this point. The origins of a signal at 783 cm^{-1}, which according to the measured frequency might suggest the presence of E-(s)-trans or Z-(s)-cis crotonaldehyde, and also of a band detected

at 719 cm^{-1}, are not clear. They might either arise form rota-isomers other than E-(s)-trans, although this has been shown to be the main component in the gas phase, or from other surface species upon which the multilayer is formed. Furthermore it cannot be excluded that these peaks might arise from overtone couplings. In the next chapter, this problem will be discussed in more detail.

6.1.5 HREELS of the Molecular Chemisorption

In this chapter, the HREELS experiments of crotonaldehyde on Pt(111) recorded in the temperature range starting at the adsorption temperature of 100 K up to 250 K shall be discussed. Essentially this is the temperature interval, in which the HREEL spectra can clearly be assigned to intact crotonaldehyde species on the surface. Also the TPD results discussed previously do not exhibit any fragmentation signals at these temperatures. In contrast, above 250 K the HREELS results show strong changes and allow to follow the decomposition processes already observed in the TPD investigations (Sec. 6.1.6).
All HREEL spectra presented in this section have been recorded with a primary energy of 4.7 eV in specular geometry. Hence the selection rules of the dipolar regime apply. The angle of incidence of the primary electrons enclosed with the surface normal has been chosen at 60°. In order to investigate the evolution of the vibrational spectra with increasing temperatures, the sample has been annealed quickly (i.e. flashed) to specific temperatures, but due to technical requirements of HREELS (electrostatic stray fields arising from the potential changes of the sample upon heating, inconstant heating currents due to PID control, etc.) it had to be cooled down to 100 K again for the measurement. The temperature of 100 K is the minimal temperature reached upon isolation of the sample from the heating power circuit. It is assumed in these experiments, that the recooling from the annealing temperature back to 100 K before starting the HREEL experiments does not induce any additional effects, i.e. reversible phase changes or alike, and that the spectra observed are therefore equivalent to those that would have been recorded at the desired temperatures neglecting temperature-dependent peak broadening.
The individual temperature steps have been deduced from the desorption temperatures determined by TPD. For the comparison of HREELS and TPD it has to be taken into account that TPD is essentially an "out of equilibrium" method while HREELS measurements correspond to a thermal equilibrium situation. Aside from this, also different annealing rates have been applied in TPD or during the flashing steps, respectively.

The first HREEL spectra to be discussed represent an annealing series of a multilayer of 4.5L crotonaldehyde adsorbed on Pt(111) at 100 K (Fig. 6.18). These spectra are very instructive and are closely related to the phenomena observed in the TPD experiments previously, i.e. the molecular desorption states of the multilayer (α_1, 143 K), the reversible adlayer (α_3, 177 K) and the intermediate state α_2 (160 K). In combination with the exposure dependent spectra series presented later in this section, the surface composition at submonolayer coverages is determined and possible origins of these low temperature desorption states of molecular crotonaldehyde are suggested.
The similarity of the fingerprints of the HREEL spectra presented in Fig. 6.18 to the one of the multilayer indicates clearly that the surface species observed in the temperature range below 300 K are derived from crotonaldehyde. The differences between the HREEL spectrum of the multilayer at 100 K and the spectra up to 169 K are very small in terms of frequency shifts and relative intensities, but a few changes are recognized that may be significant. These have been marked by dashed lines.
The vibrational spectrum recorded at 150 K corresponds to a mixed phase of surface species after desorbing the crotonaldehyde multilayer. After annealing to 169 K the partial desorption of α_2 occured. The subsequentially recorded spectrum varies only very slighty from the 150 K data

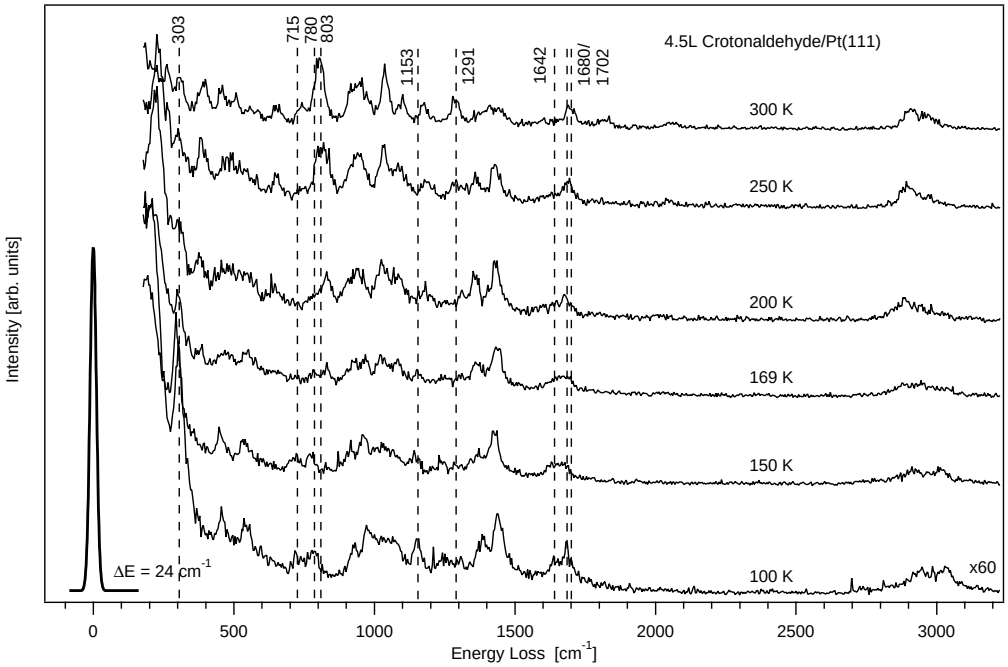

Figure 6.18: HREELS of 4.5L crotonaldehyde/Pt(111), 100-300 K. The HREEL spectra have been recorded in specular geometry at an incidence angle of 60° (primary energy 4.7 eV).

and may be considered basically equal. It is slightly better defined and resolved, which might be due to a surface reordering. Among the minor changes that can be noticed is dissappearance of a weak loss peak at 715 cm^{-1}, while in contrast an additional signal at 831 cm^{-1} starts to develop subtly (it can be recognized best in the spectrum at 200 K). Following the desorption of the reversible adlayer (α_3) at 177 K, a spectrum at 200 K has been measured. This HREEL spectrum has several features in common with the crotonaldehyde multilayer, yet especially in the frequency range between 500 cm^{-1} and 1300 cm^{-1} significant changes in the fingerprint are evident. At least 6 distinct vibrational bands are found here, which are broadened beyond the experimental resolution of ca 24 cm^{-1} and overlap partially.

The loss signals around 715 cm^{-1}, 780 cm^{-1} and 1153 cm^{-1}, which seem to characterize the low temperature adsorption states, are no longer observed, but the signal at 831 cm^{-1} has grown sizable instead. Since above 200 K no further desorption of intact crotonaldehyde occurs, the crotonaldehyde species contributing to the 200 K HREEL spectrum must be strongly and irreversibly adsorbed. Therefore this is the HREEL spectrum, which shall be analyzed and compared to the DFT results in detail in the following paragraphs. Indeed, as these strongly adsorbed crotonaldehyde entities only undergo a decomposition, one can expect that their activation energies of the desorption must be larger than the corresponding activation barriers of the decomposition pathway.

The HREEL spectrum at 250 K is essentially the equivalent to the spectrum of the irreversibly adsorbed monolayer species recorded at 200 K and shall not be analyzed further. In contrast, the experimental spectrum at 300 K exhibits again important changes, which may be assigned to the start of the fragmentation reactions. This decomposition pathway will be investigated more closely in Sec. 6.1.6.

In the next paragraphs the identification of the strongly bonded crotonaldehyde species mea-

sured on Pt(111) at 200 K will be discussed. The spectroscopic fingerprints of these structures are not only visible at lower temperatures, but also up to 300 K, when the decomposition of these species starts. The analysis of the experimental HREEL spectrum is carried out in the following manner: Firstly, characteristical loss peaks, which require certain specific adsorption structures to be present, are interpreted. Then all experimental signals not yet reproduced by these complexes are interpreted by remaining strongly adsorbed species. Finally, the presence of weaker bound species is examined by comparison of the experimental data to loss signals computed to be intense. In general the analysis of the experiments shows that the three most stable structures from DFT are present on the surface and two additional adsorption complexes cannot be ruled out. All other adsorption structures, notably all structures corresponding to the Z-(s)-trans or Z-(s)-cis rota-isomers are excluded either on the basis of the vibrational fingerprints or by weak adsorption energies.

At 1686 cm^{-1} the calculated ν(C1=O) stretching frequency of the η^2-diσ(CC)-E-(s)-trans form agrees with HREELS experiments. The systematic error arising from the computation of the frequency at the harmonic level seems to be negligibly small in this case. In order to reproduce the loss peak shape, which is broadened to lower frequencies, the η^2-diσ(CC)-E-(s)-cis adsorption complex is also taken into account. The corresponding ν(C1=O) stretching mode is calculated at 1610 cm^{-1} ; also from the match of its remaining intense vibrational modes this structure cannot be eliminated.

Most of the vibrational loss peaks measured below 1500 cm^{-1} can already be assigned to these two identified adsorption structures. At 1429 cm^{-1} and 1355 cm^{-1} two characteristic peaks are measured and correspond to the bending δ'(CH_3), δ"(CH_3) and the umbrella u(CH_3) vibrations. Although these signals are present in all calculated adsorption modes, they exhibit no significant variations. It can be shown - keeping in mind the difficulties arising from *Davydov* splitting and the periodic DFT model - by a convolution of all these normal modes that the double-feature shape is well reproduced by DFT (see Fig. B.1, App. B.2). Between 1078 cm^{-1} and 827 cm^{-1} the measured intense peaks are assigned to the out-of-plane γ'(CH_3), γ"(CH_3) and γ(C2-H2) torsional normal modes, which can be expected to be intense from the dipole selection rules.

In order to reproduce the loss peak at 827 cm^{-1} with sufficient intensity, the η^3-diσ(CC)-σ(O)-E-(s)-cis adsorption geometry is needed, which has a signal computed at 860 cm^{-1} corresponding to a γ'(CH_3) mode. It is slightly more stable than the two η^2-diσ(CC) adsorption complexes. Also the dominant ν(Pt-O) stretching mode computed at 302 cm^{-1}, which is not coupled to the substrate-C=C stretching vibrations in this case, agrees well with the experiment.

Due to the overall weak intensity of the η^4 structures in the fingerprint region, the identification of these candidates in a complex mixed phase is difficult. Nonetheless, the highly stable η^4-diσ(CC)-diσ(CO)-E-(s)-trans and η^4-π(CC)-diσ(CO)-E-(s)-cis adsorption complexes need to be included into the set of identified structures. The necessity of the η^4-E-(s)-trans structure is underlined by the experimental loss peak at 369 cm^{-1} and the band from 459 cm^{-1} to 536 cm^{-1}, which are interpreted by the symmetric molecule-substrate stretching mode ν_s(PtC2-PtC3) computed at 371 cm^{-1} and the coupled ν_{as}(PtO-PtC1) and δ(C2=C3-C4) (452 cm^{-1}) normal modes. The η^4-E-(s)-cis adsorption complex gives a better understanding of the experimental loss signals at 641 cm^{-1} and 940 cm^{-1}, which are assigned to the γ_s(C2H2-C3H3) mode calculated at 938 cm^{-1} with medium intensity and the backbone deformation vibration δ(O=C1-C2) at 659 cm^{-1} with weak intensity. A medium intense normal mode ν_{as}(PtO+PtC1-PtC2+PtC3) computed at 325 cm^{-1} must also be considered to contribute to the measured loss intensity at 298 cm^{-1}.

The intensity difference observed between the theoretical and the experimental data for several normal modes is mainly ascribed to the ideal periodicity in the theoretical models, while no ordered superstructure is detected in LEED experiments. Different orientations of adsorption structures, such as for instance for a diσ(CC) form, which can be rotated into six distinctive

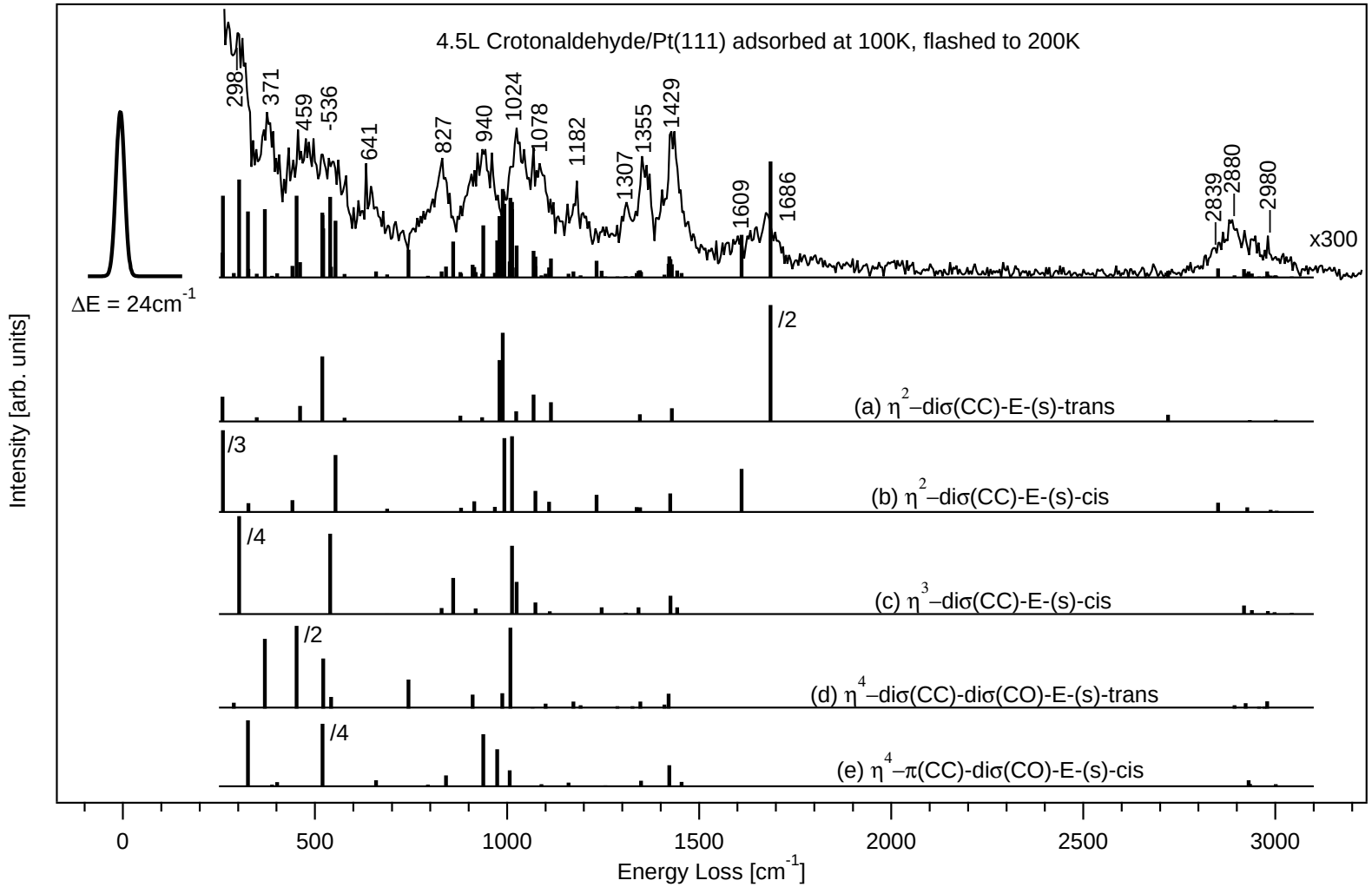

Figure 6.19: Computed DFT EEL spectra for the most stable adsorption structures, and HREEL spectrum of 4.5L crotonaldehyde adsorbed at 100 K on clean Pt(111) subsequently flashed to 200 K.

ω cm^{-1}	Intensity $\times 10^6$ au		Normal mode
3046	0.001		ν(C4-H4)
3019	0.009		ν(C2-H2)
3001	0.065		ν_{as}(C4-H5,6)
2965	0.006		ν(C3-H3)
2933	0.055		ν_s(C4-H5,6)
2720	0.30		ν(C1-H1)
1686	10.7	s	ν(C1=O)
1429	0.61		δ'(CH_3)
1414	0.024		δ"(CH_3)
1346	0.33		u(CH_3)
1338	0.017		δ_s(C2H2-C3H3)+δ(C1H1)
1317	0.011		δ_s(C2H2-C3H3)-δ(C1H1)
1207	0.001		δ_{as}(C2H2-C3H3)
1115	0.88		ν(C2=C3)
1069	1.2	vw	ν(C3-C4)
1024	0.47		ν(C1-C2)
989	4.1	m	γ"(CH_3)
980	2.8	w	γ(C2H2)
935	0.18		γ(C1H1)
910	0.003		γ(C3H3)
878	0.26		γ'(CH_3)
577	0.17		δ(O=C1-C2)
519	3.0	w	ν_{as}(PtC2-PtC3)
461	0.71		δ(C2=C3-C4)
348	0.18		ν_s(PtC2-PtC3)
259	1.1	vw	τ(C1-C2)
245	0.32		δ(C1-C2=C3)
231	0.67		τ(CH_3)
208	0.27		τ(C2=C3)
139	6.5		fR
107	1.6		fT
93	0.003		fT
68	0.0		fR

Table 6.10: Vibrational analysis of the η^2-diσ(CC)-E-(s)-trans structure of crotonaldehyde/Pt(111). The letters following the computed intensities refer to the relative strength, i.e. (v)w = (very) weak, m = medium and (v)s = (very) strong. For strong vibrational couplings of more than two normal modes, the coupling of the components is indicated by + (in phase) or - (anti-phase). The abbrevations fR and fT refer to frozen translations and frozen rotations.

ω cm^{-1}	Intensity $\times 10^6$ au		Normal mode
3042	0.0		ν(C4-H4)
3012	0.022		ν(C2-H2)
3003	0.052		ν(C3-H3)
2987	0.089		ν_{as}(C4-H5,6)
2927	0.21		ν_s(C4-H5,6)
2851	0.42		ν(C1-H1)
1610	2.0	m	ν(C1=O)
1425	0.85	vw	δ'(CH_3)
1414	0.011		δ"(CH_3)
1347	0.21		δ_s(C2H2-C3H3)-δ(C1H1)
1340	0.015		u(CH_3)
1338	0.21		δ_s(C2H2-C3H3)+δ(C1H1)
1233	0.77	vw	δ_{as}(C2H2-C3H3)
1109	0.46		ν(C2=C3)
1073	0.96	vw	ν(C3-C4)
1013	3.5	s	γ(C3H3)
993	3.4	s	ν(C1-C2)
968	0.23		γ_{as}(C1H1-C2H2)
915	0.49		γ"(CH_3)
880	0.19		γ_s(C1H1-C2H2)
831	0.006		γ'(CH_3)
688	0.15		δ(O=C1-C2)
554	2.6	s	ν_{as}(PtC2-PtC3)
441	0.54		ν_s(PtC2-PtC3)
327	0.40		δ(C2=C3-C4)
260	13.3	vs	τ(C1-C2)
241	5.0	s	τ(CH_3)
230	2.4	s	δ(C1-C2=C3)
186	0.075		τ(C2=C3)
139	14.9	vs	fR
113	1.2		fT
98	0.98		fR
47	0.54		fR

Table 6.11: Vibrational analysis of the η^2-diσ(CC)-E-(s)-cis structure of crotonaldehyde/Pt(111). The letters following the computed intensities refer to the relative strength, i.e. (v)w = (very) weak, m = medium and (v)s = (very) strong.

ω cm^{-1}	Intensity $\times 10^6$ au		Normal mode
3042	0.052		ν(C2-H2)
3035	0.002		ν(C4-H4)
2998	0.090		ν(C3-H3)
2980	0.14		ν_{as}(C4-H5,6)
2939	0.19		ν(C1-H1)
2918	0.39		ν_s(C4-H5,6)
1443	0.32		ν(C1=O)
1425	0.84		δ'(CH_3)
1415	0.0		δ"(CH_3)
1357	0.019		δ_s(C2H2-C3H3)
1342	0.30		u(CH_3)
1309	0.061		δ(C1H1)
1246	0.31		δ_{as}(C2H2-C3H3)
1111	0.13		ν(C2=C3)
1074	0.53		ν(C3-C4)
1025	1.5	w	ν(C1-C2)
1013	3.1	m	γ"(CH_3)
925	0.001		γ_{as}(C1H1-C2H2)
918	0.26		γ(C3H3)
860	1.7	w	γ'(CH_3)
829	0.29		γ_s(C1H1-C2H2)
688	0.021		δ(O=C1-C2)
539	3.7	m	ν_{as}(PtC2-PtC3)
416	0.006		δ(C2=C3-C4)
351	0.003		ν_s(PtC2-C3)
302	18.0	vs	ν(Pt-O)
248	4.7	m	δ(C1-C2=C3)
238	2.6	w	τ(CH_3)
202	2.7	w	τ(C1-C2)
166	0.60		τ(C2=C3)
119	0.015		fT
82	1.6		fT
64	0.52		fR

Table 6.12: Vibrational analysis of the η^3-diσ(CC)-E-(s)-cis structure of crotonaldehyde/Pt(111). The letters following the computed intensities refer to the relative strength, i.e. (v)w = (very) weak, m = medium and (v)s = (very) strong.

ω cm^{-1}	Intensity $\times 10^6$ au		Normal mode
3047	0.001		ν(C4-H4)
2978	0.29		ν_{as}(C4-H5,6)
2971	0.050		ν(C2-H2)
2957	0.046		ν(C3-H3)
2923	0.20		ν_s(C4-H5,6)
2894	0.10		ν(C1-H1)
1420	0.63		δ'(CH_3)
1410	0.14		δ"(CH_3)
1347	0.28		u(CH_3)
1326	0.059		δ_s(C2H2-C3H3)
1287	0.053		δ_{as}(C2H2-C3H3)+δ(C1H1)
1191	0.098		δ_{as}(C2H2-C3H3)-δ(C1H1)
1172	0.28		ν(C1=O)
1100	0.18		ν(C2=C3)
1066	0.012		ν(C3-C4)
1009	3.7	m	γ"(CH_3)
988	0.65		ν(C1-C2)
910	0.59		γ'(CH_3)
891	0.005		γ_{as}(C2H2-C3H3)
849	0.006		γ_s(C2H2-C3H3)
743	1.3	w	γ(C1H1)
542	0.49		ν_{as}(PtC2-PtC3)
521	2.3	m	δ(O=C1-C2)
480	0.007		δ(C1-C2=C3)
452	7.3	s	ν_{as}(PtO-PtC1),δ(C2=C3-C4)
369	3.2	m	ν_s(PtC2-PtC3)
289	0.22		ν_s(PtO-PtC1)
248	0.13		τ(C1-C2)
222	0.002		τ(C2=C3)
210	0.031		τ(CH_3)
163	0.24		δ(C2=C3-C4)
133	0.012		fT
93	0.18		fR

Table 6.13: Vibrational analysis of the η^4-diσ(CC)-diσ(CO)-E-(s)-trans structure of crotonaldehyde/Pt(111). The letters following the computed intensities refer to the relative strength, i.e. (v)w = (very) weak, m = medium and (v)s = (very) strong.

ω cm^{-1}	Intensity $\times 10^6$ au		Normal mode
3067	0.005		ν(C3-H3)
3056	0.027		ν(C2-H2)
3033	0.001		ν(C4-H4)
3001	0.11		ν_{as}(C4-H5,6)
2934	0.12		ν(C1-H1)
2930	0.28		ν_s(C4-H5,6)
1454	0.22		δ_s(C2H2-C3H3)
1422	0.97	vw	δ'(CH_3)
1406	0.019		δ"(CH_3)
1349	0.25		u(CH_3)
1299	0.0		δ(C1H1)
1256	0.044		δ_{as}(C2H2-C3H3)
1205	0.0		ν(C2=C3)
1159	0.18		ν(C1=O)
1089	0.098		ν(C3-C4)
1007	0.75		γ"(CH_3)
974	1.7	w	ν(C1-C2)
938	2.4	m	γ_s(C2H2-C3H3)
878	0.021		γ_{as}(C2H2-C3H3)
841	0.50		γ'(CH_3)
794	0.77		γ(C1H1)
659	0.27		δ(O=C1-C2)
520	11.2	vs	ν_{as}(PtO-PtC1)-ν_{as}(PtC2-PtC3)
402	0.20		ν_{as}(PtO-PtC1)+ν_{as}(PtC2-PtC3)
388	0.076		δ(C2=C3-C4)
325	3.0	m	ν_s(PtO-PtC1)-ν_s(PtC2-PtC3)
283	0.017		ν_s(PtO-PtC1)+ν_s(PtC2-PtC3)
231	0.007		τ(CH_3)
228	0.16		δ(C1-C2=C3)
180	1.1		τ(C2=C3)
169	0.18		τ(C1-C2)
120	0.0		fT
107	0.68		fR

Table 6.14: Vibrational analysis of the η^4-π(CC)-diσ(CO)-E-(s)-cis structure of crotonaldehyde/Pt(111). The letters following the computed intensities refer to the relative strength, i.e. (v)w = (very) weak, m = medium and (v)s = (very) strong.

directions (three for an unsubstituted C=C bond) on a surface plane preserving a hexagonal symmetry, can lead to a mutual stabilization or destabilization of the adsorption energies. Even worse, a coupling of the vibrational normal modes and the dipole moments may occur (Chap. 3.2.2). This leads to frequency shifts and significantly changes the HREELS intensities of vibrational loss peaks. Consequently the degree of complexity encountered when trying to identify specific adsorption geometries among others in a mixed phase is increased seriously and a very careful analysis of the vibrational spectra, especially of broad vibrational bands, is required. The overestimation of the HREELS loss intensities becomes more apparent in the convolution of the DFT spectra with a Gaussian (FWHM 24 cm^{-1}), which is presented in Fig. B.1 in App. B.2). Aside from the ν(C1=O) vibrations of the two η^2 structures around 1680 cm^{-1}, mainly the intense out-of-plane normal modes γ"(CH_3)[6] of all adsorption forms (around 980 cm^{-1}) and the asymmetric stretching modes ν_{as}(PtC2-PtC3) and ν_{as}(PtC1-PtO) (both around 500 cm^{-1}) for diσ-coordinated entities have extraordinarily large intensities. It can not be argued at this point, whether the latter phenomenon might also be partially caused by different surface coverages of the five strongly bonded adsorption structures (all are treated to be present in equal amounts, which of course contradicts thermodynamics).

Interesting conclusions towards the interaction mode and interaction strength can be deduced from the frequency shifts of the C-C and C-O stretching vibrations of the molecular backbone, which are usually affected strongly. Since these vibrations are mostly of weak intensity for the flat adsorption modes, only the theoretical values are used. At large it is found, that the frequencies are very sensitive to the coordination geometry. The exact adsorption strength, which would induce additional slight changes, cannot be derived unambiguously from these frequencies, because they are actually also strongly influenced by the additional interactions of the remaining double bond moiety and the configuration of the rota-isomer. The position of the stretching frequency ν(C2=C3) is usually around 1109-1115 cm^{-1} for the structures exhibiting a diσ(CC) interaction between the molecule and the substrate. The complementary π(CC) interaction mechanism leads to bands around 1205 cm^{-1}. Also the ν(C1=O) normal mode is a very sensitive probe to the interaction mechanism. While for the η^2-diσ(CC) and η^2-π(CC) adsorption structures frequencies in the vicinity of 1610-1686 cm^{-1} result, the additional O-Pt coordination specific to the η^3-adsorption forms shifts this peak to ca 1443 cm^{-1}. The largest redshifts are determined for the complexes exhibiting a diσ(CO) interaction to the surface. Here the frequencies are commonly found around 1165 cm^{-1}.

Finally the coverage dependence of the HREEL spectra in the molecular regime below 250 K is analyzed by comparing various coverages adsorbed at 100 K (Fig. 6.20) and subsequently annealed to 150 K (Fig. 6.21) and 200 K (Fig. 6.22), respectively.
It is most instructive to begin with the discussion of the HREELS data taken at the adsorption temperature of 100 K. Comparing the multilayer of 4.5L crotonaldehyde with the 2.0L HREEL spectrum does not reveal any significant changes. Hence, the 2.0L spectrum corresponds to a multilayer adsorption state, too. At lower coverages, some small differences are noted. Looking at the dashed line marked at 715 cm^{-1} in Fig. 6.20 it can be seen that a weak loss peak is present from the multilayers down to 1.5L, but it disappears completely at smaller exposures. From TPD it has already been shown that this exposure corresponds roughly to the start of the molecular desorption state α_2 at 160 K growing out of the desorption state α_3, which has been found to appear at 177 K for exposures larger than ca 1.2L (see Chap. 6.1.1). Consistent with the results from the TPD experiments, other signals seem to shift slightly and exhibit variations of the relative intensities at these low exposures. On the one hand, the loss peaks detected

[6]Since the molecules adsorb rather flat on Pt(111), the vibrations belonging to the A" symmetry races in the gas phase rota-isomers and also the molecule-substrate modes exhibit a normal coordinate component orthogonal to the surface.

at 967 cm^{-1} and 780 cm^{-1} have decreased sizably in the 1.0L HREEL spectrum; the latter one even shifts strongly to 755 cm^{-1} in the 0.5L experiment. At the same time the loss signal around 1153 cm^{-1} decreases in intensity and also the peak arising from the δ"(CH_3) and u(CH_3) normal modes of the various strongly adsorbed species shifts from 1379 cm^{-1} to approximately 1354 cm^{-1} in this submonolayer HREEL spectrum.
Interestingly most of the other loss signals in these experiments such as for instance the ν(CO) stretching modes at 1647 cm^{-1} and 1684 cm^{-1} do not show any significant variations and appear very similar to the spectrum of the strongly and irreversibly chemisorbed crotonaldehyde structures identified in the 200 K HREELS experiment of 4.5L crotonaldehyde analyzed above. Hence it is obvious that the HREEL spectra are dominated by the irreversibly bound species, yet also the reversibly adsorbed crotonaldehyde (correlated with α_2 and α_3) contributes to a small degree.
Like the vibrational spectra between 200 K and 300 K, the submonolayer HREEL spectrum of 0.5L crotonaldehyde at 100 K can be interpreted as a mixed phase of the strongly bound adsorption complexes investigated with DFT. A confrontation of the experimental fingerprint with the computed harmonic frequencies is given in Fig. B.2 in App. B.2.
Although many features of this spectrum are in common with the HREELS data of 4.5L crotonaldehyde interpreted by the two η^2, the η^3 and the two η^4 coordination geometries of the E-(s)trans and E-(s)-cis rota-isomers, slight differences point to a change in the surface species. Combining these differences and the common features, it is concluded that the submonolayer at 100 K is best matched by only three of the previously assigned structures: the η^2-diσ(CC)-E-(s)-trans, the η^4-π(CC)-diσ(CO)-E-(s)-cis and the η^4-diσ(CC)-diσ(CO)-E-(s)-trans forms. The intense loss peak at 755 cm^{-1} is derived from the γ(C1H1) vibration of the η^4-diσ(CC)-diσ(CO)-E-(s)-trans form (DFT at 743 cm^{-1}). The decrease of the intensity at 827 cm^{-1} might suggest a reduction in the relative coverage of the η^3-diσ(CC)-σ(O)-E-(s)-cis structure. Also the η^2-diσ(CC)-E-(s)-cis structure is no longer very important for an analysis, because the intensity measured around 1647 cm^{-1} is comparably small. Therefore a trend to a preference of the flat η^4 coordination types of high hapticity is recognized from the combined study with HREELS and DFT.
Indeed, this trend is in line with previous results obtained from a similar approach by Loffreda et al. [53] on the system acrolein/Pt(111). These authors observed a transition from the η^2 structures, which require less space on the surface, to the flat η^4 geometries at low coverage situations in their vibrational measurements and their corresponding DFT computations.

The nature of the desorption state α_3 (reversible adlayer) and its sometimes resolved weak shoulder α_2 (intermediate species) is very difficult to assess by HREELS. In view of the very small variation in the maximum temperatures, their overlapping behavior and of course the methodical discrepancy between HREELS annealing experiments and TPD, it is very doubtful to achieve a clear-cut interpretation. Yet some subtle transitions in the HREELS data of the 4.5L series can be noticed (Fig. 6.18) and can furthermore be correlated to coverage dependent HREEL experiments performed in the low temperature range, too.
In the series of HREEL spectra recorded after flashing various precoverages of crotonaldehyde to 150 K (Fig. 6.21) additional features are recognized that help to understand the adsorption behavior at low temperatures. First of all, the multilayer state is known to be desorbed at this temperature. According to TPD, at sufficiently high coverages contributions of the irreversibly adsorbed crotonaldehyde, the reversible adlayer and the intermediate species can be expected. The focus in the analysis of this series shall, thus, lead to four characteristic loss signals here. At 715 cm^{-1} the peak present in the 4.5L, 2.0L and 1.5L HREEL spectra disappears at lower coverages. Also the signals at 780 cm^{-1}, 970 cm^{-1} and 1153 cm^{-1} are only detected at precoverages above 1.0L, while they are strongly deteriorated in the 0.5L spectrum. In contrast to these four features, a dominant loss peak at 828 cm^{-1} is observed in the submonolayer spectrum. It

can also be found in the 1.0L data, yet with a strongly damped intensity. The latter loss peak has already been discussed above in the 4.5L HREEL spectrum at 200 K and is assigned to the two irreversibly bonded η^2 and the η^3 species. Some subtle differences found between the spectrum at 200 K and this submonolayer spectrum indicate that a reordering process of the surface species is induced by the annealing at such low precoverages. Tentatively one might argue that a transition of the mixed phase of three major components (η^2-diσ(CC)-E-(s)-trans, η^4E-(s)-trans and η^4-E-(s)-cis) to a more complex phase including additionally the η^2-diσ(CC)-E-(s)-cis and the η^3-E-(s)-cis forms would conincide with the subtle differences.
Finally after annealing to 200 K, all initial precoverages exhibit the same spectral signature in the HREEL experiments (Fig. 6.22). Neither significant coverage-dependent shifts nor sizable changes in the relative loss intensities of the various well-resolved peaks are detected. Thus the interpretation of the 4.5L HREEL spectrum at 200 K presented above is valid here.
Comparing the low temperature HREELS coverage series, in particular the loss signals at 715 cm^{-1}, 780 cm^{-1}, 967 cm^{-1} and 1153 cm^{-1} seem to change systematically with the precoverage and the temperature and thus are suitable for the interpretation of the partial desorption phenomena α_2 and α_3.
At large the three losses at 780 cm^{-1}, 967 cm^{-1} and 1153 cm^{-1} are present for coverages above ca 1.2L and behave similarly and thus they seem to be specific for the reversible adsorption state. After annealing the sample to temperatures above the desorption temperature of α_3 at 177 K, these frequencies can hardly be detected anymore[7]. Therefore it is assumed that in this temperature and exposure range, a mixture of the irreversibly adsorbed crotonaldehyde structures and reversibly adsorbed crotonaldehyde may be present on the surface. This is schematically shown in Tab. 6.15; here Φ_2 denotes this mixed surface composition.
Judging from the coverage (exposures above 1.5L) and the temperature range (up to only 150 K, see Fig. 6.21), in which the peak at 715 cm^{-1} is found, the latter is probably characteristic for the intermediate adsorption state α_2 of crotonaldehyde. This adsorption species must be present on the surface in addition to the mixed phase Φ_2, which in Tab. 6.15 is marked as Φ_1. Going to even larger initial exposures, the multilayer desorption state is determined at temperatures below 144 K.
The assignment of these frequencies is complicated by the fact that according to the desorption activation energies derived from TPD these species are bonded just slightly stronger than the multilayer. Hence, none of the chemisorbed surface complexes obtained in the DFT optimizations may be considered here. The discrepancy between the experiments and the fits of the computed EEL spectra supports this assumption.
One possible explanation that may not be exlcuded here might be a surface reordering process (or "microscopic phase change") accompanied by a partial desorption of adsorbed molecules. Another possibility might be an extrinsic adsorption states, for example a second physisorbed adlayer on top of irreversibly chemisorbed species. Depending on the amount of the additionally physisorbed crotonaldehyde, such a state might even be discriminatable in TPD by slight temperature differences to the multilayer desorption temperature. Yet a comparison of the computed gas phase frequencies to these peaks is hardly conclusive. Ignoring the uncertainty of the intensities that might be expected experimentally - as the exact nature of the species is unknown - the measured vibrations do not necessarily have to be related to the normal modes in the gas phase.
Nonetheless it must be stressed again at this point that an unambiguous assignment of the measured loss peaks and the related desorption states seen in TPD is not possible on the basis of the available data. Possibly deeper insight into this problem might be obtained from further DFT calculations including higher coverage situations of mixed surface species.

[7] Readsorption or weaker signals arising at these frequencies from the irreversibly adsorbed species might lead to weak signals at temperatures above 177 K.

Exposure	100 K	150 K	169 K	200 K
0.5L	submono.	irrev.	irrev.	irrev.
1.0L	Φ_2	Φ_2	(Φ_2)	irrev.
1.5L	Φ_2	Φ_2	(Φ_2)	irrev.
2.0L	multi.	Φ_1	(Φ_2)	irrev.
4.5L	multi.	Φ_1	Φ_2	irrev.

Table 6.15: Schematic representation of the surface phases identified from the exposure dependent TPD and HREELS experiments for crotonaldehyde/Pt(111). At 100 K, a transition from a submonolayer HREELS spectrum to a mixed phase Φ_1 containing additionally the reversibly adsorbed species (α_3) and the intermediate adsorbed species (α_2) occurs before spectra of a multilayer are observed at high precoverages. Increasing the temperature, these reversibly coadsorbed states desorb consecutively (Φ_1 appears below the desorption state α_2 leading to Φ_2; see text) until only the fingerprint of the five irreversibly bonded crotonaldehyde structures remains.

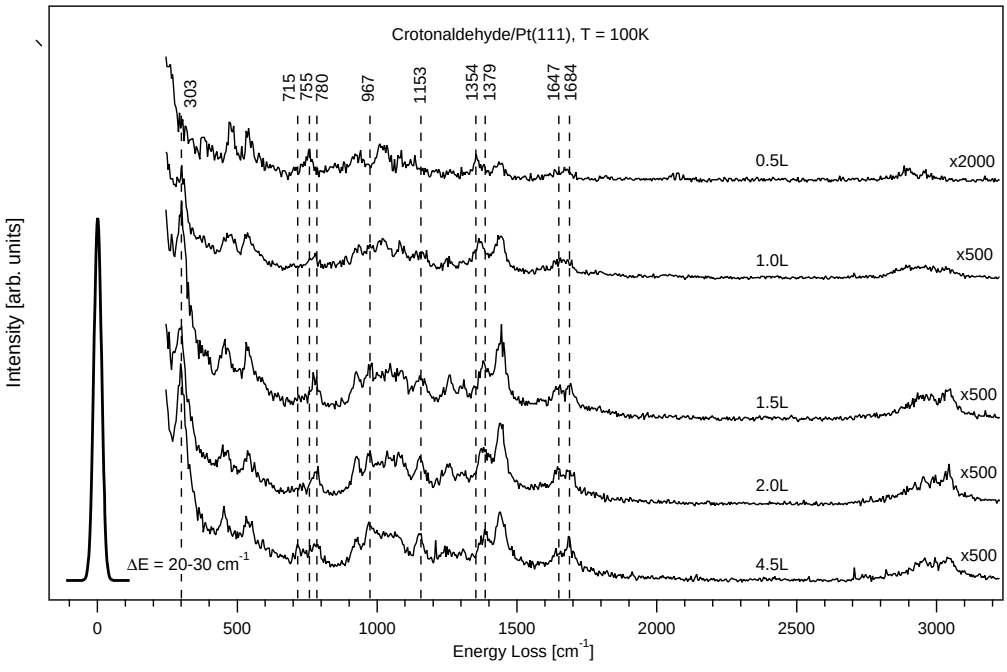

Figure 6.20: HREELS series of various initial precoverages of crotonaldehyde on Pt(111) at 100 K. All HREEL spectra have been recorded in specular geometry at an incidence angle of 60° with a primary energy of 4.7 eV.

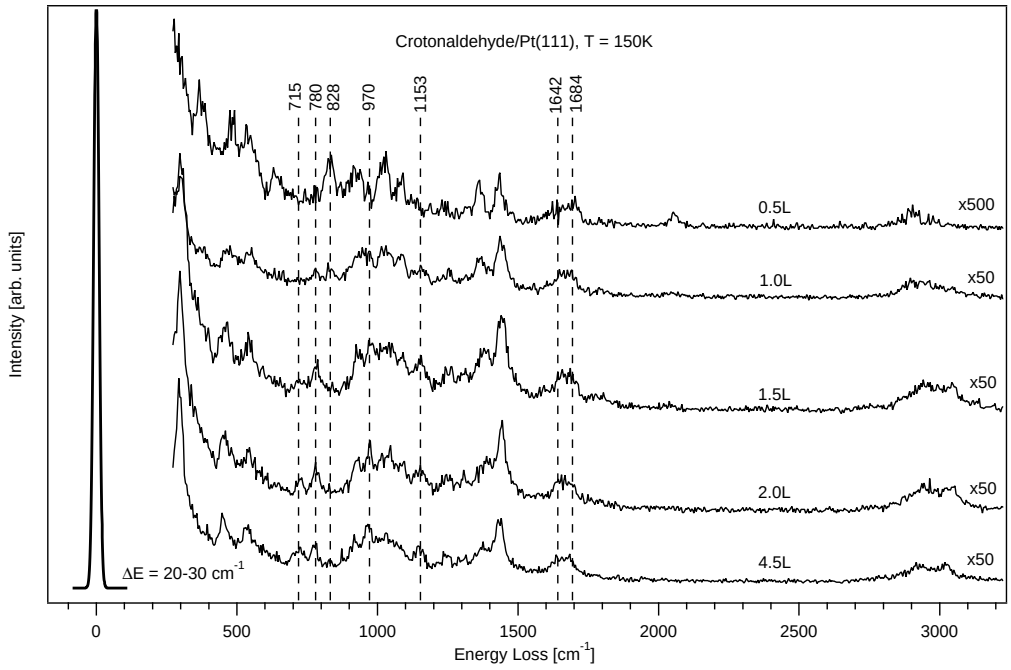

Figure 6.21: HREELS series recorded after annealing the various initial precoverages of crotonaldehyde/Pt(111) to 150 K.

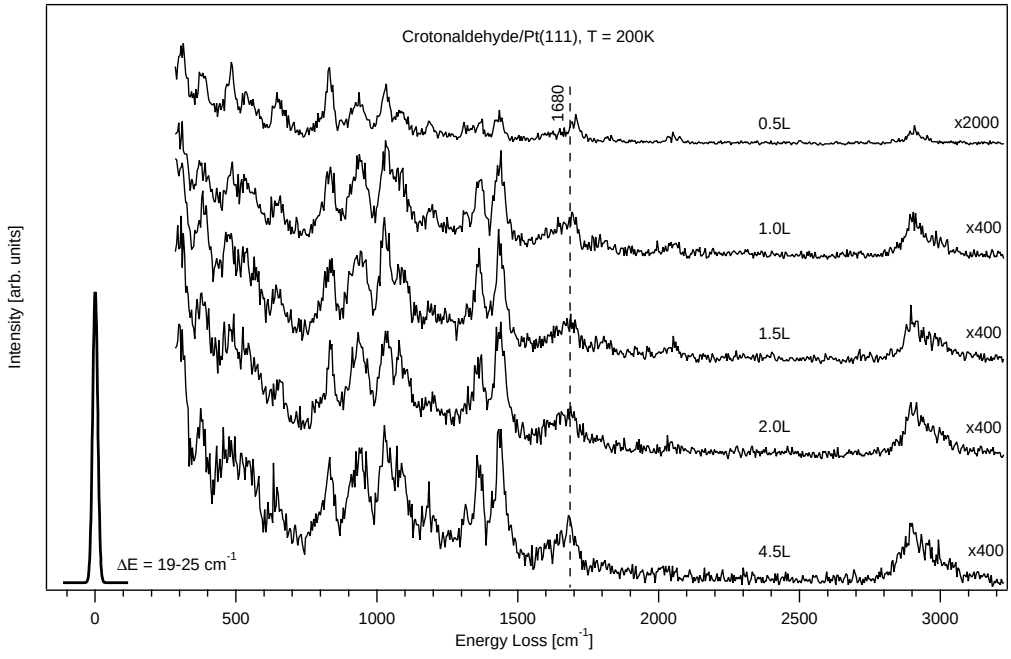

Figure 6.22: HREELS series recorded after annealing the various initial precoverages of crotonaldehyde/Pt(111) further up to 200 K.

6.1.6 The Decomposition Process of Crotonaldehyde on Pt(111)

As already observed in the TPD measurements (Chap. 6.1.1), crotonaldehyde decomposes above 250 K on Pt(111). This leads to several distinct desorption states of CO and H_2 between 275 K and 425 K. The decomposition process can also be followed closely in the HREEL spectra by annealing selected precoverages of crotonaldehyde to higher temperatures[8]. Complex vibrational patterns of mixed phases of various surface species are detected, which owing to their complexity are also highly informative.
Starting at 250 K, first changes in the vibrational spectra point to the start of the decomposition process (see Fig. 6.18). Obviously, the loss signals of the ν(C=O) vibrations between 1642 cm^{-1} and 1680 cm^{-1} previously assigned to the η^2 adsorption structures, which had been broad below 250 K, are replaced by a sharp loss peak centered at 1702 cm^{-1} (see Fig. 6.18). This is interpreted as a clear sign of a transformation involving at least the η^2-diσ(CC)-E-(s)-trans and η^2-diσ(CC)-E-(s)-cis adsorption modes in the initial stage of the reaction. A new surface intermediate must be developing, which still includes a C=O function. Parallely, the loss signal measured at 828 cm^{-1} in all HREEL spectra around 200 K broadens upon heating to 250 K before it appears as a clear-cut peak centered at 803 cm^{-1} in the experiments recorded at 300 K. Furthermore an additional loss peak begins to develop around 1291 cm^{-1} at this stage (Fig. 6.18).
An in-depth analysis of the experimental HREEL spectra at 250 K and 300 K employing computed vibrational data infers two interesting facts. On the one hand, a new intermediate arising from the fragmentation reaction must now be present on the surface, which would explain the characteristic loss peaks at 1702 cm^{-1} and 803 cm^{-1}. On the other hand, a major change in the mixed phase of irreversibly adsorbed crotonaldehyde is observed: Not only the two η^2-diσ(CC) structures can be ruled out clearly at 300 K, but also the amount of the η^3-E-(s)-cis form on the surface is decreased significantly. Its dominant vibrational normal modes calculated at 302 cm^{-1}, 539 cm^{-1} and 860 cm^{-1} are attenuated sizably at 300 K. Above this temperature, the experiments show that the η^3 form is no longer present.
One can show that the computed vibrational spectra of the η^4-E-(s)-trans and η^4-E-(s)-cis adsorption geometries, unlike the coordination structures of lower hapticity, remain compatible with the HREEL measurements recorded around 300 K. Especially the peaks measured around 300 cm^{-1}, 384 cm^{-1} (wide), 459 cm^{-1} and 515 cm^{-1}, 641 cm^{-1} (wide) and 940 cm^{-1} substantiate this conclusion (Tab. 6.12). In the absence of the η^2 and η^3 adsorption complexes, also the loss signals detected at 1040 cm^{-1}, 1182 cm^{-1}, 1350 cm^{-1} and the shoulder at 740 cm^{-1} may be assigned to the two η^4 structures. Finally after a further annealing procedure, also these species decompose and their characteristic loss peaks decrease continuously up to a temperature of 350 K, above which the fit of the theoretical data to the experiments is no longer satisfactory.

Although the transformations taking place between 200 K and 300 K are quite evident, the processes above 300 K eventually lead to more obvious changes in the HREEL spectra (Fig. 6.23). Small fragments arising from the decomposition of the surface species begin to build up around room temperature, too. At first only weak loss signals of coadsorbed CO are seen in the HREEL spectra around 300 K. They are assigned to CO adsorbed on top (2057 cm^{-1}, ν(CO), and 471 cm^{-1}, ν(Pt-C)) and in bridge (1823 cm^{-1}, ν(CO), and 398 cm^{-1}, ν_s(Pt-C)) sites. Upon annealing the sample to about 350 K, just below the onset of the CO desorption measured by TPD, these signals gain intensity and finally saturate. Within the usual deviations due to coverage dependent shifts known for CO on Pt(111) [57], the experimental frequencies of these

[8]Despite the good agreement of the TPD and HREELS results that will be discussed in this section, one has to keep in mind that the HREELS data have been recorded in a thermodynamical equilibrium situation (after recooling) while TPD is an out-of-equilibrium method.

loss peaks are in good accordance with the data of other groups. Paffet et al. [37] for instance give the values of 2105 cm^{-1} and 470 cm^{-1} for the on-top and 1865 cm^{-1} and 395 cm^{-1} for the bridge adsorption site whereas Steininger et al. [154] determined the frequencies of both sites at ca 2100/470 cm^{-1} and 1850/380 cm^{-1}, respectively.
The CO accumulation on the surface is accompanied by a deterioration of the loss signal at 1702 cm^{-1}, which was already suggested to be characteristic for the new intermediate formed in the initial reaction steps. Hence, it must be this intermediate that in a subsequent elementary step undergoes a dissociation of the CO group and leads - besides the accumulation of CO - to the formation of (a) hydrocarbon species on the Pt(111) surface.

Extending the present argumentation by including the first desorption state of hydrogen measured on Pt(111) around 300 K (β_1, see Fig. 6.6), it can be suggested that in the first elementary step the η^2 and η^3 adsorption structures of crotonaldehyde loose the aldehydic hydrogen (H1) around 250-300 K and form a stable surface intermediate. This intermediate dissociates the aldehydic function and leads to a hydrocarbon species. Around 325 K also the η^4 adsorption modes begin to fragment. Finally the resulting hydrocarbon species formed on Pt(111) passes through further dissociation reactions as evidenced by the reaction limited desorption states of molecular hydrogen measured at higher temperatures with TPD.
It is difficult to give a reason for the increased temperatures seemingly necessary for the fragmentation of the flat η^4 adsorbates. Without detailed studies of the activation barriers of the various elementary steps in the decomposition pathway, only plausible reasons may be outlined here. Assuming that the dehydrogenations of the different adsorption modes on Pt(111) lead to the same surface intermediate[9] a somewhat larger activation barrier might be expected for the flat η^4 forms due to their higher hapticity. This expectation is supported by the finding that this surface intermediate, which will be discussed below, exhibits a stable, very specific geometry, and, thus, most probably all of the irreversibly adsorbed crotonaldehyde structures can be expected to enter this decomposition channel. Yet also a transformation in the adsorbate phase of stable crotonaldehyde geometries preceeding the first elementary step of the decomposition cannot be ruled out without further investigations.

The HREEL spectra recorded after annealing the sample to temperatures between 325 K and 375 K reveal only small variations in the general fingerprints but moreover a homogeneous decrease of the loss intensities. Around 400 K, the HREEL spectra show major changes again. As the quality of the HREEL spectra deteriorates seriously beyond 400 K, indicating that complex processes lead to rather undefined and difficult to detect reaction products, any analysis of these spectra becomes increasingly difficult and might not lead to clear conclusions. Therefore no attempt has been made in this work to interprete the HREELS data above 400 K.

In order to investigate the potential elementary steps and their corresponding reaction intermediates in more detail, a large number (> 80) of possible surface species ranging from hydrogenated and dehydrogenated crotonaldehyde products to various saturated and unsaturated hydrocarbons have been calculated.
While some of these considered structures have already been identified or at least suggested in earlier studies on the adsorption, the hydrogenation or the dehydrogenation of hydrocarbons such as acetylene (Pt: [148, 152, 155], Pd: [156]), ethene (Pt: [132, 148, 149, 154, 157, 158, 159], Pd: [156, 160]), propene [132, 150, 151, 157, 161, 162, 163, 164], propyne [165, 166], 1- and 2-butene [150, 151, 157, 167], iso-butene [132, 150, 151, 157] and 1,3-butadiene [168, 169] over transition metal surfaces like Ni(111), Pd(111) or Pt(111), others are studied here for the first

[9] The same dehydrogenation intermediate was obtained from several DFT optimizations with different initial geometries, i.e. the η^2-diσ(CC)-E-(s)-trans, the η^3-E-(s)-cis and the η^4-E-(s)-trans forms. It does no longer show a cis-trans isomerization, because its C=O moiety is tilted up from the surface.

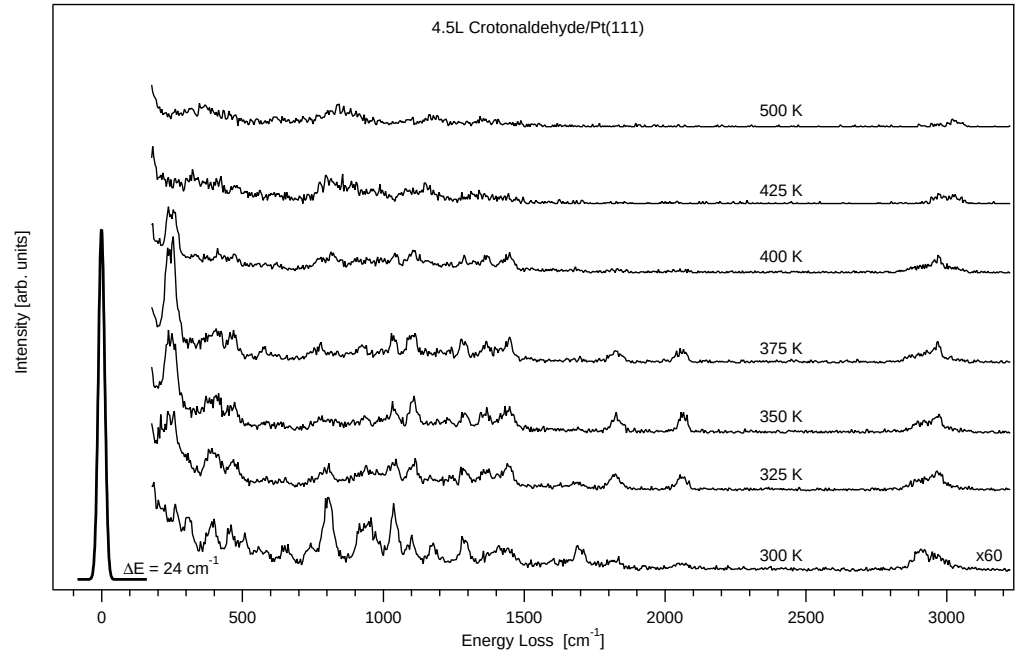

Figure 6.23: HREELS of 4.5L crotonaldehyde/Pt(111), 300-500 K. The HREEL spectra have been recorded in specular geometry at an angle of incidence of 60° with a primary energy of 4.7 eV.

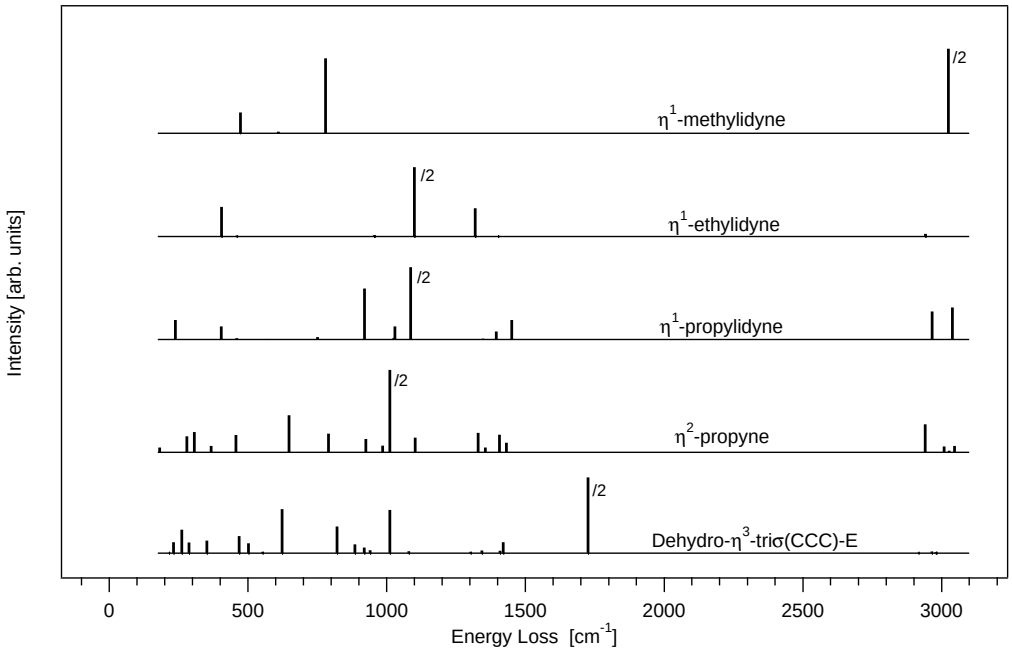

Figure 6.24: Computed HREEL spectra of potential fragments arising from the decomposition of crotonaldehyde on Pt(111).

time. Also conclusions derived from the adsorption of C_1-C_4 alcohols [170] or the formation of specific alkylidyne species [165, 166, 171] on Pt(111) pointed to certain intermediates, which might also be encountered in this decomposition pathway.
Caused by the numerous conceiveable reaction pathways and intermediates, the identification of these solely by comparison of the experiments with computed HREEL spectra turned out to be quite difficult. While the majority of the hydrocarbon structures considered can already be eliminated in this manner, in some cases an unambiguous assignment of the experimental loss peaks has been hampered by the similarity of vibrational properties of related species. Nonetheless the number of suitable structures can be constricted systematically by taking into account the reaction free energies of the competing steps, which is given by the difference of the stabilities between products and reactants calculated at the same coverage. The reaction free energies vary relatively strongly and allow to exclude thermodynamically unfavorable reaction steps by considering the Hammond postulate[10]even without regarding the exact free enthalpies and the corresponding activation barriers of the elementary processes. However, the free energies are calcutated within a "zero temperature" and "zero pressure" model and do not include the zero-point corrections or any entropy terms (via partition functions). Consequently they represent only an approximation to the true free enthalpies.
By taking into account the energetics and the results of the vibrational analysis, the most probable decomposition pathway can be proposed. The important elementary steps (bold arrows) and the surface intermediates identified spectroscopically (marked with boxes) are presented in Figs. 6.25 and 6.26.

The discussion of the decomposition pathways starts with the most stable adsorption structure of crotonaldehyde on Pt(111): the η^3-E-(s)-cis form. As an initial assumption for the theoretical investigations, several hydrogenated and dehydrogentated reaction intermediates originating from this adsorption mode have been included in the analysis. Importantly, not only the hydrogenation products like 1-butanal, 2-butenol and 1-butanol and but also the monohydrogenated "first" radical intermediates can be eliminated on the basis of their vibrational fingerprints. Hence no self-hydrogenation or hydrogenation from the background gas takes place under UHV conditions on Pt(111).
Looking at the "first" monodehydrogenation of crotonaldehyde, one finds three possible species depending on which hydrogen is abstracted: either the aldehydic hydrogen H1, or one of the vinylic hydrogens H2 and H3 may be dissociated from the molecule. In each case, the resulting dehydro-η^3 moiety forms a specific adsorption complex with strong interactions to the Pt(111) surface that can easily be understood from its unsaturated radical character. Energetically the abstraction of the aldehydic hydrogen H1 is clearly favored in this dehydrogenation step. It is exothermic at -62.5 kJ/mol. The other monodehydrogenated species can also be eliminated on the basis of their vibrational fingerprints. These are not compatible with the HREELS experiments, too.
The occurrence of this dissociation forming a dehydro-η^3-E-crotonaldehyde-H1 intermediate shown in Fig. 6.27(a) (Fragment CFr1) in the first elementary step is also confirmed by its spectroscopical identification; its vibrational spectrum is plotted in Fig. 6.24 and the assignment of its normal modes is given in Tab. 6.16. Geometrically the dehydro-η^3-E structure is bonded above a 3-fold hollow site with the carbons C1, C2 and C3 sitting on a platinum atom each and the C=O group tilted away from the surface. The C-C bond lengths are elongated significantly (C1-C2: 1.50 Å; C2-C3: 1.50 Å; C3-C4: 1.51 Å) and indicate a pure single-bond character. Looking at the short bond distance of C1=O (1.21 Å), which is typical for a C=O double bond, it becomes clear that the tetravalency of the carbons is conserved. In fact, for the most stable

[10]This principle formulated by G.S. Hammond and J.E. Leffler states that the transition state bears the greater resemblance in terms of geometry and energetics to the less stable species.

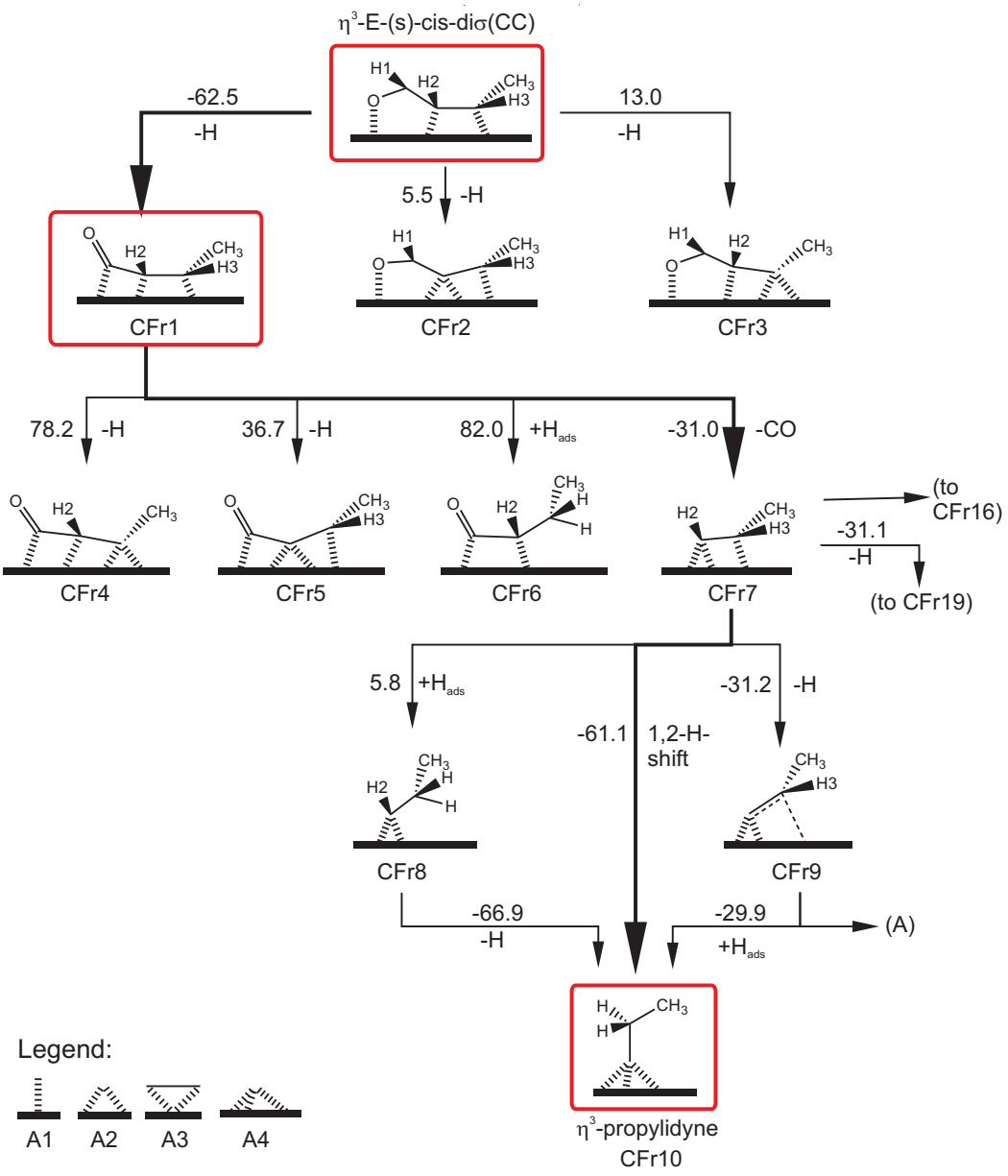

Figure 6.25: Potential initial decomposition pathways of crotonaldehyde/Pt(111). The bold arrows indicate the most probable decomposition route. Marked with boxes are the surface intermediates that have been identified above 250 K by the combination of HREELS and DFT. All free energy values of the elementary steps in this scheme are given in kJ/mol. Legend: Structure type A1 corresponds to a singly-bonded species (i.e. top), A2 to a bridge site, A3 represents a π-type metallacycle structure and A4 refers to a threefold hollow site configuration.

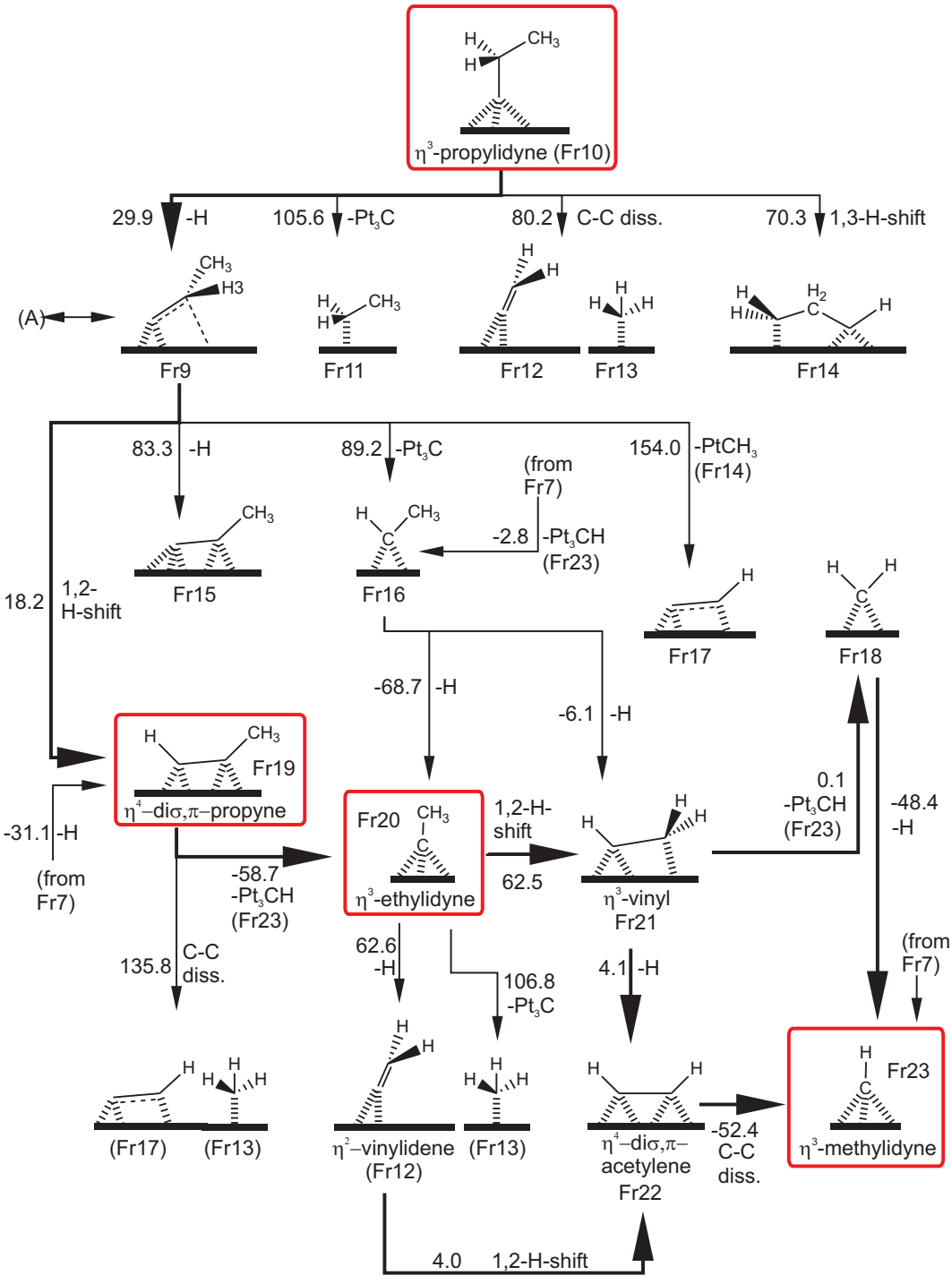

Figure 6.26: Consecutive decomposition pathways of crotonaldehyde/Pt(111). The bold arrows indicate the most probable decomposition route. All free energy values of the elementary steps in this scheme are given in kJ/mol. The same symolism as used in Fig. 6.25 is also employed here.

geometries and binding sites of all of the surface species considered in this work the tetravalency of carbon is never violated (of course metastable subvalent structures are possible, too). The molecule-metal bond distances are typical for the vinyl backbone of the dehydro-η^3-E structure with 2.12 Å (Pt2-C3) and 2.14 Å (Pt3-C2) except Pt1-C1. The latter adsorption bond is shortened slightly to 2.02 Å.
At 1725 cm^{-1} the ν(CO) stretching mode (Tab. 6.16) agrees with the experimental loss peak at 1702 cm^{-1} that is detected between 250 K and 325 K. It is quite intense here caused by the reorientation of the C=O function. Also the new loss signals at 803 cm^{-1} and 1291 cm^{-1} that are observed concommitantly to the new CO stretching mode at 1702 cm^{-1} can be assigned to vibrations of this intermediate. Computed at 821 cm^{-1} the γ(C3H2) out-of-plane deformation mode results in sizable loss intensity in agreement to the intense peak at 803 cm^{-1}. The experimentally weak signal at 1291 cm^{-1} can be attributed to the corresponding in-plane δ(C3H2) vibration obtained at 1303 cm^{-1}, though its intensity seems to be somewhat underestimated in the theoretical analysis. Justified by the close structural relationship to the two η^4 geometries remaining on the surface at these temperatures, the rest of the computed normal modes of the dehydro-η^3-E-H1 complex coincides well with the vibrations of the latter and are therefore hardly useful to discern this initial reaction intermediate.

For the next elementary step of the decomposition process again several competing possibilities have to be considered. Among subsequent dehydrogenations of the dehydro-η^3-E-crotonaldehyde-H1 complex (CFr1), also rehydrogenations of other molecular parts or cleavages of the carbon-carbon bonds of the molecular backbone have to be taken into consideration. From all these, the only exothermic elementary reaction is the release of the C=O moiety (-31 kJ/mol; the CO remains strongly bonded in a Pt-top site). The resulting surface intermediate could be called an η^3-1-prop-1-enyl (CFr7, see Fig. 6.25) and resembles a C_3 hydrocarbon bonded to the Pt(111) by a bridge type configuration of the terminal carbon C1 and an additional interaction Pt-C2. Since the subsequent fragmentation step of this new intermediate will be shown to be a strongly exothermic hydrogen rearrangement, it can be expected to exhibit only a small activation barrier and, thus, renders species CFr7 comparably unstable. Rather not unexpected for this reason, the vibrational traces of this structure could not be identified in the experimental data.
Reverting to the small amounts of propene desorption measured in some experiments around 330 K (δ_1, see Fig. 6.9) in the present work, this surface species could also explain the latter desorption phenomenon. Essentially the η^2-propenyl is the same surface species that would result from an exothermic dehydrogenation of diσ(CC) bonded propene on Pt(111) (Δ = -20.3 kJ/mol). In spite of the proposal of such a reaction intermediate by Zaera et al. [162, 163], which may be expected in the decomposition of propene/Pt(111) forming an η^3-propylidyne, no exact structure has ever been identified spectroscopically thus far (see [165, 171]).

Upon the abstraction of the CO moiety between 300 K and 350 K and the resultant build up of CO adsorbed in on-top and bridge sites follows a 1,2-hydrogen shift in the η^3-1-prop-1-enyl intermediate. This becomes evident from the fact that the forming η^3-propylidyne intermediate (CFr10, see Fig. 6.27(c)) is unambiguously identified in the experimental HREEL spectra. Any alternative route consisting of a dehydrogenation and a bimolecular rehydrogenation step via CFr8 or CFr9 is expected to be disfavored with respect to this sizably exothermic reaction (ΔF = -61.1 kJ/mol), which should proceed via an early transition state with a comparably low activation barrier.
The η^3-propylidyne intermediate (CFr10) is a highly stable alkylidyne structure and is usually observed in the dehydrogenation of propene on transition metal surfaces. The temperature range in which this structure forms during the decomposition of crotonaldehyde is in excellent agreement to its evolution in the case of heating propene adsorbed on Pt(111), where it has

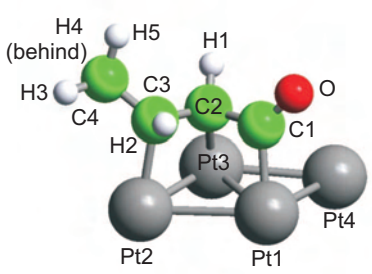

(a) Dehydro-η^3-triσ(CCC)-E-H1

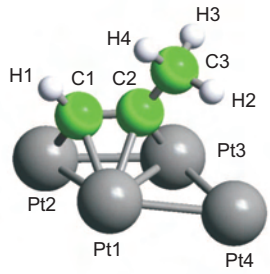

(b) η^4-propyne

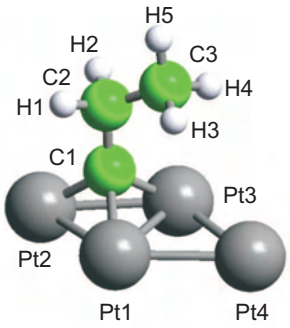

(c) η^3-propylidyne

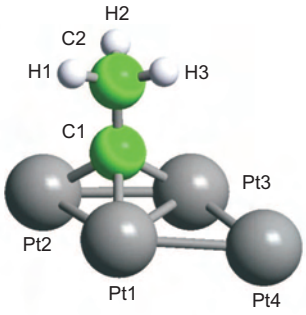

(d) η^3-ethylidyne

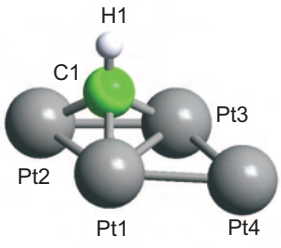

(e) η^3-methylidyne

Figure 6.27: The optimized geometries of fragments identified by HREELS and DFT arising from the decomposition process of crotonaldehyde on the Pt(111) surface.

ω cm^{-1}	Intensity $\times 10^6$ au		Normal mode
3040	0.0		ν(C4-H3)
2980	0.047		ν(C2-H1)
2980	0.090		ν_{as}(C4-H3,5)
2965	0.14		ν(C3-H2)
2916	0.028		ν_s(C4-H3,5)
1725	12.7	vs	ν(C1=O)
1420	0.93		δ"(CH_3)
1409	0.21		δ'(CH_3)
1342	0.22		u(CH_3)
1303	0.11		δ(C3H2)
1177	0.009		δ(C2H1)
1080	0.15		ν(C2=C3)
1065	0.001		ν(C3-C4)
1011	3.6	s	γ"(CH_3)
941	0.24		ν(C1-C2)
919	0.48		γ(C2H1)
886	0.73		γ'(CH_3)
821	2.2	m	γ(C3H2)
623	3.7	s	ν_{as}(PtC1-PtC2-PtC3)
552	0.10		δ(O=C1-C2)
502	0.82		ν_{as}(PtC1+PtC2-PtC3)
468	1.4	w	δ(C2=C3-C4)
352	1.05	w	ν_s(PtC1+PtC2+PtC3)
287	0.89		fT
262	2.0	m	δ(C1-C2=C3)
232	0.92		τ(CH_3)
216	0.039		τ(C2=C3)
143	0.18		fT
119	0.054		fR
75	0.20		τ(C1-C2)

Table 6.16: Vibrational analysis of the dehydro-η^3-triσ(CCC)E-crotonaldehyde-H1 species (CFr1) on Pt(111), theoretical coverage 1/9 ML. The letters following the computed intensities refer to the relative strength, i.e. (v)w = (very) weak, m = medium and (v)s = (very) strong.

ω cm^{-1}	Intensity $\times 10^6$ au		Normal mode	HREELS[a] cm^{-1}	RAIRS[b] cm^{-1}	HREELS[c] cm^{-1}
3040	0.002		ν_{as}(C3-H3,4)		2960	2980
3038	0.27		ν(C3-H5)			
2973	0.001		ν_{as}(C2-H1,2)			
2965	0.24	w	$\nu_s(CH_3)$		2917	
2938	0.0		ν_s(C2-H1,2)			2920
1450	0.16		δ'(CH_3)	1450	1450	1465
1435	0.002		δ"(CH_3)	1450	1374	1400
1395	0.067		$\delta(CH_2)$	1404	1408	1465
1346	0.005		u(CH_3)	1364		
1262	0.0		$\gamma(CH_2)$	1280		1295
1226	0.001		γ"(CH_3)	1220	1079	1055
1086	1.2	s	ν(C1-C2)	1110	1104	1115
1030	0.11		ν(C2-C3)	1040		940
1026	0.015		τ(C2-C3)	1040		
920	0.43	m	γ'(CH_3) + $\nu_s(Pt_3C)$	928	1041	825
751	0.020		δ(C1-C2-C3)	766		
568	0.004		ν_{as}(Pt1C-Pt2C+Pt3C)	576		
460	0.009		ν_{as}(Pt1C+Pt3C-Pt2C)	467	440	
404	0.11		$\nu_s(Pt_3C)$ + γ'(CH_3)	394		
245	0.001		$\tau(CH_3)$	245		250
238	0.16		fR	245		
150	0.17		fT			
102	0.095		fR			
52	0.29		τ(C1-C2)			

Table 6.17: Vibrational analysis of the η^3-propylidyne (CFr10) bonded in a threefold hollow site on Pt(111) (coverage 1/4). For comparison the experimental wavenumbers of the 350 K HREEL spectrum as well as the previous experimental values by Zaera et al. [162] and Avery et al. [150] are listed in the order of their corresponding original assignments, which differ from the conclusions of the present work.

[a]Present work, 4.5L crotonaldehyde annealed to 350 K.
[b]from Ref. [162]
[c]from Ref. [150]

been detected between 290 K and roughly 350 K by LEED [165], TPD [151, 163] and vibrational spectroscopies [150, 163]. Due to the complexity of the mixed phase of surface intermediates no LEED superstructure could be observed at higher temperatures in this work.

Present as a minority component at 300 K, propylidyne accumulates up to 325 K and even becomes a dominant surface species between 350 K and 400 K in these experiments. The optimized geometry indicates a saturated character for the carbon backbone (r(C1-C2) = 1.50 Å; r(C2-C3) = 1.53 Å), which is supported by the typical single-bond frequencies of the ν(CC) stretching modes computed at 1030 and 1086 cm^{-1}. Apparently in agreement with high stability of this intermediate, the three Pt-C bonds are computed to be short (2.03 Å).

In the experimental HREEL spectra most of the vibrations of propylidyne (Fig. 6.24) can be discerned unambiguously. Their assignment from the DFT analysis is presented in Tab. 6.17 together with literature values taken from RAIRS measurements of Zaera et al. [162] and HREELS results of Avery et al. [150]. Some attention must be paid to the sequence of the values reproduced in Tab. 6.17 from the literature, because these are sorted according to their original assignments instead of their frequencies in this case. It is noticed instantly that the interpretation of

ω cm^{-1}	Intensity $\times 10^6$ au		Normal mode	HREELS[a] cm^{-1}
3046	0.060		ν(C1-H1)	
3027	0.015		ν(C3-H2)	
3009	0.054		ν_{as}(C3-H3,4)	
2940	0.26	w	ν_s(CH_3)	
1431	0.089		δ'(CH_3)	1450
1407	0.16		δ"(CH_3)	1416
1356	0.046		ν(C1-C2)	1364
1330	0.18		u(CH_3)	
1103	0.14		δ(C1H1)	1110
1012	1.5	s	γ'(CH_3)	1040 (wide)
985	0.062		γ"(CH_3)	988
925	0.12		ν(C2-C3)	928
790	0.17		γ(C1H1)	798
648	0.35	w	ν_s(Pt1C+Pt2C)-ν_s(Pt3C+Pt4C)	650
457	0.16		δ(C1-C2-C3), ν_s(Pt1C+Pt2C)+ν_s(Pt3C+Pt4C)	467
367	0.061		ν_{as}(Pt1C-Pt2C)-ν_{as}(Pt3C-Pt4C)	360 (shoulder)
307	0.19		ν_{as}(Pt1C-Pt2C)+ν_{as}(Pt3C-Pt4C)	301 (shoulder)
280	0.15		ν_s(Pt1C+Pt2C)+ν_s(Pt3C+Pt4C), δ(C1-C2-C3)	260 (wide)
182	0.045		fT	
153	0.48	m	τ(CH_3)	
121	0.010		fR	

Table 6.18: Vibrational analysis of the η^4-diσ(CC)-π(CC)-propyne (CFr19) bonded in a three-fold hollow site on Pt(111) (coverage 1/9).

[a]Present work, 4.5L crotonaldehyde annealed to 325 K.

the vibrational loss signals measured by these authors differs from the results of the present theoretical computation. Especially the ν(C1-C2) stretching mode obtained at 1086 cm^{-1}, which is oriented normal to the surface, is dominant for η^3-propylidyne, although it may not serve as a clear indicator for this species on its own. This problem is caused by the related η^3-ethylidyne species, which exhibits a similarly intense loss peak nearby.
Other weak, but still very characteristic normal modes of η^3-propylidyne like the ν(C2-C3) at 1030 cm^{-1}, the symmetrically coupled γ'(CH_3) deformation and the ν_s(Pt_3C) molecule-metal stretching vibration at 920 cm^{-1} have to be adducted for the analysis. Even as well serves the torsion mode τ(CH_3) at 245 cm^{-1}, which lies very close in frequency to a hindered rotation at 238 cm^{-1}. All of these vibrations are recognized easily in the experimental data at temperatures above 350 K, but the weaker ones of them interfere with loss peaks of the previously discussed surface complexes at lower temperatures.
A comparison of these assignments to the conclusions of Zaera et al. [162] or Avery et al. [150] yields a good agreement for the more intense vibrations. Only a few of the in-plane and out-of-plane deformation modes (or sometimes called rocking modes in the latter case) of the methylene- and methyl-hydrogens have been assigned to very different measured signals by these authors based on their purely experimental studies.

The stability of the η^3-propylidyne intermediate, which may be the base for the simplicity of its experimental detection, can be appreciated from the high endothermicity of the reaction free energies of the next elementary steps. There are numerous sequences of dissociation and rearrangement steps possible that finally lead from the C_3 species to smaller hydrocarbons like Pt_3C-H or even surface carbon ("surface graphite").

For the sake of simplicity only the most competetive reaction steps are shown in Fig. 6.26. As seen from the reaction energetics, the η^1-propylidyne structure can be expected to give off a single hydrogen from the methylene group (29.9 kJ/mol). This forms the highly unsaturated intermediate CFr9, which has already been encountered on the parallel route of the preceding 1,2-H-shift. A branching of the pathways from CFr7 to CFr9 or the propylidyne (CFr10) may, hence, not be excluded at this stage without reliable knowledge of the activation barriers and kinetics of these reaction steps. Remarkably, a concerted elimination of two hydrogens from C2 and C3 resulting in a 'C-CH-CH2' surface species and also cleavages of the C-C bonds of η^3-propylidyne are clearly unprobable.
The subsequent fragmentation of CFr9 is an endothermic 1,2-H-shift as the less unfavorable reaction energetics of the alternative reaction steps permit to predict. This hydrogen rearrangement results in another known structure, the η^4-diσ(CC)-π(CC)-propyne (CFr19), which was suggested from LEED experiments performed by Koestner et al. [165] after propyne adsorption on Pt(111).
Judging from the adsorption energy of -191.9 kJ/mol calculated at a coverage of 1/4 monolayer, this structure is again comparably stable. The adsorption complex is centered around a 3-fold hollow site and develops four Pt-C interactions from the C1-C2 triple-bond that are best described by a η^4-diσ(CC)-π(CC) coordination. The Pt-C bond lengths differ by roughly 10% for the two diσ (Pt2-C1 2.05 Å; Pt3-C2 2.02 Å) and the π type bonds (Pt1-C1 2.20; Pt1-C2 2.25 Å).
One might expect such a small molecule to be most likely intensively studied, but only a few useful results are presently available in the literature. Aside from the LEED studies cited above, the DFT investigations of Valcárcel et al. [166] on the propyne interaction with Cu(111) provide useful insights. In comparable DFT computations these authors obtained a much smaller adsorption energy of -73.3 kJ/mol for a 2×2 supercell on Cu(111). Despite the huge discrepancies between the adsorption energies of propyne on Cu(111) and Pt(111), the elongation of the C1-C2 axis is found to be nearly uniform: It is stretched to 1.39 Å on Pt(111) and 1.37 Å on Cu(111) compared to the theoretical gas phase value of 1.21 Å. In contrast, the C-C bond length of the methyl group is as expected less influenced with 1.50 Å(gas phase 1.45 Å). The small elongation determined on Pt(111) may be ascribed primarily to electronic effects.
In the case of the propyne intermediate, the identification in the experimental HREEL spectra is not unquestionable. The problem originates from the mix of different surface species encountered during the decomposition process, which lead to ambiguities in the assignments of the peaks. While almost all of the computed frequencies of η^4-diσ(CC)-π(CC)-propyne listed in Tab. 6.18 (the theoretical HREEL spectrum is plotted in Fig. 6.24) match an experimental loss peak, these can at the same time be interpreted by the previously discussed intermediates. Nonetheless, because its theoretical HREEL spectrum is compatible with the experiments between 325 K and 350 K, it cannot be excluded without further hints. A good indicator of the presence of the η^4-diσ(CC)-π(CC)-propyne structure might be the γ'(CH_3) vibration calculated at 1012 cm^{-1}. It could explain the broadening of the experimental signal measured between 920 and 1050 cm^{-1} at 325 K, while in the HREEL spectra recorded at lower temperatures two sharp peaks are discernable at 940 cm^{-1} and 1040 cm^{-1} instead. Induced by the relatively low loss intensity measured around 1012 cm^{-1}, it can be concluded that propyne does not constitute a dominant component of the mixed surface phase.
It is interesting to direct the discussion also to the ν(C1-C2) stretching vibration of this adsorption complex. The computed frequency of this normal mode of 1356 cm^{-1} correlates well with the bond length of 1.39 Å and points to a significantly unsaturated character inherent in the C1-C2 bond after adsorption. Caused by an orientation parallel to the surface it shows only a low intensity and is therefore difficult to assign in the experiments.

The fragmentation of the η^4-diσ(CC)-π(CC)-propyne proceeds by a bond cleavage of the C-C

bond parallel to the surface. This is confirmed by HREELS and supported by the DFT total energy considerations. As a consequence of the decomposition a second highly stable alkylidyne species on Pt(111) is encountered: The η^3-ethylidyne structure (CFr20, see Fig. 6.27(d)). Similar to the propylidyne formation from propene it is very common during the dehydrogenation of ethene on transition metal surfaces and has also been characterized thoroughly during the recent decades with a variety of experimental techniques including LEED, TPD, HREELS and PES [132, 149, 154, 159, 165] as well as theoretically ones [155, 156, 160]. Upon annealing ethene adsorbed on Pt(111), for instance, ethylidyne evolves after a molecular hydrogen desorption generally measured around 302 K [132, 149]. The corresponding HREELS experiments recorded between room temperature and ca 365 K show the spectrum of an ordered ethylidyne phase [149, 154, 159].

As a byproduct in the course of the ethylidyne formation a η^3-methylidyne fragment is generated, which is a third alkylidyne species found in the present decomposition pathway. Like ethylidyne it is apparently very stable, too, and its exothermic formation energy seems to induce a preference for this dissociation channel (ΔF = -58.7 kJ/mol) over the other possibilities. In addition, as can be expected from the unsaturated character of the initial complex, any further dehydrogenation steps of propyne are obviously unfavorable.

Structurally the ethylidyne species is closely related to the η^3-propylidyne in terms of geometry. With a C-C bond length of 1.49 Å this intermediate behaves like an alkane with a typical C-C single bond. The three Pt-C1 bonds are symmetry-equivalent here in contrast to the ones in propylidyne and hence show the same bond distance of 2.02 Å.

The geometrical data obtained in the present four layer slab calculations are in good accordance to the ones of Watwe et al. [155], who in their total energy analysis used mostly simpler two layer models with frozen metal atoms. These authors find a formation energy of -156 kJ/mol for ethylidyne and coadsorbed hydrogen from gas phase ethylene, which is slightly more exothermic than the value of -142.1 kJ/mol calculated in this work. Such a formation might occur by a 1,2-H-shift and subsequent dehydrogenation step starting from either a diσ(CC) or a π(CC) coordinated ethene species, both of which having been identified successfully on Pt(111) in the past. The product of the 1,2-H-shift, the η^3-ethylidene is depicted as CFr16 in the 2^{nd} scheme of the decomposition pathway (Fig. 6.26). At an assumed coverage of 1/4 monolayer of ethene, this rearrangement would be slightly exothermic at -8.3 kJ/mol for a π(CC)-ethene adsorbate, but sizably endothermic at 26.9 kJ/mol for the diσ(CC) form.

Employing the computed vibrational spectrum of ethylidyne shown in Fig. 6.24 a clear identification of this intermediate is possible in the HREEL experiments recorded between 325 K and 400 K. Even at 300 K a small contribution of this intermediate cannot be ruled out since the most characteristic vibrations can be discerned with weak loss intensities. The derived assignments of the loss signals are presented in Tab. 6.19. Best suited for an identification of this structure is the combination of the intense u(CH_3) umbrella, the ν(C1-C2) stretching and symmetric ν_s(Pt_3C) normal modes computed at 1319 cm^{-1}, 1099 cm^{-1} and 405 cm^{-1}, respectively. In the experimental HREEL spectra these closely match the loss peaks at ca 1280 cm^{-1}, 1105 cm^{-1} and 394 cm^{-1}.

Furthermore several dipole forbidden vibrations such as the asymmetric ν_{as}(Pt_3C) molecule-surface stretching mode[11] at 460 cm^{-1} or the γ(CH_3) deformation modes at 956 cm^{-1} also agree with experimental frequencies (467 cm^{-1} and 928 cm^{-1} resp.), but are not obtained with significant intensities in the theoretical analysis. This discrepancy in the intensities observed may have its origin in an additional coupling to surface phonons or likewise to contributions from the impact scattering mechanism that are missing in the theoretical analysis.

The confrontation of the computed normal frequencies of ethylidyne with previous HREEL studies of Steininger et al. [154] and Pelster [159] given in Tab. 6.19 shows a good correspon-

[11] Two normal modes are computed degenerate in accordance with the surface point symmetry.

ω cm^{-1}	Intensity $\times 10^6$ au		Normal mode	HREELS[a] cm^{-1}	HREELS[b] cm^{-1}
3015	0.0		$\nu_{as}(CH_3)$ (deg.)	2952	2952
2941	0.045		$\nu_s(CH_3)$	2888	2888
1400	0.006		$\delta(CH_3)$ (deg.)	1420	1403
1319	0.48	w	u(CH_3)	1347	1339
1099	2.3	s	ν(C1-C2)	1129	1121
956	0.016		$\gamma(CH_3)$ (deg.)	984	984
462	0.002		$\nu_{as}(Pt_3C)$ (deg.)	597	460
405	0.49	w	$\nu_s(Pt_3C)$	427	419
162	0.29		fR	307	282
152	0.0		fT		
113	0.37	w	fT		

Table 6.19: Vibrational analysis of the η^3-ethylidyne (CFr20) bonded in a threefold hollow site on Pt(111) (coverage 1/4) and comparison to previous results in the literature [154, 159].

[a] from Ref. [154]
[b] from Ref. [159]

dance, too. On first sight, similar assignments of the normal modes made by these authors confirm the actual results. Yet at a closer look, a few small differences are found: The assignment of a peak measured by Steininger et al. at 597 cm^{-1} to the asymmetric $\nu_{as}(Pt_3C)$ metal-molecule stretching vibration, which is very specific for this type of coordination[12], does obviously disagree with the outcome of the present calculations and the results of Pelster et al., which suggest the loss peaks around 460 cm^{-1} (this work: 467 cm^{-1}) to be the correct signals. Furthermore, the experimentally determined loss signals at 307 cm^{-1} [154] and 282 cm^{-1} [159] are not reproduced by the present calculations; besides the broad experimental peak around 245 cm^{-1}, which has been assigned to propylidyne (see above), and the weak shoulder at 301 cm^{-1} measured in the 325 K spectrum, no further loss signal is observed nearby. Due to the neglect of any coupling to phonons in the present analysis, the origin of this problem cannot be resolved.

The final elementary steps of the decomposition process continuing from ethylidyne are even more confusing and difficult to treat without any knowledge of the activation barriers involved. Again a number of hydrogen rearrangements, dehydrogenations and rehydrogenation steps followed by the dissociation of the remaining C-C bond can be conceived that end up with η^3-methylidyne moieties in 3-fold hollow sites. In a strongly endothermic step (60.9 kJ/mol[13]) the latter can ultimately be dehydrogenated to an atomic carbon species.
The route of a dehydrogenation of C2 to an η^2-vinylidene species (CFr12) and subsequent 1,2-H-shift to η^4-diσ(CC)-π(CC)-acetylyne (CFr22)[14] is almost identical to the sequences possible with an initial hydrogen rearrangement to the η^2-vinyl moiety (CFr21) in terms of total energies. Even a reaction mechanism with a C-C bond cleavage involving a bridge-bonded η^3-methylidene intermediate seems possible[15].

[12] Related normal modes of propylidyne and methylidyne are computed at 460 cm^{-1} and 472 cm^{-1}. Note that the assignment differs for the latter surface species.
[13] This value corresponds to methylidyne and carbon adsorbed in an fcc site.
[14] The adsorption energy of acetylene from the computations in the 2×2 supercell is -205.3 kJ/mol; Watwe et al. obtained a value of -236 kJ/mol [155] on Pt(111) in their fixed two layer slab computation while Pallassana et al. found a sligthly smaller value of -168 for a comparable three layer slab calculation on Pd(111) [160].
[15] The energy balance for a dissociative adsorption of methane on Pt(111) forming a η^1-methyl species and hydrogen coadsorbed in an fcc site is -2.8 kJ/mol. A subsequent dehydrogenation to η^1-methylidene is endothermic

ω cm^{-1}	Intensity $\times 10^6$ au	Normal mode	HREELS[a] cm^{-1}	HREELS[b] cm^{-1}
3024	0.028	ν(C-H)		3060
778	0.013	$\nu_{as}(Pt_3C)$ + fT (deg.)	775	
610	0.0	$\nu_s(Pt_3C)$	588	640
472	0.0	fT + $\nu_{as}(Pt_3C)$ (deg.)	467	

Table 6.20: Vibrational analysis of the η^3-methylidyne (CFr23) bonded in a threefold hollow site on Pt(111) (coverage 1/4).

[a]Actual work, 4.5L crotonaldehyde annealed to 350 K.
[b]From Ref. [150]: HREELS experiments of propene on Pt(111) at 425 K.

The last surface intermediate identified by HREELS is the η^3-methylidyne structure. Bonded in a 3-fold hollow site (fcc here) it exhibits three relatively short Pt-C bonds (2.01 Å) and a C-H bond of usual length (1.10 Å).
The vibrational properties, which are plotted in Fig. 6.24 and listed in Tab. 6.20 lead to a unambiguous identification of this species in the temperature intervall from 350 K to at least 400 K. At 300 and 325 K this surface species can also be suggested to be present, although the associated loss peaks are closely matched by similarly intense vibrational losses of the η^4-diσ(CC)-π(CC)-propyne and the dehydro-η^3-E-crotonaldehyde-H1 intermediates here.
The measured loss peaks at 775 cm^{-1} and 588 cm^{-1} (in the 4.5L/350 K HREEL spectrum) are assigned to the asymmetric $\nu_{as}(Pt_3C)$ stretching vibration and its symmetric counterpart with computed frequencies of 778 cm^{-1} and 610 cm^{-1}, respectively. The asymmetric molecule-metal stretching mode is strongly coupled with a hindered translation in this case. The corresponding linear combination of these two vibrational normal modes, in which the hindered translation is the dominant component, is computed at 472 cm^{-1} and may be assigned to the experimental signal at 467 cm^{-1}. Based on the comparison of HREEL spectra with IR measurements of a similar cobalt-complex, Avery et al. proposed this intermediate to form during the decomposition of propene on Pt(111) at temperatures as high as 425 K [150].

Summing up the analysis of the high temperature HREELS data between 250 K and 400 K briefly, altogether 6 intermediates have been identified with the assistance of the DFT vibrational analysis. All of these intermediates are connected by an optimal decomposition pathway determined from the total free energy differences, which is depicted in Fig. 6.28.
The temperatures at which the different species are compatible with the experiments can be divided coarsely into two regions. At first the η^2 and η^3 adsorption structures of crotonaldehyde release the aldehydic hydrogen (H1) around 250-300 K followed by the η^4 adsorption modes up to 350 K. This is considered as the first temperature intervall of the decomposition regime. The intermediate formed here is the dehydro-η^3-E-crotonaldehyde-H1 species detected between 250 K and 325 K. As confirmed by the build up of CO bonded in bridge and on top sites, this intermediate gives off the C=O function and leads to the formation of η^3-propylidyne, a highly stable alkylidyne structure. This intermediate is identified in the experiments between 300 K and 400 K. Around 350 K it even constitutes a dominant component of the mixed adsorbate phase on Pt(111).
At temperatures above 300 K several additional reaction intermediates are assigned in the HREEL spectra and mark the higher temperature region of the decomposition process. From 325 K to 350 K small amounts of η^4-diσ(CC)-π(CC)-propyne seem to be formed during the

at 20.5 kJ/mol.

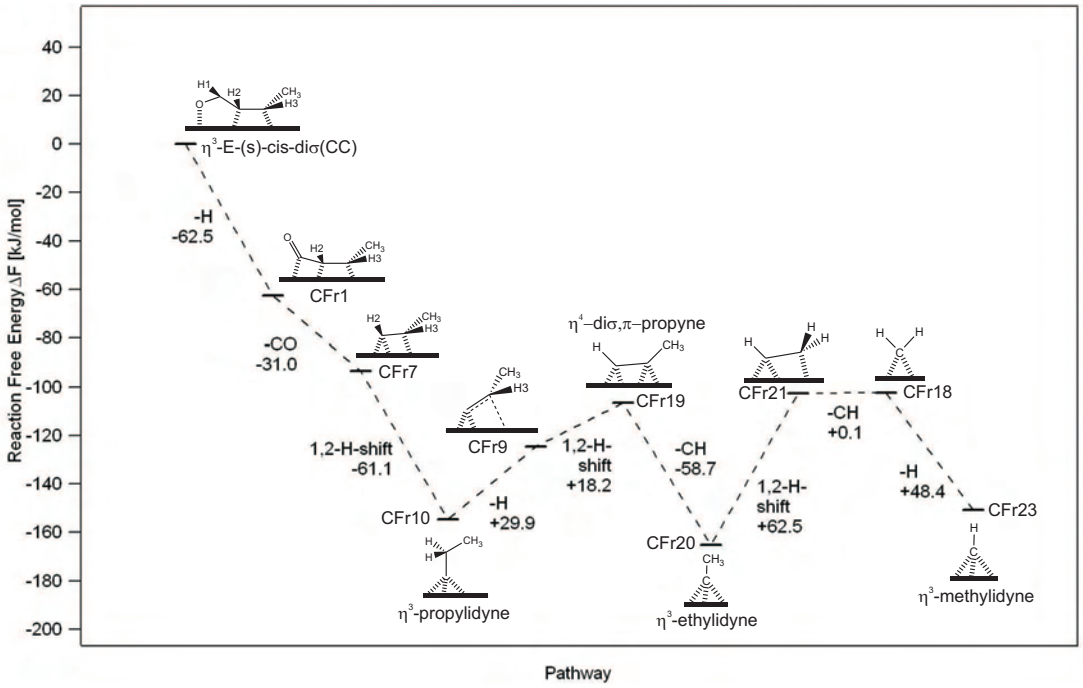

Figure 6.28: Energetics of the minimum energy decomposition pathway of crotonaldehyde/Pt(111). All relative energies are given in kJ/mol.

fragmentation of the propylidyne, while at the same time an η^3-ethylidyne species evolves on the surface and is found to be another dominant surface component up to 400 K. Its further dissociation is possibly complex and leads to badly defined vibrational spectra. Nonetheless, finally an η^3-methylidyne structure can be recognized in the HREELS experiments between 300 and 400 K.

6.1.7 Deuterium Coadsorption Experiments

One of the aims of this study was to investigate the hydrogenation reactions of crotonaldehyde under UHV conditions. Therefore experiments were conducted with a coadsorption of crotonaldehyde and deuterium using TPRS and HREELS.
During the TPRS experiments a heating rate of 2 K/s was employed together with two different sensitivity settings of the mass spectrometer as already described in section 6.1.1. Additionally to the masses observed on adsorption of pure crotonaldehyde, also the masses of HD, D_2 and the various possible deuterated products (D4-butanol, D2-butanal and D2-buten-2-ol) were followed in the TPRS experiments.
Two complementary series of TPRS experiments have been recorded depending on the sequence of adsorbing the reactants: Either crotonaldehyde was adsorbed at 100 K onto a deuterium precovered Pt(111) surface or deuterium was dosed after precovering the surface with increasing exposures of crotonaldehyde. The ratio of the gas exposures of deuterium and crotonaldehyde was chosen at 6:1 in all experiments to ensure that a sufficient excess of deuterium was available for potential reactions.

The primary result of these experiments is that no desorption of deuterated products could be

observed in the two experimental series. All of the TPR spectra of 70 amu, 74 amu and 78 amu did not indicate any additional signals except the regular low temperature desorption states of molecular crotonaldehyde, which have been discussed in section 6.1.1.
The TPRS experiments with adsorption of crotonaldehyde on a D_2 precovered surface are highlighted at this point. In the exposure series of m/z = 2 (Fig. 6.29) little difference compared to the TPD series of pure crotonaldehyde/Pt(111) (Fig. 6.6) is observed. Due to the higher SEM voltage employed here, the desorption state β_1 around 290 K (310 K with 12L D_2 and 1.9L CrA) is always resolved well. While the temperature at the desorption maximum of β_1 varies slightly, the peak position of the reaction limited desorption state β_2 is found with hardly any deviation at 425 K.
The analysis of the peak areas of β_1 and β_2 reveals again a saturation effect at exposures of about 9L D_2 and 1.5L crotonaldehyde. At higher exposures, the peak areas still remain constant within the errorbar.
The peak area ratios of the peaks β_1 : β_2 are determined to be constant for all of the performed experiments, showing that - as expected - always the same relative amount of hydrogen of 1:1 is dissociated from crotonaldehyde during the decomposition process. The small deviations observed in the peak area ratios might originate form hydrogen coadsorption form the background gases. Finally, despite a wide but weak background of H_2 up to 650 K, no additional well-defined desorption state of hydrogen is noticed at temperatures above 450 K.

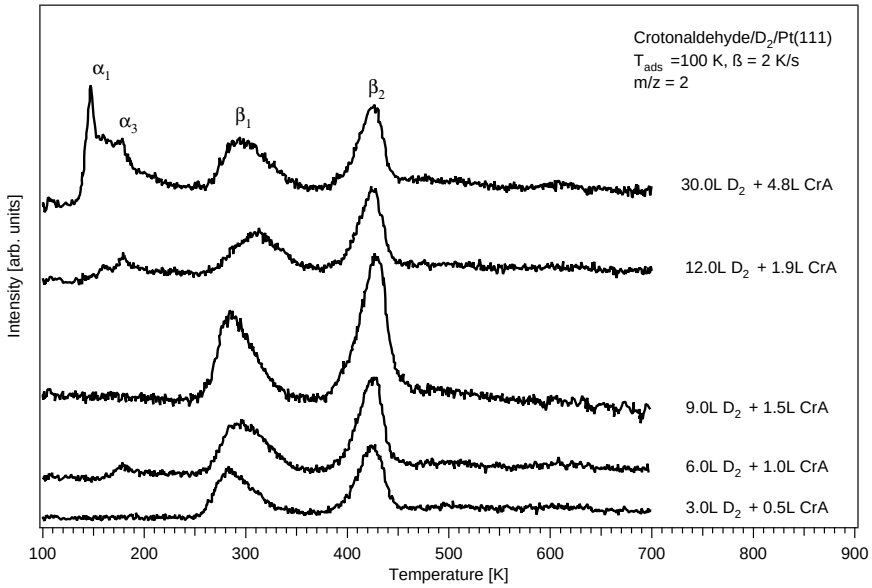

Figure 6.29: TPR spectra of crotonaldehyde adsorbed on a D_2 precovered Pt(111) surface, m/z=2.

Additional information on the effect of deuterium coadsorption is obtained from the TPRS series of HD (m/z = 3, see Fig. 6.30). Here the desorption state β_2 is measured again constantly at 428 K without noticeable shifts, whereas the signal of β_1 deviates between 270 K and 304 K. Furthermore, the peak areas of the TPRS signals do not clearly indicate a saturation effect because of their relatively large variations of up to 25%. Despite this problem, the ratio of the peak areas β_1 to β_2 again shows a constant value of 3:1 in this case. It is totally different from the one determined from the TPRS H_2 spectra. Based on the present results, the reason for this discrepancy in the relative amounts of HD desorbing in both processes can not be

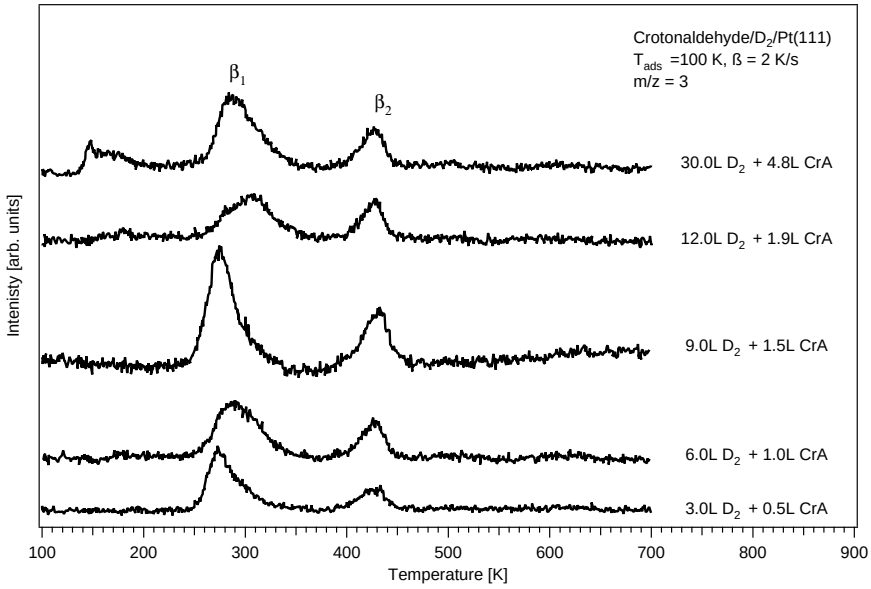

Figure 6.30: TPR spectra of crotonaldehyde adsorbed on a D_2 precovered Pt(111) surface, m/z=3.

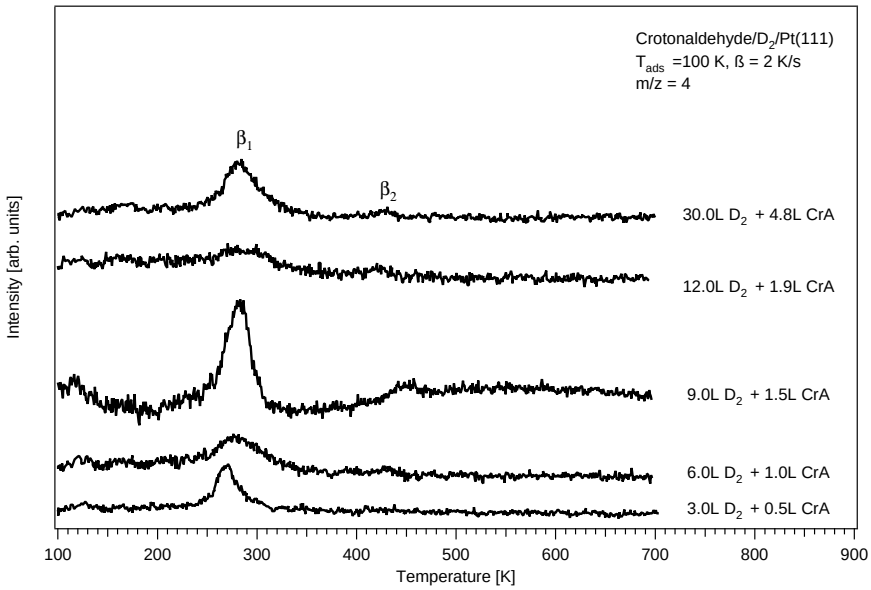

Figure 6.31: TPR spectra of crotonaldehyde adsorbed on a D_2 precovered Pt(111) surface, m/z=4.

deduced here. One possible origin of this phenonemon that might have to be adducted for an argumentation could be given by the different statistical probabilities for a deuteration or H-D exchange of the various present surface species, which might lead to a higher degree of deuteration for the thermodynamically weaker CH-bonds and, hence, are detected at lower desorption (i.e. activation) temperatures.

The TPRS exposure series of crotonaldehyde on a deuterium precovered Pt(111) surface recorded for m/z = 4 shows primarily the desorption of D_2 around 275 ± 10 K (Fig. 6.31). The molecular deuterium in this state desorbs after a recombination step from the surface and thus is quite sensitive to intermolecular interactions with other surface moieties and the condition of the sample itself. Therefore the observed shifts and large deviations of the peak intensities are not very surprising.
Obviously it can be added to the conclusions from these TPRS experiments that only a very small fraction of the present surface species are deuterated twice. Hardly any desorption of D_2 is measured at higher temperatures around 425 K.
By inverting the sequence of reaction gas exposition to precovering the sample with crotonaldehyde, a somewhat surprising result is found: The adsorption of D_2 is strongly inhibited on a crotonaldehyde covered Pt(111) surface. The TPRS experiments recorded for m/z = 4 (not presented) do not indicate any clearly distinguishable desorption state of D_2, neither around 300 K nor at higher temperatures. For this reason it is concluded that even submonolayer coverages of crotonaldehyde decrease the sticking coefficient of D_2 dramatically.

The TPRS data of the mass signal m/z = 2 (Fig. 6.32) recorded for increasing coverages of deuterium and crotonaldehyde is essentially identical to the TPRS series discussed above (Fig. 6.29). Similar desorption state maxima are assigned here, β_1 around 280 ± 10 K and β_2 close to 426 K, respectively. Even the peak areas determined by numerical integration correspond well within a small errorbar of 10%.

Turning in the present series of measurements finally to the TPRS results for m/z = 3 (Fig. 6.33), basically the same desorption states are found again compared to the data presented in Fig. 6.30. The major difference one quickly notices is the much deteriorated intensity measured here. It confirms the decrease of the sticking coefficient proposed above. In spite of huge errors in the peak area integration caused by the small signal intensities, also the peak area ratios of β_1 and β_2 seem be close to 1:1. This finding is in excellent accordance to the TPRS results of H_2 desorption in these coadsorption experiments. It agrees furthermore well with the fact that only very little D_2 desorption is observed in these TPR spectra.

From hydrogenation studies of α,β-unsaturated aldehydes like acrolein or crotonaldehyde it is already known[16] that a hydrogenation reaction often requires the reactants, especially hydrogen, to be offered at high pressures [6, 7, 8, 12, 25, 28].
The TPRS experiments performed in this thesis seem to confirm this general trend. Although one might initially have expected a formation of products on the Pt(111) surface under the coadsorption conditions in UHV, these could not be detected by TPRS. Nonetheless such a formation of adsorbed products may not be ruled out on the grounds of desorption studies. Therefore also HREELS experiments have been performed at various temperatures after coadsorption of crotonaldehyde on a D_2 precovered Pt(111) surface (Fig. 6.34).

The close comparison of the HREEL spectra recorded after coadsorption (see Fig. 6.34) and the ones of a pure crotonaldehyde adsorption (Fig. 6.23) shows hardly any changes. At 300 K only

[16] See Chap. 2.

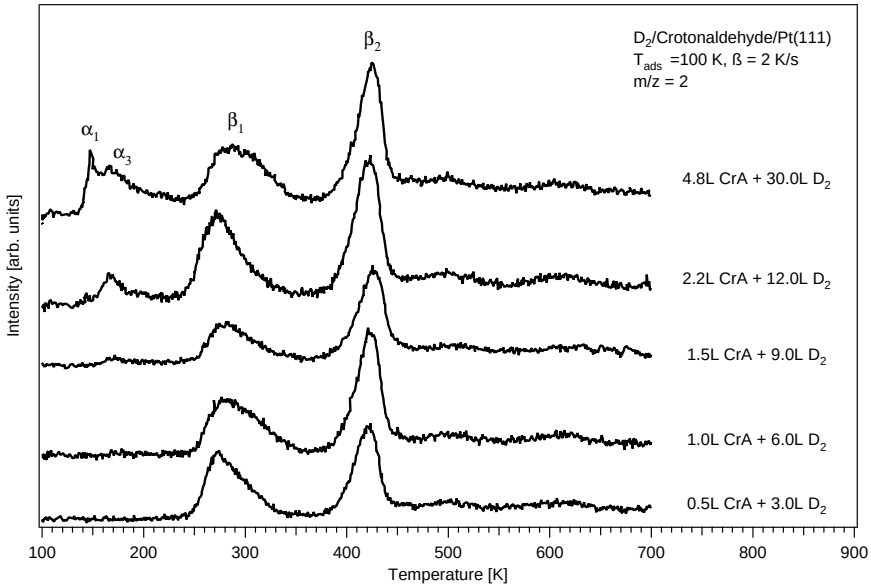

Figure 6.32: TPR spectra of D_2 adsorbed on a crotonaldehyde precovered Pt(111) surface, m/z=2.

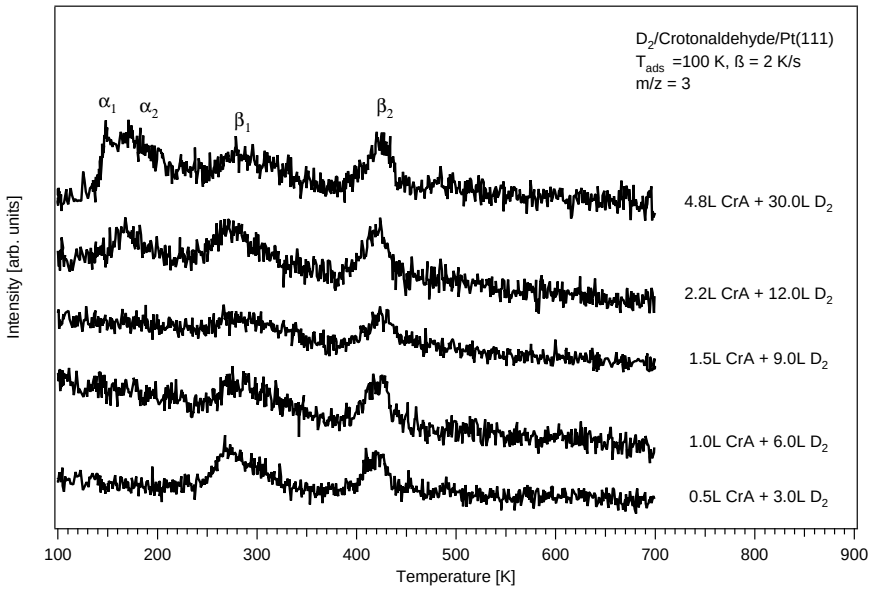

Figure 6.33: TPR spectra of D_2 adsorbed on a crotonaldehyde precovered Pt(111) surface, m/z=3.

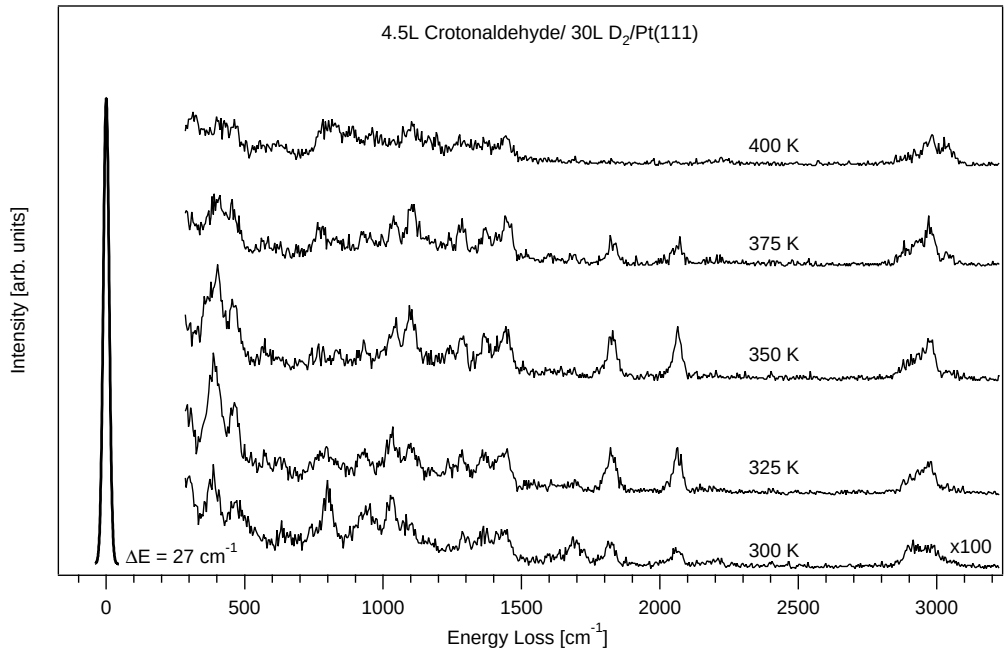

Figure 6.34: HREELS spectra recorded after subsequent annealing steps of a multilayer of crotonaldehyde coadsorbed on a D_2 precovered Pt(111) surface.

a very weak yet broad additional loss signal centered around ca 2200 cm^{-1} is measured. In fact this is very surprising taking into account the significant desorption peaks of HD measured at high temperatures in the corresponding TPRS experiments (Fig. 6.30).
Due to its low intensity and large frequency distribution of ca 50 cm^{-1} it is not clear, how many C-D vibrations it has to be attributed to. Nor can any suggestion be made towards the surface species from which these normal modes arise. The frequency of the complementary C-H vibration(s) may be estimated at ca 2970 cm^{-1} by applying an averaged isotopic shift of 1.321, which has been derived from vibrational measurements [172] on the adsorption of ethene and its perdeuterated C_2D_4 counterpart on Pd(111)[17].
From all the experiments of crotonaldehyde and deuterium coadsorption shown here hardly any clear conclusion may be drawn. Obviously there is a small fraction of either a H-D exchange or a deuteration of one of the adsorbed surface species present around 300 K. Since at this temperature the decomposition of crotonaldehyde has already begun, even the decomposition products may be involved in the deuteration.

[17]The value derived from the harmonic oscillator using the masses of H and D is precisely $\sqrt{2}$. The deviation arising from an anharmonicity is 7%. The experiments performed by Hamm [172] on Pd(111) correlate the vibrational frequencies of diσ-bonded ethene and D4-ethene. For all normal modes the according isotopic shifts are given in the latter work.

6.2 Crotonaldehyde Adsorption on $Pt_3Sn(111)$

The $Pt_3Sn(111)$ surface alloy with its p(2×2) superstructure is the first model catalyst upon which the crotonaldehyde adsorption is investigated here. With a surface fraction of 25% of Sn it may be considered as an intermediate model between pure Pt(111) and the tin richer $Pt_2Sn(111)$ surface alloy.
The electronic structure of this surface and the geometrically available adsorption sites differ from Pt(111) and one can expect new adsorption structures to be present. Since there are no longer pairs of threefold hollow sites of pure platinum neighboring each other, a site blocking effect could come into play. Various new coordination types of crotonaldehyde can be conceived, which are characterized by oxygen-tin or even carbon-tin interactions. This effectively more than doubles the possible adsorption forms that have to be considered in the analysis of this system.
As there is little known on the adsorption and interaction of crotonaldehyde with a $Pt_3Sn(111)$ surface alloy in the literature, this work presents the first results of experimental and theoretical investigations on this system.

6.2.1 TPD and TPRS results

TPD measurements performed for several precoverages of crotonaldehyde on the $Pt_3Sn(111)$ surface alloy show a qualitatively similar behavior as on Pt(111). The intensities of all mass signals is significantly reduced here in comparison to the ones on Pt(111). Obviously - and not very surprisingly - a much smaller fraction of the exposed amount of crotonaldehyde sticks on the surface alloy. Also a strong effect originating from the quality of the prepared surface alloy is recognized. The desorption peaks are affected sizably by defects like for instance remaining patches of pure Pt(111). Although the quality of the surface alloy has in every case been controlled by LEED experiments[18], it is by no means easy to obtain identical surface conditions.

The TPD results of the crotonaldehyde parental ion (m/z = 70) are presented in Fig. 6.35. Like on pure Pt(111) two low temperature desorption states are found around 145 K and 175 K (Redhead analysis: 44.8 ± 1.5 kJ/mol and 36.9 ± 1.5 kJ/mol[19]) with characteristic exponentially decreasing signal tails extending to higher temperatures. The crotonaldehyde exposure required to form a multilayer of ca 1.5L is about 30% lower than the comparable exposure on Pt(111), which indicates that the saturation coverage of the monolayer has been reduced by the alloying. From the similarity of the desorption rate maximum temperatures one might expect the low temperature behavior of crotonaldehyde to be analogous on this alloy and on Pt(111), but, as will be shown in Sec. 6.2.3, the HREELS experiments contradict this expectation.
In the light of much weaker adsorption strengths of molecules like α,β-unsaturated aldehydes on the $Pt_3Sn(111)$ surface alloy [13, 45] and the lack of any desorption traces of small hydrocarbons such as for i.e. propene in the TPD measurements, the desorption of sizable amounts of CO and H_2 at high temperatures on a Pt-Sn surface alloy seems to be a surprise. However, from TPD it is obvious that crotonaldehyde is still bonded so strongly to the surface that an intact desorption is prevented. This finding is well supported by the observation that no desorption of intact crotonaldehyde is observed at exposures below 0.4L, yet still the desorption states of CO and H_2 remain detectable. Like on Pt(111), the activation energy for the desorption process must therefore be larger than the activation for a decomposition reaction.
The TPD spectra of CO shown in Fig. 6.36 clearly exhibit relatively wide but well-defined desorption states around 350±5 K. In excellent agreement with the desorption temperature of a

[18] The size of the LEED spots is reciprocal to the realspace dimensions of the diffracting domains.
[19] Also on the $Pt_3Sn(111)$ surface alloy a frequency factor of 10^{-13} Hz was employed. The heating ramp in the TPD experiments was chosen at 2 K/s.

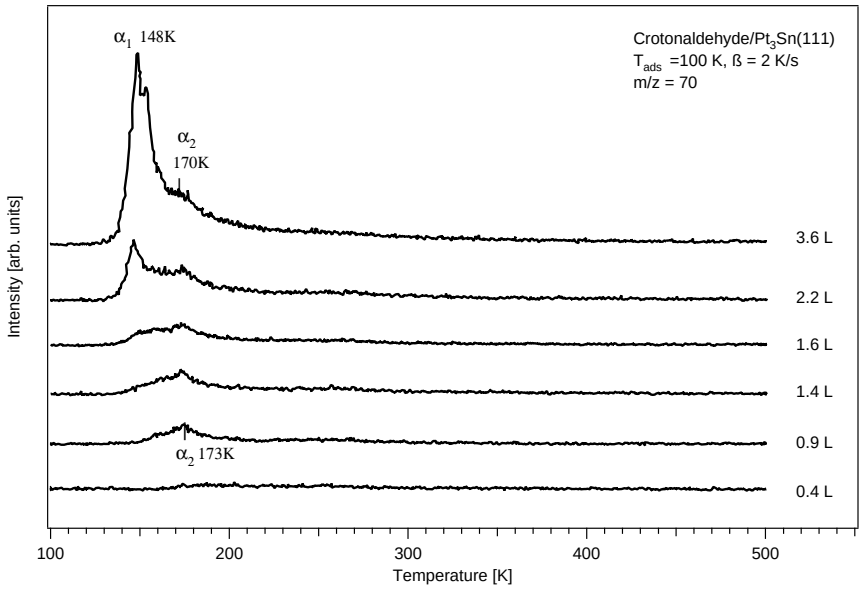

Figure 6.35: TPD spectra (m/z = 70) taken after crotonaldehyde adsorption on the $Pt_3Sn(111)$-p(2×2) surface.

saturation coverage of CO on a $Pt_3Sn(111)$ surface alloy determined by Koel and coworkers [37] (353 K), this temperature is significantly lower than the CO desorption measured in the decomposition process of crotonaldehyde on Pt(111) (380 K to 390 K). The activation barrier for the desorption determined by the Redhead method of 91.5±1.5 kJ/mol is consequently reduced by ca 10% and points to effects induced by the alloying that lead to a weakening of the CO adsorption energy on this alloy surface [37].
Although the error bar in the quantitave analysis of the CO desorption is large[20], a rough estimate of the peak areas has been made. It suggests that the amount of crotonaldehyde undergoing a decomposition, i.e. the surface coverage of irreversibly adsorbed crotonaldehyde, decreases significantly on the Pt_3Sn surface alloy and may be as low as 50-75% of the amount undergoing decomposition on Pt(111).
Concerning the associative desorption of H_2, which must accompany the decomposition process on $Pt_3Sn(111)$, only very weak signals around 340 K are detected (Fig. 6.37). They are very broad (width of ca 40 K) and undefined compared to the various desorption states of H_2 observed on Pt(111). The temperature of the desorption maximum coincides with that obtained after atomic hydrogen deposition on a clean $Pt_3Sn(111)$ surface alloy (T_{des} = 350 K at saturation coverage [37]) and indicates that this process is limited by the recombination.

In a small number of coadsorption experiments of crotonaldehyde and deuterium or hydrogen the reactivity of crotonaldehyde on the Pt-Sn surface alloys was also probed by TPRS in this thesis. Yet no observation of any crotonaldehyde reaction could be made, because the initial sticking probability of dissociative adsorption of D_2 on both Pt-Sn surface alloys is essentially zero under the actual experimental conditions [173].

[20]The TPD spectrum of 3.4L of crotonaldehyde is shown in Fig. 6.36 in order to exemplify the problem of reproducibility of the surface alloy. Yet also other TPD experiments with a better reproducibility have been recorded.

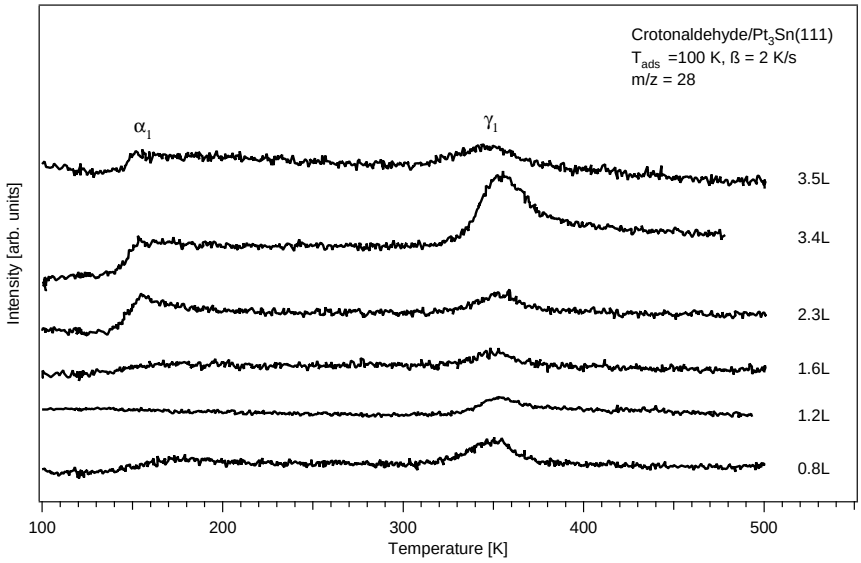

Figure 6.36: TPD spectra taken after crotonaldehyde adsorption on the $Pt_3Sn(111)$ surface, m/z=28.

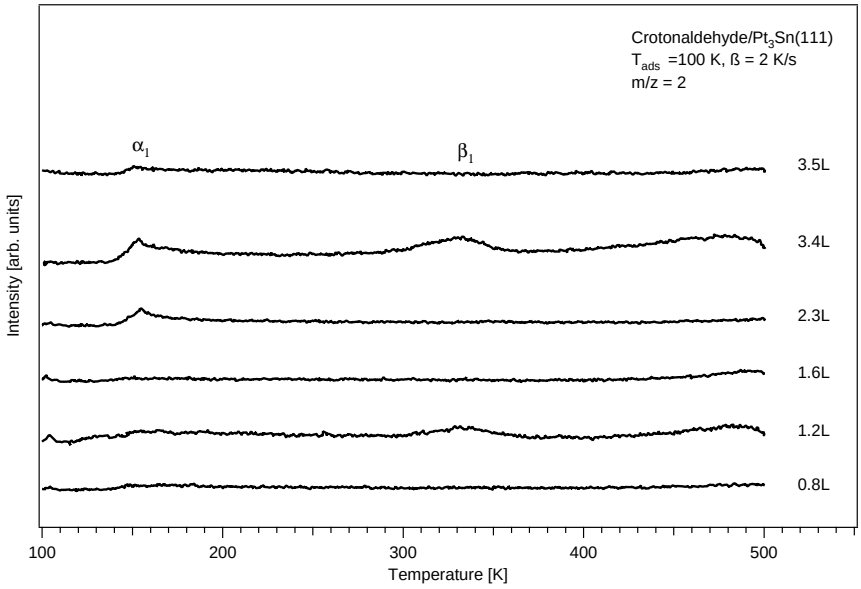

Figure 6.37: TPD spectra taken after crotonaldehyde adsorption on the $Pt_3Sn(111)$ surface, m/z=2.

6.2.2 Stable Crotonaldehyde Structures on $Pt_3Sn(111)$

The characterization of the stable adsorption structures on the $Pt_3Sn(111)$-p(2×2) surface alloy turned out to be highly complex because of the sheer number of conceivable types of coordination for each of the four rota-isomers of crotonaldehyde. The possibility to form specific oxygen-tin or carbon-tin interactions besides the "usual" bonds to platinum gives rise to various "exotic" complexes that need to be characterized for the subsequent analysis of the HREEL spectra. As will be discussed below, many types of coordination show a transition from O-Pt bonds observed on Pt(111) to more attractive O-Sn interactions. As most of the related structures interacting only with Pt do not present local minima on this surface alloy, but are still conceivable, a true "site-blocking" effect of Sn can be ruled out. Basically, there is no such effect for crotonaldehyde on either of the two surface alloys.
All calculations on $Pt_3Sn(111)$ have been carried out on a $(2\sqrt{3} \times 2\sqrt{3})$ supercell consisting of a single alloy layer of 9 Pt and 3 Sn atoms placed above a three layer platinum bulk. This model represents a low coverage of 1/12 ML of adsorbed crotonaldehyde. In general the calculations on the Pt-Sn surface alloys are considerably slower than on Pt(111). This is particularly true for Pt_3Sn due to the increased size of the supercell. Technically, the alloying with Sn leads to a sizable increase in computational demand and sometimes even creates severe problems with the convergence in the electronic minimization scheme when employing the *RMM-DIIS* algorithm. In such cases a slower, but more reliable *Davidson* algorithm had to be used instead.

The bonding distances of the most stable adsorption geometries on $Pt_3Sn(111)$ are listed in Tab. 6.21. Firstly it is seen that the adsorption energies decrease significantly for all flat structures on this surface alloy compared to Pt(111). Structures that are closely related on both surfaces like the η^2-diσ(CC) forms (see Figs. 6.39(c) and 6.39(d)) or the η^3-diσ(CC)-OPt and η^4-π(CC)-diσ(CO)-OPt complexes are destabilized on average by ca 40 to 50 kJ/mol.
The changes in the structural parameters for these complexes are rather small in contrast to the large decrease in adsorption energies. While C-C and C-H bond distances of the molecular backbone are influenced only subtly by the alloying (<1% variation), the bonding to the surface platinum atoms is affected more evidently. The Pt-C bond lengths increase only slightly between 0.02 Å and 0.04 Å[21]; the Pt-O bonds are elongated strongly by 0.08 Å to 0.12 Å.
Usually, besides the lowering of the DOS at the *Fermi* edge and the shift of the *d*-band center of gravity (see Chap. 5.3), which are suggested to lead to an decrease of the overlap and the bond strengths [39, 45, 132], also the transfer of electron density from Sn to Pt (0.10 e^-) determined by Delbecq et al. [45] is referred to in the literature to explain the weakening of the adsorption energies. The unsaturated molecules such as alkenes are mainly electron donors and their interaction strength with the surface is easily influenced by charge transfers. The electron-enrichment of the Pt atoms on the surface alloy leads therefore to a weakening of the bonds, which is considered as increased *Pauli* repulsion of the π-electrons of the adsorbate and the *d*-electrons of the platinum [45].
Generally the adsorption energy consists of three contributions, which can be elucidated by "separating" the molecule-surface complex into its components: The distortion energies of the molecule and the surface as well as the interaction term between both. For this task the supercell with the optimized adsorption complex is decomposed into the adsorption induced deformed surface and the correspondingly distorted molecule. The differences of the total free energies of the components with the ones of the gas phase and free surface structures, respectively, give the deformation energy costs (Fig. 6.38), which include both geometric effects as well as changes in the electronic configurations of the components. Much like the energy conservation principle leading to *Hess*' law in thermodynamics, the interaction energy is finally deduced from the specific constituents and the adsorption energy of the complex [174]. As long as no extensive

[21] Only r(C2-Pt) of the η^3-Z-(s)-cis-diσ(CC)-OPt complex is elongated by a larger value of 0.06 Å.

Adsorption energies [kJ/mol]	E-(s)-trans	E-(s)-cis	Z-(s)-trans	Z-(s)-cis
η^1-top-OPt	unstable	unstable	unstable	unstable
η^1-top-OSn	-33.2	-8.9	-10.5	-11.8
η^1-top-OSn(2)	-30.8	excluded	excluded	excluded
η^2-diσ(CO)-OPt	unstable	unstable	unstable	unstable
η^2-diσ(CO)-OSn	excluded	excluded	excluded	excluded
η^2-diσ(CC)	-32.9	-34.0	-19.7	-25.6
η^2-π(CC)	-2.1	-5.7	-10.3	unstable
η^2-diσ(C3,O)-OSn	unstable	unstable	unstable	unstable
η^3-diσ(CC)-OPt	unstable	-25.5	unstable	-17.4
η^3-diσ(CC)-OSn	unstable	-51.2	unstable	-47.8
η^3-π(CC)-OPt	unstable	unstable	unstable	unstable
η^3-π(CC)-OSn	unstable	unstable	unstable	unstable
η^4-diσ(CC)-diσ(CO)-OSn	-37.9	unstable	-29.9	unstable
η^4-π(CC)-diσ(CO)-OSn	-22.7	-41.7	-19.6	-26.1
η^4-diσ(CC)-diσ(CO)-OPt	unstable	unstable	unstable	unstable
η^4-π(CC)-diσ(CO)-OPt	unstable	-14.0	unstable	unstable

Table 6.21: Calculated adsorption energies of crotonaldehyde on $Pt_3Sn(111)$-p(2×2) at a theoretical coverage of $\Theta = 1/12$. Note that some structures such as the η^2-diσ(CO)-OSn coordination type were not considered due to its presumably low adsorption strength [45] or geometrical constraints. Furthermore different types of η^4 structures including π(CO) interactions turned out to be unstable.

charge transfer between the molecule and the surface occurs, or if the charge transfer is rather homogeneous for the compared adsorption structures[22], this concept is reasonable.

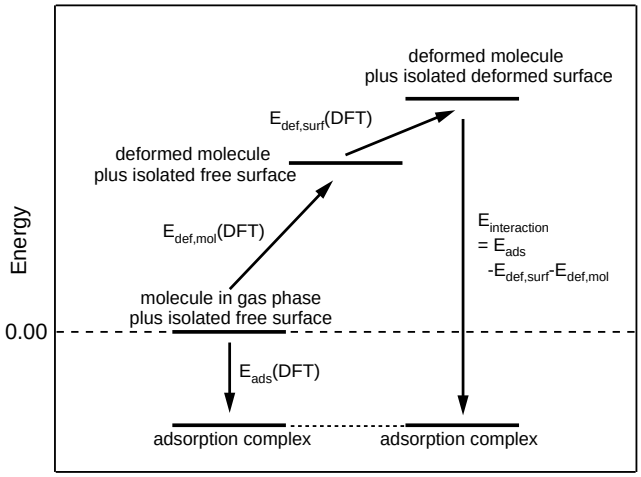

Figure 6.38: Schematic representation of the separation of the contributions to the adsorption energy analoguous to *Hess* law (for the explanation of all terms consider the text).

In fact it is found for the η^2-E-(s)-trans structure on Pt(111) and the surface alloy with this approach that the energy cost of deforming the molecule from the gas phase geometry is high and roughly homogeneous (144 kJ/mol on Pt(111) and 149 kJ/mol on Pt_3Sn). A small variation is seen in the distortion energy of the surfaces, which is somewhat softer for Pt_3Sn (41 kJ/mol) versus Pt(111) (53 kJ/mol). As the platinum atoms involved in the two σ-type bonds are lifted up much further on the surface alloy by ca 0.31 Å than on Pt(111) (ca 0.17 Å), it is evident that the alloying with Sn creates a much "softer" surface. In contrast to the large buckling induced by the interaction of the molecule, the displacement of the Pt atoms parallel to the surface plane are quite small with generally less than 0.05 Å on Pt(111) as well as on Pt_3Sn. Distortions like the ones found in this case have also been calculated previously for acrolein on Pt-Sn surfaces by Delbecq et al. [45], who correctly correlate the displacements with the changes in the coordination sphere of the surface atoms. Basically, each surface atom only tries to obey the bond order conservation principle. The major impact on the adsorption energies remaining now is governed by the interaction term, i.e. the electronic stabilization of the system upon interaction of both components. This term is significantly larger on Pt(111) with -273 kJ/mol than on Pt_3Sn with -222 kJ/mol, confirming that the decrease in adsorption energies is - as usually expected - determined primarily by the electronic effect of a much weaker bonding on the alloy surface.

Switching from adsorption complexes adsorbing on Pt atoms only to potential candidates including a bond to Sn, it is immediately found that C-Sn interactions are highly repulsive. Any initial geometry conceived with a C-Sn bond evolved into another optimized structure evading this unfavorable bonding situation.

In contrast, oxygen-tin bonds are found to be very attractive and lead to the most stable adsorption structures on $Pt_3Sn(111)$: The η^3-diσ(CC)-OSn coordination type realized for the E-(s)-cis (-51.2 kJ/mol, Fig. 6.39(e)) and Z-(s)-cis (-47.8 kJ/mol, Fig. 6.39(f)) rota-isomers. The bond lengths of theses complexes hardly differ from the structural parameters of their pure η^3-diσ(CC)-OPt counterparts. Especially the computed r(O-Sn) distances correspond closely within less than 0.04 Å. Compared to the r(O-Pt) values on pure Pt(111) of about 2.20 Å, the longer r(O-Sn) bond distances of ca 2.36 Å on the alloy surface coincide qualitatively with the increase in the *Van der Waals* radius from 1.75 Å for Pt to 2.17 Å for Sn [129]. Despite the small

[22] Methods using localized orbitals would allow to study the polarization and electron transfer effects using the *constrained space orbital variation* (CSOV) method [175]. In the periodic approach the electron transfer might be determined by projections of the orbitals on the MO's of prenal, but systematical and numerical problems are significant in this case. It is expected to be small and homogeneous for all considered adsorption structures.

deviations of the molecule-surface bond lengths, crotonaldehyde induces very different outward relaxations of the surface atoms like already observed for the η^4 modes[23].

At first glance it seems that the relatively large adsorption energies of these surface species may be ascribed to the highly oxophilic character of Sn. Yet as will be proven in the next section, the interaction strength of the O-Sn bond contributes only very little to the stability of this type of coordination.

For the η^1-top and η^4 coordination types it is also necessary to form an O-Sn bond in order to realize stable structures with sufficient adsorption energies. Several of the η^4 forms that represent very stable structures on pure Pt(111) are no longer stable on the $Pt_3Sn(111)$ surface alloy. Only the η^4-diσ(CC)-diσ(CO)-OSn and η^4-π(CC)-diσ(CO)-OSn forms (Figs. 6.40(a) to 6.40(c)) exhibit a sizable stability around -40 kJ/mol for the E and -25 kJ/mol for the corresponding Z isomer. Structurally they bear a close resemblance to the related adsorption complexes on pure Pt(111). Except for r(O-Sn), which is elongated similarly to bonds obtained in the η^3 coordination type by ca 0.08 Å, the bond lengths vary less than 1%. The surface deformations obtained for the η^4 forms are interesting in the sense that these geometries lead to a lowering of neighboring, non-bonded Sn atoms towards the bulk. This new phenomenon, which is not found for the related structures on Pt(111), originates from the sterical repulsion between the protruding Sn atoms and the methyl substituent on the vinylic bond. Caused by the attractive interactions of crotonaldehyde to the surface the covalently interacting Pt and Sn atoms are lifted up sizably on both surfaces. For the two η^4-diσ(CC) coordination types, the Pt atoms below C3 are relaxed outward by 0.18 on Pt(111) and 0.26 Å on $Pt_3Sn(111)$. The atoms below C2, C1 and O are shifted outward by consistently 0.08 Å on Pt(111) and even by 0.19, 0.14 and 0.13 Å on the surface alloy. Slight differences due to the change of coordination to π(CC) are found for the other η^4 structures, which show outward relaxations of 0.35, 0.20 and 0.10 Å for the atoms interacting with C3/C2, C1 and O on $Pt_3Sn(111)$ (0.22, 0.11 and 0.06 Å on Pt(111)). Since, generally, the buckling of the substrate atoms is more pronounced for the corresponding adsorption modes on this surface alloy, the induction of outward relaxation of the Pt (and Sn) atoms by the molecule seems to be easier here. This points towards a generally lower "surface modulus" of the Pt_3Sn surface, a finding that will be discussed in more detail in the following sections.

Unlike the new η^1-top-OSn adsorption species, the entire original η^1-top-OPt forms turned out to be unstable on the surface alloy and "desorbed" during the optimizations. They are basically replaced by analogous structures on a Sn top site, which in terms of adsorption strength and bond length come up with another little surprise. At first glance they seem to be interacting stronger with the surface atom than their counterparts on pure Pt(111).

Particularly two related η^1-top-E-(s)-trans-OSn adsorption complexes are obtained that differ only in the orientation of their molecular axis towards the surface (Figs. 6.39(a) and 6.39(b)). Although both adsorption complexes are sizably bonded with adsorption energies of around -30 kJ/mol (i.e. ca 10 kJ/mol greater stability than on Pt(111)), one finds their O-Sn bonds severely elongated by nearly 0.3 Å to 2.49 Å and 2.54 Å, respectively.

These contradicting result may be understood from the different electronic properties of the component tin in the surface alloys. Here the separation of the adsorption energy into the constituting terms points to a weak chemisorption or even physisorption of crotonaldehyde on the surface alloy in contrast to a sizable chemisorption on Pt(111). The cost for the distortion of the molecule is negligible for both systems (below 7 kJ/mol), whereas the major influence here arises from the surface distortion energy: It is essentially zero on $Pt_3Sn(111)$, but 38 kJ/mol on Pt(111)[24]. Consequently the interaction term on Pt(111) must be much larger on Pt(111) than

[23]The outward relaxation of the Pt atoms below C3/C2 is 0.17/0.16 Å on Pt(111) and 0.30/0.26 Å on the surface alloy. The effect of the O-metall interactions is very small, leading to a protrusion of 0.05 Å for Pt and 0.09 Å for Sn.

[24]Interestingly, the outward shift of the bonding surface atom is around 0.07 Å on Pt(111), but with ca 0.12 Å

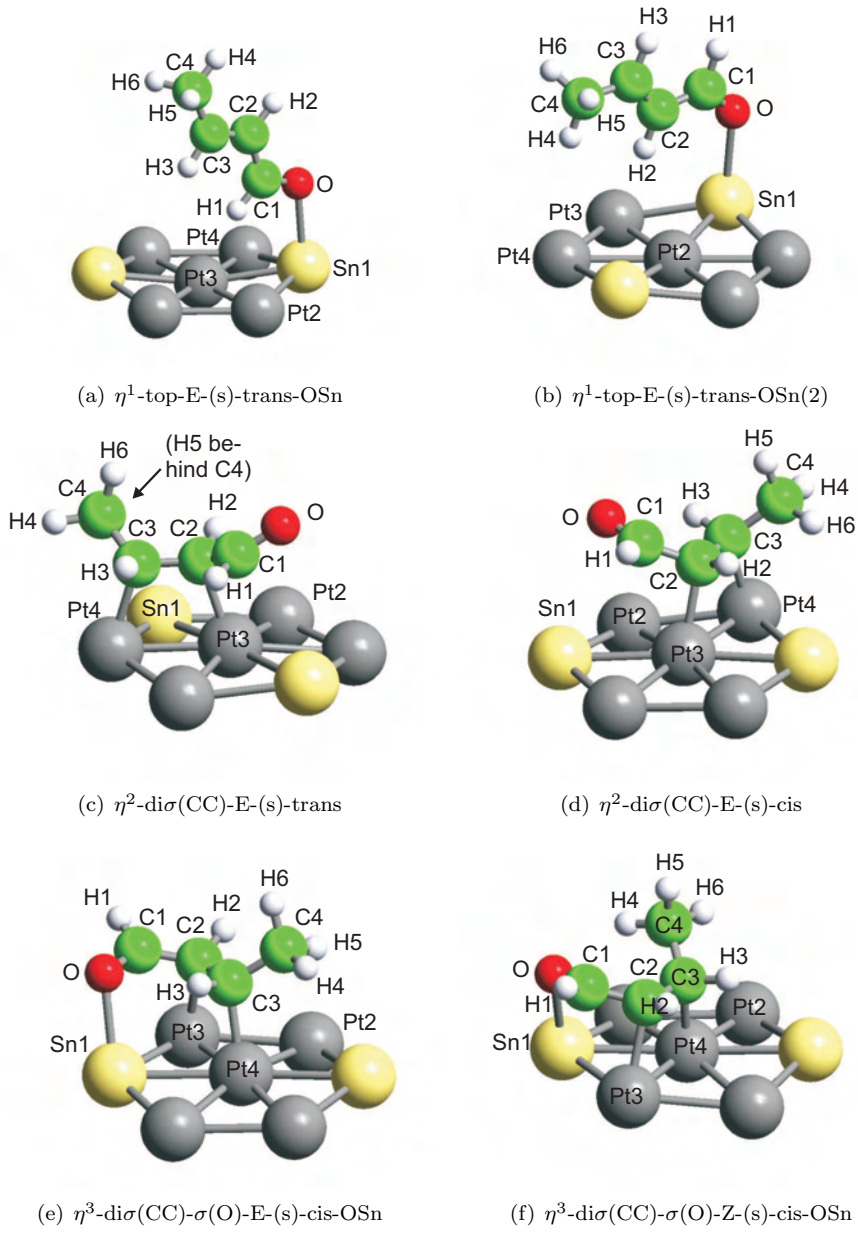

(a) η^1-top-E-(s)-trans-OSn

(b) η^1-top-E-(s)-trans-OSn(2)

(c) η^2-diσ(CC)-E-(s)-trans

(d) η^2-diσ(CC)-E-(s)-cis

(e) η^3-diσ(CC)-σ(O)-E-(s)-cis-OSn

(f) η^3-diσ(CC)-σ(O)-Z-(s)-cis-OSn

Figure 6.39: Optimized adsorption geometries of the most stable η^2 and η^3 structures of crotonaldehyde on $Pt_3Sn(111)$.

on $Pt_3Sn(111)$, which is indeed found: the molecule-surface interaction stabilizes the system by -69 kJ/mol on pure Pt(111) and by only -37 kJ/mol on the surface alloy.
This analysis, furthermore, explains the trend of a relative stabilization of the η^1-top forms compared to the η^2-diσ(CC) structures on the surface alloy. It is now easily understood from the energy balances that the huge cost of deforming the molecule upon adsorption has to be overcompensated by the interaction term in order to obtain a sizable adsorption energy. This

larger for Sn on the surface alloy.

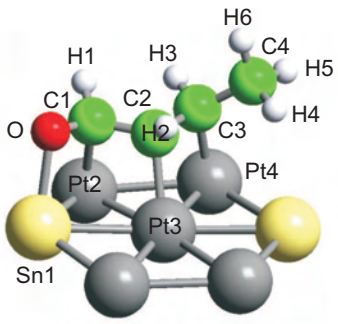

(a) η^4-diσ(CC)-diσ(CO)-E-(s)-trans-OSn

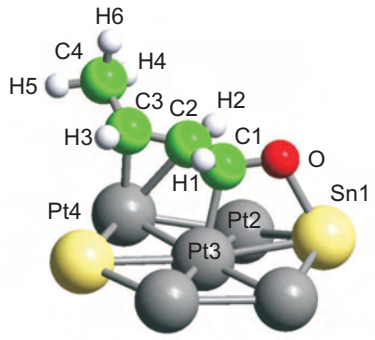

(b) η^4-π(CC)-diσ(CO)-E-(s)-trans-OSn

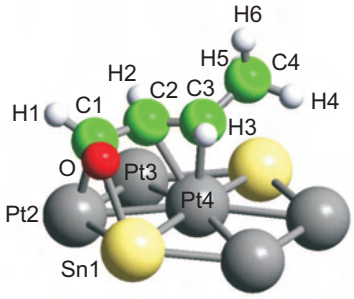

(c) η^4-π(CC)-diσ(CO)-E-(s)-cis-OSn

Figure 6.40: Optimized adsorption geometries of the most stable η^4 structures of crotonaldehyde on $Pt_3Sn(111)$.

is the case for the η^2 structures on Pt(111), but on the surface alloy the smaller interaction strength leads to a lowering of their adsorption energy. At the same time the energy balance of the η^1 complex on Pt(111) accounts only for a small adsorption energy due to the large distortion cost of the surface. On the other hand the analogous η^1 coordination geometries adsorbed on Sn exhibit just a negligible surface rearrangement and thus even the much smaller interaction energies of these structures are already sufficient to generate a competetive adsorption energy. Obviously any simple correlation between the adsorption energies and the interaction strength on different surfaces, which is normally valid for small molecules like for i.e. mono-alkenes, fails badly for complex multifunctional molecules. As a major result of this thesis it is concluded that the interplay between the adsorption-induced distortion of the adsorbate and the surface with the actual interaction strength is more complicated than a simple picture may represent. The adsorption energies are found to be no clear indicator of the interaction strength of a molecule. A counter-example may be given for instance by the case of a strongly interacting species, which due to a huge distortion cost of an adsorption complex is adsorbed only weakly (small E_{ads}). On another surface, where the deformation energies of the surface and the molecule are much smaller, a related species showing the same interaction strength may exhibit a comparably large adsorption energy E_{ads}. This example corresponds nicely to the case of the η^1-top configurations on Pt(111) and $Pt_3Sn(111)$.

Geometry	η^1-top-E-(s)-trans-OSn	η^1-top-E-(s)-trans-OSn(2)	η^2-diσ(CC)-E-(s)-trans	η^2-diσ(CC)-E-(s)-cis	η^3-diσ(CC)-σ(O)-E-(s)-cis-OSn	η^3-diσ(CC)-σ(O)-Z-(s)-cis-OSn
r(O-C1)	1.24	1.24	1.23	1.23	1.27	1.27
r(C1-C2)	1.44	1.44	1.49	1.48	1.44	1.44
r(C2-C3)	1.35	1.35	1.50	1.49	1.49	1.50
r(C3-C4)	1.48	1.48	1.52	1.52	1.52	1.52
r(C1-H1)	1.12	1.11	1.12	1.12	1.10	1.11
r(C2-H2)	1.09	1.10	1.10	1.10	1.09	1.10
r(C3-H3)	1.10	1.10	1.10	1.10	1.10	1.10
r(C4-H4)	1.10	1.10	1.10	1.10	1.10	1.09
r(C4-H5)	1.11	1.10	1.10	1.10	1.10	1.10
r(C4-H6)	1.11	1.10	1.10	1.11	1.10	1.11
r(O-M)	2.49	2.54	-	-	2.37	2.36
r(C1-M)	-	-	-	-	-	-
r(C2-M)	-	-	2.16	2.17	2.23	2.24
r(C3-M)	-	-	2.15	2.15	2.14	2.13

Table 6.22: Bond distances of the most stable η^2 and η^3 adsorption geometries of crotonaldehyde on $Pt_3Sn(111)$-p(2×2). All distances r are given in Å.

Geometry	η^3-diσ(CC)-E-(s)-cis-OPt	η^3-diσ(CC)-Z-(s)-cis-OPt	η^4-diσ(CC)-diσ(CO)-E-(s)-trans-OSn	η^4-π(CC)-diσ(CO)-E-(s)-trans-OSn	η^4-π(CC)-diσ(CO)-E-(s)-cis-OSn
r(O-C1)	1.27	1.27	1.33	1.35	1.34
r(C1-C2)	1.45	1.44	1.49	1.47	1.47
r(C2-C3)	1.50	1.51	1.49	1.43	1.42
r(C3-C4)	1.52	1.52	1.52	1.51	1.50
r(C1-H1)	1.11	1.09	1.11	1.11	1.10
r(C2-H2)	1.10	1.10	1.10	1.10	1.09
r(C3-H3)	1.10	1.10	1.10	1.10	1.09
r(C4-H4)	1.11	1.10	1.10	1.10	1.10
r(C4-H5)	1.10	1.10	1.10	1.10	1.10
r(C4-H6)	1.11	1.11	1.10	1.10	1.10
r(O-M)	2.36	2.32	2.20	2.20	2.20
r(C1-M)	-	-	2.26	2.20	2.23
r(C2-M)	2.21	2.21	2.20	2.41	2.31
r(C3-M)	2.12	2.12	2.14	2.18	2.21

Table 6.23: Bond length of the η^3-diσ(CC)-OPt adsorption geometries and the most stable η^4 forms of crotonaldehyde on $Pt_3Sn(111)$ (distances r in Å).

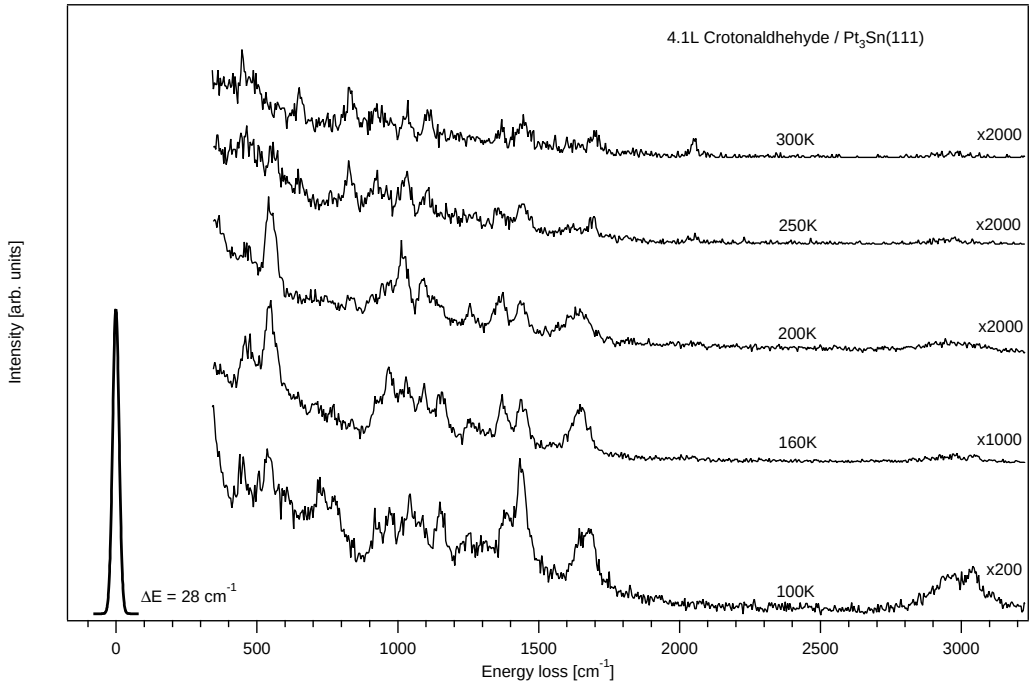

Figure 6.41: HREELS of 4.1L crotonaldehyde/$Pt_3Sn(111)$, 100-300 K. The HREEL spectra have been recorded in specular geometry at an angle of incidence of 60° (primary energy of 4.7 eV).

6.2.3 HREELS Experiments

The HREELS experiments of crotonaldehyde on the $Pt_3Sn(111)$-p(2×2) surface show characteristic changes compared to the multilayer spectrum. An exemplary temperature dependent HREELS series starting with a multilayer adsorption (4.1L) of the aldehyde at 100 K is presented in Fig. 6.41. Like the spectra on Pt(111) it is recorded in the specular geometry at an angle of incidence of 60° with a primary energy of 4.7 eV.

Clearly the HREEL spectrum recorded just after the adsorption at 100 K can be identifed as a multilayer. The vibrational fingerprint of the multilayers measured for high exposures of crotonaldehyde on Pt(111) (Sec. 6.1.4) match this spectrum quite well. Small disagreements in the intensities may point to a slightly changed environment of the physisorbed molecules, i.e. on top of a chemisorbed first layer.

After annealing the sample quickly to 160 K the multilayer is desorbed. The HREELS data measured at this stage are easily distinguished from previous multilayer spectra by a strong increase in the relative intensities of the loss signals at 475 cm^{-1}, 552 cm^{-1}, 975 cm^{-1} and 1374 cm^{-1}. Hence it can be expected that the characteristics of this spectrum, which will be discussed further in following paragraphs, may be ascribed to specific, chemisorbed crotonaldehyde species. Aside from annealing a high precoverage of crotonaldehyde, this spectroscopic fingerprint is also obtained from low exposures such as 0.6L crotonaldehyde at 100 K (not depicted). Upon annealing to 160 K the latter spectrum was found to be unaltered, but at 200 K strong changes similar to those in the 4.1L spectrum at this temperature occurred.
Despite the similarity of the low temperature TPD peaks on $Pt_3Sn(111)$ and Pt(111), the

first significant differences between the adsorption behavior of crotonaldehyde on both surfaces become obvious here. The HREELS data on the surface alloy exhibit a number of discrepancies in peak positions and relative intensities as opposed to the experiments of crotonaldehyde on Pt(111) at 169 K. Indeed many features measured here can also be observed in the problematic spectrum on pure platinum, but are shifted by roughly 10 cm^{-1} like, for instance, the losses at 475 cm^{-1}, 552 cm^{-1} and 725 cm^{-1}. They are found at 467 cm^{-1}, 544 cm^{-1} and 715 cm^{-1} on Pt(111) respectively. Furthermore, because these peaks and, in addition, the loss signals at 781 cm^{-1} (Pt: 780 cm^{-1}) and 1374 cm^{-1} (Pt: 1379 cm^{-1}) have gained intensity and seem to be more prominent here, it is justified to consider the low temperature adsorption properties of crotonaldehyde on the $Pt_3Sn(111)$ surface alloy to differ from its behavior on Pt(111).

The analysis of the experimental spectrum with the computed HREEL spectra of the local minima structures from DFT gives rise to the conclusion that the adsorbed layer is composed of four components, two of which are predominant. The other two components of the mixed phase are present as minority species (together ca 30%). The confrontation of the experimental spectrum and the computed vibrational data is presented in Fig. 6.42.

The dominant surface species are the η^2-diσ(CC)-E-(s)-trans (Tab. 6.25) and η^2-diσ(CC)-E-(s)-cis (Tab. 6.26) adsorption geometries. Already on Pt(111) it was shown that this coordination type belongs to the group of strongly adsorbed structures and can be identified in the vibrational spectra. The presence of η^2-diσ(CC) coordinated species is evidenced by the experimental signals at 1652 cm^{-1} and 975 cm^{-1}. Both signals are constituted by normal modes of the E-(s)-trans and E-(s)-cis rota-isomers that are very close in frequency.

Concerning the remaining vibrational losses, the assignment on $Pt_3Sn(111)$ is nearly identical to Pt(111) and only small shifts of ca 10 cm^{-1} are observed in both the measurements and the calculations.

More important insights are obtained from the measured signal at 1261 cm^{-1} , which gains a fraction of its intensity from the asymmetrically coupled δ_{as}(C2H2-C3H3) vibrations, which are computed around 1245 cm^{-1}. The intensity of this experimental signal extending to higher wavenumbers cannot be explained by the η^2-diσ(CC) forms and will have to be accounted for by another surface complex.

Also the measured peak at 1156 cm^{-1} cannot be explained satisfactorily by the vibrations of the η^2-diσ(CC) forms. Quite close are the ν(C2=C3) stretching modes computed at 1124 cm^{-1} for the E-(s)-trans and at 1128 cm^{-1} for the E-(s)-cis isomers, but these are weak and even shifted slighty so that other adsorption structures must be expected to contribute to the computed intensity. The ν(C3-C4) vibrations of the methyl substituents are detected around 1100 cm^{-1} with somewhat larger intensity. They are computed at 1077 cm^{-1} and 1083 cm^{-1} for the two η^2 structures.

An interesting phenomenon is found for the corresponding ν(C1-C2) modes here. While the vibration of the η^2-diσ(CC)-E-(s)-trans structure is calculated basically inactive at 1039 cm^{-1}, the analogous normal mode of the η^2-diσ(CC)-E-(s)-cis structure is intense at 1003 cm^{-1} and thus contributes to the measured signal at 1035 cm^{-1}. Due to a different coupling of the normal modes, it is the γ"(CH_3) of the E-(s)-trans form that is very intense at 999 cm^{-1}. For the E-(s)-cis form it is found with medium intensity at 932 cm^{-1}.

The experimental loss signals around 975 cm^{-1} and 926 cm^{-1} can be assigned to a whole set of out-of-plane γ deformation modes of the vinylic, the aldehydic and the methyl hydrogens. Since the normal modes corresponding to the sizably intense peak at 926 cm^{-1} are computed to be weak, the necessity for the presence of another surface species is recognized again.

In the lower frequency region, very characteristic and dominant loss signals at 552 cm^{-1} and 475 cm^{-1} can be traced back specifically to the η^2-diσ(CC) coordinated species, too. For the leading contributions of the normal modes assigned to these loss peaks, namely the ν_{as}(PtC2-PtC3) vibration of the E-(s)-trans complex computed at 524 cm^{-1} and the ν_{as}(PtC2-PtC3) mode (548 cm^{-1}) and its symmetric counterpart ν_s(PtC2-PtC3) (452 cm^{-1}) of the E-(s)-form,

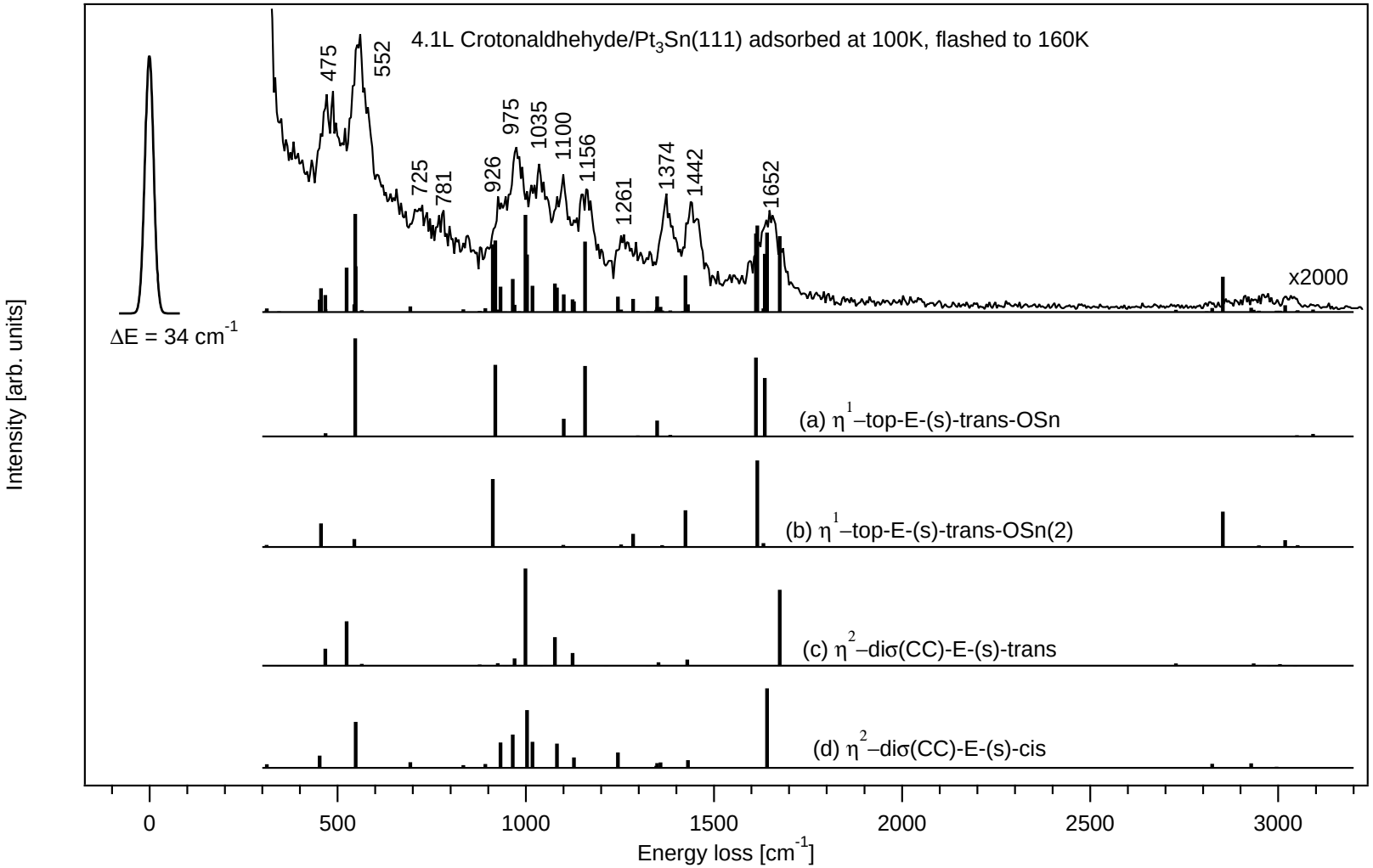

Figure 6.42: Comparison of the computed DFT HREEL spectra for the most stable adsorption structures with the experimental spectrum of 4.1L crotonaldehyde on a $Pt_3Sn(111)$ surface alloy annealed to 160 K after adsorption at 100 K.

the destabilization of the adsorption energies does not manifest itself in significant shifts.
Finally an intense and broad peak measured around 256 cm^{-1} may be assigned to a combination of the δ(C1-C2=C3) deformation and the τ(C1-C2) torsion vibration of the molecular backbone of the E-(s)-cis structure obtained in the DFT analysis at 253 cm^{-1} with large intensities; the E-(s)-trans form does not exhibit any similar loss signal here.
In general the frequencies of the carbon-carbon stretching modes ν(CC) are computed with small blueshifts of 8 to 25 cm^{-1} from the values found on Pt(111). The low frequency modes, especially the ν_{as}(PtC2-PtC3) and the ν_s(PtC2-PtC3) vibrations, which are expected to be more sensitive to variations of the molecule-interaction, are shifted only slightly by about 10 cm^{-1}. This phenomenon is very surprising in the light of the much weaker adsorption energies computed at the same time, but a probable reason can be given from the decomposition of the adsorption energies.
Judged from the similarity of frequencies, the shapes of the vibrational potential wells seem to be comparable and the harmonic levels do not vary significantly. This is consistent with the small change of the bond lengths and allows to conclude that the potential hyperplane is primarily just shifted by a constant value corresponding to the decrease of the adsorption energy. By a decomposition of the adsorption energy into its three distinct parts, the molecule-surface interaction, the distortion energy of the molecule and the distortion cost of the surface, one obtains three physical contributions, which must be correlated with the frequency changes in specific types of normal modes.
Since the molecule distortions on both surfaces are nearly equal (ca 149 and 154 kJ/mol for trans and cis, respectively; see Tab. 6.24) for the two η^2 structures, it is not very surprising that the alloying does not affect the fingerprint modes of the molecule itself noticeably and, thus, the small frequency shifts are confirmed. In contrast, both the surface distortion and the interaction energies are decreased on the $Pt_3Sn(111)$ surface alloy (41/-222 and 40/-228 vs. 53/-273 kJ/mol for Pt(111)). Although this finding might motivate the expectation of more pronounced variations in the molecule-surface stretching region as well as for the surface phonons, the computed shifts of the symmetric and the asymmetric ν(PtC2-PtC3) stretching vibrations remain quite small.

Turning to the experimental loss peaks at 1652 cm^{-1}, 1374 cm^{-1}, 1156 cm^{-1} and 926 cm^{-1}, which cannot be explained satisfactorily with the fingerprints of the two η^2-diσ(CC) structures, additional contributions of at least one more adsorption mode have to be included.
From the theoretical vibrational spectra it is evident that the structures of higher haptic-ity, namely the η^3 configurations representing the most stable structures at a low coverage of 1/12 ML, are not compatible with the experiment at 160 K. The phenomenon of a hapticity change with surface coverage is not unknown. Already Loffreda and coworkers [53] were able to show in similar studies on the adsorption of acrolein on Pt(111) that the adsorption energies of α,β-unsaturated aldehydes can depend strongly on the surface coverage. For the latter system, the high coverage regime (ca 1/4 ML) is dominated by low-coordinated η^2-diσ(CC) structures, while towards smaller coverages a transition to the η^3 and η^4 geometries occurs.
Because the system crotonaldehyde/$Pt_2Sn(111)$ behaves very similar to the adsorption on $Pt_3Sn(111)$, the coverage dependence of the adsorption energies and vibrational data has been investigated prototypically in the first case (see Chap. 6.3). Nonetheless in contrast to the ad-sorption energies the spectroscopic fingerprints of the various structures depend only weakly on the chosen coverage and can therefore be employed for the analysis of both low as well as high coverage situations.
The analysis of the remaining candidates finally leads to the vertical adsorption complexes of the η^1-top-E-(s)-trans-OSn coordination type, bonded to a Sn atom by the aldehydic oxygen, which not only show a very good agreement with the overall fingerprint discussed so far, but furthermore allows to understand the missing intensities in the problematic cases.

Adsorption mode	adsorption energy	surface deformation	molecule deformation	interaction term
Pt(111)				
η^1-top-(s)-E-trans	-23.5	38	7	-69
η^2-π(CC)-E-(s)-trans	-44.4	61	47	-153
η^2-diσ(CC)-E-(s)-trans	-76.0	53	144	-273
η^2-diσ(CC)-E-(s)-cis	-73.6	52	141	-266
η^3-diσ(CC)-σ(O)-E-(s)-cis	-76.9	53	136	-266
η^4-diσ(CC)-diσ(CO)-E-(s)-trans	-80.2	52	211	-342
η^4-π(CC)-diσ(CO)-E-(s)-cis	-68.7	59	106	-233
Pt_3Sn(111)				
η^1-top-E-(s)-trans-OSn	-33.2	2	2	-37
η^2-diσ(CC)-E-(s)-trans	-32.9	41	149	-222
η^2-diσ(CC)-E-(s)-cis	-34.0	40	154	-228
η^3-diσ(CC)-σ(O)-E-(s)-cis-OSn	-51.2	35	144	-230
η^4-π(CC)-diσ(CO)-E-(s)-cis-OSn	-41.7	37	110	-189

Table 6.24: Decomposition of the adsorption energies of crotonaldehyde on Pt(111) (Θ = 1/9 ML) and Pt_3Sn(111) (Θ = 1/12 ML) into the energy costs for deforming the surface and the molecule and the energy gain of the interaction in the optimized surface complex. All energy contributions are given in kJ/mol.

The analogous structures on Pt(111) have not been competitive in terms of adsorption energies, but on Pt_3Sn(111) the η^1-top-E-(s)-trans-OSn and its more horizontally aligned relative, the η^1-top-E-(s)-trans-OSn(2) geometry, are computed to be adsorbed as strongly as the already identified η^2-diσ(CC) structures. Hence these two adsorption complexes contribute to the HREEL spectrum recorded at 160 K.

At 256 cm^{-1} and 238 cm^{-1} the δ(C1-C2=C3) normal modes computed of the two η^1-top-E-(s)-trans-OSn structures (Tabs. 6.27 and 6.28) amplify the large intensity already obtained from η^2-diσ(CC)-E-(s)-cis and help to explain the unusual width of the band detected at 256 cm^{-1}. However, due to their high loss intensity in this frequency region only a small fraction of η^1 would already lead to the dominant signal observed here. Just below these frequencies, namely at 127 cm^{-1} and 110 cm^{-1} the ν(Pt-O) stretching modes are obtained for both structures. The latter normal modes found at 107 cm^{-1} on Pt(111) are slightly blueshifted.

Also the shoulder at 926 cm^{-1} can be explained by the γ'(CH_3) vibrations of both η^1 forms calculated with medium loss intensity at 919 cm^{-1} and 912 cm^{-1}. Again a small fraction (around 20-30%) of these geometries in the mixed surface phase would lead to a sufficient augmentation of the intensity to account for the experimental loss signal.

A clear indicator of the presence of the more vertically oriented η^1-top-E-(s)-trans-OSn adsorption complex is given by the computed ν(C1-C2) stretching mode at 1157 cm^{-1}, which nearly exactly matches the experimental loss peak at 1156 cm^{-1}. Without inclusion of this η^1 complex, this signal is barely explainable.

Furthermore the loss signals detected at 1374 cm^{-1} and 1442 cm^{-1}, which are represented only weakly by the η^2 structures, are augmented favorably by the u(CH_3) and δ'(CH_3) deformation modes of the vertical and the horizontal η^1 geometries. Though they are calculated at somewhat lower frequencies of 1350 cm^{-1} and 1424 cm^{-1} respectively, they improve the overall fit of the loss intensities.

In the characteristic double bond stretching region the ν(C2=C3) and the ν(C1=O) stretching frequencies uncover another surprising result. For both η^1 adsorption geometries the ν(C1=O)

vibrations are obtained essentially at identical values of 1611 cm^{-1} and 1615 cm^{-1} ; likewise also the ν(C2=C3) modes nearly coincide at 1635 cm^{-1} and 1632 cm^{-1}. The computed normal modes thus agree well with the loss at 1652 cm^{-1}, which exhibits the width of the corresponding signal at 200 K on Pt(111), but is evidently more intense and defined. While the width was explained previously on Pt(111) as a consequence of the disordering and random orientation, here it may in addition be understood simply from the variety of vibrations of the η^2 and η^1 that are assigned within this frequency window. Only the characteristically increased intensity is very different on the surface alloy and hence must be due to the new η^1 structures.
The improved agreement achieved by considering the η^1-top-OSn geometries together with the η^2-diσ(CC) forms to be present on the surface at low temperature can be confirmed by comparison of the measurements with a *Gaussian* convolution of the DFT spectra. It is depicted in Fig. B.3 of App. B.3.[25]
Interestingly the shifts of the ν(C2=C3) vibrations (1635 and 1632 cm^{-1}) from the gas phase frequency of 1642 cm^{-1} are of a similarly small size as those found for the η^1-top-E-(s)-trans geometry on Pt(111) (at 1633 cm^{-1}). Even more important, yet puzzling at first place, are the reduction of the blueshifts of the ν(C1=O) vibrations (1611 and 1615 cm^{-1}), which is obtained at 1706 cm^{-1} in the gas phase and at 1562 cm^{-1} for the η^1 form on Pt(111). Despite the much smaller perturbation of the normal modes here, the adsorption energy on the $Pt_3Sn(111)$ surface alloy is much larger (-33.2 and -30.8 kJ/mol vs. -23.5 kJ/mol on Pt(111), Tab. 6.24). This finding is again solely understood by the decomposition of the adsorption energy. In agreement with the elongation of the molecule-metal bond, which is above 2.5 Å here vs. 2.22 Å on Pt(111), the coinciding decrease of the interaction term on the surface alloy clearly suggests a weaker interaction and, hence, a smaller perturbation of the vibrational normal modes.

By annealing the sample to 200 K the overall shape of the HREEL spectrum is transformed dramatically. The measured loss peaks at 475 cm^{-1}, 914 cm^{-1}, 967 cm^{-1} and 1156 cm^{-1} are damped severely in contrast to the signals at 552 cm^{-1} and 1023 cm^{-1}, which are now dominating the whole fingerprint region. In the comparable low coverage HREEL spectrum of 0.6L crotonaldehyde annealed to 200 K the latter signals are even more intense. Moreover it is observed that the peak in the double bond stretching region around 1652 cm^{-1} has become wider and is less intense. The transformation of the HREEL spectra from 160 K to 200 K is accompanied by the partial desorption process evidenced by TPD (α_2, Fig. 6.35).
From the previous discussion, where it was shown that the bands at 926 cm^{-1} (926 cm^{-1} at 200 K), 975 cm^{-1} (967) and 1156 cm^{-1} as well as a part of the intensity measured at 1370 cm^{-1} (1374) and 1442 cm^{-1} (1442) originate from a small fraction of η^1-top-E-(s)-trans-OSn surface species, a decrease of this surface fraction of the η^1 species can be derived. A discrepancy arises at this point for the loss peak detected at 552 cm^{-1}, because it had gained a significant part of its intensity from the η^1 forms at 160 K.

The whole transformation observed here is understood as a surface reordering process that converts the low haptictity η^1 and η^2 coordination types to flat η^3-diσ(CC) geometries. The η^1 forms, which are less stable structures in a low coverage environment, can in turn be basically excluded above 200 K.
The spectroscopic traces of the η^3-diσ(CC)-E-(s)-cis structure (Tab. 6.29) are observed in several experimental peaks. Primarily the huge increase of the loss intensity at 1023 cm^{-1} is assigned to methyl scissoring vibration γ"(CH_3) computed at 1017 cm^{-1}. Besides that partially also the intense ν(C1-C2) mode of the η^2-diσ(CC)-E-(s)-cis complex (1003 cm^{-1}) and the γ"(CH_3)

[25]Note that the intensities of both η^2-diσ(CC) adsorption structures have been doubled in convolution (b) in order to exemplify the small surface coverage fractions of η^1-top-OSn complexes required for a satisfying agreement. Probably even a smaller amount of η^1 complexes is present. The half-width of this *Gaussian* function is determined by the resolution of the experiments.

ω cm^{-1}	Intensity $\times 10^6$ au		Normal mode
3045	0.001		ν(C4-H4)
3016	0.011		ν(C2-H2)
3004	0.092		ν_{as}(C4-H5,6)
2974	0.0		ν(C3-H3)
2934	0.15		ν_s(CH_3)
2728	0.14		ν(C1-H1)
1674	9.8	vs	ν(C1=O)
1429	0.39		δ"(CH_3)
1418	0.021		δ'(CH_3)
1356	0.005		δ_s(C1H1-C2H2)
1352	0.23		u(CH_3)
1324	0.025		δ_{as}(C1H1-C2H2)+δ(C3H3)
1214	0.009		δ_{as}(C1H1-C2H2)-δ(C3H3)
1124	0.82		ν(C2=C3)
1077	1.9	m	ν(C3-C4)
1039	0.001		ν(C1-C2)
999	6.3	s	γ"(CH_3)
970	0.48		γ_{as}(C1H1-C2H2)
945	0.026		γ_s(C1H1-C2H2)
926	0.16		γ(C3H3)
877	0.064		γ'(CH_3)
564	0.12		δ(O=C1-C2)
524	2.9	m	ν_{as}(PtC2-PtC3)
467	1.1		δ(C2=C3-C4)
345	0.040		ν_s(PtC2-PtC3)
263	0.87	w	τ(C1-C2)
247	0.79	w	δ(C1-C2=C3)
218	0.72	w	τ(CH_3)
205	0.21		τ(C2=C3)
128	0.74		fT
105	8.2	vs	fT
91	1.0	w	fR
21	0.12		fR

Table 6.25: Vibrational analysis of the η^2-diσ(CC)-E-(s)-trans structure of crotonaldehyde on Pt_3Sn(111) at a theoretical coverage of Θ = 1/12 ML. The letters following the computed intensities refer to the relative strength, i.e. (v)w = (very) weak, m = medium and (v)s = (very) strong. For strong vibrational couplings of more than 2 normal modes, the coupling of the components is indicated by + (in phase) or - (anti-phase). The abbreviations R and T refer to hindered translations and hindered rotations.

ω cm^{-1}	Intensity $\times 10^6$ au		Normal mode
3051	0.002		ν(C4-H4)
3017	0.004		ν(C3-H3)
2995	0.081		ν_{as}(C4-H5,6)
2990	0.009		ν(C2-H2)
2928	0.28		ν_s(CH_3)
2824	0.27		ν(C1-H1)
1641	5.1	s	ν(C1=O)
1431	0.50		δ"(CH_3)
1416	0.019		δ'(CH_3)
1358	0.35		δ(C1H1)
1349	0.31		δ_s(C2H2-C3H3)
1347	0.14		u(CH_3)
1245	1.0		δ_{as}(C2H2-C3H3)
1128	0.68		ν(C2=C3)
1083	1.6	m	ν(C3-C4)
1018	1.7	m	γ_s(C1H1-C2H2)+γ(C3H3)
1003	3.8	s	ν(C1-C2)
965	2.2	m	γ_{as}(C1H1-C2H2)
932	1.7	m	γ"(CH_3)
893	0.24		γ_s(C1H1-C2H2)-γ(C3H3)
834	0.18		γ'(CH_3)
693	0.37		δ(O=C1-C2)
548	3.0	m	ν_{as}(PtC2-PtC3)
452	0.80		ν_s(PtC2-PtC3)
312	0.23		δ(C2=C3-C4)
253	9.0	vs	δ(C1-C2=C3)
232	3.4	s	τ(C1-C2)
213	0.31		τ(CH_3)
184	0.12		τ(C2=C3)
112	3.6	s	fT
101	0.026		fT
76	3.8	s	fR
24	59.1	vs	fR

Table 6.26: Vibrational analysis of the η^2-diσ(CC)-E-(s)-cis structure of crotonaldehyde on $Pt_3Sn(111)$ at a theoretical coverage of $\Theta = 1/12$ ML.

ω cm^{-1}	Intensity $\times 10^6$ au		Normal mode
3092	0.15		ν(C2-H2)
3068	0.012		ν(C3-H3)-ν(C4-H4)
3049	0.067		ν(C3-H3)+ν(C4-H4)
2999	0.0		ν_{as}(C4-H5,6)
2957	0.004		ν_s(CH_3)
2810	0.036		ν(C1-H1)
1635	3.8	m	ν(C2=C3)
1611	5.1	s	ν(C1=O)
1429	0.013		δ'(CH_3)
1419	0.015		δ"(CH_3)
1383	0.094		δ(C1H1)
1350	1.0	w	u(CH_3)
1297	0.049		δ(C3H3)
1244	0.004		δ(C2H2)
1157	4.6	m	ν(C1-C2)
1101	1.1		ν(C3-C4)
1034	0.007		γ"(CH_3)
993	0.004		γ_s(C1H1-C2H2)+γ(C3H3)
965	0.014		γ_{as}(C1H1-C2H2)
919	4.6	m	γ'(CH_3)
784	0.0		γ_s(C1H1-C2H2)-γ(C3H3)
546	6.3	m	δ(O=C1-C2)
468	0.19		δ(C2=C3-C4)
311	0.041		τ(C2=C3)
256	22.7	vs	δ(C1-C2=C3)
208	0.004		τ(C1-C2)
146	0.032		τ(CH_3)
127	4.3	m	ν(Pt-O)
103	0.027		fT
92	1.5	w	fR
86	0.016		fT
63	9.6	s	fR
36	38.8	vs	fT

Table 6.27: Vibrational analysis of the η^1-top-E-(s)-trans-OSn structure of crotonaldehyde on $Pt_3Sn(111)$ at a theoretical coverage of $\Theta = 1/12$ ML.

ω cm^{-1}	Intensity $\times 10^6$ au		Normal mode
3051	0.11		ν(C4-H4)
3031	0.002		ν(C3-H3)
3018	0.44		ν(C2-H2)
2991	0.005		ν_{as}(C4-H5,6)
2948	0.086		ν_s(CH_3)
2852	2.3	w	ν(C1-H1)
1632	0.24		ν(C2=C3)
1615	11.2	vs	ν(C1=O)
1424	2.4	m	δ'(CH_3)
1418	0.043		δ"(CH_3)
1362	0.099		δ(C1H1)
1350	0.0		u(CH_3)
1285	0.85		δ_s(C2H2-C3H3)
1253	0.16		δ_{as}(C2H2-C3H3)
1170	0.011		ν(C1-C2)
1099	0.12		ν(C3-C4)
1025	0.017		γ"(CH_3)
982	0.034		γ_s(C1H1-C2H2)+γ(C3H3)
958	0.012		γ_{as}(C1H1-C2H2)
912	4.4	s	γ'(CH_3)
774	0.0		γ_s(C1H1-C2H2)-γ(C3H3)
544	0.50		δ(O=C1-C2)
456	1.5	w	δ(C2=C3-C4)
312	0.12		τ(C2=C3)
238	13.8	vs	δ(C1-C2=C3)
186	0.018		τ(C1-C2)
147	1.5	w	τ(CH_3)
110	26.7	vs	ν(Pt-O)
94	4.5	m	fR
75	1.2	w	fT
52	0.025		fT
21	27.9	vs	fR
1	0.0		fT

Table 6.28: Vibrational analysis of the η^1-top-E-(s)-trans-OSn(2) structure of crotonaldehyde on $Pt_3Sn(111)$ at a theoretical coverage of $\Theta = 1/12$ ML.

vibration of the corresponding E-(s)-trans form (999 cm^{-1}) account for the intensity increase. Around 1261 cm^{-1} and 1442 cm^{-1} further contributions of the η^3-diσ(CC)-E-(s)-cis structure improve the match of the theoretical analysis. In detail these are the δ_{as}(C2H2-C3H3) and the important ν(C1=O) normal modes computed with medium intensities at 1259 cm^{-1} and 1460 cm^{-1}, respectively.

A clear sign speaking against a significant surface fraction of the related η^3-diσ(CC)-Z-(s)-cis adsorption complex, which is only slightly less stable than the one of the E-(s)-cis isomer, is found at 1442 cm^{-1}. With the isomeric Z-form a problem would arise from the corresponding ν(C1=O) stretching mode calculated to be intense at 1474 cm^{-1}. Upon convolution of the data with a *Gaussian*, it would lead to an erroneously large shift of the simulated peak. Furthermore and even ruling out such a surface species more evidently, are the vibrational normal modes γ_s(C2H2-C3H3) and δ(C2=C3-C4) computed with sizable intensities at 875 cm^{-1} and 421 cm^{-1} in regions of only weakly intense experimental peaks that have already been account for by the other structures.

Additional traces of the η^3-diσ(CC)-E-(s)-cis surface species are attributed to the peaks at 842 cm^{-1} (γ'(CH_3), 877 cm^{-1}) and at 552 cm^{-1} (ν_{as}(PtC2-PtC3), 533 cm^{-1}). Especially the latter peak, which loses its contribution of the η^1-top-E-(s)-trans-OSn structure, remains dominant at 200 K.

Finally the ν_s(PtC2-PtC3) and ν(Pt-O) molecule-surface stretching modes are computed at 335 cm^{-1} and 316 cm^{-1}, respectively, with large intensities. Yet they seem to be hidden by the high loss intensity of the η^2 forms, which give rise to the signal detected at 259 cm^{-1}. Above 250 K the intensity of the latter vibrations is damped sufficiently so that a similarly intense and broad peak at 298 cm^{-1} is resolved.

The comparison of the computed frequencies of the η^3-diσ(CC)-σ(O)-E-(s)-cis-OSn structure on the Pt_3Sn(111) surface alloy with the corresponding species on Pt(111) leads to similar conclusion as the comparison of the η^2-diσ(CC) adsorption complexes. Generally the perturbation on the frequency shifts caused by the alloying is below 15 cm^{-1}, even for the various molecule-surface stretching vibrations and the ν(C1=O) mode of the aldehydic function interacting either with Sn or with Pt. This might again seem to be unphysical in the light of a significant decrease of the adsorption energy from -76.9 kJ/mol on Pt(111) to -51.2 kJ/mol on Pt_3Sn(111), but it is easily understood from the separation of the adsorption energies, which shows that the molecule distortion cost is nearly exactly the same with 144 kJ/mol on the alloy versus 136 kJ/mol on Pt(111). Again, as found already for the other structures above, the surface restructuring is much easier for the alloy (35 vs. 53 kJ/mol on Pt) and consequently the interaction term weakens sizably on Pt_3Sn(111) (-230 vs. -267 kJ/mol).

Although one could expect to deduce the strength of the additional O-Sn interaction for this coordination type by comparison with the otherwise geometrically related η^2-diσ(CC) complexes, this problem turns out to be more difficult. Indeed the interaction strength of the η^3 (-230 kJ/mol)and the η^2-diσ(CC)-E-(s)-cis (-228 kJ/mol) complex are very similar, which suggests an only very small contribution by the O-Sn bond here. From this picture, the higher stability of the η^3 species must result mainly from the decrease of its deformation energies for molecule and surface compared to the η^2 form (with 154 and 40 kJ/mol, respectively). Seemingly, the discrepancy in the deformation energies (15 kJ/mol) and the additional O-Sn interaction amount to the 17 kJ/mol that must equal the difference in the relative stabilities. This contribution of the additional oxygen interaction thus seems to be much too small and points to a systematic deficiency of the decomposition approach for the η^3 adsorption structures. The problem may arise from the assumption that the additional bond does not induce changes on the diσ(CC) moiety, while in the reality the overlap for the Pt-C bonds probably weakens somewhat due to the slight changes in the Pt-C-C-Pt geometry. On the other hand, also any charge transfer between molecule and surface is neglected here, and hence the picture is simplified further. Yet one can conclude that the oxophilic Sn leads to a significant stabilization

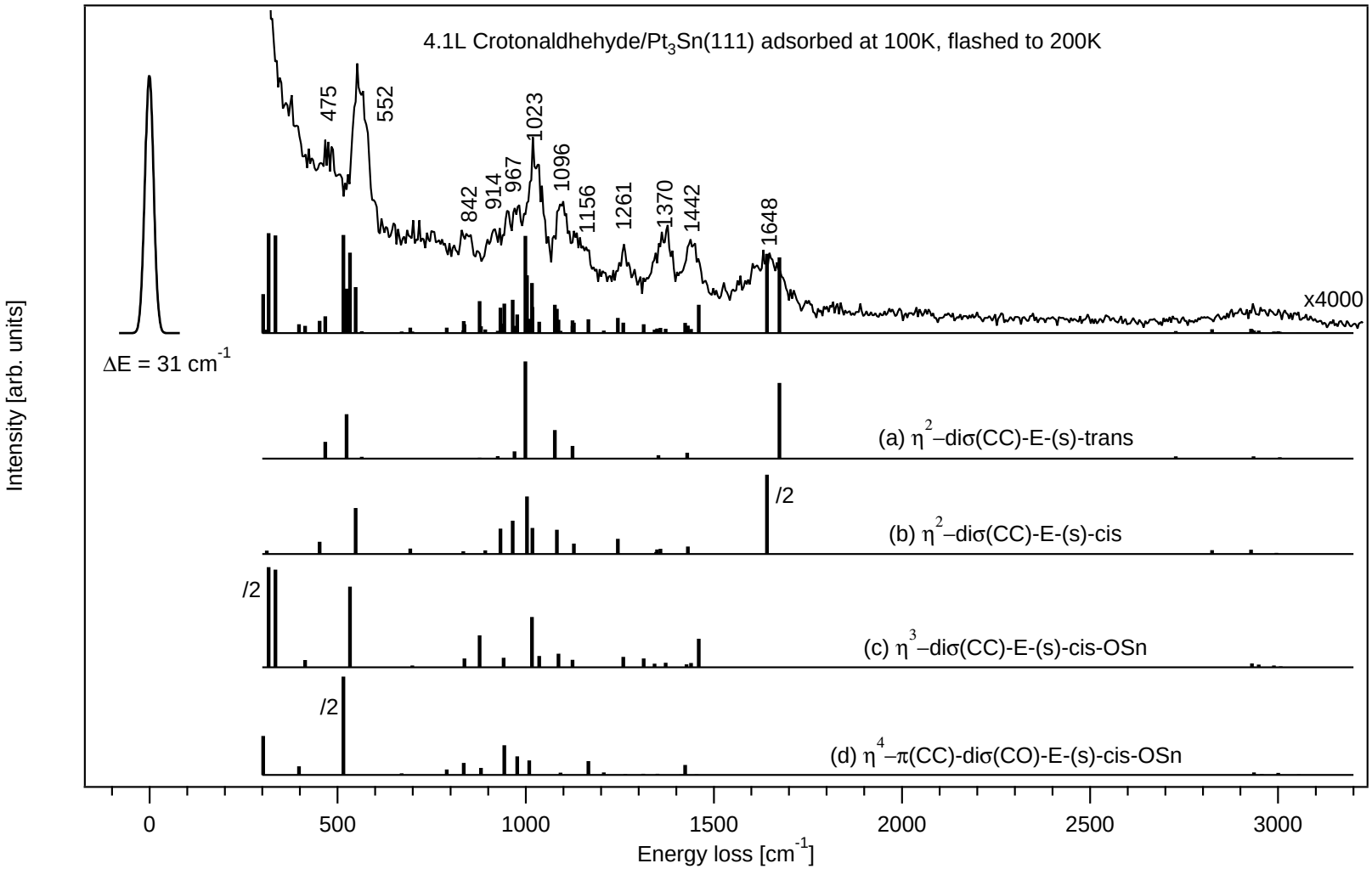

Figure 6.43: Comparison of the computed DFT HREEL spectra for the most stable adsorption structures with the experimental spectrum of 4.1L crotonaldehyde on a $Pt_3Sn(111)$ surface alloy annealed to 200 K after adsorption at 100 K.

of the adsorption structures compared to the other coordination types on the surface alloys.
Thus far the fit of the computed HREEL spectra of the η^3-diσ(CC)-σ(O)-E-(s)-cis-OSn, η^2-diσ(CC)-E-(s)-trans and η^2-diσ(CC)-E-(s)-cis adsorption structures with the experimental data is already very convincing (see Fig. B.4, App. B.3). However, another coordination type of the E-(s)-cis rota-isomer is found to be hardly distinguishable on either energetic or spectroscopic grounds from the already identified ones.
Unlike the η^4 structures of the E-(s)-trans or Z-(s)-trans isomers, which can be excluded easily by a number of mismatches of loss peaks computed intense in experimentally empty regions, most of the detectable vibrational signals of the η^4-π(CC)-diσ(CO)-E-(s)-cis-OSn (Tab. 6.30) complex happen to coincide with normal modes already assigned successfully before. As most of the normal modes of the η^4 coordination complexes are weak, these structures are quite difficult to detect here. The coincidences and the low loss intensities render the influence exerted by the additional vibrations on the HREEL spectra small.
Two computed normal modes, the ν(C1=O) at 1166 cm^{-1} and the γ_{as}(C2H2-C3H3) deformation at 835 cm^{-1}, behave even favorable by augmenting weak intensities and improving the accordance with the experimental loss peaks at 1156 cm^{-1} and 842 cm^{-1}. Caused by the much weaker interaction mechanism of the π-type, the ν(C2=C3) mode of the η^4 form is obtained at a high frequency of 1454 cm^{-1} with a small dynamical dipole moment.
A fundamental problem arises from the totally asymmetric molecule-surface stretching mode ν_{as}(PtO-PtC1)-ν_{as}(PtC2-PtC3) calculated with an enormous intensity at 515 cm^{-1}. As this frequency shows a large discrepancy of 47 cm^{-1} (i.e. 10%) from the experimental loss peak at 552 cm^{-1}, the question about the error bar of the computed normal modes in the low frequency region must be raised. Probably due to the neglect of anharmonicity effects and the limited slab thickness, the errors seem to be bigger. Nonetheless, the fit of the computed vibrational spectrum of the η^4-π(CC)-diσ(CO)-E-(s)-cis-OSn adsorption mode with the experimental HREELS data is very good within the error bars of DFT and the HREELS. Also the convolution shows a slight improvement (Fig. B.4, App. B.3) and confirms that this structure is present in the mixed adsorbate phase at 200 K.
After annealing the sample to temperatures of 250 K and above, the HREEL spectra follow the decomposition of the surface species measured with TPD and show further dramatic changes. From the damping of a number of the vibrational loss peaks correlated with the two η^2-diσ(CC) and the η^3-diσ(CC)-σ(O)-E-(s)-cis-OSn surface species - especially in the double bond stretching region around 1650 cm^{-1} - it is obvious that these surface species decompose here. New signals obtained for instance at 649 cm^{-1} and 828 cm^{-1} point to the development of new surface intermediates similar to the ones discussed on Pt(111) that are produced by fragmentation reactions.

In an analysis based on the combination of high-resolution XPS measurements of the core-level shifts of the Pt $4f_{7/2}$, Sn $4d_{5/2}$ and C 1s levels with DFT total energy calculations, Göthelid et al. [13] proposed the surface species on the $Pt_3Sn(111)$-p(2×2) surface alloy to consist solely of the η^3-diσ(CC)-σ(O)-E-(s)-cis-OSn and the η^1-top-E-(s)-trans-OSn adsorption complexes. This conclusion is primarily based on their DFT optimizations using a two-layer model. Neither the adsorption energies of -36.7 kJ/mol and -25.5 kJ/mol of the latter adsorption complexes, nor the geometry parameters these authors give seem to be sufficiently converged compared to the quality of the actual calculations. Hence it is clear that the much simpler two-layer model is a completely inadequate approximation and may lead to qualitatively incomplete or even unrealistic results.
The question now arises as to the interpretation of the subtle variations of the C 1s core levels, which these authors detected on the $Pt_3Sn(111)$ model-catalyst. The core-level shifts are consistent with the η^1 and η^3 structures, but since the majority of the photoemission peaks measured are quite weak and very broad, it is difficult to argue on whether any additional level

ω cm^{-1}	Intensity $\times 10^6$ au		Normal mode
3054	0.029		ν(C2-H2)
3030	0.005		ν(C4-H4)
3006	0.051		ν(C3-H3)
2988	0.11		ν_{as}(C4-H5,6)
2948	0.17		ν(C1-H1)
2930	0.25		$\nu_s(CH_3)$
1460	1.8	m	ν(C1=O)
1440	0.28		δ"(CH_3)
1427	0.19		δ'(CH_3)
1372	0.29		δ_s(C2H2-C3H3)
1342	0.23		u(CH_3)
1314	0.57		δ(C1H1)
1259	0.68		δ_{as}(C2H2-C3H3)
1124	0.49		ν(C2=C3)
1087	0.87		ν(C3-C4)
1036	0.74		ν(C1-C2)
1017	3.3	s	γ"(CH_3)
941	0.63		γ_s(C2H2-C3H3)
932	0.022		γ_{as}(C2H2-C3H3)-γ(C1H1)
877	2.1	m	γ'(CH_3)
837	0.57		γ_{as}(C2H2-C3H3)+γ(C1H1)
699	0.10		δ(O=C1-C2)
533	5.2	s	ν_{as}(PtC2-PtC3)
413	0.47		δ(C2=C3-C4)
335	6.3	s	ν_s(PtC2-PtC3)
316	12.9	vs	ν(Pt-O)
281	0.043		$\tau(CH_3)$
254	0.99		δ(C1-C2=C3)
216	0.26		τ(C1-C2)
142	2.0	m	τ(C2=C3)
126	1.8	m	fR
103	0.39		fT
74	0.41		fR

Table 6.29: Vibrational analysis of the η^3-diσ(CC)-σ(O)-E-(s)-cis-OSn structure of crotonaldehyde on $Pt_3Sn(111)$ at a theoretical coverage of $\Theta = 1/12$ ML.

ω cm^{-1}	Intensity $\times 10^6$ au		Normal mode
3067	0.0		ν(C3-H3)
3055	0.033		ν(C2-H2)
3024	0.0		ν(C4-H4)
3000	0.13		$\nu_{as}(CH_3)$
2956	0.066		ν(C1-H1)
2936	0.17		$\nu_s(CH_3)$
1454	0.024		ν(C2=C3)
1423	0.66		δ"(CH_3)
1414	0.024		δ'(CH_3)
1350	0.073		u(CH_3)
1312	0.083		δ(C1H1)
1264	0.042		δ_{as}(C2H2-C3H3)
1208	0.17		δ_s(C2H2-C3H3)
1166	0.91		ν(C1=O)
1092	0.16		ν(C3-C4)
1009	0.94		γ"(CH_3)
978	1.2	w	ν(C1-C2)
943	1.9	w	γ_s(C2H2-C3H3)
881	0.46		γ'(CH_3)
835	0.78		γ_{as}(C2H2-C3H3)
790	0.36		γ(C1H1)
670	0.11		δ(O=C1-C2)
515	12.7	vs	ν_{as}(PtO-PtC1)-ν_{as}(PtC2-PtC3)
397	0.57		ν_{as}(PtO-PtC1)+ν_{as}(PtC2-PtC3)
391	0.003		δ(C2=C3-C4)
302	2.5	m	ν_s(PtO-PtC1)-ν_s(PtC2-PtC3)
242	0.17		δ(C1-C2=C3)
234	0.097		ν_s(PtO-PtC1)+ν_s(PtC2-PtC3)
229	0.74		$\tau(CH_3)$-t(C2=C3)
184	1.1		τ(C1-C2)
158	0.063		$\tau(CH_3)$+t(C2=C3)
115	0.32		fT
52	0.003		fR

Table 6.30: Vibrational analysis of the η^4-π(CC)-diσ(CO)-E-(s)-cis-OSn structure of crotonaldehyde on $Pt_3Sn(111)$ at a theoretical coverage of $\Theta = 1/12$ ML.

stemming from the η^2-diσ(CC) structures unambiguously identified in this work are also in the data of Göthelid [13] et al.

A major conclusion from the observation of only small vibrational shifts for the corresponding structures on Pt(111) and the $Pt_3Sn(111)$ surface alloy discussed above is the fact that there is no simple, general correlation of the absolute adsorption energies and the vibrational frequency shifts for such complex, multifunctional molecules. Although the trend of an increase of vibrational shifts with larger adsorption energies is valid for small adsorbates such as ethene, the adsorption energy of a complex interacting molecule may very well increase sizably while the vibrational shifts, compared to the unperturbed gas phase value, simultaneously become smaller. In order to understand the frequency changes and to analyze the molecule-surface interaction it is thus inevitable to understand the basic contributions to adsorption energy. The correlation of the vibrational properties must subsequently be performed with the respective distortion energies of the surface, of the molecule and the interaction term between both.

6.3 The Bonding of Crotonaldehyde on $Pt_2Sn(111)$

The results of the investigations on the adsorption of crotonaldehyde on the tin richer $Pt_2Sn(111)$-$(\sqrt{3}\times\sqrt{3})R30°$ surface alloy are surprisingly similar to the ones on $Pt_3Sn(111)$ discussed in the previous chapter. Due to the high tin fraction in the superstructure of $Pt_2Sn(111)$ the distribution of the platinum surface atoms allows to access bridge and on-top sites, but threefold hollow sites consisting of pure platinum are no longer available on the surface. This allows to exclude a number of high hapticity geometries that were already only weakly bonded in the Pt_3Sn case. Therefore it might be expected that the effects of Sn observed previously will be even more evident here. As it will be shown, this in fact is true. Arising from the strongly varying interaction strength of the Pt-C and Sn-O bonds also the HREEL spectra recorded on $Pt_2Sn(111)$ exhibit a coverage dependence of the encountered adsorption modes. Hence this system has been chosen as a prototype for the theoretical study of low and high coverage situations of crotonaldehyde on the Pt-Sn surface alloys.

6.3.1 TPD Results

The TPD results of crotonaldehyde on the $Pt_2Sn(111)$-$(\sqrt{3}\times\sqrt{3})R30°$ surface alloy support the trend of decreasing adsorption strength with increasing surface tin fraction. In contrast to Pt(111) and the $Pt_3Sn(111)$ surface alloy no decomposition of crotonaldehyde at higher temperatures has been monitored in this case. Instead the activation energy of the initial fragmentation reactions is higher than the competing barrier of the desorption process.
Since the desorption peaks of crotonaldehyde (m/z =70) are very weak when employing the sensitivity setting used on Pt(111), additional TPD experiments have been performed with a higher SEM voltage. This TPD data presented in Fig. 6.44 exhibits a worsened signal/noise ratio, but nonetheless it allows a clearer identification of the desorption states. The most important new feature detected here is the monolayer desorption state α_3 of intact crotonaldehyde at 231 K. This temperature corresponds to an activation barrier of 59.6±1.5 kJ/mol (Redhead method [56], frequency factor $\nu = 10^{-13}$ Hz, heating rate 2 K/s) for the desorption process. In combination with the fact that no fragments such as propene, hydrogen or CO have been detected by TPD or HREELS at higher temperatures it can be concluded that crotonaldehyde chemisorbs reversibly on this surface alloy.
Similar to the findings on Pt(111) and $Pt_3Sn(111)$, two low temperature desorption peaks are detected. From the depicted TPD series the desorption of the multilayer (α_1) is determined at ca 143 K (36.3±1.5 kJ/mol) in excellent agreement with the corresponding multilayer desorption

states on the two other investigated surfaces. Also the desorption state α_2 is measured again at 170 K (44.4±1.5 kJ/mol).

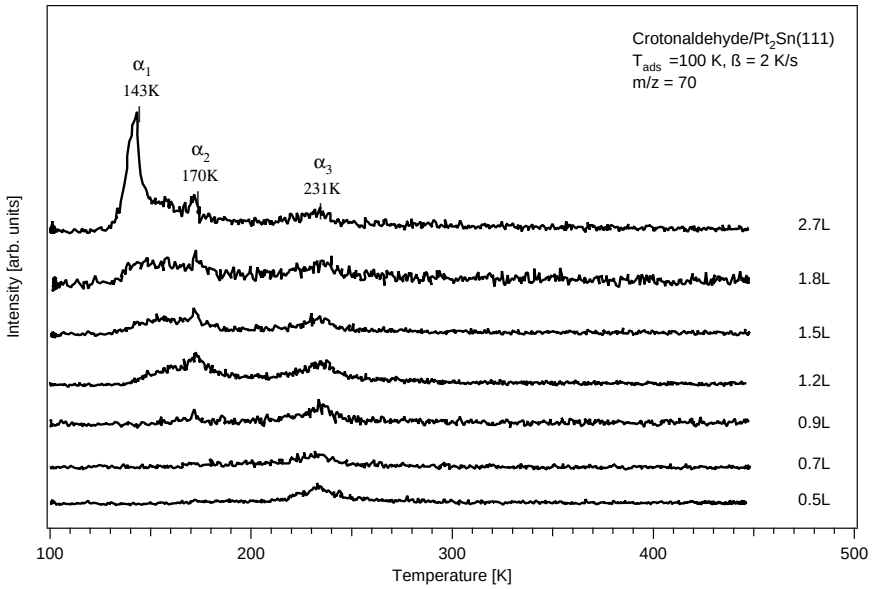

Figure 6.44: TPD spectra of crotonaldehyde adsorbed on the $Pt_2Sn(111)$ surface recorded with a more sensitive secondary electron multiplier voltage, m/z=70.

6.3.2 Adsorption Structures of Crotonaldehyde on $Pt_2Sn(111)$

Novel insights into the bonding of crotonaldehyde on the $Pt_2Sn(111)$ surface alloy are obtained in this investigation by the optimization of a large variety of possible adsorption modes. Extending the number of existing structures from previous studies of other groups [45], it was found that most of the initially conceived geometries turned out to be very unstable and transformed into other more stable configurations. Nonetheless still a large number of 14 stable complexes has been found of which 6 exhibit a sizable adsorption energy. Generally also the optimizations on $Pt_2Sn(111)$ yield the result that an O-Sn interaction of the aldehydic function is required to adsorb the molecule sufficiently while Sn-C interactions are highly repulsive.

Although it is very tempting to convey a general message of a homogeneous decrease of the adsorption energies upon increase of the surface tin fraction, this pictures is too simple to describe the present results of the total energy calculations correctly. While a comparison of the adsorption energies on this surface alloy, which are summarized in Tab. 6.31, to the ones found on Pt(111) shows a strong decrease, the variations from the values computed on $Pt_3Sn(111)$ do not exhibit a simple trend.

Indeed the most stable coordination types on the $Pt_2Sn(111)$-$(\sqrt{3} \times \sqrt{3})R30°$ surface alloy turn out to be bonded as strong as on $Pt_3Sn(111)$, indicating that the adsorption is a very local phenomenon. This is the case for all of η^2-diσ(CC) (-33.7 kJ/mol[26] and -20.7 kJ/mol; Figs. 6.45(a) and 6.45(b)) and η^3-diσ(CC)-OSn structures (-49.1 kJ/mol, Fig. 6.45(e), and -38.7 kJ/mol).

On the other hand for some adsorption modes like for instance the η^4-π(CC)-diσ(CO)-OSn

[26] Due to the use of the PAW scheme instead of Ultra-soft pseudopotentials the adsorption energies obtained here differ slightly from those computed by Delbecq et al. [45] earlier.

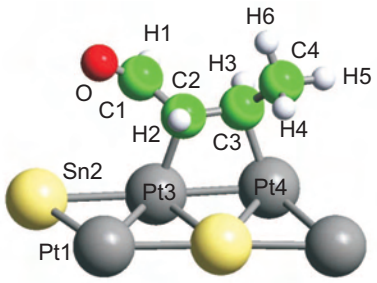

(a) η^2-diσ(CC)-E-(s)-trans

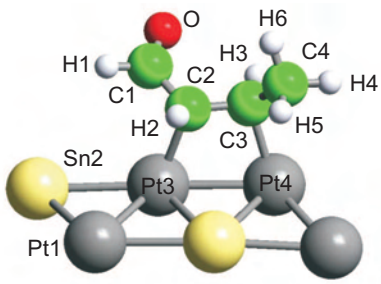

(b) η^2-diσ(CC)-E-(s)-cis

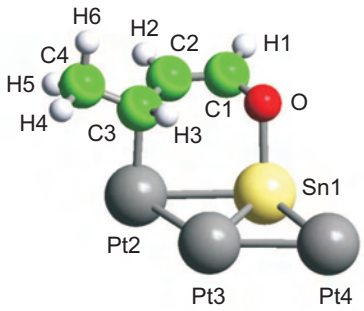

(c) η^2-diσ(C3,O)-E-(s)-cis-OSn

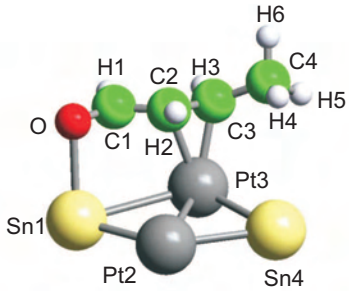

(d) η^3-π(CC)-E-(s)-trans-OSn

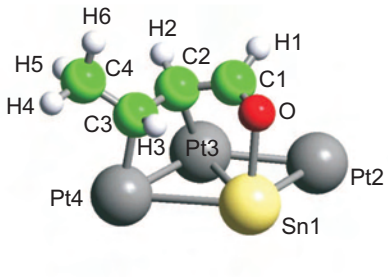

(e) η^3-diσ(CC)-σ(O)-E-(s)-cis-OSn

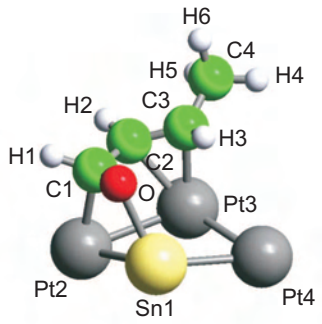

(f) η^4-π(CC)-diσ(CO)-E-(s)-cis-OSn

Figure 6.45: Optimized adsorption geometries of the most stable coordination types of crotonaldehyde on the $Pt_2Sn(111)$-$(\sqrt{3}\times\sqrt{3})R30°$ surface alloy. The geometries of the two η^2-diσ(CC) complexes shown above have been optimized on a 3×2 supercell and the structures of higher hapticity on a 3×3 supercell.

Adsorption energies [kJ/mol]	E-(s)-trans	E-(s)-cis	Z-(s)-trans	Z-(s)-cis
η^1-top-OPt	unstable	not considered	not considered	not considered
η^1-top-OSn	unstable (-21.6 [45])	not considered	not considered	not considered
η^2-diσ(CO)-OPt	unstable	unstable	unstable	unstable
η^2-diσ(CO)-OSn	unstable	-2.0	unstable	unstable
η^2-diσ(CC)	-33.7 (-25.9 [45])	unstable	-20.7	unstable
η^2-π(CC)	-17.6	unstable	-10.7	-11.2
η^2-diσ(C3,O)-OPt	unstable	unstable	unstable	unstable
η^2-diσ(C3,O)-OSn	unstable	-33.1	unstable	-20.5 (-32.0 [45])
η^3-diσ(CC)-OPt	unstable	excluded	unstable	excluded
η^3-diσ(CC)-OSn	excluded	-49.1 (-26.8 [45])	excluded	-38.7 (-42.8 [45])
η^3-π(CC)-OSn	-32.5	unstable	-25.4	-15.4
η^4-diσ(CC)-diσ(CO)-OSn	excluded	excluded	excluded	excluded
η^4-π(CC)-diσ(CO)-OSn	unstable	-29.0	not stable	-13.0 (-25.9 [45])
η^4-diσ(CC)-diσ(CO)-OPt	excluded	unstable	excluded	unstable
η^4-π(CC)-diσ(CO)-OPt	unstable	excluded	unstable	excluded
Various other adsorption modes incl. C-Sn bonds	unstable	unstable	unstable	unstable

Table 6.31: Calculated adsorption energies of crotonaldehyde on the $Pt_2Sn(111)$-$(\sqrt{3} \times \sqrt{3})R30°$ surface alloy at a low theoretical coverage of $\Theta = 1/9$. Note that no structures of the η^3-π(CC)-OPt type have been considered due to the already weak adsorption strenght of the related geometries interacting with Sn. Furthermore, several structures have been "excluded", because the initial structure was already sterically too strained to lead to a stable geometry.

(Fig. 6.45(f)) a decrease of about 13 kJ/mol compared to the analogous forms on $Pt_3Sn(111)$ is obtained. Various other coordination types are even completely destabilized and do not represent local minima here any more. Remarkable in this context is the η^1-top-OSn type that was first described by Delbecq et al. [45] as a stable geometry with an adsorption strength of -21.6 kJ/mol, but which could not be reproduced in the actual calculations. By a close analysis of the computational parameters in both extremely long and costly optimizations it was found that the combination of the dipole corrections in z-direction together with the tighter convergence requirements on the residual forces at the local minima chosen in this work lead to very slow but steady "desorption" of the molecule from the initial structure. Thus this coordination type has only been artificially stable with the more relaxed convergence criteria employed by Delbecq et al. Besides the destabilization of several structures, entire sets of other coordination types such as for i.e. the η^4-diσ(CC)-diσ(CO) cannot be constructed with pure Pt-C interactions on this surface any more due its $(\sqrt{3} \times \sqrt{3})R30°$ tin superstructure.

The appearance of new coordination types, which become accessible on $Pt_2Sn(111)$ leads again to an extensive set of possible surface complexes that may contribute to the HREEL spectra.
Especially interesting because of its untypical coordination is the new η^2-diσ(C3,O)-OSn form (Fig. 6.45(c)) with an upright molecular carbon backbone. It can be described as metallacycle bonded to a Sn atom by the aldehydic oxygen and to a neighboring Pt atom by the vinylic carbon C3. Of the two double bonds only one is conserved and shifted to C1=C2 as confirmed by the short bond distance of 1.38 Å. The C1-O distance with 1.31 Å and r(C2-C3) with 1.44 Å are quite long compared to gaseous crotonaldehyde. While the r(Pt-C3) distance to the surface is very typical for a σ bond at 2.18 Å, the O-Sn bond is relatively short at 2.17 Å. As the adsorption energies of this structure type found for the E-(s)-cis and Z-(s)-cis forms are reasonably high with -33.1 kJ/mol and -20.5 kJ/mol, respectively, these complexes are potential candidates that need to be included in the vibrational analysis.
Also quite stable are the new η^3-π(CC)-OSn geometries (Fig. 6.45(d)) realized for the E-(s)-trans, Z-(s)-trans and Z-(s)-cis rota-isomers. This coordination was unstable on the previous, platinum richer surfaces and seemingly is only accessible here due to the lack of proper adsorption sites allowing for a better stabilization. With -32.5 kJ/mol and -25.4 kJ/mol the corresponding E-(s)-trans and Z-(s)-trans configurations of this type exhibit sizable adsorption energies whereas the Z-(s)-cis geometry is somewhat weaker at -15.4 kJ/mol. The difference observed for the adsorption energies is also reproduced in the r(O-Sn) bond distances, which are 2.43 Å and 2.41 Å for the two trans isomers, but is strongly elongated to 2.64 Å for the Z-(s)-cis complex. The C3-Pt and C2-Pt bonds computed at rather typical values of 2.16±0.02 and 2.24±0.01 Å for all of the three geometries act strongly on the surface atoms and pull those up extremely in this coordination type. The Pt atoms below C2/C3 are relaxed outward by ca 0.99±0.03 Å and the protrusions of the interacting Sn atoms are raised by ca 0.16 Å from their equilibrium value. However, these impressive surface bucklings are not the only effects due to the adsorption of crotonaldehyde on $Pt_2Sn(111)$. For the first time on this surface alloy also significant displacements of the interacting metal atoms parallel to the surface plane are found, which are in the size of 0.1 to 0.35 Å. The surface atoms in nearest-neighbor positions to the interacting ones are consequently also affected by slight shifts of up to 0.05 Å. These values are much larger than those observed previously on Pt(111) and $Pt_3Sn(111)$, where interacting surface atoms were usually displaced by less than 0.05 Å in the plane. The directions in which for instance the Pt atoms bonded to C2 and C3 are displaced arise mainly from their tendency to evade the sterical hinderance of the methyl-hydrogens and to optimize the bond length and, hence, the overlapp of the C-Pt and O-Sn interactions.
As already mentioned in the discussion of the spectroscopic data of crotonaldehyde on $Pt_3Sn(111)$, the theoretical investigation of crotonaldehyde on the $Pt_2Sn(111)$ surface alloy has further been performed with an emphasize on the *coverage dependence* of the adsorption

Adsorption mode	adsorption energy		surface deformation		molecule deformation		interaction term	
Θ	1/6	1/9	1/6	1/9	1/6	1/9	1/6	1/9
η^2-diσ(CC)-E-(s)-trans	-19.7	-33.7	70	67	158	146	-248	-247
η^2-diσ(CC)-E-(s)-cis	-29.5		66		164		-260	
η^3-diσ(CC)-σ(O)-E-(s)-cis-OSn		-49.1		59		139		-246
η^4-π(CC)-diσ(CO)-E-(s)-cis-OSn	-16.4	-29.0	53	60	108	113	-177	-202

Table 6.32: Decomposition of the adsorption energies of crotonaldehyde on $Pt_2Sn(111)$ (Θ = 1/6 and 1/9 ML) into the energy costs for deforming the surface and the molecule and the energy gain of the interaction in the optimized surface complex (kJ/mol).

energies and the computed HREELS data. Therefore a set of representative adsorption geometries has been reoptimized at higher coverage in a 3×2 supercell to analyze the trends of the adsorption energies.

From Tab. 6.33 it becomes evident that a higher coverage situation corresponds to a decrease of the adsorption energy per molecule. Except for the η^2-diσ(CC)-E-(s)-cis form, which was not stable at Θ = 1/9 ML coverage, the adsorption energies are reduced by roughly 13 kJ/mol for the considered geometries. The smaller adsorption energy obtained for the η^4-π(CC)-diσ(CO)-OSn structure and the complete destabilization of the η^3 complexes points again to the realization of lower hapticities at higher coverages that was proposed from the HREEL spectra on $Pt_3Sn(111)$. This can also be rationalized from the weaker interaction per molecule-surface bond that is generally lower for the η^4 structures in comparison to the coordination types of lower hapticities on a given surface. In fact, as judged from the adsorption energy, the η^2 coordination types represent the most stable structures in a high coverage environment.

Microscopically the decrease in the adsorption energy for the η^4 structure is correlated with a weaker interaction at higher coverage as rationalized from the separation of the energy contributions (Tab. 6.32). The deformation costs of the molecule and the surface induced by the adsorption increase slightly towards lower coverages, 53 and 108 kJ/mol for 1/6 ML vs. 60 and 113 kJ/mol for 1/9 ML, but the weaker interaction energy of -177 kJ/mol at high coverage (-202 kJ/mol for 1/9 ML) disfavors this coordination type.

The investigation of the 3×2 supercell furthermore allows to analyze structural changes upon the variation of the coverage. The bond distances of the most stable adsorption complexes are presented in Tab. 6.34. It is found that the influence of the coverage on the converged geometries is usually very small, and barely a few bonds vary by more than 0.01 Å in their lengths. In fact only the molecule-surface bond distance r(C2-Pt) of the vinylic carbon in the η^4-π(CC)-diσ(CO)-E-(s)-cis-OSn complex is decreased somewhat more pronounced by 0.05 Å, which can be ascribed to the more strained sterical situation in the smaller supercell.

The deformation energies deviate also only weakly with the coverage, but at least for the η^2-E-(s)-trans species, the change accounts for the reduced adsorption energy at higher coverage. In the 3×2 supercell the computed adsorption energy amounts to -19.7 kJ/mol while it is more stable with -33.7 kJ/mol at 1/9 ML coverage. Since the interaction term between the molecule and the surface does not vary much with the coverage for this adsorption structure (-248 kJ/mol at 1/6 ML and -247 kJ/mol at 1/9 ML), the decrease in the cost for the deformation of the molecule to 146 kJ/mol together with a lower deformation energy of the surface of 68 kJ/mol explains the stabilization of the adsorption complex at lower coverages.

A comparison of the bond distances of the η^2, η^3 and η^4 structures on $Pt_2Sn(111)$ at a coverage of 1/9 ML and the corresponding structures on $Pt_3Sn(111)$ (1/12 ML) shows generally only very small variations in the range of 0.01 Å to 0.04 Å. While the geometrical parameters of

Adsorption energies [kJ/mol]	E-(s)-trans	E-(s)-cis	Z-(s)-trans	Z-(s)-cis
η^2-diσ(CC)	-19.7 (-13.8 [45])	-29.5 (-22.9 [45])	-8.4	
η^2-π(CC)	-16.8			
η^2-diσ(C3,O)-OSn		-27.1 (-25.0 [45])		
η^3-diσ(CC)-OSn		(unstable [45])		
η^3-π(CC)-OSn	unstable			
η^4-π(CC)-diσ(CO)-OSn		-16.4 (-13.4 [45])		

Table 6.33: DFT adsorption energies of selected important adsorption geometries of crotonaldehyde on the $Pt_2Sn(111)$-$(\sqrt{3} \times \sqrt{3})R30°$ surface alloy at a high theoretical coverage of $\Theta = 1/6$. Only the structures known to be competitive at 1/9 ML coverage have been considered. The other structures (missing entries) turned out not to be required for the interpretation. The reference values given are taken from Ref. [45]. These authors added the dipole corrections along the surface normal only in the form of a single point calculation at the structure optimized before.

Geometry	η^2-diσ(CC)-E-(s)-trans	η^2-diσ(CC)-E-(s)-trans	η^2-diσ(CC)-E-(s)-cis	η^3-diσ(CC)-σ(O)-E-(s)-cis-OSn	η^4-π(CC)-diσ(CO)-E-(s)-cis-OSn	η^4-π(CC)-diσ(CO)-E-(s)-cis-OSn
Supercell	3×3	3×2	3×2	3×3	3×3	3×2
r(O-C1)	1.23	1.23	1.23	1.28	1.34	1.34
r(C1-C2)	1.48	1.49	1.48	1.44	1.47	1.47
r(C2-C3)	1.50	1.50	1.50	1.49	1.42	1.42
r(C3-C4)	1.52	1.52	1.52	1.52	1.51	1.51
r(C1-H1)	1.12	1.12	1.12	1.11	1.10	1.10
r(C2-H2)	1.10	1.10	1.10	1.10	1.09	1.09
r(C3-H3)	1.10	1.10	1.10	1.10	1.09	1.09
r(C4-H4)	1.10	1.10	1.10	1.10	1.10	1.10
r(C4-H5)	1.10	1.10	1.10	1.10	1.10	1.10
r(C4-H6)	1.11	1.10	1.10	1.11	1.10	1.10
r(O-M)	-	-	-	2.34	2.16	2.27
r(C1-M)	-	-	-	-	2.25	2.24
r(C2-M)	2.16	2.16	2.17	2.25	2.32	2.27
r(C3-M)	2.14	2.14	2.13	2.13	2.20	2.20

Table 6.34: Bond distances of important optimized geometries of crotonaldehyde on $Pt_2Sn(111)$. All distances r of the stable structures at both high theoretical coverage ($\Theta = 1/6$) and at low theoretical coverage ($\Theta = 1/9$) are given in Å.

the η^2 forms are very similar, the structures of higher hapticity indicate slightly influenced bonding configurations due to the different Sn protrusion on this surface. The bond lengths of the aldehydic oxygen to surface Sn atoms is typically shortened by ca 0.03 Å in the η^3 and η^4 geometries on $Pt_2Sn(111)$ whereas the Pt-C bond lengths show both small elongations (esp. r(C1-Pt) and r(C2-Pt)) and shortenings (r(C3-Pt)) of less than 0.02 Å.

Despite the consistence of the geometry parameters of the adsorption complexes, the surface deformations induced by the molecules are large and their energy expense much larger compared to Pt(111) or Pt_3Sn. In fact, this is a general trend observed for all adsorption modes.

For instance the deformation cost of the surface and the interaction energy amounts to 60 and -202 kJ/mol, respectively, for the η^4-π(CC)-diσ(CO)-E-(s)-cis-OSn complex on Pt_2Sn, while the corresponding contributions on Pt_3Sn are computed to be only 37 and -189 kJ/mol, respectively. Even the corresponding adsorption structure on Pt(111) shows a similar deformation cost for the molecule at 106 kJ/mol and, hence, very similar frequencies[27]. As observed for the η^3-π(CC)-OSn geometries before, the displacements of the interacting atoms are large. The Pt atom interacting with the vinylic C2=C3 moiety in a π(CC) type is pulled up by 0.50 Å and shifted at the same time by roughly 0.2 Å in the surface plane just away from Pt4 (see Fig 6.45(f)). Less affected is the position of the Pt atom below C1, which is displaced by ca 0.18 Å towards C1 and pulled up by 0.25 Å, and also the interacting Sn that shows deviations of ca 0.1 (in plane, along the direction of the C1-O axis) and 0.20 Å (protrusion) to the equilibrium position, respectively. Also for the η^3-diσ(CC)-σ(O)-E-(s)-cis-OSn and the η^2-diσ(CC) structures an increase of the surface deformation energy on the Pt_2Sn surface alloy is computed. Such separation of the contributions leads to energy costs for deforming the molecule and the surface of 139 and 59 kJ/mol in the η^3-diσ(CC)-σ(O)-E-(s)-cis-OSn and 146 and 67 kJ/mol in the η^2-diσ(CC)-E-(s)-trans complex. Both complexes show an outward relaxation of the Pt atoms in the diσ(CC) configurations of roughly 0.4 Å and planar shifts of up to 0.23 Å[28].

The increase of the surface deformation energy shows that the higher Sn fraction leads to a "softer" surface that is deformed stronger by the adsorption of a multifunctional molecule. On average the surface deformation energies are in the range of ca 54 kJ/mol on Pt(111), whereas they are somewhat more favorable with ca 38 kJ/mol on Pt_3Sn (1/12 ML), but grow strongly to ca 62 kJ/mol on Pt_2Sn.

In order to obtain a more profound understanding of the deformation energies on the three model catalyst surfaces, potential curves have been computed for the outward shift of single Pt and Sn atoms from their equilibrium positions on the surface. As evident from Fig. 6.46, the energy cost to pull up a Sn atom on the two surface alloys is quite small and does not vary significantly with the surface Sn fraction. In contrast, the energy cost of rising Pt atoms is much larger and very sensitive to the surface composition. The energy expense is highest for pure Pt(111) and decreases with the surface Sn fraction[29].

In the "softer" potential curves, the increase of the deformation costs on Pt_2Sn is even more of a very surprising and counterintuitive trend. It may only be rationalized by the additional displacements in the surface plane, which were not observed on the Pt-richer surfaces.

As said before, the adsorption energies of related structures on both surface alloys are similar. Together with the similarity in the molecule deformations, the larger surface restructuring leads to a significant increase of the interaction terms on Pt_2Sn. The interaction contributions calcu-

[27] Together with the adsorption energy of -68.7 kJ/mol a somewhat larger interaction term of -233 kJ/mol was calculated therefore on Pt(111).

[28] For η^3-diσ(CC)-σ(O)-E-(s)-cis-OSn the in-plane/out-of-plane displacements of ca 0.18/0.40 Å below C3, 0.22/0.34 Å below C2 and ca 0.21/0.19 Å below O are computed. For the η^2-diσ(CC)-E-(s)-trans geometry the effects are apparently even larger, being ca 0.22/0.51 Å below C3 and 0.15/0.38 Å below C2. In many cases on $Pt_2Sn(111)$ the large displacements of the interacting surface atoms lead, furthermore, to a lowering of neighboring surface atoms, which was of the size of ca 0.05 Å for Pt and up to 0.16 Å for Sn.

[29] Keep in mind that this is just a "single" atom picture ignoring effects from deformations of neighbors and also displacements in the surface plane.

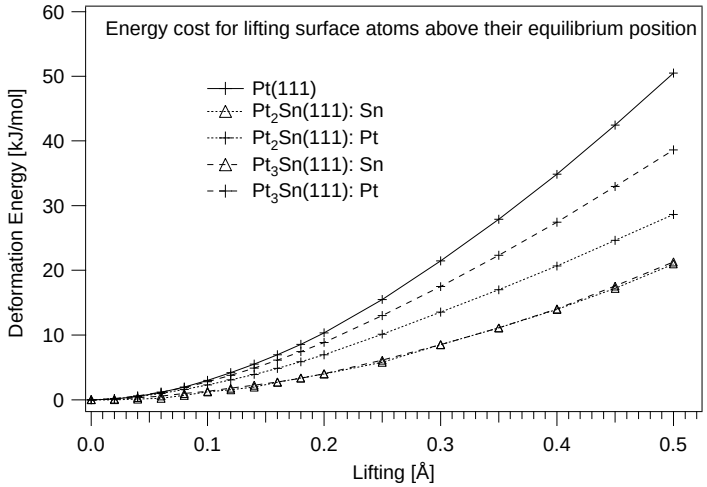

Figure 6.46: Computed DFT potential energy curves of outwards up single Pt or Sn atoms on Pt(111) ($\Theta = 1/9$), $Pt_3Sn(111)$ ($\Theta = 1/12$) and $Pt_2Sn(111)$ ($\Theta = 1/9$). In each case a only single atoms has been displaced in the direction of the surface normal.

lated on this base are -248 kJ/mol for the η^2-diσ(CC)-E-(s)-trans structure (Pt_3Sn: -222 kJ/mol, Pt(111): -273 kJ/mol), -246 kJ/mol for η^3-diσ(CC)-σ(O)-E-(s)-cis-OSn (-230/-266 kJ/mol) and -202 kJ/mol for η^4-π(CC)-diσ(CO)-E-(s)-cis-OSn (-189/-233 kJ/mol).

Importantly, this shows clearly that the simple picture of decreasing bond strengths with increasing *d*-band shift and charge transfer from Sn to Pt [45], from which one would expect the adsorption energy to decrease systematically with increasing Sn fraction for an alkene acting mainly as electron donor, is not valid for such complex systems any more. In fact it seems that the factors causing a decrease of the adsorption strength are more complicated and require a detailed study of the corresponding energetic contributions.

6.3.3 HREELS Experiments

On the $Pt_2Sn(111)$ surface alloy a similar behavior as on Pt_3Sn is found. The experimental HREELS spectra of 4.7L crotonaldehyde adsorbed at 100 K and annealed to higher temperatures are presented in Fig. 6.47. A high coverage phase, which is detected by HREELS after a flash to 155 K, can be explained with η^2-diσ(CC)-E-(s)-trans and η^2-diσ(CC)-E-(s)-cis structures. This is consistent with their relative stabilities. As discussed in the previous Sec. 6.3.2, the latter geometries are computed to be the most stable species at a high theoretical coverage of 1/6 ML. After annealing the sample further to 200 K, a partial desorption of intact crotonaldehyde (TPD: α_2 at ca 170 K) accompanies an overall reshaping of the fingerprint region in HREELS. The HREELS data at 200 K resemble the shape found for crotonaldehyde on the Pt_3Sn surface alloy at the same temperature. Thus it is not surprising that also on $Pt_2Sn(111)$ the low coverage phase (more exactly: high temperature phase) corresponds to a mixture of the η^2-diσ(CC)-E-(s)-trans, the η^3-diσ(CC)-σ(O)-E-(s)-cis-OSn and the η^4-π(CC)-diσ(CO)-E-(s)-cis-OSn adsorption complexes.

By comparison of the HREELS measurements after annealing to 155 K (Fig. 6.48) with those performed on Pt_3Sn at 160 K several small changes are recognized. While the intensities of the bands at 924 cm^{-1}, 977 cm^{-1}, 1029 cm^{-1} and 1646 cm^{-1} are not very strong, significant discrepancies of the intensities relative to the rest of the spectrum show up that can be correlated with the transition of a mixed phase of η^1 and η^2 structures on the Pt_3Sn surface alloy to a phase consisting of η^2-diσ(CC) structures on Pt_2Sn.
The increase in the intensity of the loss peak at 977 cm^{-1} is explained by the intense γ(C2H2) normal mode of the η^2-diσ(CC)-E-(s)-trans form computed at 972 cm^{-1} (see Tab. 6.35 for the

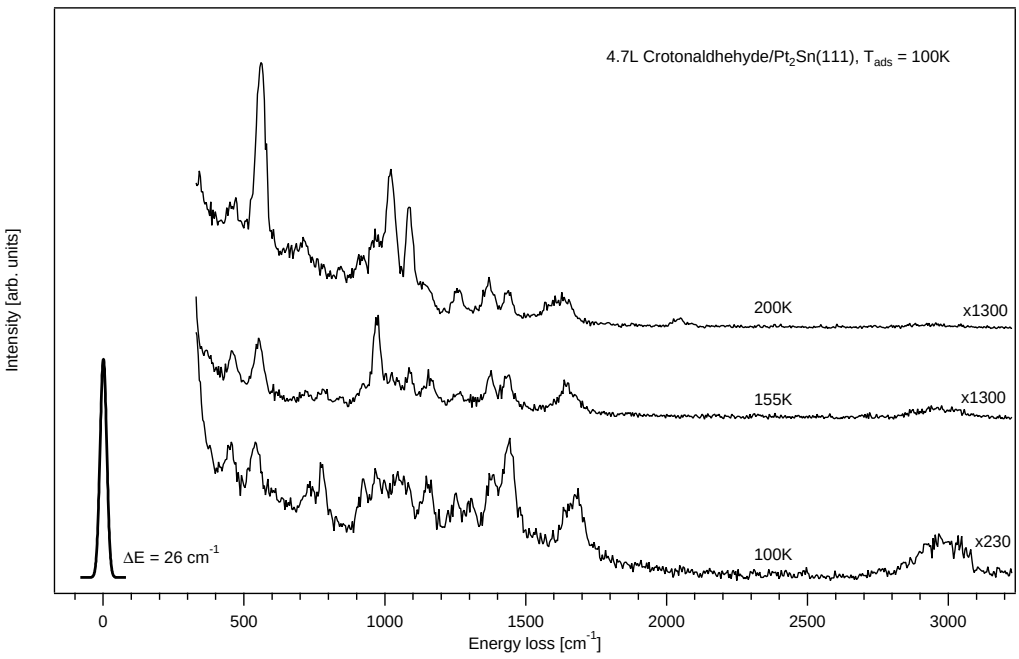

Figure 6.47: A series of HREEL spectra recorded after an exposure of 4.7L crotonaldehyde to the $Pt_2Sn(111)$ surface alloy at 100 K and subsequent annealing steps up to 200 K. The HREEL spectra have been recorded in specular geometry at a 60° angle of incidence with a primary energy of 4.7 eV.

assignments) and the highly intense ν(C1-C2) stretching vibration of the η^2-diσ(CC)-E-(s)-cis complex at 984 cm^{-1} (Tab. 6.36). Despite rather small shifts from the intense bands of the η^2 structures calculated at a low coverage on Pt_3Sn (999 cm^{-1} and 965 cm^{-1}), the assignment of the leading components of the normal modes is slightly changed here.
In contrast to the increase of intensity at 977 cm^{-1}, the experimental loss signals at 924 cm^{-1} and 1029 cm^{-1} are damped on $Pt_2Sn(111)$. Concommitantly the loss peak at 1646 cm^{-1} becomes less symmetric and somewhat weaker, but still remains as broad as on Pt(111) or Pt_3Sn (FWHM is 90 cm^{-1} from ca 1600 cm^{-1} to 1690 cm^{-1}).
This group of signals was assigned primarily to the dominant η^2-diσ(CC)-E-(s)-trans and η^2-diσ(CC)-E-(s)-cis structures on the $Pt_3Sn(111)$ surface alloy. Moreover a small fraction of the two η^1-top-E-(s)-trans-OSn adsorption complexes was adducted to explain the discrepancy between the comparably large measured intensities of these peaks and the rather weak computed ones for the corresponding normal modes of the η^2 forms.
Consequently the deterioration of the three loss signals in this case can be understood as an indicator of the absence of any such η^1-top-OSn form, which is not even stable in the DFT optimizations on this surface alloy. Furthermore, since the overall shape and intensity of this spectrum is not completely different from the one on Pt_3Sn, again the necessity for only a small fraction of the η^1 structures on $Pt_3Sn(111)$ is underlined.
Besides a big loss signal growing out of the elastic peak at 311 cm^{-1}, two broad and intense bands at 557 cm^{-1} and 465 cm^{-1} are recorded in the low frequency part of the spectrum. Identical to the assignment on $Pt_3Sn(111)$, they are found to arise from vibrational modes of both η^2 bonded crotonaldehyde species. The η^2-diσ(CC)-E-(s)-trans complex contributes the asymmetric ν_{as}(PtC2-PtC3) vibration computed with sizable dynamical dipole moment at 531 cm^{-1} (Pt_3Sn: 524 cm^{-1}) and the δ(C2=C3-C4) backbone deformation mode at 473 cm^{-1} (467 cm^{-1}). From the isomeric E-(s)-cis complex again the asymmetric and the symmetric ν(PtC2-PtC3) molecule-surface stretching vibrations contribute to experimental data. They are calculated at 564 cm^{-1} (Pt_3Sn: 548 cm^{-1}) and at 468 cm^{-1} (452 cm^{-1}), respectively. Evidently the different substrate and the variation of the coverage hardly influence the frequencies for the η^2-E-(s)-trans structure. This is rationalized by the deformation energies of the molecule, which are very similar on both surface alloys (149 kJ/mol on Pt_3Sn, 158 at $\Theta = 1/6$ on Pt_2Sn). The same phenomenon is observed for the frequencies of the E-(s)-cis form, which are shifted typically by ca 16 cm^{-1} and, hence, point to a weaker bonding in the small supercell on Pt_2Sn as compared to the low coverage on $Pt_3Sn(111)$.
The shoulder visible in the HREEL spectrum at 924 cm^{-1} must be assigned to the in-phase coupling of the symmetric γ_s(C1H1-C2H2) vibrations with the γ(C3H3) mode computed at 938 cm^{-1} and the corresponding anti-phase linear combination at 907 cm^{-1}. At 1090 cm^{-1} the sizably intense ν(C3-C4) stretching vibration of the methyl substituent tilted away from this surface in the η^2-diσ(CC)-E-(s)-cis coordination type and the ν(C2=C3) mode of the isomeric E-(s)-trans form are measured in agreement with the calculated frequencies of 1095 cm^{-1} and 1088 cm^{-1}, respectively.
Probably due to their quasi coplanar orientation, the remaining C-C stretching modes are mostly weak. They are computed at 1037 cm^{-1} (ν(C1-C2)) and 1002 cm^{-1} (ν(C3-C4)) for the η^2-diσ(CC)-E-(s)-trans form and at 1125 cm^{-1} (ν(C2=C3)) and 984 cm^{-1} (ν(C1-C2)) for the E-(s)-cis isomer. Except for the ν(C3-C4) vibration of the η^2-E-(s)-trans, where caused by a different coupling of the modes it is the leading contribution of the softer normal mode at 1002 cm^{-1}, the frequencies are perturbed by less than ca 15 cm^{-1} from the values computed for the more stable counterparts on Pt(111) and are thus consistent with the arguments derived from the energetic analysis.
A problem arises for the measured loss peak at 1162 cm^{-1}. From the computed HREELS data this peak can be assigned to the γ"(CH_3) vibration of the η^2-E-(s)-trans form computed at 1124 cm^{-1} and the ν(C2=C3) stretching mode of the related E-(s)-cis form at 1125 cm^{-1}.

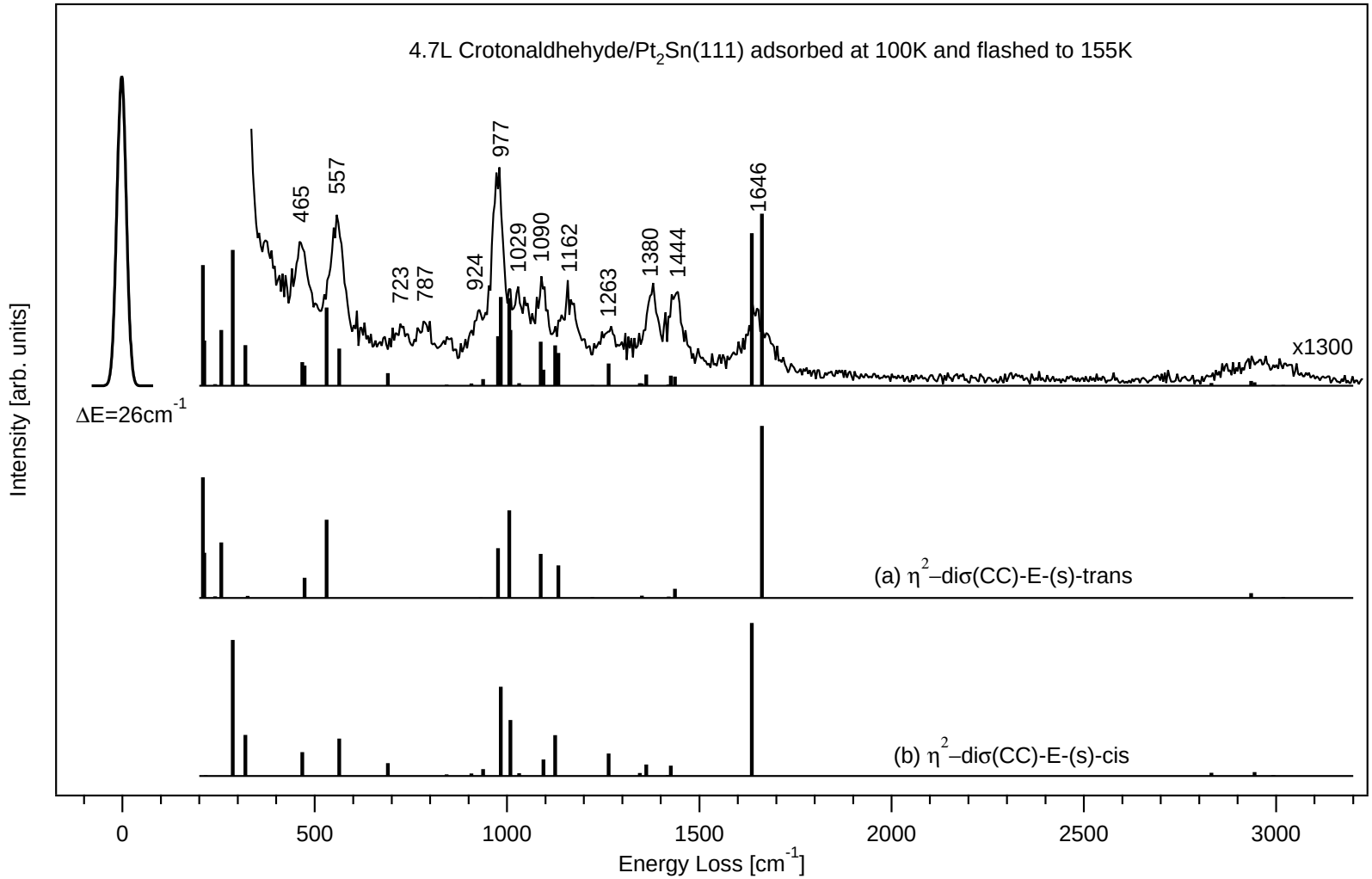

Figure 6.48: Comparison of the computed DFT HREEL spectra for the most stable adsorption structures with experimental spectrum of 4.7L crotonaldehyde exposure to a $Pt_2Sn(111)$ surface alloy annealed to 155 K after adsorption at 100 K.

The frequencies therefore show a misfit of about 3% to the experimental value, which is unusually large in comparison to the typical error of 1%.
On the $Pt_3Sn(111)$ surface alloy, a similar problem was solved previously by taking into account the η^1-top-OSn adsorption complex that provided an intense loss signal at 1157 cm^{-1} good in agreement with the measured peak at 1156 cm^{-1}. Since the corresponding η^1 coordination type is not stable on $Pt_2Sn(111)$, this discrepancy cannot be understood with the present theoretical analysis based on the harmonic approach. Nonetheless, by the comparison of the convoluted vibrational spectra of the η^2-diσ(CC)-E-(s)-trans and the η^2-diσ(CC)-E-(s)-cis forms with the recorded HREELS data (see App. B.4, Fig. B.5) a good agreement is found for this system.

Upon the transformation induced by annealing the sample to 200 K, the experimental spectra are dominated by three loss signals at 1090 cm^{-1}, 1021 cm^{-1} and 561 cm^{-1}. On Pt_3Sn basically the same signals were detected at 1090 cm^{-1}, 1021 cm^{-1} and 561 cm^{-1}. The bands at 1090 cm^{-1} and 1021 cm^{-1} are assigned to ν(C2=C3) of the η^2-diσ(CC)-E-(s)-trans geometry (DFT: 1081 cm^{-1}) and to the γ"(CH_3) vibrations of the η^3-diσ(CC)-σ(O)-E-(s)-cis-OSn (1016) and η^4-π(CC)-diσ(CO)-E-(s)-cis-OSn (1015 cm^{-1}) adsorption sites, respectively, combined with ν(C3-C4) of the η^2 form (1002 cm^{-1}).
A closer look at the optimized geometry of the η^2 complex reveals, why the ν(C2=C3) and ν(C3-C4) modes are obtained at softer frequencies and with a little increased intensity in this case relative to Pt(111). The reason of this phenomenon is twofold. Firstly, a coupling of these normal modes with the asymmetric ν_{as}(PtC2-PtC3) stretch is found, explaining the increase of intensity. Secondly, a specific coupling results from the presence of Sn. As discussed previously, on Pt_2Sn a weakening of the interactions and consequently a lengthening of the Pt-C bonds is calculated. At the same time the Pt-Pt bond interacting with C=C is strengthened as evidenced by a shorter distance of 2.71 Å on Pt_2Sn compared to 2.82 Å on Pt(111). The result is a distortion of the adsorption geometry, in which the C2=C3 axis is no longer parallel to the Pt-Pt axis and the C=C-C=O dihedral angle (146°) is closer to the gas phase value (180°) than for the related structure on Pt(111) (137°). Such a distortion accounts for a resonance between the ν(C2=C3) and ν(C3-C4) vibrations on Pt_2Sn and thus for the low frequency shift observed for ν_{as}(C3-C4). Less intense, the ν(C2=C3) vibration of the η^3 structure has a calculated value of 1120 cm^{-1}.
In accordance with the much weaker π-type interaction mechanism of the C2=C3 bond with the surface, the corresponding normal mode of the η^4-π(CC)-diσ(CO)-E-(s)-cis-OSn form is obtained at 1459 cm^{-1}. Despite of the significant decrease of the adsorption energy of this structure from -41.7 kJ/mol Pt_3Sn to -29.0 kJ/mol on this surface, the computed vibrations are very similar for this coordination type, too. Again the separation of the adsorption energy shows that the distortion cost of the molecule does not vary much (113 kJ/mol here vs. 110 kJ/mol on Pt_3Sn) and confirms this finding.
Also on $Pt_2Sn(111)$ the effect of the additional alloy component Sn on the adsorption is especially pronounced in the low frequency region below 600 cm^{-1}, representing the ν(M-C) and ν(M-O) stretching modes and the molecular bending and torsional modes that are very sensitive to geometrical changes.
While on Pt(111) a broad band between 460 and 540 cm^{-1} was observed, on $Pt_2Sn(111)$ it becomes narrower and much more intense at 561 cm^{-1}. According to DFT, the corresponding asymmetric stretching modes ν_{as}(PtC2-PtC3) of the identified adsorption complexes result in one dominant and well defined loss peak at 525 cm^{-1} for the η^2 and the η^3 complexes and at 515 cm^{-1} for the η^4 form. This low frequency shift is in excellent agreement with the decrease of the molecule-surface interaction strength.
Therefore DFT supports the argumentation that the presence of Sn reduces remarkably the number of competitive adsorption forms on both Pt-Sn surface alloys and increases the intensity in the molecule-metal frequency region. The higher loss intensities measured for this peak on the

ω cm^{-1}	Intensity $\times 10^6$ au		ω cm^{-1}	Intensity $\times 10^6$ au		Normal mode
$\Theta = 1/9$ ML			$\Theta = 1/6$ ML			
3051	0.008		3056	0.002		ν_{as}(C3-H4,5)
3011	0.055		3018	0.046		ν_s(C3-H4,5)
3007	0.022		3009	0.025		ν(C2-H2)
2962	0.006		2967	0.002		ν(C3-H3)
2936	0.22		2935	0.33		ν(C4-H4)
2750	0.001		2800	0.025		ν(C1-H1)
1661	10.0	vs	1663	11.4	vs	ν(C1=O)
1434	0.43		1437	0.61		δ'(CH_3)
1422	0.007		1421	0.096		δ"(CH_3)
1361	0.016		1347	0.025		δ_s(C1H1-C2H2)
1352	0.16		1351	0.16		u(CH_3)
1327	0.044		1324	0.004		δ_{as}(C1H1-C2H2)-δ(C3H3)
1221	0.002		1222	0.049		δ_{as}(C1H1-C2H2)+δ(C3H3)
1124	1.34	w	1133	2.2	w	γ"(CH_3)
1081	3.4	m	1088	2.9	m	ν(C2=C3)
1037	0.004		1037	0.025		ν(C1-C2)
1002	6.2	s	1006	5.8	s	ν(C3-C4)
972	2.4	m	977	3.3	m	γ(C2H2)
940	0.078		927	0.007		γ(C1H1)
925	0.11		931	0.039		γ(C3H3)
884	0.001		888	0.002		γ'(CH_3)
556	0.077		567	0.009		δ(O=C1-C2)
525	5.4	s	531	5.2	s	ν_{as}(PtC2-PtC3)
469	1.1	w	473	1.4	w	δ(C2=C3-C4)
328	0.014		326	0.14		ν_s(PtC2-PtC3)
261	6.8	s	257	3.7	m	τ(C1-C2)
245	0.44		241	0.11		δ(C1-C2=C3)
221	1.2	w	213	3.0	m	τ(CH_3)
203	0.24		210	8.0	vs	τ(C2=C3)
127	1.4		152	0.95		fT
88	1.3		103	10.2	vs	fR
80	12.0	vs	100	0.95		fR
35	2.3		33	1.3	w	fR

Table 6.35: Vibrational analysis of the η^2-diσ(CC)-E-(s)-trans structure of crotonaldehyde on Pt_2Sn(111) at high ($\Theta = 1/6$ ML) and low coverage ($\Theta = 1/9$ ML).

ω cm^{-1}	Intensity $\times 10^6$ au		Normal mode
3059	0.016		ν_{as}(C3-H4,5)
3021	0.002		ν_s(C3-H4,5)
3005	0.004		ν_{as}(C2H2-C3H3)
2992	0.057		ν_s(C2H2+C3H3)
2944	0.24		ν(C6-H6)
2832	0.19		ν(C1-H1)
1636	10.2	vs	ν(C1=O)
1426	0.67		δ'(CH_3)
1418	0.054		δ"(CH_3)
1362	0.75		δ_{as}(C2H2-C3H3)
1350	0.0		δ_s(C2H2-C3H3)+δ(C1H1)
1345	0.18		u(CH_3)
1265	1.5		δ_s(C2H2-C3H3)-δ(C1H1)
1125	2.7	m	ν(C2=C3)
1095	1.1		ν(C3-C4)
1031	0.17		γ_{as}(C1H1-C2H2)
1009	3.7		γ"(CH_3)
984	5.9	s	ν(C1-C2)
938	0.45		γ_s(C1H1-C2H2)+γ(C3H3)
907	0.16		γ_s(C1H1-C2H2)-γ(C3H3)
843	0.084		γ'(CH_3)
691	0.85		δ(O=C1-C2)
564	2.5	m	ν_{as}(PtC2-PtC3)
468	1.6		ν_s(PtC2-PtC3)
320	2.7	m	δ(C2=C3-C4)
287	9.0	vs	δ(C1-C2=C3)
253	0.016		τ(C1-C2)
216	0.038		τ(CH_3)
192	0.77		τ(C2=C3)
133	6.4	s	fR
118	0.092		fT
94	0.055		fR
79	0.82		fT

Table 6.36: Vibrational analysis of the η^2-diσ(CC)-E-(s)-cis structure of crotonaldehyde on $Pt_2Sn(111)$ (theoretical coverage $\Theta = 1/6$).

surface alloys can be understood from another change in the coupling pattern of the η^4-π(CC)-diσ(CO)-E-(s)-cis-OSn form, which is due to a distortion of the adsorption geometry enforced by the protrusion of the Sn. The ν_{as}(PtC2-PtC3) vibration becomes more active here because of an additional coupling to the ν(Sn-O) stretching mode.
Moreover around 280 cm^{-1} a highly intense and broad loss signal is measured (FWHM 100 cm^{-1}), which is shifted from the value of 259 cm^{-1} on Pt_3Sn. Since essentially all identified adsorption complexes show comparably active normal modes in this region, the width and intensity of this peak can be rationalized easily. The torsional mode τ(C1-C2) of the η^2 form, which draws a large dynamical dipole moment from the lifting of the oxygen, is computed at 261 cm^{-1}. The η^3 structure augments the intensity with the symmetric ν_s(PtC2-C3) (DFT: 322 cm^{-1}) and the ν(Sn-O) modes (313 cm^{-1}). Finally the second active molecule-surface stretching mode of the four linear combinations assigned for the η^4 species, the ν_s(PtO-PtC1)-ν_s(PtC2-PtC3) normal mode that shows an anti-symmetric lifting and weakening of the O=C1 and the C2=C3-CH_3 moieties, respectively, is also calculated with a frequency close to 310 cm^{-1}.
Although all adsorption complexes contribute in this low frequency region, the resolution of the HREELS experiments and the larger errors of the harmonic analysis of low frequency modes decoupled from the surface phonons hinders the assignment of the three surface components here. The redshift of the experimental peak from 311 cm^{-1} at 155 K to 280 cm^{-1}, which might indicate a reduction of the interaction strength to the surface, cannot be understood without further in-depth investigations on a thicker model slabs with inclusion of the surface phonons.

In summary the results of the vibrational investigations of the adsorption of crotonaldehyde on the Pt_2Sn(111) surface alloy show an adsorption behavior similar to Pt_3Sn(111). The increase surface fraction of Sn leads to a reduction of the number of competitive adsorption structures and, hence, to a simplification of the measured HREEL spectra compared to the other surfaces. Curiously the absolute adsorption energies for the stable structures compare very well on both the surface alloys. This is in fact counterintuitive as a decrease of the adsorption strength with rising surface Sn concentration was expected. The deformation energies of the surface induced by adsorption are larger on Pt_2Sn(111) (around 62 kJ/mol) than on Pt(111) (54 kJ/mol) or Pt_3Sn(111) (38 kJ/mol), which is due to the additional displacements of the Pt and Sn atoms in the surface plane here. Also this is very surprising because according to physical intuition Pt_3Sn should be more similar in its properties to Pt(111), because of the higher Pt fraction as compared to Pt_2Sn.
In contrast, the deformation costs of the molecule, which depend primarily on the coordination type rather than on the considered surface, are very similar (on average 132, 139 and 132 kJ/mol for the flat complexes on Pt, Pt_3Sn and Pt_2Sn(111), respectively). These are confirmed by the similarity of the vibrational spectra and geometrical parameters that are observed for a given coordination type on all three surfaces. Although the normal modes with frequencies above 500 cm^{-1} permit to differentiate between the various structures, the changing adsorption strengths seem to influence only the vibrations in the molecule-surface stretching region below 500 cm^{-1} sizably.
Together the deformation terms and the adsorption energies allow to deduce the interaction strength and give deeper insights into the effects of alloying the Pt(111) surface with Sn. Like the surface deformation energy these do consequently not vary continuously between Pt(111) and Pt_2Sn, but are very specific for each surface. From an average of ca -260 kJ/mol on Pt(111), the interaction strength decreases by 10% to ca -230 kJ/mol for the related η^2, η^3 and η^4 forms on Pt_2Sn and yet even more to ca -220 kJ/mol (20%) on the Sn-poorer Pt_3Sn(111) surface.
Since the geometries of the free surfaces and the adsorption complexes of the corresponding η^2, η^3 and η^4 forms on all surfaces are very similar, an important conclusion can be drawn here: The broken trend of the surface deformation energies and the interaction strengths must originate from the different electronic properties of the three model catalyst surfaces.

ω cm^{-1}	Intensity $\times 10^6$ au		Normal mode
3049	0.001		ν_{as}(C3-H4,5)
3041	0.048		ν(C2-H2)
3006	0.18		ν_s(C3-H4,5)
2986	0.014		ν(C3-H3)
2937	0.31		ν(C1-H1)
2930	0.61		ν(C6-H6)
1451	2.1	w	ν(C1=O)
1429	0.64		δ'(CH_3)
1422	0.021		δ"(CH_3)
1378	0.38		δ_s(C2H2-C3H3)
1353	0.073		u(CH_3)
1307	1.0		δ(C1H1)
1257	0.98		δ_{as}(C2H2-C3H3)
1125	0.44		ν(C2=C3)
1078	1.1	w	ν(C3-C4)
1035	0.33		ν(C1-C2)
1016	5.0	m	γ"(CH_3)
935	0.29		γ_{as}(C1H1-C2H2)-γ(C3H3)
924	0.024		γ_{as}(C1H1-C2H2)+γ(C3H3)
871	2.9	m	γ_s(C1H1-C2H2)
832	0.34		γ'(CH_3)
698	0.0		δ(O=C1-C2)
526	7.6	s	ν_{as}(PtC2-PtC3)
409	0.48		δ(C2=C3-C4)
322	10.9	vs	ν_s(PtC2-C3)
313	13.1	vs	ν(Sn-O)
247	2.5	w	δ(C1-C2=C3)
231	0.005		τ(CH_3)
187	1.5		τ(C1-C2)
152	1.2		τ(C2=C3)
115	0.17		fT
94	1.8		fT
90	0.41		fR

Table 6.37: Vibrational analysis of the η^3-diσ(CC)-σ(O)-E-(s)-cis-OSn structure of crotonaldehyde on $Pt_2Sn(111)$ (theoretical coverage $\Theta = 1/9$).

ω cm^{-1}	Intensity $\times 10^6$ au $\Theta = 1/9$ ML		ω cm^{-1}	Intensity $\times 10^6$ au $\Theta = 1/6$ ML		Normal mode
3068	0.0		3078	0.007		ν_{as}(C2H2-C3H3)
3055	0.028		3066	0.058		ν_s(C2H2-C3H3)
3043	0.001		3044	0.002		ν_{as}(C3-H4,5)
3011	0.035		3013	0.051		ν(C6-H6)
2951	0.065		2953	0.078		ν(C1-H1)
2938	0.37		2940	0.66		ν_s(C3-H4,5)
1459	0.072		1460	0.13		ν(C2=C3)
1431	0.61		1433	0.61		δ'(CH_3)
1417	0.038		1417	0.001		δ"(CH_3)
1359	0.042		1352	0.052		u(CH_3)
1311	0.090		1308	0.043		δ(C1H1)
1261	0.045		1268	0.033		δ_{as}(C2H2-C3H3)
1209	0.40		1204	0.30		δ_s(C2H2-C3H3)
1158	1.1	vw	1156	0.48		ν(C1=O)
1086	0.16		1086	0.20		ν(C3-C4)
1015	1.8	w	1015	1.6	w	γ"(CH_3)
981	1.0	vw	982	0.007	vw	ν(C1-C2)
963	3.0	w	998	2.9	w	γ_s(C2H2-C3H3)
892	0.15		899	0.087		γ_{as}(C2H2-C3H3)
853	0.63		851	0.93		γ'(CH_3)
783	0.62		789	0.34		γ_s(C1H1)
662	0.43		669	0.28		δ(O=C1-C2)
519	14.3	vs	511	14.2	vs	ν_{as}(PtO-PtC1)-ν_{as}(PtC2-PtC3)
401	0.66		396	0.97		ν_{as}(PtO-PtC1)+ν_{as}(PtC2-PtC3)
388	0.002		390	0.33		δ(C2=C3-C4)
310	2.0	w	313	3.2	w	ν_s(PtO-PtC1)-ν_s(PtC2-PtC3)
245	0.56		246	1.6	vw	ν_s(PtO-PtC1)+ν_s(PtC2-PtC3)
239	0.16		223	0.082		δ(C1-C2=C3)
218	0.27		203	0.0		τ(CH_3)
179	1.1	vw	170	0.73		τ(C2=C3)
156	0.031		144	0.63		τ(C1-C2)
99	0.93		95	0.64		fT
85	0.39		70	0.11		fR

Table 6.38: Vibrational analysis of the η^4-π(CC)-diσ(CO)-E-(s)-cis-OSn structure of crotonaldehyde on Pt_2Sn(111) at high ($\Theta = 1/6$ ML) and low coverage ($\Theta = 1/9$ ML).

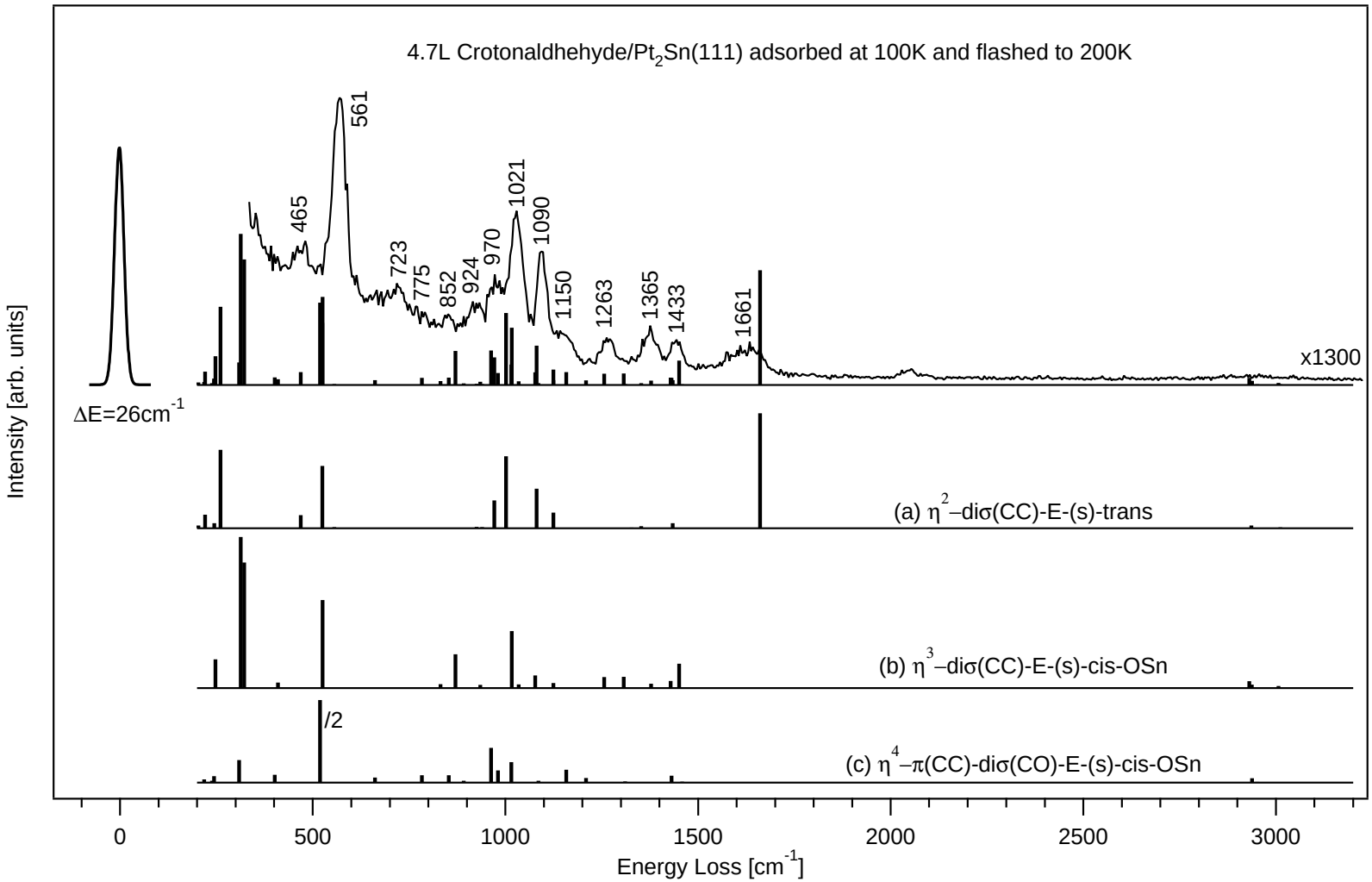

Figure 6.49: Comparison of the computed DFT HREEL spectra for the most stable adsorption structures with experimental spectrum of 4.7L crotonaldehyde exposed to a $Pt_2Sn(111)$ surface alloy annealed to 200 K after adsorption at 100 K.

6.4 Summary of the Most Important Results of the Crotonaldehyde Adsorption on Pt(111), $Pt_3Sn(111)$ and $Pt_2Sn(111)$ surface alloys

Pt(111):

- The combination of HREELS and DFT leads to the identification of the η^2-diσ(CC)-E-(s)-trans, η^2-diσ(CC)-E-(s)-cis, η^3-diσ(CC)-σ(O)-E-(s)-cis, η^4-diσ(CC)-diσ(CO)-E-(s)-trans and the η^4-π(CC)-diσ(CO)-E-(s)-cis structures. These stable coordination types show very similar adsorption energies and exhibit related, but characteristic vibrational fingerprints.
- Above 250 K the decomposition of irreversibly adsorbed crotonaldehyde species is detected by TPD with the desorption of CO (395 K) and H_2 (ca 310 and 425 K).
- The analysis of the HREEL spectra of the decomposition process with DFT points to five reaction intermediates that seem to be sufficiently stable for a detection. In the sequence of their appearance during the decomposition pathway proposed these are the dehydro-η^3-E-crotonaldehyde-H1 radical, the η^2-propyne, η^1-propylidyne, η^1-ethylidyne and finally the η^1-methylidyne surface species.

$Pt_3Sn(111)$ and $Pt_2Sn(111)$:

- While on the Pt_3Sn surface alloy a similar behavior as on Pt(111) was found, the weaker adsorption on Pt_2Sn results in a monolayer desorption at ca 236 K.
- On both surfaces a high coverage phase with structures of low hapticity such as η^1 and η^2 is measured at low temperatures (160 K and 155 K, resp.) and a low coverage situation of high hapticity forms is formed at higher temperatures (200 K).
- From the theoretical analysis the high coverage phase is concluded to consist of the η^2-diσ(CC)-E-(s)-trans and η^2-diσ(CC)-E-(s)-cis structures on both surface alloys. On Pt_3Sn the energetically competitive η^1-top-E-(s)-trans-OSn forms cannot be excluded.
- The low coverage mixed phase observed on both surfaces at 200 K is nearly identical. It is attributed to the η^2-diσ(CC)-E-(s)-trans, the η^3-diσ(CC)-σ(O)-E-(s)-cis-OSn and the η^4-π(CC)-diσ(CO)-E-(s)-cis-OSn adsorption complexes. On Pt_3Sn also the η^2-diσ(CC)-E-(s)-cis structure, which is not stable on Pt_2Sn, is present.
- The alloying with Sn leads to a simplification of the mixed adsorbate phases and to a decrease of the interaction strengths. Slight distortions of the adsorption geometries due to changes of the substrate induced by protruding Sn lead to a slightly different coupling of the normal modes and to small frequency shifts and intensity variations. The general correlation of the vibrational frequencies of atoms involved in surface bonding to the adsorption energies is no longer valid for complex, multifunctional molecules. The adsorption energy has to be decomposed into deformation contributions of the molecule and the surface plus the interaction term of both in order to understand the vibrational properties.
- The different properties of Pt(111), Pt_3Sn and Pt_2Sn are primarily due to electronic effects. The adsorption energies on the surface alloys are very similar, but about 20-30% smaller than on Pt(111). The interaction strength and the deformation cost of the surface do not exhibit a constant trend, but are specific for each surface. The surface atom displacements from the equilibrium positions induced by crotonaldehyde increase in the sequence Pt(111), Pt_3Sn and Pt_2Sn.

Chapter 7

The Prenal Adsorption

The second molecule, i.e. prenal (3-Methyl-2-buten-1-al), was chosen to study the effects of substitution on the adsorption and the vibrational properties. Even less is known about the properties of prenal in the literature than for crotonaldehyde. Despite the number of investigations published on the reactivity and the adsorption of α,β-unsaturated aldehydes on the Pt(111) single crystal surface and Sn-Pt surface alloys, to date there are no experimental studies known to the author neither on the adsorption and vibrational properties of prenal on these model catalyst surfaces nor the gas phase IR spectrum. Basically the only data available since the start of this thesis are from the DFT studies on the adsorption on Pt(111) by Delbecq et al. [45, 51].
Compared to crotonaldehyde, the behavior of prenal is expected to be much simpler. In the gas phase and on the surface only two isomers, namely (s)-trans and (s)-cis prenal (Fig. 7.1), have to be taken in consideration since the β-carbon is now fully substituted. This decreases the number of conceivable surface complexes greatly.

7.1 Prenal on Pt(111)

The adsorption and the vibrational properties of prenal have been studied on all three model catalyst surfaces. Before these investigations, also the gas phase properties of the molecule have been characterized in order to establish a reference.

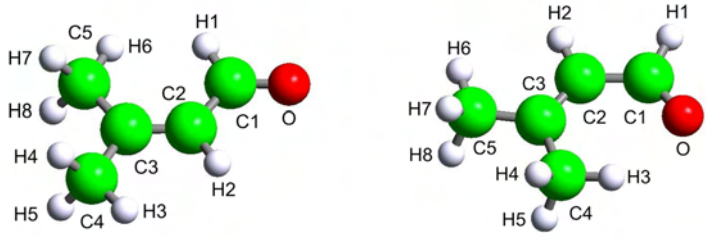

(a) (s)-trans (b) (s)-cis

Figure 7.1: The two isomers of prenal in the gas phase. Both differ only in the relative alignment of the aldehydic and the vinylic function.

In many aspects prenal behaves very similar to crotonaldehyde on Pt(111). Hence the discussions in this chapter follow the same outline. First the TPD studies (Sec. 7.1.1), which give information on subsequent desorption states and the decomposition of prenal are presented. Then the stable structures of prenal on Pt(111) obtained from the DFT calculations are discussed (Sec. 7.1.3). In combination with the HREELS measurements performed for several different initial exposures between 100 K and 500 K, the actually present prenal structures (Sec. 7.1.4) are identified and the decomposition process is characterized (Sec. 7.1.5). Finally, also deuterium coadsorption experiments have been carried out using TPD and HREELS. Like for crotonaldehyde, no deuteration is detected for prenal (Sec. 7.1.6).

7.1.1 TPD Results of Prenal/Pt(111)

The TPD studies of prenal have been conducted in a similar manner as those of crotonaldehyde. Selected exposures of prenal were adsorbed on a clean Pt(111) surface at 100 K and the sample was heated up with a heating rate of 2 K/s up to 800 K in all experiments.
Already the gas phase mass spectrum of prenal shows a complex fragmentation pattern (Fig. 7.2) that leads to a number of signals appearing simultaneously. In the present experiments, the desorption of intact prenal led to the observation of sizable signals at m/z = 84 (parental ion), 69, 55, 41 and 39. The desorption states and the decomposition processes of prenal on Pt(111) detected by TPD are very much reminiscent of the behavior of crotonaldehyde.

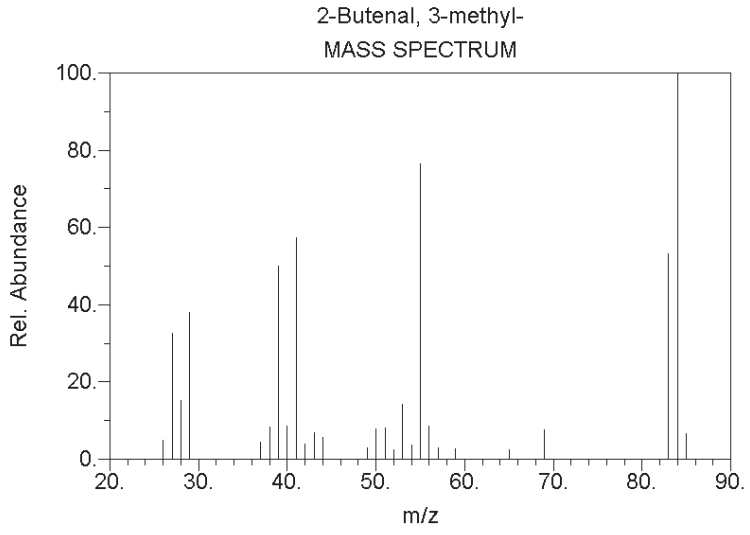

Figure 7.2: Prenal gas phase mass spectrum (electron impact ionization). The mass spectrum was taken from the NIST internet database [135].

First all desorbing mass fragments between 1 and 100 amu have been identified before they were investigated in detail as a function of exposure. Below ca 200 K prenal desorbs intact and the recorded 2D-TPD spectrum presented in Fig. 7.3 exhibits the complete signal set of 84 , 69, 55, 41 and 39 amu. Due to the high SEM voltage applied to the channeltron for detecting the otherwise relatively weak signals of prenal, high background traces arising from CO_2 (44 amu), CO/N_2 (28 amu), $H_2O/OH/O$ (18, 17 and 16 amu) and H_2 (2 amu) are recorded in this experiment. Also a small trace of m/z =70 (crotonaldehyde) that seems to be a coadsorbed

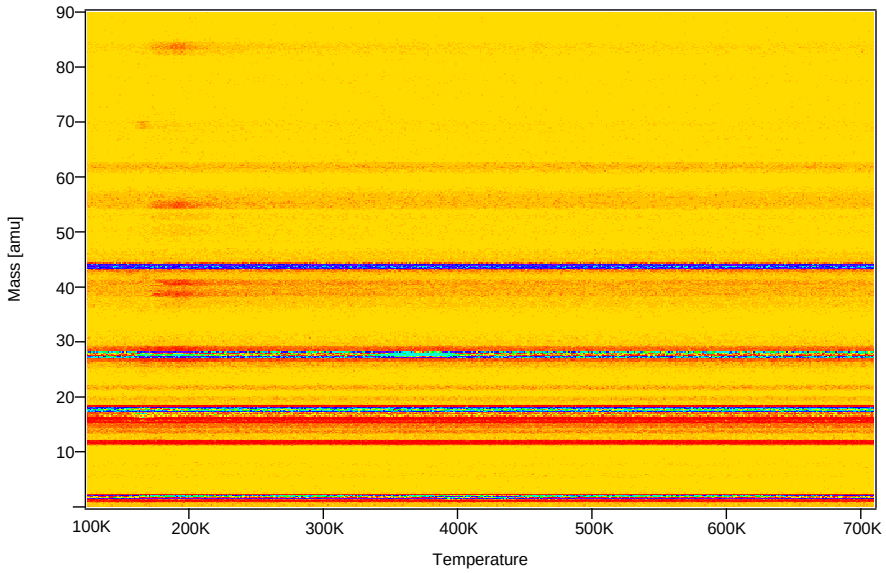

Figure 7.3: TPD experiment in the mass range of 1 to 100 amu after adsorption of 4.2L prenal on Pt(111) at 100 K. A high voltage has been applied to the SEM in order to study the weak signals of the prenal fragments in this case.

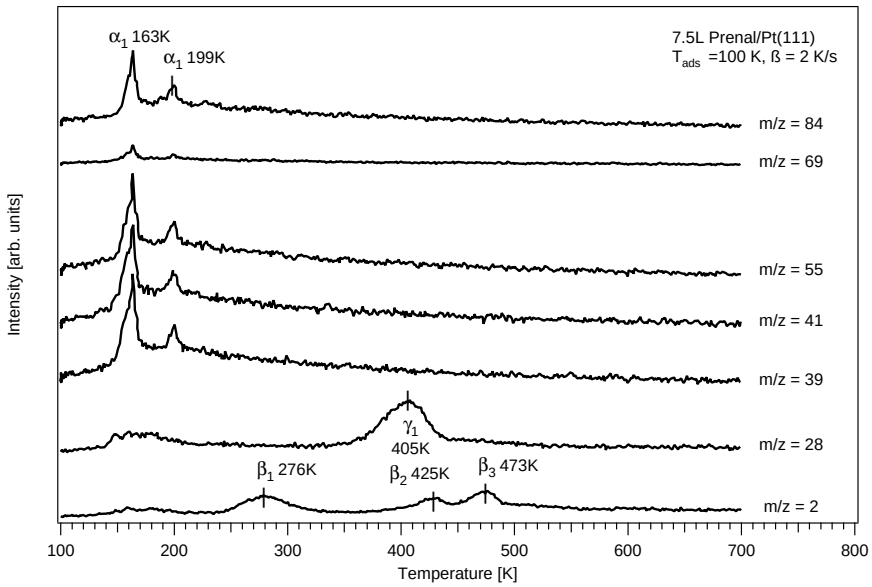

Figure 7.4: TPD experiment after adsorption of 7.5L prenal on Pt(111) at 100 K. Mind that the signals of m/z=28 and m/z=2 have been recorded with a lower channeltron voltage (sensitivity) than m/z=39,41,55,69,84.

contamination from the liquid doser is found at ca 155 K. Above 250 K the desorption states of CO and H_2 indicate again a decomposition process of the stable prenal surface species in several reaction steps. However, this decomposition process obviously does not lead to desorption of smaller hydrocarbons such as for ethene or isobutylene and, hence, must lead to a mixed phase of hydrogen-poor surface species or even surface carbon decontaminations.
In order to give a clearer overview of the general desorption and decomposition behavior of prenal on Pt(111) at this point, a combination of two TPD experiments (low SEM voltage for CO and H_2; high sensivity for the hydrocarbon fragments m/z = 39, 41, 55, 69 and 84) performed for an identical exposure of 7.5L is shown in Fig. 7.4. The appearing desorption states marked in this figure will be discussed in detail in the following paragraphs with the two experimental series performed to probe the coverage dependence of the intact desorption and the fragmentation.

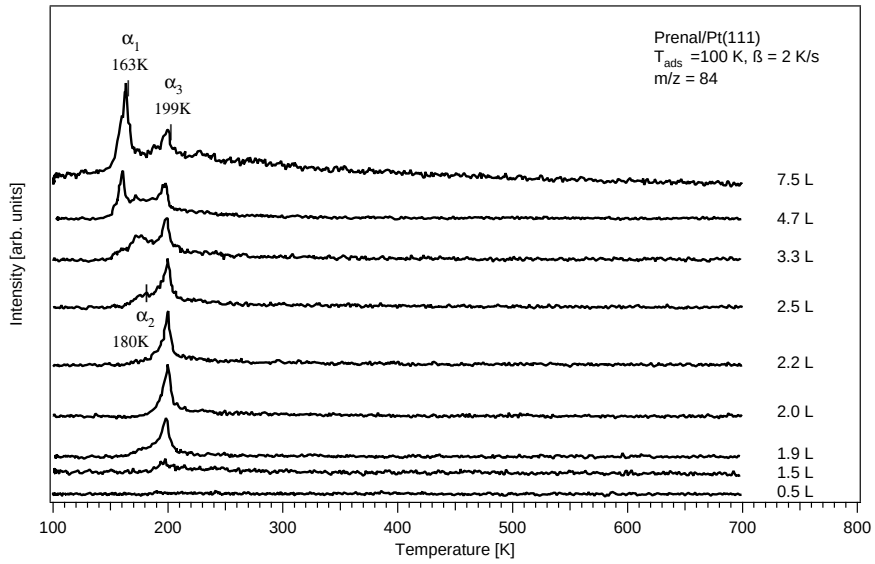

Figure 7.5: Prenal TPD spectra of m/z=84 as a function of coverage.

Like crotonaldehyde, also prenal shows three low temperature desorption states below 200 K (Figs. 7.5 and 7.6). At very low exposures below ca 1.5L, no desorption of intact prenal is observed. As will be shown in the HREELS measurements in Sec. 7.1.4, prenal is evidently irreversibly adsorbed on the Pt(111) surface in this exposure range. Starting at exposures around 1.5L a desorption state α_3 appears at 199 K that is of unknown origin. This desorption state, which is of 1^{st} order since no temperature shift of the desorption rate maximum is discerned, saturates for exposures around 2.0L as can be confirmed from the integrated peak areas. Like the corresponding desorption state of crotonaldehyde (at ca 177 K), it may be understood either as a partial desorption process accompanying a reordering on the surface or a prenal species bonded in an extrinsic adsorption state.
For exposures between 2.0L and about 3L a shoulder to this signal develops on the low-temperature side at 180 K (α_2), but cannot be resolved satisfactorily anymore for larger exposures. Here the multilayer desorption state α_1 at 163 K overlaps with the former signal.
A rough estimate of the amount of prenal correlated with the two low temperature desorption states and the irreversibly adsorbed species (that decompose above 200 K) similar to the one performed for crotonaldehyde in Chap. 6.1.1 suggests that also the majority of the adsorbed prenal is irreversibly bound, whereas the saturated reversibly bonded states α_2 and α_3 account

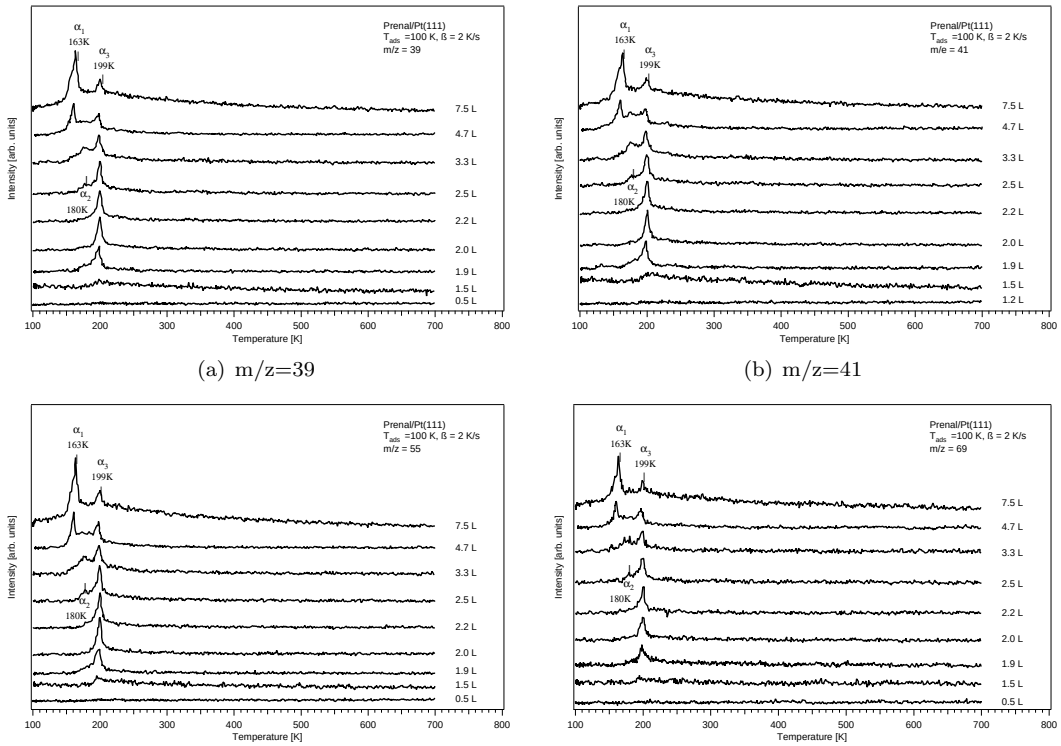

(a) m/z=39 (b) m/z=41

(c) m/z=55 (d) m/z=69

Figure 7.6: TPD spectra of prenal on Pt(111) as a function of coverage: m/z=39, 41, 55 and 69. The TPD spectra are essentially identical to the ones of the prenal parental ion (84 amu) and given here only for sake of completeness.

for less than 30% for the surface species. From the coverage dependence of the peak areas of α_2 at 177 K and α_3 at 199 K a ratio of 1:4 is estimated, which corresponds to similar exposures of ca 1L required to saturate both states subsequently after filling the irreversible monolayer with an exposure of ca 1.2L prenal. Assuming furthermore that the sticking coefficient of the strongly bonded species is unity, $\sigma(irrev.) \equiv 1$, and the one of the weaker bound prenal forms is significantly smaller, say $\sigma(\alpha_3) \equiv 0.5$, one obtains for $\sigma(\alpha_2) = \sigma(\alpha_3)/4 \approx 0.13$. From the multiplication of the required exposures with the corresponding sticking coefficients the relative amount of the surface components is estimated roughly. It shows a ratio of 10:4:1 for the irreversible, the reversible state α_3 and the badly-resolved intermediate desorption state α_2, which again underlines the dominance of the irreversibly adsorbed prenal structures and the generally only small amounts of intact desorbing prenal. This must be kept in mind for the analysis of loss intensities of the HREEL spectra recorded at low temperatures, which consequently are dominated by the vibrational properties of these strongly adsorbed prenal structures.

Using the Redhead approach [56] for a 1^{st} order desorption with a frequency factor of 10^{-13} Hz, desorption energies of 51.1 (199 K), 45.3 (177 K) and 42.4 kJ/mol (163 K) are calculated with an errorbar of 1.3 kJ/mol. The detected desorption states and their corresponding activation energies are closely related to the results of crotonaldehyde/Pt(111) discussed in Chap. 6.1.1. Generally the activation barriers of prenal are slightly larger by 5 kJ/mol than those of crotonaldehyde for each of the three desorption states, i.e. the desorption temperatures are

higher by roughly 15-20 K. This trend may also be expected from the melting and the boiling points of prenal, which at ambient pressures are higher compared to crotonaldehyde. The boiling point of prenal is ca 409 K at 760 Torr (crotonaldehyde 377 K [137]), its melting point ca 253 K [176] (CrA. 197 K [137]).

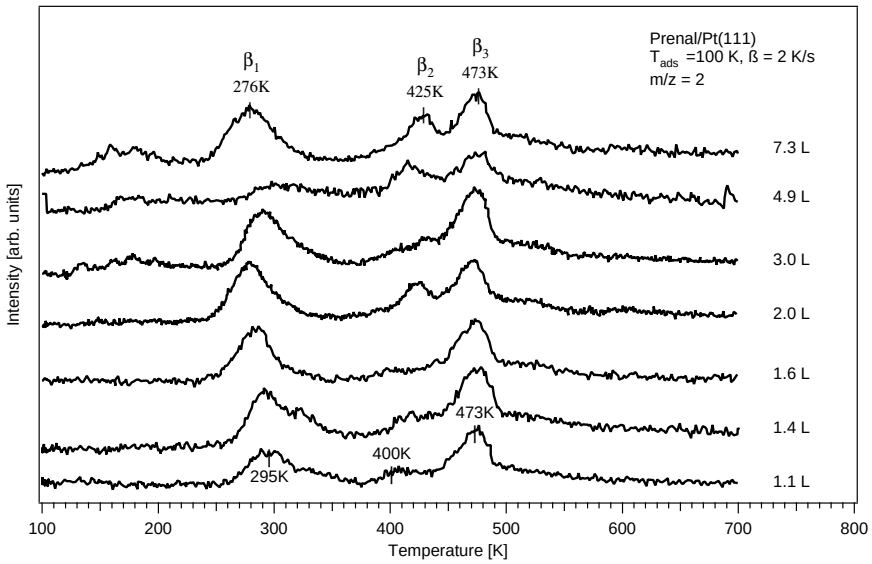

Figure 7.7: TPD spectra of m/z=2 as a function of prenal exposure.

Further TPD experiments have been carried out to investigate the thermal stability of prenal on Pt(111) and to identify subsequent fragmentation stages. Three signals of molecular hydrogen are observed around ca 280 K (β_1), 425 K (β_2) and 473 K (β_3). The desorption order of the recorded states and their coverage dependence are deduced from an exposure series between submonolayer to multilayer coverages (Fig. 7.7). Contrary to the TPD series of prenal presented above, the desorption of molecular hydrogen in all three states is found already at very low exposures.

The three desorption peak areas saturate around 1.2L in rough agreement with the first appearance of the desorption of intact prenal at 199 K (α_3). Therefore it is expected that prenal, like crotonaldehyde, forms a phase of strongly adsorbed surface complexes, which decompose above 250 K before desorption. The positions of the desorption rate maxima of H_2 show different trends in the actual experiments. While the exact temperature of the desorption state at 473 K depends only weakly on the prenal coverage, the two other signals shift from 295 K and 400 K at low exposures (1.1L) to 276 K and 425 K at high coverages. Hence it is concluded that the desorption state around 280 K is desorption limited and of 2^{nd} order. Remarkably, this peak and the signal at 473 K always show long high temperature tails. Experiments of pure H_2 on Pt(111) put the desorption of H_2 between 390 K at low exposures and 315 K at higher doses [37], which points to a temperature shift induced by repulsive lateral interactions with other surface species in this case.

Moreover, the signals at 425 K and 473 K clearly arise from the decomposition of irreversibly bound prenal on the surface and are reaction limited desorption processes. Since the relative peak areas of the signals at ca 280 K and 425 K are constant compared to the signal at 473 K, it can be excluded that the H_2 desorption observed at low temperature arises from hydrogen coadsorbed from the background during the experiments. Unlike the absolute TPD intensities,

the relative peak areas are more reproducible. The ratio of $1 : 0.7 \pm 0.3 : 1.4 \pm 0.3$ for the integrals of the peaks at ca 280 K, 425 K and 473 K, respectively, amounts to a sum of 3.1 ± 0.4. However, the determination of the peak areas is complicated by the fact that the peaks show extensive high-temperature tails. Although the number of stepwise dissociated hydrogens can often be estimated from the integration of the TPD peaks, it is not easily possible for systems like prenal or crotonaldehyde on Pt(111). In these cases the problems seem to originate from the fact that different surface species are present, which decompose in different elementary steps at similar temperatures and, thus, lead to various potential origins of hydrogen dissociation for each desorption state. Yet in combination of TPD with the HREELS results discussed in Sec. 7.1.5 it can be assumed that at least the dissociation of the aldehydic hydrogen of the stable prenal structures contributes to the desorption at 280 K here.

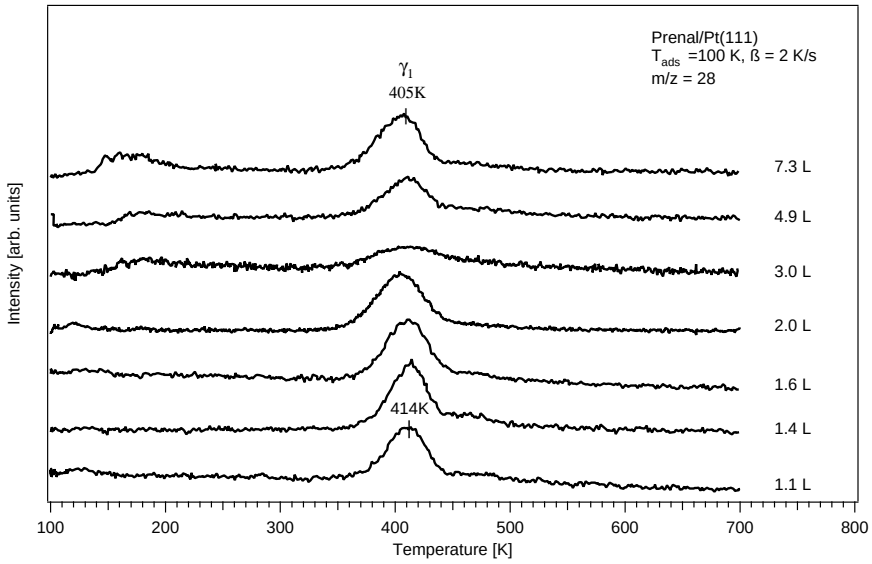

Figure 7.8: TPD spectra of m/z=28 as a function of prenal exposure.

Around 406 K desorption of CO is measured in the TPD exposure series (Fig. 7.8). Also this signal shows a saturation effect that corresponds to the filling of the irreversibly adsorbed prenal monolayer, because the peak areas are found to increase only slightly above 1.1L. The temperature shift determined for this signal from 414 K at low to 405 K at high precoverages is rather small. These determined temperatures coincide well with the desorption of intermediate amounts of pure CO from Pt(111). At very low exposures Paffett et al. [37] have observed the desorption of CO adsorbed on Pt(111) at 450 K, while at higher coverages the desorption shifts to 375 K [37].

In order to confirm the saturation effect of the CO desorption peak, coadsorption experiments with CO have been performed on clean Pt(111) surfaces for prenal, too (Fig. 7.9). First CO was adsorbed on the clean Pt(111) surface at 100 K followed by the adsorption of prenal. Already at very small CO exposures one finds an increase of the CO desorption peak area accompanied by a sizeable decrease of the desorption temperature. The CO desorption temperature of 0.9L CO coadsorbed with 2.0L prenal is lowered by ca 20 K to 389 K. Even more pronounced is the shift of the onset of this desorption signal, which lowers from ca 370 K for pure prenal (0.8L) to ca 312 K for the coadsorbed molecules (0.9L CO and 2.0L prenal). This proves that the

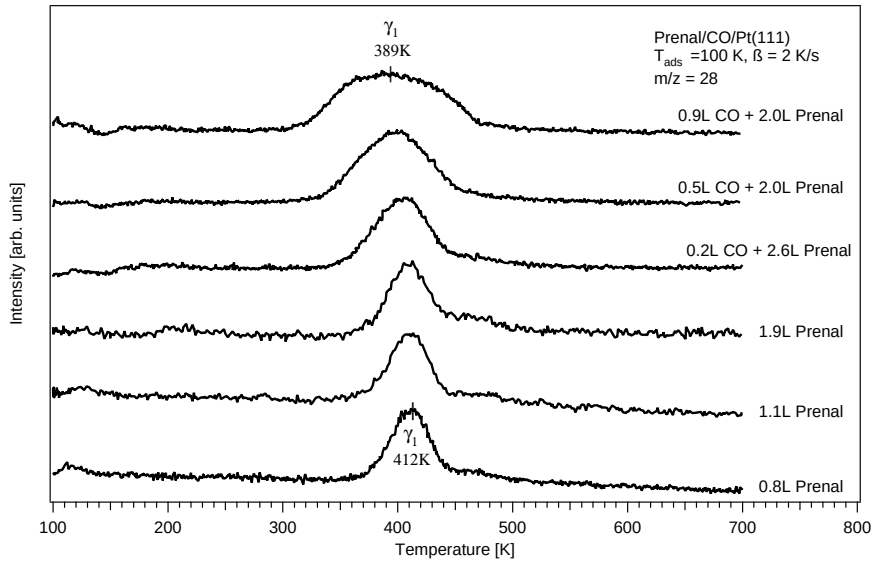

Figure 7.9: TPD spectra taken after prenal and CO coadsorption, m/z=28.

CO detected in the TPD experiments of pure prenal shown in Fig. 7.8 must arise from the decomposition of the aldehydic function of the irreversibly adsorbed prenal species.

7.1.2 Prenal in the Gas Phase and the Multilayer

In order to support the qualitative analysis of the HREEL spectra of an adsorbed multilayer of prenal, the vibrational spectra of both (s)-trans and (s)-cis prenal have been computed in the gas phase first. Like in the previous case of crotonaldehye, the gas phase geometry and the vibrational frequencies serve as a reference for the analysis of the effects of the molecule-surface interaction. Using different levels of theory and different basis sets, the relative stability of both isomers and the gas phase composition have been estimated.
The geometries of both prenal isomers were fully optimized in the framework of the Resolution-of-the-Identity [138] Density-Functional-Theory (RI-DFT) implemented in Turbomole 5 [126], using the Becke-Perdew 86 parameterization [80, 81, 83] and the Karlsruhe SVP, TZVP and TZVPP basis sets, respectively, for C, O and H. The vibrational spectra have been obtained at the RI-BP86/TZVP level. The internal coordinates of the optimized geometries are given for completeness in Tab. C.1, App. C.1 (RI-BP86/TZVP).

In comparison to the gas phase calculations of crotonaldehyde, the energetic differences between the two prenal isomers are much smaller (Tab. 7.1). Consequently the effect of the basis set size is more important here. At the RI-BP86/SVP level, the basis set is clearly insufficient. Here the (s)-cis isomer is 1.9 kJ/mol lower in energy than the (s)-trans structure, which is expected to be the ground state isomer. This trend is reversed for the larger TZVP and TZVPP basis sets, with which the (s)-cis isomer becomes slightly less stable than (s)-trans prenal (2.9 and 3.7 kJ/mol, resp.). Hence it is obvious that a correct description of the molecule in the gas phase requires a flexible basis that should be augmented with additional polarization functions. In fact also the much more extensive CCSD(T) optimization performed with Molpro [124] in a correlation-consistent cc-pVDZ basis [139] leads to a similarly wrong description of the stabilities, although

Relative energies [kJ/mol]	(s)-cis to (s)-trans	transition state
RI-BP86/SVP	-1.9	41.5
RI-BP86/TZVP	2.9	39.9
RI-BP86/TZVPP	3.7	39.8
VASP	3.3	-
Molpro CCSD(T)/cc-pVDZ	-1.1	33.9

Table 7.1: Energies of the (s)-cis prenal rota-isomer and the isomerization transition state relative to the (s)-trans form (0 kJ/mol) at various levels of theory.

the value of -1.1 kJ/mol relative to the (s)-trans isomer is well within the estimated error bar of the computations.
The corresponding VASP gas phase optimizations carried out in the $20 \times 13 \times 13$ Å^3 box are of an intermediate qualitity to the RI-BP86/TZVP and RI-BP86/TZVPP results. The (s)-trans isomer is 3.3 kJ/mol lower in energy than (s)-cis prenal. The optimized structural parameters of both isomers are given in Tab. 7.2. They coincide very closely with the parameters of crotonaldehyde (see Tab. 6.2, Sec. 6.1.2). Among the minor changes are small angle deformations and slight bond elongations of about 0.01 Å for r(C2-C3) and r(C3-C4), which originate from the substitution effect of the additional methyl group on the β-carbon.

Using the RI-DFT/TZVPP energy difference of 3.7 kJ/mol in a *Boltzmann* approach, one obtains for the composition of the gas phase roughly 19% of (s)-cis prenal and 81% (s)-trans prenal. The fraction of (s)-trans prenal is thus much lower here than in the case of crotonaldehyde (98.4% alone for the E-(s)-trans isomer). The interconversion of both isomers in the gas phase depends, of course, strongly on the mechanism and the activation barrier, which has been calculated here by the rotation around the conjugated C2-C1 axis at the RI-BP86/TZVPP level, too. For the rotational potential curve of the δ(CCCO) dihedral angle one finds a maximum at 90° . It corresponds to a rotational barrier of 39.8 kJ/mol relative to (s)-trans prenal. As expected, the highly correlated CCSD(T)/cc-pVDZ value for the rotational barrier is much lower at 33.9 kJ/mol since the description the electronic wavefunction at the transition state improves strongly with the number of included configurations. This value has been computed by the optimization of the transition state structure with a single frozen internal coordinate, namely the δ(CCCO) dihedral angle that was fixed at 90° .
The values computed for the activation barrier between different conformations of prenal are of the same order as those obtained for crotonaldehyde in Chap. 6.1.2. They also agree well with theoretical result of Loncharich et al. [143] for acrolein (37.2 kJ/mol, RHF/6-31G*) and the experimental value of the corresponding activation barrier for crotonaldehyde of de Groot et al. [142] (30.9 kJ/mol). The energy cost to break the conjugation between the C=C and C=O double bonds is consequently only weakly influenced by the substitution pattern. In the gas phase, an interconversion of prenal between the (s)-trans and (s)-cis isomers is, therefore, improbable for all of the α, β-unsaturated aldehydes.

Both the (s)-trans and (s)-cis isomers of prenal belong to the symmetry group C_s and thus the normal coordinates of their vibrations can be divided into 23 vibrations of A' and 13 vibrations of A" symmetry. The calculated vibrational spectra of both prenal isomers are presented in Tab. 7.3 and are plotted together with a HREEL spectrum of a prenal multilayer (4.9L at 100 K) in Fig. 7.10. Only a short comparison of the calculated IR spectra of both isomers and the assignment of the measured bands shall be given here.
For the task of differentiating both isomers by IR spectra, characteristic bands from the computed intensities can be deduced. The most important variations in the spectral pattern con-

cern the ν(C2=C3) and ν(C1=O) stretching vibrations. While these are found at 1633 and 1677 cm^{-1} (RI-DFT) respectively for the (s)-trans isomer, the same vibrations of the (s)-cis form lie further apart at 1604 cm^{-1} and 1695 cm^{-1}. Additionally it is the ν(C1=O) normal mode, which is dominant for the (s)-trans isomer, whereas for (s)-cis prenal ν(C2=C3) is more intense. The lowest C-H stretching vibrations, the aldehydic ν(C1-H1), also differ sizably. For the (s)-trans isomer it is calculated at 2806 cm^{-1}. In the case of (s)-cis prenal it is found at slightly lower frequency of 2784 cm^{-1}.

The fingerprint region of the molecular deformation vibrations displays two signals very specific for each isomer. Here the (s)-trans form has two sizeably IR active modes at 1183 and 1034 cm^{-1} corresponding to asymmetrically coupled ν(C3-C4) and ν(C3-C5) stretching vibrations in the first, and the symmetrically coupled in-plane γ vibrations of the methyl group hydrogens in the second band. The according vibrations of the (s)-cis form with a similar coupling are computed at 1196 cm^{-1} and 970 cm^{-1}, yet only the γ normal mode is IR active in this case. Another specific signal of (s)-cis prenal assigned to the δ(O-C1-C2) deformation mode is computed at 717 cm^{-1} with medium intensity. It is thus found in a region, in which the intensity of (s)-trans prenal is only weak. Upon adsorption of 4.9L prenal at 100 K the HREEL spectrum of a multilayer is recorded on Pt(111). The comparison of the loss peak positions with calculated IR spectra shows a good agreement and confirms the accuracy of the calculated frequencies. Judging from the comparison of the experimental and calculated frequencies (RI-DFT and VASP), the errors are expected to be of the order of 15 cm^{-1} (i.e. ca 1.5%) except for the ν(C-H) stretching frequencies, for which again somewhat larger errors are observed due to anharmonicity and Fermi-resonances. Although frequencies obtained with the VASP approach do not differ significantly from the RI-DFT results, they are in slightly better agreement with the experimentally identified peaks discussed below.

Parameter	(s)-trans	(s)-cis
r(O-C1)	1.23	1.23
r(C1-C2)	1.46	1.46
r(C2-C3)	1.36	1.36
r(C3-C4)	1.50	1.50
r(C3-C5)	1.50	1.50
r(C1-H1)	1.12	1.12
r(C2-H2)	1.09	1.09
r(C4-H3)	1.10	1.09
r(C4-H4,5)	1.10	1.10
r(C5-H6)	1.09	1.10
r(C5-H7,8)	1.10	1.10
r(H-Bond)		2.21
α(O-C1-C2)	123.4	127.6
α(C1-C2-C3)	126.3	127.9
α(C2-C3-C4)	120.2	124.4
α(C2-C3-C5)	124.9	120.1
α(O-C1-H1)	119.5	119.1
α(C1-C2-H2)	114.3	114.0
α(H3-C4-C3)	112.2	112.4
α(H4,5-C4-C3)	110.5	109.7
α(H6-C5-C3)	114.0	112.5
α(H7,8-C5-C3)	109.9	110.3
δ(O-C1-C2-C3)	180.0	0.0
δ(C1-C2-C3-C4)	180.0	0.0
δ(C1-C2-C3-C5)	0.0	180.0
δ(H1-C1-C2-C3)	0.0	180.0
δ(O-C1-C2-H2)	0.0	180.0
δ(H3-C4-C3-C2)	0.0	0.0
δ(H4-C4-C3-C2)	-121.4	125.3
δ(H5-C4-C3-C2)	121.4	-125.3
δ(H6-C5-C3-C2)	0.0	0.0
δ(H7-C5-C3-C2)	121.8	-121.9
δ(H8-C5-C3-C2)	-121.8	121.9

Table 7.2: Geometries of the rota-isomers of prenal calculated in the gas phase using VASP. All distances r are given in Å and all angles in degree. The value r(H-bond) denotes the closest, non-covalent H-O distance.

As seen from Fig. 7.10 all vibrations of (s)-trans prenal can be assigned in the HREELS spectrum, yet due to the experimental resolution of ca 30 cm^{-1} (FWHM) several vibrations are not resolved well enough and broad loss peaks are measured instead. The computed ν(C1=O) and ν(C2=C3) stretching vibrations (1677 and 1633 cm^{-1}, VASP 1679 and 1637 cm^{-1}) lead to a wide but rather weak loss peak. At 1448 cm^{-1} and 1383 cm^{-1} a double feature is detected together with a small shoulder at

1322 cm^{-1}. In this frequency range the DFT analysis allows to assign the full variety of the C-H deformation vibrations δ_s'(CH_3), δ_s"(CH_3), u(CH_3) as well as the aldehydic δ(C1H1) and the vinylic δ(C2H2). The important C-C single bond stretching modes are more difficult to assign as they show a coupling. While ν(C1-C2) is calculated at 1117 cm^{-1} (VASP: 1130 cm^{-1}) in agreement with the experimental peak at 1136 cm^{-1}, the frequencies of the ν(C3-C4) and ν(C3-C4) vibrations of both methyl groups are split due to their coupling. They are obtained at 1183 cm^{-1} for the asymmetrical and 832 cm^{-1} for the symmetrical combination (VASP: 1193 and 842 cm^{-1}) and can be assigned to the loss peaks measured at 1197 cm^{-1} and 841 cm^{-1}, respectively. Dispersed in between the two bands are the loss peaks arising from combinations of the out-of-plane γ(CH) modes of the methyl, the vinylic and the aldehydic hydrogens. In the low frequency range finally the deformation vibrations of the molecular backbone lead to three sizable experimental signals at 529 cm^{-1} (δ(O-C1-C2), 520 cm^{-1}), 464 cm^{-1} (δ(C2-C3-C4), 467 and ω(C2=C3,C4,C5), 458 cm^{-1}) and 351 cm^{-1} (δ(C3-C4-C5), 347 cm^{-1}).
Since most of the vibrational frequencies calculated for (s)-cis prenal are close to the corresponding normal modes of the (s)-trans isomer, the differentiation of both isomers in the multilayer spectrum is complicated. The only normal mode of (s)-cis prenal, which does not overlap closely with vibrations of (s)-trans prenal, is the δ(O-C1-C2) deformation mode computed at 717 cm^{-1} (VASP: 722 cm^{-1}), but this vibration could not be observed in the HREELS spectrum. Hence it seems that no significant fraction of the slightly less stable (s)-cis isomer is present in the condensed multilayer.

A comparison of the important stretching modes of the (s)-trans and (s)-cis prenal isomers to E-(s)-trans and E-(s)-cis crotonaldehyde allows to analyse the influence of the additional methyl substituent onto the vibrational frequencies in the gas phase. This substitution effect consists of a small decrease of the frequencies notably of the ν(C1=O) and ν(C2=C3) stretching vibrations by 21 and 7 cm^{-1} for the prenal trans structure and of 15 and 16 cm^{-1} for the corresponding double bond vibrations of the (s)-cis form. The correlation of the C-C single bond stretching modes of prenal and crotonaldehyde, especially ν(C3-C4), is rather difficult due to differences in the aforementioned couplings, but the ν(C1-C2) normal mode of the conjugating single bond of (s)-trans prenal shows a redshift of 15 cm^{-1}. However, like the C-C stretching modes of the methyl groups also the latter vibration is coupled with the out-of-plane γ(C-H) deformation modes and complicates the analysis severely. Thus for instance the ν(C1-C2) vibrations of the (E-)(s)-cis forms are found to be the main contribution of the normal modes at very different frequencies for both molecules. Finally also other normal modes such as for instance the ν(C-H) vibrations show in general small redshifts of up to 10 cm^{-1}. Hence it is obvious that the mesomeric +M effect of the additional methyl group weakens the bonds of the molecular backbone slightly.

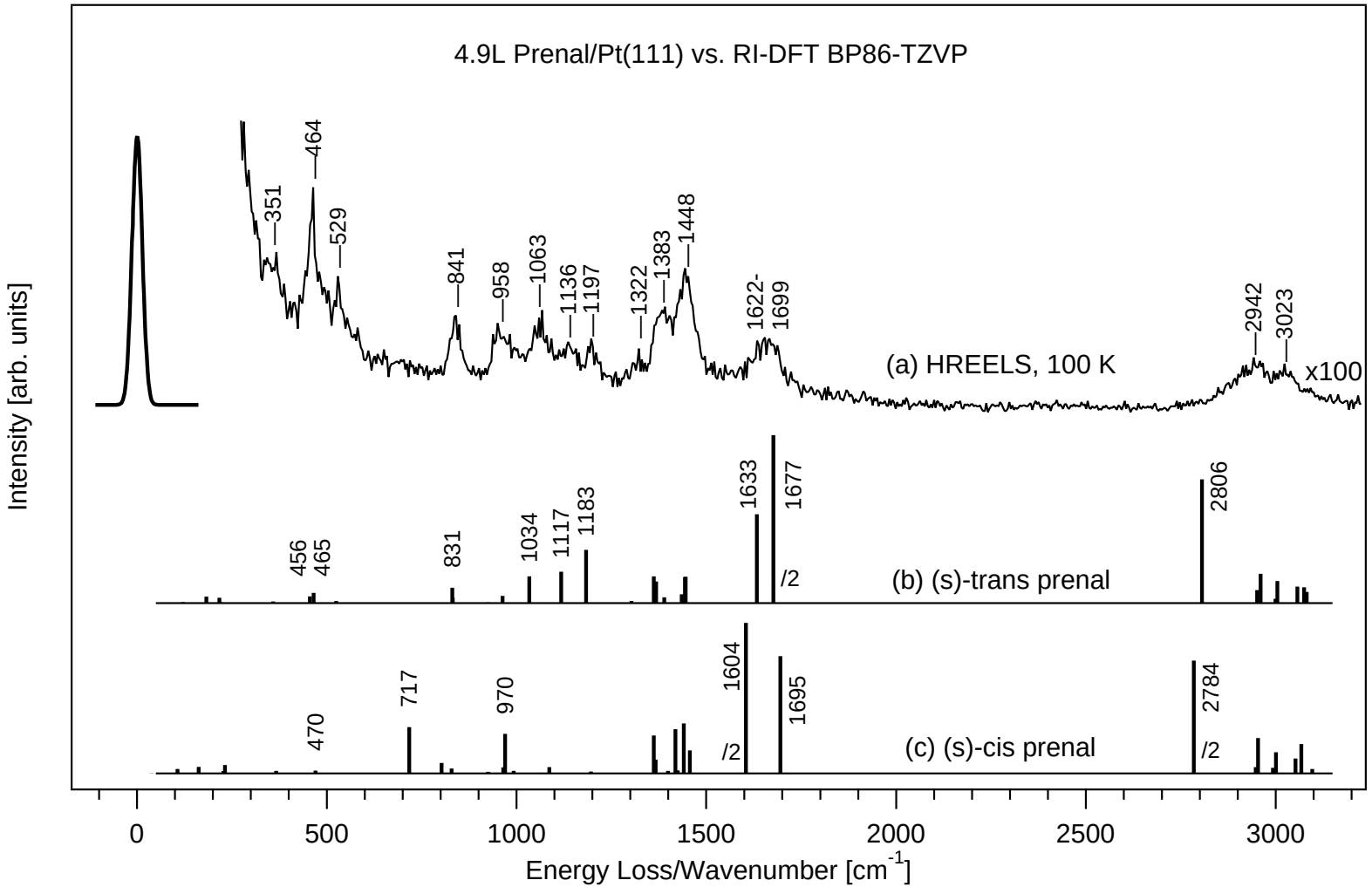

Figure 7.10: Comparison of the multilayer HREEL spectrum of 4.9L prenal/Pt(111) at 100 K with the corresponding RI-DFT BP86/TZVP IR spectra (gas phase, numerical harmonic frequencies). The HREEL spectrum has been recorded in specular geometry at an angle of incidence of 60° with a primary energy of 4.7 eV.

(s)-trans					(s)-cis				
VASP	RI-BP86/TZVP				VASP	RI-BP86/TZVP			
ω	ω	Inten.	Sym.	Assignment	ω	ω	Inten.	Sym.	Assignment
3089	3082	9.5	A'	ν(C2-H2)	3099	3096	3.7	A'	ν(C4-H3)
3084	3075	13.7	A'	ν(C5-H6)	3079	3068	25.4	A'	ν(C2-H2)
3065	3057	14.4	A'	ν(C4-H3)	3063	3053	13.1	A'	ν(C5-H6)
3007	3005	19.1	A"	ν_{as}(C4-H4,5)+ν_{as}(C5-H7,8)	3011	3001	18.4	A"	ν_{as}(C4-H4,5)+ν_{as}(C5-H7,8)
3001	2999	3.8	A"	ν_{as}(C4-H4,5)-ν_{as}(C5-H7,8)	3003	2993	4.9	A"	ν_{as}(C4-H4,5)-ν_{as}(C5-H7,8)
2970	2960	25.6	A'	ν_s(C4-H3,4,5)+ν_s(C5-H6,7,8)	2971	2954	30.8	A'	ν_s(C4-H3,4,5)+ν_s(C5-H6,7,8)
2958	2952	11.4	A'	ν_s(C4-H3,4,5)-ν_s(C5-H6,7,8)	2965	2948	5.4	A'	ν_s(C4-H3,4,5)-ν_s(C5-H6,7,8)
2825	2806	107.8	A'	ν(C1-H1)	2799	2784	196.5	A'	ν(C1-H1)
1679	1677	292.5	A'	ν(C1=O)	1699	1695	102.1	A'	ν(C1=O)
1637	1633	77.3	A'	ν(C2=C3)	1607	1604	262.4	A'	ν(C2=C3)
1444	1445	22.8	A"	δ_s'(C4H3-C5H3)	1452	1457	20.1	A"	δ_s'(C4H3-C5H3)
1435	1443	22.6	A'	δ_s(C4H3-C5H3)	1439	1440	43.6	A'	δ_s(C4H3-C5H3)
1427	1436	7.5	A'	δ_{as}(C4H3-C5H3)	1421	1425	2.7	A"	δ_{as}'(C4H3-C5H3)
1421	1422	0.2	A"	δ_{as}'(C4H3-C5H3)	1409	1419	38.4	A'	δ_{as}(C4H3-C5H3)
1381	1389	5.0	A'	δ(C1H1)	1393	1399	2.3	A'	δ(C1H1)
1359	1368	18.8	A'	u_s(C4H3-C5H3)	1359	1366	11.9	A'	u_s(C4H3-C5H3)
1356	1362	23.4	A'	u_{as}(C4H3-C5H3)	1358	1362	33.1	A'	u_{as}(C4H3-C5H3)
1300	1303	1.8	A'	δ(C2H2)	1330	1333	0	A'	δ(C2H2)
1193	1183	46.4	A'	ν_{as}(C3C4-C3C5)	1202	1196	1.7	A'	ν_{as}(C3C4-C3C5)
1130	1117	27.4	A'	ν(C1-C2)	1089	1086	5.4	A'	ν(C1-C2)
1058	1062	0.4	A"	γ_s'(C4H3-C5H3)	1061	1065	0.6	A"	γ_s'(C4H3-C5H3)
1035	1034	23.3	A'	γ_s(C4H3-C5H3)	992	993	2.4	A"	γ(C1H1)
979	982	0.4	A"	γ(C1H1)	977	970	34.5	A'	γ_s(C4H3-C5H3)
968	963	6.2	A"	γ_{as}'(C4H3-C5H3)	962	965	5.2	A"	γ_{as}'(C4H3-C5H3)
921	925	0.6	A'	γ_{as}(C4H3-C5H3)	925	925	1.6	A'	γ_{as}(C4H3-C5H3)
842	832	4.7	A'	ν_s(C3C4-C3C5)	831	829	4.2	A'	ν_s(C3C4-C3C5)
836	831	13.4	A"	γ(C2H2)	800	803	9.1	A"	γ(C2H2)
520	525	1.8	A'	δ(O-C1-C2)	722	717	40.3	A'	δ(O-C1-C2)
467	465	8.9	A'	δ(C2-C3-C4)	473	470	2.4	A'	ω(C2=C3,C4,C5)
458	456	5.8	A"	ω(C2=C3,C4,C5)	385	386	0.4	A"	δ(C3-C4-C5)
347	359	1.4	A'	δ(C3-C4-C5)	362	366	2.3	A'	δ(C2-C3-C4)
227	220	0.8	A"	τ(C2=C3)	235	232	7.2	A"	δ(C1-C2=C3)
213	217	4.7	A'	δ(C1-C2=C3)	218	227	2.1	A'	τ(C2=C3)
187	183	5.7	A"	τ(C1-C2)	159	162	5.5	A"	τ(C5-H6,7,8)
124	121	0.7	A"	τ(C5-H6,7,8)	113	107	3.7	A"	τ(C1-C2)
85	114	0.4	A"	τ(C4-H3,4,5)	57	38	0.3	A"	τ(C4-H3,4,5)

Table 7.3: Computed IR spectra of the two isomers of prenal in the gas phase (frequencies in cm^{-1}). The IR intensities have only been computed in the RI-DFT approach.

7.1.3 Prenal Adsorption Structures on Pt(111)

The most stable adsorption structures of prenal computed on Pt(111) are of similar coordination types as those of crotonaldehyde. Extending the knowledge of the adsorption geometries from the starting point of the previous studies of Delbecq et al. [51], all heretofore known and several new geometries have been considered in both a low coverage 3×3 supercell ($\Theta = 1/9$) and a higher coverage 3×2 supercell ($\Theta = 1/6$). The free adsorption energies of all obtained stable local minima (see Figs. 7.11 and 7.12) are presented in Tab. 7.4.

The computed adsorption energies in this work are in good agreement with the previous results of Delbecq et al. [51] taking into account the change from ultra-soft pseudopotentials to the PAW scheme and the additional dipole corrections in the present work.

Clearly the structures of the system prenal/Pt(111) can be separated into a group of highly stable and a group of weakly bonded adsorption complexes, too. Among the most stable structures are again the η^4-diσ(CC)-diσ(CO), the η^4-π(CC)-diσ(CO), the η^3-diσ(CC)-σ(O) and the η^2-diσ(CC) forms of both prenal isomers, which show adsorption energies in the range of -47.2 to -58.6 kJ/mol at a low coverage of $\Theta = 1/9$. Compared to the related, strongly bonded adsorption complexes of crotonaldehyde, the substitution of a hydrogen by a methyl group on the β-carbon lowers the adsorption energies by roughly 25% (i.e. 20-25 kJ/mol). The exact origin of this decrease, which may arise from electronic as well as sterical effects, will be investigated in greater detail in the following discussion.

An opposite trend, i.e. a stabilization of the adsorption complex compared to the analogous structure of crotonaldehyde is obtained for the η^1-top and the η^2-diσ(CO) coordination types of (s)-trans prenal. Here adsorption energies are more favorable by 4 to 9 kJ/mol for prenal, but still these structures are not competitive to the group of strongly bonded species. The corresponding η^1-top complex of (s)-cis prenal is computed to be destabilized slightly (5 kJ/mol), whereas the η^2-diσ(CO) form of the latter isomer is totally unstable at 1/9 ML coverage.

This leads to the variations of the adsorption energies as a function of coverage, which are also of interest to explain the weak coverage dependence of the crotonaldehyde/Pt(111) system (Chap. 6.1.5). As concluded previously from the HREEL spectra after various exposures of crotonaldehyde to Pt(111), which are essentially identical at 200 K, even at low coverages the surface species present are the five η^2, η^3 and η^4 complexes of the two E isomers. For very small exposures at 100 K, the submonolayer HREEL spectrum suggests an increase of the relative amount of the η^2-E-(s)-trans and the two η^4 forms, but nonetheless all five highly stable structures contribute to the spectroscopic pattern.

Similar to crotonaldehyde the vibrational data of the irreversibly bonded structures of prenal/Pt(111) around 200 K do not indicate major changes of the surface composition with coverage[1]. This is reproduced nicely by the adsorption energies computed in the different supercells[2]. In the high coverage situation ($\Theta = 1/6$ ML) the same adsorption modes are found to be the most stable ones like at lower coverage ($\Theta = 1/9$ ML). Therefore it is expected at this point that the interpretation of the HREELS data above 200 K will be rather independent of the initial coverage and will be closely related to the analysis of crotonaldehyde.

Structurally the effects of the different coverages are very small. The deviations of the bond lengths found for prenal in both supercells is generally below 0.01 Å for most adsorption modes. Slightly larger deviations have been obtained for the aldehydic part of the η^3-diσ(CC)-σ(O) geometry, which obviously arise from a higher sterical repulsion exerted by the closer distance of the neighboring molecules in the smaller supercell. Here the r(C1=O) bond length is shortened by 0.04 Å at lower coverage (1.27 Å) and consequently the molecule-surface bond r(O-Pt) is weaker and elongated by 0.07 Å to 2.25 Å. The distortion of the molecule and the weaker O-Pt

[1] The HREELS results of prenal on Pt(111) and their interpretation will be given in detail in the next Sec. 7.1.4.

[2] Consequently also the adsorption energy per surface area as a measure of the (total free) energy of the whole system confirms this trend.

Adsorption energies [kJ/mol]	(s)-trans		(s)-cis	
	$\Theta = 1/9$ ML	$\Theta = 1/6$ ML	$\Theta = 1/9$ ML	$\Theta = 1/6$ ML
η^1-top	-32.1 (-34.7* [51])	-18.8 (-31.4* [51])	-19.6	unstable
η^2-diσ(CO)	-23.7 (-17.6 [51])	-20.3	unstable	-12.6
η^2-π(CC)	-31.7	-10.8	-29.8	-16.4
η^2-diσ(CC)	-54.2 (-50.2 [51])	-46.2 (-43.4 [51])	-47.8 (-42.3 [51])	-41.1
η^2-diσ(C3,O)	unstable	unstable	unstable	unstable
η^3-diσ(CC)-σ(O)	unstable	unstable	-49.5 (-45.6 [51])	-38.1 (-39.3 [51])
η^3-π(CC)-σ(O)	unstable	unstable	unstable	unstable
η^4-diσ(CC)-diσ(CO)	-58.6 (-57.3 [51])	-31.3 (-30.5 [51])	excluded	excluded
η^4-π(CC)-diσ(CO)	excluded	excluded	-47.2 (-49.0 [51])	-37.0

Table 7.4: Calculated adsorption energies of prenal on Pt(111) at theoretical coverages of $\Theta = 1/9$ and $\Theta = 1/6$ ML. The reference values given in some cases are taken from Ref. [51]. Except for the values marked with an asteric the results of Delbecq et al. have been obtained without the use of dipole corrections. The structures "excluded" have not been optimized, because the initial structure was already sterically too strained to lead to a stable geometry.

bond, furthermore, lead to a smaller r(C2-Pt) distance (shortened by 0.03 Å to 2.20 Å).
Interestingly it is again the η^1-top-(s)-trans form, which exhibits a distinctive elongation of the O-Pt bond by 0.11 Å to 2.33 Å at a coverage of 1/6 ML. This elongation coincides with the decrease of the adsorption energy from -32.1 to -18.8 kJ/mol, but is moreover accompanied by a significant tilting of the molecular plane towards the surface in the adsorption geometry. While the angle between the surface plane and the (O,C1,C2,C3)-plane is close to 90° in the vertical structure at 1/9 ML coverage, it is reduced to ca 66° at 1/6 ML[3]. Since no additional interaction is generated in this manner, this tilting is understood as a consequence of the higher sterical repulsion.
A comparison of the optimized bond lengths of prenal with the corresponding parameters of the related crotonaldehyde structures points to a few small but systematic variations due to the new methyl substituent. The variations can be summed up as follows: Firstly, both the C2=C3 and the C3-methyl bonds are slightly longer by ca 0.01 to 0.02 Å in basically all of the prenal adsorption structures, suggesting minimally weaker bond strengths. In contrast, the influence on the important C1=O and C1-C2 bonds or on the hydrogen bond distances is negligible as the deviations here are well below ±0.01 Å. Consequently it is not very surprising that also the molecule-surface interactions of the aldehydic part in the adsorption geometries is much less affected (Δr(O-Pt) and Δr(C1-Pt) $< \pm 0.01$ Å) than the vinylic part, which now has to compensate the additional sterical strain and the electronic change due to the positive inductive effect of the second methyl substituent (+I effect). For the η^2-π(CC) forms, the r(C2-Pt) bond length is 0.01 to 0.02 Å shorter compared to the corresponding structures of crotonaldehyde,

[3]The η^1-top adsorption modes have also been considered at an extremely high coverage of 1/4 ML. Here the (s)-trans complex is weakly stable with -9.3 kJ/mol whereas the (s)-cis relative represents no longer a local minimum. Also at this coverage the adsorption complex is tilted strongly and r(O-Pt) is quite long at 2.34 Å.

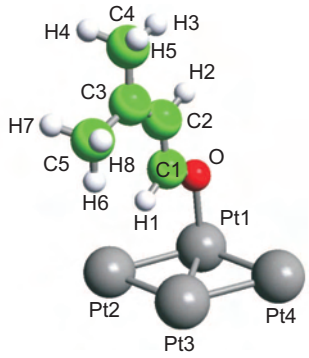

(a) η^1-top-(s)-trans

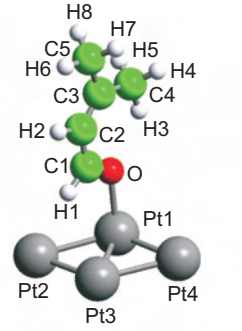

(b) η^1-top-(s)-cis

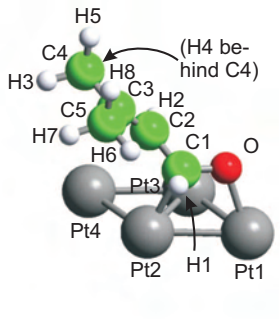

(c) η^2-diσ(CO)-(s)-trans

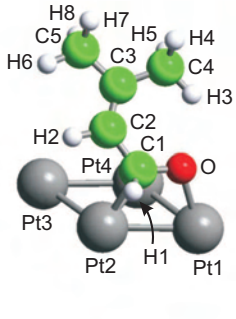

(d) η^2-diσ(CO)-(s)-cis

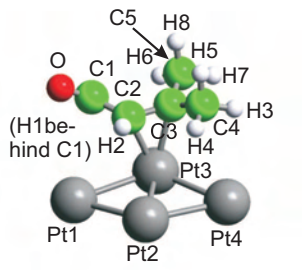

(e) η^2-π(CC)-trans

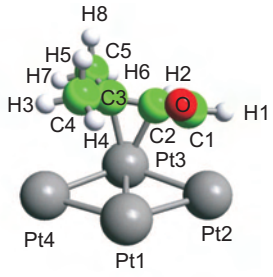

(f) η^2-π(CC)-(s)-cis

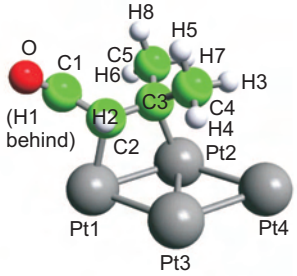

(g) η^2-diσ(CC)-(s)-trans

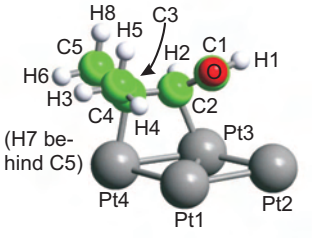

(h) η^2-diσ(CC)-(s)-cis

Figure 7.11: Optimized η^1 and η^2 adsorption geometries of prenal on Pt(111).

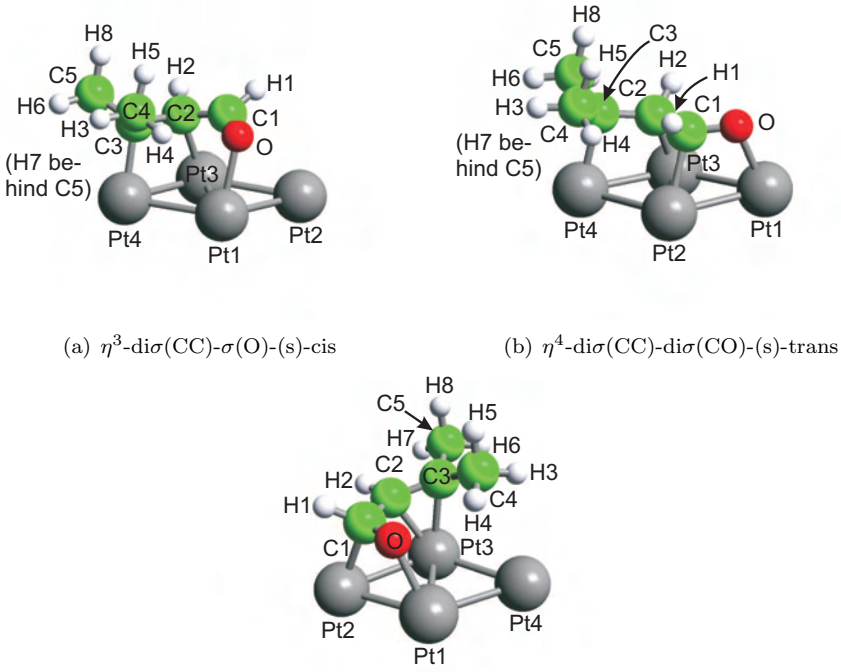

(a) η^3-diσ(CC)-σ(O)-(s)-cis

(b) η^4-diσ(CC)-diσ(CO)-(s)-trans

(c) η^4-π(CC)-diσ(CO)-(s)-cis

Figure 7.12: Optimized η^3, η^4-diσ(CC)-diσ(CO) and η^4-π(CC)+diσ(CO) adsorption geometries of prenal on Pt(111).

whereas r(C3-Pt) closer to the methyl groups is stretched by 0.07 to 0.09 Å. Hence, the additional methyl substituent leads to a tilting of the C2=C3 axis by ca 9° away from the surface plane (ca 1.5° for crotonaldehyde). A similar variation of r(C3-Pt) is found for the η^4-π(CC)-diσ(CO)-(s)-cis form, but here also the three other bonds to the surface are somewhat longer (0.05 Å for C2, 0.02 Å for C1 and O).

Unlike the structures with a π(CC) interaction mechanism, the η^2, η^3 and η^4 geometries characterized by a diσ(CC) coordination show only slight elongations of r(C3-Pt) that are typically between 0.02 and 0.04 Å. Since the bond distance of C2 to Pt is even computed to be hardly longer (0.01 Å) compared to crotonaldehyde, the sterical influence of the additional methyl groups is concluded to be much smaller for this coordination type than for the forms having a π(CC) interaction.

Concerning the subtrate, the relaxation of the interacting Pt atoms out of the surface is generally about 10% larger for prenal (0.02-0.05 Å) than for crotonaldehyde. The displacements of the relaxed Pt atoms within the surface plane induced by the bonding are of the same size, being generally below 0.05 Å. Just in the η^4 complex a few slightly larger displacements of up to 0.1 Å are noticed. Typically the surface atoms bonded to a carbon atom are pulled up between 0.07 to 0.25 Å by prenal, whereas the protrusions induced by crotonaldehyde on the Pt(111) surface were around 0.08 to 0.20 Å. Also the bonds to the aldehydic oxygen lead to a buckling of the Pt out of the surface plane by roughly 0.05 to 0.08 Å. This observation may be rationalized by the increased sterical demand of prenal, which requires the larger outward relaxation in order to minimise the repulsive interactions between the molecule and the surface.

Further insights into the substitution effects are obtained from the decomposition of the ad-

Geometry	η^1-top-(s)-trans	η^1-top-(s)-cis	η^2-diσ(CO)-(s)-trans	η^2-π(CC)-trans	η^2-π(CC)-cis
r(O-C1)	1.25	1.25	1.34	1.23	1.23
r(C1-C2)	1.44	1.44	1.46	1.49	1.49
r(C2-C3)	1.36	1.36	1.36	1.43	1.43
r(C3-C4)	1.50	1.50	1.50	1.51	1.51
r(C3-C5)	1.50	1.50	1.50	1.51	1.51
r(C1-H1)	1.11	1.11	1.11	1.12	1.12
r(C2-H2)	1.09	1.09	1.10	1.10	1.10
r(C4-H3)	1.10	1.09	1.10	1.10	1.09
r(C4-H4)	1.10	1.10	1.10	1.11	1.11
r(C4-H5)	1.10	1.10	1.10	1.10	1.10
r(C5-H6)	1.09	1.10	1.10	1.10	1.10
r(C5-H7)	1.10	1.10	1.11	1.11	1.11
r(C5-H8)	1.10	1.10	1.10	1.10	1.10
r(O-M)	2.22	2.18	2.09	-	-
r(C1-M)	-	-	2.25	-	-
r(C2-M)	-	-	-	2.20	2.21
r(C3-M)	-	-	-	2.29	2.31
r(O-H)		2.18			2.43

Table 7.5: Bond length of the optimized η^1 and η^2-diσ(CC) adsorption geometries of the prenal on Pt(111) (Θ = 1/9 ML). All distances r are given in Å. r(O-H) denotes a short distance of a methyl hydrogen to the aldehydic oxygen in the respective adsorption complex.

Geometry	η^2-diσ(CC)-(s)-trans	η^2-diσ(CC)-(s)-cis	η^3-diσ(CC)-σ(O)-(s)-cis	η^4-diσ(CC)-diσ(CO)-(s)-trans	η^4-π(CC)-diσ(CO)-(s)-cis
r(O-C1)	1.23	1.23	1.27	1.34	1.33
r(C1-C2)	1.50	1.49	1.45	1.49	1.48
r(C2-C3)	1.52	1.51	1.51	1.51	1.43
r(C3-C4)	1.50	1.52	1.53	1.52	1.51
r(C3-C5)	1.52	1.53	1.53	1.53	1.51
r(C1-H1)	1.12	1.12	1.11	1.10	1.11
r(C2-H2)	1.10	1.10	1.10	1.10	1.10
r(C4-H3)	1.10	1.10	1.09	1.10	1.09
r(C4-H4)	1.11	1.11	1.11	1.11	1.11
r(C4-H5)	1.10	1.10	1.10	1.10	1.10
r(C5-H6)	1.10	1.10	1.10	1.10	1.10
r(C5-H7)	1.11	1.11	1.11	1.11	1.11
r(C5-H8)	1.10	1.10	1.10	1.10	1.10
r(O-M)	-	-	2.25	2.11	2.14
r(C1-M)	-	-	-	2.21	2.21
r(C2-M)	2.14	2.16	2.20	2.17	2.23
r(C3-M)	2.18	2.18	2.14	2.17	2.29
r(O-H)			2.36		2.27

Table 7.6: Bond distances of the optimized η^2, η^3 and η^4 adsorption geometries of the prenal on Pt(111) (Θ = 1/9 ML).

Adsorption mode	adsorption energy	surface deformation	molecule deformation	interaction term
η^1-top-(s)-trans	-32.1	39	5	-76
η^2-π(CC)-trans	-31.7	67	50	-148
η^2-diσ(CC)-(s)-trans	-54.2	57	158	-270
η^2-diσ(CC)-(s)-cis	-47.8	56	148	-252
η^3-diσ(CC)-σ(O)-(s)-cis	-49.5	59	162	-270
η^4-diσ(CC)-diσ(CO)-(s)-trans	-58.6	55	142	-255
η^4-π(CC)-diσ(CO)-(s)-cis	-47.2	65	115	-227

Table 7.7: Decomposition of the adsorption energies of prenal on Pt(111) ($\Theta = 1/9$ ML) into the energy costs for deforming the surface and the molecule as well as the energy gain of the interaction in the optimized surface complex. All energy contributions are given in kJ/mol.

sorption energies into the respective deformation costs of the molecule and the surface and the interaction term, which is presented in Tab 7.7. It is easily recognized that the average deformation cost of the surface is a little more costly (ca 58 kJ/mol for the most stable forms) than for the corresponding structures of crotonaldehyde (55 kJ/mol), which coincides excellently with the increased effects of sterical strain on the geometry parameters. Also the energy expenses invested to distort the molecule upon adsorption are somewhat higher compared to crotonaldehyde, but their increases are very inhomogeneous for the different coordination types (between 7 and 26, i.e. on average about 15 kJ/mol[4]).
Hence, it must be concluded that the decrease of the adsorption energies of prenal by roughly 23 kJ/mol is primarily due to increased sterical demands of the additional methyl group (about 18 kJ/mol additional deformation costs) and to a lesser degree also to a weaker molecule-surface interaction, which is calculated to be about 5 kJ/mol less favorable (roughly 255 kJ/mol) compared to crotonaldehyde (ca 260 kJ/mol on average, ca 275 kJ/mol including the η^4-(s)-trans form). Evidently the methyl group leads to a higher repulsion with the surface and, therefore, to a weaker overlap of the molecular orbitals of prenal with the bands of the metallic substrate.

[4]The molecule distortion energy for the η^4-diσ(CC)-diσ(CO)-(s)-trans adsorption complexes of both molecules on Pt(111) differs enormously (prenal 142, crotonaldehyde 211 kJ/mol) although the geometrical parameters do not support this. Additionally to the geometrical deformation, a change in the electronic structure of the crotonaldehyde complex has occured. Consequently, the computed interaction terms of both complexes differ considerably and have to be ignored for the analysis of the general substitution effect here.

7.1.4 HREELS Experiments of the Molecular Adsorption

The HREELS experiments have been carried out for different exposures of prenal adsorbed at 100 K followed by annealing steps to given temperatures, which have been chosen based on the TPD results[5]. After each annealing step the sample was cooled down again to 100 K to perform the HREELS measurements. All HREEL spectra presented have been taken with a primary electron energy of 4.7 eV in the specular reflection mode. Since also most of the possible adsorption structures are only of C_1 symmetry, all vibrational normal modes are expected to be dipole active. Thus, no off-specular experiments have been performed. A HREELS annealing series of 4.9L prenal adsorbed on Pt(111) with temperature steps between 100 K and 300 K is presented in Fig. 7.13.

As already discussed in Sec. 7.1.2, the vibrational fingerprint detected after the adsorption of a sufficiently large exposure of prenal at 100 K reveals a physisorbed multilayer. After heating the sample to 169 K in order to desorb the multilayer phase, the HREELS loss intensities are decreased significantly. Besides the relative intensities also the width of several loss peaks are changed and small frequency shifts are recognized. In the ν(C-H) stretching region, which extends here from 2730 cm^{-1} to 3050 cm^{-1}, two sizeable peaks can be found at 2875 cm^{-1} and 2940 cm^{-1}. In the multilayer spectrum the ν(C-H) signals extend up to 3100 cm^{-1} with major peaks obtained at 2942 cm^{-1} and 3023 cm^{-1}.

Heating up the sample sequentially to higher temperatures, the low temperature desorption states α_2 (180 K) and α_3 (reversible layer, 199 K) seen in TPD are supposed to be desorbed. Moreover, the decomposition of the irreversibly adsorbed prenal species starts between 250 K and 300 K (first H_2 desorption around 280 K) and is followed in the HREELS spectra. While up to 205 K no further changes in the ν(C-H) stretching region can be detected, some differences appear again at higher temperatures. In particular, the loss intensity at 2875 cm^{-1} decreases at 250 K until at 300 K only a single maximum is measured at 2955 cm^{-1}.

In the ν(C=C) and ν(C=O) stretching region, only one asymmetric, broad and weak loss signal from 1600 to 1700 cm^{-1} is obtained between 169 K and 250 K. This already points towards an adsorption mode with a rather flat orientation and interaction with the substrate by only one double bond. The maximum around 1660 cm^{-1} coincides not only with the computed ν(C1=O) stretching mode of the η^2-diσ(CC)-(s)-trans (1666 cm^{-1}, vibrational assignments in Tab. 7.8) complex, but also with the corresponding, intense normal mode of the η^2-diσ(CC)-(s)-cis form (1655 cm^{-1}, Tab. 7.9). As in the case of crotonaldehyde, several of the bands of these adsorption modes including ν(C1=O), the ν(C1-C2) (around 1040 cm^{-1}), the symmetrically coupled γ_s"(CH_3) (ca 900 cm^{-1}) as well as the molecule-surface stretching vibrations (500 cm^{-1}) are computed to be intense in regions, in which experimentally rather weak but very broad features are detected. This problem is enhanced further by the contributions of the η^3 and η^4 complexes that will be discussed in the next paragraphs. Again it is ascribed mainly to the ideal periodicity in the theoretical models, while no ordered superstructure is detected in any of the LEED experiments performed for various exposures below 400 K. Hence a *Davydov* splitting between different configurations (for i.e. orientations on the surface) of the adsorption modes may be expected here (Chap. 3.2.2).

Another uncertainty adding to the problem of interpreting the intensity discrepancies is due to the different surface coverages of the strongly bonded structures, which must be expected from their slightly varying adsorption energies. For simplicity of the analysis these are treated to be present in equal coverage fractions. The measured signal of the ν(C1=O) vibrations remains unchanged up to 205 K, when it starts to shift to higher frequencies. At 300 K it is measured with increased relative intensity at 1700 cm^{-1}.

[5]Keep in mind that TPD is an "out of thermodynamical equilibrium" method while HREELS measurements corresponds to an equilibrium situation. Aside from this, also different heating rates have been applied in TPD or during the annealing.

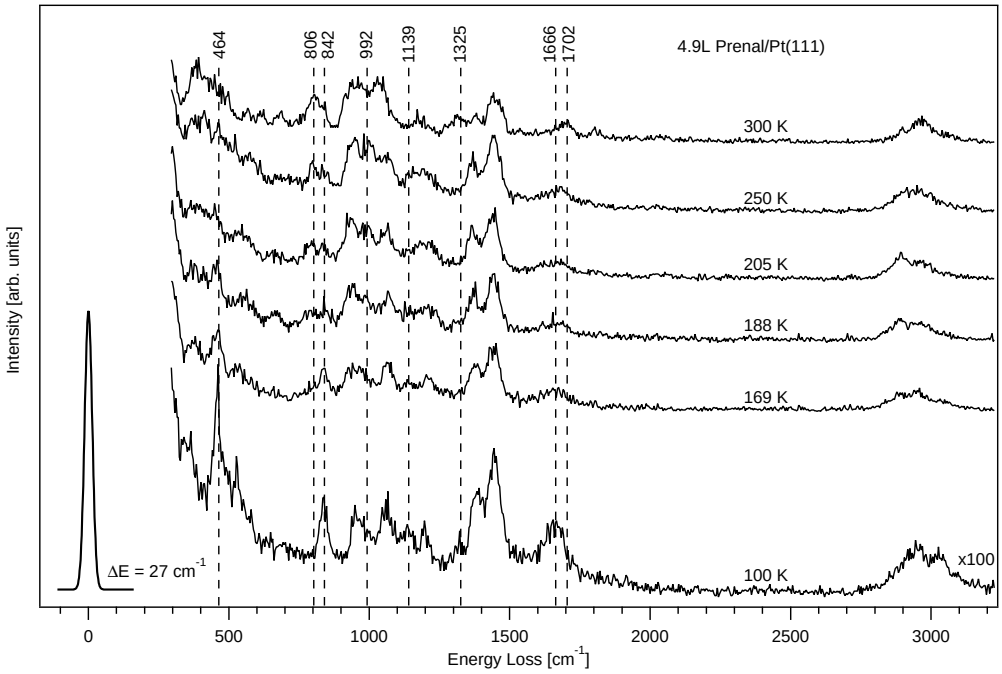

Figure 7.13: HREELS of 4.9L prenal/Pt(111), 100-300 K. The HREEL spectra have been recorded in specular geometry at an angle of incidence of 60° with a primary energy of 4.7 eV.

At 842 cm^{-1} a sizably intense loss peak identifies the presence of the η^3-diσ(CC)-σ(O)-(s)-cis structure, which is the only one to be sufficiently active in this region with its out-of-plane deformation mode γ_s(C1H1-C2H2) computed at 860 cm^{-1} (Tab. 7.11). This loss peak is found to be more intense in the HREEL spectra at lower temperatures, especially at 169 K. Together with the start of the decomposition of prenal above 250 K, a new signal appears at 806 cm^{-1} and indicates a new surface species.

Two more surface complexes, namely the η^4-diσ(CC)-diσ(CO)-(s)-trans (Tab. 7.11) and the η^4-π(CC)-diσ(CO)-(s)-cis (Tab. 7.12) structures, are found to be compatible with the experimental HREELS data. Although it is hardly possible to identify each of these structures by a single measured loss peak, they are energetically as stable as the η^2 and η^3 geometries and their computed HREEL spectra improve the fit obtained thus far. Therefore these structures are considered to be present in the mixed phase of strongly adsorbed prenal species.

The comparison of the convolution of the theoretical data with a *Gaussian* (App. C.1, Fig. C.1) is less satisfying for prenal/Pt(111) than it was for crotonaldehyde/Pt(111). This may result on the one hand from the temperature dependent shifts of the experimental loss peaks below 1000 cm^{-1}, which are more pronounced for prenal, but on the other hand also from the uncertainty in choice of the theoretical coverage. Moreover contributions from impact scattering have to be kept in mind. Nonetheless the DFT analysis leads unambiguously to the exclusion of the remaining, less strongly adsorbed coordination types such as for instance the η^1-top or the η^2-diσ(CO) forms as these show vibrational fingerprints very different from the experimental data[6]. However, the overestimation of the loss intensities mentioned above becomes more apparent in the convolution. Another problem appearing in addition arises from the intense γ_s'(C4H$_3$-C5H$_3$) mode of the

[6]The structures of the η^2-π(CC) type posses vibrational patterns that are quite similar to those of the η^2-diσ(CC) geometries, but due to their weaker adsorption energies and since the HREEL spectra of the η^2-diσ(CC) structures are already sufficient to explain the experimental data, they are excluded.

η^2-(s)-cis form calculated at 892 cm^{-1} . It is shifted to lower frequency as compared to the experimental loss at 923 cm^{-1}, with which it is correlated (error is thus about 30 cm^{-1} or 3%). This leads to a slight intensity discrepancy[7] around 900 cm^{-1}.
Also the measured intensities around 992 cm^{-1} and 1220 cm^{-1} seem to be underestimated in the DFT calculations. Despite the large number of vibrations from all strongly adsorbed species that agree with the experimental frequency of 992 cm^{-1}, they do not sum up in intensity sufficiently to explain the measured feature. The frequencies fitting well with the experiment originate from various γ'_s(C4H$_3$-C5H$_3$), γ''_s(C4H$_3$-C5H$_3$), γ'_{as}(C4H$_3$-C5H$_3$) and γ_{as}(C1H1-C2H2) vibrations, but these are computed to be weak. In contrast, at slightly higher frequencies the ν(C1-C2) normal modes of the η^2-(s)-trans (1039 cm^{-1}), the η^2-(s)-cis (1036 cm^{-1}) and the η^3-(s)-cis (1063 cm^{-1}) structures are obtained with high intensities[8]. These normal modes are attributed to the experimental loss signal at 1064 cm^{-1}, yet they are expected furthermore to distribute their intensities due to vibrational couplings and disorder and, hence, to account partially for measured intensity in the region between 1000 cm^{-1} and 1100 cm^{-1}.
Looking at the intensity of the signal at 992 cm^{-1} in the HREELS experiments at lower temperatures no significant variation is observed after desorbing the multilayer (169 K). Up to 300 K yet, the intensity increases sizably until it cannot be discerned from the peaks at 923 cm^{-1} and 1029 cm^{-1} anymore. Consequently the fit of the DFT analysis with the experimental data is better at lower temperatures and it is suggested that another possible reason for the intensity problem may arise from surface fragments, which obviously start to appear at 205 K.
A badly resolved feature in the HREEL spectrum that originates from at least two peaks merging at 1220 cm^{-1} and 1183 cm^{-1} represents a similar problem. At 1220 cm^{-1} mainly the frequencies of the δ_{as}(C1H1-C2H2) vibration of the η^2-(s)-trans (1262 cm^{-1}) and the η^4-(s)-trans (1234) forms as well as the ν(C2=C3) mode of η^2-(s)-cis (1205, inactive) can be assigned, yet they are weak, too. For the peak at 1183 cm^{-1} a larger set of computed vibrations must be taken into account, but some of these are shifted significantly to lower frequencies. As this would mean untypically large frequency errors of up to 55 cm^{-1} (ca 5%) for the medium intense ν_{as}(C3C4-C3C5) vibrations of the η^2-(s)-trans (1130 cm^{-1}), the η^2-(s)-cis (1127) and the η^3-(s)-cis (1130) structures, these can only be considered to reproduce the basic intensity recognized between the peaks at 1064 and 1183 cm^{-1}. Excellently within the error bar of the DFT frequencies are the ν(C2=C3) normal modes of the η^2-(s)-trans (1189 cm^{-1}), η^3-(s)-cis (1181) and the η^4-(s)-trans (1184) structures plus the ν(C1=O) stretching vibration of the η^4-(s)-cis (1186) geometry. These vibrations agree with the experiment and account for sufficient loss intensity.
Very well reproduced is also the double feature in the experimental HREEL spectrum around 1445 cm^{-1} and 1361 cm^{-1} which is very much reminiscent of similar peaks found for crotonaldehyde before. It originates from a variety of coupled deformation modes of the methyl substituents as well as coupled normal modes arising from deformation vibrations of the vinylic and the aldehydic hydrogens. In particular, the symmetric δ'_s(C4H$_3$-C5H$_3$) and u$_s$(C4H$_3$-C5H$_3$) vibrations are computed to be intense for the identified adsorption modes. The corresponding anti-symmetric modes δ'_{as}(C4H$_3$-C5H$_3$) and u$_{as}$(C4H$_3$-C5H$_3$) as well as the δ_s(C1H1-C2H2) vibration contribute to a lesser degree to the detected intensity, but allow to understand the width of the experimental peaks.

[7] As shown in Fig. C.2 and Fig. C.3 of App. C.1, the fit of the experimental and theoretical HREEL spectra is even best if also the η^2-diσ(CC)-(s)-cis structure is excluded based on its misfit at 892 cm^{-1}. Yet since the frequency error of this mode is only 3% and since it is energetically very similar to the other four stable η^2, η^3 and η^4 adsorption complexes, it must be included into the set of identified structures.

[8] Since the ν(C-C) stretching modes are usually subject to small anharmonicities, too, the frequencies may be overestimated by 5 to 20 cm^{-1} in the DFT analysis.

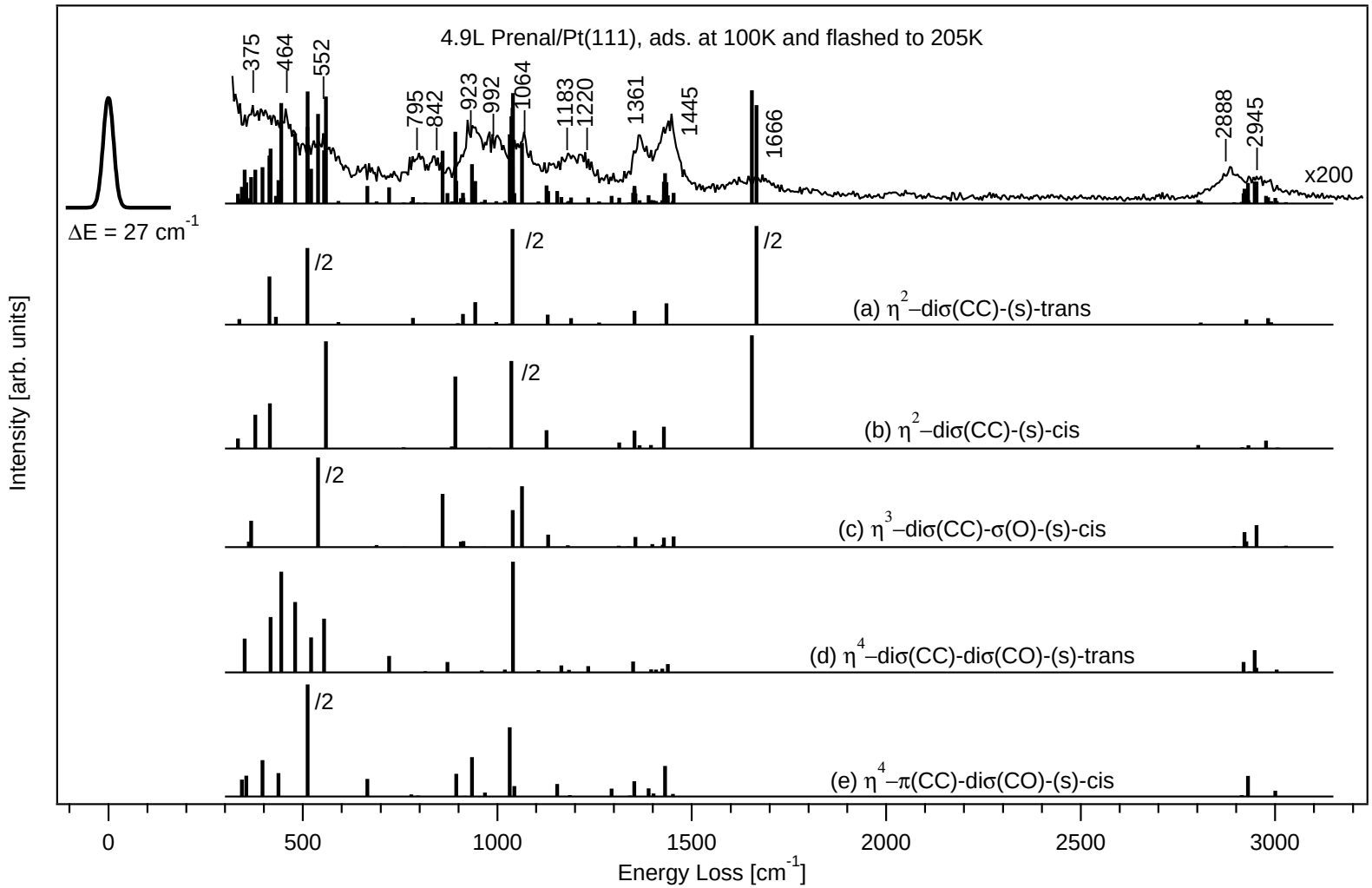

Figure 7.14: Computed DFT HREEL spectra for the most stable adsorption structures and HREEL spectrum of 4.9L prenal adsorbed at 100 K on Pt(111) subsequently flashed to 205 K.

Exemplarily for the systems crotonaldehyde/Pt(111) and prenal/Pt(111) the coverage dependence of the frequencies and the loss intensities has been studied in this case using the small 3×2 and the 3×3 supercell. Generally it is observed that the dependence of the computed frequencies and intensities on the chosen theoretical coverage is small. The frequencies shift typically less than 5 cm^{-1}, which is well below the DFT precision. Since the theoretical spectra of the five stable prenal species calculated at a coverage of 1/6 ML reproduce the experimental HREELS data nearly equally well and do not add to the understanding of this system, it is not presented here.

The treatment of the effect of an additional methyl substituent on the vibrations is not as simple as its effect on the adsorption energies. Normally it can be illustrated by a comparison of the frequencies of the normal modes of substituted and unsubstituted molecules, a concept which works out quite well in the gas phase. The correlation of the frequencies does, in fact, only make sense if the character of the normal coordinates of the substituted molecule does not differ too much from the vibrations of the reference. Then the frequencies may be correlated with the bond strengths. On the surface, however, the character, i.e. the coupling of the vibrations in the normal modes, is found to change strongly for the α,β-unsaturated aldehydes due to different distortions of the molecules. The basis of the comparison is thus inconsistent even for "simple" adsorption modes such as the η^2-diσ(CC) coordination type and the analysis may be misleading. In the gas phase the substitution effect of prenal leads to small redshifts of the frequencies of the C-C and C-O stretching modes in the molecular backbone. Although the other normal modes are sensitive to the influence of the 2^{nd} methyl group, too, these modes are best suited for a simple analysis. The frequency of the ν(C2=C3) vibration is reduced by 5 cm^{-1} for the (s)-trans and 14 cm^{-1} for the (s)-cis form from the values of the two E isomers of crotonaldehyde. Consistently also the frequencies of the ν(C1-C2) and the ν(C1=O) vibrations, which sense only an indirect, purely electronic +I effect from the 2^{nd} methyl group, decrease in the two prenal isomers[9]. Nonetheless it seems that the bond strength of the aldehydic C-O bond is weakened slightly more than the C1-C2 or C2=C3 bonds.

Despite the changing basis of the normal coordinates, generally a systematic blueshift of the interacting double bonds, mainly C2=C3, is observed in the computed vibrational frequencies of the adsorption complexes. This is in line with the decrease of the DFT binding energies due to the 2^{nd} methyl group, which require the corresponding double bonds to retain a higher bond strength (bond order) and exhibit higher frequencies than the counterparts of crotonaldehyde.

Although upon adsorption finally also the molecule-surface modes are expected to be sensitive to the substitution pattern, their coupling with other vibrations is very complex and troubles any simple correlation. Additionally, the neglect of the coupling to the surface phonons in the theoretical model hampers a full, quantitative analysis in the low frequency region. Without going too much into details of the comparisons of the molecule-surface stretching modes, it is observed experimentally that the loss signals for prenal (229, 375-464, 552 cm^{-1}) are shifted a little to higher (harder) frequencies compared to crotonaldehyde at 200 K (222, 298/shoulder, 371, 459-536 cm^{-1}). Although this is supported qualitatively by the calculations, the computed shifts are much larger at roughly 40 cm^{-1} since the couplings change the vibrational assignment strongly. As commonly a redshift would be expected with a weakening of the bond strength, such as proven for example for CO or ethene, this finding is very counterintuitive, but it seems to be definitely a physical phenomenon[10]. Therefore it becomes clear that the molecule-surface

[9] The frequencies decrease by 27 and 13 cm^{-1} for the (s)-trans and by 14 and 81 cm^{-1} for the (s)-cis isomer, respectively. In the latter case already the problem of changed couplings leads to a different assignment of the normal modes and the analysis becomes less precise here.

[10] Similar studies on the adsorption and vibrational properties of cyclopentene on Pt(111) and Pt-Sn surface alloys by F. Delbecq, C. Becker, J. Breitbach et al. lead to the same phenomenon. In these studies, the low frequency peaks in the HREEL spectra are assigned unambiguously from the DFT analysis and both approaches show consistently that the molecule-surface vibrations are hardly shifted despite a huge decrease of the adsorption energy.

stretching modes do not always allow a simple rationalization of the substitution effect and the correlated changes of the adsorption strength.
In the η^2-diσ(CC) structures a strong increase of ν(C2=C3) is found for prenal. The frequency in the structure of the (s)-trans isomer is blueshifted by 74 cm^{-1} compared to the one of E-(s)-trans crotonaldehyde, while the frequency of the (s)-cis sturcture is shifted even by 96 cm^{-1}. This confirms nicely the lower rehybridisation of C2=C3 and the decrease in the interaction strength of the double bond with the platinum surface, which is 3 kJ/mol for the (s)-trans and much larger at 14 kJ/mol for the (s)-cis geometry. As the weakening of the interaction strength of the η^2-diσ(CC)-(s)-trans structure itself is very small, also an effect from the substitution on the bond order may be recognized in the frequency shift.
The ν(C1=O) and ν(C1-C2) stretching modes are influenced, too, but here the trends are not straight forward. For the η^2-diσ(CC)-(s)-trans structure the two normal modes shift in opposite directions (-20 and +15 cm^{-1} variation, resp.), whereas for the η^2-diσ(CC)-(s)-cis form the corresponding vibrational frequencies are blueshifted by 45 and 43 cm^{-1} and consequently support the finding of a much weaker interaction compared to crotonaldehyde.
Moreover the ν(C2=C3) stretching mode of the η^3-diσ(CC)-σ(O)-(s)-cis structure shows a strong blueshift of 70 cm^{-1} for prenal. Puzzling in this case, the stronger C2=C3 bond character is in contrast to a slightly increased interaction strength with the surface in this geometry (4 kJ/mol)[11]. Due to the problem of a changing basis of normal coordinates, even the qualitative analysis becomes difficult here. Although it might be suggested that this finding indicates a weaker interaction of the C2=C3 moiety in this coordination type and thus requires the contribution of the Pt-O bond to achieve the calculated interaction strength of 270 kJ/mol (similar to the η^2 forms), any conclusion seems to be badly substantiated without further support. Consistent with the additional O-Pt interaction, the frequencies of the ν(C1=O) and ν(C1-C2) vibrations are blueshifted less than in the η^2-(s)-cis form, i.e. by only 10 and 38 cm^{-1}, respectively, here.
The picture obtained for the η^4-diσ(CC)-diσ(CO)-(s)-trans and the η^4-π(CC)-diσ(CO)-(s)-cis coordination types underlines the weaker bonding to the surface by frequency increases of ν(C2=C3) of 84 and 184 cm^{-1}, respectively, but is also not intuitive concerning the ν(C1=O) stretching mode. It is redshifted by 8 cm^{-1} for the (s)-trans and blueshifted by 27 cm^{-1} for the (s)-cis adsorption complex.
In conclusion, the substitution effect influences the frequencies of the "internal" stretching modes in two ways. Firstly, they are affected indirectly by the change of the molecule-surface interaction strength. Secondly, the new substituent influences the bond strengths and the vibrational frequencies of the molecular modes directly, which is already recognized in the gas phase. Both effects seem to vary strongly as a function of the coordination type, but the shifts due to changes of the molecule-surface interaction are estimated to be generally larger. Nonetheless, the analysis of the substitution effect is hampered in this work strongly by the inconsistency of the basis of normal coordinates for both molecules in their respective coordination geometries and any further (semi-)quantitative analysis does probably only lead to badly supported conclusions at best.

[11] It might be interesting at this point to note that the ν(C2=C3) and ν(C1=O) vibrations of the η^1-top-(s)-trans geometry are redshifted by 15 and 17 cm^{-1}, respectively, whereas ν(C1-C2) is constant. These values are slightly smaller than the pure substitution shift in the gas phase. Thus the increase in the interaction strength to the surface leads to a weakening of the "internal" bonds of prenal, too.

ω cm^{-1}	Intensity $\times 10^6$ au		Normal mode
3038	0.001		ν(C4-H3)
3033	0.000		ν(C2-H2)
3003	0.005		ν_s($C5H_3$)
2989	0.098		ν(C1-H1)
2981	0.27		ν_s($C4H_3$)
2926	0.21		ν_{as}(C5-H7,8)
2921	0.012		ν_{as}(C4-H4,5)
2809	0.093		ν(C5-H6)
1666	8.4	s	ν(C1=O)
1435	0.90	w	δ'_s($C4H_3$-$C5H_3$)
1422	0.043		δ''_s($C4H_3$-$C5H_3$)
1412	0.013		δ'_{as}($C4H_3$-$C5H_3$)
1401	0.026		δ''_{as}($C4H_3$-$C5H_3$)
1352	0.59		u_s($C4H_3$-$C5H_3$)
1349	0.029		δ_s(C1H1-C2H2)
1333	0.005		u_{as}($C4H_3$-$C5H_3$)
1262	0.093		δ_{as}(C1H1-C2H2)
1189	0.27		ν(C2=C3)
1130	0.42		ν_{as}(C3C4-C3C5)
1039	8.1	s	ν(C1-C2)
1032	0.04		γ'_s($C4H_3$-$C5H_3$)
997	0.11		γ''_s($C4H_3$-$C5H_3$)
962	0.009		γ'_{as}($C4H_3$-$C5H_3$)
943	0.96	w	γ_{as}(C1H1-C2H2)
912	0.45		γ_s(C1H1-C2H2)
898	0.06		γ''_{as}($C4H_3$-$C5H_3$)
783	0.28		ν_s(C3C4-C3C5)
591	0.11		ν_{as}(PtC2-PtC3)
511	6.5	s	ν_s(PtC2-PtC3)
431	0.33		δ(O=C1-C2)
413	2.0	m	δ(C3-C4,5)
337	0.23		δ(C2=C3-C4,C5)
283	0.011		τ_s(CH_3)
265	0.32		τ_{as}(CH_3)
255	0.25		δ(C1-C2=C3)
236	0.65		ω(C2=C3,C4,C5)
220	0.074		τ(C2=C3)
192	0.81		τ(C1-C2)
113	4.7		fT
96	5.1		fR
92	1.6		fT
52	2.9		fR

Table 7.8: Vibrational analysis of the η^2-diσ(CC)-(s)-trans structure of prenal/Pt(111). The harmonic frequencies ω are given in cm^{-1}. The letters following the computed intensities refer to the relative strength, i.e. (v)w = (very) weak, m = medium and (v)s = (very) strong. For strong vibrational couplings of more than two normal modes, the coupling of the components is indicated by + (in phase) or - (anti-phase). The abbreviations fR and fT refer to hindered translations and hindered rotations.

ω cm^{-1}	Intensity $\times 10^6$ au		Normal mode
3043	0.016		ν(C5-H6)
3033	0.001		ν(C4-H3)
3006	0.045		ν_{as}(C5-H7,8)
2978	0.005		ν(C2-H2)
2976	0.34		ν_{as}(C4-H4,5)
2931	0.14		ν_s($C5H_3$)
2915	0.055		ν_s($C4H_3$)
2802	0.15		ν(C1-H1)
1655	4.8	s	ν(C1=O)
1428	0.93		δ'_s($C4H_3$-$C5H_3$)
1417	0.032		δ''_s($C4H_3$-$C5H_3$)
1407	0.005		δ'_{as}($C4H_3$-$C5H_3$)
1395	0.15		δ''_{as}($C4H_3$-$C5H_3$)
1366	0.14		δ_{as}(C1H1-C2H2)
1353	0.76		u_s($C4H_3$-$C5H_3$)
1333	0.0		u_{as}($C4H_3$-$C5H_3$)
1313	0.26		δ_s(C1H1-C2H2)
1205	0.001		ν(C2=C3)
1127	0.78		ν_{as}(C3C4-C3C5)
1036	7.4	s	ν(C1-C2)
1012	0.008		γ''_s($C4H_3$-$C5H_3$)
979	0.028		γ_{as}(C1H1-C2H2)
963	0.004		γ'_{as}($C4H_3$-$C5H_3$)
901	0.001		γ''_{as}($C4H_3$-$C5H_3$)
892	3.1	m	γ'_s($C4H_3$-$C5H_3$)
883	0.088		γ_s(C1H1-C2H2)
759	0.047		ν_s(C3C4-C3C5)
679	0.016		δ(O=C1-C2)
559	4.6	s	ν_{as}(PtC2=C3)
415	1.9	w	ν_s(PtC2=C3)
378	1.4	w	δ(C3-C4,C5)
333	0.42		δ(C1-C2=C3)
290	0.30		τ_s(CH_3)
270	0.24		τ_{as}(CH_3)
240	5.9	s	τ(C1-C2)
231	0.38		δ(C2=C3,4,5)
222	0.118		ω(C2=C3,4,5)
208	0.80		τ(C2=C3)
101	0.59		fT
85	9.8	s	fT
76	11.0	vs	fR
0	0	-	-

Table 7.9: Vibrational analysis of the η^2-diσ(CC)-(s)-cis complex of prenal/Pt(111).

ω cm^{-1}	Intensity $\times 10^6$ au		Normal mode
3069	0.002		ν(C4-H3)
3028	0.062		ν(C2-H2)
3018	0.021		ν(C5-H6)
3015	0.0		ν_{as}(C4-H4,5)
2952	0.94		ν_{as}(C5-H7,8)
2926	0.24		ν(C1-H1)
2921	0.63		ν_s($C4H_3$)
2894	0.051		ν_s($C5H_3$)
1453	0.45		ν(C1=O)
1429	0.40		δ_s''($C4H_3$-$C5H_3$)
1425	0.10		δ_s'($C4H_3$-$C5H_3$)
1408	0.008		δ_{as}"($C4H_3$-$C5H_3$)
1398	0.12		δ_{as}'($C4H_3$-$C5H_3$)
1355	0.43		u_s($C4H_3$-$C5H_3$)
1338	0.032		δ_s(C1H1-C2H2)
1331	0.004		u_{as}($C4H_3$-$C5H_3$)
1312	0.059		δ_{as}(C1H1-C2H2)
1181	0.084		ν(C2=C3)
1130	0.54		ν_{as}(C3C4-C3C5)
1063	2.6	m	ν(C1-C2)
1039	1.6	w	γ_s"($C4H_3$-$C5H_3$)
967	0.019		γ_{as}'($C4H_3$-$C5H_3$)
923	0.029		γ_{as}(C1H1-C2H2)
913	0.25		γ_{as}"($C4H_3$-$C5H_3$)
906	0.24		γ_s'($C4H_3$-$C5H_3$)
860	2.3	m	γ_s(C1H1-C2H2)
760	0.021		ν_s(C3C4-C3C5)
690	0.089		ν_s(PtC2-PtC3)
539	7.6	m	ν_{as}(PtC2-PtC3)
416	0.0		δ(C3-C4,5)
367	1.1	w	ν(Pt-O)
361	0.23		δ(C2=C3,4,5)
293	0.68		τ_s(CH_3)
280	17.7	s	τ(C1-C2)
264	1.5	w	δ(C1-C2=C3)
243	0.012		τ_{as}(CH_3)
219	1.7	w	τ(C2=C3)
209	0.62		δ(O=C1-C2)
163	0.091		ω(C2=C3,4,5)
116	0.59		fT
90	0.16		fT
76	2.6		fR

Table 7.10: Vibrational analysis of the η^3-diσ(CC)-σ(O)-(s)-cis complex of prenal/Pt(111).

ω cm^{-1}	Intensity $\times 10^6$ au		Normal mode
3043	0.019		ν(C5-H6)
3038	0.003		ν(C4-H3)
3004	0.11		ν_{as}(C5-H7,8)
2951	0.19		ν_{as}(C4-H4,5)
2947	0.94	m	ν(C1-H1)
2934	0.040		ν_s($C5H_3$)
2918	0.44		ν_s($C4H_3$)
2896	0.018		ν(C2-H2)
1438	0.35	w	δ_s'($C4H_3$-$C5H_3$)
1424	0.14		δ_s"($C4H_3$-$C5H_3$)
1408	0.11		δ_{as}'($C4H_3$-$C5H_3$)
1396	0.13		δ_{as}"($C4H_3$-$C5H_3$)
1349	0.45	w	u_s($C4H_3$-$C5H_3$)
1330	0.001		u_{as}($C4H_3$-$C5H_3$)
1307	0.0		δ_s(C1H1-C2H2)
1234	0.26		δ_{as}(C1H1-C2H2)
1184	0.11		ν(C2=C3)
1164	0.28		ν(C1=O)
1106	0.094		ν_{as}(C3C4-C3C5)
1040	4.9	s	γ_s"($C4H_3$-$C5H_3$)
1020	0.11		ν(C1-C2)
960	0.074		γ_{as}'($C4H_3$-$C5H_3$)
936	0.001		γ_s'($C4H_3$-$C5H_3$)
902	0.008		γ_{as}"($C4H_3$-$C5H_3$)
872	0.44	w	γ_{as}(C1H1-C2H2)
815	0.045		ν_s(C3C4-C3C5)
722	0.69	w	γ_s(C1H1-C2H2)
554	2.3	m	ν_{as}(PtC2-PtC3)
521	1.5	m	δ(O=C1-C2)
480	3.0	m	ν_{as}(PtO-PtC1)
444	4.3	s	δ(C2=C3,4,5)
417	2.3	m	ν_s(PtC2-PtC3)
350	1.4	m	δ(C3-C4,5)
293	0.061		τ_s(CH_3)
281	0.0		ν_s(PtO-PtC1)
249	0.043		δ(C1-C2=C3)
245	0.004		τ_{as}(CH_3)
214	0.009		ω(C2=C3,4,5)
196	0.0		τ(C2=C3)
149	0.002		τ(C1-C2)
126	0.033		fT
74	0.059		fR

Table 7.11: Vibrational analysis of the η^4-diσ(CC)-diσ(CO)-(s)-trans complex of prenal/Pt(111).

ω cm^{-1}	Intensity $\times 10^6$ au		Normal mode
3084	0.001		ν(C4-H4)
3033	0.008		ν(C5-H6)
3021	0.021		ν(C2-H2)
3001	0.25		ν_{as}(C4-H3,5)
2998	0.012		ν_{as}(C5-H7,8)
2930	0.88		ν_s($C4H_3$)
2922	0.027		ν_s($C5H_3$)
2914	0.070		ν(C1-H1)
1451	0.11		δ_s"($C4H_3$-$C5H_3$)
1431	1.3	w	δ_s'($C4H_3$-$C5H_3$)
1412	0.021		δ_{as}'($C4H_3$-$C5H_3$)
1402	0.14		δ_{as}"($C4H_3$-$C5H_3$)
1389	0.35		ν(C2=C3)
1352	0.66		u_s($C4H_3$-$C5H_3$)
1340	0.041		u_{as}($C4H_3$-$C5H_3$)
1308	0.005		δ(C1H1)
1294	0.33		δ(C2H2)
1186	0.065		ν(C1=O)
1154	0.54		ν_{as}(C3C4-C3C5)
1044	0.45		γ_s'($C4H_3$-$C5H_3$)
1032	2.9	m	γ_s"($C4H_3$-$C5H_3$)
968	0.17		γ_{as}'($C4H_3$-$C5H_3$)
935	1.7	w	ν(C1-C2)
917	0.034		γ_{as}"($C4H_3$-$C5H_3$)
894	0.97		γ(C2H2)
796	0.042		γ(C1H1)
779	0.092		ν_s(C3C4-C3C5)
666	0.75		δ(O=C1-C2)
512	9.5	s	ν_{as}(PtO-PtC1)-ν_{as}(PtC2-PtC3)
437	1.0		ν_{as}(PtO-PtC1)+ν_{as}(PtC2-PtC3)
396	1.6	w	δ(C3-C4,5)
354	0.89		δ(C2=C3,4,5)
343	0.72		ν_s(PtO-PtC1)-ν_s(PtC2-PtC3)
280	0.58		ν_s(PtO-PtC1)+ν_s(PtC2-PtC3)
245	0.37		δ(C1-C2=C3)
225	0.089		τ_s(CH_3)
196	0.22		τ(C2=C3)
179	0.35		τ_{as}(CH_3)
154	2.64		ω(C2=C3,4,5)
133	1.0		τ(C1-C2)
103	0.002		fT
82	0.25		fR

Table 7.12: Vibrational analysis of the η^4-π(CC)-diσ(CO)-(s)-cis complex of prenal/Pt(111).

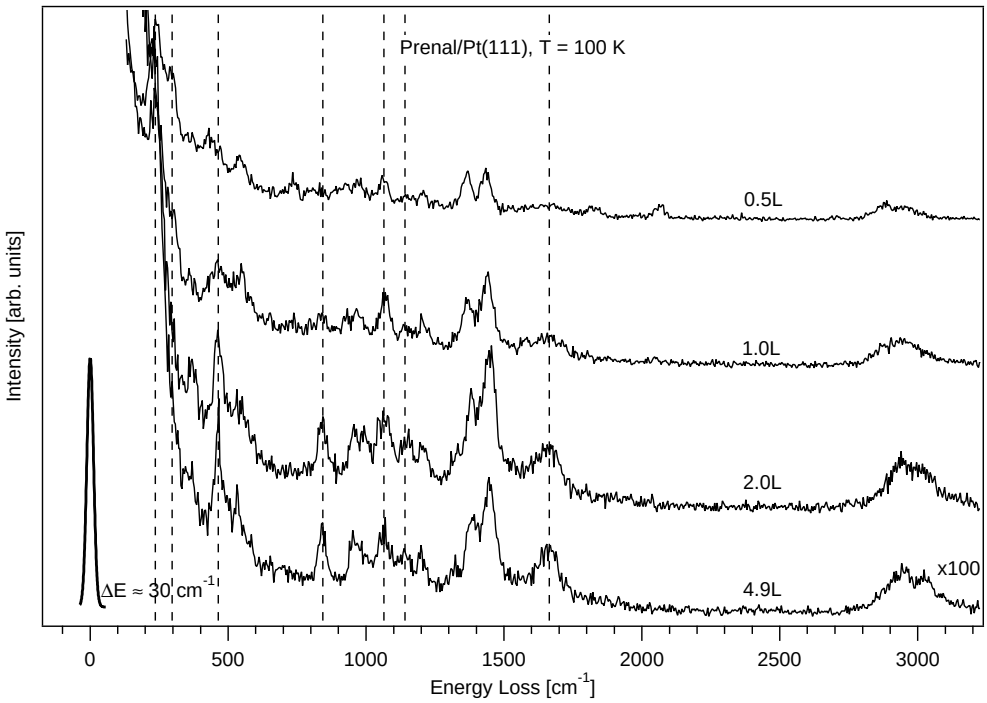

Figure 7.15: HREELS series of various inital precoverages of prenal on Pt(111) at 100 K. All HREEL spectra have been recorded in specular geometry at an angle of incidence of 60° with a primary energy of 4.7 eV.

Further HREELS experiments of prenal have been carried out as a function of coverage in order to investigate the effects correlated with the different low temperature desorption states detected by TPD. After annealing the sample to 188 K and above (Figs. 7.16 and 7.17), the HREELS experiments of various initial coverages characterized in the TPD studies (Sec. 7.1.1) as multilayer (4.9L) or submonolayer (below 1L) are essentially identical. Slight decreases of the overall intensities point to lower coverages, but neither the frequencies nor the relative peak intensities vary significantly. In line with the lower coverages a small amount of coadsorbed CO (2061 cm^{-1}, top sites and 1820 cm^{-1}, bridge sites [37]) builds up during the measurements for prenal exposures below 1L.
Basically the only coverage dependency is found at temperatures below the multilayer desorption at 163 K. This is shown by the HREELS experiments performed just after adsorption of prenal at 100 K, which are depicted in Fig. 7.15. A number of signals, among them the loss peaks at 240 cm^{-1}, 464 cm^{-1}, 842 cm^{-1}, 1064 cm^{-1}, ca 1150 cm^{-1} and ca 1660 cm^{-1} that have been discussed in detail above, are damped relatively to the other measured peaks for exposures below 1L. Further changes are visible in the ν(C-H) stretching region, which shifts strongly and shrinks in width. The HREELS results of 0.5L and 1.0L prenal/Pt(111) at 100 K coincide very well with the spectrum of 4.9L annealed to 205 K. Hence, it seems that the spectrum of 2.0L corresponds still mainly to a physisorbed prenal species, while the HREELS experiments of less than 1L prenal lead immediately to the formation of the irreversibly chemisorbed η^2, η^3 and η^4 prenal structures, which have already been identified from 169 K to 205 K.
Therefore no strong coverage dependence of the irreversibly adsorbed prenal species on Pt(111) is found and the origin of the low temperature desorption states α_2 (180 K) and α_2 (199 K) cannot be understood from the present results.

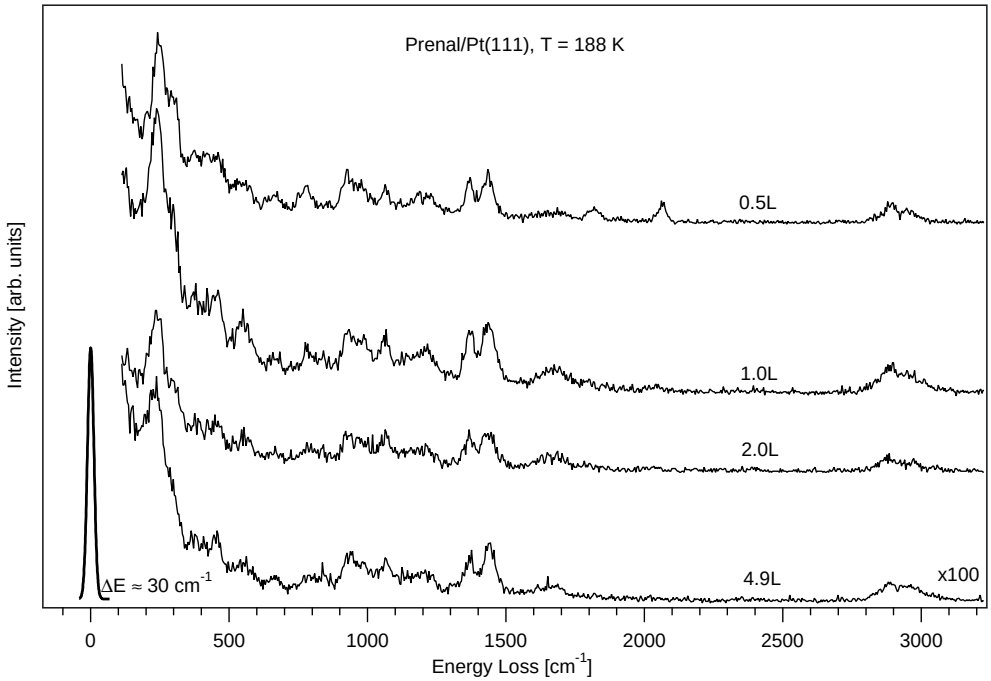

Figure 7.16: HREELS series of various inital precoverages of prenal on Pt(111) at 188 K. All HREEL spectra have been recorded in specular geometry at an angle of incidence of 60° with a primary energy of 4.7 eV.

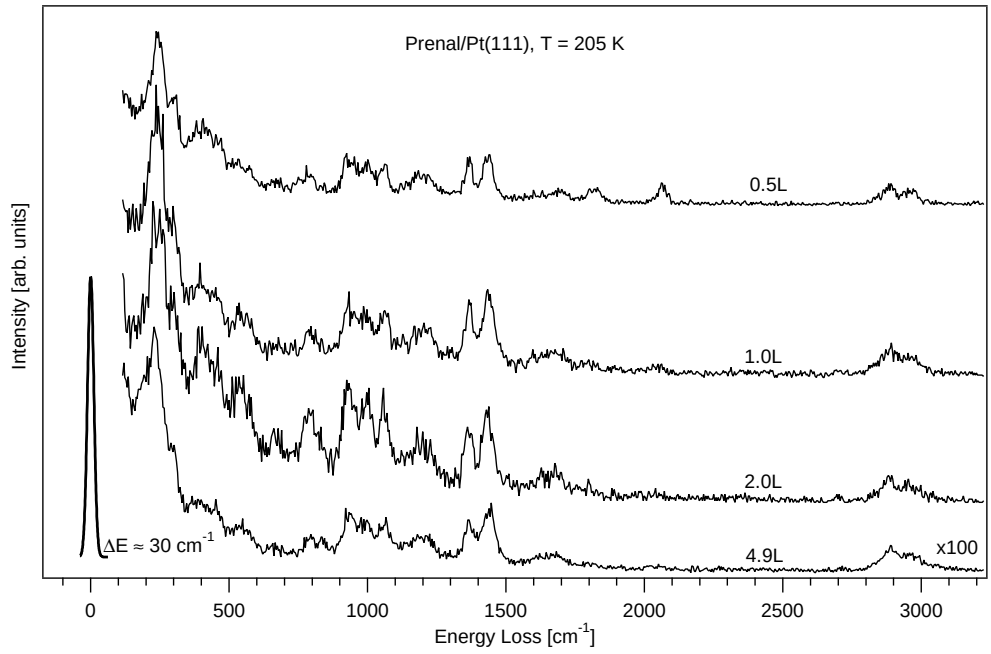

Figure 7.17: HREELS series of various inital precoverages of prenal on Pt(111) at 205 K. All HREEL spectra have been recorded in specular geometry at an angle of incidence of 60° with a primary energy of 4.7 eV.

7.1.5 HREELS of the Decomposition Process on Pt(111)

Above 250 K the decomposition pathway of prenal starts (TPD: first desorption of H_2 around 280 K) and leads to drastic changes in the measured HREEL spectra. Typical HREELS data of the temperature range from 325 K to 480 K are presented in Fig. 7.18. As the vibrational characteristics of the irreversibly adsorbed prenal species can still be observed at temperatures up to 315 K or partially even 350 K, it can be suggested that a part of it is still present intact on Pt(111), while another part is already decomposed and stable intermediates with a "close" structural relationship have been formed on the surface.

First signs of CO adsorbed in bridge sites are detected at 300 K with the development of the loss peak at 1800 cm^{-1}. Due to intermolecular interactions, this signal is shifted to lower wavenumbers compared to the value of 1865 cm^{-1} (2105 cm^{-1} for top adsorption sites) measured by Paffett et al. with HREELS for a saturation coverage of CO on Pt(111) [37]. Between 325 K and 375 K CO populates both the bridge (1805 cm^{-1}) and the top (2040 cm^{-1}) sites. At the same time, the ν(C1=O) vibration of the adsorbed η^2 prenal species grows more intense around 1700 cm^{-1} (blueshift of ca 35 cm^{-1}) and becomes a much better defined peak with a width of 45 cm^{-1}. At 440 K, after the desorption of CO is measured by TPD (desorption maximum at 414 K), no more traces of either molecularly adsorbed CO or CO in an aldehydic function can be observed by vibrational spectroscopy. Therefore it is concluded that above 440 K only pure hydrocarbons are left on the surface and decompose further under release of hydrogen.

Like the discussion of the decomposition process of crotonaldehyde already taught, the analysis of a decomposition pathway is very difficult. Also for prenal the huge number of conceivable surface intermediates and the five stable adsorption complexes that may contribute at the same time in the high temperature HREEL spectra demand a very careful analysis, especially concerning the overlapping loss intensities. However, in terms of frequencies numerous intermediates, such as for instance the other potential first (de-)hydrogenation products, can be ruled out easily and unambiguously by the DFT results.

The first stable intermediate in the decomposition process that can be identified is the dehydro-η^3-triσ(CCC)-prenal-H1 (Fig. 7.21) radical structure, which is formed by a dissociation of the aldehydic hydrogen H1[12]. Choosing the most stable adsorption complex of prenal, η^3-diσ(CC)-σ(O)-(s)-cis, as a starting point, this first fragmentation reaction is strongly exothermic with -73.1 kJ/mol and it is significantly more favorable than an alternative dissociation of the vinylic H2 or a methly hydrogen (Fig. 7.20)[13]. As expected the aldehydic C-H bond is the weakest bond of the unsaturated aldehydes. The resulting optimized structure is very similar to the related dehydrogenation product of crotonaldehyde, i.e. the dehydro-η^3-triσ(CCC)-E-H1 geometry (see Chap. 6.1.6). Its bonds to the surface are comparably short, because the structure sits optimally around a threefold hollow site. The r(Pt1-C1) distance is 2.02 Å, and r(Pt3-C2) and r(Pt4-C3) are computed at 2.14 and 2.15 Å, respectively. Consistent with the chemical intuition, the bond orders of the C1-C2 and C2-C3 bonds are reduced to single bonds (lengths of 1.50 and 1.51 Å), whereas the C1=O moiety retains its double bond character and exhibits a short distance of 1.21 Å.

The appearance of characteristic vibrational bands of the dehydro-η^3-triσ(CCC)-H1 intermediate coincides with the blueshift and reshaping of ν(C1=O) at ca 1700 cm^{-1} as well as the damping of a number of loss peaks assigned previously to the five irreversibly bonded prenal forms at temperatures from 325 K up to 375 K. Since this damping is most pronounced for the loss peaks at 375 cm^{-1} (all η^2, η^3 and η^4 forms), 806 cm^{-1} (η^2-(s)-trans), 923 cm^{-1} (shoulder, both η^2 and the η^4-(s)-cis forms) and 1064 cm^{-1} (all), it seems that basically all stable prenal

[12] In order to limit the computational demand, for the first two dissociation steps only the stable intermediates originating from the η^3-diσ(CC)-σ(O)-(s)-cis prenal structure have been considered theoretically. All of the other (s)-cis and (s)-trans adsorption forms are expected to lead to the same intermediate. The satisfying interpretation of the experimental spectra, which follows in this chapter, seems to confirm this approximation retrospectively.

[13] Hence it is even more exothermic for the less strongly bonded prenal adsorption geometries.

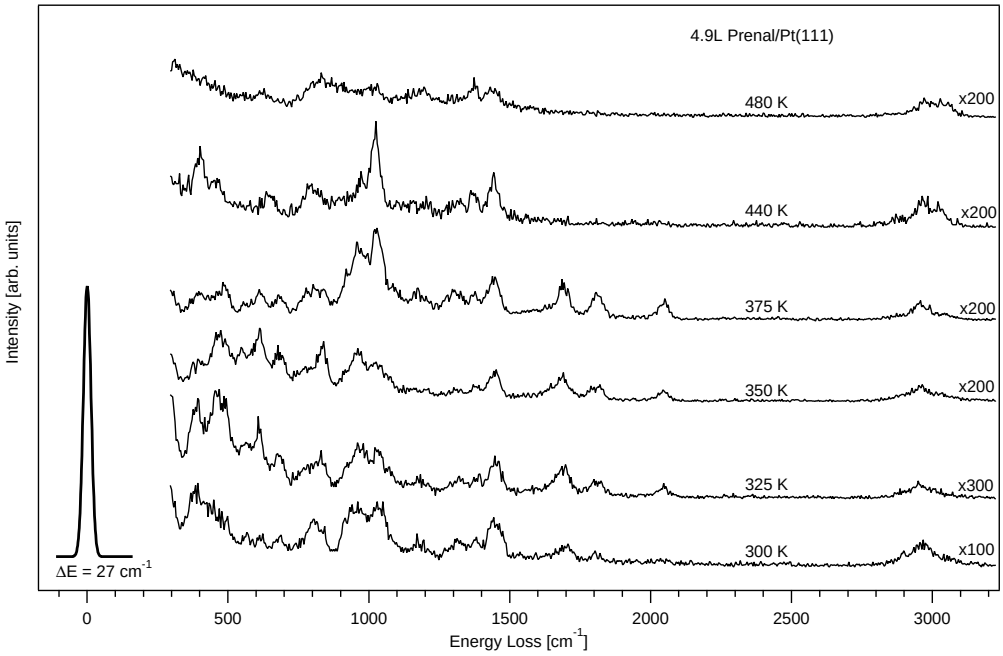

Figure 7.18: HREELS of 4.9L prenal/Pt(111), 300-500K. The HREEL spectra have been recorded in specular geometry at an angle of incidence of 60° (primary energy of 4.7 eV).

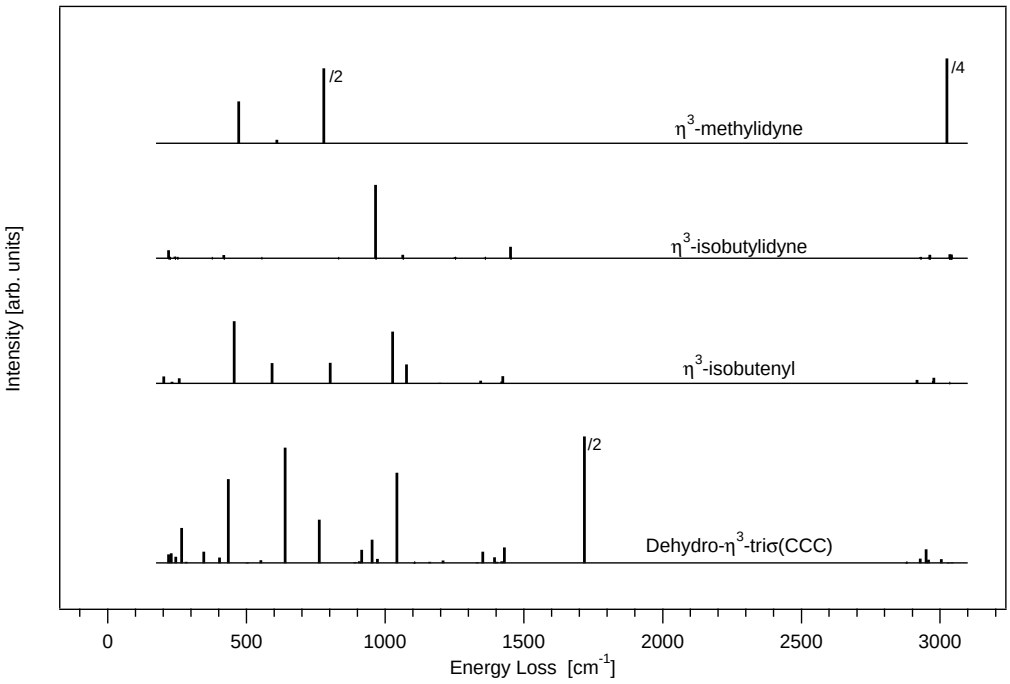

Figure 7.19: Computed HREEL spectra of potential fragments arising from the decomposition of prenal on Pt(111).

adsorption complexes are affected simultaneously. In fact, several intense vibrational features of the η^3-(s)-cis complex (for example those around 550, 842 and 992 cm^{-1}) seem to be present somewhat longer, but the coincidence of these frequencies with the computed loss peaks of the new dehydro-η^3-triσ(CCC)-H1 intermediate prevents any unambiguous assignment here.
Employing the theoretical assignments given in Tab. 7.13 and the plot of the bar diagram shown in Fig. 7.19, specific vibrational losses of the new intermediate can be deduced in combination with the HREEL spectra. Of course, as mentioned above, the ν(C1=O) stretching mode computed at 1718 cm^{-1} reproduces nicely the blueshift observed in the experiments and is thus well suited for an identification. Further normal modes specific to this intermediate are computed around 435 cm^{-1} (totally symmetric linear combination ν_s(PtC1-PtC2)+ν(PtC3), intense and broad peak from 360 to 506 cm^{-1} in the experiment; probably this mode must be assigned to the peak shifted to 392 cm^{-1}) and at 640 cm^{-1}, where the highly intense ν_{as}(PtC1-PtC2) vibration of this structure agrees well with the new loss peak at 611 cm^{-1} that is present between 325 and 375 K. Despite the deviation of these frequencies of roughly 30 cm^{-1} caused by the neglect of the coupling to the surface phonons, anharmonicity and coverage-dependent interactions between the various surface species, the agreement with the experiments is very satisfying. Disadvantageously, hardly any characteristic changes can be traced back to the dehydro-η^3-triσ(CCC)-H1 fragment in the fingerprint region. Here only the symmetrically coupled "out-of-plane" γ_s"($C4H_3$-$C5H_3$) wagging mode of the hydrogens of both methyl groups is sufficiently intense at 1042 cm^{-1}, but the corresponding experimental feature detected in this range has already been assigned to a number of intense vibrations originating from all five stable prenal structures and is thus of little help. Other vibrations of this new fragment are calculated with weak loss intensity between 922 and 953 cm^{-1} as well as between 1352 and 1429 cm^{-1}, but also these are of little use for an identification.
The proceeding decomposition of the five stable prenal adsorption forms seems to be finished at roughly 350 K as evidenced by TPD and HREELS. Since at this temperature the first H_2 desorption β_1 is completed and the ν(C1=O) stretching mode at 1691 cm^{-1} has become an intense and well-defined peak, while at the same time several peaks assigned to the stable adsorption structures of prenal are gone, it is concluded that mainly fragment species populate the surface now. Hence the remaining peaks in HREEL spectra have to be explained solely by loss signals originating from the decomposition products. Moreover, between 375 K and 440 K even the dehydro-η^3-triσ(CCC)-H1 intermediate must be decomposed completely since no more ν(C1=O) stretching mode is visible in the latter HREEL spectrum.
Therefore it seems to be the most promising strategy at this point to use primarily the HREELS data recorded at 350 K for the spectroscopic identification of the various "first" decomposition intermediates, among them the dehydro-η^3-triσ(CCC)-prenal-H1 fragment (Fig. 7.22).
Continuing the DFT analysis with the next decomposition step it turns out that the release of the CO moiety from the dehydro-η^3-triσ(CCC)-H1 intermediate is energetically more advantageous than other conceivable reactions, among them a dehydrogenation of the vinylic H2 or the rehydrogenation of C3. With the CO fragment staying adsorbed on a top site, the evolving η^3-isobutenyl intermediate (PFr5, Fig. 7.21(b)) is reached in an exothermic step with a free reaction energy of -38.7 kJ/mol. Like the preceeding dissociation step of prenal, this elementary step is slightly more exothermic than the corresponding dissociation identified for crotonaldehyde, which showed reaction free energies of -62.5 and -31.0 kJ/mol, respectively. The final optimized geometry of the η^3-isobutenyl intermediate can be described as a diσ(CC) coordination of the unsaturated C1C2 moiety, which due to its radical character is turned in such a manner that the terminal C1 is bonded in a bridge configuration. Consequently the distances r(C1-Pt) are very short at 2.08 Å as compared to 2.14 Å for the bond length of C2 sitting on top of Pt3. The σ(C2-Pt3) bond is understood to be elongated furthermore by the tendency to avoid the sterical strain arising from the repulsion of the methyl groups and the surface.
From the configurations of the carbons C1 and C2 it is clear that the C1-C2 bond has a single

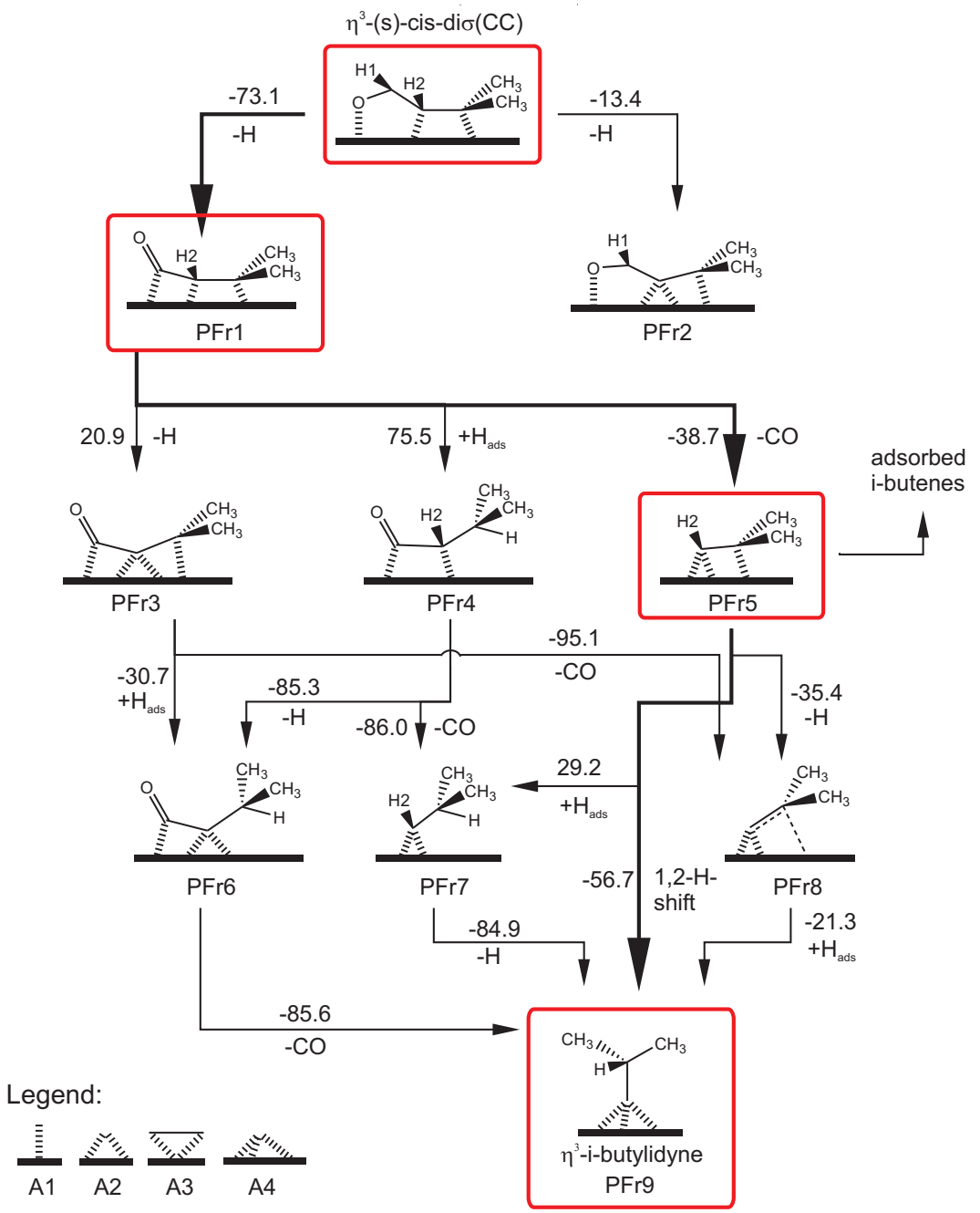

Figure 7.20: Potential initial decomposition steps of prenal/Pt(111). The bold arrows indicate the most probable decomposition route. Marked with boxes are the surface intermediates that have been identified above 250 K by the combination of HREELS and DFT. All relative energies in this scheme are given in kJ/mol. Legend: Coordination type A1 corresponds to a singly-bonded species (i.e. top), A2 to a bridge site, A3 represents a π-type metallacycle structure and A4 refers to a threefold hollow site configuration.

ω cm^{-1}	Intensity $\times 10^6$ au		Normal mode
3042	0.012		ν(C4-H2)
3030	0.005		ν(C5-H5)
3004	0.17		ν_{as}(C4-H3,4)
2958	0.13		ν(C2-H1)
2949	0.57		ν_{as}(C5-H6,7)
2928	0.19		ν_s($C4H_3$)
2879	0.015		ν_s($C5H_3$)
1718	10.6	s	ν(C1=O)
1429	0.65		δ_s'($C4H_3$-$C5H_3$)
1421	0.070		δ_s"($C4H_3$-$C5H_3$)
1403	0.046		δ_{as}"($C4H_3$-$C5H_3$)
1394	0.24		δ_{as}'($C4H_3$-$C5H_3$)
1351	0.47		u_s($C4H_3$-$C5H_3$)
1332	0.010		u_{as}($C4H_3$-$C5H_3$)
1209	0.11		δ(C2H1)
1160	0.057		ν(C2=C3)
1105	0.015		ν_{as}(C3C4-C3C5)
1042	3.8	m	γ_s"($C4H_3$-$C5H_3$)
972	0.17		ν(C1-C2)
953	0.98		γ_{as}'($C4H_3$-$C5H_3$)
915	0.56		γ(C2H1)
907	0.075		γ_{as}"($C4H_3$-$C5H_3$)
892	0.042		γ_s'($C4H_3$-$C5H_3$)
763	1.8	m	ν_s(C3C4-C3C5)
640	4.8	s	ν_{as}(PtC1-PtC2)
552	0.12		δ(C1-C2=C3)
503	0.0		ν_s(PtC1-PtC2)-ν(PtC3)
435	3.5	m	ν_s(PtC1-PtC2)+ν(PtC3)
403	0.23		δ(C2=C3,4,5)
346	0.47		δ(C3-C4,5)
283	0.053		τ_s(CH_3)
267	1.5	w	τ(C2=C3)
245	0.26		τ_{as}(CH_3)
229	0.41		τ(C1-C2)
220	0.36		ω(C2=C3,4,5)
183	0.30		δ(O=C1-C2)
126	0.002		fT
91	0.29		fT
56	0.011		fR

Table 7.13: Vibrational analysis of the dehydro-η^3-triσ(CCC)-prenal-H1 species (PFr1) on Pt(111) (coverage 1/9). The letters following the computed intensities refer to the relative strength, i.e. (v)w = (very) weak, m = medium and (v)s = (very) strong. The coupling of different vibrations is indicated by (+) (in phase) and (-) (anti-phase movement).

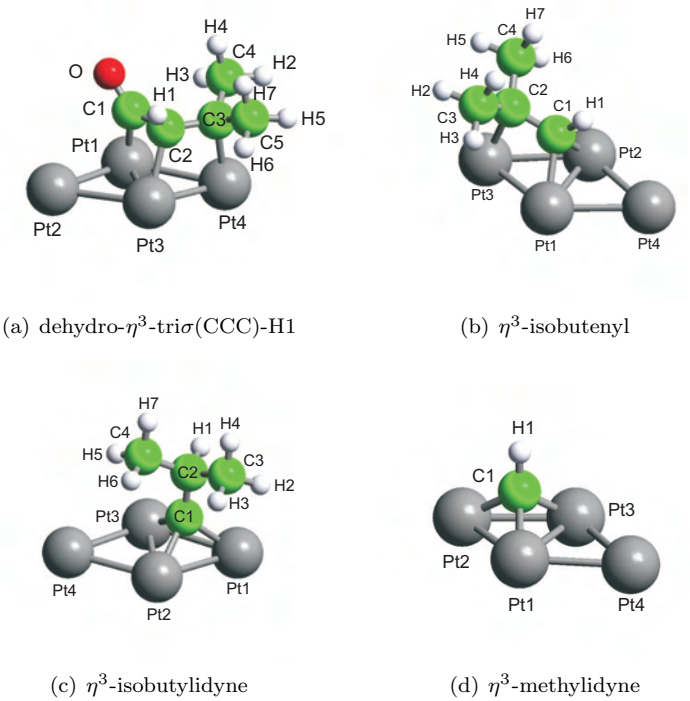

(a) dehydro-η^3-triσ(CCC)-H1 (b) η^3-isobutenyl

(c) η^3-isobutylidyne (d) η^3-methylidyne

Figure 7.21: Schemes of the optimized geometries of the fragments identified by HREELS and DFT appearing during the decomposition of prenal on the Pt(111) surface.

bond character. This is confirmed by both the typical r(C1-C2) distance of 1.49 Å and the ν(C1-C2) stretching frequency computed at 1197 cm^{-1} with a negligible loss intensity. In terms of characteristic loss peaks, also the η^3-isobutenyl radical is very difficult to identify unambiguously in the mixed phase of the already assigned adsorption geometries and intermediates, but its calculated vibrational frequencies and its HREEL intensities (Tab. 7.14) fit very well to the experimental data measured between 325 and 375 K and therefore it cannot be excluded. One could say that this radical form is nearly concealed by the vibrational features of the previously discussed surface species.

The best hints for the presence of this intermediate are deduced again in the low frequency region between 400 and 800 cm^{-1}, which exhibit only a few comparably weak and badly resolved loss signals from the prenal adsorption complexes below 300 K. At 802 cm^{-1} (ν_s(C2C3-C2C4)), 592 cm^{-1} (partially symmetric ν_s(Pt1C1-Pt2C1)-ν(Pt3C2)) and 456 cm^{-1} (totally symmetric ν_s(Pt1C1-Pt2C1)+ν(Pt3C2)), three intense vibrations of the η^3-isobutenyl radical can be correlated with the experimental peaks at ca 797 cm^{-1}, 550 cm^{-1} and 465 cm^{-1}. Most probably the measured intensity of the double peak around 465 cm^{-1} and the signal at 550 cm^{-1}, which below 325 K were significantly weaker, must be attributed to η^2-isobutenyl since the other surface species are by far less intense here.

Further loss signals computed with large intensities are obtained from the "vertical" δ(C1H1) angular deformation mode and the γ_s"($C3H_3$-$C4H_3$) methyl wagging vibration computed at 1077 and 1026 cm^{-1}, respectively, but in this frequency range barely any of the other surface species is inactive. The precision of the computed frequencies, the uncertainity of the theoretical model towards the coverage, the disorder, anharmonicity etc. and also the limited experimental resolution do not allow to differentiate the various contributions of all prenal adsorbates and decomposition intermediates in detail for these signals.

ω cm^{-1}	Intensity $\times 10^6$ au		Normal mode
3033	0.016		ν_s(C3H2-C4H5)
3031	0.0		ν_{as}(C3H2-C4H5)
2978	0.24		ν_{as}(C3-H3,H4)
2975	0.11		ν_{as}(C4-H6,H7)
2949	0.006		ν(C1-H1)
2916	0.16		$\nu_s(C3H_3)+\nu_s(C4H_3)$
2912	0.007		$\nu_s(C3H_3)-\nu_s(C4H_3)$
1424	0.31		δ_s"($C3H_3$-$C4H_3$)
1421	0.079		δ_s'($C3H_3$-$C4H_3$)
1403	0.0		δ_{as}"($C3H_3$-$C4H_3$)
1397	0.0		δ_{as}'($C3H_3$-$C4H_3$)
1344	0.12		u_s($C3H_3$-$C4H_3$)
1324	0.013		u_{as}($C3H_3$-$C4H_3$)
1197	0.032		ν(C1-C2)
1106	0.003		ν_{as}(C2C3-C2C4)
1077	0.79	m	δ(C1H1)
1026	2.2	s	γ_s"($C3H_3$-$C4H_3$)
956	0.011		γ_{as}'($C3H_3$-$C4H_3$)
931	0.007		γ_s'($C3H_3$-$C4H_3$)
901	0.001		γ_{as}"($C3H_3$-$C4H_3$)
802	0.86	m	ν_s(C2C3-C2C4)
697	0.009		γ(C1H1)
592	0.86	m	ν_s(Pt1C1-Pt2C1)-ν(Pt3C2)
520	0.007		ν_{as}(Pt1C1-Pt2C1)
456	2.6	s	ν_s(Pt1C1-Pt2C1)+ν(Pt3C2)
377	0.002		δ(C2-C3-C4)
280	0.007		τ(C1-C2)
258	0.21		δ(C1-C2-C3,C4)
232	0.068		$\tau(C3H_3)+\tau(C4H_3)$
202	0.30		$\tau(C3H_3)-\tau(C4H_3)$
157	0.040		fR
149	0.21		fT
117	0.004		fR

Table 7.14: Vibrational analysis of the η^3-isobutenyl species (PFr5) on Pt(111) (coverage 1/9).

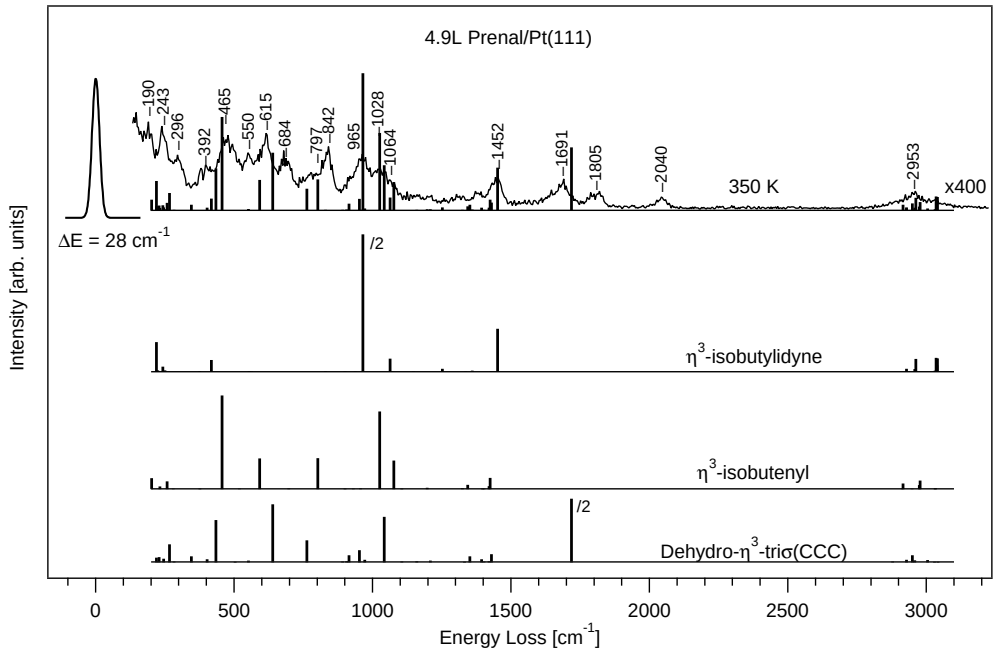

Figure 7.22: Comparison of a typical HREEL spectrum of 4.9L prenal/Pt(111) annealed to 350 K and the computed HREEL spectra of the dehydro-η^3-triσ(CCC)-prenal-H1, the η^3-isobutenyl and the η^3-isobutylidyne species.

Between 300 K and 375 K a third decomposition product is found that helps to interpret the experimental HREELS data. The highly stable η^3-isobutylidyne complex (PFr9, Fig. 7.21(c)) can be identified on the Pt(111) surface. It is proposed to evolve from the η^3-isobutenyl radical by a 1,2-hydrogen shift with a free energy of -56.7 kJ/mol. Competing sequences of a hydrogenation of C2 and a dehydrogenation of C1 or vice versa are expected to be disfavored by larger activation barriers as the reaction free energies are sizably more positive[14]. Moreover, none of the two possible intermediates from the two alternative routes, namely PFr7 or PFr8, possess vibrational fingerprints consistent with the measured HREEL spectra. Structurally η^3-isobutylidyne is closely related to other alkylidynes by its typical, short Pt-C bonds in the threefold hollow site configuration[15].

Like its smaller counterparts ethylidyne and propylidyne detected during the decomposition of crotonaldehyde, this species seems to be kinetically relatively stable, because its accumulation on the surface at temperatures up to 375 K can be easily recognized in the HREEL spectra. At higher annealing temperatures such as 440 K, the signals of this species are found to be damped strongly in the HREEL spectra. Since TPD showed a H_2 desorption state β_2 around 425 K, it is suggested that the η^3-isobutylidyne complex undergoes further fragmentation reactions between 375 and 440 K and only a small surface fraction remains intact and contributes to the higher temperature spectrum.

Since the excellent fits of the computed HREEL spectra of the dehydro-η^3-triσ(CCC)-prenal-H1 and the η^3-isobutenyl structures with the experiment have been discussed above, it is now required to analyse the spectroscopic features, especially those unaccounted for so far, with the

[14] This expectation is based on the *Hammond* principle.

[15] Due to the symmetry reduction induced by the methyl substituents, the distance r(C1-Pt2) is slightly shorter at 2.02 Åthan r(C1-Pt1,3) at 2.03 Å. The C-C bond lengths r(C1-C2) and r(C2-C3,4) correspond to typical single bonds with values of 1.51 and 1.54 Å, respectively.

fingerprint of the η^3-isobutylidyne species (Fig. 7.22). This is possible by its extremely intense ν(C1-C2) stretching mode computed at 965 cm^{-1}, which is oriented nearly perfectly along the surface normal and coincides well with the experimental signal at 960 cm^{-1} (Tab. 7.15). This vibration, which is close to the two loss peaks arising from several normal modes of at least the η^2-(s)-trans, η^2-(s)-cis and the η^4-(s)-cis prenal adsorption complexes overlapping at ca 923 and 992 cm^{-1} in the 205 K to 300 K HREEL spectra, is generally well resolved in the experiments recorded after annealing to higher temperatures. At 350 K it explains the comparably intense experimental feature basically alone.

Also at 1452 cm^{-1} an excellent agreement of a measured loss peak and the active δ_s"($C3H_3$-$C4H_3$) deformation mode of the methyl hydrogens of this intermediate is found and improves the correspondence of the intensities obtained at slightly lower frequencies from the related deformation modes of the dehydro-η^3-triσ(CCC)-prenal-H1 and the η^2-isobutenyl forms with the experimental data. Together with the γ_s'($C3H_3$-$C4H_3$) (1064 cm^{-1}), the ν_{as}(Pt1C-Pt3C-Pt2C) (418 cm^{-1}) and the τ(C1-C2) (220 cm^{-1}) normal modes, the η^1-isobutylidyne structure thus agrees quite well with the experimental results and supports the interpretation.

Previous investigations of other groups on the adsorption and reactive behavior of various alkenes on Pt(111) reported the appearance of η^1-isobutylidyne in the high temperature decomposition of irreversibly adsorbed isobutene [132, 150, 151]. TPD experiments performed to follow such decomposition steps and to determine the stochiometric constitution of the remaining surface species showed a desorption state of isobutene between 268 K and 280 K, which was correlated to decreasing coverages of isobutene[16], while at very low initial coverages only a strongly chemisorbed monolayer of isobutene was formed. This monolayer decomposed in several steps between ca 300 and 700 K, leading to subsequent desorption peaks of H_2 at 330 K, 400 K, 480 K, 535 K and 628 K [132]. Quite consistent with the analysis of Avery et al. [150], the surface intermediates resulting from the dehydrogenation steps were assigned to compositions in the range of C_4H_7, $C_4H_{4.5-5}$ and C_4H_3, before above 535 K a set of mixed species with an average composition of $C_4H_{1.5}$ was proposed.

The HREELS measurements of Avery et al. [150], who successfully identified the spectroscopic fingerprint of η^3-isobutylidyne at 300 K (the assignments of these authors are given Tab. 7.15), present furthermore a good reference to examine the quality of the DFT frequency calculations. Comparing the measured peak positions and intensities of the actual experiments to their results, a good agreement with deviations of less than 20 cm^{-1} is found, which is ascribed to coverage effects and intermolecular interactions between the various surface species present in both experiments. Essentially the same vibrations are intense and even the assignments deduced by Avery et al. [150] on purely experimental grounds are closely related to the more detailed DFT analysis given here. Even most of the computed frequencies agree excellently with features in the measured HREEL spectra of the present work, but in some cases slightly larger discrepancies are obtained. For instance the three coupled ν_{as}(Pt1C,Pt2C,Pt3C) normal modes are computed to be too weak to be correlated with experimental peaks around 550 cm^{-1}. As other species like η^3-methylidyne (Pt_3CH, see Chap. 6.1.6) exhibit intense band in this frequency range, only the lowest molecule-surface stretching mode at 418 cm^{-1} can be assigned tentatively to the loss peak measured at 405 cm^{-1} (Avery: 440 cm^{-1}).

Slight discrepancies are also found for the coupled ν(C1-C2) stretching and the $\gamma(CH_3)$ rocking modes that according to the experiments of Avery and coworkers appear at 1080 cm^{-1} (shoulder, weak), 1010 cm^{-1} and 800 cm^{-1}, respectively. Since the spectrum published by this group (resolution ca 55 cm^{-1}) shows a complex pattern of loss peaks from both isobutene adsorption structures and the decomposition products at 300 K, their assignment of the experimental data is not unambiguous. The problem arises in particular from the two signals at 800 and 1010 cm^{-1},

[16] The corresponding desorption activation energies were determined at 68 to 72 kJ/mol by Tsai et al. [132]. No superstructures due to isobutene or its fragments were observed in low and high temperature LEED experiments by these authors.

which in the spectra recorded by this group at 300 K appear nearly similarly intense, while in the one taken after annealing to 420 K the peak at 800 cm^{-1} becomes very weak. Hence one of both signals, probably the one at 800 cm^{-1}, ought to be due to a different surface species, which is not yet decomposed at 420 K in contrast to the η^3-isobutylidyne species causing the vibrational loss at 1010 cm^{-1}.

In the actual results, two intense but wide loss peaks are present at 965 cm^{-1} and 1028 cm^{-1} in a frequency region that is otherwise badly resolved in the experiments. The first peak coincides perfectly with the computed ν(C1-C2) vibration (also 965 cm^{-1}) and is, thus, assigned to it here, even though it is redshifted by roughly 45 cm^{-1} from the value of 1010 cm^{-1} given by Avery and coworkers. Although the shift is rather large, its origin may be the varying interactions between the different surface species on Pt(111) in the two HREELS experiments. Finally, the signal at 800 cm^{-1} detected by Avery et al. agrees well with the symmetrically coupled ν(C2-C3)+ν(C2-C4) normal mode calculated by DFT at 831 cm^{-1}. In the actual HREELS measurements it appears at 793 cm^{-1}. However, one must keep in mind that η^3-methylidyne is also active around 780-800 cm^{-1} and, thus, because it is assumed to be present in significant amounts, an unambiguous assignment is not possible with the limited resolution of HREELS.

As mentioned before, following the increase of the relative intensities of the loss peaks attributed to the η^3-isobutylidyne structure at 375 K, the damping of its signals in the HREEL spectrum at 440 K suggests the onset of its decomposition. Avery et al. suggested purely from their experimental data that the decomposition of the isobutylidyne species at 420 K on Pt(111) leads to a C_{3v} symmetric, cage-like $(Pt_2CH)_3CH$ species, which is positioned over a threefold hollow site and is bonded to the surface by bridge configurations of the three terminal CH groups, while the central CH fragment is oriented along the surface normal. Due to its high symmetry and its orientation, the $(Pt_2CH)_3CH$ species was proposed to exhibit only three active bands at 2985 cm^{-1} (ν(CH)), 1010 cm^{-1} (ν_s(CC)) and 655 cm^{-1} (ν_s(CPt_2)).

Surprisingly, in the DFT calculations carried out for the analysis of the prenal decomposition pathway this species was, indeed, found to be a stable local minimum. Yet its vibrational properties obtained differ significantly from the predictions of Avery et al. Although the theoretical results show a similarly surprising agreement for the ν(C-H_{center}) stretching mode of the central CH group computed at 2979 cm^{-1}, which was assigned by Avery et al. to a peak at 2985 cm^{-1}, the signals computed in the fingerprint region do not correspond well. The only intense modes for this structure are computed at 1125 cm^{-1}, 659 cm^{-1} and 447 cm^{-1}. They are assigned respectively to the symmetric ν(C-C) stretching (breathing) mode, which is coupled to an angular $\delta(CH)$ deformation vibration of the terminal CH groups along the C-C axis, the coupled symmetric δ(CCCC) deformation mode and the symmetrically coupled ν(C-Pt_2) molecule surface stretching vibration.

In contrast to these DFT results, Avery et al. assigned an experimental signal at 1010 cm^{-1} to the ν(C-C) modes (similar frequency like in η^3-isobutylidyne) of the $(Pt_2CH)_3CH$ species and a loss peak at 655 cm^{-1} to the corresponding ν(C-Pt_2) stretching modes. Moreover, the latter experimental loss peak was, in addition, assigned to η^3-methylidyne complexes bonded in threefold hollow sites (Fig. 7.21(d); vibrational assignments in Tab. 7.16), which according to their interpretation evolve from the dissociation of the $(Pt_2CH)_3CH$ species between 420 K and 490 K. Definitely, this signal is not well suited for a differentiation between the latter two surface species. Therefore, in the light of the new results obtained in this thesis, the validation of the experimental assignments of $(Pt_2CH)_3CH$ given by Avery et al. is not possible and a correction must rather be proposed, pointing to yet another surface species to be formed in the decomposition of η^3-isobutylidyne.

Although isobutylidyne shows close counterparts to the vibrational bands of the $(Pt_2CH)_3CH$ intermediate, the change in the relative intensities observed indicates that the latter is not formed in the decomposition pathway of prenal either. Including only the contributions of the discussed three intermediates at 350 K, most of the experimental loss signals are accounted for.

ω cm^{-1}	Intensity $\times 10^6$ au		Normal mode	HREELS[a] cm^{-1}	HREELS[b] cm^{-1}
3041	0.15		ν_{as}(C3-H2,4)		
3038	0.073		ν_{as}(C4-H5,7)		
3035	0.16		ν_{as}(C3-H3,4)	(2953)	2970, ν_{as}(CH$_3$)
3032	0.014		ν_{as}(C4-H6,7)		
2963	0.14		ν_s(C3H$_3$)		2880, ν_s(CH$_3$)
2959	0.030		ν_s(C4H$_3$)		
2929	0.033		ν(C2-H1)		
1452	0.48	w	δ_s"(C3H$_3$-C4H$_3$)	1452	1460, δ_{as}(CH$_3$)
1440	0.001		δ_s'(C3H$_3$-C4H$_3$)		
1429	0.001		δ_{as}"(C3H$_3$-C4H$_3$)		
1427	0.001		δ_{as}'(C3H$_3$-C4H$_3$)		1400, δ_s(CH$_3$)
1359	0.011		u$_s$(C3H$_3$-C4H$_3$)	1367	
1336	0.002		u$_{as}$(C3H$_3$-C4H$_3$)	1327	
1252	0.034		δ(C1H1)		1280, δ(CH)
1251	0.0		γ(C1H1)		
1149	0.001		γ_s"(C3H$_3$-C4H$_3$)		
1070	0.0		ν(C2-C3)-ν(C2-C4)		1080, 1010, 800
1064	0.15		γ_s'(C3H$_3$-C4H$_3$)	1028	coupled ν(CC)
965	3.1	s	ν(C1-C2)	965	and γ(CH$_3$)
937	0.001		γ_{as}'(C3H$_3$-C4H$_3$)		
901	0.0		γ_{as}"(C3H$_3$-C4H$_3$)		
831	0.007		ν(C2-C3)+ν(C2-C4)	(797, Pt$_3$CH)	
562	0.0		ν_{as}(Pt1C-Pt2C+Pt3C)	(615, Pt$_3$CH)	645, ν(CPt), δ(CCC)
554	0.005		ν_{as}(Pt1C+Pt2C-Pt3C)	(465, Pt$_3$CH)	
418	0.13		ν_{as}(Pt1C-Pt3C-Pt2C)	405	440, ν(CPt)
376	0.004		δ(C2-C3-C4)		
251	0.014		τ(C3H$_3$)+τ(C4H$_3$)		
242	0.057		δ(C1-C2-C3,C4)		
225	0.016		τ(C3H$_3$)-τ(C4H$_3$)		
220	0.33		τ(C1-C2)		
125	0.28		fT		
104	0.012		fT		
54	0.001		fR		

Table 7.15: Vibrational analysis of the η^3-isobutylidyne (PFr9) bonded in a threefold hollow site on Pt(111) (coverage 1/9).

[a]Actual work, 4.9L prenal annealed to 350 K.
[b]From Ref. [150]: HREELS experiments of isobutene on Pt(111) at 420 K.

ω cm^{-1}	Intensity $\times 10^6$ au	Normal mode	HREELS[a] cm^{-1}	HREELS[b] cm^{-1}
3024	0.028	ν(C-H)	2964	2970
778	0.013	ν_{as}(Pt$_3$C) + fT (deg.)	793	800
610	0.0	ν_s(Pt$_3$C)	643	(640 fr. propene)
472	0.0	fT + ν_{as}(Pt$_3$C) (deg.)	465	

Table 7.16: Vibrational analysis of the η^3-methylidyne (CFr23, see decomposition reactions of crotonaldehyde in Chap. 6.1.6) bonded in a threefold hollow site on Pt(111) (coverage 1/4).

[a]Actual work, 4.9L prenal annealed to 440 K.
[b]From Ref. [150]: HREELS experiments of isobutene on Pt(111) at 490 K.

Still missing is particularly an assignment of the scattering losses at 296 cm^{-1}, 684 cm^{-1} and 842 cm^{-1}, but their origin cannot be deduced easily here. Despite the large number of hydrocarbon intermediates considered in the theoretical calculations, including basically all possible C_2H_x ($1 \leq x \leq 5$) and C_3H_x ($3 \leq x \leq 7$) species and numerous C_4H_x ($4 \leq x \leq 9$) forms, the next fragments showing a vibrational pattern compatible with the experiment is η^1-methylidyne. In the HREELS spectra after annealing steps between 325 K to 440 K, the bands assigned to η^3-methylidyne coincide with vibrations of other identified surface species and, thus, are not sufficient for an independent assignment. At 480 K yet, the recorded spectra are badly defined and show various very broad signals (FWHM of up to 150 cm^{-1}). Notably the intense, characteristic loss peaks attributed to the hydrocarbon species have basically disappeared and, hence, also the hydrocarbon species. Instead, the signal at ca 825 cm^{-1}, obviously shifted from the 797 cm^{-1} loss peak of isobutylidyne, and the unresolved intensity around 460 and 640 cm^{-1} point to the formation of a highly disordered phase of η^3-methylidyne and surface carbon.
Also a comparison of the HREEL spectra to experimental data of similar species[17] available from the literature did not yield any useful conclusions. Thus, although a number of the important intial decomposition steps could be identified for prenal successfully, the fragmentation steps leading from η^3-isobutylidyne to the smaller C3 or C2 hydrocarbon species and finally to η^3-methylidyne and surface carbon remain unclear at this point. Possibly, a complete investigation of all conceivable reaction steps of isobutylidyne might give new insights on the missing elementary steps of the decomposition pathway.

The conclusions on the decomposition pathway of prenal are linked closely to the results obtained for the fragmentation of crotonaldehyde presented in Chap. 6.1.6 and should be compared at this point. For both α,β-unsaturated aldehydes, the first three reaction steps lead to structurally very similar intermediates. This is not very surprising since the influence of the additional methyl group at the β-carbon is mainly of an indirect nature (the already discussed electronical influence and sterical repulsions). It is generally the aldehydic hydrogen, which is dissociated in a first elementary step from the intact adsorption complexes of the molecules. The reaction free energies are quite close in both cases, i.e. -62.5 kJ/mol for crotonaldehyde and -73.1 kJ/mol for prenal (relative to the η^3-(s)-cis forms). Also common is the second elementary step, in which both dehydro-aldehyde intermediates (CFr1 and PFr1) are decarbonylated to pure hydrocarbons (CFr7 and PFr5). It is slightly more favorable for prenal (-38.7 kJ/mol), although the difference to crotonaldehyde (-31.0 kJ/mol) is not large. Finally, in the last comparable reaction step of both pathways, a 1,2-hydrogen shift leads to the formation of very stable alkylidyne species. For crotonaldehyde, the η^3-propylidyne intermediate (CFr10) has been identified, whereas from the prenal fragmentation an η^3-isobutylidyne (PFr9) complex is produced on Pt(111). Both intramolecular hydrogen shifts are exothermic at -61.1 kJ/mol and -56.7 kJ/mol, respectively, and indicate only a small influence due to the additional methyl group.

[17] For instance some experimetal data is available on ethyl, ethylidene [149], ethylidiyne [148, 149, 150], 1- and 2-propyl, n-propylidene, n-propylidyne [150, 151, 161, 162, 163].

7.1.6 Deuterium Coadsorption Experiments

One of the aims of this study was to investigate the reactivity of prenal concerning the hydrogenation reactions under UHV conditions. Therefore a number of coadsorption experiments of prenal and hydrogen as well as deuterium have been conducted using TPD and HREELS.
For the TPD experiments the same heating rate of 2 K/s was employed as before together with two different sensitivity settings of the SEM of the mass spectrometer. Additionally to the masses observed in desorption experiments of pure prenal, also the masses of HD, D_2 and the various possible deuteration products (D4-3-methyl-butanol, m/z = 92, D2-3-methyl-butanal and D2-3-methyl-2-butenol, both m/z = 88) as well as their dominating fragments were investigated. Two series of experiments have been recorded by either adsorbing prenal (at 100 K) on a deuterium precovered surface or adsorbing deuterium after exposing the Pt(111) surface to increasing exposures of prenal. The ratio of exposures of deuterium to prenal was chosen at 6:1 in all experiments to ensure that a sufficient excess of deuterium was available for any reaction.
Firstly, as the primary result of these experiments it must be concluded that no desorption of deuterated or hydrogenated products has been observed in either of the experimental series. In the TPD spectra of the m/z = 84, 88 and 92 (not shown), no additional signals except the regular low temperature desorption peaks of molecular prenal have been found. Therefore, in line with the related experiments preformed for crotonaldehyde in this thesis and various hydrogenation studies of other α,β-saturated aldehydes in the literature [6, 7, 8, 12, 25, 28], it is evident that the hydrogenation requires higher pressures of the reactants, especially those of hydrogen or deuterium.
In the case of a deuterium precovered sample, prenal does stick on the surface and its desorption can be observed afterwards in the TPD experiments. Hence in this sequence, even large exposures of both reactants can be readily coadsorbed on the surface. This is evidenced in the TPD spectra of HD (3 amu, Fig. 7.24), in which two signals around ca 281 K (β_1) and 475 K (β_3) are recorded, which can be resolved down to low coverages of both reactants (3.0L D_2 and 0.5L prenal). The intermediate desorption state measured with weak intensity around 425 K (β_2) requires relatively high exposures to be distinguishable.
Importantly, the appearance of reaction-limited HD desorption states at T >> 300 K proves that deuterium must have been incorporated into the prenal molecule by a H-D exchange reaction (regular desorption of HD at ca 290K). This phenomenon will be further analyzed in the HREELS spectra below. Furthermore, as expected, the analysis of the integrated desorption peak areas does not reveal any information beyond the fact that due to the coadsorption of increasing amounts of D_2 the peak area of the first, desorption-limited signal around 290 K grows much faster compared to the area of the signal at 475 K.
The TPD spectra of deuterium (m/z = 4, Fig. 7.25) recorded concommitantly show only a single signal shifting from 290 K at low coverages to 267 K for higher exposures of both reactants. No monomolecular dissociation of D_2 from the deuterated prenal species occurs at higher temperatures after the H-D exchange. The TPD spectra of m/z = 2 (Fig. 7.23) indicate the desorption of hydrogen at slightly different temperatures (300-290 K, 410-420 K and 471 K) from HD, but are furthermore similar to the series from pure prenal. Hence, from the latter observations it is deduced that the H-D exchange in the strongly adsorbed prenal species is selective towards a certain hydrogen substituent. The desorption states appearing in TPD are linked specifically to the different hydrogens (or deuterium) in the surface species and the dissociation proceeds stepwise. Around 475 K HD is dissociated in a reaction limited step, whereas the signal at 420 K corresponds purely to a dissociation of H_2.
In order to resolve the question whether deuterium also sticks on a surface already precovered with prenal, similar TPD experiments have been carried out with inversion of the sample exposition to the reactant gases. Like the first procedure also here no hydrogenation or deuteration products could be detected. If (small amounts) of such products had been formed, they decom-

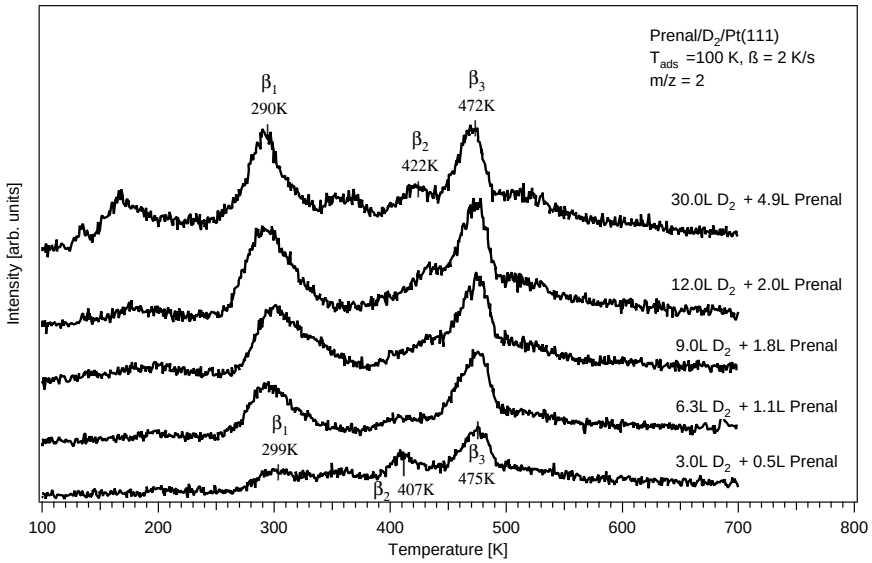

Figure 7.23: TPD spectra after prenal adsorption on a D_2 precovered Pt(111) surface, m/z=2.

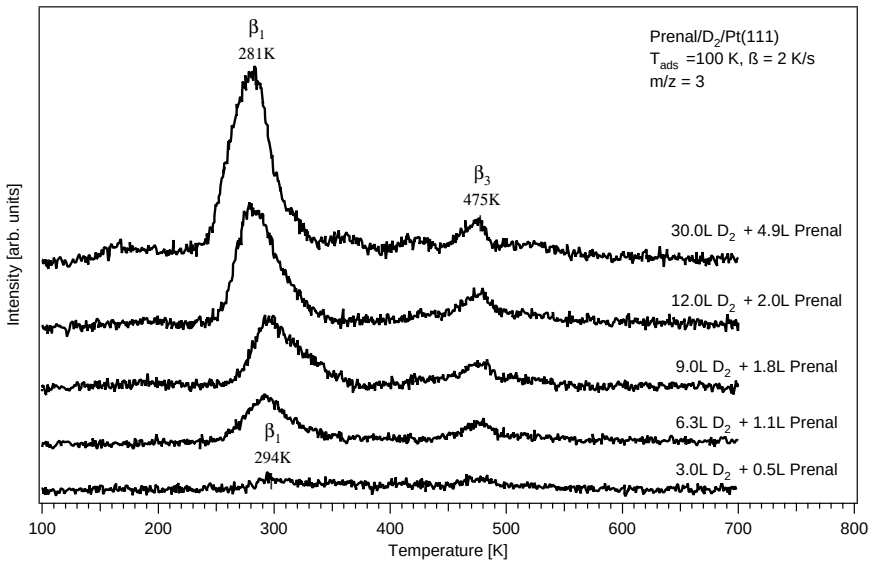

Figure 7.24: TPD spectra after prenal adsorption on a D_2 precovered Pt(111) surface, m/z=3.

posed readily at higher temperatures without giving new signals in addition to those already attributed to the prenal decomposition. Interestingly, deuterium (resp. hydrogen) does stick only weakly on a prenal precovered surface. Large exposures of D_2 are required to detect even very weak desorption signals of HD (Fig. 7.27). The spectra measured of $m/z = 2$ show the usual decomposition behavior known from the pure prenal adsorption (Fig. 7.26), while no signals of $m/z = 4$ could be detected up to 800 K at all (not shown).

Finally the nature of the H-D exchange reaction, i.e. of the hydrogen(s) that are selectively exchanged, has been investigated using HREELS. Fig. 7.28 shows the HREELS spectra taken

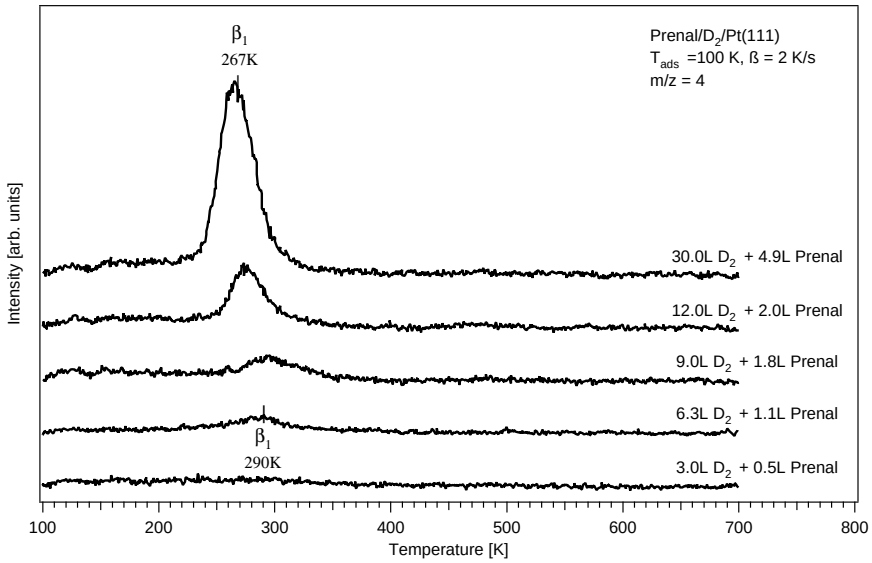

Figure 7.25: TPD spectra after prenal adsorption on a D_2 precovered Pt(111) surface, m/z=4.

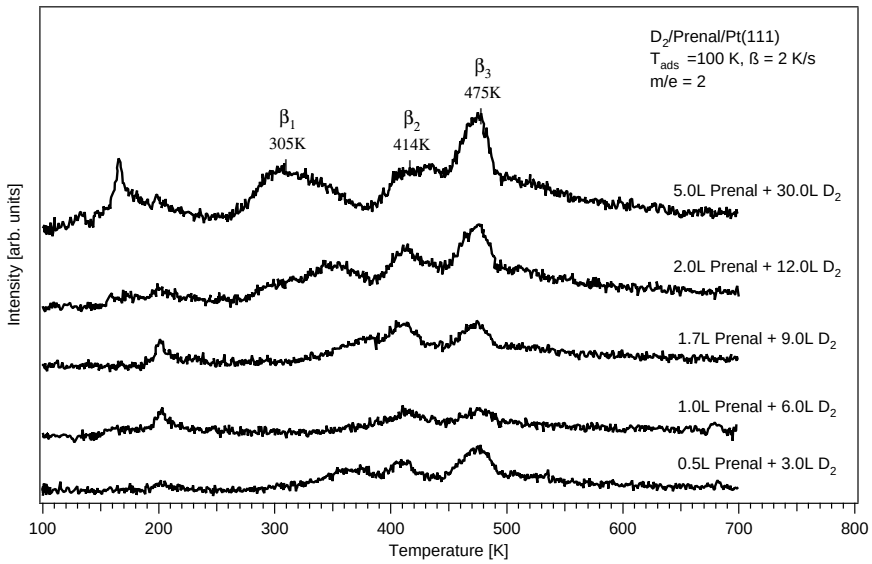

Figure 7.26: TPD spectra after D_2 adsorption on a prenal precovered Pt(111) surface, m/z=2.

after adsorption of 4.9L prenal onto a surface precovered with 30L D_2 at 100 K. The spectra are recorded at a much lower resolution of ca 45 cm^{-1} in order to increase the detectable intensities. Below 300 K no changes are found in the HREELS spectra compared to the spectra of pure prenal on Pt(111). Starting at 300 K, a very weak signal is measured around 2210 cm^{-1} besides the already discussed fingerprints and small amount of coadsorbed CO arising from the decomposition of the stable prenal species. This signal is attributed to a C-D vibrational mode of a deutero-prenal species or one of its first decomposition intermediates. The weakness of this new ν(C-D) stretching mode compared to the sizable desorption peak β_3 around 475 K in TPD is

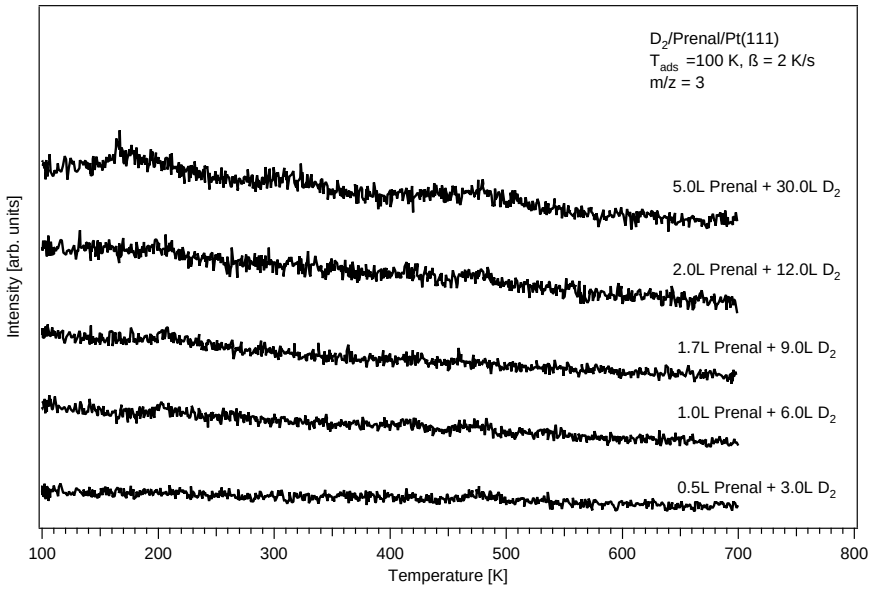

Figure 7.27: TPD spectra after D_2 adsorption on a prenal precovered Pt(111) surface, m/z=3.

rather surprising and might indicate a flat orientation of this C-D stretching vibration parallel to the sample surface.

Since the rotation barriers around the C-C axis of the two methyl groups are expected to be very low[18], an unhindered rotation leads to a coalescence of the distinct ν(C-H) vibrations of all three hydrogens and, thus, all of them become relatively intense. Thus these can be excluded as candidates for the exchanged hydrogen. On the other hand, the hydrogens (deuterium) of the aldehydic and the vinylic functions are oriented more or less coplanar with the surface in the strongly bonded η^2, η^3 and η^4 adsorption modes and are, thus, better candidates to explain the weak scattering intensities observed for the C-D stretching mode. In fact, since it has been shown in Sec. 7.1.5 that the aldehydic hydrogen is dissociated in the first step of the decomposition process of prenal around 300 K and this new ν(C-D) signal remains visible until after the HD desorption at 475 K, an exchange of the vinylic hydrogen H2 seems to be most probable.

A tentative correlation of this loss peak at 2210 cm^{-1}, which shifts even slightly higher to 2230 cm^{-1} at 400 K, with the losses of the corresponding, not exchanged C-H stretching modes of the prenal adsorption complexes is possible by using the averaged isotopic shift of 1.321[19] deduced from vibrational analyses of ethene and D4-ethene on Pd(111) [172]. From this the frequency of the unexchanged ν(C2-H2) stretching mode may be estimated at roughly 2920 cm^{-1}, which might consequently be correlated to a weak low frequency shoulder of the loss signal measured at 2955 cm^{-1} in the HREEL spectra above 300 K. Yet, as neither the exact isotopic shifts of this vibration in the different prenal species or in the decomposition intermediates (at T$\geq$>400 K) nor the exact theoretical frequencies of the various ν(C-H) modes (anharmonicty problem) are known, a further proof would be required to confirm the suggested exchange on the vinylic C2-H2 bond.

In summary the hydrogen and the deuterium coadsorption experiments of prenal on Pt(111) do not lead to the formation and subsequent desorption of any hydrogenation/deuteration products.

[18] See Chap. 6.1.2.

[19] See Chap. 6.1.7. The isotopic shifts of the harmonic oscillator of precisely $\sqrt{2}$ is derived from the ratio of the masses of H and D. The deviation arising from the anharmonicity is thus 7%.

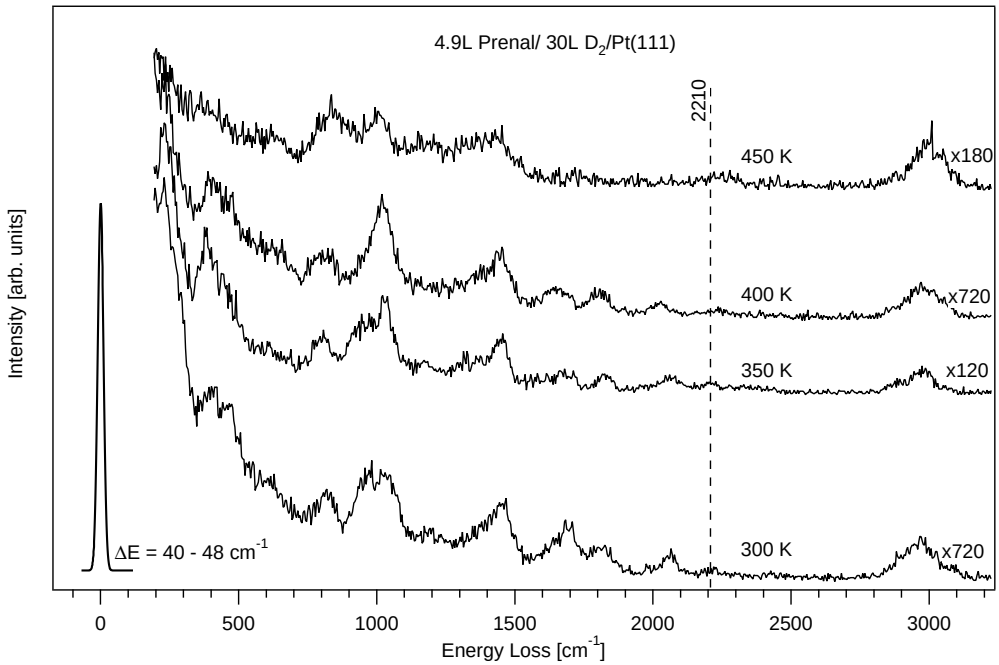

Figure 7.28: HREELS spectra recorded after subsequent annealing steps of 4.9L prenal coadsorbed on a D_2 (30L) precovered Pt(111) surface. The HREEL spectra are recorded at a very large resolution in order to increase the loss electron count rates.

Only a weak H-D exchange reaction takes place on the C2-H2 bond of the stable prenal surface complexes at temperatures around 300 K and, thus, in addition to the usual H_2 desorption signals also the elimination of HD appears in the decomposition process at higher temperatures.

7.2 Prenal on $Pt_3Sn(111)$

Also in the case of prenal adsorption on the $Pt_3Sn/Pt(111)$ surface alloy with its p(2×2) superstructure a good understanding can be developed by combining the HREELS experiments with the DFT calculations. As will be shown, its characteristic Sn protrusions above the surface and its electronic structure lead to very interesting effects upon the prenal adsorption properties.

Up to this work, no similar experiments have been reported to the knowledge of the author. Basically the only reference prior to these results is presented by Delbecq et al. [45], who determined a number of potential adsorption geometries of prenal using DFT and pointed to a preference of the top adsorption modes of the (s)-trans isomer on surface tin atom on both $Pt_2Sn(111)$ and $Pt_3Sn(111)$.

Given this prediction from theory, TPD, LEED and HREELS experiments have been carried out to investigate the stable adsorption structures and to probe the molecule-surface interactions. By a more comprehensive DFT analysis of all reasonably stable adsorption modes and a full characterization of their vibrational properties, results are obtained that allow - also in this case only in conjunction with the experimental data - to address the identification of the actually present geometries and to assess their interaction mechanisms with the surface.

7.2.1 TPD Results

The TPD experiments of prenal on the Pt_3Sn surface alloy have been performed in the same manner as the studies discussed in the previous chapter. A constant heating rate of $\beta = 2$ K/s up to the final temperature of 450 K was applied to the sample and two different sets of experiments have been carried out to record either the desorption of CO and H_2 or the mass signals stemming from prenal (m/z = 84) or its fragments generated in the QMS (69, 55, 41, 39 amu). Various initial exposures have been investigated on freshly prepared Pt_3Sn/Pt(111) surface alloys to analyse the coverage dependent formation of monolayer and multilayer features.

Firstly, it was found that prenal does not decompose on Pt_3Sn(111) up to 450 K. No signals of desorbing CO or H_2 could be detected above of the signal level caused by the background gases in the chamber. The desorption of intact prenal occurred in two distinct states at low temperatures. As already detected on pure Pt(111), the multilayer that is formed from sufficiently large initial exposures above 1.5L, desorbs at 161 K (α_1, Fig. 7.29). For smaller exposures, only the desorption state α_2 could be detected at ca 184 K, which is suggested to arise from a monolayer adsorption. In contrast to the behavior of prenal on Pt(111), this desorption state was observed even for very small amounts of prenal on the surface alloy, but it was always quite badly defined and showed a typical width of several 10 K with its high temperature side tailing well beyond 200 K. Thus, also for larger exposures above the multilayer formation threshold, the signal α_2 was difficult to resolve due to the overlap with the more intense multilayer desorption peak and the slow pumping speed of this aldehyde. The comparison of the peak areas of the monolayer desorption states with the low temperature desorption states on Pt(111) suggests a significant decrease in the surface coverages on the surface alloy, since the peak area corresponds to only about 66±15% (due to the badly defined signals, peak area integration and baseline corrections are rather difficult and the errors consequently large).

From the detected desorption rate maximum temperatures, the activation barriers for the desorption states have been estimated using the Redhead method [56] with a frequency factor of $\nu = 10^{13}$ Hz. Similar values for the activation energies as compared to the low temperature desorption states of prenal on Pt(111) are obtained, which importantly are only slightly

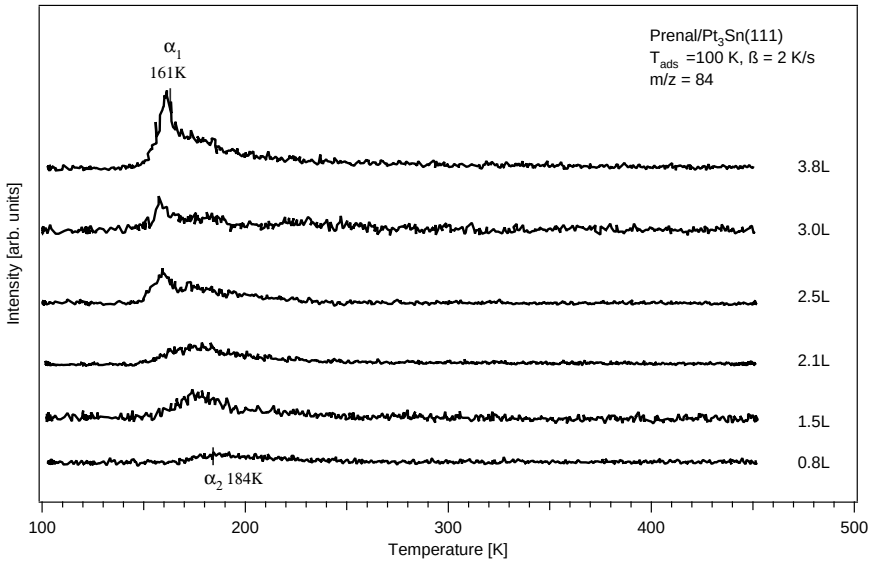

Figure 7.29: TPD spectra of prenal adsorbed on the Pt_3Sn(111) surface, m/z=84.

larger than the adsorption energy of the multilayer (α_1). Compared to the desorption energy of 41.1±1.5 kJ/mol for α_1, the value for the desorption state α_2 is determined at 47.1±1.5 kJ/mol, which points to a rather weak adsorption on $Pt_3Sn(111)$. Therefore it is expected from the TPD results that any prenal species that may desorb again from the surface alloy, is weakly bonded.

7.2.2 Stable Structures from DFT Optimizations

The DFT analysis of the prenal/$Pt_3Sn(111)$ model system results in a number of stable configurations with weak adsorption energies and two sizably stable geometries: Two η^1-top-(s)-trans-OSn coordination structures differing only in their orientation relative to the surface are found to interact sizably with the Sn atoms.

Taking up the optimizations performed previously by Delbecq et al. [45], also for prenal on $Pt_3Sn(111)$ the theoretical investigations have been extended to a much larger set of conceivable geometries (Tab. 7.17) in this work and finally the vibrational properties of all stable configurations have been characterized. Actually only such initial coordination types have been excluded from this study, which could be ruled out from the previous study of Delbecq and coworkers [45] or from the present results of prenal and crotonaldehyde on the various model catalysts. Thus for example the η^2-diσ(CO) forms are adsrobed typically very weakly or even become totally unstable like for prenal on $Pt_2Sn(111)$ and do not represent interesting candidates for the analysis.

Generally, like in the case of crotonaldehyde on the surface alloys, also for prenal a reduction of the adsorption energies by roughly 66% and a simplification of the manifold of potential adsorption complexes is found. Besides the two strongly bonded η^1-(s)-trans-top-OSn forms, barely six other optimized geometries with a flat orientation exhibit a negative adsorption energy. Among these flat structures, η^3-diσ(CC)-σ(O)-(s)-cis-OSn is the most stable one at -20.4 kJ/mol. This value corresponds nicely to the reference energy of -16.7 kJ/mol calculated by Delbecq et al., who, using less strict convergence thresholds on the residual forces and no dipole corrections during their optimizations, arrived at a very similar geometry (deviations of the bond lengths well below 0.005Å).

A comparison of the new local minima to those computed for the related complexes on Pt(111) does not reveal any drastic changes in the bond lengths of the prenal molecules themselves (Tab. 7.19), but some elongations of the molecule-surface bonds are recognized that coincide with the decrease of the adsorption energies. These change are more pronounced on the Pt-C bonds of the aldehydic C1=O moiety, whereas the surface bonds of the vinylic C2=C3 part are influenced only slightly. This can be seen particularly well from the nearly unchanged geometries of the η^2-diσ(CC) and the η^2-π(CC) complexes.

While the latter changes of the vinylic C2=C3 coordinations from the related prenal geometries on Pt(111) can be ascribed to the weaker interactions (Tab. 7.18), which arise from the negative polarization of Pt on the surface alloys [45], the elongations of r(O-Sn) must be due to the transition from an oxygen-platinum to an oxygen-tin interaction.

The separation of the adsorption energies into their constituents, the deformation costs for the surface and the molecule and finally the remaining interaction strengths, performed as described in Chap. 6.2.3, points to a strong decrease of the interaction terms of roughly 35 kJ/mol (ca 15%) and slightly lower deformation costs for the surface on $Pt_3Sn(111)$ (8 kJ/mol, i.e. a lowering of about 10%) compared to Pt(111)[20]. This is in line with the findings of the corresponding crotonaldehyde systems. Unlike the behavior of crotonaldehyde, the increase of the deformation costs invested into the distortion of the molecule in the flat adsorption complexes by the alloying of the surface is more pronounced for prenal (increase on average to ca 160 kJ/mol from

[20]The interaction terms of the flat η^2, η^3 and η^4 coordination types are on average about -255 and -224 kJ/mol on Pt and Pt_3Sn, respectively. The corresponding deformation energies of the surface are ca 58 and 50 kJ/mol.

Adsorption energies [kJ/mol]	(s)-trans	(s)-cis
η^1-top-OPt	excluded	excluded
η^1-top-OSn	-39.1 (-32.2 [45])	-17.3
η^1-top-OSn-2	-30.8	excluded
η^2-diσ(CC)	-9.7	unstable
η^2-π(CC)	-1.1	unstable
η^2-diσ(C3,O)-OPt	unstable	unstable
η^2-diσ(C3,O)-OSn	excluded	unstable
η^3-π(CC)-σ(O)-OPt	unstable	unstable
η^3-diσ(CC)-σ(O)-OPt	unstable	unstable
η^3-π(CC)-σ(O)-OSn	unstable	unstable
η^3-diσ(CC)-σ(O)-OSn	unstable	-20.4 (-16.7 [45])
η^4-diσ(CC)-diσ(CO)-OPt	excluded	unstable
η^4-π(CC)-diσ(CO)-OPt	unstable	unstable
η^4-diσ(CC)-diσ(CO)-OSn	-16.7 (-11.3 [45])	unstable
η^4-π(CC)-diσ(CO)-OSn	excluded	-11.4 (-16.3 [45])

Table 7.17: Calculated adsorption energies of the stable prenal species on $Pt_3Sn(111)$ at a theoretical coverage of $\Theta = 1/12$ ML. Note that no coordination structures of the η^2-diσ(CO) type interacting either with Sn or with Pt have been considered as these were already on pure Pt(111) only very weakly bonded and are completely unstable on $Pt_2Sn(111)$. The structures "excluded" have not been optimized, because their initial structure was already too strained to lead to a stable geometry. The reference values given in brackets are taken from Ref. [45] (the dipole corrections were employed in the latter study only in a single-point calculation for the geometry optimized before).

ca 145 kJ/mol on Pt(111); from ca 132 kJ/mol on Pt(111) to 139 kJ/mol on Pt_3Sn for crotonaldehyde[21]), which is ascribed to the sterical repulsions of the additional methyl substituent and the surface tin atoms.

[21] Again, like for crotonaldehyde, the η^4-diσ(CC)-diσ(CO)-(s)-trans structures cause some problems in estimating the average energy constituents since the deformation costs of prenal on both surfaces vary surprisingly strongly by about 100 kJ/mol, which must be ascribed to a different electronic situation. Excluding this problematic case, the molecule deformation energies are close for the remaining flat adsorption geometries on Pn and Pt_3Sn.

Adsorption mode	adsorption energy	surface deformation	molecule deformation	interaction term
η^1-top-(s)-trans-OSn	-39.1	2	2	-43
η^1-top-(s)-trans-OSn-2	-30.8	3	2	-36
η^2-π(CC)-trans	-1.1	59	52	-112
η^2-diσ(CC)-(s)-trans	-9.7	47	167	-224
η^3-diσ(CC)-σ(O)-(s)-cis-OSn	-20.4	44	168	-232
η^4-diσ(CC)-diσ(CO)-(s)-trans-OSn	-16.7	46	244	-306
η^4-π(CC)-diσ(CO)-(s)-cis-OSn	-11.4	60	146	-217

Table 7.18: Decomposition of the adsorption energies of prenal on $Pt_3Sn(111)$ ($\Theta = 1/12$ ML) into the energy costs for deforming the surface and the molecule and the energy gain of the interaction in the optimized surface complex. All energy contributions are given in kJ/mol.

The energetic phenomena shall be discussed exemplarily for the η^3-diσ(CC)-σ(O)-OSn adsorption complex and correlated with the changes in the optimized structure. Here the bond distance r(O-Sn) is elongated by 0.16 Å to 2.41 Å, which is quite close to the 2.36 Å of the related E-(s)-cis crotonaldehyde complex. The r(C2-Pt) and r(C3-Pt) bond lengths are affected less evidently, increasing by 0.07 Å to 2.23 Å in the first and shortening by 0.02 Å to 2.16 Å in the latter case. In contrast to the significant changes of the molecule-surface coordination parameters, the internal structure of prenal is basically the same on both Pt(111) and $Pt_3Sn(111)$. Hence, it is easily rationalized that the molecule deformation energies are very close (162 and 168 kJ/mol, resp.), but the interaction strength decrease strongly from -270 kJ/mol on Pt(111) to -232 kJ/mol. Considering the surface displacements, outward relaxations of 0.28 and 0.38 Å are computed for the Pt atoms below C2 and C3. These are typical for a diσ(CC) coordination[22]. However, the protrusion of Sn atoms bonded to the aldehydic oxygen is close to their equilibrium values, but it is translated by ca 0.15 Å within the surface plane away from the molecule, probably allowing for a better overlapp. In contrast, the Sn atoms in close vicinity of the methyl-groups are relaxed inward by roughly 0.09 Å due to sterical repulsion. Neither for the other surface atoms, nor for the in-plane positions of the interacting Pt atoms, displacements larger than about 0.05 Å are observed. Despite these structural changes, which are larger than the deformations of the corresponding complexes on Pt(111)[23], the deformation energy of the surface is smaller. The fact that it, indeed, decreases on the alloy surface must again be originating from the "softer" distortion potential curves, which have been discussed in Chap. 6.3.2.

Although the η^4-π(CC)-diσ(CO)-(s)-cis-OSn form shows a surprising increase of its molecular deformation term, which can be rationalized easily from the huge changes of the optimized molecule-surface bond lengths[24], this seems to be rather an exception of the previously proposed trend. Yet, from the problematic cases of both η^4 complexes it becomes obvious that despite the general trends of the studied adsorption systems, a closer analysis of the details of the adsorption mechanisms is indispensable in order to achieve a basic understanding.

Finally, turning to the two most stable structures of the η^1-top-(s)-trans-OSn type, the same correlation of a weaker interaction strength (-43 and -36 kJ/mol, i.e. ca 33 and 40 kJ/mol lower than on Pt(111), see Tab. 7.18) and a bond elongation of r(O-Sn) of 0.21 and 0.28 Å for both candidates, respectively, can be deduced like for crotonaldehyde on $Pt_3Sn(111)$. Caused by the "softer" alloy surface in contrast to Pt(111) and the already protruding position of the Sn

[22] For the η^2-diσ(CC)-(s)-trans form, the Pt atoms below C2 and C3 are lifted by 0.30 and 0.39 Å.

[23] I.e. the outward relaxtions of the η^3-diσ(CC)-σ(O) form on Pt(111) are 0.05 (below O), 0.18 (C2) and 0.21 Å (C3), which is again typical for a diσ(CC) coordination. The surrounding Pt atoms are "pushed" inwards by ca 0.02 to 0.06 Å.

[24] The bond distances are changed here from the ones on Pt(111) by Δr(O-Sn)=+0.16 Å, Δr(C1-Pt)=+0.30 Å, Δr(C2-Pt)=-0.11 Å and Δr(C3-Pt)=+0.28 Å.

Geometry	η^1-top-(s)-trans-OSn	η^1-top-(s)-trans-OSn-2	η^1-top-(s)-cis-OSn	η^2-diσ(CC)-(s)-trans	η^2-π(CC)-(s)-trans	η^3-diσ(CC)-σ(O)-(s)-cis-OSn	η^4-diσ(CC)-diσ(CO)-(s)-trans-OSn	η^4-π(CC)-diσ(CO)-(s)-cis-OSn
r(O-C1)	1.25	1.25	1.25	1.23	1.23	1.27	1.34	1.29
r(C1-C2)	1.43	1.44	1.44	1.49	1.48	1.45	1.48	1.44
r(C2-C3)	1.36	1.36	1.36	1.51	1.43	1.51	1.51	1.50
r(C3-C4)	1.50	1.49	1.50	1.53	1.51	1.53	1.53	1.53
r(C3-C5)	1.50	1.50	1.49	1.53	1.51	1.53	1.53	1.53
r(C1-H1)	1.11	1.11	1.11	1.12	1.12	1.11	1.10	1.11
r(C2-H2)	1.09	1.10	1.09	1.10	1.09	1.10	1.10	1.10
r(C4-H3)	1.10	1.10	1.10	1.10	1.10	1.09	1.10	1.10
r(C4-H4)	1.10	1.10	1.10	1.11	1.11	1.11	1.11	1.11
r(C4-H5)	1.10	1.10	1.10	1.10	1.10	1.10	1.10	1.10
r(C5-H6)	1.09	1.09	1.10	1.10	1.10	1.10	1.10	1.10
r(C5-H7)	1.10	1.10	1.10	1.11	1.10	1.11	1.11	1.11
r(C5-H8)	1.10	1.10	1.10	1.10	1.10	1.10	1.10	1.10
r(O-M)	2.43	2.50	2.37	-	-	2.41	2.17	2.30
r(C1-M)	-	-	-	-	-	-	2.23	2.51
r(C2-M)	-	-	-	2.16	2.20	2.23	2.22	2.25
r(C3-M)	-	-	-	2.17	2.27	2.16	2.16	2.18
r(O-H)			2.46			2.39		2.55

Table 7.19: Bond length of the optimized adsorption geometries of prenal on $Pt_3Sn(111)$ ($\Theta = 1/12$ ML). All distances r are given in Å. r(O-H) denotes a short distnace of a methyl hydrogen to the aldehydic oxygen in the respective adsorption complex.

atoms, neither the interacting Sn atom nor the molecule are distorted significantly from their equilibrium geometries in the adsorption complex (the interacting Sn atoms show small outward relaxations of 0.12 and 0.18 Å , respectively, while no displacements larger than 0.02 Å are computed for the other metal atoms or the in-plane components of Sn). Therefore, with the deformation costs of surface and molecule being negligible on $Pt_3Sn(111)$, the weaker molecule-surface interaction strengths translate immediately into moderate adsorption energies of -39.1 and -30.8 kJ/mol for both complexes.

In summary, from the DFT structure study of prenal on $Pt_3Sn(111)$ it may be concluded that weaker electronic interactions (ca 15% weaker) lead to a simplification of the number of encountered types of stable coordinations. Despite the lower energetic costs for the adaptation of the surface upon forming the flat adsorption complexes (10% lower), the interactions are weakened to such an extend that they can no longer compensate the deformation energies of the molecule (up to 10% larger) sufficiently in order to generate sizable adsorption energies. Therefore the only adsorption forms that appear relatively strongly bonded are the η^1-top-(s)-trans-OSn types, which do not require any deformation energy to create the interacting complex.

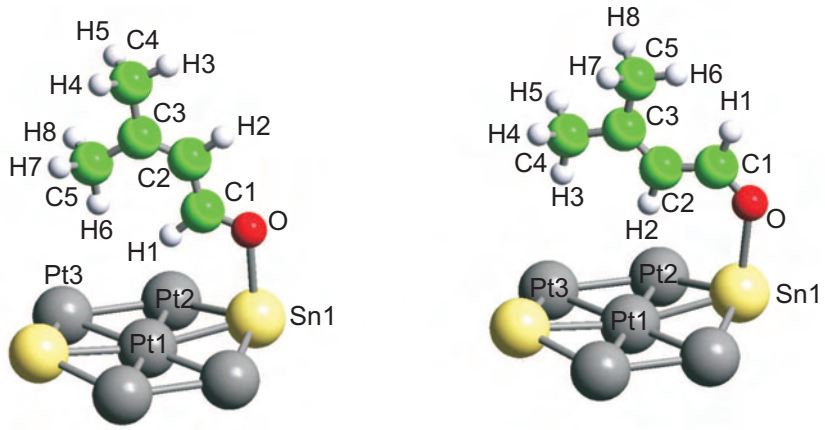

(a) η^1-top-(s)-trans-OSn (b) η^1-top-(s)-trans-OSn-2

Figure 7.30: Optimized η^1-top-(s)-trans-OSn adsorption geometries of prenal on $Pt_3Sn(111)$.

7.2.3 HREELS of prenal on the $Pt_3Sn(111)$ surface alloy

Experimentally the TPD results discussed in Sec. 7.2.1 point to a completely reversible adsorption of prenal on the $Pt_3Sn(111)$ surface alloy, since no desorption of CO, H_2 or hydrocarbon fragments could be detected up to 450 K. However, the HREELS experiments recorded for several initial exposures of prenal between 0.5L and 10L on this surface do not comply with this expectation.

A representative series of HREEL spectra measured after annealing the alloyed sample with 3.0L prenal to temperatures from 100 K to 250 K is presented in Fig. 7.31. It shows at the bottom again a typical spectrum of a multilayer of prenal (Chap. 7.1.2) recorded after adsorption at 100 K, whereas at intermediate temperatures between 170 K and 200 K the vibrational fingerprints are characteristically different from the multilayer and moreover from those observed on Pt(111). The desorption of the multilayer just below 170 K leads generally to a strong damping of the scattered intensities, but the desorption state α_2 (184 K at $\beta = 2$ K/s) supposed to be removed by annealing to 200 K affects the loss intensities only slighty. As the HREEL spectra at 170 K and 200 K are - besides the damping of a few loss signals - basically indentical and no significant shifts are recognized neither with temperature nor with coverage[25], they are considered the HREELS data of the interesting monolayer species and will be used for the DFT analysis described below.

All HREELS experiments performed above 200 K lead to surprisingly well-defined and still comparably intense spectra that can be distinguished easily from the ones at lower temperatures. These experiments are reminiscent of the data obtained after annealing a prenal covered Pt(111) sample to 440 K (see Chap. 7.1.5 for the detailed interpretation of this data), which were discussed in the decomposition process of prenal. Among others, especially the signals at 454 cm^{-1}, 639 cm^{-1} and 1027 cm^{-1} allow to correlate the data observed here to the ones on Pt(111). Furthermore some very weak signals at 1740 cm^{-1} measured between 250 K and 400 K indicate CO adsorbed on platinum bridge sites (no signals were observed from CO at higher frequencies), which, given the fact that below 200 K no coadsorbed CO was detected, must be

[25]Indeed no significant coverage dependence of the HREEL spectra between 170 K and 400 K could be detected on $Pt_3Sn(111)$ by comparing the various initial exposures chosen between 0.5L and 10L.

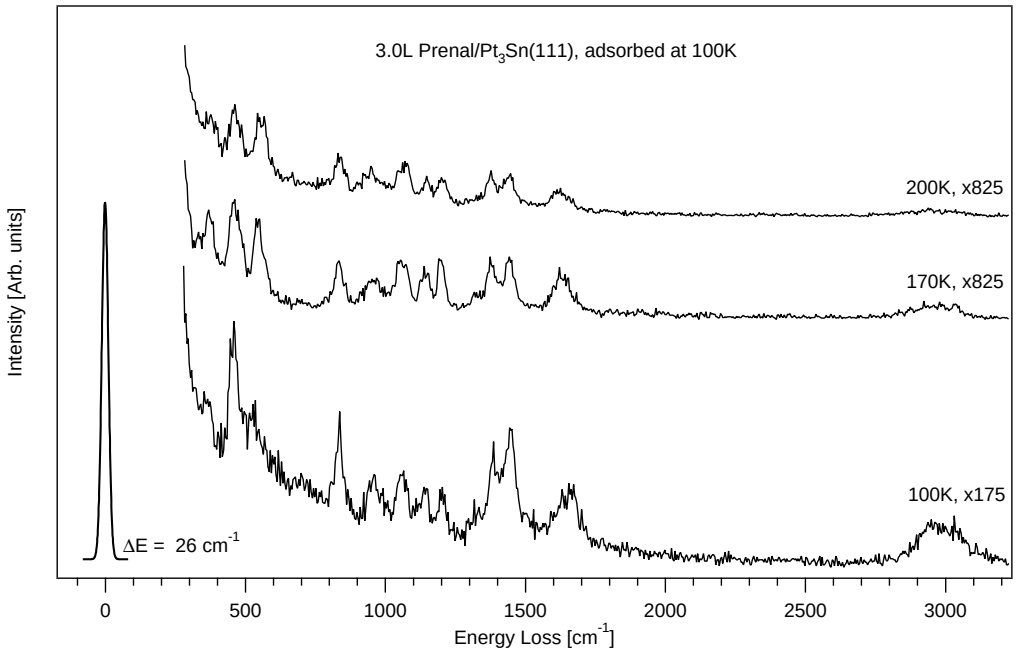

Figure 7.31: HREELS experiments with 3.0L prenal/$Pt_3Sn(111)$, 100-200 K. The spectra have been recorded in specular geometry at an angle of incidence of 60° (primary energy of 4.7 eV).

originating from the prenal adsorption complexes.
Taking into account the TPD and HREELS results, two possibilities need to be considered: The first possibility is an irreversibly adsorbed species that besides the species desorbing at low temperature (184 K) is also present on the surface alloy, but decomposes at high temperatures. The second possibility points "simply" to an interpretation of the HREELS data above 200 K as adsorption and decomposition of prenal on defect sites, which would include remaining pure platinum patches.
From the loss intensities, which do not decrease significantly between 200 K and 250 K as would be expected for a limited surface defect density, rather a decomposition of prenal on $Pt_3Sn(111)$ is proposed here. Indeed, this would even be consistent with the similar behavior of crotonaldehyde detected on $Pt_3Sn(111)$. The problem of the missing CO and H_2 desorption peaks from the proposed decomposition of prenal in the TPD experiments is yet somewhat puzzling. Since the amount of prenal adsorbed on this surface alloy is rather small compared to Pt(111)[26], the desorption peaks of CO and H_2 stemming from the small fraction of irreversibly adsorbed prenal might just have been hidden in the noise signal of the background gases.
Turning now to the interpretation of the monolayer HREEL spectra recorded at 170 K, again a full vibrational assignment can be given from the DFT calculations. In agreement with the DFT total energy results, the computed HREEL spectra of the two most stable adsorption complexes of the η^1-top-(s)-trans-OSn type are compatible with the experimental data between 170 and 200 K, whereas the fingerprints of the weaker bonded, flat adsorption modes fail to reproduce it[27]. Already in the study of Delbecq et al. [45] these authors had suggested that the η^1-top-OSn coordination type should lead to the most stable adsorption forms, which is hereby proven.

[26] Rough estimates from the HREELS loss intensities and TPD put the coverage on $Pt_3Sn(111)$ to about 1/3 to 1/5 of the one on Pt(111).

[27] Although the vibrational characteristics of the η^2-diσ(CC)-(s)-trans complex fit satisfactorily with the experimental features, it must be excluded due to its weak adsorption energy.

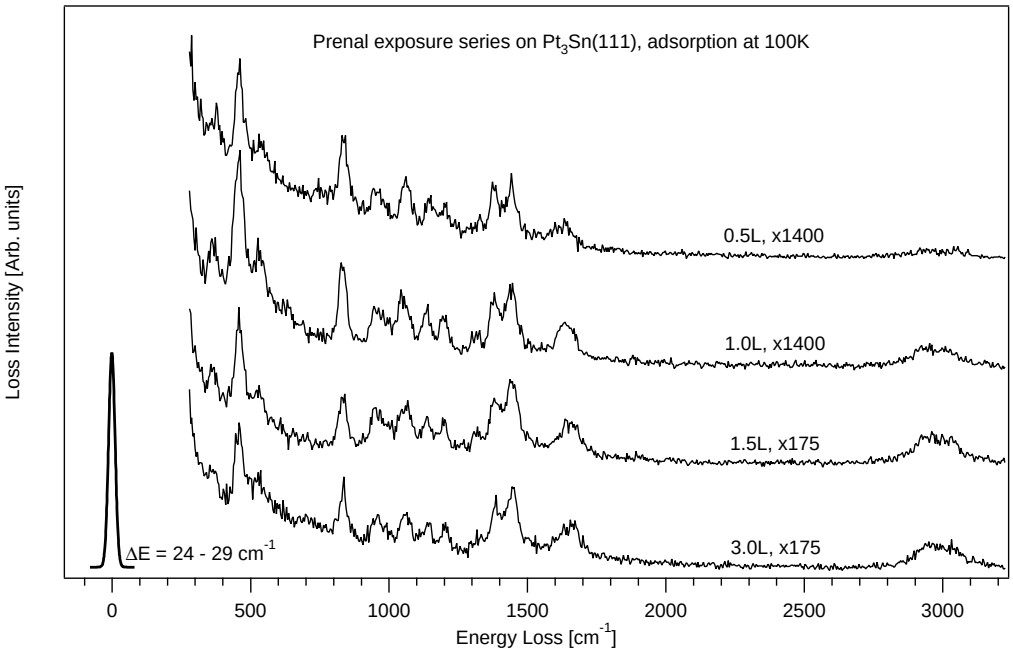

Figure 7.32: HREELS exposure series of prenal on $Pt_3Sn(111)$ recorded after adsorption at 100 K. The HREEL spectra have been recorded in specular geometry at an angle of incidence of 60° with a primary energy of 4.7 eV.

In terms of vibrational frequencies, neither the experimental data nor the computed vibrations of the two η^1-top-(s)-trans-OSn forms differ strongly from the values determined in the prenal multilayer. This is quite intuitive, because the molecules are essentially unperturbed and far from the surface, while only the aldehydic part directly senses the comparably weak interaction with the surface of -43 and -36 kJ/mol, respectively. For the differentiation of these adsorption complexes from the multilayer or gas phase features, one thus has to rely on the relative intensities. Obvious from the specific vertical orientations of both top structures, the loss intensity patterns are highly characteristic and well suited for an identification.
Some indications speaking against significant contributions of any weakly bonded, i.e. physisorbed prenal species at 170 K or 200 K, which have also been suggested before in the case of Pt(111) (low temperature desorption states of prenal and crotonaldehyde below 200 K) can be found in the experimental data. Aside from the shift of the peak in the ν(C=O) and ν(C=C) stretching region from ca 1660 cm^{-1} in the multilayer to 1616 cm^{-1}, also the three intense peaks at 380, 470 and 548 cm^{-1} show a different pattern than before at 100 K and hence suggest the presence of strongly bonded structures. However, otherwise only the spectra of the isolated prenal molecules are reproduced by the unperturbed frequencies.
As it turns out during the analysis, the second η^1-(s)-trans-top-OSn-2 species exhibits only two really intense losses at 1358 and 1589 cm^{-1}, which coincide with similarly intense signals of the first η^1-(s)-trans-top-OSn form. This complicates the differentiation between those two vertical structures (Fig. 7.33; the convolution is presented in App. C.2, Fig. C.4). Nonetheless, the second form may not be ruled out from either its sizable adsorption energy or its spectrum, which adds some weak but necessary intensity for the assignment of the experimental features at 836 and 955 cm^{-1}, and must thus be present, too.
The assignment of the experimental features to the vibrations of the two η^1-(s)-trans-top-OSn adsorption structures is very simple in this case and the agreement of the frequencies surprisingly

good. Seemingly, the simpler the constitution of the mixed adsorbate phase, the lower its degree of disordering and the higher the interaction strength, the better is the description of the experimental data obtained with the periodic DFT approach. Nonetheless, also here some discrepancies of the frequencies and especially the computed intensities are found.
In the range above 2500 cm^{-1}, only weak signals from the ν(C-H) stretching modes are recorded in agreement with the weak intensities of the computed normal modes. Due to anharmonicity and *Fermi*-couplings, no assignment can be made here. Most importantly, the ν(C1=O) and ν(C2=C3) vibrations of the two η^1 complexes lead to a broad and intensive loss signal between 1590 and 1650 cm^{-1}, which is very specific for this η^1-top-OSn or the η^2-diσ(CC) coordination type. As the latter flat structure has been excluded because of its weak adsorption energy on the Pt_3Sn surface alloy, the experimental peak may be attributed unambiguously to the two η^1 species. The DFT calculations indicate as expected that the ν(C1=O) normal modes (1616 and 1615 cm^{-1}, see Tabs. 7.20 and 7.21) of these adsorption complexes show larger redshifts of ca 60 cm^{-1} compared to the gas phase due to the interaction with the surface than the corresponding ν(C2=C3) vibrations (1588 and 1583 cm^{-1}), which are redshifted by about 45 cm^{-1}. The ν(C1=O) and ν(C2=C3) vibrations appear at 1677 and 1633 cm^{-1} in the gas phase calculations, respectively. From the comparison to the frequencies of the η^1-(s)-trans adsorption complex of prenal on Pt(111) it is concluded, moreover, that the weakening of the interaction strength here affects only the vibrational frequencies of the ν(C1=O) mode. While the latter was computed on Pt(111) with a larger redshift at 1545 cm^{-1}, the ν(C2=C3) and the ν(C1-C2) stretching frequencies showed essentially the frequencies like those obtained on Pt_3Sn(111).
Around 1442 and 1374 cm^{-1}, the large family of deformation modes δ'(CH_3), δ"(CH_3) and u(CH_3) gives loss signals that fit excellently to the experiments. Particularly the latter umbrella modes show a considerable coupling to the in-plane deformation vibrations δ(C1H1) and δ(C2H2) of the aldehydic and the vinylic hydrogens, which results in further linear combinations of these normal modes that are assigned to the weak experimental signal at 1326 cm^{-1}.
In this frequency range also the first discrepancy of the calculated vibrations and the experimental loss peaks becomes obvious with the u($C5H_3$)-δ(C2H2) normal mode of η^1-(s)-trans-top-OSn-2 at 1358 cm^{-1} : In contrast to the experimental peak it is computed with dominating intensity. At the same time, the experimental peaks at 836 cm^{-1} and 955 cm^{-1}, which agree well with the computed frequencies of the γ_s(C1H1-C2H2) and ν_s(C3C4-C3C5) normal modes in the first and the asymmetrically coupled γ'(CH_3), γ"(CH_3) and the γ_{as}(C1H1-C2H2) deformation modes in the second case, are underestimated strongly in their intensity. The origin of these intensity misfits is very difficult to establish without further studies, but it might be partially due to contributions of impact scattering on the experimental side as well as the neglect of the phonons on the theoretical side, which might lead to some intensity transfer from the lower frequency modes. Finally also small contributions of (s)-trans prenal re- or coadsorbed roughly parallel to the surface in a physisorptive manner would also lead to intense losses at these frequencies (833 and 956 cm^{-1}) and can not be excluded easily [28].
In the intermediate range of the fingerprint region, several signals are resolved at 1055, 1140 and 1197 cm^{-1}. The broad feature at 1055 cm^{-1} originates from the symmetrically coupled γ_s'($C4H_3$-$C5H_3$) "in-plane" deformation modes calculated at 1038 cm^{-1}, which in contrast to the related "out-of-plane" symmetric counterparts γ_s"($C4H_3$-$C5H_3$) at 1055/1052 cm^{-1} are sizably active. At 1140 cm^{-1} the important ν(C1-C2) stretching mode of the first η^1-(s)-trans-top-OSn form becomes intense because of its orientation normal to the surface. It is computed with a dominant scattering intensity at 1156 cm^{-1}, while the corresponding mode of the second top form at 1154 cm^{-1} is basically forbidden.

[28] These spectra will be discussed in the following Chap. 7.3.2. Further intense signals of such a physisorbed species would appear at 454 and 1435 cm^{-1}, while all other vibrations would be barely recognizable.

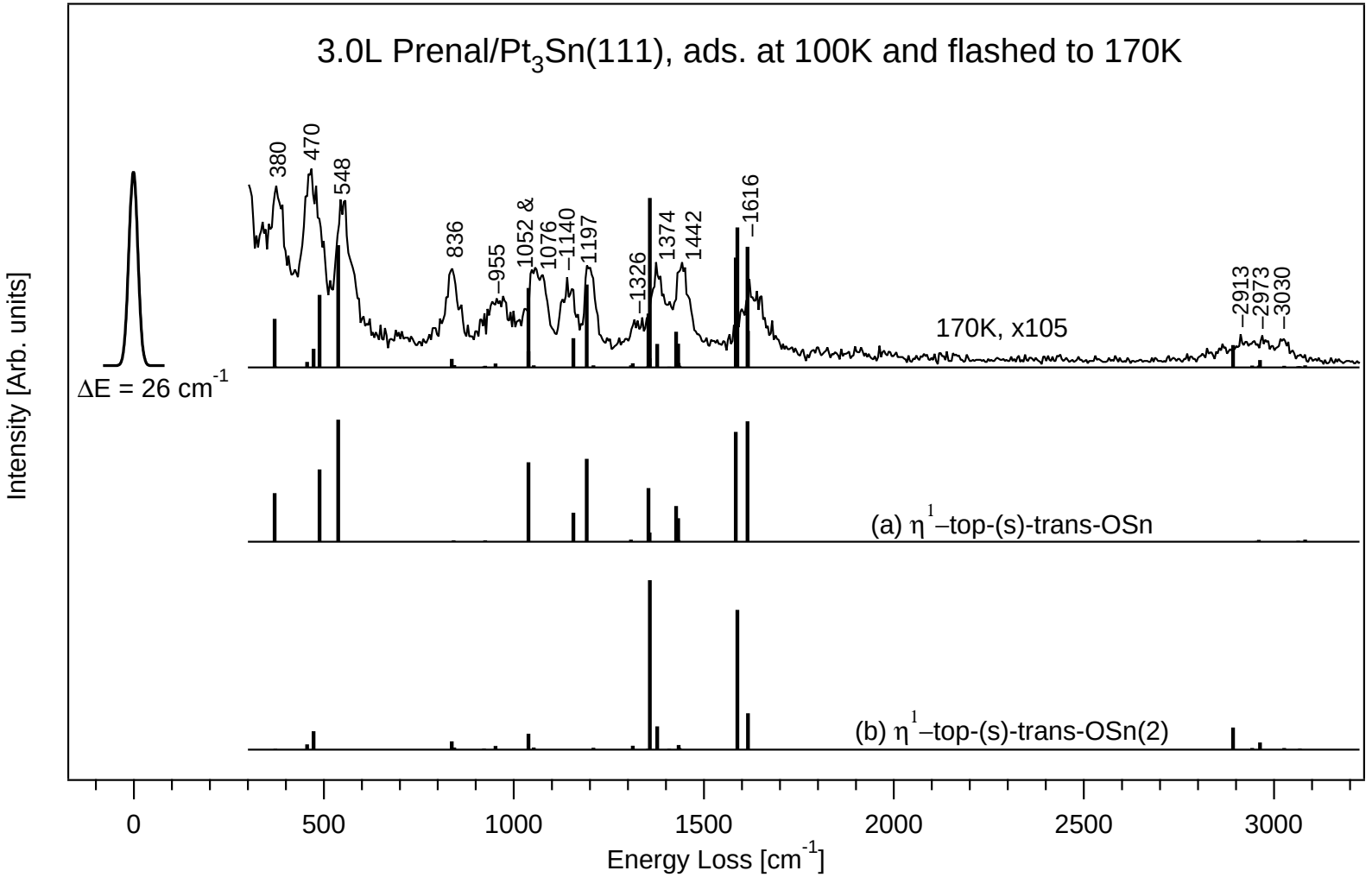

Figure 7.33: Computed DFT HREEL spectra for the two stable η^1-top-(s)-trans-OSn adsorption complexes of prenal on $Pt_3Sn(111)$ and a HREEL spectrum of 3.0L prenal adsorbed at 100 K that was subsequently flashed to 170 K.

ω cm^{-1}	Intensity $\times 10^6$ au		Normal mode
3082	0.10		ν(C2-H2)
3066	0.002		ν(C5-H6)
3064	0.051		ν(C4-H3)
3005	0.0		ν_{as}(C4-H4,5)+ν_{as}(C5-H7,8)
2999	0.0		ν_{as}(C4-H4,5)-ν_{as}(C5-H7,8)
2960	0.093		ν_s($C4H_3$)+ν_s($C5H_3$)
2955	0.032		ν_s($C4H_3$)-ν_s($C5H_3$)
2847	0.014		ν(C1-H1)
1615	5.9	m	ν(C2=C3)
1584	5.4	m	ν(C1=O)
1434	0.085		δ''_s($C4H_3$-$C5H_3$)
1432	1.2	w	δ'_s($C4H_3$-$C5H_3$)
1427	1.7	w	δ'_{as}($C4H_3$-$C5H_3$)
1407	0.0		δ''_{as}($C4H_3$-$C5H_3$)
1386	0.022		u($C4H_3$)-δ(C1H1)
1358	0.45		u($C5H_3$)-δ(C2H2)
1354	2.6	w	δ(C1H1)+u($C5H_3$)
1308	0.10		δ(C2H2)+u($C4H_3$)
1192	4.1	m	ν_{as}(C3C4-C3C5)
1156	1.4	w	ν(C1-C2)
1055	0.001		γ_s"($C4H_3$-$C5H_3$)
1038	3.9	m	γ_s'($C4H_3$-$C5H_3$)
979	0.0		γ_{as}"($C4H_3$-$C5H_3$)
954	0.001		γ_{as}(C1H1-C2H2)
924	0.073		γ_{as}'($C4H_3$-$C5H_3$)
841	0.076		ν_s(C3C4-C3C5)
837	0.002		γ_s(C1H1-C2H2)
538	6.0	m	δ(O=C1-C2)
489	3.5	m	δ(C2=C3-C4,C5)
467	0.0		ω(C2=C3,C4,C5)
371	2.4	w	δ(C3-C4,5)
266	15.9	vs	δ(C1-C2=C3)
240	0.017		τ(C2=C3)
179	0.008		τ($C5H_3$)
131	0.005		τ(C1-C2)
104	8.2	s	ν(Sn-O)
86	0.0		τ($C4H_3$)
78	4.3		fR
67	4.1		fR
54	17.2	vs	fT
51	0.87		fT
19	5.7		fR

Table 7.20: DFT analysis of the vibrational properties of the first η^1-(s)-trans-top-OSn structure of prenal/Pt_3Sn(111). The letters following the computed intensities refer to the relative strength, i.e. (v)w = (very) weak, m = medium and (v)s = (very) strong. For strong vibrational couplings of more than two normal modes, the coupling of the components is indicated by + (in phase) or - (anti-phase). The abbreviations fR and fT refer to hindered translations and hindered rotations.

ω cm^{-1}	Intensity $\times 10^6$ au		Normal mode
3068	0.054		ν(C5-H6)
3044	0.004		ν(C4-H3)
3027	0.079		ν(C2-H2)
3010	0.003		ν_{as}(C5-H7,8)
2993	0.001		ν_{as}(C4-H4,5)
2963	0.35	vw	ν_s($C5H_3$)
2943	0.085		ν_s($C4H_3$)
2892	1.1	w	ν(C1-H1)
1616	1.88	w	ν(C2=C3)
1588	6.8	s	ν(C1=O)
1436	0.081		δ_s'($C4H_3$-$C5H_3$)
1433	0.22		δ_s"($C4H_3$-$C5H_3$)
1425	0.0		δ_{as}'($C4H_3$-$C5H_3$)
1409	0.036		δ_{as}"($C4H_3$-$C5H_3$)
1377	1.1	w	u($C4H_3$)-δ(C1H1)
1358	8.2	s	u($C5H_3$)-δ(C2H2)
1352	0.038		δ(C1H1)+u(C5H3)
1313	0.20		δ(C2H2)+u(C4H3)
1209	0.10		ν_{as}(C3C4-C3C5)
1154	0.001		ν(C1-C2)
1052	0.10		γ_s"($C4H_3$-$C5H_3$)
1038	0.78	vw	γ_s'($C4H_3$-$C5H_3$)
969	0.020		γ_{as}"($C4H_3$-$C5H_3$)
952	0.19		γ_{as}(C1H1-C2H2)
921	0.047		γ_{as}'($C4H_3$-$C5H_3$)
843	0.11		ν_s(C3C4-C3C5)
837	0.41		γ_s(C1H1-C2H2)
534	0.004		δ(O=C1-C2)
473	0.90		δ(C2=C3-C4,C5)
456	0.26		ω(C2=C3,C4,C5)
372	0.039		δ(C3-C4,5)
253	13.0	vs	δ(C1-C2=C3)
239	1.3	w	τ(C2=C3)
195	0.028		τ($C5H_3$)
144	0.63		τ(C1-C2)
126	0.55		τ($C4H_3$)
108	17.2	vs	ν(Sn-O)
79	1.6		fR
77	7.6	s	fR
66	2.8		fT
41	3.6		fT
(-19)			(imaginary, rotation around the surface normal)

Table 7.21: Vibrational analysis of the second η^1-(s)-trans-top-OSn-2 structure of prenal/Pt_3Sn(111). The harmonic frequencies ω are given in cm^{-1}. The imaginary frequency obtained from the vibrational analysis of the optimized structure corresponds to a rotation around the surface normal of the molecule on top of Sn.

Another important peak ascribed to the ν(C-C) stretching modes in the fingerprint region is measured at 1197 cm^{-1} consistent with the computed frequencies of the asymmetrically coupled methyl stretching vibrations ν_{as}(C3C4-C3C5), which are obtained at 1192 and 1209 cm^{-1} from the DFT analysis. Due to a partial coupling to the deformation vibrations, only the signal of the first η^1-(s)-trans-top-OSn complex is active here, too.
At last also the loss peaks in the low frequency region have to be assigned. Here an intense signal at 548 cm^{-1} arises from the δ(O=C1-C2) deformation modes computed for both complexes at 538 and 534 cm^{-1}, respectively, which vibrate normal to the surface. Despite the "frozen surface" approximation in the vibrational analysis by DFT, the computed frequencies seem to be extremely accurate in the low frequency region.
At 470 cm^{-1} another experimental peak is well reproduced by DFT. This experimental feature must be assigned clearly to the coupled δ(C2=C3-C4,C5) deformation modes of the vinylic moiety calculated at 489 and 473 cm^{-1}, respectively, since the ω(C2=C3,C4,C5) wagging modes of both adsorption forms are barely active. The corresponding deformation modes of the methyl substituents, i.e. the δ(C3-C4,5) normal modes, are found at slightly lower frequency of 380 cm^{-1}. Here, too, only the computed normal mode of the first η^1-(s)-trans-top-OSn complex at 371 cm^{-1} is intense, whereas the one of the second form at 371 cm^{-1} is very weak.
Finally, of great interest are of course also the molecule-surface stretching modes ν(Sn-O), which in this case could not be resolved experimentally from the elastic peak. Their corresponding theoretical frequencies are 104 and 108 cm^{-1}. Compared to the ν(Pt-O) vibration of the η^1-(s)-trans species on Pt(111) at 125 cm^{-1}, these values exhibit a redshift of about 20 cm^{-1}, confirming the weaker interaction with the surface alloy. In both adsorption structures the ν(Sn-O) vibrations show a coupling to the δ(C1-C2=C3) deformation modes of the molecular backbone, which gives rise to a second linear combination of consequently also very intense normal modes. This time the leading term comes from the δ(C1-C2=C3) vibrations. Calculated at 266 and 253 cm^{-1}, respectively, these may be assigned to the dominating loss peak measured at 248 cm^{-1}, completing the vibrational analysis of prenal on the Pt_3Sn surface alloy.
The formation of the two η^1-top-OSn species of prenal on $Pt_3Sn(111)$ is contrary to the mixed phase of crotonaldehyde on this surface alloy, which includes besides the η^1-top also the flat η^2, η^3 and η^4 adsorption modes (Chap. 6.2). However, this change in behavior can be well understood from the decomposition of the adsorption energies. Caused by the much larger deformation energies of prenal as compared to crotonaldehyde in the corresponding high-hapticity coordination types, and furthermore by the slightly higher energy costs for adapting the surface alloy to the molecule in the case of prenal, a much larger interaction strength of prenal with $Pt_3Sn(111)$ would be required to stabilize the flat adsorption modes sufficiently[29]. But as the interaction terms of crotonaldehyde and prenal are surprisingly similar on this model catalyst, the flat molecule-surface complexes are only favorable for crotonaldehyde. In contrast, the negligible deformation energies required for the formation of the η^1-top-OSn species lead immediately to sizable adsorption energies and render these structures the competitive ones for prenal.

7.3 Prenal on $Pt_2Sn(111)$

The case study of the prenal adsorption on the tin-richer $Pt_2Sn(111)$-$(\sqrt{3} \times \sqrt{3})R30°$ surface alloy represents a counter-example to the successful analysis of the crotonaldehyde and prenal adsorption systems discussed in the previous chapters. For the first time during the investigations, the adsorption of prenal on this model catalysts leads to contradictory results. The

[29]The deformation energies of prenal and crotonaldehyde are on average about 160 and 139 kJ/mol for both molecules in flat adsorption modes. The distortion of the $Pt_3Sn(111)$ surface alloy by prenal and crotonaldehyde amounts to 50 and 38 kJ/mol, respectively, and the averaged interaction terms are about -224 and -217 kJ/mol.

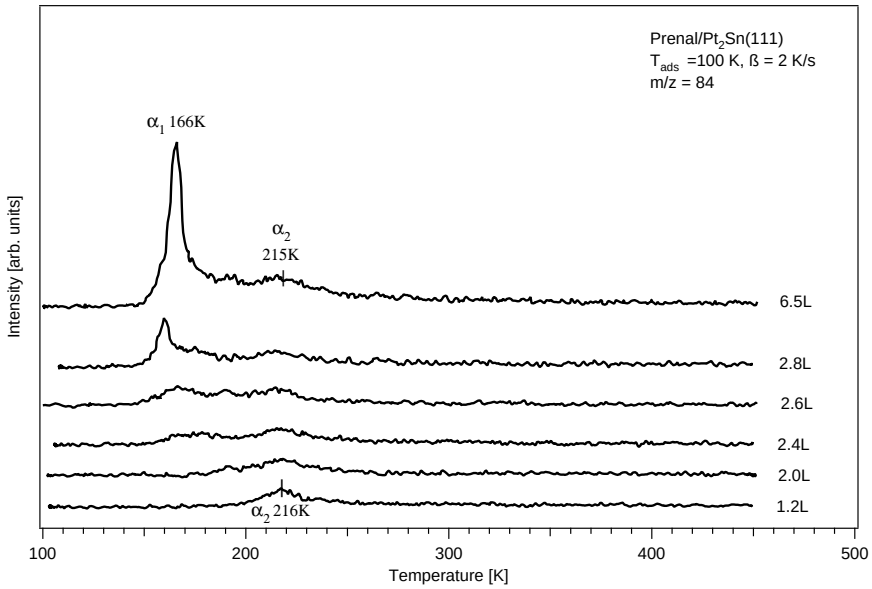

Figure 7.34: TPD spectra of various exposures of prenal to the $Pt_2Sn(111)$ surface, m/z=84, recorded with increased SEM voltage on the QMS. A slow heating rate of 2 K/s was employed between the adsorption temperature of 100 K up to 500 K.

interpretation of the HREEL spectra turns out to be impossible with the computed vibrational data of the stable adsorption forms from DFT, which themselves are not very convincing as their adsorption energies are very weak. Probably due to the increase of the deformation energies of the surface and the weak interaction strength inherent to this surface alloy, prenal does adsorb strongly on $Pt_2Sn(111)$.
Nonetheless, despite these problems, possible reasons for the failure of the theoretical approach for this adsorption system can be pointed out and a basic understanding of the observed phenomena is derived from the TPD and HREELS experiments.

7.3.1 Suggestions from the TPD Experiments

The TPD experiments carried out on the $Pt_2Sn(111)$ surface alloy shown in Fig. 7.34 indicate the formation of a prenal monolayer at low temperatures. As no fragments such as CO, H_2 and hydrocarbons have been detected in the temperature range between the adsorption at 100 K and the chosen upper limit of 450 K, it is concluded that prenal desorbs only intact from the surface.
Consistent with the reduction of the adsorption energies from crotonaldehyde to prenal observed already on Pt(111) and the $Pt_3Sn(111)$ surface alloy, the desorption of the monolayer takes place at slightly lower temperatures of ca 216 K as compared to the desorption state of intact crotonaldehyde at 231 K. In TPD experiments performed with the same QMS setting (sensitivity is chosen by the SEM voltage) as on Pt(111) and $Pt_3Sn(111)$, the multilayer desorption state could also be resolved around 166 K, but in spite of a good signal to noise ratio the desorption of the monolayer could hardly be recognized above the prenal background. Already from this finding it is clear that the amount of prenal adsorbed in the monolayer on the $Pt_2Sn(111)$ surface alloy is even smaller than on the previous surfaces[30].

[30]Due to the change in the QMS recording parameters, a direct comparison of the integrated peak areas is not sensible.

For the desorption rate maximum of prenal at 216 K an activation energy of 55.6 ± 1.5 kJ/mol is calculated by the Redhead analysis [56] (frequency factor of $\nu = 10^{13}$ Hz). This corresponds to a ca 20% stronger interaction to the surface compared to the multilayer (42.4 ± 1.5 kJ/mol), which represents a well-defined signal at 166 K for exposures above ca 2.6L. At smaller exposures down to 2.0L, it can still be discerned as a badly-defined and broad peak that always extends well beyond 200 K.

7.3.2 Conflicting Results from DFT and HREELS

In this case the DFT investigations of the system prenal/Pt_2Sn(111) did not allow a direct interpretation of the measured HREEL spectra. Although DFT optimizations of numerous initial structures were performed, the number of adsorption complexes obtained finally was rather manageable and showed only very weak adsorption strengths (Tab. 7.22). Essentially just the η^3-π(CC)-σ(O)-(s)-trans-OSn and the η^3-diσ(CC)-σ(O)-(s)-cis-OSn geometries (Fig. 7.35) exhibited adsorption energies below -10 kJ/mol at the chosen theoretical coverage of 1/9 ML. Also for prenal on Pt_2Sn it is a necessity to form an oxygen-tin interaction in order to bond to the surface. Other coordination types like the η^2-diσ(CC) and η^2-π(CC) forms are bonded negligibly or are even totally unstable as for example various of the η^4 complexes.
The problems encountered with the system prenal/Pt_2Sn(111) point to a general deficiency of the chosen theoretical model. Since the slab model (esp. thickness and coverage) and the theoretical parameters (k-point mesh, smearing parameters etc.) are considered to be sufficiently converged, which is underlined by the previous successful analysis of the adsorption of crotonaldehyde on this surface alloy, the main cause for the trouble of the theoretical description here may be the selected DFT functional.
It is well-known that the typical DFT functionals, among them the employed GGA approximation Perdew-Wang 91, fail to describe weak interactions correctly [92, 94, 95, 96, 98, 99, 100]. In particular, the *London* dispersion forces of *Van der Waals* interactions are described incompletely, leading to an underestimation of attractive terms in the calculations. Also hydrogen-bridge bonds, which might be expected to become especially important for the α,β-unsaturated aldehydes in case the interaction with the substrate is weak, are badly described by the PW91 functional [92].
Especially the η^1-top-OSn structures, which could be identified on Pt_3Sn(111) between 180 K and 200 K, do not represent local minima on this surface alloy anymore. While Delbecq et al. [45], based on their calculations using the US-PP scheme, pointed to the former as probable adsorption forms on both Pt-Sn surface alloys, the actual calculations performed in the PAW formalism with dipole corrections along the surface normal virtually resulted in the desorption of the molecules. Turning off the dipole correction potentials during the optimizations, at least for the η^1-top-(s)-trans-OSn form a stable minimum is found with an adsorption energy of -29.9 kJ/mol[31]. Nonetheless, the stabilization of structures due to the large dipole moment component along the surface normal, when no correction is applied, is considered unphysical.
The geometrical parameters of the stable adsorption modes obtained on the Pt_2Sn(111) surface alloy, which are given in Tab. 7.35, compare extremely well to the corresponding structures on Pt_3Sn(111). Only in a few cases the deviations of the bond distances are up to 0.02 Å, but otherwise they are below 0.01 Å.
The exception to this agreement is just the η^4-π(CC)-diσ(CO)-(s)-cis-OSn structure with its adsorption energy of -4.6 kJ/mol. Here, besides strong variations of the molecule-surface distances, also elongations of the double bonds C1=O and C2=C3 of 0.04 and 0.07 Å and a shortening of r(C1-C2) by 0.04 Å occurs and confirms the weaker adsorption as the geometry becomes

[31] Without these dipole corrections, even a stable η^1-top-(s)-trans-OPt adsorbed on a Pt top site (-9.9 kJ/mol) is obtained, whereas all η^1-top complexes of the (s)-cis isomer remain unstable. Furthermore, several of the η^3 and η^4 structures remain stable until the dipole corrections are included.

more similar to the free prenal. As to the bonds to the surface, mostly r(O-Sn) and r(C1-Pt) are affected by shortenings of 0.10 and 0.22 Å, while the surface bonds of the vinylic carbons vary much less (-0.03 Å for r(C2-Pt), +0.06 Å for r(C3-Pt)). This in fact would indicate a stronger adsorptive bonding. Basically the geometry of this coordination type resembles more the corresponding structure on Pt(111), which is confirmed further by its deformation energy of the molecule (107 kJ/mol, see Tab. 7.23). On Pt(111) this energy amounts to 115 kJ/mol whereas the value calculated for the molecule deformation on $Pt_3Sn(111)$ is significantly larger at 146 kJ/mol. In the light of a decrease of the interaction strength of this coordination structure from Pt(111) (-227) over $Pt_3Sn(111)$ (-217) to $Pt_2Sn(111)$ (-166 kJ/mol), it is thus concluded that the adsorption is weakened, but that the different geometrical constraints of this surface alloy lead to shortenings of the molecule-surface bonds.

In contrast to the similarity of the optimized molecule structures to the ones on $Pt_3Sn(111)$, the displacements of the surface atoms from their equilibrium positions show a characteristically different trend. As already concluded from the studies of crotonaldehyde, the formation of the adsorption complexes on $Pt_2Sn(111)$ requires strong shifts of the metal atoms parallel to the surface plane, which were not observed on the other model catalysts. These displacements explain not only the much larger surface deformation energies computed on this surface alloy, but finally even the strong weakening of the adsorption for prenal (Tab. 7.23).

The in-plane displacements of the metal atoms are particularly apparent for the metal atoms interacting covalently with prenal. For the latter η^4-π(CC)-diσ(CO)-(s)-cis-OSn complex, for example, the Sn atom (Fig. 7.35(f)) is lifted by the interaction with the aldehydic function by 0.14 Å, while at the same time it is displaced roughly by 0.08 Å along the C1=O direction away from the molecule. Far larger deformations are found generally for the Pt atoms. The Pt bonded to carbon C1 of the aldehydic moiety is relaxed outward by 0.24 Å and shifted in-plane by 0.18 Å towards C1, whereas the Pt interacting in π(CC) type with the vinylic carbons is lifted by 0.61 Å and shifted by 0.20 Å into a position just below C3.

The surface deformations calculated for the other stable adsorption structures lead to a similar picture. Typical outward relaxations of 0.40 and 0.64 Å occur for the Pt atoms below C2 and C3 in the η^2-diσ(CC)-(s)-trans form, while their shifts parallel to the surface are about 0.30 and 0.15 Å correspondingly.

The η^3-diσ(CC)-σ(O)-(s)-cis-OSn structure behaves alike due to its diσ(CC) interaction[32]. Its additional σ(O) bond leads to a small increase of the protrusion of the affected Sn atom by 0.05 Å and an in-plane displacement of 0.10 Å just like in the η^4 case discussed above.

Moreover, it might be interesting to mention that the two η^3-π(CC)-σ(O)-OSn structures exhibit the largest deformations of the metal atoms bonded to the molecule. Here the Pt atoms below the vinylic carbons are lifted up by as much as 1.18 and 0.87 Å in the (s)-trans and (s)-cis forms, respectively, and the Sn atoms bonded to the aldehydic oxygens by 0.15 and 0.23 Å. The planar shifts of the Pt atoms are calculated at roughly 0.36 and 0.27 Å, but those of Sn are negligible. The significant in-plane shifts are expected to arise from the tendency to optimize the overlapp of the covalent molecule-surface bonds, while the outward relaxations might be a consequence of the sterical repulsion and the bond order conservation principle for the interacting metal

[32]The Pt atoms below C2 and C3 are lifted up by 0.39 and 0.54 Å and displaced by 0.34 and 0.23 Å parallel to the alloy plane.

Adsorption energies [kJ/mol]	(s)-trans	(s)-cis
η^1-top-OPt	unstable	unstable
η^1-top-OSn	unstable (-27.5* [45])	unstable
η^2-diσ(CO)-OPt	unstable	unstable
η^2-diσ(CO)-OSn	unstable	unstable
η^2-diσ(CC)	-7.4 (-2.5 [45])	unstable
η^2-π(CC)	-6.1 (-3.8 [45])	-3.6
η^2-diσ(C3,O)-OPt	unstable	unstable
η^2-diσ(C3,O)-OSn	excluded	not stable (-2.9 [45])
η^3-π(CC)-σ(O)-OPt	excluded	unstable
η^3-diσ(CC)-σ(O)-OPt	unstable	excluded
η^3-π(CC)-σ(O)-OSn	-20.0 (-16.3 [45])	-7.5
η^3-diσ(CC)-σ(O)-OSn	excluded	-16.5 (-11.3 [45])
η^4-diσ(CC)-diσ(CO)-OPt	excluded	unstable
η^4-π(CC)-diσ(CO)-OPt	excluded	excluded
η^4-diσ(CC)-diσ(CO)-OSn	excluded	excluded
η^4-π(CC)-diσ(CO)-OSn	excluded	-4.6 (-0.9 [45])

Table 7.22: DFT adsorption energies of prenal on $Pt_2Sn(111)$ at a theoretical coverage of $\Theta = 1/9$. A large number of structures could be "excluded" from the optimizations, because already the sterical situation of the initial structure was too unfavorable to lead to a reasonably stable geometry. The reference values given are taken from Ref. [45]. These authors added the dipole corrections along the surface normal only in the form of a single point calculation at the structure optimized before.

Adsorption mode	adsorption energy	surface deformation	molecule deformation	interaction term
η^2-π(CC)-trans	-6.1	74	40	-120
η^2-diσ(CC)-(s)-trans	-7.4	68	150	-225
η^3-diσ(CC)-σ(O)-(s)-cis-OSn	-16.5	59	156	-232
η^4-π(CC)-diσ(CO)-(s)-cis-OSn	-4.6	55	107	-166

Table 7.23: Decomposition of the adsorption energies [kJ/mol] of prenal on $Pt_2Sn(111)$ ($\Theta = 1/9$ ML) into the energy costs for deforming the surface and the molecule and the energy gain of the interaction in the optimized surface complex.

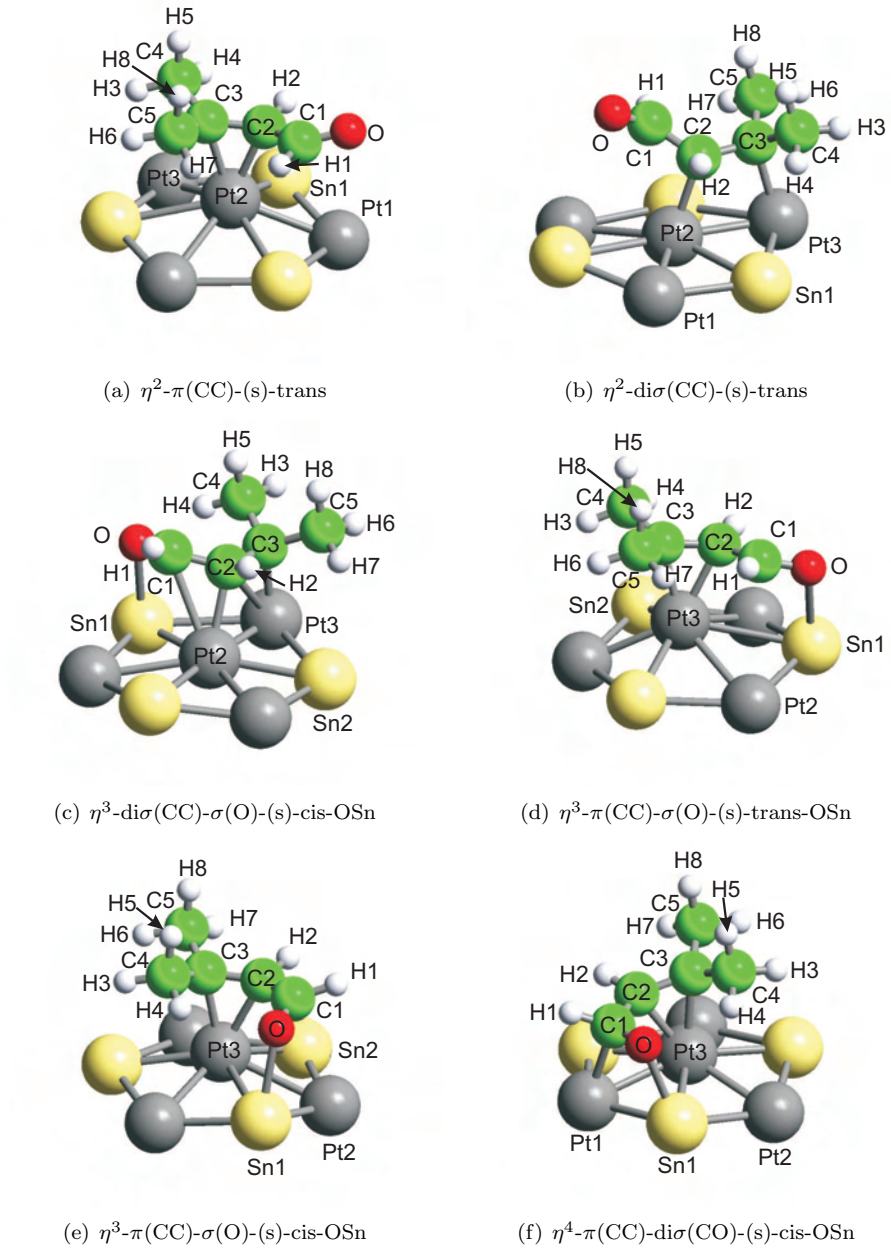

(a) η^2-π(CC)-(s)-trans

(b) η^2-diσ(CC)-(s)-trans

(c) η^3-diσ(CC)-σ(O)-(s)-cis-OSn

(d) η^3-π(CC)-σ(O)-(s)-trans-OSn

(e) η^3-π(CC)-σ(O)-(s)-cis-OSn

(f) η^4-π(CC)-diσ(CO)-(s)-cis-OSn

Figure 7.35: Optimized structures of the most stable η^2 and η^3 adsorption modes of prenal on $Pt_2Sn(111)$ at a theoretical coverage of 1/9 ML.

Geometry	η^2-diσ(CC)-(s)-trans	η^2-π(CC)-(s)-trans	η^2-π(CC)-(s)-cis	η^3-diσ(CC)-σ(O)-(s)-cis-OSn	η^3-π(CC)-σ(O)-(s)-trans-OSn	η^3-π(CC)-σ(O)-(s)-cis-OSn	η^4-π(CC)-diσ(CO)-(s)-cis-OSn
r(O-C1)	1.23	1.23	1.23	1.27	1.27	1.27	1.33
r(C1-C2)	1.48	1.47	1.48	1.41	1.43	1.44	1.47
r(C2-C3)	1.51	1.43	1.43	1.51	1.41	1.44	1.43
r(C3-C4)	1.53	1.51	1.51	1.53	1.51	1.52	1.51
r(C3-C5)	1.53	1.51	1.51	1.53	1.52	1.52	1.52
r(C1-H1)	1.12	1.12	1.12	1.11	1.11	1.11	1.11
r(C2-H2)	1.10	1.09	1.10	1.10	1.09	1.09	1.10
r(C4-H3)	1.10	1.10	1.09	1.09	1.10	1.09	1.09
r(C4-H4)	1.11	1.11	1.11	1.11	1.11	1.11	1.11
r(C4-H5)	1.10	1.10	1.10	1.10	1.10	1.10	1.10
r(C5-H6)	1.10	1.10	1.10	1.10	1.10	1.10	1.10
r(C5-H7)	1.11	1.11	1.11	1.11	1.11	1.11	1.11
r(C5-H8)	1.10	1.10	1.10	1.10	1.10	1.10	1.10
r(O-M)	-	-	-	2.41	2.43	2.41	2.20
r(C1-M)	-	-	-	-	-	-	2.29
r(C2-M)	2.17	2.19	2.19	2.24	2.21	2.30	2.28
r(C3-M)	2.16	2.25	2.23	2.15	2.18	2.19	2.24
r(O-H)			2.39	2.42		2.44	2.36

Table 7.24: Bond lengths of the optimized adsorption geometries of prenal on $Pt_2Sn(111)$ (Θ = 1/9 ML). All distances r are given in Å. r(O-H) denotes a short distance of a methyl hydrogen to the aldehydic oxygen in the corresponding adsorption complex.

atoms [51], which gain new bonds and must therefore reduce the overlapp with the metal bands. The metal atoms surrounding the directly interacting ones in the first surface layer usually adjust their positions according to the displacements of the latter centers in the various adsorption complexes. This manifests itself typically in planar shifts of ca 0.10 Å and inward relaxations of 0.05 Å, which, due to sterical repulsion, appear to be even larger for atoms below the methyl groups (up to 0.15 Å, for instance, for Sn).

The additional large in-plane displacements of the metal atoms on $Pt_2Sn(111)$ account for the high energy costs of the deformation of this surface alloy (ca 61 kJ/mol for the η^2, η^3 and η^4 complexes) as compared to $Pt_3Sn(111)$ (50 kJ/mol) or Pt(111) (58 kJ/mol). This phenomenon, already discussed for crotonaldehyde in Chap. 6.3.2, is quite surprising, because the Pt_2Sn surface exhibits the "softest" modulus of all three considered surface alloys for the outward relaxation of a surface atom.

A consequence of the high surface deformation costs is a lowering of the adsorption energies (Tab. 7.23). Together with the similarity of the molecule deformation costs on both Pt-Sn surface alloys and the lowering of the interaction terms, which decrease from Pt(111) (ca -255) over $Pt_3Sn(111)$ (-224) to $Pt_2Sn(111)$ (-208 kJ/mol) for the high-hapticity forms, a weakening of the adsorption energies results. This weakening is, in fact, dramatic with the consequence that no sizably bonded adsorption complex results for prenal on this model catalyst.

The problem of the weakly bonded adsorption structures is also reflected in the experimental HREEL spectra, which have been recorded for a number of initial exposures ranging from 0.5L to 10L. Independent of the exposure, i.e. the prenal coverage, only small shifts and slight changes

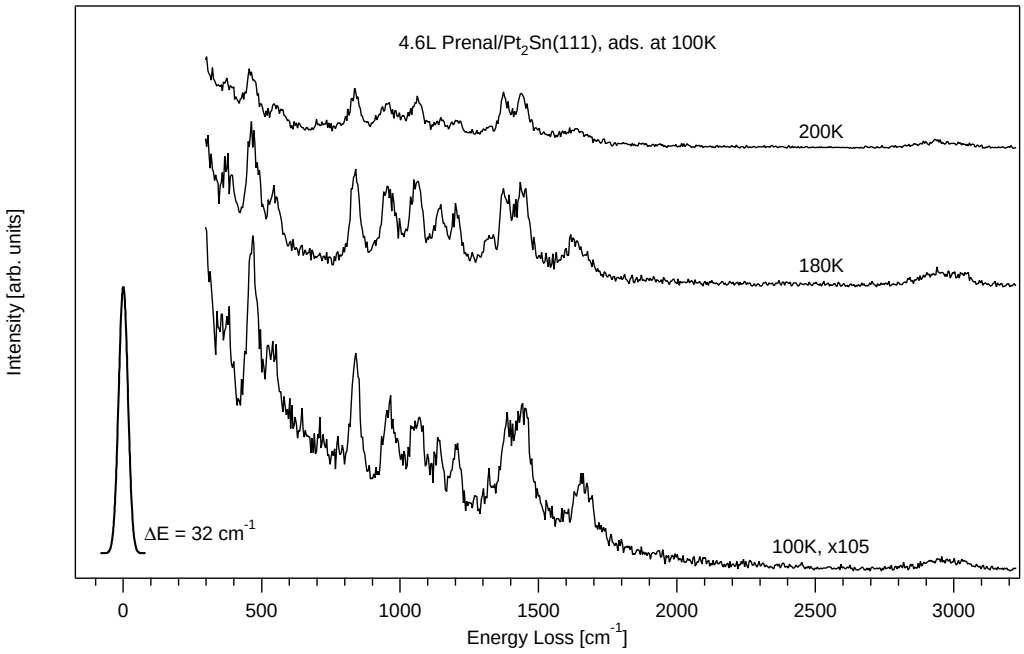

Figure 7.36: HREELS experiments after exposure of 4.6L prenal to $Pt_2Sn(111)$ at 100 K. The HREEL spectra have been recorded in specular geometry at an angle of incidence of 60° (primary energy of 4.7 eV).

in loss intensities are found in the HREEL spectra recorded after annealing to temperatures of 100 K (adsorption), 180 K, 200 K (both after desorption of multilayer, see TPD results in Chap. 7.3.1) and above 250 K (desorption of monolayer).

The HREELS experiments carried out for the different exposures at 100 K always show the spectroscopic fingerprint known from the multilayer on Pt(111) or Pt_3Sn, although the absolute loss intensities decrease with the surface coverage. Even for small sample coverages such as expected from an exposure of 0.5L prenal, no significant changes in frequencies or relative intensities are observed.

After annealing the prenal precovered sample to 180 K, slight changes in the relative loss intensities indicate a surface reordering of the adsorbate layer. This can be followed for instance in the experimental HREELS series of 4.6L prenal as presented in Fig. 7.36. This vibrational spectrum is well-defined and shows a number of comparably sharp and intense bands in the fingerprint region, all of which have a close counterpart in the multilayer.

The overall shape of the 180 K HREEL spectrum is reminiscent of the data recorded at similar temperatures for prenal on $Pt_3Sn(111)$, which was interpreted satisfactorily with the computed vibrational properties of the two η^1-top-(s)-trans-OSn adsorption structures. Both species exhibited mostly the unperturbed vibrational frequencies of prenal in the gas phase, since they are only bonded on top of one surface tin atom through the aldehydic oxygen. In contrast their specific vertical orientations lead to a characteristic intensity pattern, which matched the experimental data well. In terms of experimental frequencies and loss intensities, the HREEL spectra on $Pt_2Sn(111)$ coincide partially well with the solved case on $Pt_3Sn(111)$, although some discrepancies are found. Thus for instance the loss intensities at the low frequencies of 380, 470 and 553 cm^{-1} as well as the peaks at 1202 and 1625 cm^{-1} are at least 30% weaker on $Pt_2Sn(111)$, which renders this spectrum in fact more similar to the multilayer characteristics.

Since the DFT optimizations did not lead to any stable η^1-top-OSn adsorption geometry on this surface alloy, it must be suggested that the latter HREEL spectrum at 180 K corresponds to a very weakly bonded, i.e. physisorbed surface species. As this is not directly supported by DFT, further experimental studies are necessary to confirm this suggestion.
After annealing the sample to 200 K, the HREEL spectra are varied slightly (Fig. 7.37). The overall intensity is somewhat lowered, which is in agreement to the extending desorption tail measured for the multilayer state α_1 between 166 K and about 230 K. Apparently the signals between 380 and 553 cm^{-1} and the peaks at 1202 and 1625 cm^{-1} are still damped stronger in comparison to the other loss peaks, rendering the data again different from the one on $Pt_3Sn(111)$. However, the HREEL spectrum differs also from the multilayer data, but the discrepancies are not very pronounced. Mostly the peak in the double bond stretching region at ca 1625 cm^{-1} seems to be rather weak as compared to the relative intensity of the same signal at 100 K, yet other signals show small changes in relative intensities, too.
The general approach followed in this thesis to analyze the experimental measurements with the computed HREEL data, first of the most stable adsorption structures, afterwards also of the remaining geometries that might be present on the surface, fails in this case. Using only the most stable sites such as η^3-diσ(CC)-σ(O)-(s)-cis-OSn (Tab. 7.25 to 7.28), one is not only unable to reproduce the HREEL spectra satisfactorily, but even finds several signals that are not present experimentally. Particularly large discrepancies are evident around 375, 956, 1371 and 1444 cm^{-1} between the experimental data at 200 K and the DFT results, where the intensity obtained from the theoretical results is insufficient to account for the measured loss peaks. Additionally the theoretical frequencies of the ν(C1=O) vibrations of the η^3-π(CC)-σ(O)-(s)-trans-OSn (1500 cm^{-1}) and the η^3-diσ(CC)-σ(O)-(s)-cis-OSn (1480 cm^{-1}) forms show large errors of ca 50 cm^{-1} to the experimental value of 1444 cm^{-1}, which is a phenomenon not encountered so far. Indeed surprising is also the appearance of a loss signal at 1625 cm^{-1}, because the η^2-diσ(CC) and η^2-π(CC) species are extremely weakly bonded and other structures usually exhibiting vibrations in this range have not been obtained from the DFT optimizations. In contrast to this disagreement, the best correspondence is achieved by considering the calculated spectra of η^2-diσ(CC)-(s)-trans and η^2-π(CC)-(s)-trans (both ca -2 kJ/mol). These calculated spectra show the smallest differences to the gas phase and multilayer frequencies. In the light of their nearly negligible bond energies, which are expected to be below the precision of PW91, they have to be excluded nonetheless.
Finally, after annealing the sample to temperatures above 250 K, no further defined HREEL spectra are recorded, indicating that the prenal species have desorbed.

In summary, this is the first case during the present studies of α,β-unsaturated aldehydes on model catalysts, in which the combination of HREELS and DFT fails to reach a convincing explanation. The problem seems to be originating from the deficiency of the DFT GGA functional PW91 to describe weak interactions such as for example the dispersion forces and hydrogen bridge bonds correctly, which are expected to be especially important for prenal/$Pt_2Sn(111)$. Hence, both the theory and the experiment have difficulties with this system when considered on their own. Having in mind the results of prenal/$Pt_3Sn(111)$, it is also not possible to arrive at a satisfying conclusion from the purely experimental point of view.
Taking into account the weak calculated adsorption energies (> -20.0 kJ/mol) as well as the small changes between the multilayer HREEL spectrum at 100 K and the spectra at higher temperatures, the combination of the results from both approaches allows to suggest that prenal is only physisorbed on this surface alloy.

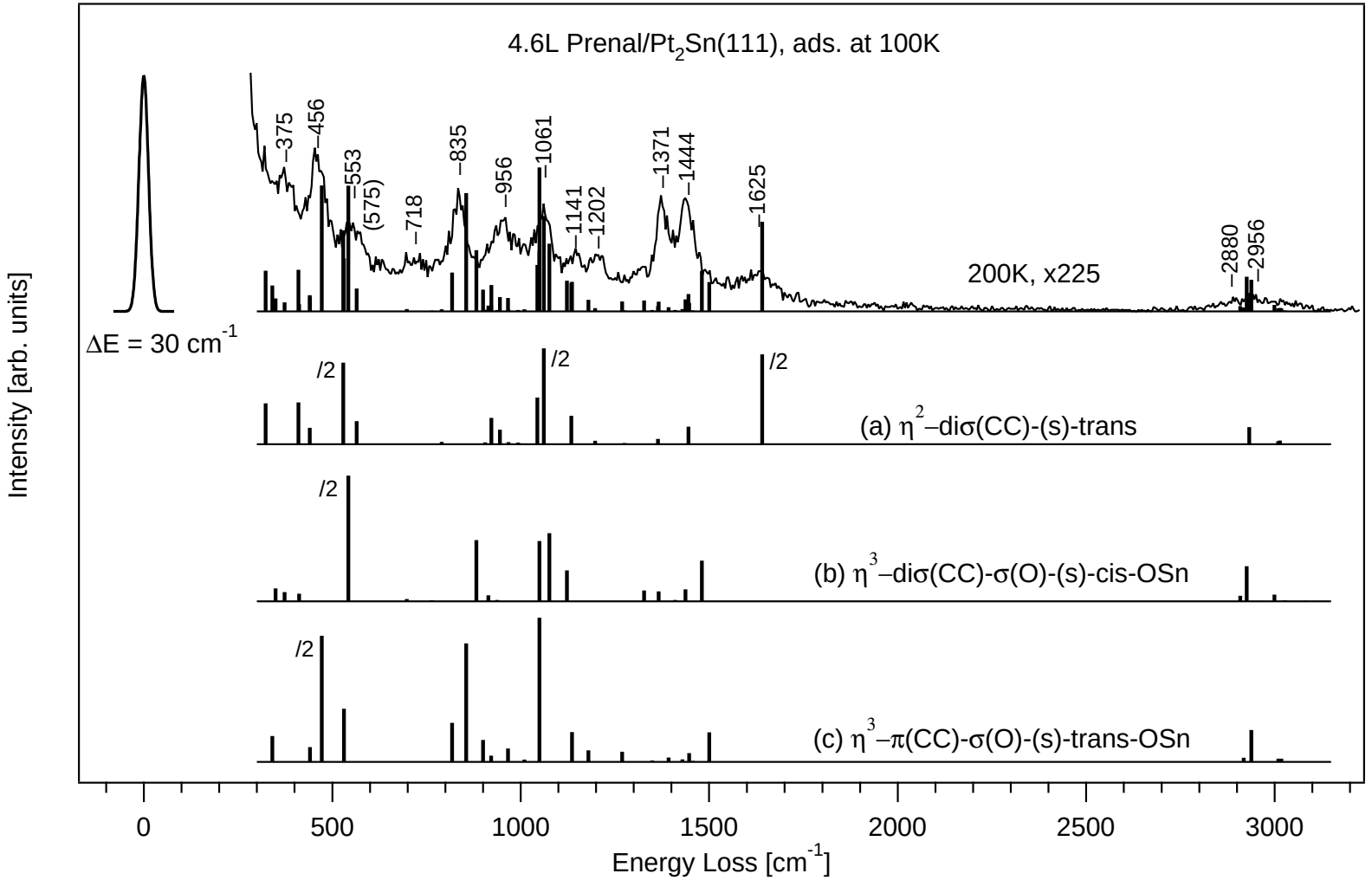

Figure 7.37: Computed DFT HREEL spectra of the most stable adsorption complexes of prenal on $Pt_2Sn(111)$ and the HREEL spectrum of 4.6L prenal adsorbed at 100 K that was subsequently flashed to 200 K. As evident, the agreement between the theoretical data and the experiment is bad in this case.

ω cm^{-1}	Intensity $\times 10^6$ au		Normal mode
3051	0.019		ν(C4-H3)+ν(C5-H6)
3049	0.004		ν(C4-H3)-ν(C5-H6)
3014	0.16		ν_{as}(C5-H7,8)
3009	0.13		ν_{as}(C4-H4,5)
3006	0.003		ν(C2-H2)
2933	0.74		ν_s($C5H_3$)
2927	0.001		ν_s($C4H_3$)
2822	0.014		ν(C1-H1)
1640	7.7	s	ν(C1=O)
1445	0.76		δ_s'($C4H_3$-$C5H_3$)
1432	0.019		δ_s"($C4H_3$-$C5H_3$)
1424	0.011		δ_{as}'($C4H_3$-$C5H_3$)
1411	0.025		δ_{as}"($C4H_3$-$C5H_3$)
1369	0.030		δ_s(C1H1-C2H2)
1364	0.23		u_s($C4H_3$-$C5H_3$)
1345	0.001		u_{as}($C4H_3$-$C5H_3$)
1275	0.047		δ_{as}(C1H1-C2H2)
1198	0.15		ν(C2=C3)
1134	1.2	w	ν_{as}(C3C4-C3C5)
1061	8.2	s	ν(C1-C2)
1044	2.0	w	γ_s"($C4H_3$-$C5H_3$)
993	0.064		γ(C2H2)
967	0.088		γ_{as}'($C4H_3$-$C5H_3$)
944	0.62		γ(C1H1)
922	1.1	w	γ_s'($C4H_3$-$C5H_3$)
906	0.077		γ_{as}"($C4H_3$-$C5H_3$)
790	0.10		ν_s(C3C4-C3C5)
565	0.99		ν_{as}(PtC2-PtC3)
529	7.0	s	δ(O=C1-C2)
440	0.70		δ(C2=C3,4,5)
410	1.8	w	δ(C3-C4,C5)
323	1.8	w	ν_s(PtC2-PtC3)
286	0.091		τ_s(CH_3)
257	0.29		τ_{as}(CH_3)
244	2.3	w	δ(C1-C2=C3)
242	0.72		ω(C2=C3,4,5)
210	0.15		τ(C2=C3)
205	3.8	m	τ(C1-C2)
115	2.2		fT
90	1.5		fT
70	16.8		fR
52	0.116		fR

Table 7.25: Vibrational analysis of the η^2-diσ(CC)-(s)-trans structure of prenal on Pt_2Sn(111) ($\Theta = 1/9$ ML).

ω cm^{-1}	Intensity $\times 10^6$ au		Normal mode
3083	0.028		ν(C4-H3)
3043	0.0		ν(C5-H6)
3028	0.047		ν(C2-H2)
3020	0.020		ν_{as}(C4-H4,5)
3000	0.29		ν_{as}(C5-H7,8)
2925	1.5	vw	ν_s($C4H_3$)
2918	0.015		ν_s($C5H_3$)
2909	0.24		ν(C1-H1)
1480	1.7	vw	ν(C1=O)
1437	0.52		δ_s'($C4H_3$-$C5H_3$)
1431	0.001		δ_s"($C4H_3$-$C5H_3$)
1419	0.008		δ_{as}'($C4H_3$-$C5H_3$)
1409	0.067		δ_{as}"($C4H_3$-$C5H_3$)
1366	0.43		u_s($C4H_3$-$C5H_3$)
1351	0.017		δ_s(C1H1-C2H2)
1343	0.001		u_{as}($C4H_3$-$C5H_3$)
1327	0.47		δ_{as}(C1H1-C2H2)
1190	0.0		ν(C2=C3)
1122	1.3	vw	ν_{as}(C3C4-C3C5)
1076	2.9	w	ν(C1-C2)
1049	2.6	w	γ_s"($C4H_3$-$C5H_3$)
971	0.004		γ_{as}"($C4H_3$-$C5H_3$)
938	0.061		γ_{as}(C1H1-C2H2)
915	0.001		γ_{as}'($C4H_3$-$C5H_3$)
914	0.26		γ_s'($C4H_3$-$C5H_3$)
882	2.6	w	γ_s(C1H1-C2H2)
764	0.039		δ(O=C1-C2)
698	0.11		ν_s(C3C4-C3C5)
543	10.8	m	ν_{as}(PtC2-PtC3)
412	0.32		δ(C3-C4,C5)
374	0.39		δ(C2=C3,4,5)
350	0.56		ν_s(PtC2-PtC3)
301	20.9	vs	ν(O-Sn)
287	0.008		τ_s(CH_3)
265	0.040		δ(C1-C2=C3)
238	0.20		τ_{as}(CH_3)
218	0.21		ω(C2=C3,4,5)
214	0.33		τ(C2=C3)
146	1.8		τ(C1-C2)
112	1.0		fR
104	1.1		fT
91	0.31		fT

Table 7.26: Vibrational analysis of the η^3-diσ(CC)-σ(O)-(s)-cis-OSn structure of prenal on $Pt_2Sn(111)$ (Θ = 1/9 ML).

ω cm^{-1}	Intensity $\times 10^6$ au		Normal mode
3067	0.001		ν(C2-H2)
3060	0.016		ν(C5-H6)
3048	0.001		ν(C4-H3)
3018	0.14		ν_{as}(C5-H7,8)
3010	0.14		ν_{as}(C4-H4,5)
2938	1.4	w	ν_s($C5H_3$)
2932	0.0		ν_s($C4H_3$)
2918	0.18		ν(C1-H1)
1500	1.3	w	ν(C1=O)
1456	0.046		δ_s'($C4H_3$-$C5H_3$)
1446	0.37		δ_s"($C4H_3$-$C5H_3$)
1429	0.11		δ_{as}'($C4H_3$-$C5H_3$)
1417	0.028		δ_{as}"($C4H_3$-$C5H_3$)
1392	0.19		ν(C2=C3)
1362	0.027		u_s($C4H_3$-$C5H_3$)
1349	0.063		u_{as}($C4H_3$-$C5H_3$)
1314	0.023		δ(C1H1)
1269	0.44		δ(C2H2)
1179	0.50		ν(C1-C2)
1136	1.3	w	ν_{as}(C3C4-C3C5)
1049	6.2	s	γ_s"($C4H_3$-$C5H_3$)
1009	0.092		γ_s'($C4H_3$-$C5H_3$)
966	0.58		γ_{as}'($C4H_3$-$C5H_3$)
921	0.26		γ_{as}"($C4H_3$-$C5H_3$)
900	0.94	vw	γ(C1H1)
855	5.1	s	γ(C2H2)
817	1.7	w	ν_s(C3C4-C3C5)
531	2.3	m	δ(O=C1-C2)
472	10.8	vs	ν_{as}(PtC2-PtC3)
441	0.63	vw	δ(C2=C3,4,5)
358	0.029		δ(C3-C4,C5)
341	1.1	w	ν_s(PtC2-PtC3)
282	1.12	w	τ_s(CH_3)
257	10.1	vs	ν(O-Sn)
248	6.3	s	τ_{as}(CH_3)
214	2.9	m	τ(C1-C2)
189	0.61		ω(C2=C3,4,5)
177	3.7	m	δ(C1-C2=C3)
134	0.82		τ(C2=C3)
80	3.11		fT
61	0.38		fT
45	0.30		fR

Table 7.27: Vibrational analysis of the η^3-π(CC)-σ(O)-(s)-trans-OSn structure of prenal on $Pt_2Sn(111)$ ($\Theta = 1/9$ ML).

ω cm^{-1}	Intensity $\times 10^6$ au		Normal mode
3101	0.009		ν_{as}(C4-H4,5)
3052	0.015		ν_{as}(C5-H7,8)
3045	0.031		ν(C2-H2)
3022	0.029		ν(C4-H3)
3013	0.060		ν(C5-H6)
2940	1.0		ν_s($C4H_3$)
2935	0.021		ν(C1-H1)
2930	0.21		ν_s($C5H_3$)
1456	0.0		ν(C2=C3)
1436	0.69		δ_s"($C4H_3$-$C5H_3$)
1418	0.028		δ_s'($C4H_3$-$C5H_3$)
1410	0.032		δ_{as}'($C4H_3$-$C5H_3$)
1393	0.41		δ_{as}"($C4H_3$-$C5H_3$)
1363	0.20		u_s($C4H_3$-$C5H_3$)
1350	0.003		u_{as}($C4H_3$-$C5H_3$)
1326	0.12		δ(C1H1)
1291	0.18		δ(C2H2)
1194	1.3	w	ν(C1=O)
1150	0.92		ν_{as}(C3C4-C3C5)
1046	0.88		γ_s'($C4H_3$-$C5H_3$)
1043	3.4	m	γ_s"($C4H_3$-$C5H_3$)
982	0.28		γ_{as}"($C4H_3$-$C5H_3$)
951	0.97		γ(C2H2)
930	0.027		ν(C1-C2)
913	0.17		γ_{as}'($C4H_3$-$C5H_3$)
781	0.36		ν_s(C3C4-C3C5)
774	0.35		γ(C1H1)
670	1.5	w	δ(O=C1-C2)
512	14.2	s	ν_{as}(PtO-PtC1)-ν_{as}(PtC2-PtC3)
425	0.99		ν_{as}(PtO-PtC1)+ν_{as}(PtC2-PtC3)
396	1.5	w	δ(C3-C4,C5)
359	0.34		δ(C2=C3,4,5)
332	0.80		ν_s(PtO-PtC1)-ν_s(PtC2-PtC3)
255	1.7	w	δ(C1-C2=C3)
235	0.12		τ_s(CH_3)
215	0.15		ν_s(PtO-PtC1)+ν_s(PtC2-PtC3)
212	0.004		τ(C2=C3)
194	0.40		τ_{as}(CH_3)
166	1.8	w	ω(C2=C3,4,5)
121	0.13		τ(C1-C2)
90	1.7		fR
80	0.32		fT

Table 7.28: Vibrational analysis of the η^4-π(CC)-diσ(CO)-(s)-cis-OSn structure of prenal on $Pt_2Sn(111)$ (Θ = 1/9 ML).

7.4 Important Conlusions from the Studies of Prenal

Pt(111):

- For prenal, the analysis of the HREEL spectra with DFT leads to the identification of the η^2-diσ(CC)-(s)-trans, η^2-diσ(CC)-(s)-cis, η^3-diσ(CC)-σ(O)-(s)-cis, η^4-diσ(CC)-diσ(CO)-(s)-trans and the η^4-π(CC)-diσ(CO)-(s)-cis adsorption complexes. These structures are the most stable forms for prenal on Pt(111). They exhibit similar adsorption energies, but characteristic vibrational fingerprints.
- The identified adsorption modes are adsorbed irreversibly according to TPD and decompose above 250 K. This can be followed by the desorption of CO (405 K) and H_2 (ca 276, 425 and 473 K) in the TPD investigations.
- During the decomposition, three reaction intermediates are formed with a significant stability, which allowed to identify them by the combination of DFT and HREELS. Sequentially appearing during the decomposition process are the dehydro-η^3-prenal-H1 and η^3-isobutenyl surface species as well as the η^3-isobutylidyne surface species.
- Coadsorption experiments of prenal with D_2 fail to produce any hydrogenation products under UHV conditions. Instead only a weak H-D exchange is observed.

$Pt_3Sn(111)$ and $Pt_2Sn(111)$:

- The HREELS and DFT results on the Pt_3Sn surface alloy point to a similar behavior as on Pt(111), i.e. the formation of irreversibly adsorbed species that decompose above 250 K, but the desorption of fragments such as CO remained below the detection limit of TPD. The theoretical analysis of the HREELS data at 200 K leads to the identification of two energetically competitive, vertical structures of the η^1-top-(s)-trans-OSn type. As most of the vibrational frequencies of the two identified η^1-top-(s)-trans-OSn geometries are similar to the gas phase values of free prenal, the HREELS *intensities* have to be adducted for their identification.
- In contrast, the DFT study of prenal on $Pt_2Sn(111)$ results in a number of only very weakly bonded adsorption complexes, whose spectroscopic properties are not consistent with the low temperature HREELS experiments at 180 or 200 K. Especially the η^1-top forms are no longer stable in the DFT optimizations. Also the TPD experiments indicate a weaker adsorption on $Pt_2Sn(111)$ (monolayer desorption at ca 216 K). Taking into account the changes between the HREEL spectra recorded at 100 K and after annealing to 200 K, only weakly bonded, i.e physisorbed prenal is present on the Pt_2Sn surface alloy. Although the DFT adsorption energies would support the trend of a weaker interaction, the chosen DFT model (GGA functional PW91, slab thickness) fails to describe the interactions correctly.
- The differences of the properties of Pt(111), Pt_3Sn and Pt_2Sn arise from electronic effects, since basically for all coordination types some local minina are found by DFT. The alloying of Pt(111) with Sn reduces both the adsorption energies and, more importantly, the interaction strength of prenal. This weakening of the adsorption leads to a decrease of the number of competitive, chemisorbed structures on $Pt_3Sn(111)$. On the Pt_2Sn surface alloy, HREELS and DFT suggest only a physisorption. The interaction strength of prenal and the deformation cost of the surface do not show a constant trend, but are specific for each surface. Like for crotonaldehyde, the surface atom displacements from the equilibrium positions induced by prenal increase in the sequence Pt(111), Pt_3Sn and Pt_2Sn. On Pt_2Sn the surface atoms are not only relaxed outward, but they are shifted sizably parallel to the surface plane, too.

Chapter 8

Summary

In the present work, the interactions of the multifunctional molecules prenal and crotonaldehyde with mono- and bimetallic model catalyst surfaces have been investigated with a combined experimental (TPD, LEED and HREELS) and theoretical (DFT) approach. Although the morphology of well-ordered model catalyst surfaces in a UHV environment is rather simple in contrast to real catalysts under reaction conditions (the often discussed "materials gap" and "pressure gap"), these investigations are essential in order to lay the base for a detailed understanding and control of the reactivity of processes at surfaces. Thus the studies of the α,β-unsaturated aldehydes on Pt(111) and Pt-Sn surface alloys have been carried out with the goal of understanding the effects of the alloying on the adsorption as well as on the selective hydrogenation to either saturated aldehydes or unsaturated alcohols, which are the desired product in chemical and pharmaceutical industries.

The first major conclusion of this thesis is that with the combined approach of spectroscopic experiments and theoretical calculations it is generally possible to identify different surface species in a mixed phase. The interpretation of highly complex HREEL spectra of multifunctional molecules is nonetheless a very demanding task for the experimental techniques as well as for the theoretical computations.
From the vibrational analysis a few simple rules can be derived, which may help to distinguish the various possible surface configurations. The most useful indicator is the presence of a loss peak in the double-bond stretching region between 1600 and 1700 cm^{-1}. Such a peak is characteristic for the more vertical structures such as the η^1-top and the various η^2 forms (π and diσ coordinations of the C=C or C=O moieties). Due to the different possible isomers of the molecules (trans and cis for prenal and in addition E and Z for crotonaldehyde), this peak may shift slightly or even broaden. Also the presence of η^1-top species, which besides the ν(C=C) stretching mode around 1650 cm^{-1} are characterized by a band from the ν(C=O) vibration near 1560-1610 cm^{-1}, causes a close-lying second peak that has been rather difficult to resolve using HREELS in the present experiments. Furthermore all these peaks may be broadened by couplings to other surface species and disorder, which can lead to overlapping and makes the identification of a certain species very difficult.
In case that no intensity is observed in the double-bond stretching region, the aldehydes must be adsorbed in a flat η^3 or η^4 configuration with interactions of both C=C and C=O to the surface. Also the η^2-diσ(C3,O) metallacycles, which are stable on the Pt_2Sn surface alloy, do not exhibit any intense signals in the 1600 to 1700 cm^{-1} frequency range and must, thus, be identified by loss signals in the fingerprint region.
In the frequency region up to 1450 cm^{-1} , a large variety of different normal modes (the ν(CC), δ, γ, ω, τ modes, the hindered modes and, of course, the molecule-surface stretching vibrations)

of the molecular backbone can be found, but it is very difficult to predict the relative intensities of these vibrational signals qualitatively. These normal modes tend to shift sizably due to the different adsorption configurations, the interaction strength and especially also due to different vibrational couplings, which render an analysis of the HREEL spectra from the purely experimental point of view extremely complicated. In order to understand the features observed in the fingerprint region, a detailed analysis of the vibrational experiments by structure calculations and corresponding theoretical vibrational analysis needs to be performed. Only by a close comparison of the measured signals with the simulated DFT data, it is possible to identify the various components of a mixed phase of adsorbates. Thus, the identification of the η^3 and η^4 structures or the differentiation between the multitude of η^2 forms is only feasible by such a dual approach. Neither the vibrational experiments, nor any total energy results coming from the DFT calculations are sufficient for an analysis of such mixed phases of complex molecules when considered on their own.

The identification of the actually present adsorbate complexes opens the way for thorough characterization not only of the vibrational properties, but also of the interactions and bonding mechanisms of these structures.

The adsorption of crotonaldehyde:

Of the two considered α,β-unsaturated aldehydes, crotonaldehyde is the more complex system, because four rota-isomers, namely the E and Z isomers of the (s)-trans and (s)-cis forms, exist close in energy in the gas phase. On the surface, consequently, a large set of adsorption structures has to be considered in the analysis.

Generally the adsorption of crotonaldehyde on Pt(111) is characterized by several low temperature desorption states of intact molecules in TPD, while at temperatures above 250 K the desorption of CO (395 K) and H_2 (ca 310 and 425 K) indicate a decomposition process of irreversibly bonded crotonaldehyde species. Although TPD is not very useful for a further characterization of the adsorption, it still gives a good overview on the temperature-dependent behavior of the molecule and points to interesting temperature and coverage ranges, which have subsequently been studied using HREELS.

After the desorption of the multilayer (ca 143 K) and two more low temperature states (160 and 177 K), whose origin might be a partial desorption and reordering or some weakly bonded species, HREEL spectra of strongly adsorbed crotonaldehyde have been recorded at 200 K. The analysis of spectra using the vibrational computations from DFT leads to the identification of five structures with very similar stabilities (-69 to -80 kJ/mol), i.e. the η^2-diσ(CC)-E-(s)-trans, η^2-diσ(CC)-E-(s)-cis, η^3-diσ(CC)-σ(O)-E-(s)-cis, η^4-diσ(CC)-diσ(CO)-E-(s)-trans and the η^4-π(CC)-diσ(CO)-E-(s)-cis complexes. As expected, the stable adsorbate configurations exhibit related, yet characteristic vibrational fingerprints.

The analysis of the decomposition products above 250 K measured with HREELS using extensive geometry optimizations and vibrational characterizations of potential surface intermediates with DFT allows to identify five reaction species, which seem to be sufficiently stable for the experimental detection. Despite the huge number of more than 50 conceivable intermediates ranging from dehydrogenated fragments of crotonaldehyde down to pure hydrocarbons as small as η^1-methylidyne (Pt_3CH), a decomposition pathway is proposed. In the sequence of their appearance during the decomposition, the dehydro-η^3-E-crotonaldehyde-H1 radical, the η^2-propyne, η^1-propylidyne, η^1-ethylidyne and finally the η^1-methylidyne surface species are identified by HREELS and DFT between 250 and 450 K.

In order to investigate the selective hydrogenation on Pt(111), also coadsorption experiments of crotonaldehyde with D_2 or H_2 have been carried out. Yet these failed to yield any hydro-

genation products under UHV conditions. Instead, a weak H-D exchange reaction is observed by HREELS. Nonetheless, from the present results it is possible to draw the conclusion that the hydrogenation of crotonaldehyde must be very unselective on pure Pt(111), since in three of the five stable adsorption geometries both the C=C and the C=O double bonds participate in the adsorption and, hence, are activated [6, 7, 25]. This is consistent with results of previous studies, which showed indeed that Pt(111) exhibits a very low selectivity, especially towards the unsaturated alcohol 2-butenol [6, 7, 25]. Moreover, one might expect from the two η^2-diσ(CC) structures an increased fraction of a hydrogenation of the thermodynamically preferred C=C bond to butanal, the saturated aldehyde, which is also consistent with the literature.

Switching to the adsorption of crotonaldehyde on the Pt-Sn surface alloys, the situation does not change dramatically. On the $Pt_3Sn(111)$ surface alloy, a high temperature decomposition similar to the behavior on Pt(111) is detected by HREELS and TPD, while on $Pt_2Sn(111)$ a monolayer desorption state of intact aldehyde at ca 236 K points to a much weaker interaction. From the interpretation of the HREELS experiments with the DFT calculations, a pronounced coverage dependence is deduced on both surfaces. Around 160 K (155 K on Pt_2Sn), a high coverage phase with structures of low hapticity such as η^1 and η^2 is formed, whereas after annealing to higher temperatures (200 K), a partial desorption and reordering to a low coverage situation of high hapticity complexes is detected.
The theoretical analysis shows that the high coverage phase consists of the η^2-diσ(CC)-E-(s)-trans and η^2-diσ(CC)-E-(s)-cis structures on both surface alloys ($E_{ads} \approx -20$ to -33 kJ/mol). However, on Pt_3Sn two energetically competitive η^1-top-E-(s)-trans-OSn forms ($E_{ads} \approx -30$ kJ/mol) cannot be excluded. Also very similar are the low coverage mixed phases at 200 K on both surface alloys. These are interpreted well by the DFT spectra of the η^2-diσ(CC)-E-(s)-trans ($E_{ads} \approx -33$ kJ/mol), the η^3-diσ(CC)-σ(O)-E-(s)-cis-OSn ($E_{ads} \approx -50$ kJ/mol) and the η^4-π(CC)-diσ(CO)-E-(s)-cis-OSn adsorption complexes ($E_{ads} \approx -42$ and -29 kJ/mol on Pt_3Sn and Pt_2Sn, resp.). On Pt_3Sn also the η^2-diσ(CC)-E-(s)-cis structure ($E_{ads} \approx -34$ kJ/mol), which is not stable on Pt_2Sn, agrees with the experiments.
Generally it is observed from the calculated adsorption energies that the complexes require the formation of an oxygen-tin bond in order to be reasonably stable. On the other hand, an oxygen-platinum bond hardly strengthens the adsorption on the Pt-Sn alloy surfaces.
Also the experimental studies of the selective hydrogenation of crotonaldehyde on both surface alloys were unsuccessful. The reason for this is the low sticking probability for molecular hydrogen or deuterium, which is reduced essentially to zero by the alloying with Sn [173]. Therefore conclusions can only be drawn from the identified adsorption modes. In this case, the coverage effects may be expected to lead to a pressure dependence of the selectivity and reactivity of crotonaldehyde on the Pt-Sn model surfaces.
At low coverages the flat η^2, η^3 and η^4 species imply a low selectivity in the hydrogenation, but at high coverages the performance of both model catalysts might be different. While on $Pt_2Sn(111)$ the η^2-diσ(CC) forms account for the saturated aldehyde as primary product, on $Pt_3Sn(111)$ additionally a small fraction of vertical η^1-top-OSn complexes is present on the sample. Ignoring the desorption energies of the different products in a crude approximation, it is the latter type of coordination that should lead to an increased selectivity towards formation of the unsaturated alcohol on the Pt_3Sn model catalyst, since the C=O bond is activated by the adsorption here[1].
The expectation of a change in the selectivity of the crotonaldehyde hydrogenation from the unselective model catalysts Pt(111) and $Pt_2Sn(111)$ to $Pt_3Sn(111)$ is yet disproved by the experimental studies of several other groups. According to the explanation of Marinelli et al. [6, 7]

[1] Although a desired product may be formed with a low energy barrier and a high selectivity, the performance of catalyst may still appear to be bad if other, undesired products may desorb much easier and, hence, the desired product only blocks the surface.

and Jerdev et al. [12], the different alloy phases do not lead to an increase in selectivity alone. The saturated aldehyde (butanal) always remains the primary product when the hydrogenation is performed at moderate reactant pressures and temperatures [12] (5 Torr H_2, 0.05 Torr crotonaldehyde, 350 K $\leq T_{rec} \leq$ 395 K), but the activity of the Pt-Sn catalysts is about twice as high as the one detected for Pt(111). Also a preoxidation of the Pt-Sn surface alloys does not alter the selectivity significantly. It just decreases the activity of the catalyst drastically [12].

The adsorption of prenal:

The investigation of the prenal adsorption on Pt(111) results in a picture similar to observations made for crotonaldehyde. Since prenal has only two energetically close isomers, namely the (s)-trans and (s)-cis forms, the studies of prenal turn out to be less complex.

The TPD experiments showed the desorption state of the multilayer at ca 163 K and two low temperature desorption states of intact prenal at about 180 K (badly resolved) and 199 K. The occurrence of the two distinguishable states cannot be explained from the present data. The HREEL spectra recorded after annealing the sample to 200 K are interpreted as a mixed phase of the most stable adsorption structures found in the DFT optimizations, which are of the same types of coordination as found for crotonaldehyde. For prenal, the analysis leads to the identification of the η^2-diσ(CC)-(s)-trans, η^2-diσ(CC)-(s)-cis, η^3-diσ(CC)-σ(O)-(s)-cis, η^4-diσ(CC)-diσ(CO)-(s)-trans and the η^4-π(CC)-diσ(CO)-(s)-cis adsorption modes. These complexes are adsorbed slightly weaker with -47 to -59 kJ/mol than the corresponding crotonaldehyde forms, which is a consequence of the substitution effect induced by the 2^{nd} methyl group on the β-carbon.

The five identified adsorption structures are adsorbed irreversibly in the sense that they do not desorb intact at higher temperatures, but according to TPD decompose above 250 K. This is evidenced by the desorption of CO (405 K) and H_2 (ca 276, 425 and 473 K), which is observed by HREELS. Three reaction intermediates, which seem to be reasonably stable on the surface at high temperatures, are identified by the combination of DFT and HREELS. Sequentially appearing during the proposed decomposition pathway are first the dehydro-η^3-prenal-H1 and η^2-isobutenyl radicals as well as the η^1-isobutylidyne fragment.

In agreement with the experiments on the selective hydrogenation of crotonaldehyde, the coadsorption experiments of prenal with D_2 or H_2 lead to a weak H-D exchange reaction instead of producing the desired hydrogenation products. Therefore it must be proposed that the hydrogenation process of prenal on Pt(111) is also unselective, since the same types of adsorption structures are identified here.

On the Pt-Sn model catalysts the behavior of prenal shows striking differences compared to pure platinum. The HREELS and DFT studies on the $Pt_3Sn(111)$ surface alloy lead to the identification of two related, energetically competitive η^1-top-(s)-trans-OSn geometries, which are adsorbed moderately strong (-39.1 and -30.8 kJ/mol). As these structures are bonded just by the aldehydic oxygen, most of their vibrational frequencies are unperturbed as compared to the gas phase values of free prenal and, hence, the HREELS *intensities* have to be adducted for their identification.

Very troublesome is the system prenal/$Pt_2Sn(111)$, which does not allow an unambiguous conclusion. The origin of the problems is seen immediately from the DFT calculations, which resulted in a number of only very weakly bonded adsorption structures. Importantly the η^1-top forms are no longer stable in the present DFT optimizations using the PAW scheme with dipole corrections along the surface normal. As the error bar of the DFT approach becomes significant for such small bonding energies, it is not very surprising that the interpretation of the low

temperature HREELS experiments (180 and 200 K) by the vibrational analysis with DFT fails in this case. A possible explanation for this phenomenon is available from the experimental side instead. Since the TPD experiments indicate a weaker adsorption on $Pt_2Sn(111)$ (monolayer desorption at ca 216 K, no decomposition) while the HREELS experiments show nearly unperturbed frequencies and loss intensities as compared to the multilayer spectra, a weakly bonded, i.e physisorbed prenal state may be proposed on this surface alloy. Although the DFT adsorption energies would support the trend of a weaker interaction, the DFT GGA functional PW91 fails to describe the nonbonded and dispersion interactions correctly, which are expected to become more important as the covalent adsorption bonds are weakened.

Concerning the selective hydrogenation of prenal, a strong increase in the yield of unsaturated alcohol might be expected from Pt(111) to $Pt_3Sn(111)$ due to the reordering of the surface complex to the vertical η^1-top forms. The role of the physisorbed species on $Pt_2Sn(111)$ is yet unclear. The expected change is in agreement to the experimental results of Marinelli et al. [6, 7], who found an improved selectivity on silica-supported Pt catalysts that are alloyed with Sn. In this case, an overall increase of the fraction of unsaturated alcohol (from 13 to 29% for crotonaldehyde, from 20 to 77% for prenal) was observed. Nonetheless it remains unresolved whether a different, catalytically active phase is formed on the supported catalyst under real conditions, which causes the measured improvement of the selectivity as compared to the unselective performance of the $Pt_2Sn(111)$ and $Pt_3Sn(111)$ model catalysts.
However, although the hydrogenation reaction could not be carried out successfully for crotonaldehyde or prenal in this work, the results of the adsorption on the model catalysts are still indispensable to gain an understanding of the basic interaction mechanisms of such multifunctional molecules with surfaces.

General conlcusions:

All three model catalysts exhibit characteristic electronic and geometrical properties, which are the key to the changes in the adsorption modes. In terms of adsorption energy, tin induces a destabilization of the molecule-surface interaction. The adsorption energies for corresponding complexes on the surface alloys, e.g. for the η^2-diσ(CC) structures, are very similar, but about 20-30% smaller than on Pt(111). Although qualitatively a much larger number of possible adsorption complexes can be conceived on the Pt-Sn surface alloys, the presence of Sn simplifies the number of competitive stable adsorption forms, thereby leading to less complex HREEL spectra than on Pt(111).
It was suggested that from $Pt_3Sn(111)$ to $Pt_2Sn(111)$ an increase in the electron transfer from Pt to Sn and a *d*-band lowering leads to a decrease of the adsorption strength, which is presently also found in both the calculations and the experiments of prenal and crotonaldehyde. Since structures of all coordination types (η^2, η^3 and η^4) are obtained on all model catalyst surfaces as local minima in the DFT optimizations, the weakening of the adsorption strength must be governed by electronic effects, while any site-blocking may be ruled out.
Importantly it is concluded that the picture of explaining weaker adsorption energies and bond strengths by increasing *d*-band shifts away from the Fermi level and larger charge transfers, as it is usually recalled in the literature, is not valid in such a simple manner for a multifunctional molecule interacting through a complex mechanism with the surface anymore.
Despite the destabilization of the interactions on the Pt-Sn surface alloys, the computed vibrational frequencies of the ν(C-C) and ν(C-O) stretching modes affected by surface bonds do not allow a simple correlation of the frequency shifts with the adsorption energies. The vibrational properties of the various structures on the three model catalysts have to be analyzed in detail in order to understand the changes in the adsorption energies and

geometries. Due to slight distortions of the adsorption geometries caused by changes of the substrate, different couplings of the normal modes are found, which complicates the analysis. Even for related types of coordination on the three model catalysts, this prevents a correlation of the interesting stretching frequencies usually sensitive to the adsorption strength.

Deeper insights in the variation of the adsorption energies, not only with increasing Sn fraction, but also for the different types of coordination and coverages, are obtained from the decomposition of the adsorption energies into its components, i.e. the deformation energy of the surface as well as the deformation energy of the molecule in the optimized complexes, and finally the interaction term deduced from both. Thus numerous factors causing a decrease of the bond strength are accessible through the detailed analysis of the corresponding energetic contributions. The energy decomposition is valid, if the electron transfer between the molecule and the surface in the adsorbate complex is small, which is assumed in the present cases.
From the comparison of the energy contributions of prenal and crotonaldehyde bonding on the model catalyst surfaces it is concluded that neither the deformation cost of the surface nor the interaction strength to the molecule exhibit a constant trend as a function of the tin fraction, but are specific for each surface. The surface deformation costs can be correlated with the displacements of the metal atoms from the equilibrium positions. On Pt_3Sn and Pt_2Sn an outward relaxation of a Sn atom requires small energy costs of similar size, while an outward relaxation of a Pt atom is more costly. In fact the energy cost for this outward shift of Pt decreases from Pt(111) over Pt_3Sn(111) to Pt_2Sn(111), which accounts for the larger displacements found in adsorption geometries on the Pt-Sn surface alloys as compared to Pt(111). In contrast to the absolute distortions, the deformation energies are lowest on Pt_3Sn (38 and 50 kJ/mol for the flat crotonaldehyde and prenal adsorption forms, resp.), but rise on Pt(111) (ca 54 and 58 kJ/mol, resp.) and Pt_2Sn (ca 62 and 61 kJ/mol, resp.). Interestingly, the reason for this increase on Pt_2Sn(111) is found in a combination of the large outward relaxations with sizable shifts for the metal atoms parallel to the surface plane, which do not occur on the other model catalysts.

Quite similar, the deformation costs of the molecule are very specific for the coordination type of the formed adsorption species. Here, for example, the deformation energies are smallest for the η^1 and η^2-π(CC) coordination types (below 10 and 50 kJ/mol, resp.) of both aldehydes on the three surfaces, which is in accordance with the smallest distortions of the molecules from their gas phase geometries. Hence it is not surprising that most of the vibrational normal modes in these geometries, except those of atoms interacting directly, appear very close to the unperturbed gas phase frequencies. Due to the low interaction strengths of these configurations on the model catalysts, even the frequencies of vibrations concerning atoms bonded to the substrate are redshifted only moderately.
In contrast, large deformation energies are found for the η^2-diσ(CC) and the numerous η^3 and η^4 types of coordination (typically between 110 for the η^4-π(CC) and 170 kJ/mol for the η^3 forms of prenal and between 105 and 160 kJ/mol for crotonaldehyde, although for both molecules much larger values are obtained in some cases, which is ascribed to changes in the electronic configurations). This allows to rationalize the large frequency shifts of the normal modes of these geometries, since basically the whole molecule is distorted strongly by the adsorption. In particular, in the fingerprint region above 600 cm^{-1}, significant changes occur that are characteristic of the different adsorption modes and their deformation energies.

The deformation costs of the molecules are slightly larger on Pt_3Sn(111), but of a similar size on Pt(111) and Pt_2Sn(111). While the increase from Pt(111) to Pt_3Sn (132 to 139 kJ/mol and 145 to 160 kJ/mol for crotonaldehyde and prenal, resp.) is concluded to originate from the repulsive interactions of the molecules with the neighboring metal atoms, particularly the protruding Sn

atoms, the in-plane displacements of the surface atoms on Pt_2Sn reduce the deformation energies to similar values as on Pt(111) (132 and 137 kJ/mol). Caused by the second methyl substituent, the deformation energies are commonly slightly larger for prenal.
This also gives the reason for the formation of η^1-top-OSn species on $Pt_3Sn(111)$. For crotonaldehyde, these structures present only a fraction of the surface species present at high coverages and low temperatures, but prenal exclusively forms such η^1-top-OSn structures. Especially for prenal the flat high-hapticity geometries (η^2 to η^4) show such high deformation costs (160 kJ/mol) that much larger interaction strengths would be required to turn them into competitive candidates.
Since the deformations of the molecule and the surface due to the usual buckling of Sn are basically negligible in the η^1 coordination type on this surface alloy, the weak interaction term (-43 and -36 kJ/mol, resp.) translates immediately into the computed adsorption energies (-39.1 and -30.8 kJ/mol). For crotonaldehyde on $Pt_3Sn(111)$ the interaction strength in the flat adsorption complexes remains strong enough to compensate the higher deformation energies of the molecule. Hence, at low coverages the η^2, η^3 and η^4 structures appear energetically more stable than the η^1-top-OSn forms. In the high coverage regime, the situation changes. Here η^1 forms are competitive to the η^2-diσ(CC) species, whereas the η^3 and η^4 structures are no longer present on the sample.
This behavior of the high-hapticity forms has been confirmed by the explicit theoretical coverage dependent treatment of crotonaldehyde on $Pt_2Sn(111)$. It can be understood from a significant decrease of the interaction terms, which affects only the flat η^3 and η^4 structures.
The detailed analysis leads furthermore to the finding that the complete destabilization of the η^1 coordination types of both aldehydes on the Pt_2Sn surface alloy must originate from the weakening of the interaction energies with the substrate, which in the light of usually negligible deformation energies is ascribed to the different electronic properties of this model catalyst.
On Pt(111), in contrast, an outward relaxation of the interacting metal atom induces sizable deformation costs for the η^1 structures of crotonaldehyde and prenal (ca 39 kJ/mol). Therefore the interaction terms (around -70 kJ/mol) are reduced by about half and consequently result in a similar adsorption energy as found on Pt_3Sn.

Derived from the adsorption energies and the deformation costs, the interaction terms are computed. The interaction strengths between the unsaturated aldehydes and the surfaces decrease strongly from Pt(111) to the Pt-Sn surface alloys, which is ascribed, as mentioned before, to the change of the electronic properties. For the stable high-hapticity configurations of crotonaldehyde and prenal, the weakening is on average as much as 15% (from -260 and -255 kJ/mol, resp., to -217 and -224 kJ/mol on Pt_3Sn and -229 and -208 kJ/mol on Pt_2Sn).
Interestingly, the interaction terms do not vary strongly and systematically between the two different surface alloys, which contrasts the trends of the deformation energies in the adsorption complexes.
Also in order to understand the vibrational properties, the interaction terms are much more useful than the absolute adsorption energies. The weakening of the interactions on the surface alloys as compared to Pt(111) causes primarily specific changes in the *low frequency region* below ca 400 cm^{-1}. Here the influence of the *substrate* can be revealed easily. The *fingerprint region* above 400 cm^{-1} is generally *only* typical for a certain *type of coordination* and *isomer*. Here only very small changes (below ca 20 cm^{-1}) in frequencies and slight deviations in intensities are found for a given configuration on all three surfaces. This major finding is very counterintuitive, as usually correlations between the shifts of important vibrations, like for example the ν(C1=O) and ν(C2=C3) modes, and the adsorption energy are expected [57].

Another topic in the focus of this thesis is the substitution effect distinguishing crotonaldehyde from prenal. It is first analyzed thoroughly on Pt(111) by the energy decomposition approach, indicating that the decrease of the adsorption energies of roughly 23 kJ/mol from crotonaldehyde

to prenal is primarily due to increased sterical demands of the latter and only to a lesser degree to a weaker molecule-surface interaction. The deformation energies of both the molecule and the surface in the five flat adsorption complexes increase by an average of 13 and 5 kJ/mol for prenal, respectively, whereas the interaction terms are about 20 kJ/mol less favorable (roughly 255 kJ/mol) compared to crotonaldehyde (ca 275 kJ/mol on average). In the vibrational spectra, the substitution effect is detected in a systematic blueshift of interacting double bond stretching frequencies ν(C1=O) and ν(C2=C3), especially for the configurations including a diσ(CC) bond. On $Pt_3Sn(111)$, the substitution effect manifests itself in an increase of the deformation costs of the surface (38 and 50 kJ/mol for crotonaldehyde and prenal, resp.) and the molecule (139 and 160 kJ/mol), too.
Therefore it must be concluded that the major effect of the additional methyl group of prenal, especially in the flat configurations, is a higher sterical repulsion with the surface. The larger deformation energies are consistent with the increased distortions in the adsorbate structures of prenal, which indicate significantly larger outward relaxations and distortions on the vinylic part compared to crotonaldehyde.

In summary, this study shows that a joint experimental and theoretical approach not only allows the identification of possible adsorption structures and reaction intermediates, but even provides a deeper understanding of the vibrational spectra of the adsorbed molecules. Finally it reveals the details of the interaction of the reactants with the surfaces, which opens a very promising route to study the properties of the various model catalysts. Often controversly discussed topics like the alloying effects or the changes correlated with different substitution patterns may be resolved by this strategy and render it extremely useful.
Continuing such detailed studies of numerous other, chemically interesting model systems with this approach may lead to the required knowledge for tailoring special catalysts according to the desired interaction properties, which govern the reactivity and selectivity in the catalytic processes.
Using better time-resolved spectroscopical methods such as for example the Reflection Absorption Infrared Spectroscopy (RAIRS) or Sum-frequency Generation (SFG) in conjunction with the DFT characterization, it may even be possible to analyze catalytic surface reactions in situ. Such reaction studies might then be compared to kinetical models, which can be constructed from the total energy results based on the identified and characterized adsorption structures and intermediates. Combining in situ studies with *ab initio* thermodynamics and kinetics, the full description of catalytical processes and catalysts comes into reach.

Bibliography

[1] M. Bartok, K. Felföldi, *Stereochemistry of Heterogeneous Metal Catalysis (Chapter VII)* (John Wiley, Chichester, 1985).

[2] K. Bauer, D. Garbe, eds., *Common Fragrance and Flavor Materials. Preparation, Properties and Uses.* (Wiley VCH, New York, 1985).

[3] F. Zaera, *Chem. Rev.* **95**, 2651 (1995).

[4] R. L. Augustine, *Catalysis for the Synthetic Chemists* (Marcel Dekker, New York, 1996).

[5] B. E. Bent, *Chem. Rev.* **96**, 1361 (1996).

[6] T. B. L. W. Marinelli, S. Nabuurs, V. Ponec, *J. Catal.* **151**, 431 (1995).

[7] T. B. L. W. Marinelli, V. Ponec, *J. Catal.* **156**, 51 (1995).

[8] D. Goupil, P. Fouilloux, R. Maurel, *React. Kinet. Catal. Lett.* **35**, 185 (1987).

[9] Z. Poltarzewski, S. Galvagno, R. Pietropaolo, P. Staiti, *J. Catal.* **102**, 190 (1986).

[10] C. Xu, J. W. Peck, B. E. Koel, *J. Am. Chem. Soc.* **115**, 751 (1993).

[11] D. G. Blackmond, A. Waghray, *Catalysis of Organic Reactions, Chemical Industries Series, in Chap.: The role of alkali promoters in the selective hydrogenation of 3-methyl 2-butenal.* (Dekker, New York, 1995).

[12] D. I. Jerdev, A. Olivas, B. E. Koel, *J. Cat.* **205**, 278 (2002).

[13] E. Janin, H. von Schenck, S. Ringler, J. Weissenrieder, T. Åkermark, M. Göthelid, *J. Cat.* **215**, 245 (2003).

[14] A. Borgna, B. G. Anderson, A. M. Saib, H. Bluhm, M. Hävecker, A. Knop-Gericke, A. E. T. Kuiper, Y. Tamminga, J. W. Niemantsverdriet, *J.Phys.Chem. B* **108**, 17905 (2004).

[15] N. Iwasa, M. Takizawa, M. Arai, *Appl. Catal. A: Gen.* **283**, 255 (2005).

[16] K. Judai, S. Abbet, A. S. Wörz, U. Heiz, C. R. Henry, *J. Am.Chem. Soc.* **126**, 2732 (2004).

[17] S. Abbet, A. Sanchez, U. Heiz, W.-D. Schneider, A. M. Ferrari, G.Pacchioni, N. Rösch, *J. Am. Chem. Soc.* **122 (14)**, 3455 (2000).

[18] K. von Bergmann, *Diplomarbeit, Universität Bonn* (2000).

[19] A. Wiltner, *Diplomarbeit, Universität Bonn* (2001).

[20] T. V. W. Jansses, S. Völkening, T. Zambelli, J. Wintterlin, *J. Phys. Chem. B* **102**, 6521 (1998).

[21] J. Breitbach, D. Franke, G. Hamm, C. Becker, K. Wandelt, *Surf. Sci.* **507-510**, 18 (2002).

[22] Q. Y. Yang, K. J. Maynard, A. D. Johnson, S. T. Ceyer, *J. Chem Phys.* **102**, 7734 (1995).

[23] J. Jenck, J. E. Germain, *J. Catal.* **65**, 133 (1980).

[24] V. Ponec, *Appl. Catal. A* **149**, 27 (1997).

[25] P. Beccat, J. C. Bertolini, Y. Gauthier, J. Massardier, P. Ruiz, *J. Catal.* **126**, 451 (1990).

[26] R. M. Makouangou, D. Y. Murzin, A. E. Dauscher, R. A. Touroude, *Ind. Eng. Chem. Res.* **33**, 1881 (1994).

[27] T. Birchem, C. M. Pradier, Y. Berthier, G. Cordier, *J. Catal.* **146**, 503 (1994).

[28] T. Birchem, C. M. Pradier, Y. Berthier, G. Cordier, *J. Catal.* **161**, 68 (1996).

[29] P. Claus, *Topics in Catalysis* **5 (No. 1-4)**, 51 (1998).

[30] F. Coloma, J. M. Coronado, C. H. Rochester, J. A. Anderson, *Catal. Lett.* **51**, 155 (1998).

[31] A. Dandekar, M. A. Vannice, *J. Catal.* **183 (2)**, 344 (1999).

[32] P. Reyes, M. del C Aguirre, I. Melián-Cabrera, M. L. Granados, J. L. G. Fierro, *Bol. Soc. Chil. QuM-mm.* **vol. 47 no.4**, 547 (2002).

[33] K. Liberková-Šebková, L. Červený, R. Touroude, *Res. on Chem. Interm.* **29(6)**, 609 (2003).

[34] M. Galeotti, A. Atrei, U. Bardi, G. Rovida, M. Torrini, *Surf. Sci.* **313**, 349 (1994).

[35] M. T. Paffett, R. G. Windham, *Surf. Sci.* **208**, 34 (1989).

[36] M. T. Paffett, S. C. Gebhard, R. G. Windham, B. E. Koel, *Surf. Sci.* **223**, 449 (1989).

[37] M. T. Paffett, S. C. Gebhard, R. G. Windham, B. E. Koel, *J. Phys. Chem.* **94**, 6831 (1990).

[38] S. H. Overbury, D. R. Mullins, M. T. Paffett, B. E. Koel, *Surf. Sci.* **254**, 45 (1991).

[39] M. Batzill, D. E. Beck, B. E. Koel, *Surf. Sci.* **466**, L821 (2000).

[40] H. Zhao, B. E. Koel, *Surf. Sci.* **573**, 413 (2004).

[41] H. Zhao, B. E. Koel, *J. Cat.* **234**, 24 (2005).

[42] Y. Jugnet, R. Sedrate, J. C. Bertolini, *J. Cat.* **229**, 252 (2005).

[43] S. H. Overbury, Y.-S. Ku, *Phys. Rev. B* **46**, 7868 (1992).

[44] A. Krupski, A. Bailly, M. C. Saint-Lager, R. Baudoing-Savois, P. Dolle, C. Becker, K. Wandelt, *in preparation* (2006).

[45] F. Delbecq, P. Sautet, *J. Catal.* **220**, 115 (2003).

[46] A. Ruban, B. Hammer, P. Stolke, H. L. Schriver, J. K. Nørskov, *J. Mol. Cat. A* **115**, 421 (1997).

[47] J. Oudar, *Z. Phys. Chem.* **197**, 125 (1996).

[48] J. C. de Jesús, F. Zaera, *Suf. Sci.* **430**, 99 (1999).

[49] E. Janin, S. Ringler, J. Weissenrieder, T. Åkermark, U. O. Karlsson, M. Göthelid, D. Nordlund, H. Ogasawara, *Surf. Sci.* **482-485**, 83 (2001).

[50] F. Delbecq, P. Sautet, *J. Catal.* **152**, 217 (1995).

[51] F. Delbecq, P. Sautet, *J. Catal.* **211**, 398 (2002).

[52] R. Hirschl, F. Delbecq, P. Sautet, J. Hafner, *J. Catal.* **217**, 354 (2003).

[53] D. Loffreda, Y. Jugnet, F. Delbecq, J. C. Bertolini, P. Sautet, *J. Phys. Chem. B* **108**, 9085 (2004).

[54] D. Loffreda, *Surf. Sci.* **600**, 2103 (2006).

[55] D. Loffreda, F. Delbecq, F. Vigné, P. Sautet, *J. Am. Chem. Soc.* **128**, 1316 (2006).

[56] P. A. Redhead, *Vaccum* **12**, 203 (1962).

[57] H. Ibach, D. L. Mills, *Electron Energy Loss Spectroscopy and Surface Vibrations* (Academic Press, New York, 1982).

[58] M. Henzler, W. Göpel, *Oberflächenphysik des Festkörpers* (Teubner Taschenbücher, Stuttgart, 1992).

[59] D. L. Mills, *Surf. Sci.* **48**, 59 (1975).

[60] B. N. J. Persson, *Surf. Sci.* **92**, 265 (1980).

[61] E. Fermi, *Z. Physik* **71**, 250 (1931).

[62] D. A. King, *Surf. Sci.* **47**, 384 (1975).

[63] J. L. Falconer, R. J. Madix, *J. Catal.* **48**, 262 (1977).

[64] J. L. Falconer, J. A. Schwarz, *Catal. Rev.-Sci. Eng.* **25**, 141 (1983).

[65] E. Habenschaden, J. Küppers, *Surf. Sci.* **138**, L147 (1984).

[66] A. M. de Jong, J. W. Niemantsverdriet, *Surf. Sci.* **233**, 355 (1990).

[67] C. Becker, *Dissertation, Universität Bonn* (1993).

[68] G. Ertl, J. Küppers, *Low Energy Electrons and Surface Chemistry* (VCH Verlagsgesellschaft mbH, Weinheim, 1985).

[69] R. L. Park, H. H. Madden, *Surf. Sci.* **11**, 188 (1968).

[70] E. A. Wood, *J. Appl. Phys.* **35**, 1306 (1964).

[71] J. Breitbach, *Dissertation, Universität Bonn* (2002).

[72] G. Kresse, J. Hafner, *Phys. Rev. B* **47**, 558 (1993).

[73] G. Kresse, J. Hafner, *Phys. Rev. B* **48**, 13115 (1993).

[74] G. Kresse, J. Furthmueller, *Phys. Rev. B* **54**, 11169 (1996).

[75] M. Born, J. R. Oppenheimer, *Ann. Der Physik* **84**, 457 (1927).

[76] P. Hohenberg, W. Kohn, *Phys. Rev.* **136**, 864 (1964).

[77] W. Kohn, L. J. Sham, *Phys. Rev. A* **140**, 1133 (1965).

[78] R. Hirschl, *Dissertation, Universität Wien* (2002).

[79] K. Burke, J. P. Perdew, M. Levy, *Modern Density Functional Theory: A Tool for Chemistry* (Elsevier, Amsterdam, 1995).

[80] A. D. Becke, *Phys. Rev. A* **38**, 3098 (1988).

[81] S. H. Vosko, L. Wilk, M. Nusair, *Can. J. Phys.* **58**, 1200 (1980).

[82] J. P. Perdew, Y. Wang, *Phys. Rev. B* **45**, 13244 (1992).

[83] J. P. Perdew, *Phys. Rev. B* **33**, 8822 (1986).

[84] C. Lee, W. Yang, R. G. Parr, *Phys. Rev. B* **37**, 785 (1988).

[85] J. P. Perdew, M. Ernzerhof, K. Burke, *J. Chem. Phys.* **105**, 9982 (1996).

[86] K. Doll, *Surf. Sci.* **573**, 464 (2004).

[87] A. Seidl, A. Görling, P. Vogl, J. A. Majewski, M. Levy, *Phys. Rev. B* **53(7)**, 3764 (1996).

[88] J. Harris, R. O. Jones, *J. Phys. F.* **4**, 1170 (1974).

[89] A. D. Becke, *J. Phys. Chem.* **98**, 5648 (1993).

[90] P. J. Stevens, F. J. Devlin, C. F. Chablowski, M. J. Frisch, *J. Phys. Chem.* **80**, 11623 (1994).

[91] S. Chawla, G. A. Voth, *J. Chem. Phys.* **108(12)**, 4697 (1998).

[92] S. Tsuzukia, H. P. Lüthi, *J. Chem. Phys.* **114**, 3949 (2001).

[93] H. Rydberg, B. Lundqvist, D. Langreth, M. Dion, *Phys. Rev. B* **62**, 6997 (2000).

[94] H. Rydberg, M. Dion, N. Jacobson, E. Schröder, P. Hyldgaard, S. I. Simak, D. C. Langreth, B. I. Lundqvist, *Phy. Rev Lett.* **91**, 126402(1) (2003).

[95] M. Dion, H. Rydberg, E. Schröder, D. C. Langreth, B. I. Lundqvist, *Phys. Rev. Lett.* **92**, 246401(1) (2004).

[96] X. Xu, W. A. G. III, *PNAS* **101**, 2673 (2004).

[97] D. C. Langreth, M. Dion, H. Rydberg, E. Schröder, P. Hyldgaard, B. I. Lundqvist, *Int. J. of Quant. Chem.* **101**, 599 (2005).

[98] Y. Andersson, D. C. Langreth, B. Lundqvist, *Phys Rev. Lett.* **76**, 102 (1996).

[99] E. Hult, H. Rydberg, B. I. Lundqvist, D. C. Langreth, *Phys. Rev. B* **59(7)**, 4708 (1999).

[100] W. Kohn, Y. Meir, D. E. Makarov, *Phys Rev. Lett.* **80(19)**, 4153 (1998).

[101] J. P. Perdew, A. Zunger, *Phys. Rev. B* **23**, 5048 (1981).

[102] R. O. Jones, O. Gunnarsson, *Rev. Mod. Phys.* **61(3)**, 689 (1989).

[103] D. J. Chadi, M. L. Cohen, *Phys. Rev. B* **8**, 5747 (1993).

[104] H. J. Monkhorst, J. D. Pack, *Phys. Rev. B* **13**, 5188 (1976).

[105] N. D. Mermin, *Phys. Rev.* **137**, A 1441 (1965).

[106] M. Methfessel, A. T. Paxton, *Phys. Rev. B* **40**, 3616 (1989).

[107] P. E. Blöchl, O. Jepsen, O. K. Andersen, *Phys. Rev. B* **49**, 16223 (1994).

[108] J. C. Philips, L. Kleinman, *Phys. Rev. B* **116**, 287 (1959).

[109] G. Kresse, *Dissertation, Technische Universität Wien* (1997).

[110] Y.-M. Juan, E. Kaxiras, R. G. Gordon, *Phys. Rev. B* **51**, 9521 (1995).

[111] M. Fuchs, M. Bockstedte, E. Pehlke, M. Scheffler, *Phys. Rev. B* **57**, 2134 (1998).

[112] D. R. Hamann, M. Schluter, C. Chiang, *Phys. Rev. Lett.* **43**, 1494 (1979).

[113] G. P. Kerker, *J. Phys.* **C 13**, L189 (1980).

[114] D. Vanderbilt, *Phys. Rev. B* **32**, 8412 (1985).

[115] W. C. Topp, J. J. Hopfield, *Phys. Rev. B* **7(4)**, 1295 (1973).

[116] A. M. Rappe, K. M. Rabe, E. Kaxiras, J. D. Joannopoulos, *Phys. Rev. B* **41**, 1227 (1990).

[117] N. Troullier, J. L. Martins, *Phys. Rev. B* **43**, 1993 (1991).

[118] D. Vanderbilt, *Phys. Rev. B* **41(11)**, 7892 (1990).

[119] P. E. Blöchl, *Phys. Rev. B* **41**, 5414 (1990).

[120] P. E. Blöchl, *Phys. Rev. B* **50(24)**, 17953 (1994).

[121] G. Kresse, D. Joubert, *Phys. Rev. B* **59(3)**, 1758 (1999).

[122] D. Loffreda, *These, Universtité Lyon* (2001).

[123] E. B. Wilson, *J. Chem. Phys.* **7**, 104752 (1939).

[124] MOLPRO 2000 is an ab-initio program package written by H.-J. Werner und P. J. Knowles, with contributions from R. D. Amos, A. Bernhardsson, A. Benning, P. Celanie, D. L. Cooper, M. J. O. Deegan, A. J. Dobbyn, F. Eckert, C. Hampel, G. Hetzer, T. Korona, R. Lindh, A. W. Lloyd, S. J. McNicholas, F. R. Manby, W. Meyer, M. E. Mura, A. Nicklass, P. Palmieri, R. Pitzer, R. Rauhut, M. Schutz, H. Stoll, A. J. Stone, R. Tarroni and T. Thosteinsson .

[125] M. J. Frisch, G. W. Trucks, H. B. Schlegel, G. E. Scuseria, M. A. Robb, J. R. Cheeseman, Montgomery, Jr., J. A., T. Vreven, K. N. Kudin, J. C. Burant, J. M. Millam, S. S. Iyengar, J. Tomasi, V. Barone, B. Mennucci, M. Cossi, G. Scalmani, N. Rega, G. A. Petersson, H. Nakatsuji, M. Hada, M. Ehara, K. Toyota, R. Fukuda, J. Hasegawa, M. Ishida, T. Nakajima, Y. Honda, O. Kitao, H. Nakai, M. Klene, X. Li, J. E. Knox, H. P. Hratchian, J. B. Cross, V. Bakken, C. Adamo, J. Jaramillo, R. Gomperts, R. E. Stratmannk, O. Yazyev, A. J. Austin, R. Cammi, C. Pomelli, J. W. Ochterski, P. Y. Ayala, K. Morokuma, G. A. Voth, P. Salvador, J. J. Dannenberg, V. G. Zakrzewski, S. Dapprich, A. D. Daniels, M. C. Strain, O. Farkas, D. K. Malick, A. D. Rabuck, K. Raghavachari, J. B. Foresman, J. V. Ortiz, Q. Cui, A. G. Baboul, S. Clifford, J. Cioslowski, B. B. Stefanov, G. Liu, A. Liashenko, P. Piskorz, I. Komaromi, R. L. Martin, D. J. Fox, T. Keith, M. A. Al-Laham, C. Y. Peng, A. Nanayakkara, M. Challacombe, P. M. W. Gill, B. Johnson, W. Chen, M. W. Wong, C. Gonzalez and J. A. Pople, *Gaussian Inc., Wallingford, CT* (2004).

[126] R. Ahlrichs, M. Bär, M. Häser, H. Horn, C. Kölmel, *Chem.Phys. Lett.* **162**, 165 (1989).

[127] P. Pulay, *Chem. Phys. Lett.* **73**, 393 (1980).

[128] D. Loffreda, *private communications* .

[129] J. Huheey, E. Keiter, R. Keiter, *Inorganic Chemistry: Principles of Structure and Reactivity* (HarperCollins, New York, 1993), fourth edn.

[130] A. Atrei, U. Bardi, J. X. Wu, E. Zanazzi, G. Rovida, *Surf. Sci.* **290**, 286 (1993).

[131] T. B. Massalsi, *Binary Alloy Phase Diagramms* (ASM International, Materials Park, OH, 1990), second edn.

[132] Y.-L. Tsai, C. Xu, B. Koel, *Surf. Sci.* **385**, 37 (1997).

[133] J. A. Rodriguez, S. Chaturvedi, T. Jirsak, J. Hrbek, *J. Chem. Phys.* **109**, 4052 (1998).

[134] Y. Teraoka, *Surf. Sci.* **235**, 249 (1990).

[135] P. J. Linstrom, W. G. Mallard, eds., *NIST Chemistry WebBook (http://webbook.nist.gov)*, vol. NIST Standard Reference Database Number 69 (National Institute of Standards and Technology, Gaithersburg MD, 20899, June 2005).

[136] W. V. Steele, R. D. Chirico, A. B. Cowell, S. E. Knipmeyer, A. Nguyen, *J. Chem. Eng. Data* **47**, 667 (2002).

[137] *Hazardous Substances Data Bank data are provided by the National Library of Medicine (US)* .

[138] K. Eichkorn, O. Treutler, H. Öhm, M. Häser, R. Ahlrichs, *Chem. Phys. Lett.* **240**, 283 (1995).

[139] R. Poirier, R. Kari, I. Csizmadia, eds., *Handbook of Gaussian Basis Sets* (Elsevier, Amsterdam, 1985).

[140] S. Thakur, V. P. Gupta, *Ind. J. of Pure and App. Phys.* **36**, 177 (1998).

[141] J. R. Durig, S. C. Brown, V. F. Kalasinsky, *Spectrochimica Acta A* **32**, 807 (1976).

[142] M. S. D. Groot, J. Lamb, *Proc. Roy. Soc. (A)* **242**, 36 (1957).

[143] R. J. Loncharich, T. R. Schwartz, K. N. Houk, *J. Am. Chem. Soc.* **109**, 14 (1987).

[144] C. E. Blom, R. P. Müller, H. H. Günthard, *Chem. Phys. Lett.* **73**, 483 (1980).

[145] A. Grassi, P. Longo, A. Musco, W. Porzio, A. Srivanti, *J. Organomet. Chem.* **289**, 439 (1985).

[146] P. Ganis, I. Orabona, F. Ruffo, A. Vitagliano, *Organometallics* **17**, 2646 (1998).

[147] C. Becker, T. Pelster, M. Tanemura, J. Breitbach, K. Wandelt, *Surf. Sci.;* **433**, 822 (1999).

[148] H. Ibach, S. Lehwald, *J. Vac. Sci. Technol.* **15 2**, 407 (1978).

[149] A. M. Baró, H. Ibach, H. D. Bruchmann, *J. Chem. Phys.* **74 7**, 4194 (1981).

[150] N. R. Avery, N. Sheppard, *Proc. R. Soc. Lond. A* **405**, 1 (1986).

[151] N. R. Avery, N. Sheppard, *Proc. R. Soc. Lond. A* **405**, 27 (1986).

[152] T. Miura, H. Kobayashi, K. Domen, *J. Phys. Chem. B* **104**, 6809 (2000).

[153] H. J. Oelichmann, D. Bougeard, B. Schrader, *J. Mol. Struct.* **77**, 149 (1981).

[154] H. Steininger, S. Lehwald, H. Ibach, *Surf. Sci.* **123**, 264 (1982).

[155] R. M. Watwe, R. D. Cortright, J. K. Nørskov, J. A. Dumesic, *J. Phys. Chem. B* **104**, 2299 (2000).

[156] M. Neurock, R. A. van Santen, *J. Phys. Chem. B* **104**, 11127 (2000).

[157] M. Salmeron, G. A. Somorjai, *J. Phys. Chem.* **86**, 341 (1982).

[158] F. Zaera, *Langmuir* **12(1)**, 88 (1996).

[159] T. Pelster, *Dissertation, Universität Bonn* (2000).

[160] V. Pallassana, M. Neurock, V. S. Lusvardi, J. J. Lerou, D. D. Kragten, R. M. van Santen, *J. Phys. Chem. B* **106**, 1656 (2002).

[161] P. S. Cremer, X. Su, Y. R. Chen, G. A. Somorjai, *J. Phys. Chem.* **100**, 16302 (1996).

[162] F. Zaera, D. Chrysostomou, *Surf. Sci.* **457**, 71 (2000).

[163] F. Zaera, D. Chrysostomou, *Surf. Sci.* **457**, 89 (2000).

[164] A. Valcárel, J. M. Ricart, A. Clotet, A. Markovits, C. Minot, F. Illas, *Surf. Sci.* **519**, 250 (2002).

[165] R. J. Koestner, J. C. Frost, P. C. Stair, M. A. V. Hove, G. A. Somorjai, *Surf. Sci.* **116**, 85 (1982).

[166] A. Valcárel, J. M. Ricart, A. Clotet, A. Markovits, C. Minot, F. Illas, *Jour. Chem. Phys.* **116**, 1165 (2002).

[167] Y.-L. Tsai, B. E. Koel, *J. Phys. Chem. B* **101**, 2895 (1997).

[168] A. Valcárel, A. Clotet, J. M. Ricart, F. Delbeq, P. Sautet, *Surf. Sci.* **549**, 121 (2004).

[169] A. Valcárel, A. Clotet, J. M. Ricart, F. Delbeq, P. Sautet, *J. Phys. Chem. B* **109**, 14175 (2005).

[170] B. Sexton, K. Rendulic, A. Hughes, *Surf. Sci.* **121**, 181 (1982).

[171] K. M. Ogle, J. R. Creighton, S. Akhter, J. M. White, *Surf. Sci.* **169**, 246 (1986).

[172] G. Hamm, *Dissertation, Universität Bonn* (2002).

[173] P. Samson, A. Nesbitt, B.E.Koel, A. Hodgson, *J. Chem. Phys.* **109**, 3255 (1998).

[174] C. Morin, D. Simon, P. Sautet, *J. Phys. Chem. B* **107**, 2995 (2003).

[175] K. Hermann, P. S. Bagus, *Appl. Phys. A* **44**, 63 (1978).

[176] *International Chemical Safety Cards data are provided by the National Institute for Occupational Safety and Health* .

List of Figures

List of Tables

Appendix A

Inhaltsangabe

Untersuchungen von Systemen mit komplexen Wechselwirkungen wie z.B. der Adsorption der α,β-ungesättigten Aldehyde Crotonaldehyd und Prenal auf Modellkatalysatoren stellen noch immer eine große Herausforderung dar. Das Wissen über die Molekül-Oberflächen-Wechselwirkungen solcher Systeme ist jedoch eine Grundvoraussetzung um die Aktivitäten und Selektivitäten der verschiedenen zur Hydrierung dieser Aldehyde verwendeten Katalysatoren zu verstehen. Zusätzlich nimmt die Komplexität, die man schon bei Betrachtung von monometallischen Oberflächen antrifft, noch zu, sobald man Legierungseffekte wie z.B. auf bimetallischen Modellkatalysatoren in die Untersuchungen einbezieht. Diese können zur Modifikation der Molekül-Substrat Wechselwirkungen führen und vermögen die Eigenschaften von Katalysatoren dramatisch zu beeinflussen.

Daher ist es die Zielsetzung dieser Arbeit, die Adsorption und die selektive Hydrierung von Crotonaldehyd und Prenal auf einer Pt(111) Einkristalloberfläche und auf zwei ultradünnen Sn-Pt(111) Oberflächenlegierungen zu studieren. Mittels zweier komplementärer, leistungsstarker Methoden, der Hochauflösenden Elektronen Energie Verlustspektroskopie (HREELS) und der Dichtefunktionaltheorie (DFT), ist es möglich, neue Einsichten in Molekül-Oberflächenwechselwirkungen, Modifikationen durch Legierungsbildung und in ablaufende Oberflächenprozesse zu gewinnen.

Zunächst gibt Kap. 2 einen Überblick über die Bedeutung von Oberflächenforschung im Bereich der heterogenen Katalyse. Mit dem Schwerpunkt der Adsorption und Wechselwirkung der Moleküle Crotonaldehyd und Prenal auf verschiedenen Modellkatalysatoroberflächen wird in Kap. 2.2 ein Rückblick auf die bisherigen Forschungsergebnisse von Hochdruck- und Ultrahochvakuum-Studien präsentiert. Nach einer allgemeinen Einführung in die experimentellen Methoden (Kap. 3) und die Grundlagen der Dichtefunktionaltheorie (Kap. 4), beschreibt Kap. 5 die Präparation und Charakterisierung der Pt(111), Pt_2Sn(111) und Pt_3Sn(111) Modellkatalysatoroberflächen.

Die hier durchgeführten TPD Messungen (Thermisch Programmierte Desorptionsspektroskopie) bezüglich Crotonaldehyd auf Pt(111) zeigen mehrere Desorptionszustände bei niedrigen Temperaturen. Zwischen 200 K und 300 K werden komplexe HREELS Spektren detektiert, die einer Kombination von verschiedenen Adsorptionsmoden auf der Oberfläche entsprechen.
Da Crotonaldehyd schon in der Gasphase in vier stabilen Rota-Isomeren vorkommt, ergeben die DFT Berechnungen eine große Anzahl von 19 stabilen Adsorptionsgeometrien auf der reinen Platinoberfläche. Der Vergleich der gemessenen und berechneten HREEL Spektren zeigt, dass eine Vielfalt von η^4, η^3 und η^2 Adsorptionsmoden zur Interpretation herangezogen werden

muss. Oberhalb von 300 K wird mittels HREELS und TPD der Zerfall der stark gebundenen Crotonaldehyd Spezies beobachtet, der zu vielen, schlecht definierten Verlustsignalen in den HREEL Spektren führt.
Auf den Sn-Pt(111) Oberflächenlegierungen muss eine viel größere Anzahl möglicher Adsorptionsgeometrien in die DFT Berechnungen miteinbezogen werden. Aufgrund der noch immer relativ hohen Bindungsenergien, welche durch die DFT Rechnungen erhalten werden, kann davon ausgegangen werden, das Crotonaldehyd auch auf den Oberflächenlegierungen chemisorbiert. Auf $Pt_2Sn(111)$ werden bei niedrigen Temperaturen hauptsächlich η^2 Adsorptionsmoden gefunden. Durch die Desorption von intaktem Crotonaldehyd kommt es bei höheren Temperaturen jedoch zu einem Phasenübergang, der zur Population von η^3 und η^4 Bindungskonfigurationen führt.
Auf $Pt_3Sn(111)$ wird Crotonaldehyd in einer Kombination verschiedener, flach-gebundener Adsorptionsgeometrien gefunden. Obwohl es hier nicht besonders stark chemisorbiert ist, zerfällt Crotonaldehyd oberhalb von 250 K, bevor es intakt desorbieren könnte.

Die Messungen von Prenal adsorbiert auf Pt(111) zeigen ebenfalls verschiedene Adsorptionszustände. Während unterhalb von 200 K die Desorption von intaktem Prenal mittels TPD beobachtet wird, befinden sich auch stark-gebundene Prenal Spezies auf der Oberfläche, die bei höheren Temperaturen zerfallen. Die HREEL Spektren bei niedrigen Temperaturen werden als Kombination aus den flachen η^4 und η^3 Adsorptionsmoden mit niedriger-koordinierten η^2 Spezies interpretiert. Die Vielfalt dieser Adsorptionsmoden auf Pt(111) bestätigen, dass die Hydrierung auf der Pt(111) Oberfläche unselektiv verläuft. Verschiedene Fragmente aus dem Zerfall von Prenal werden identifiziert und erlauben die Aufstellung von Zerfallsreaktionspfaden.

Auf der $Pt_3Sn/Pt(111)$ Oberflächenlegierung erlauben Experiment und Theorie den Schluss, dass Prenal hier in zwei vertikalen η^1 Adsorptionsmoden auf der Oberfläche vorliegt. Beide sind mittels einer O-Sn Bindung durch den Sauerstoff der Aldehydfunktion an das Sn des Modellkatalysators gebunden und sollten daher besonders selektiv die Hydrierung der C=O Bindung zeigen.
Im Gegensatz dazu ist die Interpretation der Ergebnisse von Prenal auf der $Pt_2Sn/Pt(111)$ Legierung problematischer. Erst die Kombination aus Experiment und theoretischen Rechnungen führt zu dem Ergebnis, dass Prenal auf $Pt_2Sn/Pt(111)$ nur physisorbiert vorliegt.

Generell erlauben die DFT Untersuchungen in Kombination mit der Identifikation von Adsorptionsstrukturen und deren Schwingungsmoden eine detaillierte Analyse der Wechselwirkungsmechanismen mit der Oberfläche. Es zeigt sich, dass die berechneten Adsorptionsenergien in ihre Komponenten zerlegt werden müssen, um mit den Schwingungseigenschaften der Komplexe korreliert werden zu können. Auch lassen sich durch die detaillierte Analyse der Adsorptionsenergien die tatsächlichen Wechselwirkungsstärken zur Oberfläche abschätzen, die ansonsten von den Deformationsenergien der Moleküle und der Oberfläche der entsprechenden Adsorptionskomplexe überlagert werden. So zeigt sich insbesondere, dass trotz geringerer Wechselwirkung auf den Legierungen zugleich höhere Adsorptionsenergien und verkleinerte Frequenzverschiebungen möglich sind, wenn die nötigen Deformationsenergien gering ausfallen. Des Weiteren sind die Deformationsenergien der Moleküle charakteristisch für ihren jeweiligen Koordinationstyp, während die Deformationsenergien der Oberfläche letzteren spezifisch zuzuordnen sind. Diese zeigen von Pt(111) zu $Pt_3Sn(111)$ und $Pt_2Sn(111)$ keinen stetigen Trend, da auf letzterer zusätzlich zu den immer vorhandenen Relaxationen senkrecht zur Oberfläche auch starke Verschiebungen der Metallatome in der Ebene hinzukommen.

Abschließend werden in Kap. 8 die Schlussfolgerungen, die sich aus der Kombination der experimentellen Messungen mit den theoretischen Berechnungen ergeben, zusammengefasst.

Appendix B

Additional Resources: Crotonaldehyde

B.1 RI-DFT Geometries of Crotonaldehyde

Parameter	E-(s)-trans	E-(s)-cis	Z-(s)-trans	Z-(s)-cis
r(O-C1)	1.22	1.22	1.23	1.23
r(C1-C2)	1.47	1.48	1.47	1.48
r(C2-C3)	1.35	1.35	1.35	1.35
r(C3-C4)	1.50	1.49	1.50	1.49
r(C1-H1)	1.12	1.12	1.12	1.12
r(C2-H2)	1.09	1.10	1.09	1.09
r(C3-H3)	1.10	1.10	1.10	1.10
r(C4-H4)	1.10	1.10	1.10	1.09
r(C4-H5,6)	1.11	1.10	1.10	1.10
r(H-bond)				2.30
α(O-C1-C2)	124.8	125.3	123.4	127.0
α(C1-C2-C3)	120.9	122.3	125.6	127.2
α(C2-C3-C4)	125.6	125.7	128.6	128.0
α(O-C1-H1)	120.8	120.0	119.9	119.4
α(C1-C2-H2)	116.8	116.8	114.7	114.4
α(C2-C3-H3)	117.2	116.9	116.9	116.5
α(H4-C4-C3)	112.0	112.5	114.0	112.4
α(H5,6-C4-C3)	111.0	110.7	110.0	109.8
δ(O-C1-C2-C3)	180.0	0.0	180.0	0.0
δ(C1-C2-C3-C4)	180.0	180.0	0.0	0.0
δ(H1-C1-C2-C3)	0.0	180.0	0.0	180.0
δ(O-C1-C2-H2)	0.0	180.0	0.0	180.0
δ(C1-C2-C3-H3)	0.0	0.0	180.0	180.0
δ(H4-C4-C3-C2)	180.0	0.0	0.0	0.0
δ(H5-C4-C3-C2)	120.7	121.5	121.8	122.1
δ(H6-C4-C3-C2)	-120.7	-121.5	-121.8	-122.1

Table B.1: Geometries of the crotonaldehyde rota-isomers in the gas phase calculated at the RI-DFT BP86/TZVP level using Turbomole [126]. All distances r are given in Å.

B.2 Convolution of DFT HREEL Spectra of Crotonaldehyde/Pt(111)

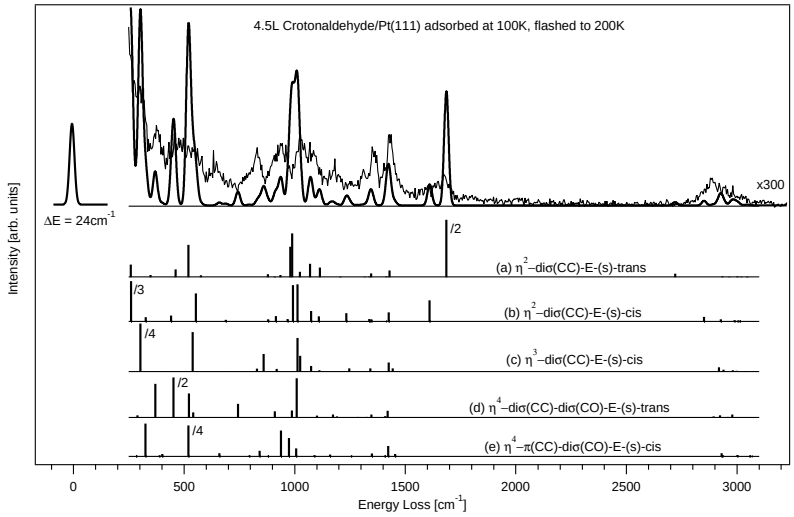

Figure B.1: Convolution (gaussians, 24 cm^{-1} FWHM) of the computed DFT HREEL spectra (a-e) for the most stable adsorption structures and the HREEL spectrum of 4.5L crotonaldehyde adsorbed at 100K on clean Pt(111) subsequently flashed to 200K.

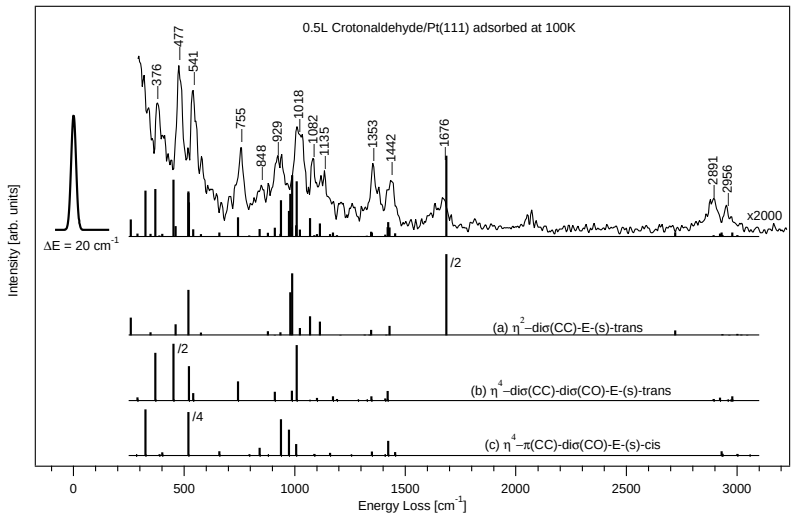

Figure B.2: Computed DFT EEL spectra for the most stable adsorption structures and the HREEL spectrum of 4.5L crotonaldehyde adsorbed at 100K on clean Pt(111) subsequently flashed to 200K.

B.3 Convolution of DFT HREEL spectra of Crotonaldehyde/$Pt_3Sn(111)$

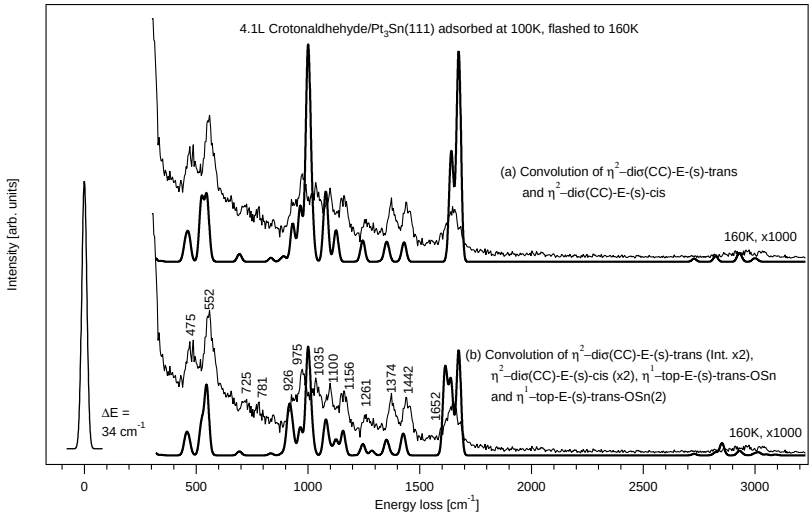

Figure B.3: Confrontation of the experimental HREEL spectrum (specular geometry at a 60° AOI (angle of incidence), primary energy 4.7 eV) of 4.1L crotonaldehyde/$Pt_3Sn(111)$ recorded after a flash to 160 K with the *Gaussian* convolutions of computed vibrational spectra. Note that the intensities of both η^2-diσ(CC) adsorption structures have been doubled in convolution (b) in order to exemplify the small surface coverage fractions of both η^1-top-OSn complexes required for a satisfactory agreement.

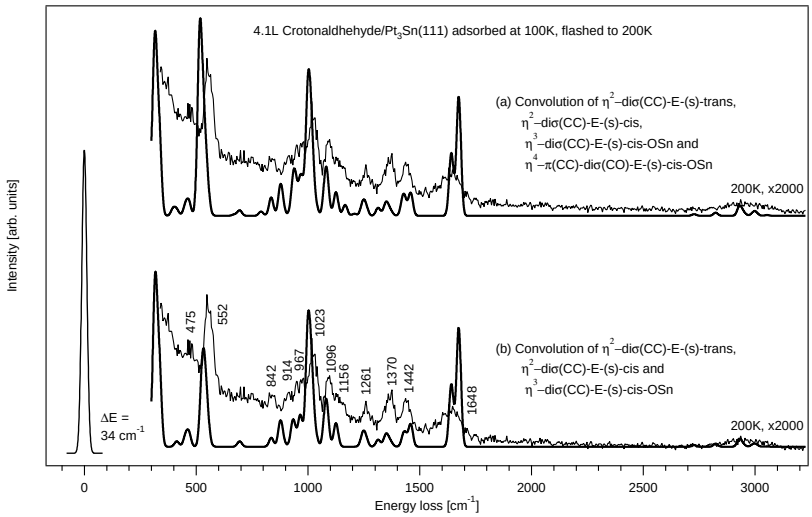

Figure B.4: Comparison of the experimental HREEL spectrum (specular geometry at a 60° AOI, primary energy 4.7 eV) of 4.1L crotonaldehyde/$Pt_3Sn(111)$ recorded after annealing to 200 K with the *Gaussian* convolutions of computed vibrational spectra of η^2, η^3 and η^4 adsorption modes.

B.4 Convolution of DFT HREEL spectra of Crotonaldehyde/$Pt_2Sn(111)$

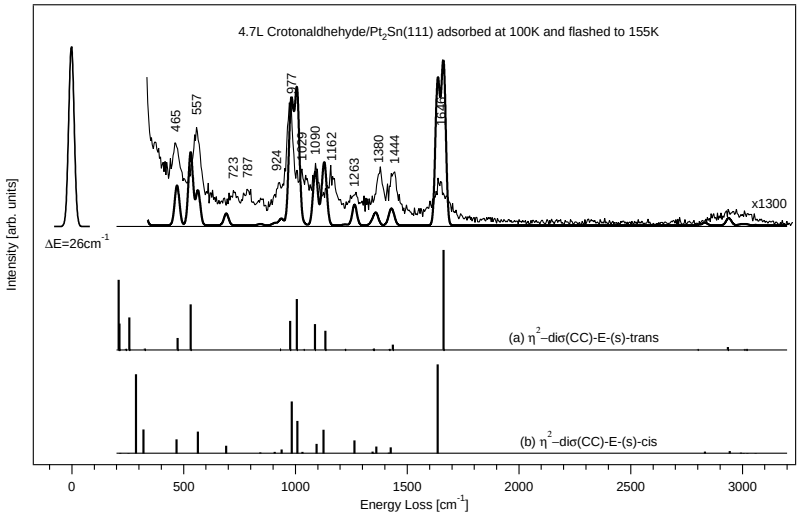

Figure B.5: Comparison of the experimental HREEL spectrum (specular geometry at a 60° AOI, primary energy 4.7 eV) of 4.7L crotonaldehyde/$Pt_2Sn(111)$ recorded after annealing to 155 K with the *Gaussian* convolutions of computed vibrational spectra of the η^2-diσ(CC) adsorption modes.

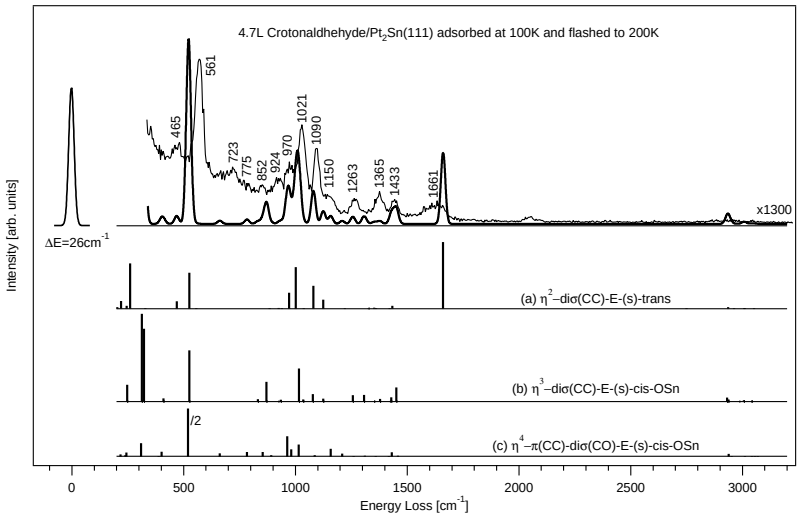

Figure B.6: Comparison of the experimental HREEL spectrum (specular geometry at a 60° AOI, primary energy 4.7 eV) of 4.7L crotonaldehyde/$Pt_2Sn(111)$ recorded after annealing to 200 K with the *Gaussian* convolutions of computed vibrational spectra of η^2, η^3 and η^4 adsorption modes.

Appendix C

Additional Resources: Prenal

C.1 RI-DFT Gas Phase Geometries of Prenal

Parameter	RI-BP86/TZVP (s)-trans	CCSD(T)/cc-pVDZ	RI-BP86/TZVP (s)-cis	CCSD(T)/cc-pVDZ
r(O-C1)	1.23	1.22	1.23	1.23
r(C1-C2)	1.46	1.48	1.47	1.49
r(C2-C3)	1.36	1.36	1.36	1.37
r(C3-C4)	1.50	1.52	1.50	1.51
r(C3-C5)	1.51	1.52	1.50	1.52
r(C1-H1)	1.12	1.12	1.12	1.12
r(C2-H2)	1.09	1.10	1.10	1.10
r(C4-H3)	1.10	1.10	1.09	1.10
r(C4-H4,5)	1.10	1.11	1.10	1.11
r(C5-H6)	1.09	1.10	1.10	1.10
r(C5-H7,8)	1.10	1.11	1.10	1.11
α(O-C1-C2)	123.4	122.0	127.8	127.3
α(C1-C2-C3)	126.5	126.0	128.2	127.6
α(C2-C3-C4)	120.3	120.4	124.4	124.9
α(C2-C3-C5)	125.0	125.1	120.0	120.1
α(O-C1-H1)	119.7	119.9	119.1	119.7
α(C1-C2-H2)	114.2	114.3	113.9	114.3
α(H3-C4-C3)	112.1	111.4	112.3	112.1
α(H4,5-C4-C3)	110.6	110.2	109.8	109.4
α(H6-C4-C3)	113.9	113.4	112.5	112.1
α(H7,8-C4-C3)	110.0	109.6	110.4	110.2
δ(H4-C4-C3-C2)	121.3	120.9	-122.0	-121.7
δ(H5-C4-C3-C2)	-121.3	-120.9	122.0	121.7
δ(H7-C4-C3-C2)	-121.7	-121.3	121.5	121.2
δ(H8-C4-C3-C2)	121.7	121.3	-121.5	-121.2

Table C.1: Geometries of the rota-isomers of prenal calculated in the gas phase using Turbomoles RI-DFT and Molpro CCSD(T) methods. All distances r are given in Å and all angles in degree.

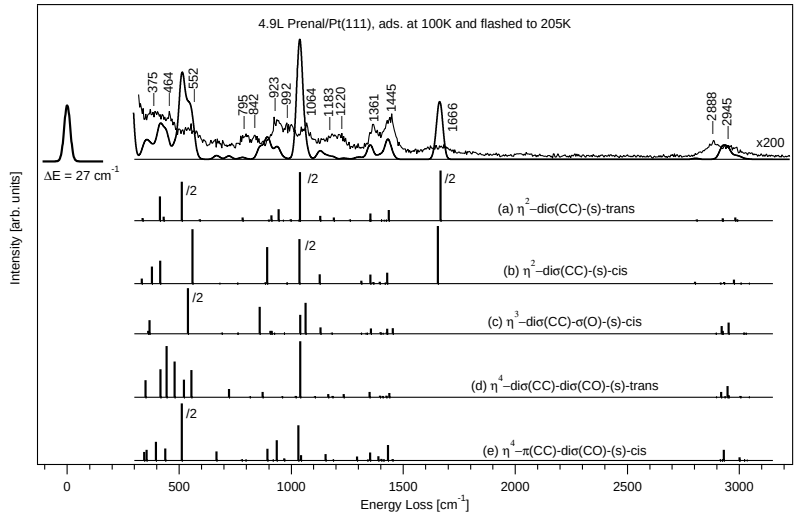

Figure C.1: Convolution (gaussians, 24 cm^{-1} FWHM) of the computed DFT HREEL spectra for the η^2-diσ(CC)-(s)-trans, η^2-diσ(CC)-(s)-cis, η^3-diσ(CC)-σ(O)-(s)-cis, η^4-diσ(CC)-diσ(CO)-(s)-trans and the η^4-π(CC)-diσ(CO)-(s)-cis adsorption complexes (a-e) and the HREEL spectrum of 4.9L prenal adsorbed at 100K on clean Pt(111) subsequently flashed to 205K.

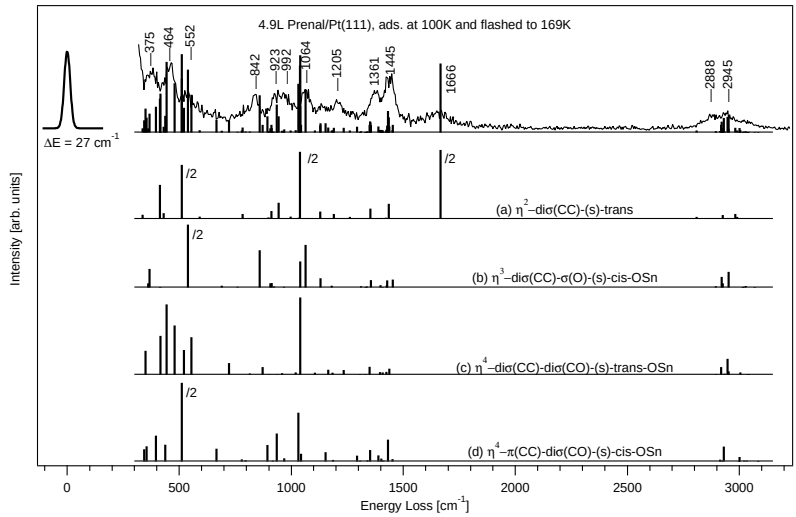

Figure C.2: Comparison of the computed DFT HREEL spectra of the η^2-diσ(CC)-(s)-trans, η^3-diσ(CC)-σ(O)-(s)-cis, η^4-diσ(CC)-diσ(CO)-(s)-trans and the η^4-π(CC)-diσ(CO)-(s)-cis adsorption structures (a-d) and the HREEL spectrum of 4.9L prenal adsorbed at 100K on clean Pt(111) subsequently flashed to 169K.

.

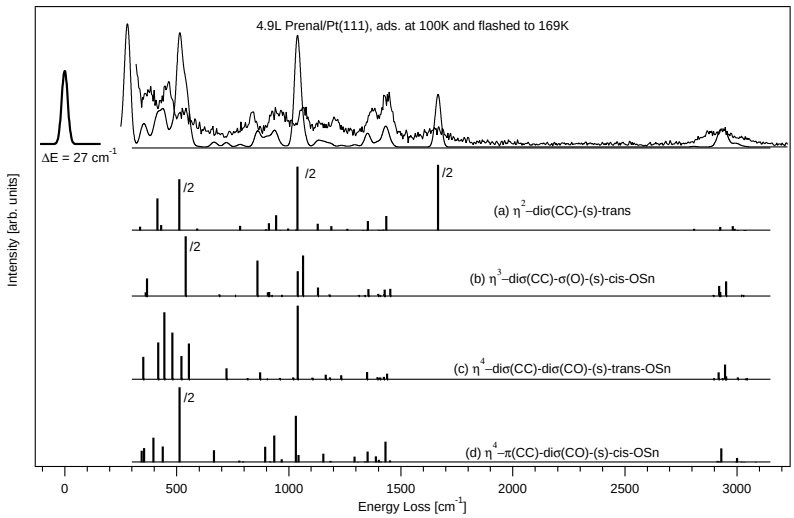

Figure C.3: Convolution (gaussians, 24 cm^{-1} FWHM) of the computed DFT HREEL spectra for the η^2-diσ(CC)-(s)-trans, η^3-diσ(CC)-σ(O)-(s)-cis, η^4-diσ(CC)-diσ(CO)-(s)-trans and the η^4-π(CC)-diσ(CO)-(s)-cis adsorption structures (a-d) and the HREEL spectrum of 4.9L prenal adsorbed at 100K on clean Pt(111) subsequently flashed to 169K.

C.2 Convolution of the DFT HREEL Spectra of Prenal/$Pt_3Sn(111)$

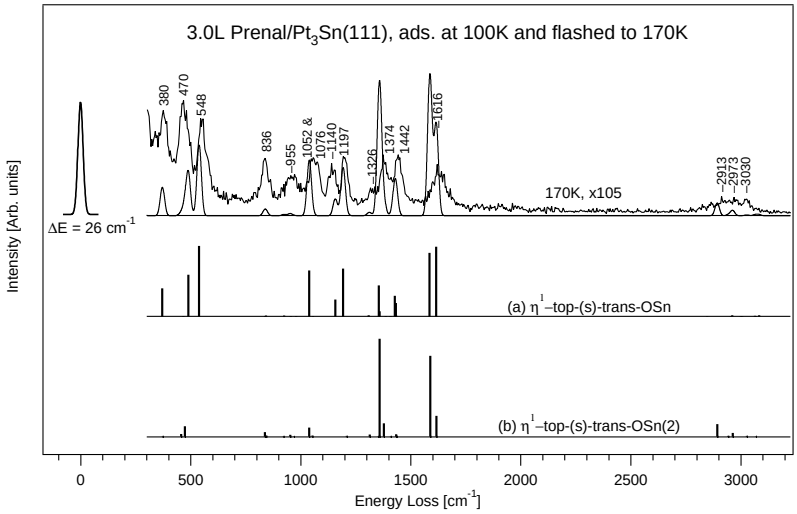

Figure C.4: Convolution (gaussians, 24 cm^{-1} FWHM) of the computed DFT HREEL spectra for the two stable η^1-top-(s)-trans-OSn adsorption complexes (a-b) and the HREEL spectrum of 3.0L prenal adsorbed at 100K on clean $Pt_3Sn(111)$ subsequently flashed to 169K.

Acknowledgements

I want to express my gratitude to *all* who contributed and supported me during the last three years in this work. Serveral persons I desire to mention here in particular:

- *Prof. Wandelt* for the opportunity to perform research in his group, for his steady encouragement and support during my PhD thesis at the Dept. of Physical Chemistry. His leadership, allowing the freedom to explore and solve many problems myself while always being helpful with advice on encountered problems, turned out to develop a very productive working atmosphere.
- *Dr. Conrad Becker* for the supervision, his hands-on assistance with experimental problems, for the uncounted fruitful scientific discussions and for proofreading this thesis and smoothing its edges.
- *Dr. Aleksander Krupski* for the many successful experiments we performed together on these systems and the excellent teamwork throughout all the last years.
- *Dr. David Loffreda*, *Dr. Françoise Delbecq*, *Dr. Yvette Jugnet* and *Dr. Philippe Sautet* for the chance to "push the frontiers ahead" in our joint scientific work, the many fruitful discussions of the enormous amount of results, and for the many nice and extremely productive visits to Lyon.
- *Prof. Peyerimhoff* for the scientific expertise, her encouragement to explore the field of periodical calclulations of solids and surfaces and finally, of course, for the contribution in the purchase of the VASP program package. For providing huge amounts of computer capacity, I have to be very thankful to her and to the Dept. of Theoretical Chemistry, namely *Dr. Barbara Kirchner*.
- *Everyone* else from the *Groups Wandelt and Sautet* not mentioned here personally, who helped me to see problems from a different view and often supported me when more than two hands or eyes were required. In particular I want to mention Dipl. Chem. Christian Breinlich and Dipl. Phys. Andreas Seemayer at this point not only for their assistance during this PhD thesis, but also for proofreading the many stages this manuscript lived through.
- The members of the mechanical and the electronical workshops, especially *P. Königshoven*, *R. Backhausen* (mech. WS) and *M. Böhmer* and *R. Paulig* (elec. WS) of our institute for their assistance in solving many urgent problems and their expertise and knowledge in adding improvements to the experimental setup.
- *Prof. T. Bredow*, *Prof. C. A. Schalley* and *Prof. K. Maier* who agreed to join the PhD-evaluation committee and to referee this thesis.
- My family: *Marcel*, *Sylvia* and *Klaus* for their patient support and guidance during the recent years in Bonn.